



Република Србија

УБ

Универзитет у Београду
Електротехнички факултет, Београд



Оснивач: Република Србија

Дозволу за рад број 612-00-02666/2010-04 од 10. децембра 2010.
године је издало Министарство просвете и науке Републике Србије

Миљан, Драјан, Дашић

рођен 3. новембра 1990. године у Параћину, Република Србија, уписан школске
2009/2010. године, а дана 5. јула 2013. године завршио је основне академске студије,
првог степена, на студијском програму Електротехника и рачунарство, обима
240 (двеста четрдесет) бодова ЕСПБ са просечном оценом 9,93 (девет и 93/100).

На основу тога издаје му се ова диплома о стеченом високом образовању и стручном називу
дипломирани инжењер електротехнике и рачунарства

Број: 1774200

У Београду, 19. новембра 2013. године

Декан
Проф. др Бранко Ковачевић

Ректор
Проф. др Владимир Бумбасијевић

00017366



Република Србија

УБ

Универзитет у Београду
Електротехнички факултет, Београд



Оснивач: Република Србија

Дозволу за рад број 612-00-02666/2010-04 од 10. децембра 2010.
године је издало Министарство просвете и науке Републике Србије

Диплома

Миљан, Драјан, Дашић

рођен 3. новембра 1990. године у Параћину, Република Србија, уписан школске
2013/2014. године, а дана 16. јула 2014. године завршио је мастер академске
студије, струко специјализована, на студијском програму Електротехника и рачунарство,
обима 60 (шездесет) бодова ЕСПБ са просечном оценом 10,00 (десет и 0/100).

На основу тога издаје му се ова диплома о стицању високог образовања и академском називу
мастер инжењер електротехнике и рачунарства

Број: 3427800

У Београду, 20. јануара 2015. године

Декан

Проф. др Бранко Ковачевић

Ректор

Проф. др Владимир Бумбаширевић

00034384



На основу члана 29 Закона о општем управном поступку («Службени гласник РС» број 18/2016 и 95/2018), и члана 149 Статута Универзитета у Београду - Физичког факултета, по захтеву МИЉАНА ДАШИЋА, мастер инжењера електротехнике, издаје се следеће

У В Е Р Е Њ Е

МИЉАН ДАШИЋ, мастер инжењер електротехнике, дана 23. септембра 2019. године, одбранио је докторску дисертацију под називом

„MODELING THE BEHAVIOUR OF CONFINED DIPOLAR AND IONIC SYSTEMS“
(„МОДЕЛОВАЊЕ ПОНАШАЊА ПРОСТОРНО ОГРАНИЧЕНИХ ДИПОЛНИХ И ЈОНСКИХ СИСТЕМА“)

пред Комисијом Универзитета у Београду - Физичког факултета, и тиме испунио све услове за промоцију у ДОКТОРА НАУКА – ФИЗИЧКЕ НАУКЕ.

Уверење се издаје на лични захтев, а служи ради регулисања права из радног односа и важи до промоције, односно добијања докторске дипломе.

Уверење је ослобођено плаћања таксе.

ДЕКАН ФИЗИЧКОГ ФАКУЛТЕТА
Проф. др Иван Белча



IEEEESTEC
5th Student projects
conference

BEST PAPER AWARD

for paper

*Design of Photonic Microring-Resonator
Based Wavelength Selective
1 x N Power Splitters*

by

M. Dašić and M. A. Popović

Organized By:
EESTEC LC Niš
IEEE Student Branch Niš
Faculty of Electronic Engineering Niš

With the cooperation of:
IEEE Serbia and Montenegro section
IEEE Electron Devices/Solid-State Circuits Chapter
IEEE Microwave Theory and Techniques Chapter



Conference Secretary

Studentski deo Optičkog društva na Univerzitetu u Beogradu
dodeljuje

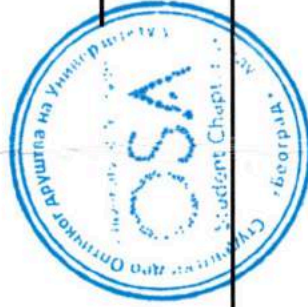
ZAHVALNICU

MILJANU DAŠIĆU

za realizaciju i podršku na manifestaciji
"DANI FOTONIKE"

na Elektrotehničkom fakultetu u Beogradu od 25.12.2018-26.12.2018.

26.12.2018.



Jovana Babić

Jovana Babić
Predsednik



Instrukcije za autore	IEEEESTEC konferencija ▾	Galerija	Dobrodošli u Niš ▾	Kontakt	Glasanje	
Project applications						SR EN



IEEEESTEC Student project conference (2014)

Danijel Danković

Sedma studentska konferencija "IEEEESTEC 7th Student project conference" održana je 27. novembra 2014. godine na Elektronskom fakultetu u Nišu (<http://ieeefak.ni.ac.rs/>). Konferenciju su organizovali studentski ogranak IEEE SB Niš, EESTEC LC Niš i Elektronski fakultet u Nišu, u saradnji sa IEEE Serbia and Montenegro Section, IEEE Electron Devices/Solid-State Circuits Chapter i IEEE Microwave Theory and Techniques Chapter.

Na sastanku IEEE SB Niš i EESTEC LC Niš održanom krajem marta 2014. godine podržana je inicijativa za organizovanjem konferencije "IEEEESTEC 7th Student project conference". IEEE Sekcija Srbija i Crna Gora je podržala ovu inicijativu.

Poziv za konferenciju poslali smo autorima radova sa prethodnih konferencija, svim studentskim organizacijama u Srbiji, studentskim ograncima IEEE-a, članovima IEEE Sekcije Srbija i Crna Gora. Ukupan broj pristiglih radova je 48 (iz oblasti: elektronika, mikroelektronika, telekomunikacije, automatika, energetika, računarstvo i informatika, fizika, mobilnost studenata...). Svi radovi su prošli fazu recenziranja, pri čemu je za svaki rad obezbeđeno minimum po pet recenzija. U procesu recenziranja pomogla su 38 nastavnika i saradnika Elektronskog fakulteta u Nišu. Na osnovu prispelih recenzija izabrana su tri najbolje ocenjena rada:

1. nagrada

Rad: Programiranje LED kocke pomocu Raspberry mikroračunara

Autori: A. Kostić, D. Aleksić

Institucija: Matematički fakultet u Beogradu - Astrofizika, Prirodno-matematički fakultet, Niš

2. nagrada

Rad: Wordarium - aplikacija za interaktivno učenje stranih reči

Autori: P. Antić, P. Živanović, M. Janković

Institucija: Elektronski fakultet, Niš

3. nagrada

Rad: Optimizacija i skaliranje energije 3D struktura samoorganizovanih magnetnih čestica

Autori: M. Dašić

Institucija: Univerzitet u Beogradu, Institut za fiziku, Laboratorija za primenu računara u nauci

U kategoriji Rad sa najboljom praktičnom realizacijom, a na osnovu Odluke Organizacionog odbora Konferencije dodeljene su nagrade:

Institucija: Elektronski fakultet u Nišu

2. nagrada

Rad: Sistem za kontrolu radnog vremena i pristupa laboratoriji realizovan na Raspberry Pi platformi

Autori: N. Živković, M. Milojević, N. Nikolić, B. Majkić, S. Stošović

Institucija: VTŠ Apps Tim, Visoka tehnička škola strukovnih studija u Nišu

3. nagrada

a) Rad: WEB kontrola osvetljenja u pametnoj kući

Autori: J. Krstić, D. Stajić

Institucija: Elektrotehnička škola Nikola Tesla, Niš

b) Rad: Projektovanje sistema za brojanje posetilaca u realnom vremenu uz pomoć TSOP senzora

Autori: M. Mitić, N. Krstić, Đorđe Veličković

Institucija: Elektronski fakultet u Nišu

Na osnovu prispelih radova Elektronski fakultet u Nišu je izdao Zbornik radova "IEEEESTEC 7th Student project conference" , ISBN: 978-86-6125-114-6. Urednici Zbornika radova su: Prof. dr Ninoslav Stojadinović, prof. dr Bratislav Milovanović, prof. dr Vera Marković, prof. dr. Goran S. Đorđević i doc. dr Danijel Danković. Konferencija je organizovana od strane Organizacionog odbora koji su činili: Doc. dr Danijel Danković, predsednik konferencije i Dušan Vučković, Darko Todorović i Miloš Marjanović, potpredsednici konferencije. Sekretarijat konferencije činili su studenti Elektronskog fakulteta u Nišu: Damir Nešić, Saša Dević, Nikola Vučić, Sandra Iljin, Miroslav Božić, Željko Kalezić, Nikola Simić, Dragana Dimitrijević, Đorđe Veličković, Miloš Mitić i Neda Dinić. Zbornik je tehnički uredio Miloš Marjanović.

Konferenciju su svečano otvorili prorektor Univerziteta u Nišu, prof. dr Zoran Nikolić, dekan Elektronskog fakulteta u Nišu, prof. dr Dragan Janković i prodekan Elektronskog fakulteta u Nišu, prof. dr Zoran Perić.

Najbolji radovi u obe kategorije usmeno su prezentovani. Svi radovi (uključujući i nagradene) su prezentovani kao poster radovi u holu Elektronskog fakulteta u Nišu. Pored mesta za postavljanje postera u četvoročasovnom radu autori su koristili i ppt prezentacije, prikaz simulacija na računaru, svojih maketa i gotovih proizvoda. Sami autori su anketom za najinteresantniji rad izabrali:

1. nagrada

Rad: Pametna ruka (Smart hand)

Autori: J. Krstić, L. Petrović, M. Mihajlović, M. Dimitrijević, M. Radomirović, S. Krstić, R. Mitić

Institucija: Elektrotehnička škola Nikola Tesla , Niš

Odlukom Organizacionog odbora Konferencije za najbolji rad IEEEESTEC konferencije, predložen za IEEE Region 8 Student Paper Contest 2015 (<http://www.ieeeer8.org/category/student-activities/awards-and-contests/student-paper-contest>) izabran je:

1. nagrada

Rad: Primena digitalnih filtara u kriptografiji

Autori: M. Petrović

Institucija: Elektronski fakultet u Nišu

Svi autori su kao promotivni materijal IEEEESTEC konferencije dobili: zbornika radova, disk, blok i kesu. Autorima najboljih radova uručene su diplome i prigodne nagrade, dar prijatelja konferencije.

Učesnici konferencije su bili iz sledećih ustanova: Elektronski fakultet u Nišu, Prirodno matematički fakultet u Nišu, Visoka tehnička škola strukovnih studija u Nišu, Elektrotehnički fakultet u Beogradu, Institut za fiziku, Univerzitet u Beogradu, Fakultet za fizičku hemiju, Univerzitet u Beogradu, Matematički fakultet u Beogradu, Matematički institut SANU, Vojna Akademija, Beograd, University of Sarajevo, Faculty of Electrical Engineering, Knjazevačka gimnazija, Tehnička škola Rade Metalac, Leskovac, ETŠ Nikola Tesla, Niš, Ei PCB Factory Niš, IRC ALFATEC Niš, Universitatea Politehnica din Bucuresti, Tennessee Tech University - TTU.

Nadamo se da će naredne godine ova konferencija biti još bolje organizovana i jos masovnija.

Математичка гимназија
Београд

МАТУРСКИ РАД
-из физике-

Испитивање ефикасности графена у заштити метала
од атома водоника

Ментор:

Миљан Дашић,

Институт за физику, Београд

Аутор:

Кристина Николић

Београд, мај 2018

термостата показују да су се термодинамички параметри довољно стабилизовали, према томе дужина трајања симулације од 5 [ps] је довољна за јасан увид у понашање система.

4. Закључак

У овом раду је посматрано понашање система који се састоји од бакарне плочице, графена и 100 атома водоника. Циљ је био испитати могућности за примену графена као заштите бакарне плочице од дифузије атома водоника. У ти сврху развијене су симулације молекуларне динамике у LAMMPS-у. Параметри у зависности од којих је испитана ефикасност графена јесу иницијална кинетичка енергија атома водоника и температура графена. Узето је 10 различитих вредности енергије и 3 различите температуре, дакле има укупно 30 симулација. Симулације су извршене на PARADOX суперрачунару Института за физику у Београду, при чему је свака од 30 симулација извршена на по једним ноду суперрачунара, а сваки нод има по 16 процесора.

Разматрана је употреба термостата за одржавање иницијалне температуре графена, као и случај без датог термостата. Закључак је да не треба применити термостат и да се систем за време трајања симулације од 5 [ps] стабилизује у довољној мери. Такође, иницијална кинетичка енергија водоника кључно одређује ефикасност графена, док је његова температура параметар далеко мањег утицаја.

Графен је одлична заштита метала од водоника када атоми водоника имају мале почетне енергије. Постоји праг који почетна енергија водоника мора да пређе да би дошло до дифузије и тај праг је на $7,5 \pm 2,5$ [eV]. На неким иницијалним енергијама водоника мањим од прага дифузије, за које је коефицијент адсорпције највећи, графен се може користити за складиштење атома водоника. Према томе, у случају високе рефлексије графен се може користити као заштита метала, а у случају високе адсорпције може се користити за складиштење атома водоника.

Истраживање се може унапредити посматрањем атома водоника који имају брзину усмерену под датим углом у односу на раван металне плочице. Осим тога, занимљиво је детаљно испитати како локација на коју атом водоника пада на графен утиче на његову интеракцију са атомом угљеника у графену.

5. Захвалност

Захваљујем се својим менторима Миљану Дашићу и Игору Станковићу, члановима Лабраторије за примену рачунара у науци Института за физику Универзитета у Београду. Такође, захваљујем се руководиоцу семинара физике Владану Павловићу и сарадницима ИС Петнице као и Милици Божанић на корисним саветима и помоћи приликом организације и реализације овог пројекта.

Ово истраживање је делом изведено као део образовних активности у оквиру Horizon 2020 пројекта DAFNEOX подржаног од стране Европске комисије.

Ispitivanje 2D struktura magnetnih čvrstih sfera u spoljašnjem magnetnom polju metodom molekularne dinamike

Neodijumske čestice predstavljaju gotovo idealne magnetne dipole. Ovakav model omogućava praćenje kretanja čestica u spoljašnjem magnetnom polju, kao i uvid u njihovu međusobnu dipol-dipolnu interakciju i interakciju sa spoljašnjim magnetnim poljem. Osnovni cilj projekta je ispitivanje dinamike dipola u spoljašnjem magnetnom polju polazeći od prstena, strukture sa minimalnom energijom pre uključivanja magnetnog polja, formiranog od N ($4 \leq N \leq 13$) čestica. Pokazano je da kada se ovoliko čestica postavi dovoljno blizu da mogu međusobno da interaguju, njihovo stabilno stanje (stanje sa minimalnom potencijalnom energijom) je prsten. Jedan od ciljeva projekta je utvrđivanje minimalne jačine magnetnog polja potrebnog da se prsten kao stabilna struktura raspadne, takođe i utvrđivanje oblasti u parametarskom prostoru $\alpha(B)$ gde se formiraju određene stabilne strukture. Sa α je označen ugao rotacije prstena u odnosu na pravac magnetnog polja na početku simulacije, a sa B je označena jačina magnetnog polja. Sve čestice, njihova međusobna interakcija i interakcija sa spoljašnjim magnetnim poljem modelovani su simulacijama. Korišćenjem tih simulacija prati se ponašanje čestica u zavisnosti od jačine spoljašnjeg magnetnog polja B i ugla rotacije α . U ovom radu ispitana je dinamika dvodimenzionalnih struktura sačinjenih od 7 i 9 čestica.

Helena Miljković (1998),
Beograd, Mileve Marić
Ajnštajn 21/54, učenica
4. razreda Matematičke
gimnazije u Beogradu

Aleksa Denčevski (1998),
Kraljevo, Zelena Gora
46/16, učenik 4 razreda
Gimnazije u Čačku

Teorijski uvod

Magnetne čestice su modelovane potencijalom koji ima dve komponente, prva je dipol-dipolna magnetna interakcija, a druga je tvrda interakcija čvrstih sfera. Dipol-dipolna interakcija predstavlja interakciju između dve čestice magnetnog momenta \vec{m}_1 i \vec{m}_2 čiji se centri nalaze na pozicijama \vec{r}_1 i \vec{r}_2 . Potencijalna energija dobijena ovom interakcijom definisana je formulom:

$$U(\vec{r}_{12}) = C \frac{1}{r_{12}^3} \left[\vec{m}_1 \cdot \vec{m}_2 - 3 \frac{(\vec{m}_1 \cdot \vec{r}_{12})(\vec{m}_2 \cdot \vec{r}_{12})}{r_{12}^2} \right]$$

gde je $r_{12} = |\vec{r}_{12}| = |\vec{r}_1 - \vec{r}_2|$, a konstanta C se može izračunati kada se dve čestice postavljaju jedna do druge pri čemu se i dipolni momenti postavljaju

MENTORI:

dr Igor Stanković, viši
naučni saradnik,
Laboratorija za primenu
računara u nauci
Instituta za fiziku
Univerziteta u Beogradu

Miljan Dašić, doktorant,
Laboratorija za primenu
računara u nauci
Instituta za fiziku
Univerziteta u Beogradu

kuglicama. Osim sila, pratimo i energiju sistema u svakom trenutku, čime određujemo njegovu dinamiku. U ovom radu je ispitivan najjednostavniji slučaj homogenog (usmereno duž x -ose koordinatnog sistema) i konstantnog polja ($B_x = \text{const}$). Variranjem ugla za koji je prsten zarotiran u odnosu na početni položaj i jačine magnetnog polja, pokriven je ceo opseg za ugao i opseg od 0 do 9 arbitrarnih jedinica za magnetno polje, pri čemu su oba opsega pokrivena ravnomerno. Prilikom ispitivanja primećeno je da se vrednost kritičnog magnetnog polja drastično menja u zavisnosti od ugla za oba ispitivana sistema. Mnogo je teže prekinuti prsten sačinjen od devet kuglica koji je zarotiran za ugao od 1.5 do 2.25 rad nego prsten koji je zarotiran za ugao od 4.5 do 5.5 rad. Takođe, primećeno je da vrednost spoljašnjeg magnetnog polja pri kojem puca prsten zavisi od broja čestica koje su orijentisane suprotno od spoljašnjeg magnetnog polja.

Tokom rada došli smo do saznanja da su ovi sistemi veoma kompleksni i da se pri tačno određenim vrednostima spoljašnjeg magnetnog polja i ugla rotacije prstena javljaju stabilne konfiguracije. Prav lanac, tipičan za sisteme sa manjom energijom i sa manjim brojem čestica, otkriven je u sistemu od 7 čestica, a u sistemu od 9 čestica nije. Takođe, prav lanac predstavlja stabilnu konfiguraciju koja se javlja između tačno dve konfiguracije, uzimajući osobine svake od njih. Prav lanac se ne mora uvek naći između dve konfiguracije ali one predstavljaju preduslov za nastanak lanaca. Između svakih konfiguracija se javlja određena deformacija jer struktura ima osobine obe ključne konfiguracije između kojih se nalazi i ne može da dođe do pucanja lanca.

Kao ključni rezultat nacrtani su fazni dijagrami koji pokazuju sve različite strukture koje se javljaju za zadati fazni prostor $\alpha(B)$. Tako možemo za zadato α pratiti dinamiku struktura, odnosno koje sve strukture se javljaju sa povećanjem magnetnog polja. Važi i obrnuto, može se na fiksnoj B zavisno od α pratiti koje se strukture pojavljuju. Primećeno je da su fazni dijagrami slični za sedam i devet kuglica. Razlog za to je nesimetričnost prstena na početku simulacije. Oba sistema su sačinjena od neparnog broja kuglica zbog čega se dipolni momenti na sličan način postavljaju u odnosu na magnetno polje.

Dalja istraživanja na ovu temu bi uključivala posmatranja sistema čestica u nehomogenom i vremenski promenljivom polju.

Zahvalnost. Zahvaljujemo se svojim mentorima dr Igoru Stankoviću, višem naučnom saradniku i Miljanu Dašiću, doktorantu, članovima Laboratorije za primenu računara u nauci Instituta za fiziku Univerziteta u Beogradu. Takođe, zahvaljujemo se rukovodiocu seminara fizike Vladanu Pavloviću, doktorantu Prirodno-Matematičkog fakulteta Univerziteta u Nišu. Pomenutim saradnicima IS Petnica i rukovodiocu našeg seminara zahvalni smo na korisnim savetima i nesebičnoj pomoći prilikom organizacije i realizacije projekta.

Ovo istraživanje je delom izvedeno kao deo obrazovnih aktivnosti u okviru Horizon 2020 projekta DAFNEOX podržanog od strane Evropske komisije (br. ugovora 645658)

Ispitivanje efikasnosti grafena u zaštiti metala od atoma vodonika metodom molekularne dinamike

U ovom radu je ispitana efikasnost grafena u zaštiti bakra od atoma vodonika. U ranijim istraživanjima proučavana je hemijska interakcija između atoma vodonika i grafena (Atsushi 2008), dok je u ovom radu akcenat na ispitivanjima mogućnosti za praktičnu primenu grafena u zaštiti metala. Napravljena je numerička simulacija za modelovanje sistema koji se sastoji od atoma bakra, vodonika i strukture grafena. Sistem je posmatran za tri različite inicijalne temperature grafena i deset različitih inicijalnih kinetičkih energija atoma vodonika. Utvrđeni su uslovi pri kojima vodonik difunduje kroz grafen, pri kojima se adsorbuje, tj. zakači na njegovu površinu i pri kojima se odbija od njega, u zavisnosti od navedenih parametara. Definisana je granična vrednost koeficijenta difuzije. Ukoliko je koeficijent difuzije manji od te vrednosti grafen se može smatrati efikasnom zaštitom. Dobijeni rezultati pokazuju da inicijalna energija vodonika određuje efikasnost grafena kao zaštite, dok je zavisnost od temperature grafena na ispitanom opsegu slaba. Na manjim energijama grafen potpuno štiti bakar od atoma vodonika, dok sa povećanjem početne kinetičke energije vodonika nakon izvesnog praga ta se efikasnost smanjuje. Takođe, iznad određene vrednosti energije grafen je kao zaštita neprimenjiv, pošto svi atomi vodonika prodru do metalne pločice. Navedeni rezultati su za sistem posmatran u opštem slučaju u kome su atomi vodonika slučajno raspoređeni i brzina im je usmerena u pravcu normale na metalnu pločicu. Istraživanje se može proširiti variranjem ovih parametara i određivanjem njihovog uticaja na vrednost koeficijenta difuzije.

Uvod

Grafen je dvodimenzionalna struktura ugljenika koji je organizovan u međusobno jako povezane šestočlane prstenove. Grafen predstavlja jedan sloj grafita.

Grafen je skoro u potpunosti providan, ali je istovremeno i veoma gust. Pored toga, električnost provodi jednako dobro kao i bakar. Kao material, grafen ima izuzetno specifična **svojstva**. To je veliki kristal, koji je veoma čvrst, sto puta čvršći od čelika, a može se rastegnuti i do 20%. Grafen je **istovremenom** i najtanji i najjači poznati materijal.

Providnost, čvrstina i gusto napakovani šestočlani prstenovi atoma ugljenika su dobri preduslovi da se grafen koristi kao zaštitni sloj površine nekog materijala od neželjenih atoma ili molekula gasova. Izloženost metala vodoniku može dovesti do promene njihove strukture, a pošto je vodonik svuda oko nas: u atmosferi, u svemiru, i u Zemlji, potrebno je naći optimalno rešenje problema zaštite metala od kontakta sa njim.

Difuzija je kretanje molekula ili atoma iz oblasti više koncentracije u oblast niže koncentracije. Ovakvo kretanje se još naziva i kretanje niz koncentracioni gradijent. Gradijent je promena jedne fizičke veličine uslovljena promenom druge, u ovom slučaju promena koncentracije sa promenom položaja. U našem sistemu smatra se da je do difuzije vodonika kroz grafen došlo ako se u bilo kom trenutku simulacije atom vodonika nalazi ispod zadate granične vrednosti. Ta granična vrednost predstavlja procenjen položaj grafena

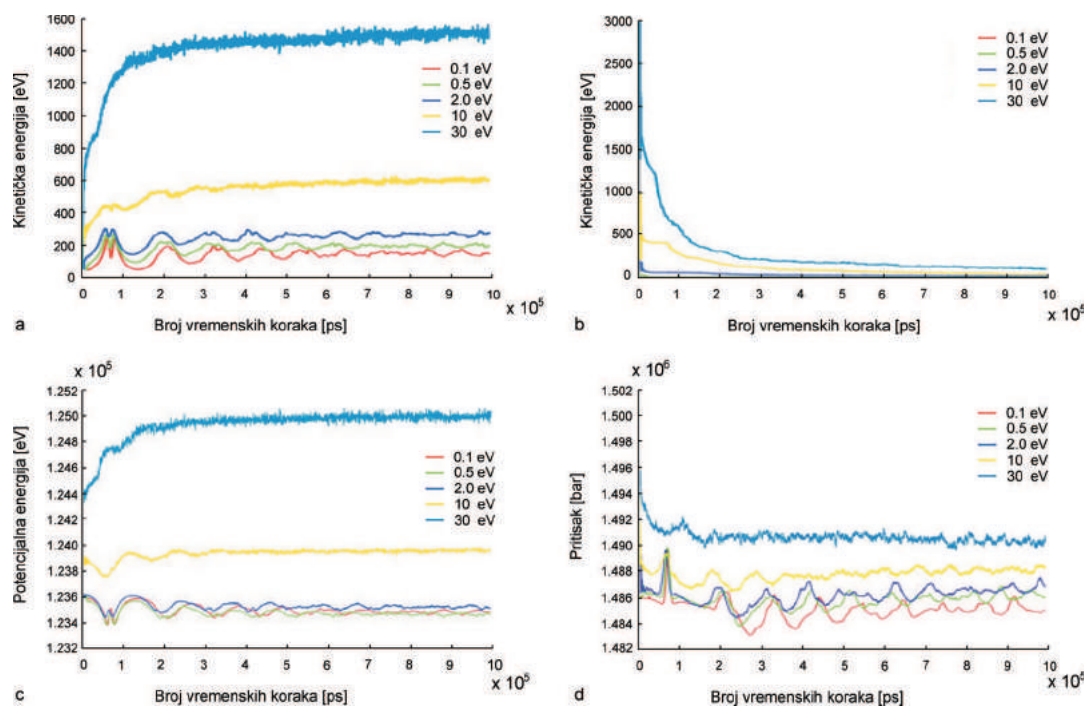
Milica Božanić (1999), Šabac, Sremska 7B/1, učenica 4. razreda Matematičke gimnazije u Beogradu

Kristina Nikolić (1999), Požarevac, Stevana Sremca 14, učenica 4. razreda Matematičke gimnazije u Beogradu

MENTORI:

Miljan Dašić, Institut za fiziku, Beograd

Igor Stanković, Institut za fiziku, Beograd



Slika 6. Zavisnost termodinamičkih parametara od vremena za različite početne energije atoma vodonika. a) kinetička energija grafena b) kinetička energija vodonika c) potencijalna energija sistema d) pritisak. Sve simulacije su za početnu temperature grafena od 800 K.

Figure 6. Dependence of thermodynamic parameters with time for different initial energies of hydrogen atoms. a) kinetic energy of graphene b) kinetic energy of hydrogen c) potential energy of the system d) pressure. All simulations are for an initial graphene temperature of 800 K.

Razmatrana je upotreba termostata za održavanje inicijalne temperature grafena, kao i slučaj bez datog termostata. Zaključak je da ne treba primeniti termostat i da se sistem za vreme trajanja simulacije od 5 ps stabilizuje u dovoljnoj meri. Takođe, inicijalna kinetička energija vodonika ključno određuje efikasnost grafena, dok je njegova temperatura parametar daleko manjeg uticaja.

Grafen je odlična zaštita metala od vodonika kada atomi vodonika imaju male početne energije. Postoji prag koji početna energija vodonika mora da pređe da bi došlo do difuzije i taj prag je na 8 ± 3 eV. Na nekim inicijalnim energijama vodonika manjim od praga difuzije, za koje je koeficijent adsorpcije najveći, grafen se može koristiti za skladištenje atoma vodonika. Prema tome, u slučaju visoke refleksije grafen se može

koristiti kao zaštita metala, a u slučaju visoke adsorpcije može se koristiti za skladištenje atoma vodonika.

Istraživanje se može unaprediti posmatranjem atoma vodonika koji imaju brzinu usmerenu pod datim uglom u odnosu na ravan metalne pločice. Osim toga, zanimljivo je detaljno ispitati kako lokacija na kojoj atom vodonika pada na grafen utiče na njegovu interakciju sa atomima ugljenika u grafenu.

Zahvalnost. Zahvaljujemo se svojim mentorima Miljanu Dašiću i Igoru Stankoviću, članovima Laboratorije za primenu računara u nauci Instituta za fiziku Univerziteta u Beogradu. Takođe, zahvaljujemo se rukovodiocu seminara fizike Vladanu Pavloviću sa Prirodno-Matematičkog fakulteta Univerziteta u Nišu. Pomenutim

Nikola Petreski i Mihailo Radojević

Analiza i razvoj modela konačnih dipolnih heliksa

Tema ovog rada su heliksi sastavljeni od konačnog broja čvrstih dipolnih sfera, poznati pod terminom konačni dipolni heliksi. Čvrste dipolne sfere intereaguju preko dve vrste interakcija: dipol-dipolnom interakcijom i tvrdom interakcijom čvrstih sfera. Iako je sistem na prvi pogled jednostavan, ispoljava kompleksno ponašanje usled prirode dipol-dipol interakcije, koja je anizotropna i dugodometna. Analizirali smo razne slučajeve interakcije heliksa sa probnom dipolnom sferom i sa identičnim heliksom, pri čemu su uzete u obzir različite magnetizacije heliksa, takozvana ST (single-thread) i MT (multi-thread) magnetizacija. Prvi deo rada predstavlja detaljnu analizu interakcija u kojima učestvuju dipolni heliksi, a drugi deo je vezan za razvoj modela konačnih dipolnih heliksa. Naime, formirali smo i ispitali dve vrste modela heliksa koje predstavljaju pojednostavljenu zamenu za heliks, i proverili koliko mogu reprodukovati zadate interakcije.

Uvod

Čestice sa stalnim dipolnim momentom, kao što su magnetne kuglice, poznate su po samoasemblirajućim osobinama. Magnetne strukture su popularne zato što imaju široku primenu u nanoelektronici i biotehnologiji (Whitesides i Grzybowski 2002). Što se tiče značaja tubularnih i helikoidnih struktura, u biologiji su to relevantni samoasemblirajući objekti koji su pronađeni u nekim vrstama bakterija i u ćelijskim mikrotubulama. Magnetne nanočestice mogu se rasporediti tako da grade helikse, što je vrlo

interesantno da se na nano nivou mogu napraviti ovakve strukture (Sellmayer 2002; Zeng *et al.* 2002).

U ovom radu posmatrano je ponašanje helikoidnih struktura sastavljenih od konačnog broja čvrstih dipolnih sfera, poznati pod terminom konačni dipolni heliksi. Pored toga modelovane su i uprošćene strukture početnog heliksa i ispitivana je njihova efikasnost. Dipolne sfere interaguju preko dve vrste interakcija: dipol-dipolna interakcija i tvrda interakcija čvrstih sfera.

Konkretno smo u ovom radu dipolne helikse implementirali u softverskom paketu Matlab. Kako se sve čestice opisuju preko prostornih koordinata i dipolnog momenta (magnetizacije) potrebno je postaviti ih u početnu konfiguraciju, pri čemu konfiguracija podrazumeva prostorni raspored i magnetizaciju. Pokazano je prethodnim radovima da interakcija između magnetnih sfera može dovesti do formiranja 3D struktura, ali da dimenzionalnost struktura zavisi od broja čestica u sistemu N . Naime, razmatrano je kako se čestice raspoređuju tako da imaju minimalnu energiju (takozvani ground state). Za mali broj čestica ($N = \{2, 3\}$) formiraju se lanci, za veći broj čestica ($3 < N < 14$) formiraju se prstenovi, dok za $N > 14$ optimalne strukture su heliksi. Jasno vidimo prelaz od 1D preko 2D do 3D struktura zavisno od broja čestica u sistemu (Boncheva *et al.* 2005).

U prvom delu rada detaljno je opisana dipol-dipol interakcija i način formiranja heliksa. Takođe, ovaj deo rada posvećen je ispitivanju zavisnosti energije dipol-dipol interakcije i sile od nametnutih uslova, poput promene rastojanja između ispitivanih struktura ili magnetizacije. Imamo slučajeve interakcije heliksa sa probnom česticom i sa identičnim heliksom. Pored ovoga, posmatran je i slučaj kada dolazi do promene

Nikola Petreski (2000), Šabac, Grmićska 3, učenik 3. razreda Šabačke gimnazije

Mihailo Radojević (2000), Šabac, Kralja Dragutina 8, učenik 3. razreda Šabačke gimnazije

MENTORI:

Miljan Dašić, Institut za Fiziku, Beograd

Igor Stanković, Institut za Fiziku, Beograd

tima) i probna čestica. Za alternirajuće dipolne momente mora biti paran broj kuglica u lancu kako bi se poništile x i y komponente uzastopnih kuglica.

Na osnovu rezultata sa grafika na slici 24 može se zaključiti da je nemoguće formirati zamenu za helikoidnu strukturu u vidu modela koje smo mi izabrali. Razlog ovome je poklapanje datih rezultata po x osi a ne poklapanje po z osi. Ovo se dešava zato što svaka čestica početnog heliksa ima z komponentu magnetnog momenta dok kod naših modela nemaju sve čestice z komponentu. U ovom slučaju ponovo možemo uočiti osetljivost dipol-dipol interakcije. Iako su modeli napravljeni tako da magnetni momenti po komponentama imaju istu sumu nije moguće modelovati na ovaj način uprošćeniju strukturu zbog ugla magnetizacije.

Zaključak

Primećeno je da intezitet ukupne sile i energija opadaju pri udaljavanju od početnog heliksa i kod probne čestice a i kod složenijih struktura kao što su heliksi. Pri rotaciji heliksa oko koordinatne ose dobijene su oscilacije ukupnog inteziteta sile i energije, simetrične u odnosu na ugao od π rad. Ovo je posledica različitog ugla magnetizacija i trenutne konfiguracije čestica. Postoji magični ugao pri kojem je energija interakcije između dva heliksa jednaka 0, ali nije jedinstven kao za slučaj dve čestice već zavisi od broja čestica u heliksu. Energija interakcije između dva heliksa je maksimalna ako su magnetni momenti paralelni, dok je minimalna kada su međusobno normalni. Uprošćeni modeli ne mogu zameniti početnu helikoidnu strukturu. Rad se može proširiti dodavanjem novih modela i uključivanjem spolašnjeg magnetnog polja.

Zahvalnost. Zahvaljujemo se svojim mentorima Miljanu Dašiću i Igoru Stankoviću, članovima Laboratorije za primenu računara u nauci Instituta za fiziku Univerziteta u Beogradu. Takođe, zahvaljujemo se rukovodiocu seminara fizike Petru Bojoviću, sa Fizičkog fakulteta Univerziteta u Beogradu. Pomenutim saradnicima IS Petnica i rukovodiocu našeg seminara zahvalni smo na korisnim savetima i pomoći prilikom organizacije i realizacije ovog rada.

Literatura



- Boncheva M., Andreev S., Mahadevan L., Winkleman A., Reichman D. R., Prentiss M. G., *et al.* 2005. Magnetic self-assembly of three-dimensional surfaces from planar sheets. *Proceedings of the National Academy of Sciences of the United States of America*, **102**: 3924.
- Grzybowski A., Brodka A. 2003. Lekner type method for summing the dipole-dipole interactions. *Molecular Physics*, **101** (8): 1079.
- Kocbach L., Lubbad S. 2010. Geometrical simplification of the dipole-dipole interaction formula. *Physics Education*, **45** (4): 345.
- Messina R., Khalil L. A., Stanković I. 2014. Self-assembly of magnetic balls: From chains to tubes. *Physical Review E*, **89**: 011202(R).
- Prokopieva T. A., Danilov V. A., Kantorovich S., Holm C. 2009. Ground state structures in ferrofluid monolayers. *Physical Review E*, **80**: 031404.
- Stanković I., Dašić M. Messina R. 2016. Structure and cohesive energy of dipolar helices. *Soft Matter*, **28** (12): 3056.
- Sellmayer D. J. 2002. Strong magnets by self-assembly. *Nature*, **420**: 374.
- Whitesides G. M., Grzybowski B. 2002. Self-Assembly at All Scales. *Science*, **295**: 2418.
- Zeng H., Li J., Liu J. P., Wang Z. L., Sun S. 2002. Exchange-coupled nanocomposite magnets by nanoparticle self-assembly. *Nature*, **420**: 395.

Nikola Petreski and Mihailo Radojević

Analysis and Development of the Model of Finite Dipole Helices

Topic of this paper is helicoides composed of the finite number of solid dipole spheres, known as the finite dipole helix. Solid dipole spheres have two types of interactions, such as: dipole - dipole interaction and hard interaction of solid spheres. Although at first glance it can be done simple, such a system exhibits complex behavior due to the nature of the dipole-dipole interaction, which is long-term and anisotropic. We explored various cases of helix interaction with the test di-

pole sphere, as well as identical helix, taking into account the different dipole orientations of the helix, the so-called ST (single-thread) and MT (multi-thread) dipole orientations. The first part of our paper presents detailed analysis of the interactions involving final dipole helix, and the other part is related to the development of the model of given helix. In modeling, the aim is to replace the helix with a simplified structure that includes a ring and a chain, and to check if such a simplified structure on interaction behaves as a model helix. We have also formed two types of helix that represent a simplified substitute for helix and check how much they can reproduce the given interactions.

Thank You

miljandasic@yah.../Inbox



Optical and Quantum Electronics (OQEL) <em@editorialmanager.com>
To: Milijan Dasic <miljandasic@yahoo.com>

Mar 6, 2018 at 7:08 PM

Dear Dr Dasic,

Thank you very much for your review of manuscript

OQEL-D-18-00137, "Full 3D Electromagnetic Wave Analysis of SOI Ring Resonators Using 2D Simulation".

We greatly appreciate your assistance.

With kind regards,

Journals Editorial Office

Springer

Thank You

miljandasic@yah.../Inbox



Optical and Quantum Electronics (OQEL) <em@editorialmanager.com>
To: Milijan Dasic <miljandasic@yahoo.com>

Nov 9, 2018 at 11:58 AM

Dear Dr Dasic,

Thank you very much for your review of manuscript

OQEL-D-18-00783R1, "Tunable slow light based on detuned coupling between graphene nanoribbon and square ring splitting modes".

We greatly appreciate your assistance.

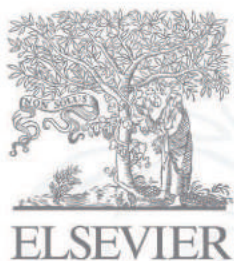
With kind regards,

Journals Editorial Office

Springer

Recipients of this email are registered users within the Editorial Manager database for this journal. We will keep your information on file to use in the process of submitting, evaluating and publishing a manuscript. For more information on how we use your personal details please see our privacy policy at <https://www.springernature.com/production-privacy-policy> or email dataprotection@springernature.com. If you no longer wish to receive messages from this journal or you have questions regarding the Editorial Manager database and the publishing process, please email our publication office, stating the journal name(s) and your email address(es): PublicationOfficeSPS@springernature.com

In compliance with data protection regulations, please contact the publication office if you would like to have your personal information removed from the database.



Tribology International

Certificate of Reviewing

Awarded since August 2017 (1 review)
presented to

MILJAN DAÅ;IC

in recognition of the review contributed to the journal

The Editors of Tribology International



6 • 1 Support to Young People

As a socially responsible company that strives to contribute to the development of the communities in which it operates, Erste Bank is primarily focused on developing young people. We see young people as a driving force of the society and as our present and future customers, colleagues and partners. We developed different support mechanisms just for them, focusing primarily on their financial education, empowerment and independence, development of their talents and leadership skills and their orientation towards further development of society.

Seventeen New Members of the SUPERSTE Club

In 2014, for the seventh consecutive time, Erste Bank organised a competition in search for talented young people whom it awards as part of the SUPERSTE Club. The awards are intended for young people aged 16 to 27 years who achieve exceptional results in the areas they engage in and who spread a positive impact on the society.

In 2014, 151 valid applications were submitted to the SUPERSTE Club competition from almost 60 towns in Serbia, and 17 most talented applicants were given recognitions and cash awards.

The total award amount was RSD 1.5 million. The winners of the main awards got RSD 200,000 each on Erste Bank Youth Cards. The Ljubiša Rajić special award for social activism also included a cash award of RSD 100,000, while those awarded based on public voting got RSD 50,000 each RSD on Erste Bank Youth Cards.

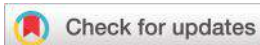
In the past six years, the Bank awarded 71 talented and creative young people with the total amount of RSD 7 million. The project has been implemented from the very beginning in cooperation with the Trag Foundation (the former Balkan Community Initiatives Fund – BCIF) and with support of the Ministry of Youth And Sport of the Republic of Serbia.



Award Winners

- The Ljubiša Rajić special award for social activism was presented to Maša Davidović (1990), National Coordinator for Human Rights and Peace (IFMSA-Serbia)
- The main award in the natural sciences, engineering and technology category went to Dušan Dimić (1990), who graduated from the Faculty of Physical Chemistry of the University of Belgrade.
- The main award in the social sciences and humanities category went to Maša Mišković (1991), winner of the Gold Medal “for outstanding achievements in learning and acquiring knowledge”.
- Two main awards in the arts category went to Irena Josifoski (1996), who has been playing cello since she was five years old, and Ivan Marković (1989), who took part in many festivals in Europe with his solo works and as director of photography.

By public voting, four more awards in the natural sciences, engineering and technology category were given to Ana Stanojević (1990), Stefan Hačko (1993), Miljan Dašić (1990) and Vladimir Petrović (1991). Based on public voting, Dušan Jovčić (1992), Nadežda Tonic (1988), Rada Mašić (1988) and Dragana Vasiljević (1989) were awarded in the social sciences and humanities category. In the arts category, the public also selected Nikola Peković (1991), Dušan Sretović (1995), Nikola Čirić (1992) and Strahinja Pavlović (1996), who distinguished themselves with their work in the arts.



Cite this: *Nanoscale*, 2019, **11**, 2521

A platform for nanomagnetism – assembled ferromagnetic and antiferromagnetic dipolar tubes†

Igor Stanković, *^a Miljan Dašić,^a Jorge A. Otálora^b and Carlos García ^c

We report an interesting case where magnetic phenomena can transcend mesoscopic scales. Our system consists of tubes created by the assembly of dipolar spheres. The cylindrical topology results in the breakup of degeneracy observed in planar square and triangular packings. As far as the ground state is concerned, the tubes switch from circular to axial magnetization with increasing tube length. All magnetostatic properties found in magnetic nanotubes, in which the dipolar interaction is comparable to or dominant over the exchange interaction, are reproduced by the dipolar tubes including an intermediary helically magnetized state. Besides, we discuss the antiferromagnetic phase resulting from the square arrangement of the dipolar spheres and its interesting vortex state.

Received 27th August 2018,
Accepted 25th November 2018

DOI: 10.1039/c8nr06936k

rsc.li/nanoscale

1. Introduction

Whether a system behaves as classical or quantum is usually determined by the ratio between its spatial dimension and quantum coherence length. Even so, there are cases where the actual size dependent behavior seems to be an illusion and transcending the scales is possible, thus allowing the study of fundamental aspects hardly accessible at the original size. Spin-ice frustration^{1–4} is an example, wherein the micro- and mesoscopic rules that govern the spin orientation of such systems can become very subtle and hard to understand. Nevertheless, Venderbos *et al.*⁵ and Mellado *et al.*⁶ have shown that similar frustrated states can also arise in arrangements of macroscopic dipolar rotors *via* classical magnetic interactions, furthermore, showing phenomena that are not visible in their microscopic counterpart. In this paper, we present a similar scenario of scale transcendence, relating magnetic nanotubes (MNTs) to self-assembled dipolar magnetic spheres arranged in tubular structures, named here *dipolar tubes*. The spheres can have radii from 10 nm to macroscopic neodymium balls. A peculiar feature of this comparison is that the tubular geome-

try of dipolar tubes breaks-up the continuous degeneracy of the ground states in the two dimensional (2D) lattices of dipolar spheres.^{7,8} As a result, we expect a number of new stable states in the tubular geometry. The curvature-induced feature opens the inquiry on its impact on the energy barriers that separate and stabilize the novel magnetic states, which will be addressed in this manuscript.

Given the lack of exchange interaction in dipolar tubes, it is most reasonable to compare them with dipolar interaction dominated MNTs where the exchange interaction is negligible. Since in MNTs the dipolar interaction dominated state is *circular* (magnetization polarized azimuthally), it can be expected that transcendence exists only with a similar circular state in dipolar tubes. As we show in the manuscript, it is found that the scale transcendence strikingly goes beyond this trivialization. In a ground state, the stray field created by MNTs should be minimal. This condition stems from micromagnetic considerations^{9–11} wherein the magnetostatic energy is minimized due to the dipolar part of the energy. Apart from the circular state, *axial* and *helical* ground states in MNTs have been predicted theoretically^{12,13} ‡ and confirmed experimentally.^{14–18} In the axial state, the magnetization is parallel to the nanotube's axis in the center of the tube and gradually turns into circular magnetization at the nanotube ends. In the helical state, the magnetization is never completely aligned with the tube's axis resulting in a circulating component of the magnetization.^{12,13} The helical and axial states spontaneously

^aScientific Computing Laboratory, Center for the Study of Complex Systems, Institute of Physics Belgrade, University of Belgrade, 11080 Belgrade, Serbia.
E-mail: igor.stankovic@ipb.ac.rs

^bDepartamento de Física & Centro Científico Tecnológico de Valparaíso-CCTVal, Universidad Técnica Federico Santa María, Av. España 1680, Casilla 110-V, Valparaíso, Chile

^cInstitute for Metallic Materials at the Leibniz Institute for Solid State and Materials Research, IFW, 01069 Dresden, Germany

†Electronic supplementary information (ESI) available. See DOI: 10.1039/C8NR06936K

‡Elsewhere in the literature the axial state is also referred to as mixed and helical as the transition state, *cf.* ref. 13. In this work, we chose to name the states based on magnetization in the center of the tube.

emerge when the dipolar interaction is comparable to the exchange interaction. Both states occur when nanotube's radius is a few tens of times larger than the exchange length. The axial state appears when the MNT length is around two to three orders of magnitude larger than its diameter, whereas the helical state is a transition configuration to the circular state that appears when the length of the tube is further reduced. Most of the previous studies on magnetic nanotubes have focused on magnetic configurations as a function of geometry for specific material parameters. Only recently Salinas *et al.*¹⁹ applied a generic model to discover that helical phases possess a high level of metastability relevant to magnetization reversal modes. Still, the origin of small energy differences between the states remained unclear. The axial and helical states create a small stray field¹³ or exponential decaying in the case of infinite structures, and therefore they could also exist in dipolar tubes.²⁰

The cylindrical magnetic geometry of MNTs has advantages for applications despite evident fabrication problems. In fact, the elongated geometry, azimuthal symmetry, and curvature of nanotubes bring reproducibility, robustness, and extra stability to nanotube's equilibrium states and magnetization dynamics,^{12,13,21–25} which makes MNTs attractive for buffering, transport and processing information using their equilibrium states, and domain wall dynamic and spin-wave excitations. In this sense, the proper understanding and characterization of equilibrium states in MNTs is, thus, a mandatory task. Under this scenario, mimicking the magnetic equilibrium features of nanotubes with dipolar tubes can facilitate and encourage developments towards alternative techniques intended to reduce the complexity of experiments. The minimal energy structures of dipolar particles have been investigated in recent theoretical studies.^{26,27} The tubular form of the ground state together with outstanding self-assembly properties of dipolar particles^{28,29} present motivation for their application as a platform for testing concepts with MNTs. For instance in experiments, tubular and helical architectures with dipolar particles were obtained *via* DNA ligations,^{30,31} confinement,^{32–34} bulk interactions – magnetic Janus colloids,³⁵ and asymmetric colloidal magnetic dumbbells.³⁶ Another interesting system with respect to magnetic order is the two dimensional self-assembled super lattices of magnetic cubes. The magnetic cubes are synthesized with two most probable orientations: axial [001]³⁷ and along the principal diagonal of the crystal, *i.e.*, cube, [111],³⁸ but the possibility of less trivial orientations should not be discounted. As a result of the interplay of square packing and magnetization defined by their crystal structure, we find axially magnetized anti-ferromagnetic states in the case of [001] and *vortex* in the case of [111] magnetized cubes.^{39,40} At this point, we would like to draw attention to two recently developed techniques with which dipolar tubes could be realised: (i) two-photon lithography⁴¹ nano-printers can fabricate complex three-dimensional structures with the resolution of up to 300 nm. The two-photon lithography technique was used to fabricate nanostructures out of polymer, metallic,⁴² and recently magnetic⁴³ materials. Such printed structures could be used as a template for the

self-assembly of magnetic particles with rhombic and square lattices. (ii) The second technique comes from micro-fluidics. The tubular structures of magnetic particles can be created by the conformal covering of the cylindrical conductive wire surface by assisting the self-ordering process of magnetic microspheres⁴⁴ *via* the application of a circular electromagnetic field induced by an injected electrical current along the wire.

With the aim of addressing our results, linking self-assembly, geometry, and magnetization states in dipolar tubes, this paper is organized as follows: section 2 introduces the dipolar interaction model and methods used. We discuss self-organization on cylindrical confinement in section 3, and *in silico* hierarchical degeneracy breakup of the infinite square and triangular lattices with an introduction of curvature in section 4. We also present a systematic study of the ground state configurations and energies resulting from the interplay between the tube's length and curvature for triangular and square arrangements in section 4. The final section, section 5, gives the conclusion and outlook.

2. Models and methods

2.1. Magnetic interaction model

Magnetic nanoparticles can have complex coupling involving both dipolar and exchange interactions. The atomic exchange interaction is relevant up to a length scale of 10 nm.⁴⁵ Thus, dipolar coupling dominates in the formation of the structures on the length scales 10 nm–100 μm , with many potential applications.^{30–35} We characterize the system using dipole–dipole interaction potential: it is assumed that each particle carries identical dipolar (magnetic) moment with magnitude $m = |\vec{m}_i|$, where $\vec{m}_i = (m_i^x, m_i^y, m_i^z)$ defines the dipolar moment of particle i . The potential energy of interaction $U(\vec{r}_{ij})$ between two point-like dipoles with centers located at \vec{r}_i and \vec{r}_j can be written as:

$$U(\vec{r}_{ij}) = \frac{\mu_0}{4\pi} \left[\frac{\vec{m}_i \cdot \vec{m}_j}{r_{ij}^3} - 3 \frac{(\vec{m}_i \cdot \vec{r}_{ij})(\vec{m}_j \cdot \vec{r}_{ij})}{r_{ij}^5} \right], \quad (1)$$

for $r_{ij} \geq d$ or ∞ otherwise, where $r_{ij} = |\vec{r}_{ij}| = |\vec{r}_j - \vec{r}_i|$ and d is particle's diameter. It is convenient to introduce the energy scale defined by $U_{\uparrow\uparrow} \equiv \mu_0 m^2 / 4\pi d^3$ that physically represents the repulsive potential value for two parallel dipoles in contact standing side by side, as clearly suggested by the notation. Thereby, the total potential energy of interaction in a given structure U_{tot} is given by

$$U_{\text{tot}} = \sum_{i>j} U(\vec{r}_{ij}). \quad (2)$$

One can then define the reduced potential energy of interaction u (per particle) of N magnetic spheres. It reads:

$$u_N = \frac{U_{\text{tot}}}{U_{\uparrow\uparrow} N}, \quad (3)$$

which will be referred to as the *cohesive energy*. The cohesive energy of a particle is directly related to the energy required to take it out from the structure. Lower cohesive energy means it

takes more energy to disintegrate the structure. The higher is the absolute value of cohesive energy the more stable is the structure. For a particular two particle head-to-tail configuration (*i.e.*, $\rightarrow\rightarrow$), we get $u_2 = -1$ per particle.

There is significant flexibility in tuning the physical and chemical properties of magnetic particles. In particular, colloids can be synthesized either from a pure magnetic material like hematite with a small spontaneous magnetization ($I_{\text{FeO}}^s \approx 2.2 \text{ kA m}^{-1}$), or large in the case of magnetite or cobalt ferrite ($I_{\text{CoFe}}^s \approx 480 \text{ kA m}^{-1}$).^{46,47} In the case of core-shell particles, a design freedom is obtained by the adjustable core to shell ratio. Here, in particular, we consider that all magnetic particles have the same magnetic moment. We assume that the particles are silica-hematite core-shell particles with outer diameter $d = 50 \text{ }\mu\text{m}$ and hematite core $d_{\text{core}} = 10 \text{ }\mu\text{m}$.⁴⁸ Assuming a single domain particle behavior, the magnetic moment m is expressed as $m = I_{\text{FeO}}^s \nu = 1.15 \text{ A }\mu\text{m}^2$, where $\nu \approx 500 \text{ }\mu\text{m}^3$ is the volume of the magnetic part of the particle. The result in this work should be independent on the particle material or size. To facilitate comparison, we present results in the scaled units with the reference magnetic interaction energy $U_{\uparrow\uparrow} = 10^{-18} \text{ J}$ calculated for hematite core/shell particles. For reference energy we take the minimum of magnetic cohesive energy of two particles in contact. The reference magnetic energy $U_{\uparrow\uparrow}$ is therefore equal to $256k_{\text{B}}T$, where $T = 300 \text{ K}$ is the temperature and k_{B} is the Boltzmann's constant. The maximal magnetic field generated by one particle at the center of the mass of the other particle (placed side by side) is $B_0 = \mu_0 m / (2\pi d^3) = 1 \text{ }\mu\text{T}$. The size of the magnetic core has a strong influence on the energy scale: for $d_{\text{core}} = 20 \text{ }\mu\text{m}$, we would obtain magnetic moment $m = I_{\text{FeO}}^s \nu = 9.2 \text{ A }\mu\text{m}^2$, and magnetic energy depends on the square of magnetic moment $U_{\uparrow\uparrow} = 67 \times 10^{-18} \text{ J}$, *i.e.*, $1.6 \times 10^4 k_{\text{B}}T$. As a result, one could tune the level of degeneracy described in latter sections with the size of the core. Also, by changing the core to shell ratio we tune the balance of interaction between particles and of particles with the field created by a conducting wire.

2.2. Isotropic interaction

When the dipolar coupling is strong, such as in nanocrystals, the particle assembly is determined unequivocally by the dipolar coupling and the particle shape. Here, we are interested in moderately interacting magnetic particles since we want to avoid the spontaneous formation of the clusters. Self-assembly requires to take advantage of forces that dominate on the micron scale and below (magnetic, contact, and van der Waals), resulting in different device designs and functionalities.⁴⁹

We describe the effect of isotropic contact and van der Waals interactions between the spherical particles using a minimal model, *i.e.*, as soft-core beads, that interact isotropically by means of a truncated and shifted Lennard-Jones potential. The interaction is defined as: $U_{\text{LJ}}^{\text{cut}}(r) = U_{\text{LJ}}(r) - U_{\text{LJ}}(r_{\text{cut}})$, $r < r_{\text{cut}}$ and $U_{\text{cut}} = 0$, $r \geq r_{\text{cut}}$, where r_{cut} is the distance at which the potential is truncated, and $U_{\text{LJ}}(r)$ is the conventional Lennard-Jones (LJ) potential, *i.e.*, $U_{\text{LJ}}(r) = -4\epsilon[(\sigma/r)^{12} - (\sigma/r)^6]$. The parameter ϵ corresponds to the energy scale of the

interaction and σ is related to the characteristic diameter of the beads d , *i.e.*, $\sigma = d/2^{1/6}$ and $d = 50 \text{ }\mu\text{m}$. The choice of the r_{cut} value determines the nature of the potential $U_{\text{LJ}}^{\text{cut}}(r)$: *repulsive*, which is also known as Weeks-Chandler-Andersen (WCA) potential for truncated Lennard-Jones potential in minimum $r_{\text{cut}} = 2^{1/6}\sigma$, and *attractive* for a commonly chosen $r_{\text{cut}} = 2.5\sigma$. The presence of attractive interactions between particles is reminiscent of a Stockmayer fluid, a simple and convenient model for representing ferrofluids^{50,51} or lattice of particles stabilized by dipolar coupling.⁵²

The colloidal structures analyzed here are modeled to represent the colloidal magnetic particles that have iron oxide inclusions inside the silica shell: *attractive* part of isotropic interaction; we choose a weak interaction between particles,⁵² $\epsilon_{\text{a}} = 3.5 \times 10^{-19} \text{ J}$ ($\epsilon_{\text{a}} = 0.3U_{\uparrow\uparrow}$ for $d_{\text{core}} = 10 \text{ }\mu\text{m}$) and $r_{\text{cut}} = 125 \text{ }\mu\text{m}$ for particles with diameter $d = 50 \text{ }\mu\text{m}$. The value of the sphere repulsive contact potential is taken as $\epsilon_{\text{r}} = 7 \times 10^{-16} \text{ J}$ for particles with the same diameter $d = 50 \text{ }\mu\text{m}$ (*i.e.*, $\epsilon_{\text{r}} = 10U_{\uparrow\uparrow}$). The magnitude of the attractive part of potential and interaction range can be varied by controlling the colloidal charge number or surface composition.⁵³

We study the system by means of Langevin molecular dynamics computer simulations (described in the following subsection): our spheres are represented by WCA potential, and carry a magnetic point dipole in their centers. A weak isotropic van der Waals (vdW) attraction between the spheres is included for a more realist approach to an experimental solution of colloidal particles. In the experiment, the colloidal particles are stabilized against irreversible agglomeration by vdW forces, either by polymers grafted to the surface, or manipulating the ionic content of the fluid. The vdW attraction between the spheres provides additional stability to the lattice composed of assembled tubes after the electromagnetic field has been switched-off. As such, our results can be scaled to different shell materials, *i.e.*, polystyrene and silica oxide, but the conclusions of this minimal model should be generic.

2.3. Interaction with conductive wire

We place the conductive wire in a suspension of spherical magnetic particles. The conductive wire is an elegant way to cover the cylindrical surface with magnetic particles. Such a system has been recently implemented by Bécu *et al.* with paramagnetic particles.⁴⁴ When replacing paramagnetic particles with magnetic particles, the magnetic fields of the ferromagnetic particles and the electromagnetic field generated by the conductive wire become independent. As a result, we obtain an additional tuning parameter – a ratio between magnetization of the particle and electromagnetic field or current of the wire. Still, the system parameters should be carefully selected to avoid the formation of kinetically trapped clusters or arcs of particles attached to the wire.

We consider a situation in which colloidal suspension is placed in the vicinity of the current conducting wire. A wire with outer diameter $2R_{\text{w}} = 50\text{--}100 \text{ }\mu\text{m}$ is connected along the z -direction. In order to generate an electromagnetic field able to attract particles at the surface of the wire, significant cur-

rents must go through the wire, giving rise to fields of several mT at the wire surface. Recent similar experiments with paramagnetic particles indicate that a 50 μm wire can support currents of up to 0.5 A for several minutes and up to 0.8 A for a short time, creating electromagnetic fields up to $B = 3.2$ mT,⁴⁴ *i.e.*, $B_w = \mu I / \pi(2R_w + d)$ for $d_w = 50$ μm wire and $d = 50$ μm particle. § We will show how the interactions between the particles and of particles with the wire can be balanced to obtain single wall tubes. Our design based on ferromagnetic particles has a freedom of tuning the ratio between two magnetic forces: interparticle magnetic force F_{mm} and electromagnetic force between ferromagnetic particles and the conductive wire F_{mi} , *i.e.*, magnitude of magnetic force between two particles depends on the square of their magnetic moments and the force between particles and conducting wire depends linearly on the magnetic moment. At the same time, magnetic moment is proportional to the cube of the core's diameter allowing the variation of the ratio for up to three orders of magnitude, therefore this ratio can be anywhere between $F_{\text{mi}}/F_{\text{mm}} = 1$ –1000 (the single wall tubes will be created only at the higher ratios).

2.4. Langevin molecular dynamics

Langevin molecular dynamics (MD)⁵⁴ was used to study the self-assembly in the vicinity of the wire under the influence of an electromagnetic field of uninsulated conductive wire. The total force of implicit solvent on each particle has the form: $\vec{f} = \vec{f}_c + \vec{f}_i + \vec{f}_r$, where f_c is the conservative force of interparticle interactions and of particles with the wire, $f_i = -(m/\xi)v$ is a frictional drag or viscous damping term proportional to the particle's velocity, and $\langle f_r \rangle = \sqrt{k_B T m / \xi}$ is the random Brownian force of the solvent. The random force term is treated as a Gaussian process that adheres to the fluctuation-dissipation theorem. The rotational degrees of freedom are, of course, governed by the equations of motion for the torque and angular velocity of a sphere. Since evolution in time is not of primary concern in this study, the values of mass, inertia and translational/rotation friction coefficients are physically inconsequential to the final state of the system. An estimate of time, per MD step, can be obtained for 50 μm -sized colloidal particles with $d_{\text{core}} = 20$ μm as $t = \sqrt{M_{\text{sp}} d^2 / U_{\uparrow\uparrow}} = 80$ ms (mass of the core-shell hematite/silica particle $M = 10$ μg). The total length of the MD simulation was thus estimated to be of the order of 15 minutes (*i.e.*, about 1000 s).

2.5. Energy minimization

The energies of finite tubes were independently computed using 10 – 10^3 initial configurations with random magnetiza-

tion (depending on the size of the system). The procedure included two steps: in the first step 'overdamped' equations of rotational motion of each particle were integrated with respect to the torque exerted on a particle (same equation as in Langevin molecular dynamics equations as in the previous section). The parameters used correspond to motion in a highly viscous fluid where angular velocity is proportional to torque, *i.e.*, in the limit where no acceleration takes place, in order to avoid any oscillations. In the second step, the resulting configurations were used as the input to a rigorous conjugate gradient minimization algorithm.⁵⁵ The second step was required since 'overdamped' rotational motion converges slowly towards the ground state ¶ for a prescribed geometry. The energies of the resulting configurations were compared – about 10% of configurations had the same energy, in the limit of numerical precision of about $\delta u/u = 10^{-7}$, corresponding to the ground state. The minimization procedure always finds dipole moments tangential to the cylindrical surface, *cf.* ref. 20.

2.6. Geometry of tubes

We refer to tubes made by stacking of rings. || In AA-tubes all constitutive rings are exactly aligned, *cf.* Fig. 1(a), and in AB-tubes every ring is shifted by half of the particle's diameter, in respect to its preceding ring, *cf.* Fig. 1(b). Alternatively, AA- or AB-tubes could be generated by rolling square or triangular lattices with cylindrical confinement, respectively.

Particle i -positions in AA tubes are calculated as: $x_i = R \cos(2\pi i/N)$, $y_i = R \sin(2\pi i/N)$, and $z_i = [i/N]d$, where $[x]$ is the greatest integer function and gives the largest integer less than or equal to x , while N is the number of particles in a constitutive ring. To simplify the discussion, we refer to N also as *curvature* since there is a correspondence with the tube's geometrical curvature $R/d = 1/2 \sin(\pi/N)$, *e.g.*, we obtain $R/d = \sqrt{2}/(\sqrt{3} - 1) \approx 1.3$ for $N = 8$ ring.

One of the ways to obtain AB tubes is stacking of a pair of two successive rings. ** In both rings particle positions are calculated based on their index i : $x_i = R \cos(2\pi i/N + \theta_i)$, $y_i = R \sin(2\pi i/N + \theta_i)$, and $z_i = [i/N]\Delta z$, where θ_i is the angular displacement of rings $\theta_i = \pi \text{mod}([i/N], 2)/N$ and

¶A simple example of a discrete ground state is two dipole cases: put two dipoles next to each other and let them orient freely in three dimensional space, they will align their moments in a head to tail configuration (coaxially).

|| Apart from self assembly on the micro-scale, it is possible to construct tubes described in this subsection manually on the macroscopic (millimetre) scale. The neodymium magnetic spheres are widely available and applicable for building model systems.⁵⁶ Neodymium magnets are made of a sintered alloy of iron, neodymium, and boron ($\text{Nd}_2\text{Fe}_{14}\text{B}$). The coercive field strength is about 10^6 A m^{-1} . Thus, the neodymium magnets can withstand high external magnetic fields. The remanence of 1 to 1.5T is at the same time not larger than that in other magnetic materials. All tubes constructed in this section can be therefore built with neodymium magnets.

**The tubes can also be created, in analogy to carbon nanotubes, by rolling a ribbon of a triangular lattice on a cylinder surface.²⁰ The cylindrical geometry is infinite in one direction and we can, in analogy with crystal lattices, generate tubes by periodical reproduction of a curved patch (unit cell) along the helical backbone with *spanning vectors* (\vec{a}_1, \vec{a}_2). This curved unit cell has n_1 particles along the \vec{a}_1 direction and n_2 particles in the \vec{a}_2 direction.

§To favor the comparison with previous research on paramagnetic particles, we present here results for wires with $2R_w = 100$ and 130 μm and particles with 50 μm diameter. Ohmic heating limits the current through wire and is proportional to the square of the current and wire radius. Since the electromagnetic field B is linearly proportional to the current and inversely proportional to the distance of centers of the particle and wire, the power is $P \propto B^2(1 + d/R_w)^2$. Therefore, we should note that the increase of the wire diameter allows higher electromagnetic field for similar dissipation.

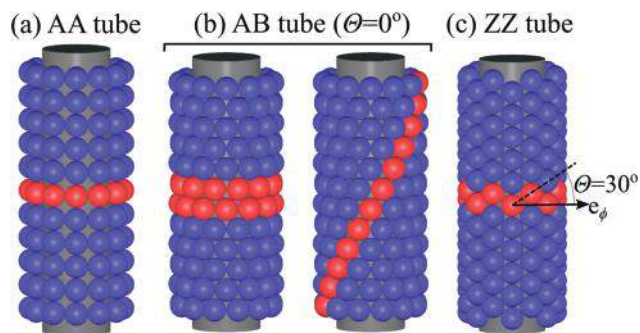


Fig. 1 Illustration of (a) AA, (b) AB, and (c) ZZ tubes. The tubes are wrapped around the confinement cylinder. Tubes can be created via ring stacking (highlighted). A single ring is enough in the case of AA and ZZ tubes. We show that AB tubes can be created in two ways. The first way is by a pair of successive rings in the case of the AB tube (left panel, see ESI movie 1†). The second way is by wrapping of the ribbon with a triangular lattice on cylindrical confinement (right panel, see ESI movie 2†). In the right panel of the AB tube, the edge of the ribbon with 12 threads is denoted. The ZZ tube can be created in three ways, stacking of zig-zag rings (pictured), wrapping 14 filaments parallel to the tube's long axis, or 14 thread ribbons oblique to the axis (see ESI movies 3 and 4†). The AB tube has a chiral angle $\theta = 0^\circ$. The lattice structure of the ZZ tube is triangular, like one of the AB tubes, while chirality is different, *i.e.*, $\theta = 30^\circ$.

$\Delta z = \sqrt{d^2 - 2R^2[1 - \cos(\pi/N)]}$ is the displacement between successive rings along AB tube's axis and $i = 1, N_{\text{tube}}$. The total number of particles in the tube N_{tube} is a multiple of the number of particles in ring N and the number of rings N_{rings} , *i.e.*, $N_{\text{tube}} = N_{\text{rings}} \cdot N$.

In addition to stacking of the rings, the tubes can be created by rolling a ribbon with a square or triangular lattice on a cylindrical surface. The right side panel in Fig. 1(b) shows an edge of the ribbon creating exactly the same structure as that by stacking of rings (see also ESI movies 1–4†). In fact, every ordered tubular structure can be generated by reproduction of a curved unit cell along the helical lines defined through curved spanning vectors in analogy to crystals in two dimensions. This curved unit cell has n_1 and n_2 particles along two spanning directions.²⁰

Still, there are geometrical limits for a ribbon with a defined structure (*i.e.*, square, rhombic or triangular). Like in carbon nanotubes, ribbons of assembled particles can be rolled at specific and discrete (“chiral”) angles. The chiral angle can take values $0 < \theta < 30^\circ$ for triangular lattices and $0 < \theta < 45^\circ$ for square lattices, where θ is the angle between the thread of particles and tangent to the cylinder radius⁵⁷ (in Fig. 1). Here, we will demonstrate how combination of the rolling angle and radius decides the tube's properties with respect to magnetic state energies. We show AB and ZZ tubes which have different chiralities, $\theta = 0^\circ$ and 30° , in Fig. 1(b) and (c), respectively. The circular arrangement of the AB tube corresponds to, the so called, armchair carbon nanotube equivalent. The curvature of the two structures is also similar $R_{\text{AB}}/d = 1.932$ and $R_{\text{ZZ}}/d = 1.945$, while the number of particles

in a constitutive ring is different, $N = 12$ and 14 for AB and ZZ tubes, respectively. An arrangement, circular or helical in the AB tube and axial or helical in the ZZ tube, corresponds to a possible choice of magnetization of tubes that is aligned with their lattice structure.

3. Ampère force driven assembly

The central mechanism driving the adhesion of particles on a conductive wire is an interplay between dipolar forces between particles and radial attractive Ampère force. The electromagnetic field of the conducting wire is strong enough to determine the orientation of all dipole moments. In order to obtain a single layer of magnetic particles, the Ampère force should dominate inter-particle dipolar forces. Here, we should point out that the Ampère force generated by the current in the wire depends linearly on the magnetic moment of the particles while magnetic dipolar interactions scale quadratically. Besides, there are symmetric and short-range forces between colloidal particles due to their surface design. We base our analysis on a simplest analytically tractable model for constitutive ring rearrangement and comparison with the MD simulations.

In the following two sections, we first give analytical results for Ampère force driven processes. After that, we compare these analytical results with the ones obtained by computer simulation for moderate and strong currents. We will show that only sufficiently strong current is able to pull and attach all particles to the wire's surface.

3.1. From self-assembled chain to ring

The first agglomeration phenomenon analyzed analytically is the strength of the curved electromagnetic field needed to reduce the radius of an arc built by magnetic particles. An elongated chain (or cluster of chains) should overcome the elastic barrier preventing its bending into the ring under the influence of a circular electromagnetic field. The origin of the resistance to deformation can be understood in terms of a transition from local (chain) to global energy minima, corresponding to a ring or stacking of the rings.^{26,58} For simplicity, we assume that the magnetic spheres have a magnetization that follows the curvature of the arc (*i.e.*, part of the ring) and that the arc backbone follows electromagnetic field streamlines (*i.e.*, co-centered with wire).

To do so, we consider a thin wire ($r_{\text{dist}}/R_{\text{wire}} > 1$). An arc with curvature d/R can be obtained by calculating the particle positions based on their index i in Euclidian space: $x_i = r_{\text{dist}} \cos(\theta_i)$, $y_i = r_{\text{dist}} \sin(\theta_i)$, and respective magnetization $m_i^x = \cos(\theta_i + \pi/2)$, $m_i^y = \sin(\theta_i + \pi/2)$, where θ is the angular displacement of particles $\theta = 2\arcsin(d/2r_{\text{dist}})$ and d the particle diameter. The combined resistive magnetoelastic force tries to straighten the chain and reduce its curvature d/r_{dist} , see dashed lines for $N = 4, 6, 12$ particles in Fig. 2(a). Due to the circular nature of the electromagnetic field, the curvature d/r_{dist} of the arc is inverse of its distance from the wire r_{dist} . The magneto-elastic force F

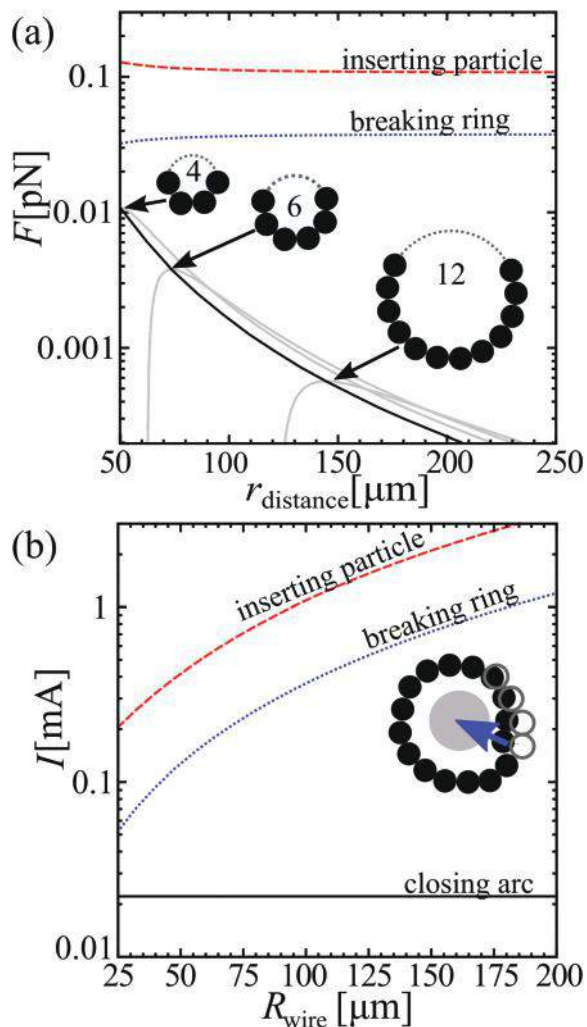


Fig. 2 Critical (a) force and (b) current required to bend and close an arc of particles and form a ring, break the ring, or insert particle between the two rings. The dependence of the forces on distance from the center of the wire r_{dist} is shown. The ring is broken when Ampère's force pushes one side of the ring inside (spirally deforming ring). The evolution of the force with the distance from wire r_{distance} is also shown in figure (a) with dotted line for $N = 4, 6$, and 12 particles. The critical current depends on wire radius R_{wire} since particles become further away from the center. The magnetic moment of the particle is $1.15 \text{ A } \mu\text{m}^2$.

increases up to the point when the arc ends start to attract each other, *cf.*, bold black line connecting maxima of force curves for different arcs in Fig. 2(a). The critical force for the chain with $N = 4$ particles has a maximum $F = 30 \text{ pN}$ at distance $r_{\text{dist}} = 50 \mu\text{m}$ and $N = 6$ particles has $F = 15 \text{ pN}$ at $r_{\text{dist}} = 70 \mu\text{m}$. Thereafter, the deformation of the chain becomes irreversible. The magneto-elastic force decreases with increasing curvature d/r_{dist} and changes the sign. The negative force means that after that point the arc closes on its own. Also, one can observe that while the critical force diminishes with distance – the highest necessary critical current is for thin wire and short arcs (*i.e.* for three particle arc). The critical force is inversely

proportional to the distance, *i.e.*, $F \sim 1/r_{\text{dist}}$. The current needed to generate sufficient electromagnetic field, $I \approx 0.02 \text{ A}$, is therefore independent of the chain length.

3.2. Attaching particles to the surface of the wire

We also observe that for a moderate current the long arc closes into a ring with a radius larger than the radius of the wire (R_{wire}). How does this ring finally attach to the surface of the wire? What is the critical force and current required to break the rings by spiral deformation? The transformation from a large ring to the adapted wire diameter involves a destabilizing field able to tear apart a ring by pulling a part of it inwards to the surface of the wire ($r_{\text{dist}} > R_{\text{wire}}$). The energy per particle of the single ring is:

$$u_r(N) = -\frac{1}{4} \sin^3\left(\frac{\pi}{N}\right) \sum_{k=1}^{N-1} \frac{\cos\left(\frac{2\pi k}{N}\right) + 3}{\sin^3\left(\frac{\pi k}{N}\right)}. \quad (4)$$

Similarly, the approximate expression for the force required to break the ring is given by (see also Fig. 2(a)),

$$F_s(N) = -\frac{3}{8} \sin^3\left(\frac{\pi}{N}\right) \sum_{k=1}^{N-1} k \frac{\cos\left(\frac{2\pi k}{N}\right) + 3}{\sin^3\left(\frac{\pi k}{N}\right)}. \quad (5)$$

Since the Ampère force reaches its strongest value in the wire surface, the ring will break in the vicinity at this position. We can therefore estimate the critical current to be $I = 2\pi(d + R_{\text{wire}})^2 F / \mu_0 m$, as shown in Fig. 2(b). The current required to break a ring is more than three times higher than the current needed to close an arc and increases with the wire radius. Still, the increase is slow ($I \sim R_{\text{wire}}^\alpha$, where $\alpha < 1$) and is compensated without the increase in current density through the wire.

The magnetic particles stick (or diffuse) on top of the triangular lattice formed on the cylindrical surfaces. Following compaction, the remaining beads coming from solvent try to pop-in between the constitutive rings of the tube. In numerical analysis, we use the fact that a ring configuration compensates for the dipole moment and the total dipole moment is zero within the ring. In far field, the electromagnetic field of the ring resembles a multipole, *i.e.*, the electromagnetic field drops with the distance as $1/r^{N+2}$, where N is the number of particles in the ring. The self-screening of inter-ring dipolar interactions takes place as soon as the rings are separated by more than one particle size. Therefore, the change in total energy depends dominantly on the distance of the touching rings, *i.e.*, the change in their interaction energy,

$$u_{ir}(N) = -\frac{1}{8} \sin^3\left(\frac{\pi}{N}\right) \times \sum_{k=0}^{N-1} \frac{2 \left\{ 3 + \cos\left[\frac{\pi(2k+1)}{N}\right] \right\} \sin^2\left[\frac{\pi(2k+1)}{2N}\right] + dz^2 S_k}{\left\{ dz^2 \sin^2\left[\frac{\pi(2k+1)}{2N}\right] + \sin^2\left(\frac{\pi}{N}\right) \right\}^{5/2}} \quad (6)$$

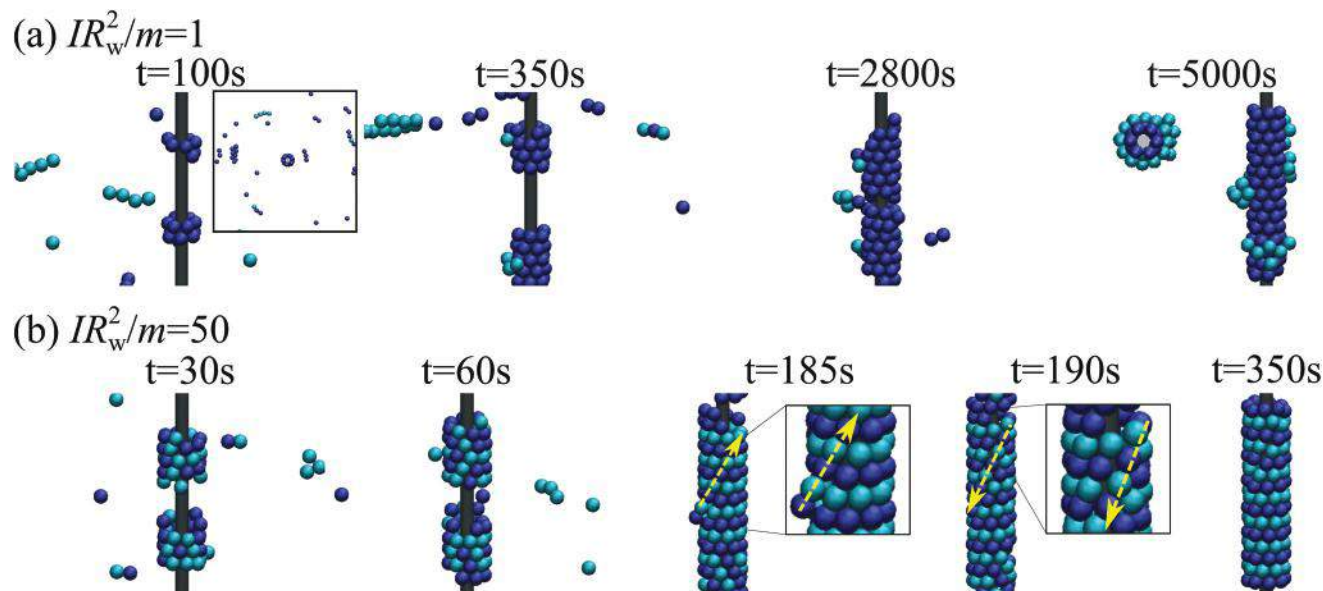


Fig. 3 Snapshots of MD simulations at moderate (a) $IR_w^2/m = 1$ and strong (b) $IR_w^2/m = 50$ currents are shown. (a) For $IR_w^2/m = 1$, we observe chains form as an oriented collection of magnetic dipoles, increasingly curved by the electromagnetic field as they approach, and eventually attach to the wire. The particles in contact with wire at $t = 1000$ s are colored differently. The animation is given as ESI movies 5 and 6† (top and side views). (b) At strong currents, $IR_w^2/m = 50$, Ampère force inserts particles into the triangular lattice. Insets between $t = 53$ s and 54 s show particles while entering moving (shear) tube's structure turning it into a quasi-stable single stranded helix. The particles belonging to successive rings are colored differently at $t = 185$ s to visualize this process. After some time, $t = 190$ s, the helix shears back into a tube with rings of magnetic particles conforming electromagnetic field lines. The animation is given as ESI movie 7.† The magnetic moment of the particle is $1.15 \text{ A } \mu\text{m}^2$, the wire radius is (a) $R_w = d = 50 \text{ } \mu\text{m}$ and (b) $R_w = 1.3d = 65 \text{ } \mu\text{m}$, and the current is (a) $I = 0.46 \text{ mA}$ and (b) $I = 23 \text{ mA}$.

where dz is the distance between touching rings and $S_k = \sum_{i=0,1,2} (-1)^i \binom{2}{i} \cos[\pi(2(k+i)-1)/N]$. We estimate the force $F_i(N) = (6/\sqrt{2})\partial u_{ir}(N)/\partial dz$ needed to push the particle between the two rings in contact, *i.e.*, at a distance:

$$dz_N^c = \sqrt{1 - \frac{1}{2} \left[1 - \cos\left(\frac{\pi}{N}\right) \right] \sin^{-2}\left(\frac{\pi}{N}\right)}. \quad (7)$$

The resulting critical force and current depend on the wire radius as shown in Fig. 2(a) and (b), respectively. For wire of $R_{\text{wire}} = 65 \text{ } \mu\text{m}$, on which 8 particles of $d = 50 \text{ } \mu\text{m}$ could form a ring, the critical current is $I = 0.4 \text{ A}$.

3.3. Dynamics of assembly

We simulate the Ampère force driven assembly of colloidal magnetic particles on a cylindrical confinement. The snapshots of evolution of the configuration with time are given in Fig. 3 and animations are given in the ESI as movies 5–7.† We model the dynamics of assembled particles with dipolar coupling in the presence of the circular electromagnetic field generated by the electrical current going through a conductive cylindrical wire which, at the same time, serves as a geometrical constraint.

In MD simulations at moderate currents, *cf.* the inset in Fig. 3(a), we observe the formation of chains composed of an oriented collection of magnetic dipoles, increasingly curved by the electromagnetic field as they approach, and eventually

attach to the wire. This process is schematically given in Fig. 2(a). The resistance to bending increases as the particles approach the wire. The chain finally bends due to the fact that the dipoles cannot align with both, the electromagnetic field lines and with each other's magnetic axis. In this frustrated configuration, the magnetic field of each dipole exerts a torque on all other dipoles.

At sufficiently high currents we observe that the system becomes rapidly compact, see Fig. 3(b). We also observe, between $t = 185$ s and $t = 190$ s in Fig. 3(b),†† how the last particle coming from solvent pushes the already formed triangular lattice structure forming a metastable single stranded helix. In this metastable state, the helix backbone and electromagnetic field are not aligned, resulting in mechanical strain on the whole structure. At $t = 350$ s, we observe that the system shears back into a stable state (tube) with constitutive rings aligned with the electromagnetic field.

Finally, we should note that a square lattice can only be obtained by self assembly on a square patterned surface. This corresponds also to the state-of-the-art in the literature.⁴¹ The latter one is limited to the self assembly of finite sized structures. Nano-scale printing allows realization of curved conductors with a complex surface geometry and opens an interesting playground for generating different packings of magnetic spheres. The Joule heating limits the current through a

†† The particles are colored differently to visualize the movement.

100 μm wire to 0.5 A.⁴⁴ Therefore, the magnetic moment of the particle is limited by the total magnetic moment of the particle and should be $m < IR_w^2/50 = 25 \text{ A } \mu\text{m}^2$, taking into account the whole size of the particle. The total magnetic moment of the particle is controlled by the volume of the ferromagnetic core and choice of the magnetic material. Once the dipolar tube had been formed, the particles would stay in place after the wire is removed. The tubular structures are mechanically stable also at finite temperatures (see movie 8 in the ESI†). We should highlight that the wire is not only a confinement structure but an efficient way to control the magnetic configuration of these tubes.

4. Magnetization of dipolar tubes

In this section, we analyze the implication of curvature and size effects on the energy landscape of triangular and square lattices. The isotropic interaction between the particles and the particles with the wire, which now serves only as a rigid cylindrical confinement, does not have influence on magnetic dipole orientation.

4.1. Characteristics of triangular and square lattices

First, we investigate the dependence of ground state energy on magnetization. All dipoles in the triangular lattice are parallel and allowed to rotate only around a fixed axis orthogonal to the plane, see Fig. 4(a), for numerical details *cf.* ref. 59. There is a continuous ground state for any in-plane angle θ with cohesive energy value $u_{\text{AB}} \simeq -2.7586$,^{††} see also ref. 7 and 8. For a square two dimensional lattice, similarly, there is a continuous degeneracy of its ground state, described in Fig. 4(b) and (c). A continuous state, in this case, involves a unit cell of four particles. The moments in a unit cell are synchronously coupled and in our notation take directions $\theta, \pi - \theta, \pi + \theta$, and $-\theta$, in the anti-clockwise direction as shown in Fig. 4(b). The ground states found are obviously antiferromagnetic, with the total dipole moment within the cell conserved and equal to zero. The most striking is the so-called *vortex state* for $\theta = \pi/4$ with a fully enclosed circulation of the magnetic dipole moment within the unit cell. The ground state cohesive energy value is $u_{\text{AA}} \simeq -2.5494$.^{§§} We will use the calculated ground state energy value as an absolute point for comparison of energies of different states in tubes with square or triangular lattice structures. We should note that both antiferromagnetic states are observed in systems of square particles as a result of the interplay between the magnetization defined by crystallinity of the cubes and the structure of the two dimensional super lattice.

^{††}The energy of the continuous ground state of the triangular lattice independent of the in-plane angle θ is

$$u_{\text{AB}} = -2\zeta(3) + 16\pi^2 \sum_{k=1}^{\infty} \sum_{l=1}^{\infty} \cos(kl\pi) K_0(kl\sqrt{3}\pi) \simeq -2.7586.$$

^{§§}The energy of the continuous ground state of the square lattice is

$$u_{\text{AA}} = -2\zeta(3) + 16\pi^2 \sum_{k=1}^{\infty} \sum_{l=0}^{\infty} k^2 \{K_0[4k(l+1)\pi] - K_0[2k(2l+1)\pi]\} \simeq -2.5494.$$

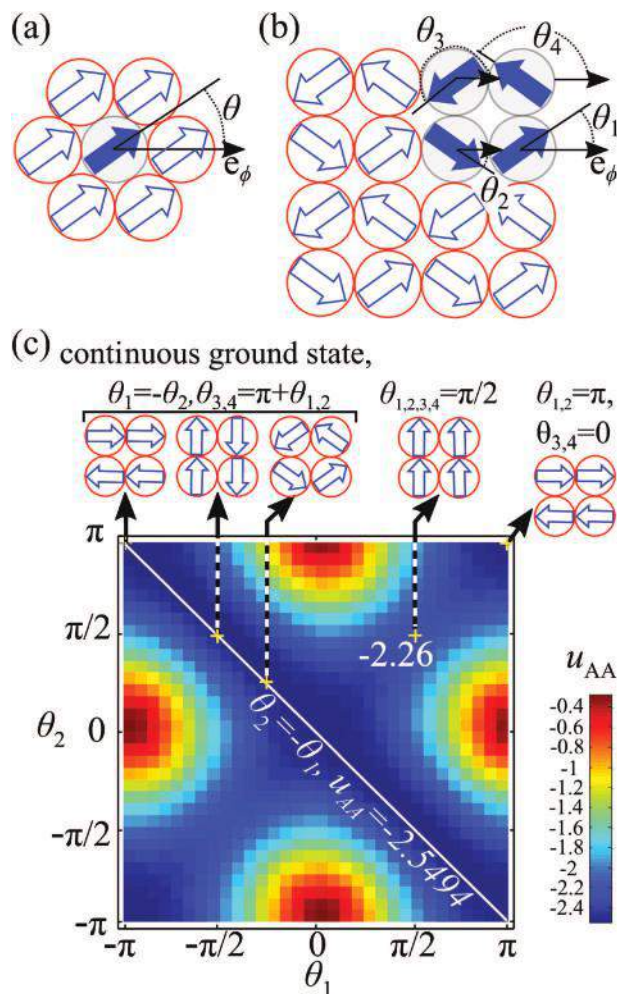


Fig. 4 Visualization of degenerate states in infinite (a) triangular and (b) square lattices, *i.e.*, respectively AB and AA packings. The dipoles are depicted as arrows located in the center of the spheres. In the case of the triangular lattice the unit cell consists of a single particle and in the case of the square lattice it consists of four particles (gray). (c) An energy landscape for the square lattice is shown with respect to two θ_1 and θ_2 out of four magnetic moments in the unit cell. Other two moments were oriented so the energy of the system is minimal. One can observe a flat valley of degenerate ground state, $\theta_2 = -\theta_1$, with energy $u_{\text{AA}} \simeq -2.5494$. The saddle point which represents a uniformly magnetized square plane with energy $u_{\text{AA}}^{\text{sd}} = -2.26$ is also marked. The curves are drawn through the discrete points and are smooth. The results are in principle scale independent. The reference magnetic energies are $U_{11} = 10^{-18} \text{ J}$ and $67 \times 10^{-18} \text{ J}$, *i.e.*, $256k_{\text{B}}T$ and $1.6 \times 10^4 k_{\text{B}}T$, for particles with magnetic moments $m = 1.15 \text{ A } \mu\text{m}^2$ and $9.2 \text{ A } \mu\text{m}^2$, respectively, where $T = 300 \text{ K}$ is the temperature and k_{B} is the Boltzmann's constant.

Commonly, magnetic cubes are represented by single dipoles placed in the center. While this is a good approximation for many systems, it only takes into account about 50% of the total volume of the cube and is neglecting the effect of the corners. Therefore one could expect degeneracy breakup due to asymmetry of the shape of the cubes. Still, the cubes are synthesized very often with curved edges, *i.e.*, as superballs, exhibiting a continuous transformation of shape from an ideal cube to a sphere⁶⁰ and they are expected to self assemble in structures

with a square symmetry.⁶¹ An extent of degeneracy breakup remains to be analyzed during this shape-shift.

4.2. Degeneracy break-up with curvature

Wrapping of the plane around the confinement cylinder will make the system quasi one-dimensional and break degeneracy. We will discuss repercussions of degeneracy breakup on cohesive energy for different dipole orientations. We analyze first the degeneracy breakup in infinite tubes: according to tube's cylindrical geometry, we represent the dipole moment of the i -th particle in cylindrical coordinates like:

$$\vec{m}_i = m_{i\phi}\vec{e}_\phi + m_{iz}\vec{e}_z, \quad (8)$$

with constraints $m^2 = m_{i\phi}^2 + m_{iz}^2$ ($i = 1, \dots, N$). The parallel component with respect to tube's axis is given by m_z and the orthogonal component is m_ϕ (*i.e.*, m_ϕ is tangential to cylinder's circumference). In Fig. 5, we follow the dependence of energy on angular parameter θ , $m_{iz} = m \sin(\theta)$. We find that the axial magnetization (*i.e.*, $\theta = \pi/2$) of dipole moments represents the ground state for both AA- and AB-tubes, and circular magnetization (*i.e.*, $\theta = 0$) is the most unfavorable as seen in Fig. 5.

Between circular and axial magnetization (*i.e.*, $0 < \theta < \pi/2$), we observe a continuous increase of energy with increasing cir-

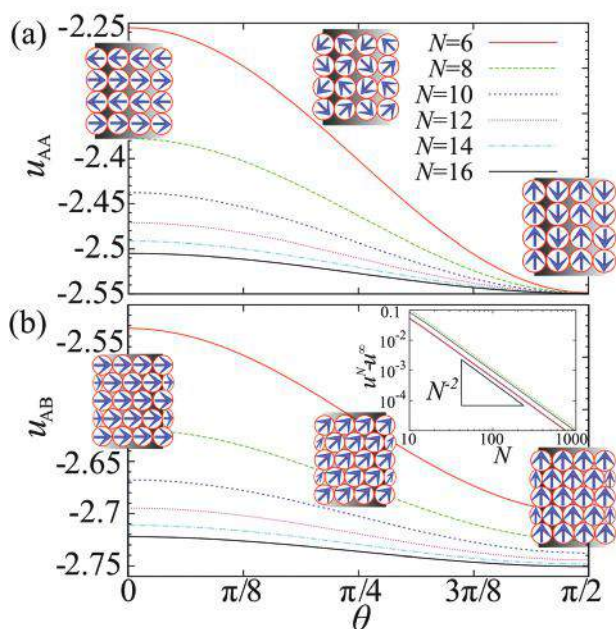


Fig. 5 Dipolar cohesive energy spectrum of configurations for dipole orientations shown in Fig. 4 on a curved surface of the infinitely long tube with (a) square AA and (b) triangular AB tubes. Breaking of degeneracy with respect to angle θ due to the curvature, *i.e.*, proportional to the number of particles in the constitutive ring N , is shown. The axial magnetization corresponds to $\theta = \pi/2$. The inset shows convergence of dipolar cohesive energies for $\theta = 0$, and $\pi/4$ to infinite two dimensional plane value u (for square lattice $u_{AA} = -2.5494$ and for triangular lattice $u_{AB} = -2.7586$). The reference magnetic energies are $U_{\uparrow\uparrow} = 10^{-18}$ J and 67×10^{-18} J, *i.e.*, $256k_B T$ and $1.6 \times 10^4 k_B T$, for particles with magnetic moments $m = 1.15 \text{ A } \mu\text{m}^2$ and $9.2 \text{ A } \mu\text{m}^2$, respectively, where $T = 300$ K is the temperature and k_B is Boltzmann's constant.

cular alignment of magnetization. These transition states, we call *vortex* in the case of square AA tubes and *helical* in the case of triangular AB tubes, *e.g.*, $\theta = \pi/4$ in Fig. 5(a) and (b), respectively. The cohesive energy, of different configurations shown in Fig. 5, converges to a continuously degenerate state with increasing curvature N , following the power law, $u^N - u^\infty \sim N^{-2}$, *cf.* the inset in Fig. 5.

Configurations (A1), (B1), (C1), (D1), and (E1) are shown in Fig. 7. The results are in principle scale independent. In this work, we have used in all examples length scale $d = 50 \mu\text{m}$.

4.3. Magnetization states in finite tubes

We will go one step further and consider finite tubes which consist of N_{rings} stacked rings. Tube's length influences ground state dipole orientation on both global and local levels. The competition between the two geometrical parameters, (i) curvature N and (ii) tube length N_{rings} , leads to different possible magnetic states of the tube. The energies of ground states, at a prescribed number of rings N_{rings} and for two curvatures $N = 8, 12$, are given in Fig. 6 for AA and AB tubes (*i.e.* square and triangular tubular structures).

Points (A2), (B2), (C2), (D2) and (E2) from the state diagram are chosen as illustrative examples in Fig. 9. The results are in principle scale independent. We used length scale $d = 50 \mu\text{m}$.

Finite AA tubes. For square AA stacked tubes with $N = 12$ curvature, the circular magnetization state is stable for ($2 \leq$

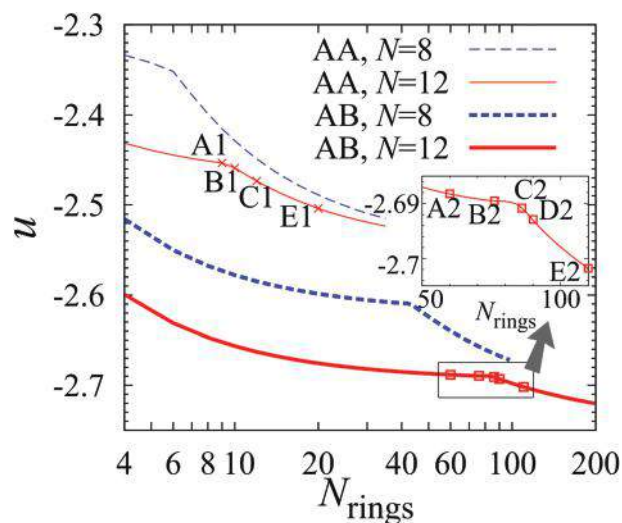


Fig. 6 Reduced cohesive energy profiles u as a function of the number of rings N_{rings} for AA and AB tubes with curvatures $N = 8$ and 12 . Configurations for points (A1), (B1), (C1), and (E1) are shown in Fig. 7 and (A2), (B2), (C2), (D2) and (E2) in Fig. 9. The curves are plotted through the discrete points and serve as guide to the eye, all points lie on the curves, and only a few listed and analysed points are shown. Before points (A1) and (B2) the magnetization is ideally circular and the energy decrease is only driven by the addition of new rings. The results are in principle scale independent. Two possible choices for reference magnetic energy could be $U_{\uparrow\uparrow} = 10^{-18}$ J and 67×10^{-18} J, *i.e.*, $256k_B T$ and $1.6 \times 10^4 k_B T$, for particles with magnetic moments $m = 1.15 \text{ A } \mu\text{m}^2$ and $9.2 \text{ A } \mu\text{m}^2$, respectively, where $T = 300$ K is the temperature and k_B is Boltzmann's constant.

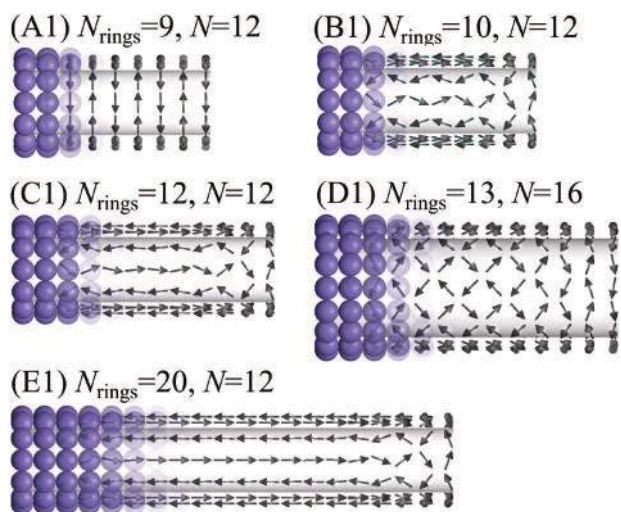


Fig. 7 Illustrative examples of characteristic ground state magnetization for tubes with AA stacking. Configurations (A1), (B1), (C1) and (E1) are obtained with curvature $N = 12$, and (D1) with $N = 16$.

$N_{\text{rings}} \leq 9$) rings. It turns out that circular magnetization is the ground state of short tubes, relative to their constitutive ring size N . The circular magnetization case $N_{\text{rings}} = 9$ is illustrated in Fig. 7(A1). The change in magnetization towards axial is abrupt for $N_{\text{rings}} = 10$ and curvature $N = 12$, see Fig. 7(B1). We observe a local antiferromagnetic circulation formed almost over the whole length except in terminal rings. The dipoles in the middle of the tube are only slightly misaligned with tube's axis (*i.e.*, for angle 0.12π). As a result of change in the magnetic order we observe, Fig. 6, that the slope of cohesive energy changes from $N_{\text{rings}} = 9$ to 10, *i.e.*, between points (A1) $u_{\text{AA}}^{12,9} = -2.4534$ and (B1) $u_{\text{AA}}^{12,10} = -2.4589$. Extending further the tube length $N_{\text{rings}} \geq 13$, we observe a well formed axial anti-ferromagnetic state with chains of alternating magnetization parallel to the tube axis.

The state diagram of AA tubes is given in Fig. 8. The calculated equilibrium states are given for different curvatures and lengths of AA. The coloring method in the state diagram is based on the local order parameter, conveniently defined as:

$$\chi_{L/2} = |2\langle (m_z/m)^2 \rangle_{L/2} - 1|, \quad (9)$$

where $(m_z/m)^2$ is the scaled intensity of local magnetization in the axial direction and $\langle \rangle_{L/2}$ is the average in the middle of the tube ($z = L/2$).^{¶¶} The idea of the order parameter is to visualize transition states (between axial and circular). Magnetic states which do not match with axial nor circular states in the middle of the tube are also referred to as *vortex states* in AA tubes. The order parameter measures the misalignment of \vec{m} from the geometry of the tube, it is $\chi_{L/2} = 1$ in circular, *i.e.*, $(m_z/m)^2 = 0$, and axial states, *i.e.*, $(m_z/m)^2 = 1$, *i.e.*, white areas comprising points (A1) and (E1) in Fig. 8 (*cf.* also Fig. 7). The

^{¶¶}In the case of even number of rings, *i.e.*, $N_{\text{tot}} = 2k$, we take two rings above/below $z = L/2$.

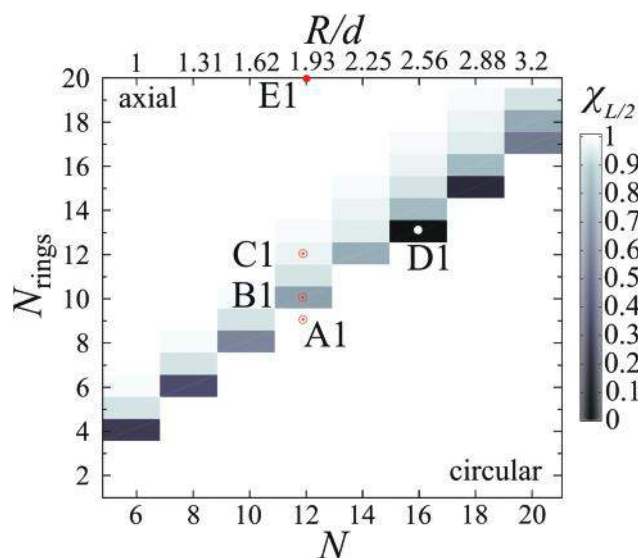


Fig. 8 State diagram of AA tubes. It is shown in 2D tube length-curvature parameter space, *i.e.*, $L(R)$ or $N_{\text{rings}}(N)$, with clear indication of axial, circular and transitional vortex magnetization states. The coloring method based on order parameter $\chi_{L/2}$, defined in eqn (9), is applied. The order parameter $\chi_{L/2}$ is zero in axial and circular magnetic states, *i.e.*, when the magnetic texture is parallel to tube geometry, and equal to unity when the magnetic structure is turned by 45° (*i.e.* equidistant from axial and circular magnetization).

state diagram contains three regions corresponding to the three classes of equilibrium states. We observe pure circular magnetization with no axial dipole component for short tubes. In the transition state, there is a change from the dominantly axial orientation of dipoles in the middle of the tube ($z = L/2$) to a vortex-like orientation at tube's ends ($z = 0, L$). We observe that a transition from a vortex to an axial state follows roughly a linear trend for $4 \leq N \leq 14$. For $N = 16$ this trend is broken and the transition occurs earlier (after a single additional ring and not two). The resulting local order parameter is very small, $\chi_{L/2} \approx 0$. This is all a result of a strong local circulation, *i.e.*, $\theta = \pi/4$, $m_\phi = m_z = m/\sqrt{2}$, *cf.* value of $\chi_{L/2}$ at point (D1) in Fig. 8 and also visualization in Fig. 7.

Finite AB tubes. In the case of AB stacked tubes (triangular lattice), for $N = 12$ curvature, the circular state is stable for ($2 \leq N_{\text{rings}} \lesssim 70$) rings. After that, only dipoles in the middle of the tube significantly start to change magnetization, *cf.* Fig. 9(A2) and (B2). Only when the local order parameter, $\chi_{L/2} \approx 0$, we observe a change in the dependence of cohesive energy on tube's length N_{rings} , *cf.* Fig. 9(C2) and Fig. 6 for $N_{\text{rings}} = 85$. The energy for configuration (C2) is $u_{\text{AB}}^{12,85} = -2.6895$. The similarity of observed state transitions with increasing length of the dipolar tube to state transitions observed in solid magnetic nanotubes is striking.^{13,18} This is surprising due to the absence of the exchange interaction in dipolar tubes. We call the transition state $\chi_{L/2} \approx 0$ the *helical state*. The helical state, both in solid and dipolar tubes, is a result of the interplay between tube's curvature and length. We find three equivalent

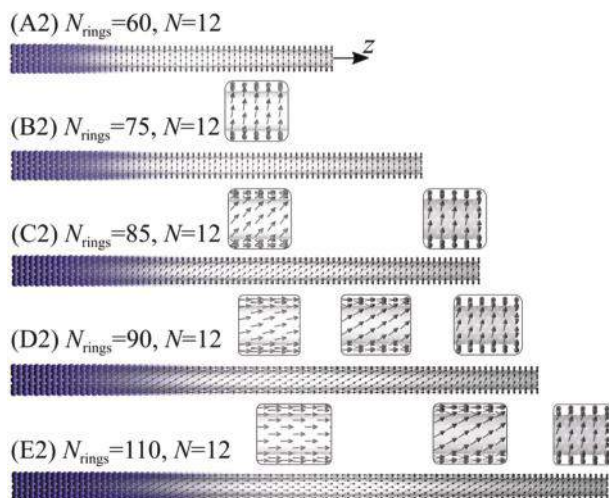


Fig. 9 Illustrative examples of characteristic ground state magnetization for tubes with AB stacking.

states: clockwise, anti-clockwise and symmetric, within numerical accuracy, as a result of broken symmetry.

There are three clear differences between transitions from circular to axial states in AA and AB tubes, as seen in Fig. 8 and 10:

- The transition occurs at smaller tube lengths in the case of AA tubes, *i.e.*, in AA-tubes for curvature $N = 12$ transition is at $N_{\text{rings}} \approx 10$ while for AB-tubes it will occur at $N_{\text{rings}} \approx 80$;
- For AA tubes, the circular state sharply changes into the transitional vortex state when the threshold length is reached. In the case of AB tubes, the transition through the helical state is gradual with increasing length;
- Edge effects at tube's ends, *i.e.*, in the vicinity of $z = (0, L)$, are much stronger in AB tubes than in the case of AA tubes, *i.e.*, in AB-tubes for curvature $N = 12$ they extend over $\Delta N_{\text{rings}} = 30$ rings on each side of the tube, compared to only up to $\Delta N_{\text{rings}} = 3$ rings.

It is insightful to compare the energies of obtained finite tubular magnetizations with the limits of an infinite planar triangular and square lattice. In the case of AB tubes for $N = 12$, $N_{\text{rings}} = 200$, we obtain $u_{\text{AB}}^{12,200} = -2.7203$ and an energy deviation of about 15% from the infinite triangular plane case. This is essentially due to the edge effects that are still non-negligible. For much shorter AA tubes, *i.e.*, $N = 12$, $N_{\text{rings}} = 35$, we are with $u_{\text{AB}}^{12,35} = -2.5233$ within 10% from the infinite plane case.

At this point we would like to draw a comparison with solid-state MNTs. In MNTs the magnetic properties are mainly defined by dipole-dipole and exchange interactions, wherein the latter stems from quantum mechanical considerations. Exchange is a short-range interaction that, in micromagnetic approximation, is typically characterized by the exchange length (l_{ex}) that is not larger than a few tens of nanometers. The quantum mechanics signature in magnetic states of nanotubes can be neglected whether by choosing curvature $R \gg l_{\text{ex}}$ or reducing the exchange length to zero. The magnetic equi-

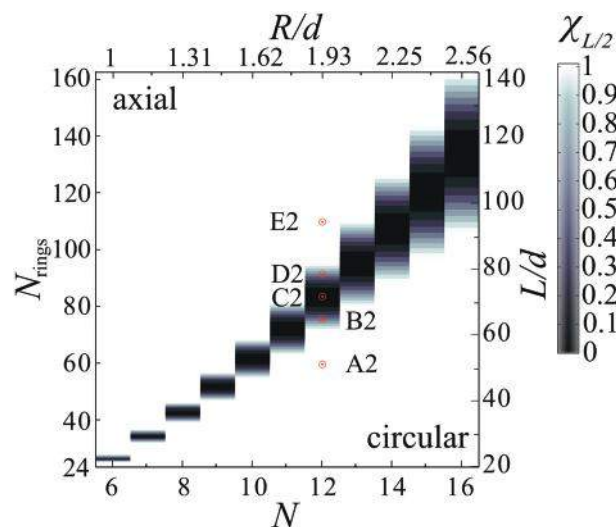


Fig. 10 State diagram of AB tubes. It is shown in 2D tube length-curvature parameter space, *i.e.*, $L(R)$ or $N_{\text{rings}}(N)$, with clear indication of axial, circular and transition helical states. The coloring method $\chi_{L/2}$, defined in eqn (9), is applied. The order parameter $\chi_{L/2}$ is zero in axial and circular magnetic states, *i.e.*, when the magnetic texture is parallel to tube geometry, and equal to unity when the magnetic structure is turned by 45° (*i.e.* equidistant from axial and circular magnetization).

brum states of MNTs are mostly defined according to the ratio between MNT dimensions, such as their length L and radius R . The radii $R_{\text{F}} \sim \eta l_{\text{ex}}$ and $R_{\text{V}} \sim \gamma l_{\text{ex}}$ are critical transition radii with $\eta = 1-10$ and $\gamma = 10-50$. In MNTs with $L \geq R$ and $R < R_{\text{F}}$ uniform axial states are the preferred ground states. At $R_{\text{F}} < R < R_{\text{V}}$ and $L \gg R$ the magnetization is in the axial state (*i.e.*, only the center of the tube is axially magnetized), and if the length is reduced to $L \approx R$ magnetization turns into the circular state. The helical state appears as a transition state between the axial and circular states as a result of a reduction of the tube's length. All these states have been predicted theoretically^{12,13} and measured experimentally just recently.¹⁴⁻¹⁸ Thus, solid state MNTs with weak or comparable exchange interaction regarding the dipolar interaction will exhibit a circular magnetic order. This is not the case in dipolar tubes, consisting of discrete (nano- or even micro-particles), where exchange interaction is not present. And still, we could find all states seen in MNTs (circular, helical, and axial). We also observe similar tendencies with respect to the tube's size. We find the circular state in short, the helical intermediary state in medium, and the axial state in long dipolar tubes.

The principal difference between the AA- and AB-tubes is the total magnetic moment. For AA-tubes the total magnetic moment is zero. In the case of AB-tubes, the axial and helical states have a finite total magnetic moment, just like MNT counterparts. Fig. 11 shows the dependence of magnetic field intensity on radial distance from the center of AA and AB tubes. The magnetic field at the closest approach of the probe particle $\Delta r/d = 1$ is always smaller than the magnetic field of a single constitutive particle $B/B_0 = 1$ in side by side $\uparrow\downarrow$ configur-

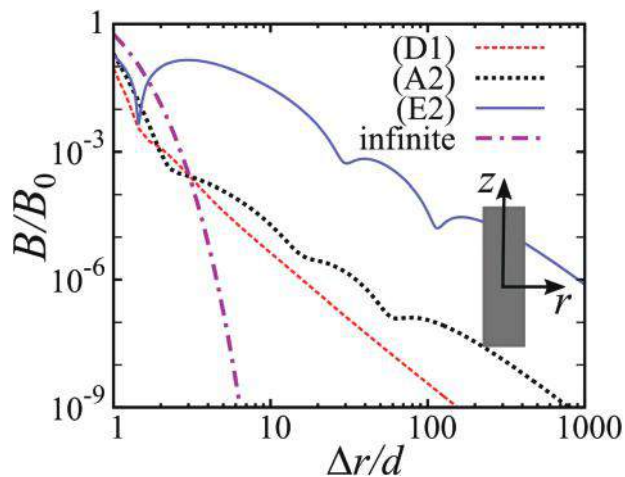


Fig. 11 Dependence of the intensity of the magnetic field B from radial distance $\Delta r = r - R$ from the center of dipolar tubes, where R is the tube radius. The magnetic field is given for the (D1) AA tube in the vortex state $L/d = 13$ long and with curvature $N = 16$, (A2) the circularly magnetized AB tube with $L/d \approx 53$ and $N = 12$, (E2) the axially magnetized AB tube with $L/d \approx 98$ and $N = 12$, and the uniformly axially magnetized infinite AB tube with the same curvature ($N = 12$). The distance $\Delta r/d = 1$ is the distance of the closest approach of the particle to the tube. The configurations of AA and AB tubes are shown in Fig. 7 and 9, respectively. We used length scale $d = 50 \mu\text{m}$. Reference magnetic field is $B_0 = 1 \mu\text{T}$ for two particles with magnetic moments $1.15 \text{ A } \mu\text{m}^2$.

ation. The vortex state in the AA tube results in a $B_{D1}(1)/B_0 = 0.09$, while in the case of AB tubes $B_{E2}(1)/B_0 = 0.19$. The smallest structure shown in Fig. 11 has more than 200 constitutive particles, *i.e.*, the (D1) AA tube in the vortex state. In all three cases of the finite tubes, the intensity of magnetic field far from the tube follows the power law on distance, *i.e.*, $B \sim \Delta r^{-3}$ for $\Delta r/L \gg 1$. Only in axially magnetized infinite AB tubes the magnetic field exponentially decays with distance $\Delta r/d$ and therefore fulfills flux closure, *cf.* also ref. 62. This result is not surprising from the micromagnetic point of view since in a finite object a singularity-free solution cannot exist for topological reasons.⁶³ Only if the system is infinite at least in one dimension, micromagnetic solutions may be constructed. As a result, magnetostatic energy is minimized, leading to similar ground states in finite MNTs and dipolar tubes, that tend to reduce the stray field but cannot make it negligible.

4.4. Chirality and degeneracy breakup

In this section, we would like to point out, how chirality of the structure influences the energy barriers between different states in dipolar tubes. The ribbons of assembled particles can be rolled at different (“chiral”) angles θ . In our self assembly experiment, combination of the magnetic field along the wire and the circular electromagnetic field will result in creating ferromagnetic tubes with a specific chiral angle. We will only briefly analyse limiting cases which are actually the most interesting ones from the point of the metastability (*i.e.*, energy differences between different states). Antiferromagnetic tubes need to be created on a cylindrical structure with a tilted

pattern. The radius of these tubes will depend on the lattice structure (*i.e.*, square or triangular) and chiral angle. Here, we will demonstrate how the combination of the rolling angle and radius decides the tube’s energy. In the previous section, we have calculated energies of different states for tubes obtained by stacking of the rings. In the following text, we will follow energy gains and losses due to change in the chirality (orientation) of tube’s lattice with its axis $\theta = 30^\circ$ in triangular and $\theta = 45^\circ$ in square lattices.

First, we will compare the energy of the infinite AB tube shown in Fig. 5(b) and the ZZ tube shown in Fig. 1(c). While the ZZ-tube is aligned with the tube’s axis, the ribbon generating AB tube is rolled under a 60° angle, see Fig. 1(b). The energy of the circular state in Fig. 5(b) is $u_{AB}^{\text{circular}} = -2.694$ for the unit ring of $N = 12$ particles and $\theta = 0$. The helical state ($\theta = \pi/3$), in Fig. 5(a), is more energetically favorable, $u_{AB}^{\text{helical}} = -2.7315$. The axially magnetized state has energy $u_{AB}^{\text{axial}} = -2.7441$ for $\theta = \pi/2$. The difference between circular and axial state energies is small, *i.e.*, less than 2% of the total energy. Already at moderate curvatures, *i.e.*, $R/d = 1.932$, the difference in the infinite triangular plane value (u_{AB}^∞) is small, $u_{AB}^{\text{axial}} - u_{AB}^\infty \approx 0.015$ or roughly 0.5% of the total energy value. If we chose chirality to align the tube’s structure with its axis, as in ZZ tubes shown in Fig. 1(c), the energy converges faster to the infinite triangular plane value. The energy difference, for the system shown in Fig. 1(c), is $u_{ZZ}^{\text{axial}} - u_{AB}^\infty \approx 0.001$. Improved convergence of the axial state comes with a marginal increase of energy difference to circular and helical states of less than 3% of the total energy value. The energies of circular and helical states, for the ZZ tube in Fig. 1(c), are $u_2^{\text{circular}} = -2.618$ and $u_2^{\text{helical}} = -2.7$, respectively. We can conclude that by changing chirality we can manipulate energy differences between different states.

The AA tube’s square lattice is aligned with the tube’s axis, see Fig. 5(a). What will happen if we turn the tube’s lattice structure by 45° ? We show the configurations and results of energy calculations in Fig. 12. To demonstrate the stability of the structure it is also realized with neodymium magnetic spheres. The striking feature is a comparably small energy increase of $u_\infty^{\text{helical}} - u_\infty^{\text{vortex}} = 1.8 \times 10^{-4}$, *cf.* Fig. 12(c). This means that in realization with a finite temperature this system would be degenerate. Since an infinite tube can never be realized, one could ask how significant is the influence of the edges? In this context we calculate energies of finite tubes consisting of $N = 208$ particles, *i.e.*, which correspond exactly to the helical and vortex configurations shown in Fig. 12(A) and (B), and obtain values $u_{208}^{\text{vortex}} = -2.4527$ and $u_{208}^{\text{helical}} = -2.4495$, respectively. Therefore, at least in these two finite configurations the energy is relatively close to each other (within 2%) and to that of infinite tubes (*i.e.*, within 5%). In contrast to AA tubes in the previous section, the local magnetic order of finite and infinite tubes shown in Fig. 12 is quite similar. The

|||| In the ZZ tube, particles form chains (so called, filaments) parallel to the tube’s axis.

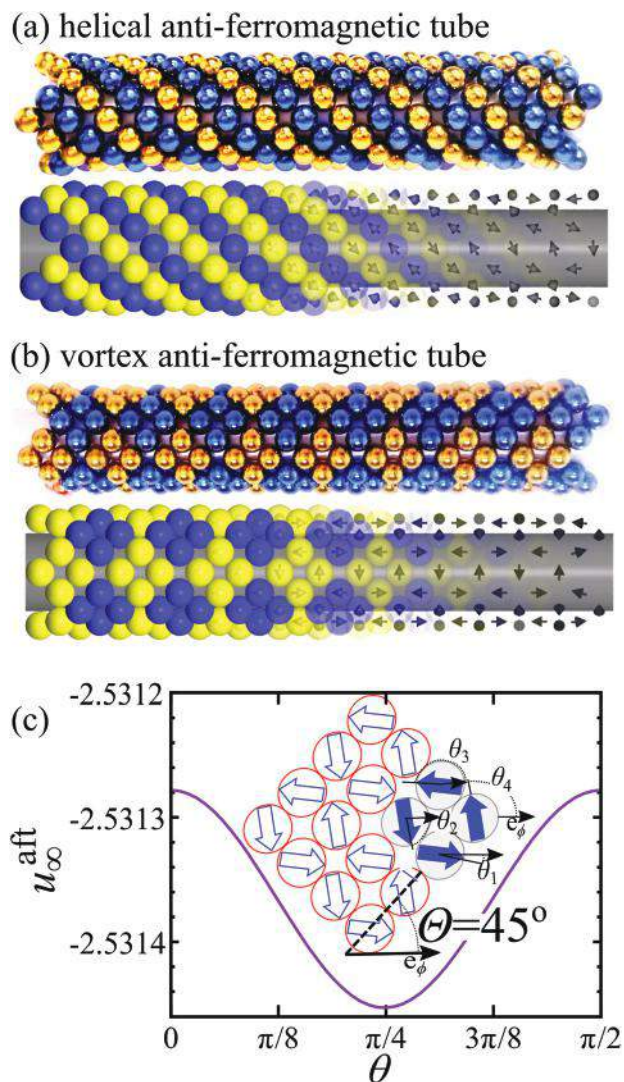


Fig. 12 The helical (a) and vortex (b) anti-ferromagnetic states realized with neodymium magnets (in upper panels) and magnetization pattern. The energy spectrum of configurations (c) for the same infinite configuration with respect to angle θ , where $\theta_1 = \theta$, $\theta_2 = -\theta$, $\theta_3 = \pi + \theta$, and $\theta_4 = \pi - \theta$. The case $\theta = \pi/4$ corresponds to helical and $\theta = 0, \pi/2$ vortex state. The chiral angle, *i.e.*, the angle between thread of particles and tangent to cylinder radius, is $\theta = 45^\circ$ and is also marked in the planar scheme of the system in panel (c). To convert results in real units, for example the reference magnetic energies $U_{11} = 10^{-18}$ J or 67×10^{-18} J could be used that correspond to $256k_B T$ or $1.6 \times 10^4 k_B T$, in cases of particles with magnetic moments $m = 1.15 \text{ A } \mu\text{m}^2$ or $9.2 \text{ A } \mu\text{m}^2$, respectively, where $T = 300 \text{ K}$ is the temperature and k_B is Boltzmann's constant.

reason is that the tubes finish the crown (zig-zag) ring which prevents formation of a continuous head-tail magnetic order.

5. Conclusion and outlook

In the first part of the paper, we demonstrate that using magnetic particles with a permanent dipolar moment gives

additional design freedom for an experiment recently proposed. Injection of an electrical current into a conductor wire induces an electromagnetic field. The radial gradient of this field owns the ability to attract magnetic beads. The particles, therefore, assemble on the wire surface. We explored the intensity of the electromagnetic field that leads to a transformation of the clusters attached to the wire into a single layer tubular structure. We further analyse the limits on the injected currents to minimize the Joule heating and steer the particle assembly. In this regard, we have found a realistic range of currents and resulting electromagnetic fields at which the assembly of spheres and its magnetic orientation are stable and controllable. Our results are generic and can be scaled to many different systems. Once the current is switched off, the circular electromagnetic field disappears, and the particles stay assembled held by interparticle interactions. From this point on, the magnetization of colloidal particles turns and relaxes to the equilibrium configuration.

In the second part of the paper, we studied the curvature-induced breakup of the continuously degenerated state when a two-dimensional ribbon of spheres is curved and transferred to the cylinder. We show that different ferromagnetic states, observed previously,^{20,26} are a result of curvature induced energy barriers that lift the continuous degeneracy in the triangular lattice. We performed a systematic investigation of the degeneracy break-up as a function of the tube length and packing symmetry (square or triangular), which lead to a number of equilibrium magnetic states of dipolar tubes. For triangular packing, we show that dipolar tubes transcend the scale. Their equilibrium states mimic the ground magnetization of magnetic nanotubes where the dipolar interaction is either comparable or dominate over the exchange interaction. Indeed, we found the circular state in short tubes, the axial state in long tubes, and the helical state in between. This is an important conclusion since it shows that all these states could exist in magnetic nanotubes also without exchange interactions. We find that the planar square lattice has a continuously degenerate antiferromagnetic state. In tubes with the square lattice, we have found remarkable magnetic vortex configurations formed spontaneously. Such a configuration was observed previously only in a system of magnetic cubes due to intricate relation between the crystallinity of the cubes and packing. Antiferromagnetic states have no analogous in the set of magnetic ground states in continuum magnetic nanotubes^{13,21} and are remarkable due to their curvature-induced stability and non-colinear texture. Indeed, these non-colinear states can be very attractive for further research on magnetization dynamics (reversal processes mediated by domain wall propagation and spin-waves) due to the macroscopic scale of dipolar tubes, and therefore less complexity in experiments.

In the context of curvilinear nanomagnetism,^{13,25} the present theoretical result could represent a departure point and alternative means to test and explore equilibrium and dynamic magnetic properties at macroscopic scales. The dipolar tubes present an alternative technique to reduce the complexity of experiments and a platform to prove concepts

for applications in magnonics at more accessible parameters (reduced frequencies and macroscopic wavelengths). The experimental realization of cylindrical magnetic objects is very demanding since curvature effects might be overshadowed by wall pinning on imperfections, such as grain boundaries and edges.²¹ The realization of presented quasi-one-dimensional or edge free ferromagnets and antiferromagnets would create an accessible platform for testing concepts of spin-based electronics (e.g., Cherenkov-like spin wave emission^{22,64} or curvature induced non-reciprocities in magnonics^{25,65}) and information technologies by getting around a requirement of robust magnetic uniformity at temperatures of technological relevance. An additional application of the tubular assemblies of dipoles could be modeling of the ordered planar systems due to the absence of the lateral edges in curved geometry and low energy barriers. Macroscopic dipoles were, for instance, successfully used to study frustrated states in spin glasses.⁶ Although the previous approach cannot be applied straightforwardly to ordered planar structures, since edge effects could overshadow properties like the response to magnetization reversal, it can motivate further studies on this topic.

Conflicts of interest

There are no conflicts to declare.

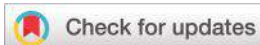
Acknowledgements

The authors acknowledge financial support from the European Commission H2020 project DAFNEOX (Grant No. 645658). Numerical calculations were run on the PARADOX supercomputing facility at the Scientific Computing Laboratory of the Institute of Physics Belgrade. I. S. and M. D. acknowledge support of the Ministry of Education, Science, and Technological Development of Republic of Serbia – projects ON171017 and III45018. I. S. and C. G. acknowledge the financial support received by the Proyecto CONICYT PIA/Basal FB 0821 and PCI/atracción de capital humano avanzado del extranjero folio MEC80170122.

References

- 1 A. P. Ramirez, A. Hayashi, R. Cava, R. Siddharthan and B. Shastri, *Nature*, 1999, **399**, 333–335.
- 2 M. J. Gingras, *Introduction to frustrated magnetism*, Springer, 2011, pp. 293–329.
- 3 H. Diep, *Frustrated spin systems*, World Scientific, 2013.
- 4 J. Loehr, A. Ortiz-Ambriz and P. Tierno, *Phys. Rev. Lett.*, 2016, **117**, 168001.
- 5 J. W. F. Venderbos, M. Daghofer, J. van den Brink and S. Kumar, *Phys. Rev. Lett.*, 2011, **107**, 076405.
- 6 P. Mellado, A. Concha and L. Mahadevan, *Phys. Rev. Lett.*, 2012, **109**, 257203.
- 7 K. De'Bell, A. B. MacIsaac, I. N. Booth and J. P. Whitehead, *Phys. Rev. B: Condens. Matter Mater. Phys.*, 1997, **55**, 15108–15118.
- 8 S. Prakash and C. L. Henley, *Phys. Rev. B: Condens. Matter Mater. Phys.*, 1990, **42**, 6574–6589.
- 9 P. Weiss, *J. Phys. Theor. Appl.*, 1907, **6**, 661–690.
- 10 A. Hubert, *Phys. Status Solidi B*, 1969, **32**, 519–534.
- 11 A. Aharoni, *Introduction to the Theory of Ferromagnetism*, Clarendon Press, 2000, vol. 109.
- 12 J. Escrig, P. Landeros, D. Altbir, E. Vogel and P. Vargas, *J. Magn. Magn. Mater.*, 2007, **308**, 233–237.
- 13 P. Landeros, O. J. Suarez, A. Cuchillo and P. Vargas, *Phys. Rev. B: Condens. Matter Mater. Phys.*, 2009, **79**, 024404.
- 14 D. Weber, D. Ruffer, A. Buchter, F. Xue, E. Russo-Averchi, R. Huber, P. Berberich, J. Arbiol, A. Fontcuberta i Morral, D. Grundler and M. Poggio, *Nano Lett.*, 2012, **12**, 6139–6144.
- 15 D. Ruffer, R. Huber, P. Berberich, S. Albert, E. Russo-Averchi, M. Heiss, J. Arbiol, A. Fontcuberta i Morral and D. Grundler, *Nanoscale*, 2012, **4**, 4989–4995.
- 16 A. Buchter, J. Nagel, D. Ruffer, F. Xue, D. P. Weber, O. F. Kieler, T. Weimann, J. Kohlmann, A. B. Zorin, E. Russo-Averchi, R. Huber, P. Berberich, A. Fontcuberta i Morral, M. Kemmler, R. Kleiner, D. Koelle, D. Grundler and M. Poggio, *Phys. Rev. Lett.*, 2013, **111**, 067202.
- 17 A. Buchter, R. Wölbing, M. Wyss, O. F. Kieler, T. Weimann, J. Kohlmann, A. B. Zorin, D. Ruffer, F. Matteini, G. Tütüncüoğlu, F. Heimbach, A. Kleibert, A. Fontcuberta i Morral, D. Grundler, R. Kleiner, D. Koelle and M. Poggio, *Phys. Rev. B: Condens. Matter Mater. Phys.*, 2015, **92**, 214432.
- 18 M. Wyss, A. Mehlin, B. Gross, A. Buchter, A. Farhan, M. Buzzi, A. Kleibert, G. Tütüncüoğlu, F. Heimbach, A. Fontcuberta i Morral, D. Grundler and M. Poggio, *Phys. Rev. B: Condens. Matter Mater. Phys.*, 2017, **96**, 024423.
- 19 H. D. Salinas, J. Restrepo and Ö. Iglesias, *Sci. Rep.*, 2018, **8**, 10275.
- 20 I. Stanković, M. Dašić and R. Messina, *Soft Matter*, 2016, **12**, 3056–3065.
- 21 R. Streubel, P. Fischer, F. Kronast, V. P. Kravchuk, D. D. Sheka, Y. Gaididei, O. G. Schmidt and D. Makarov, *J. Phys. D: Appl. Phys.*, 2016, **49**, 363001.
- 22 M. Yan, C. Andreas, A. Kákay, F. García-Sánchez and R. Hertel, *Appl. Phys. Lett.*, 2011, **99**, 122505.
- 23 A. P. Chen, N. A. Usov, J. M. Blanco and J. Gonzalez, *J. Magn. Magn. Mater.*, 2007, **316**, e317–e319.
- 24 C.-R. Chang, C. M. Lee and J.-S. Yang, *Phys. Rev. B: Condens. Matter Mater. Phys.*, 1994, **50**, 6461–6464.
- 25 J. A. Otálora, M. Yan, H. Schultheiss, R. Hertel and A. Kákay, *Phys. Rev. Lett.*, 2016, **117**, 227203.
- 26 R. Messina, L. A. Khalil and I. Stanković, *Phys. Rev. E: Stat., Nonlinear, Soft Matter Phys.*, 2014, **89**, 011202.
- 27 J. Hernandez-Rojas, D. Chakrabarti and D. J. Wales, *Phys. Chem. Chem. Phys.*, 2016, **18**, 26579–26585.
- 28 D. Morphew and D. Chakrabarti, *Nanoscale*, 2018, **10**, 13875–13882.
- 29 D. Morphew and D. Chakrabarti, *Nanoscale*, 2015, **7**, 8343–8350.

- 30 A. Kuzyk, R. Schreiber, Z. Fan, G. Pardatscher, E.-M. Roller, A. Hoge, F. C. Simmel, A. O. Govorov and T. Liedl, *Nature*, 2012, **483**, 311–314.
- 31 Y. Zhang, F. Lu, K. G. Yager, D. van der Lelie and O. Gang, *Nat. Nanotechnol.*, 2013, **8**, 865–872.
- 32 Y. Zhou and T. Shimizu, *Chem. Mater.*, 2008, **20**, 625–633.
- 33 M. A. Correa-Duarte, M. Grzelczak, V. Salgueiriño Maceira, M. Giersig, L. M. Liz-Marzán, M. Farle, K. Sieradzki and R. Diaz, *J. Phys. Chem. B*, 2005, **109**, 19060–19063.
- 34 X. Liu, I. Marangon, G. Melinte, C. Wilhelm, C. Ménard-Moyon, B. P. Pichon, O. Ersen, K. Aubertin, W. Baaziz, C. Pham-Huu, S. Bégin-Colin, A. Bianco, F. Gazeau and D. Bégin, *ACS Nano*, 2014, **8**, 11290–11304.
- 35 J. Yan, M. Bloom, S. C. Bae, E. Luijten and S. Granick, *Nature*, 2012, **491**, 578–581.
- 36 D. Zerrouki, J. Baudry, D. Pine, P. Chaikin and J. Bibette, *Nature*, 2008, **455**, 380–382.
- 37 M. Chen, J. Kim, J. Liu, H. Fan and S. Sun, *J. Am. Chem. Soc.*, 2006, **128**, 7132–7133.
- 38 J. L. C. Huaman, S. Fukao, K. Shinoda and B. Jeyadevan, *CrystEngComm*, 2011, **13**, 3364–3369.
- 39 G. Singh, H. Chan, A. Baskin, E. Gelman, N. Repnin, P. Král and R. Klajn, *Science*, 2014, **345**, 1149–1153.
- 40 S. Mehdizadeh Taheri, M. Michaelis, T. Friedrich, B. Förster, M. Drechsler, F. M. Römer, P. Bösecke, T. Narayanan, B. Weber, I. Rehberg, S. Rosenfeldt and S. Förster, *Proc. Natl. Acad. Sci. U. S. A.*, 2015, **112**, 14484–14489.
- 41 H.-B. Sun and S. Kawata, *NMR 3D Analysis Photopolymerization*, Springer, 2004, pp. 169–273.
- 42 Y.-Y. Cao, N. Takeyasu, T. Tanaka, X.-M. Duan and S. Kawata, *Small*, 2009, **5**, 1144–1148.
- 43 G. Williams, M. Hunt, B. Boehm, A. May, M. Taverne, D. Ho, S. Giblin, D. Read, J. Rarity, R. Allenspach and S. Ladak, *Nano Res.*, 2018, **11**, 845–854.
- 44 L. Bécu, M. Basler, M. L. Kulić and I. M. Kulić, *Eur. Phys. J. E: Soft Matter Biol. Phys.*, 2017, **40**, 107.
- 45 X.-M. Lin and A. C. Samia, *J. Magn. Magn. Mater.*, 2006, **305**, 100–109.
- 46 S. Sacanna, L. Rossi and D. J. Pine, *J. Am. Chem. Soc.*, 2012, **134**, 6112–6115.
- 47 W. Lowrie, *Fundamentals of geophysics*, Cambridge university press, 2007.
- 48 C.-L. Fang, K. Qian, J. Zhu, S. Wang, X. Lv and S.-H. Yu, *Nanotechnology*, 2008, **19**, 125601.
- 49 Y. Min, M. Akbulut, K. Kristiansen, Y. Golan and J. Israelachvili, *Nat. Mater.*, 2008, **7**, 527EP.
- 50 W. H. Stockmayer, *J. Chem. Phys.*, 1941, **9**, 398–402.
- 51 M. A. Miller and D. J. Wales, *J. Phys. Chem. B*, 2005, **109**, 23109–23112.
- 52 A. Baskin, W.-Y. Lo and P. Král, *ACS Nano*, 2012, **6**, 6083–6090.
- 53 A.-P. Hynninen and M. Dijkstra, *Phys. Rev. Lett.*, 2005, **94**, 138303.
- 54 S. Plimpton, *J. Comput. Phys.*, 1995, **117**, 1–19.
- 55 R. Barrett, M. W. Berry, T. F. Chan, J. Demmel, J. Donato, J. Dongarra, V. Eijkhout, R. Pozo, C. Romine and H. Van der Vorst, *Templates for the solution of linear systems: building blocks for iterative methods*, Siam, 1994, vol. 43.
- 56 A. Concha, D. Aguayo and P. Mellado, *Phys. Rev. Lett.*, 2018, **120**, 157202.
- 57 D. Wood, C. Santangelo and A. Dinsmore, *Soft Matter*, 2013, **9**, 10016–10024.
- 58 D. Vella, E. du Pontavice, C. L. Hall and A. Goriely, *Proc. R. Soc. London, Ser. A*, 2013, **470**, 20130609.
- 59 A. Grzybowski and A. Bródka, *Mol. Phys.*, 2003, **101**, 1079–1088.
- 60 J. G. Donaldson, P. Linse and S. S. Kantorovich, *Nanoscale*, 2017, **9**, 6448–6462.
- 61 J. G. Donaldson and S. S. Kantorovich, *Nanoscale*, 2015, **7**, 3217–3228.
- 62 R. Tao and J. M. Sun, *Phys. Rev. Lett.*, 1991, **67**, 398–401.
- 63 E. Feldtkeller, *IEEE Trans. Magn.*, 2017, **53**, 1–8.
- 64 J. A. Otálora, J. A. López-López, P. Vargas and P. Landeros, *Appl. Phys. Lett.*, 2012, **100**, 072407.
- 65 J. A. Otálora, A. Kákay, J. Lindner, H. Schultheiss, A. Thomas, J. Fassbender and K. Nielsch, *Phys. Rev. B: Condens. Matter Mater. Phys.*, 2018, **98**, 014403.



Cite this: *Nanoscale*, 2019, **11**, 2536

Correction: A platform for nanomagnetism – assembled ferromagnetic and antiferromagnetic dipolar tubes

Igor Stanković,^{*a} Miljan Dašić,^a Jorge A. Otálora^b and Carlos García^c

DOI: 10.1039/c9nr90017a

rsc.li/nanoscale

Correction for 'A platform for nanomagnetism – assembled ferromagnetic and antiferromagnetic dipolar tubes' by Igor Stanković *et al.*, *Nanoscale*, 2019, DOI: 10.1039/c8nr06936k.

The authors of this manuscript have noticed that the affiliations for Jorge A. Otálora and Carlos García were listed incorrectly in the original publication. A corrected affiliation list has therefore been provided with this correction.

The Royal Society of Chemistry apologises for these errors and any consequent inconvenience to authors and readers.

^aScientific Computing Laboratory, Center for the Study of Complex Systems, Institute of Physics Belgrade, University of Belgrade, 11080 Belgrade, Serbia.

E-mail: igor.stankovic@ipb.ac.rs

^bInstitute for Metallic Materials at the Leibniz Institute for Solid State and Materials Research, IFW, 01069 Dresden, Germany

^cDepartamento de Física & Centro Científico Tecnológico de Valparaíso-CCTVal, Universidad Técnica Federico Santa María, Av. España 1680, Casilla 110-V, Valparaíso, Chile





Cite this: DOI: 10.1039/c5sm02774h

Structure and cohesive energy of dipolar helices

Igor Stanković,^{*a} Miljan Dašić^a and René Messina^bReceived 11th November 2015,
Accepted 18th January 2016

DOI: 10.1039/c5sm02774h

www.rsc.org/softmatter

This paper deals with the investigation of cohesive energy in dipolar helices made up of hard spheres. Such tubular helical structures are ubiquitous objects in biological systems. We observe a complex dependence of cohesive energy on surface packing fraction and dipole moment distribution. As far as single helices are concerned, the lowest cohesive energy is achieved at the highest surface packing fraction. Besides, a striking non-monotonic behavior is reported for the cohesive energy as a function of the surface packing fraction. For multiple helices, we discover a new phase, exhibiting markedly higher cohesive energy. This phase is referred to as ZZ tube consisting of stacked crown rings (reminiscent of a pile of zig-zag rings), resulting in a local triangular arrangement with densely packed filaments parallel to the tube axis.

1 Introduction

Particles with permanent dipole moments, such as magnetic particles, are well known for their outstanding self-assembly properties.^{1–3} In biology, tubular and helical structures are relevant self-assembled objects, for instance, found in bacterial flagella⁴ and microtubules.^{5,6} Other instances of such tubular/helical structures can be found in various materials with specific building units that can be: carbon atoms,⁷ coiled carbon nanotubes,⁸ DNA,⁹ nanoparticles,¹⁰ or amphiphilic molecules.^{11–13} Self organization of cubic magnetic nanoparticles¹⁴ and asymmetric colloidal magnetic dumbbells¹⁵ into helical architectures were recently reported without the need for pre-existing templates.

On a more theoretical side, hard spherical particles confined in narrow cylinders spontaneously assemble into helical structures^{16,17} and this is also seen experimentally.¹⁸ Hard-spheres with permanent moment can be employed as a paradigm for more complex helical molecular superstructures,¹⁹ or microtubules.^{20,21} The pioneering theoretical work of Jacobs and Bean²² and later that of de Gennes and Pincus²³ shed some light on the microstructure of self-assembled unconstrained (spherical) dipoles. More recently, the paper²⁴ advocated the ground states of self-assembled magnetic structures. The authors proved that for a sufficiently high number of particles the ground state is obtained *via* ring stacking into tubes.²⁴ On the other hand, Vella *et al.*²⁵ showed an illustrative example in which a macroscopic straight portion of the chain spontaneously wraps itself building a tube. At larger scales, the Janus chain model was able to reproduce well the formation of superstructures and double helical conformations

of amphiphilic molecules.^{26,27} The competition between toroidal and rod-like conformations, as possible ground states for DNA condensation, was studied using a polymer chain model function of stiffness and short range interactions.^{28,29} Also the recently introduced polymorphic dynamics model^{30,31} was able to reproduce the behavior of the microtubule lattice based on a rough understanding of underlying atomic level processes. The general scientific problem of understanding the processes by which building blocks (dipoles) self-assemble and obtain their functionality is highly challenging.^{32–36}

The goal of this paper is to address the intimate link between microstructure and cohesive energy. Tubular helical structures can be obtained either (i) through ring stacking or (ii) by rolling one or multiple helices on a confining cylindrical surface (Section 2). The dipolar interaction model is introduced and a link between the dipole distribution and the microstructure is established in Section 3. In Section 4, starting from the most simple case corresponding to a single helix, we discuss the relationship between the surface packing and the resulting macroscopic properties such as the cohesive energy or overall polarization. Then, the more complex situation of multiple helices with densely packed constitutive particles is addressed. There, the degree of alignment (especially in the ground state) between the dipole moment orientation and the helix axis is analyzed.

2 Geometry of helices

2.1 Geometry of the single helix

In the framework of this paper, helices are composed of hard spherical particles and confined to a cylinder's surface, *i.e.*, the helices are created by rolling threads on the cylindrical surface of radius R_{cyl} . Geometrical parameters that define a single helix are: the azimuthal angular shift Γ between the centers of two

^a Scientific Computing Laboratory, Institute of Physics Belgrade, University of Belgrade, Pregrevica 118, 11080 Belgrade, Serbia. E-mail: igor.stankovic@ipb.ac.rs

^b Institut de Chimie, Physique et Matériaux (ICPM), Université de Lorraine, 1 Bd. Arago, 57070 Metz, France

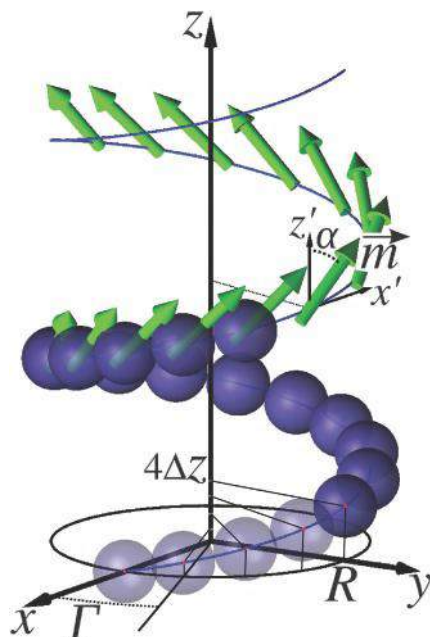


Fig. 1 Illustration of a single helix with the relevant geometrical parameters ($R, \Gamma, \Delta z$) labelled. The bold line connecting spherical particle centers represents the backbone of the helix. In the upper part of the figure, the azimuthal dipole moment orientation α is defined in a local coordinate system with its origin corresponding to the particle center. The z' -axis is parallel to the cylinder axis.

successive particles and the radius of the helix $R = R_{\text{cyl}} + d/2$, where d stands for the hard sphere diameter, see Fig. 1. The radius R represents physically the distance of the closest approach between the cylinder axis and the center of the spherical particle.

The Cartesian coordinates of particle i in a single helix are calculated as: $x_i = R \cos(i\Gamma)$, $y_i = R \sin(i\Gamma)$, and $z_i = i\Delta z$, where $i \in Z$ and assuming that one particle is at $(x, y, z) = (R, 0, 0)$. The distance between the centers of each two successive particles along the helix axis is labelled Δz , see Fig. 1. When constructing a helix, its radius R and the azimuthal angular distance Γ have to be chosen in a way that ensures non-overlapping of hard spheres. The non-overlapping constraint is expressed for any two particles i, j as

$|\overline{r}_{ij}| \geq d$. Since the helix thread is connected everywhere, any two successive particles are touching. We can obtain Δz as a function of other two variables: $\Delta z = \sqrt{d^2 + 2(\cos \Gamma - 1)R^2}$. Thereby, variables Δz , R and Γ are not independent. Clearly, with decreasing Δz (*i.e.*, increasing Γ) helices become more compact. Because of the connectivity, every particle in a helix has at least two neighbors, *i.e.*, the coordination number, n_c , is always greater or equal than two ($n_c \geq 2$). The highest packing density of the particles for the prescribed confinement radius R will be achieved when the successive helix turns touch. In this situation of touching turns, the coordination number n_c can be either four or six. Therefore, in general, $n_c \in \{2, 4, 6\}$, where the case $n_c = 2$ corresponds to non-touching turns. Based on the coordination number n_c , we can classify helices as follows (see Fig. 2a–c). Examples of helices with two neighbors $n_c = 2$ and four neighbors $n_c = 4$ at a prescribed cylindrical confinement, *e.g.*, $R/d = 1.78$, are sketched in Fig. 2a and b, respectively. For a number of well-defined radii, as discussed later in this paper, densely packed helices with six neighbors ($n_c = 6$) can be formed, see Fig. 2c. In the following sections, we will also investigate stacked rings forming the so-called tubes, also depicted in Fig. 2d–f.

2.2 Order parameters for single helices

The surface packing fraction, $\eta = S/S_{\text{avail}}$, is defined as the ratio of the area $S = \pi d^2/4$ covered by one particle and the area available for one particle S_{avail} , in an unrolled configuration.

Following the definition of the surface packing density we obtain:[†]

$$\eta = \frac{d^2}{8\Delta z R}. \quad (1)$$

For comparison we are also going to derive the packing fraction for the tubes:[‡]

• The surface packing fraction of AA tubes is given by $\eta_{\text{AA}} = N_{\text{ring}} d / 8R_{\text{AA}}$ for an AA tube with N_{ring} particles per ring and the confinement radius $R_{\text{AA}}/d = 1/[2\sin(\pi/N_{\text{ring}})]$, see Fig. 2d for a microstructure with $R_{\text{AA}}/d = 1.93$.

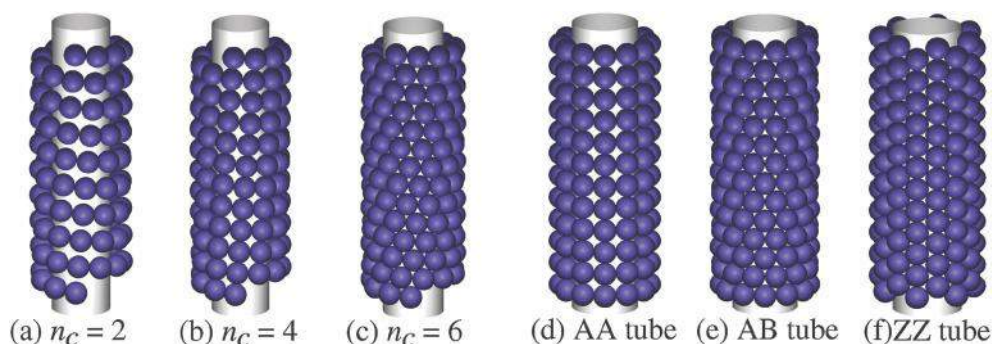


Fig. 2 Illustration of different classes of helices, based on the coordination number $n_c = 2, 4$, and 6 . (a) Helix with non-touching turns ($n_c = 2$). (b) Helix with touching turns ($n_c = 4$). (c) Densely packed helix ($n_c = 6$). The other panels illustrate the so-called (d) AA, (e) AB, and (f) ZZ tubes. The tubes can be created by strict axial stacking of unit rings. For AA and AB tubes unit rings are flat, whereas, for ZZ tubes the unit ring has a crown shape (reminiscent of the pile of 'zig-zag' rings). The radii of AA and AB tubes are the same $R/d = 1.93$.

• Similarly, for AB tubes, the packing fraction is $\eta_{AB} = N_{\text{ring}}d^2/8R_{AB}\Delta z_{AB}$, with $R_{AB} = R_{AA}$. Here, the elevation Δz_{AB} between two consecutive rings is:

$$\Delta z_{AB} = (d/2)\sqrt{2 + 2\cos(\pi/N) - \cos^2(\pi/N)}. \quad (2)$$

• For ZZ tubes, the packing fraction is $\eta_{ZZ} = N_{\text{ring}}d/8R_{ZZ}$, with the confinement radius $R_{ZZ}/d = \sqrt{3}/[4\sin(\pi/N_{\text{ring}})]$.

To further characterize the helical microstructures, we introduce an additional geometrical order parameter ξ which is valid for $n_c = 4$ and 6. This order parameter connects an individual reference particle 0 located at \vec{r}_0 in the helix with its two neighbors: its immediate successive particle 1 in the turn ($\vec{r}_{01} = \vec{r}_1 - \vec{r}_0$) and a neighboring particle 2 from the next turn ($\vec{r}_{02} = \vec{r}_2 - \vec{r}_0$), see Fig. 3(a).

The angular coordination order parameter is conveniently defined as:

$$\xi = 2 \frac{|\vec{r}_{01} \cdot \vec{r}_{02}|}{d^2}. \quad (3)$$

In the two limiting cases, the angular coordination order parameter has values: $\xi_{\text{min}} = 0$, for a locally square lattice on a cylinder (e.g., AA tubes, check Fig. 2d) and $\xi_{\text{max}} = 1$, for a locally triangular lattice (e.g. AB tubes, check Fig. 2e). In all other cases, the value of the angular coordination order parameter ξ is between those two extreme values, i.e., $0 < \xi < 1$.

2.3 Multiple helices at high surface packing fraction

The densely packed helices ($n_c = 6$) can be created, in analogy with carbon nanotubes, by rolling a ribbon of a triangular lattice on a cylinder surface.³⁷ We deal with cylindrical geometry, infinite in one direction. We can generate these helical structures by periodical reproduction of a curved patch (unit cell) along the helical line with spanning vectors (\vec{a}_1, \vec{a}_2). This curved unit cell has n_1 particles along the \vec{a}_1 direction and n_2 particles in the \vec{a}_2 direction.†

Since we deal with hard spheres and we aim to build very dense structures, the parameter space ($R, \Delta z, n_1, n_2$) is significantly restricted. We are going to find out that only two of these parameters are independent. There exists a relationship linking the elevation angle $\Theta = \arcsin(\Delta z/d)$ and the confinement radius R , see ref. 37. Bearing in mind that for any pair (n_1, n_2) or equivalently (n_2, n_1), we have a unique corresponding structure

† The available area per particle is $S_{\text{avail}} = 2\pi R\Delta z$, where the distance between successive particles along the tube axis is Δz . We take for the surface covered by particle $S = \pi d^2/4$, i.e., neglecting curvature. This results in a small overestimation of the packing fraction (less than 2% for large curvatures, e.g., $R/d = \sqrt{3}/2$).

‡ The tubes are obtained *via* ring stacking. It is convenient to calculate the surface packing fraction as the ratio of the area covered by the particles in a unit ring and the available area per ring. The surface covered is $S = N_{\text{ring}}\pi d^2/4$. The available area per ring is $S_{\text{avail}} = 2\pi R\Delta z$, where Δz is the distance between successive rings. The distance between successive rings is $\Delta z = d$ for AA and ZZ tubes.

§ The values n_1 and n_2 can be seen as the two possible widths of the ribbon generating the same helical structure.

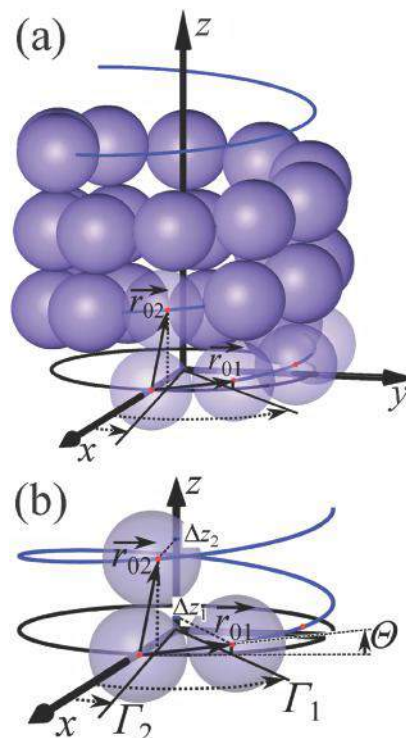


Fig. 3 (a) Illustration of a helix made of hard spheres, helix backbone (solid line), and the vectors connecting a reference particle 0 located at $(x, y, z) = (R, 0, 0)$ with its neighbors: an immediate successive particle 1 in the turn located at (\vec{r}_{01}) and a neighboring particle 2 from the next thread turn at (\vec{r}_{02}). (b) An overview of the principal geometrical parameters of $n_c = 4$ and 6 helices: elevation angle θ and azimuthal angular shifts Γ_1 and Γ_2 (see eqn (7)). In our notation, densely packed directions along the helical superstructure are called threads. The corresponding elevation distances of successive particles along helix axes $\Delta z_{1,2}$ (see eqn (9)) are also given for two possibilities for the rolling of the same helix configuration.

with $n_c = 6$, one arrives at the following two independent equations:

$$\Theta(n_1, n_2) = \arctan\left(\frac{\sqrt{3}n_2}{2n_1 + n_2}\right) \quad (4)$$

and

$$180^\circ = n_1 \arcsin\left[\left(\frac{d}{4R}\right) \frac{2n_1 + n_2}{\sqrt{n_1^2 + n_2^2 + n_1n_2}}\right] + n_2 \arcsin\left[\left(\frac{d}{4R}\right) \frac{2n_2 + n_1}{\sqrt{n_1^2 + n_2^2 + n_1n_2}}\right]. \quad (5)$$

We have solved those two equations and obtained the sets $(\Theta, R/d)$ shown in Fig. 4. For each value of R there are two different values of Θ , symmetric around $\Theta = 30^\circ$, which correspond to lattice constant pairs (n_1, n_2) and (n_2, n_1) , respectively. The (n_1, n_2) pairs are actually identical structures with opposite chirality.³⁸ The six-fold rotational symmetry of the lattice restricts $\Theta \in [0^\circ, 60^\circ]$.

We now look into properties of (n_1, n_2) pairs in order to characterize the multi-thread structure of six neighbor helices ($n_c = 6$). First, we identify the link between $n_c = 6$ -tubes and the

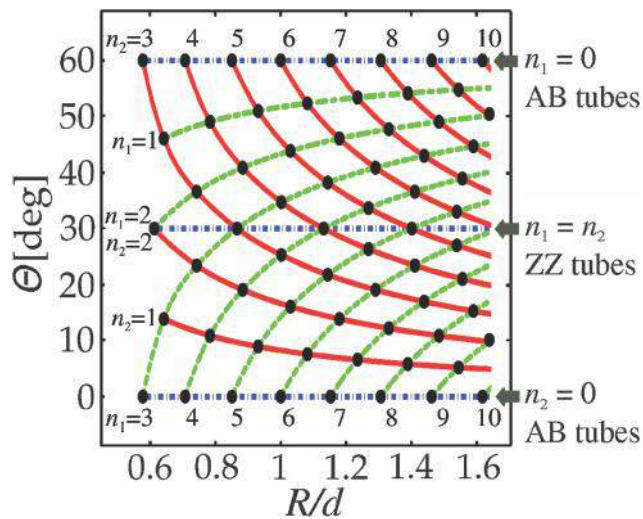


Fig. 4 Phase diagram in the $(\Theta, R/d)$ -plane showing possible unit cells characterized by (n_1, n_2) pairs. Solid lines represent unit cells with n_2 fixed, and the dashed ones represent unit cells with n_1 fixed. The three horizontal lines (dot-dashed) correspond to tubes.

(n_1, n_2) pair values. The pairs $(0, n_2)$ and $(n_1, 0)$ leading to $\Theta = 60^\circ$ and 0° , respectively, represent AB tubes, cf. Fig. 4. The pairs with $n_1 = n_2$ corresponding to $\Theta = 30^\circ$ lead to ZZ tubes that are characterized by constitutive straight filaments parallel to the ZZ tube axis, see Fig. 2f. The curve with $n_1 = 1$ (with $n_2 \geq 3$) corresponds to a single helix, $n_1 = 2$ (with $n_2 \geq 3$) to a double helix, $n_1 = 3$ (for any $n_2 \geq 4$) to a triple helix, and more generally an n_1 -helical structure is obtained when $n_2 \geq n_1 + 1$.[¶]

We employ Cartesian coordinates to express positions of particles in an n -helix similarly to the single helix case, using two indices, $i \in Z$ and $j = \{1, n\}$:

$$\begin{aligned} x_{i+jn} &= R \sin(i\Gamma_1 + j\Gamma_2) \\ y_{i+jn} &= R \cos(i\Gamma_1 + j\Gamma_2) \\ z_{i+jn} &= i\Delta z_1 + j\Delta z_2. \end{aligned} \quad (6)$$

In eqn (6), Γ_1 represents the azimuthal angular shift between each two consecutive particles along a given thread and Γ_2 is the angular shift between threads, i.e., densely packed directions in a superstructure, see Fig. 3(b). The azimuthal angle Γ_1 is merely provided by:

$$\Gamma_1 = \arccos \left[1 - \left(\frac{d}{\sqrt{2}R} \cos \Theta \right)^2 \right]. \quad (7)$$

The angular shift Γ_2 between threads is more delicate to derive. Knowing that starting from the reference particle it is possible to reach the same particle position following two paths along threads (in \vec{a}_1 or \vec{a}_2 -direction), one can arrive at a relation linking Γ_1 and Γ_2 : $360^\circ = (n_1 + n_2)\Gamma_1 - n_2\Gamma_2$.

The dependence of angular parameters Γ_1 and Γ_2 on the reduced helix radius R/d is displayed in Fig. 5, for $\Theta < 30^\circ$ in the

[¶] In our notation, multiple helices are named after the smallest unit patch dimension, i.e., the smallest number of generating threads.

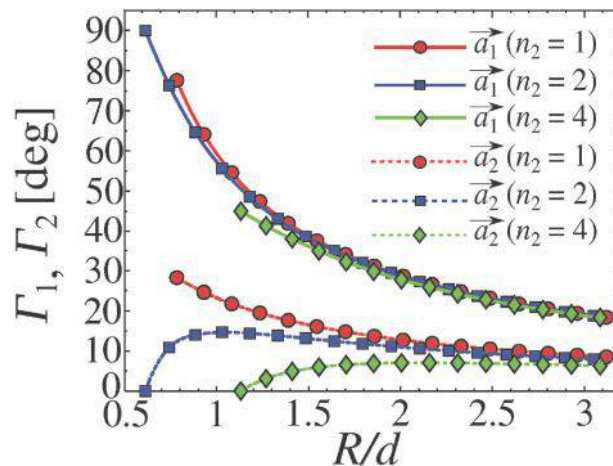


Fig. 5 Dependence of azimuthal angular shift parameters Γ_1 and Γ_2 stemming from the corresponding spanning vectors \vec{a}_1 , \vec{a}_2 , respectively, on a reduced helix radius R/d , for single ($n_2 = 1$), double ($n_2 = 2$), and quadruple ($n_2 = 4$) helices.

single helix ($n_2 = 1, n_1 \geq 4$), the double helix ($n_2 = 2, n_1 \geq n_2$) and the quadruple helix ($n_2 = 4, n_1 \geq n_2$).

As the helix radius R/d increases, the value of Γ_1 monotonically decreases, since additional particles are added to a turn. The angular parameter Γ_2 monotonically decreases only for $n_2 = 1$. The scenario becomes qualitatively different at $n_2 \geq 2$ where non-monotonic behavior is found, see Fig. 5. This feature can be rationalized as follows. The smallest compatible radii R with $n_2 \geq 2$ and $\Theta < 30^\circ$ are obtained when $n_1 = n_2$ (cf. Fig. 4) corresponding to Z tubes where $\Gamma_2 = 0$. Besides that, Γ_2 tends to zero for the vanishing cylinder curvature ($R/d \rightarrow \infty$). These are the reasons why the profile of $\Gamma_2(R/d)$ is non-monotonic when $n_2 \geq 2$.

The surface packing fraction of densely packed multiple helices is simply obtained by multiplying the surface packing fraction of a single helix with the number of threads n_2 ($\eta_{\text{multi}} = n_2\eta$, see eqn (1)):

$$\eta_{\text{multi}} = n_2 \frac{d^2}{8\Delta z_1 R}, \quad (8)$$

where the elevation distance Δz_1 (shown in Fig. 3b) is given by:

$$\Delta z_1 = \sqrt{d^2 - 4R^2 \sin^2 \left(\frac{\Gamma_1}{2} \right)}. \quad (9)$$

The calculated surface packing fraction of single ($n_2 = 1$), double ($n_2 = 2$), and quadruple ($n_2 = 4$) helices is shown in Fig. 6. At a given confinement curvature (fixed R/d), adding threads results in higher surface packing fraction, see Fig. 6.

3 Dipole moments

3.1 Dipolar interaction model

We now want to address the situation where the constitutive particles are dipolar. Each particle carries an identical dipole moment in magnitude, $m = |\vec{m}_i|$, where $\vec{m}_i = (m_i^x, m_i^y, m_i^z)$ defines

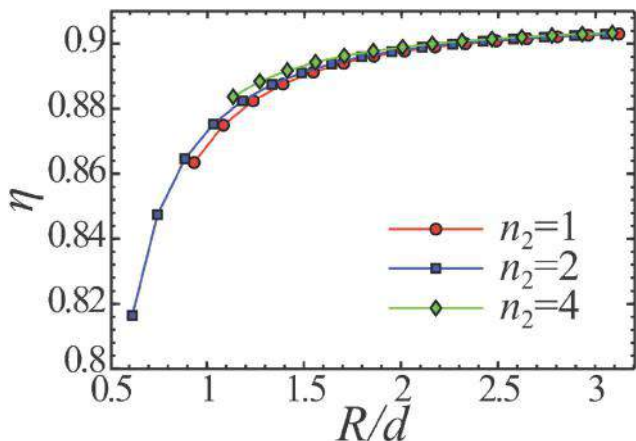


Fig. 6 Surface packing fraction η , see eqn (8) as a function of reduced helix radius R/d for single ($n_2 = 1$), double ($n_2 = 2$), and quadruple ($n_2 = 4$) helices.

the dipole moment of particle i , see also Fig. 1. The potential energy of interaction $U(\vec{r}_{ij})$ between two point-like dipoles whose centers are located at \vec{r}_i and \vec{r}_j can be written as:

$$U(\vec{r}_{ij}) = C \frac{1}{r_{ij}^3} \left[\vec{m}_i \cdot \vec{m}_j - 3 \frac{(\vec{m}_i \cdot \vec{r}_{ij})(\vec{m}_j \cdot \vec{r}_{ij})}{r_{ij}^2} \right] \quad (10)$$

for $r_{ij} \geq d$ or ∞ otherwise, where C represents a constant that depends on the intervening medium, and $r_{ij} = |\vec{r}_{ij}| = |\vec{r}_j - \vec{r}_i|$. It is convenient to introduce the energy scale defined by $U_{\uparrow} \equiv Cm^2/d^3$ that physically represents the repulsive potential value for two parallel dipoles in contact standing side by side as clearly suggested by the notation. Therefore, the total potential energy of interaction in a given structure U_{tot} is given by

$$U_{\text{tot}} = \sum_{\substack{ij \\ i > j}} U(\vec{r}_{ij}). \quad (11)$$

One can then define the reduced potential energy of interaction u (per particle) of N magnetic spheres. It reads $u = U_{\text{tot}}/(U_{\uparrow}N)$, which will be referred to as the cohesive energy.

Since we are dealing with infinitely long structures (in one direction), we shall consider only periodic structures in that direction that greatly facilitate the calculation of the cohesive energy. The method of choice is provided by the Lekner sum for systems with periodicity in one direction.³⁹ The central feature in the Lekner method is the choice of the periodic cell. For $n_c = 2, 4$, we can always find helical parameters with a finite number of particles in the unit cell. The periodicity is achieved by imposing a condition on the angular shift parameter Γ that a helix has to make an integer number of turns within the unit cell.

3.2 Dipole moment orientation prescribed by helix threads

Because of the symmetry it is intuitive to envision dipole moments following helix threads. In order to have dipole moments tangential to the helical backbone, we introduce two components of dipole moments. The parallel component with respect to the helix axis is given by $m^z = m\Delta z/d$ and the orthogonal one is given by $|\vec{m}^{xy}| = m\sqrt{1 - (\Delta z/d)^2}$. Hence, the dipole moment of particle i

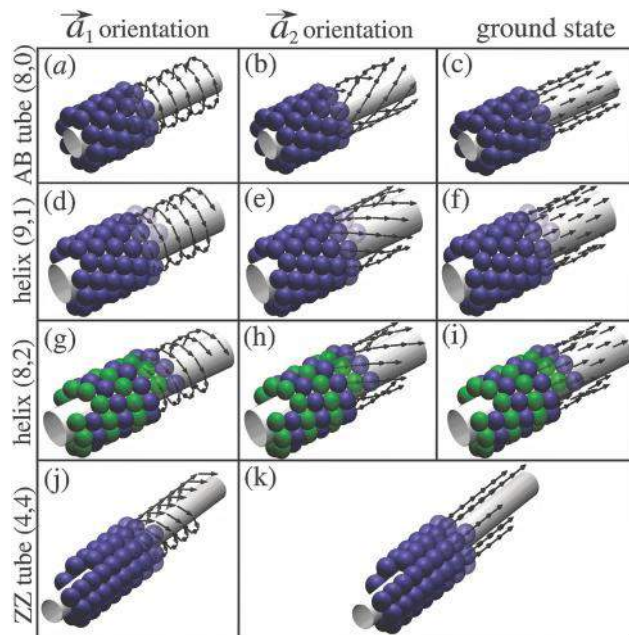


Fig. 7 The representative structures including dipole moment distributions are displayed. For AB tubes with patch parameters $(n_1, n_2) = (8, 0)$ dipole distributions which correspond to spanning unit cell vectors (a) \vec{a}_1 (oblique to cylinder's axis), (b) \vec{a}_2 (closer to cylinder's axes), and (c) ground state dipole distribution. For a single helix $(n_1, n_2) = (9, 1)$ dipole distributions which correspond to (d) \vec{a}_1 and (e) \vec{a}_2 (closer to helix axes) spanning vectors, and (f) ground state dipole distribution. For a double helix $(n_1, n_2) = (8, 2)$ dipole distributions which correspond to (g) \vec{a}_1 , (h) \vec{a}_2 (closer to helix axes) spanning vectors, and (i) the ground state dipole distribution. In the case of ZZ tubes (j) \vec{a}_1 and (k) \vec{a}_2 dipole distributions are shown. The ground state of ZZ tubes follows \vec{a}_2 dipole distribution (parallel to cylinder's axis).

in the single thread helix reads: $m_i^x = -m^{xy}\sin(i\Gamma)$, $m_i^y = m^{xy}\cos(i\Gamma)$, and $m_i^z = m_z$.

In the multi-thread case, the Cartesian dipole moment components are given by:

$$\begin{aligned} m_{i,j}^x &= -m^{xy}\sin(i\Gamma_1 + j\Gamma_2) \\ m_{i,j}^y &= m^{xy}\cos(i\Gamma_1 + j\Gamma_2) \\ m_{i,j}^z &= m\Delta z/d, \end{aligned} \quad (12)$$

where $i \in Z$ is the internal particle label within a thread and $j = \{1, n_2\}$ stands for the thread's label. In dense helices ($n_c = 4, 6$) dipole moments can follow two directions \vec{a}_1 and \vec{a}_2 . In Fig. 7, representative dipole moment distributions are shown.

3.3 Energy minimization

In general, the dipole moments do not have to follow thread structure. To find the dipole moment distribution that yields minimal energy, we first perform minimization of the cohesive energy using a constrained minimization algorithm.^{24,40} A randomly oriented dipole moment is assigned to every particle of the helical structure in the following way: dipole moment is defined in the spherical coordinate system. Two important features stemming from these energy minimization calculations are:

- (i) Dipole moments are tangential to the cylinder's surface.

(ii) The component of dipole moment in the z -axis direction m_z for a given structure is identical for all particles.†

Therefore we need just one angular parameter to characterize the dipole moment orientation. We choose the dipole moment angular parameter, $\alpha \in [-180^\circ, 180^\circ]$, relative to the z -axis, see Fig. 1. Doing so we arrive at:

$$\begin{aligned} m_{i,j}^x &= -m \sin(\alpha) \sin(i\Gamma_1 + j\Gamma_2) \\ m_{i,j}^y &= m \sin(\alpha) \cos(i\Gamma_1 + j\Gamma_2) \\ m_{i,j}^z &= m \cos(\alpha), \end{aligned} \quad (13)$$

where the indices i and j have the same meaning as in eqn (12). Consequently, the angular parameter α is most of the time a unique variable, at prescribed helical structures, entering into the energy minimization routine.

4 Cohesion energy and microstructure

4.1 Compression of a single helix

A simple way to deform a helix is to compress (or extend) it along its axis, *i.e.*, the z -direction, while ensuring the dipole moments follow the thread (for details of implementation, see Section 3.2). Compression of a helix results in a continuous increase of its surface packing fraction η . Fig. 8 shows the evolution of cohesive energy u_R with the surface packing fraction η for a single helix with reduced radius ($R/d \simeq 1.7$, chosen in the vicinity of $n_c = 6$ point). Recalling geometrical considerations in Section 2.1 the increase of the azimuthal angular shift Γ at prescribed curvature results in a continuous decrease of Δz and compression of the helix. The compression process begins with

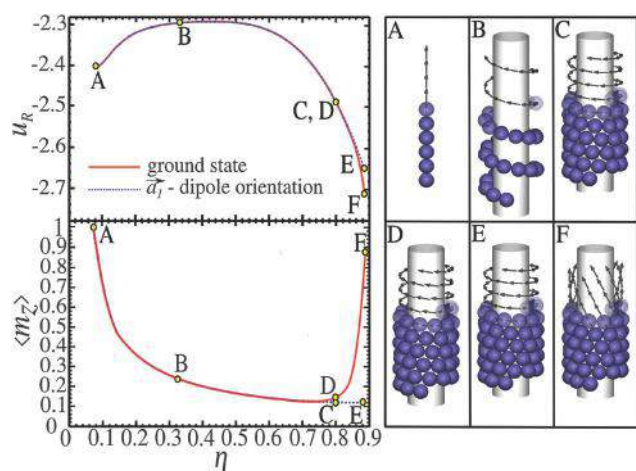


Fig. 8 Compression of a single helix on a cylindrical confinement with a fixed radius ($R/d \simeq 1.7$). Dependence of cohesive energy (upper left panel) and the overall polarization order parameter, *i.e.*, the axial component of the dipole moment (in lower left panel), on the packing fraction is shown for two characteristic dipole moment orientations: one that follows the helix, *i.e.*, the spanning vector \vec{a}_1 and the ground state dipole moment orientation obtained by energy minimization. Comparative microstructures at different η values (A–F) are depicted on the right panel. Configurations (A, B, C and E) correspond to a dipole moment distribution following the helix whereas configurations D and F correspond to ground state distributions.

a fully extended helix (*i.e.*, $\eta \rightarrow d/8R \simeq 0.073$) where the chain stands up with $\Delta z/d = 1$, and the cohesive energy of infinite chain $u \simeq -2.404$.²⁴ The compression ends when two successive turns of the helix touch, *i.e.*, the coordination number of particles in the helix changes from $n_c = 2$ to $n_c = 4$.

We also address the minimal energy of the helix with respect to the dipole moment distribution (*i.e.*, not necessarily prescribed by tangentially following the helix). From Fig. 8, we observe that $u_R = u_R(\eta)$ is non-monotonic. We can identify two regimes:

- At small packing fractions up to $\eta \lesssim 0.4$ (with no touching turns), the compression of the helix requires energy input and therefore cohesive energy increases. The reason for this is that two distant consecutive turns of the helix experience weaker attraction upon increasing η .

- In the regime of high $\eta \gtrsim 0.4$ where successive turns are allowed to be close or even touching, the cohesive energy starts to decrease as η increases, *i.e.*, the helix would compress on its own without input of energy. This is a consequence of enhanced attraction caused by the discreteness of the constitutive dipolar beads, see ref. 41.

The overall polarization order parameter $\langle m_z \rangle$ is also analysed in Fig. 8. During most of the course of the helix compression, see Fig. 8, a dipole moment orientation following the helix corresponds to the ground state structure up to $\eta \approx 0.8$, *cf.* points C and D in Fig. 8 (for details of ground state calculations, see Section 3.3). Only for very high packing fractions, *i.e.*, $\eta > 0.8$, the ground state dipole orientation starts to rapidly deviate from the helix direction accompanied by a significant reduction in cohesive energy (see points E and F in Fig. 8). The highest difference in $\langle m_z \rangle$ occurs for $\eta \approx 0.887$, where $n_c = 4$ helix with touching turns is formed, and the energy difference $u_R^E - u_R^F \simeq 0.06$.

4.2 From the square to triangular arrangement for a single helix

Having successfully parameterized helices and introduced dipole moments, it is natural to ask how cohesive energy depends on structural changes and especially on curvature. With increasing curvature the structure will change from the triangular to square arrangement and *vice versa* through a continuous series of rhombic configurations. We first study in detail systems with dipole moments following the spanning vector that are most oblique to helix axes, see Fig. 7d. For the sake of comparison with tubes (AA/AB tubes), we also chose dipole moments that are building vortices along the rings for them, *cf.* Fig. 7a. Motivation for that choice stems from a previous study,²⁴ where we have shown that finite AB tubular systems are energetically favorable, see Fig. 7a (dipole moment orientation is perpendicular to the tube's axis).

The surface packing fraction η (eqn (1)), the angular coordination order parameter ζ (see eqn (3)), and the cohesive energy per particle u_R (eqn (11)) are plotted *versus* the reduced helix radius R/d in Fig. 9.

† We have found that under some circumstances the dipole moment orientations alternate, *i.e.*, antiferromagnetic-like coupling between the neighboring threads. This actually occurs with any AA tube. Similar behavior is reported for some moderately dense $n_c = 4$ -helical structures.

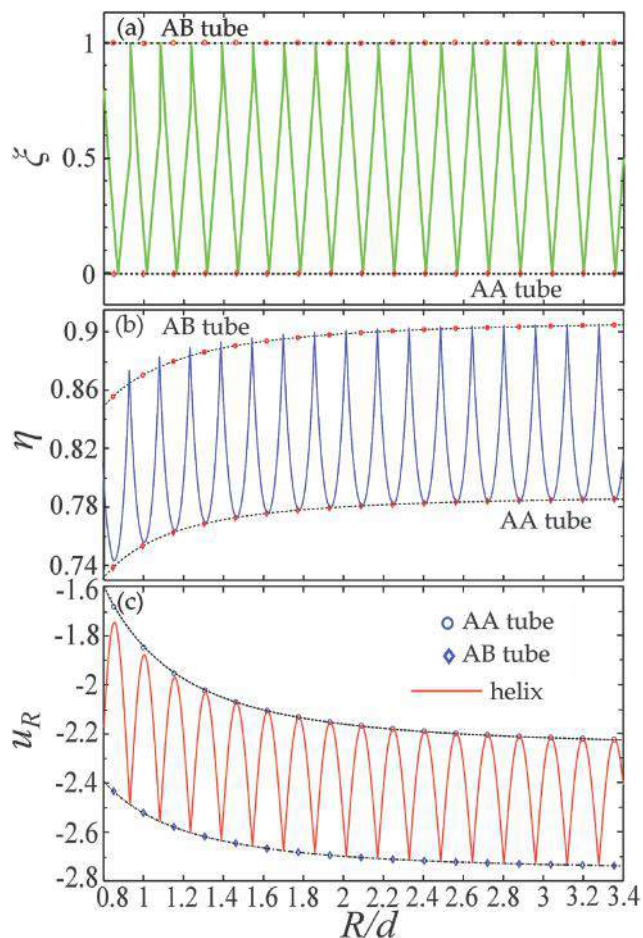


Fig. 9 Dependence of (a) the angular coordination order parameter ξ , (b) the packing density η and (c) the cohesive energy u_R on the helix radius R/d , for \vec{a}_1 dipole orientation. AA and AB tube points are clearly indicated, they bracket the parameter values of helices, like a kind of envelope (solid and dashed lines connecting the tube points are power law fits).

Actually, the energy and structural properties change in an oscillatory quasi-periodic manner and they are enveloped from both sides with the properties of AA and AB tubes, see Fig. 9. In Fig. 10 behavior of these observables is depicted within one period ($R/d \in [2.09, 2.26]$, arbitrary chosen). In one period, the number of particles (n) in a constitutive ring of (AA/AB) tubes is increased for one, *i.e.*, from n -ring to $n + 1$ -ring. Within this period, the order parameter changes from $\xi = 0$, *i.e.*, square arrangement, to $\xi = 1$, *i.e.*, triangular arrangement, *via* a continuous rhombic transformation, see Fig. 10a. The radii of densely packed helices are roughly in the middle between two corresponding (AB/AA) tube radii, see Fig. 10a. This is a result of the radial constraint and the excluded volume. Though in a single thread helical structure we cannot close rings in the plane perpendicular to the cylinder axis, one can nevertheless realize a full 360° helix turn with roughly $n + 1/2$ particles. We observe discontinuity and strong asymmetry of the angular coordination order parameter ξ at the mid-period ($R_{(13,1)}/d \approx 2.17$), see Fig. 10a. This is due to a change in the number of lateral threads n_2 , see Fig. 7e for illustration, at the mid period going from $n_2 = 9$ to $n_2 = 10$, see Fig. 10a.

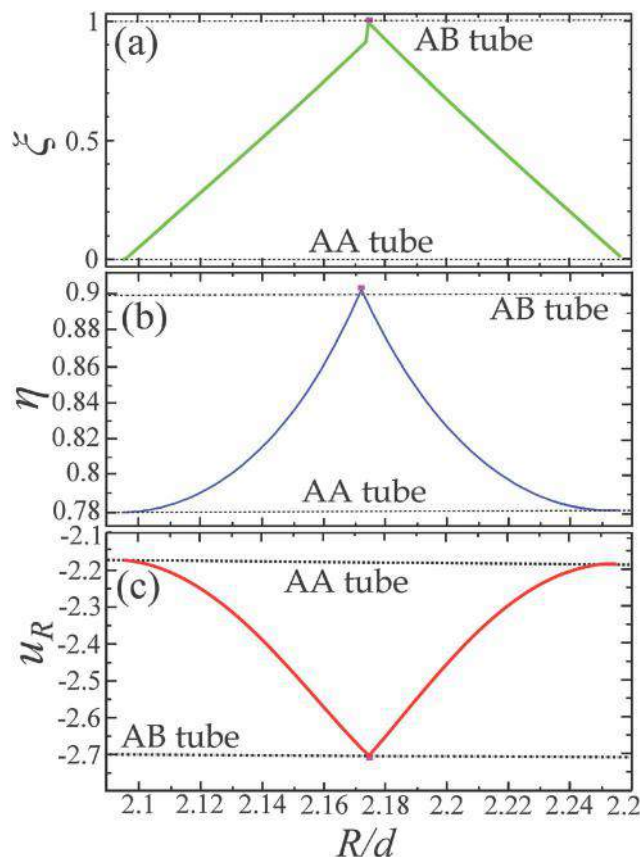


Fig. 10 Dependence of (a) the angular coordination order parameter ξ , (b) the packing density η and (c) the cohesive energy u_R on the helix radius R/d , for a segment in the vicinity of $R_{(13,1)}/d = 2.17$ of Fig. 9. Tubes AA and AB are represented by discrete points since they can be formed only with a fixed number of particles in a ring, the fitted (power law) curves serve only as a guide to the eye. The point which represents the dense helix with $(n_1, n_2) = (13, 1)$ and $R_{(13,1)}/d = 2.17$ is marked with a rectangle.

With decreasing curvature, the surface packing fraction increases globally, see Fig. 9b. We observe oscillatory behavior as the system continuously evolves from the square to triangular arrangement and *vice versa*. The AA and AB tubes still roughly bound the values taken by the surface packing fraction. At the helix radius $R/d > 3.4$, see Fig. 9b, we are already within 3% of the asymptotic expected values in the planar case. In contrast to the angular coordination parameter ξ , the surface packing density η is continuous everywhere, compare Fig. 10a and b. Moreover, at mid-period the η value is slightly (and systematically, see Fig. 9b) above the interpolated stemming from AB tubes (see Fig. 10b). In Fig. 9b and c, it can be clearly seen that the profiles of energy oscillations u_R and the surface packing fraction η are anti-correlated. The mid-period values u_R coincide with interpolated stemming from AB tube radii (confirmed by Fig. 9c and 10c).

4.3 Looking for the ground state

At this point, we would like to discuss mechanisms which govern the minimal energy dipole moment orientation near the mid-period transition point (more details about implementation are provided in Section 3.3). There are three privileged directions in

a helix: two which follow helix spanning vectors (determined by \vec{a}_1, \vec{a}_2) and the third one which is the direction of the helix axis. These privileged directions come into play in two competing mechanisms:

- The first mechanism is typically dictated by first neighbor interactions which favor dipole moments following the thread directions.

- The distant-neighbor interactions favor the distribution of dipole moments parallel to the helix axis.

We can justify these two mechanisms as follows. It is well known for a small finite system that rings are formed with dipole moments building vortices, *cf.* ref. 24. When a helix turn is projected along the z -axis, the resulting figure is highly reminiscent of the vortex discussed above. The head to tail configuration is favored at long distances, explaining the second advocated mechanism.

The abrupt change in polarization (or magnetization) in the direction of the axis $\langle m_z \rangle$, seen in Fig. 11b, is correlated with the discontinuous change in the angular coordination order parameter ξ in the vicinity of transition, see Fig. 10a. At the mid-period point $R_{(13,1)}/d = 2.17$ magnetization in the direction of the axis $\langle m_z \rangle$ is close to one, but not exactly one, see Fig. 11.

For the sake of comparison with tubes (AA/AB tubes), we choose dipole moments that are parallel with the helix axis, see Fig. 7c. The fact that the system is able to relax its dipole moment orientation to the ground state results in more dependence of energy on confinement curvature around the mid-point. The degree of asymmetry of u_R is stronger around the transition point, see Fig. 11b, than in the excited state in Fig. 10c. The ground state calculations confirm the high stability of AB tubes (see Fig. 10c).

4.4 Cohesion energy for multiple helices at high surface packing fraction

In this part, we consider the high surface packing fraction regime with $n_c = 6$. Some representative structures including dipole moment streamlines are displayed in Fig. 7. The streamlines following spanning unit cell vectors \vec{a}_1 (oblique to the helix axis) and \vec{a}_2 (more aligned to the helix axis) are also shown.** Dipole moment distributions in the ground states are also indicated for comparison in Fig. 7. In analogy with the study of a single helix case (see Section 4.2), we start analysis with a dipole moment distribution prescribed by tangentiality with the thread backbone. In Fig. 12, cohesive energy for the \vec{a}_1 -generated dipole moment distribution is shown for different helical structures.

The cohesive energy in a planar triangular lattice, $u_\infty \simeq -2.759$, represents the energy value which will be reached asymptotically ($R/d \rightarrow \infty$) for all considered structures. As already found for AB tubes in ref. 24, cohesive energy exhibits the scaling law of the form $u_R - u_\infty \sim R^{-2}$, see Fig. 12. The cohesive energies of all three helices and AB tubes are weakly dependent on the number of threads for \vec{a}_1 -generated dipole moment distribution.

** It is possible to polarize the helix by a homogeneous external field parallel to its axis. For symmetry reasons, a reversal of the magnetic field should result in the reversal of the dipole orientation. In the case of magnetic dipoles, it should also be possible to polarize the system to follow \vec{a}_1 and \vec{a}_2 spanning vectors by combination of a curling magnetic field of electric current flowing through the confining cylinder and the homogeneous external magnetic field parallel to its axis.

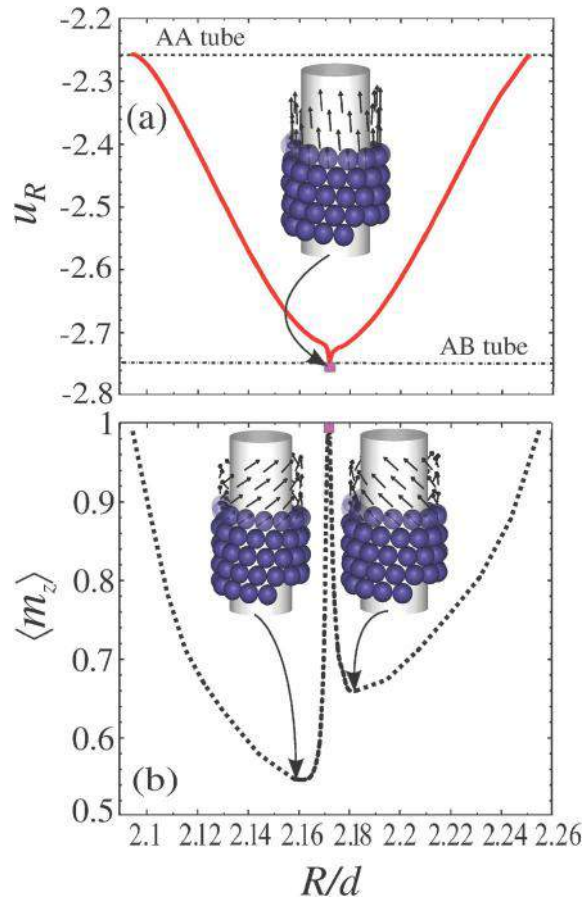


Fig. 11 Dependence of (a) cohesive energy u_R and (b) the overall polarization order parameter $\langle m_z \rangle$ on the helix radius R/d (in the ground state), for a chosen segment of Fig. 9. Tubes AA and AB are represented by discrete points since they can be formed only with a fixed number of particles in a ring, the fitted (power law) curves serve only as a guide to the eye. The point which represents the dense helix with $(n_1, n_2) = (13, 1)$ and $R_{(13,1)}/d = 2.17$, is marked with a rectangle.

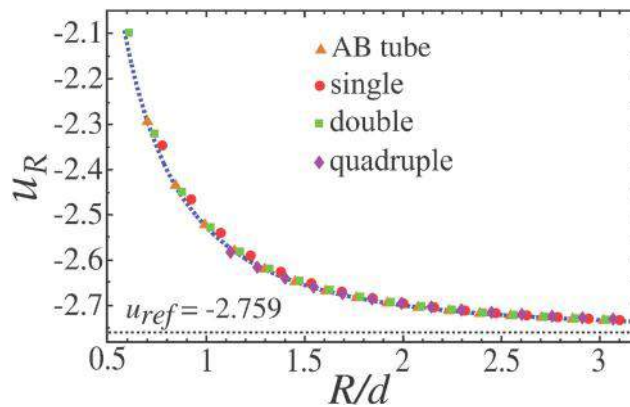


Fig. 12 Dependence of cohesive energy u_R on the helix radius R/d , for single, double, and quadruple helices at high surface packing fraction, and AB tubes, with \vec{a}_1 dipole orientation.

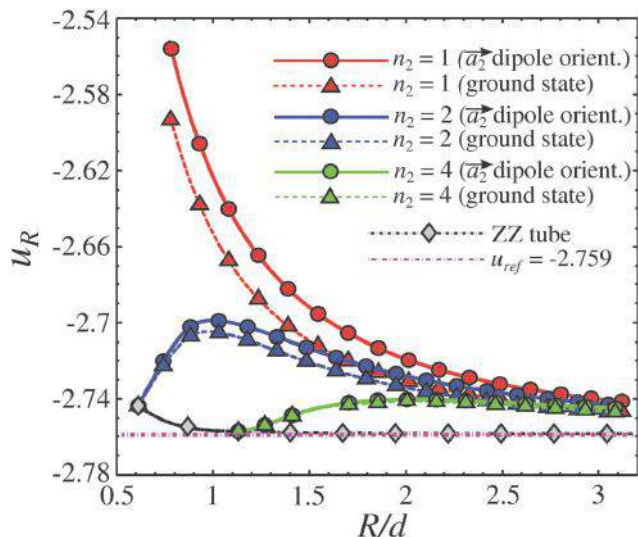


Fig. 13 Dependence of cohesive energy u_R on the helix radius R/d , for families of single, double, and quadruple helices at a high surface packing fraction, *i.e.*, $n_2 = \{1, 2, 4\}$, respectively, and AB tubes, with \vec{a}_2 and optimized dipole moment orientation.

This is in accordance with surface packing fraction behavior reported in Fig. 6. A comparison with the azimuthal angular shift parameter Γ_1 , see Fig. 5, and the corresponding cohesive energy (for \vec{a}_1 -generated dipole moment distribution) clearly reveals a correlation between these two quantities.

In Fig. 13, cohesive energy for \vec{a}_2 -generated dipole moment distribution is compared with ground state energy for a different number of threads. There exists an analogous correlation (as discussed for \vec{a}_2 -dipole distribution) between the azimuthal shift Γ_2 and the resulting cohesive energy, compare Fig. 5 and 13.

The smallest compatible radius R for multi thread helices ($n_2 = 2, 4$) is obtained for ZZ tubes ($n_1 = n_2$). In Fig. 13, the corresponding radii read $R_{(2,2)}/d = 0.61$ and $R_{(4,4)}/d = 1.13$. In this case the \vec{a}_2 and ground state dipole moment orientations are the same, see Fig. 7k. Strikingly, ZZ tube ground states converge very fast to the expected planar value u_∞ at the smallest accessible radii, *i.e.*, the largest curvature, within less than 1% of the planar case, see Fig. 13 for $R_{(2,2)}/d = 0.61$. A structural similarity of ZZ tubes, with typical experimental images of microtubules is striking, see Fig. 7k. Structurally, ZZ tubes can be created by closing the rectangular strip on a cylinder and decomposition into chains which are analogous to biological filaments which the microtubules are made of.

5 Conclusions

We have presented a study about cohesive energy of helical structures composed of hard spheres with permanent dipole moments. Helices were created by replication of a particle or patch (of particles) on a confining cylindrical surface. Even for the most simple situation, namely the single thread helix, a non-trivial behavior is found when monitoring the cohesive energy as a function of surface packing (*i.e.*, axial compression). In particular, we observe a non-monotonic dependence of the

cohesive energy on the packing fraction (or equivalently the amount of compression) as a result of a delicate interplay of dipole-dipole interactions and excluded volume effects. The lowest cohesive energy is achieved at the highest packing fraction with touching turns. In parallel, the magnetization (or polarization) order parameter, *i.e.*, the mean dipole moment per particle in $\langle m_z \rangle$, also exhibits a striking non-monotonic behavior as a function of the extent of compression. In the regime of very high surface packing fraction with local triangular arrangement compatible with certain cylinder radius (R) vs. particle diameter (d) ratio (R/d), a pronounced cohesive energy is found. Concomitantly, the magnetization order parameter indicates a sharp change in the dipole moment orientation, which tends to be parallel to the helix axis.

Finally, we compare cohesive energies of dense multiple (*i.e.*, double or quadruple) helices, as well as, AB and ZZ-tubes made up of stacking rings that can also be seen as special multiple helices. A remarkable finding is the enhanced cohesive energy for the ZZ-tube structure. The latter already emerges at strong substrate curvature with cohesive energies very close to that obtained at vanishing curvatures. In these ZZ-tube structures, an alignment of the helix threads with its axis is a microstructural signature for this low cohesive energy. As a final note, we would like to emphasize that our model mimics nicely the geometry and microstructure of microtubules. It could also provide a possible clue about the self-assembly mechanisms and cohesion within microtubular structures.

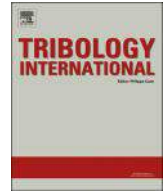
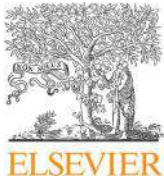
Acknowledgements

The authors acknowledge support from the bilateral Franco-Serbian PHC Pavle Savic 2014/15 Grant 32135NJ. I.S and M.D. acknowledge financial support from Ministry of Education, Science, and Technological Development of the Republic of Serbia projects ON171017 and III45018, and European Commission under H2020 projects VI-SEEM and DAFNEOX (Grant No. 675121 and 645658). Numerical calculations were run on the PARADOX supercomputing facility at the Scientific Computing Laboratory of the Institute of Physics Belgrade.

References

- 1 W. Wen, N. Wang, D. W. Zheng, C. Chen and K. N. Tu, *J. Mater. Res.*, 1999, **14**, 1186–1189.
- 2 D. J. Sellmyer, *Nature*, 2002, **420**, 374–375.
- 3 G. M. Whitesides and B. Grzybowski, *Science*, 2002, **295**, 2418–2421.
- 4 K. F. Jarrell and M. J. McBride, *Nat. Rev. Microbiol.*, 2008, **6**, 466–476.
- 5 I. M. Cheeseman and A. Desai, *Nat. Rev. Mol. Cell Biol.*, 2008, **9**, 33–46.
- 6 J. Howard and A. A. Hyman, *Nat. Rev. Microbiol.*, 2009, **10**, 569–574.
- 7 D. V. Kosynkin, A. L. Higginbotham, A. Sinitskii, J. R. Lomeda, A. Dimiev, B. K. Price and J. M. Tour, *Nature*, 2009, **458**, 872–876.

- 8 X. Zhang, X. Zhang, D. Bernaerts, G. Van Tendeloo, S. Amelinckx, J. Van Landuyt, V. Ivanov, J. Nagy, P. Lambin and A. Lucas, *EPL*, 1994, **27**, 141.
- 9 S. M. Douglas, J. J. Chou and W. M. Shih, *Proc. Natl. Acad. Sci. U. S. A.*, 2007, **104**, 6644–6648.
- 10 G. D. Lilly, A. Agarwal, S. Srivastava and N. A. Kotov, *Small*, 2011, **7**, 2004–2009.
- 11 T. Shimizu, M. Masuda and H. Minamikawa, *Chem. Rev.*, 2005, **105**, 1401–1444.
- 12 Y. Yamamoto, T. Fukushima, Y. Suna, N. Ishii, A. Saeki, S. Seki, S. Tagawa, M. Taniguchi, T. Kawai and T. Aida, *Science*, 2006, **314**, 1761–1764.
- 13 W. Zhuang, E. Kasemi, Y. Ding, M. Kröger, A. D. Schlüter and J. P. Rabe, *Adv. Mater.*, 2008, **20**, 3204–3210.
- 14 G. Singh, H. Chan, A. Baskin, E. Gelman, N. Repnin, P. Kral and R. Klajn, *Science*, 2014, **345**, 1149–1153.
- 15 D. Zerrouki, J. Baudry, D. Pine, P. Chaikin and J. Bibette, *Nature*, 2008, **455**, 380–382.
- 16 G. Pickett, M. Gross and H. Okuyama, *Phys. Rev. Lett.*, 2000, **85**, 3652–3655.
- 17 E. C. Oguz, R. Messina and H. Loewen, *EPL*, 2011, **94**, 28005.
- 18 M. A. Lohr, A. M. Alsayed, B. G. Chen, Z. Zhang, R. D. Kamien and A. G. Yodh, *Phys. Rev. E: Stat., Nonlinear, Soft Matter Phys.*, 2010, **81**, 040401.
- 19 A. Mershin, A. A. Kolomenski, H. A. Schuessler and D. V. Nanopoulos, *BioSystems*, 2004, **77**, 73–85.
- 20 E. D. Spoeerke, G. D. Bachand, J. Liu, D. Sasaki and B. C. Bunker, *Langmuir*, 2008, **24**, 7039–7043.
- 21 M. Cifra, J. Pokorný, D. Havelka and O. Kučera, *BioSystems*, 2010, **100**, 122–131.
- 22 I. Jacobs and C. Bean, *Phys. Rev.*, 1955, **100**, 1060.
- 23 P.-G. De Gennes and P. A. Pincus, *Phys. Kondens. Mater.*, 1970, **11**, 189–198.
- 24 R. Messina, L. A. Khalil and I. Stanković, *Phys. Rev. E: Stat., Nonlinear, Soft Matter Phys.*, 2014, **89**, 011202.
- 25 D. Vella, E. du Pontavice, C. L. Hall and A. Goriely, *Proc. R. Soc. London, Ser. A*, 2013, **470**, 20130609.
- 26 Y. Ding, H. C. Öttinger, A. D. Schlüter and M. Kröger, *J. Chem. Phys.*, 2007, **127**, 094904.
- 27 M. Kröger, O. Peleg, Y. Ding and Y. Rabin, *Soft Matter*, 2008, **4**, 18–28.
- 28 T. X. Hoang, A. Giacometti, R. Podgornik, N. T. Nguyen, J. R. Banavar and A. Maritan, *J. Chem. Phys.*, 2014, **140**, 064902.
- 29 R. Cortini, B. R. Caré, J.-M. Victor and M. Barbi, *J. Chem. Phys.*, 2015, **142**, 105102.
- 30 H. Mohrbach, A. Johner and I. M. Kulić, *Phys. Rev. Lett.*, 2010, **105**, 268102.
- 31 O. Kahraman, H. Mohrbach, M. M. Müller and I. M. Kulić, *Soft Matter*, 2014, **10**, 2836–2847.
- 32 D. Tomanek, S. G. Kim, P. Jund, P. Borrmann, H. Stamerjohanns and E. R. Hilf, *Z. Phys. D: At., Mol. Clusters*, 1997, **40**, 539–541.
- 33 T. A. Prokopenko, V. A. Danilov, S. S. Kantorovich and C. Holm, *Phys. Rev. E: Stat., Nonlinear, Soft Matter Phys.*, 2009, **80**, 031404.
- 34 G. Pál, F. Kun, I. Varga, D. Sohler and G. Sun, *Phys. Rev. E: Stat., Nonlinear, Soft Matter Phys.*, 2011, **83**, 061504.
- 35 V. Malik, A. V. Petukhov, L. He, Y. Yin and M. Schmidt, *Langmuir*, 2012, **28**, 14777–14783.
- 36 N. Vandewalle and S. Dorbolo, *New J. Phys.*, 2014, **16**, 013050.
- 37 D. A. Wood, C. D. Santangelo and A. D. Dinsmore, *Soft Matter*, 2013, **9**, 10016–10024.
- 38 W. T. B. Kelvin, *The molecular tactics of a crystal*, Clarendon Press, 1894.
- 39 A. Grzybowski and A. Bródka, *Mol. Phys.*, 2003, **101**, 1079–1088.
- 40 L. Assoud and R. Messina, *Phys. Rev. E: Stat., Nonlinear, Soft Matter Phys.*, 2011, **83**, 036113.
- 41 R. Messina and I. Stanković, *arXiv:1602.00861*, 2016.



Molecular dynamics investigation of a model ionic liquid lubricant for automotive applications



Konstantinos Gkagkas^{a,*}, Veerapandian Ponnuchamy^b, Miljan Dašić^c, Igor Stanković^c

^a Advanced Technology Division, Toyota Motor Europe NV/SA, Technical Center, Hoge Wei 33B, 1930 Zaventem, Belgium

^b Abylsen Belgium, 1000 Brussels, Belgium

^c Scientific Computing Laboratory, Center for the Study of Complex Systems, Institute of Physics Belgrade, University of Belgrade, 11080 Belgrade, Serbia

ARTICLE INFO

Keywords:

Friction
Molecular dynamics
Ionic liquid
Drivetrain

ABSTRACT

In the current work we present a new modelling approach for simulating meso–scopic phenomena related to lubrication of the piston ring–cylinder liner contact. Our geometry allows a variable confinement gap and a varying amount of lubricant in the gap, while avoiding the squeeze-out of the lubricant into vacuum. We have implemented a coarse grain molecular dynamics description of an ionic liquid as a lubricant which can expand into lateral reservoirs. The results have revealed two regimes of lubrication, an elasto-hydrodynamic one under low loads and one with low, velocity-independent specific friction, under high loads. The observed steep rise of normal forces at small plate-to-plate distances is an interesting behaviour that could potentially be exploited for preventing solid–solid contact and wear.

1. Introduction

Friction accounts approximately for one-third of the fuel energy consumed in passenger cars [1], therefore a deeper understanding of the lubrication mechanisms in engineering systems is necessary. Atomic-scale simulations can provide important insights which are necessary for understanding the underlying mechanisms that can affect the system behaviour, such as structural changes in lubrication layers during shear as well as the interaction between lubricants and surfaces. The field of computational lubricated nanotribology has been well established over the last decades [2,3] and the availability of increased computational resources is allowing the application of such methods in cases with increasing complexity. Recent studies of nanoscopic friction based on Molecular Dynamics (MD) include, for example, the study of fatty acids [4] and ionic liquids ILs [5] as lubricants. Wear reduction demands and the drive to keep friction low, have led to reduced lubricant film thickness down to only a few molecular layers [6–9]. MD can enable us to access and understand the behaviour of very thin films which are subjected to compression and shearing between walls [6–8].

Our specific goal is to achieve a representation of the tribological system which is relevant to automotive powertrain applications. As approximately 45% of the engine friction losses occur in the piston assembly [1], our initial target is to mimic the conditions observed in the piston ring–cylinder liner contact, in terms of pressure, temperature and shear rates. In addition, in order to be able to achieve length–

and time–scales that can be of relevance to the real–life systems, it is necessary to apply appropriate simulation methodologies, such as the use of coarse grain molecular dynamics [10–13].

In recent years, the application of ILs as advanced lubricants is being studied with a steadily increasing interest [14]. The use of ILs as both neat lubricants and additives for engine lubrication has been considered [15–17]. Significant improvements on friction and wear reduction have been observed experimentally [16], rendering this concept of potential interest to industry. However, unravelling the mechanism of nanoscopic friction in ILs together with their structure poses a great scientific challenge, and so far few studies in this direction have been performed, e.g., Ref. [18]. ILs are molten salts typically consisting of large-size organic anions and cations. Physical properties of ILs, such as negligible vapour pressure, high temperature stability (they do not evaporate or decompose at temperatures of interest for automotive industry) and high ionic conductivity render them potentially relevant to lubrication. In addition, their properties can be modified by an applied voltage using confining surfaces which are charged in order to build up an electric field across the nanoscale film. The applied potential can affect the structure of IL layers and lead to externally controllable lubricating properties [18,19]. There is also significant flexibility in tuning the physical and chemical properties of ILs which can affect lubrication such as viscosity, polarity and surface reactivity by varying their atomic composition as well as the anion–cation combination. An important observation is that ILs confined

* Corresponding author.

E-mail address: Konstantinos.Gkagkas@toyota-europe.com (K. Gkagkas).

between surfaces feature alternating positive and negative ionic layers, with an interlayer separation corresponding to the ion pair size [20,21].

Previous work employing Lennard-Jones fluids has provided insights on the complete dynamic diagram of confined liquids including wall slip, shear banding, solid friction, and plug flow. In terms of fluid complexity these studies have mainly employed mono-atomic systems, and only a few authors have considered mixtures of molecules [22,23]. In addition to inherently being a mixture of cation and anion molecules, ILs involve long range Coulomb interactions inducing long range order on far greater scales than the IL itself [5,9,24]. Detailed investigation of ILs as lubricants at the nanoscale is therefore essential for exploring the potential of implementing them in lubrication systems.

In this study, we apply a coarse-grained model for the description of nanoscopic friction mediated by a liquid lubricant because based on recent studies [18,19,21] it was shown that if the molecules interact via non-bonded potentials (Lennard-Jones and Coulombic), this can capture all main physical attributes of the IL-lubricated nanotribological system.

This paper is organised as follows: Section 2 introduces the MD setup of the solids and lubricants used, while the motivation for the choices made is provided. In Section 3, the structural properties of the modelled IL under bulk and confined conditions are discussed. The results stemming from the friction MD simulations are then presented in Section 4 followed by some concluding remarks in Section 5.

2. Model

Under typical operation of internal combustion engines, the conditions inside the combustion chamber vary significantly. Temperature can range from 300 K to values higher than 2000 K, while pressure ranges from atmospheric to values higher than 10 MPa [1]. The piston reciprocates with a sinusoidal velocity variation with speeds varying from zero to over 20 m/s. The time required for one revolution of the engine is of the order of 10 ms, while the total distance travelled by the piston over this period is of the order of 0.2 m. Such scales are typically modelled using continuum mechanics simulations. However such simulations cannot provide the physical insight which is necessary for understanding the molecule-dependent processes that affect the tribological phenomena. For this purpose, we have developed a coarse grain MD configuration that can provide useful insights to molecular processes, while remaining relevant to conditions observed in real-life systems. More specifically, in this section we will describe a setup of MD simulations developed with the aim of building a framework that incorporates meso-scale features of the piston ring-cylinder liner system and permits an efficient implementation of different solid surfaces and lubricants.

2.1. Geometry

All MD simulations in this study were performed using the LAMMPS software [25]. The geometry used in our friction simulations is shown as a schematic in Fig. 1, along with the dimensions of our system as well as the number of the MD particles used. The simulation setup was loosely inspired by previously published research by others [5,18,19,21]. By implementing such a geometry we have attempted to achieve: (i) a realistic particle squeeze-out behaviour with the formation of two lateral lubricant regions (in a similar manner to the simulations of Capozza et al. [21]) and (ii) a system that allows the lubricant to be externally pressurised. For the description of the solid surfaces we have combined rigid layers of particles moving as a single entity on which the external force or motion is imposed, denoted by “Top Action” and “Bottom Action” in Fig. 1(A), with thermalised layers (denoted by “Top Thermo” and “Bottom Thermo”) in which particles vibrate thermally at $T=330$ K. The Nose-Hoover NVT thermostat is used to control the temperature. As in previous MD simulations

[9,18,19,21,24], under similar operating conditions, the details of the adopted dissipation scheme are not expected to change the essence of the system response on mechanical deformation. The relaxation time of the Nose-Hoover NVT thermostat for the lubricant and the solids is 200 fs (cf. Ref. [9]). The plates were treated as rigid bodies, with the lower one being fixed and the upper one subjected to a z-directed force F_z (the load) as shown in Fig. 1(A) and driven along x direction at a constant velocity. The solid plates were made up of densely packed atomic layers at a FCC (111) lattice arrangement. Periodic boundary conditions were applied in the x and y directions. The bottom plate can therefore be considered to be infinite, while the top plate is surrounded by vacuum pockets on its sides, so called lateral reservoirs, in which the lubricant can freely expand. The lateral reservoirs were implemented as a mechanistic way for allowing the lubricant to be dynamically squeezed in or out as an external load or velocity is applied, or due to local fluctuations during the simulation progression. At the same time, the lubricant remains an infinite continuous body in x and y directions, similar to the conditions observed in a real tribological system from a meso-scopic point of view. This is especially important if the system experiences partial or complete crystallisation under compression, cf. Section 4 and Fig. 8.

While the total number of considered lubricant molecules is constant, the finite upper plate width and the resulting free space enables the particles to be squeezed-out even to the extent where due to structural changes the lubricant ceases wetting the solid plates. The number of lubricant molecules effectively confined inside the gap can therefore dynamically change depending on the loading conditions. This is important for exploring the possible states of a mechanical system of particles that is being maintained in thermodynamic equilibrium (thermal and chemical) with a lubricant reservoir (i.e., void spaces in tribological system). The nano-tribological system is open in the sense that it can exchange energy and particles, realising an effectively grand-canonical situation, cf. Fig. 1(b) and Ref. [26].

2.2. Solids and lubricant model

By using our simulation setup, we aim to study the lubrication properties of several lubricants. As a first step, in the current study we have implemented an ionic liquid as a lubricant. On the atomic level ILs are usually made up of large-size irregular organic anions and cations often including long alkyl chains. In the current work we have applied a simple coarse-grained model for its description, consisting of a charged Lennard-Jones system where anions and cations have different radii as already exploited in previous studies in the literature [21]. According to that, we have implemented a Lennard-Jones (LJ) 12-6 potential combined with a Coulombic electrostatic potential:

$$V(r_{ij}) = 4\epsilon_{ij} \left[\left(\frac{\sigma_{ij}}{r_{ij}} \right)^{12} - \left(\frac{\sigma_{ij}}{r_{ij}} \right)^6 \right] + \frac{1}{4\pi\epsilon_0\epsilon_r} \frac{q_i q_j}{r_{ij}} \quad (1)$$

Parameters $\{\epsilon_{ij}, \sigma_{ij}\}$ define the LJ potential between different types of particles $i, j = A, C, P$ which refer to anions, cations and solid plate atoms, respectively. The numerical values for each pair are listed in Table 1. The diameter of cations was set to $\sigma_{CC} = 5 \text{ \AA}$ and anions to $\sigma_{AA} = 10 \text{ \AA}$, in order to explore the effect of asymmetry of ion sizes (similar to Ref. [21]). Atoms of the solid plates have a diameter of $\sigma_{PP} = 3 \text{ \AA}$. The plates consist of nine densely packed layers in a FCC (111) lattice.

The ions were modelled as coarse grain particles, the charge of which was set to elementary: $q_A = -e$ and $q_C = +e$, i.e., $e = 1.6 \times 10^{-19} \text{ C}$. The ionic liquid is neutral, so the total number of cations and anions is the same: $N_C = N_A = N_{IL}/2$. In the present simulations, the number of ions used was $N_{IL} = 2500$. The dielectric constant was set to $\epsilon_r = 2$ to account for the dielectric screening, as in Refs. [19] and [21]. The LJ potential has a short-range impact, since it vanishes rapidly as the distance increases $\propto r^{-6}$, while the Coulombic

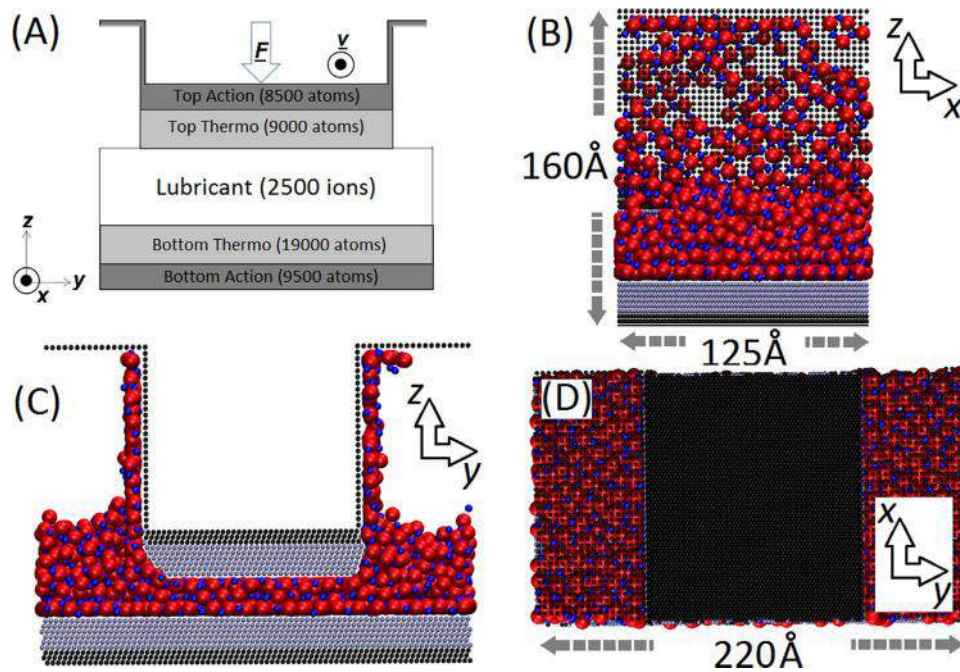


Fig. 1. (A) Schematic of the simulation setup shown as yz cross-section. There are two solid plates at the top and bottom of the system, consisting of two regions: at the outermost ones the particles are moving as a single entity (Top/Bottom Action) and at the innermost ones the particles are at a controlled temperature (Top/Bottom Thermo). The thermalised layers are in direct contact with the lubricant while the action layers are used to impose external velocity and/or force to the solid plates. (B)–(D) Side views of the typical simulation configuration and key dimensions of the geometry. (B) Side (xz) view with respect to the shear direction. (C) Front (yz) view in the direction of the top plate motion. (D) Top (xy) view of the system. The solid plates are made up of FCC (111) atomic layers. The ionic liquid is composed of an equal number of cations (blue spheres) and anions (red spheres). (For interpretation of the references to color in this figure legend, the reader is referred to the web version of this article.)

Table 1
List of LJ parameters used in simulations.

Pair ij	ϵ_{ij} [kCal/mol]	σ_{ij} [Å]
CC	0.03	5
AA	0.03	10
CA	0.03	7.5
PC	0.3	4
PA	0.3	6.5
PP	120	3

potential has a long-range impact, $\propto 1/r$. To handle long-range interactions, we have used a multi-level summation method (MSM) [27], since it scales well with the number of ions and allows the use of mixed periodic and non-periodic boundaries that are featured in our setup. To sum up, IL ions and plate atoms interact with each other via LJ potentials. In addition a Coulombic electrostatic potential is added in ion-ion interactions.

In engineering applications, the lubricant molecules typically interact with metal surfaces. Computationally efficient many-body potentials such as embedded atom method (EAM) potential [28,29] can be applied for the description of such solids. Such schemes have been employed extensively for modelling a wide range of systems including metals [29] and metal-metal oxide interfaces [30]. In addition, in order to account for the induced charges on the metallic conductor surface by the ions, the Drude-rod model developed by Iori and Corni [31] which consists of the addition of an embedded dipole into each metal atom, thus rendering it polarisable, has been applied in previous studies [5]. Since in our initial stage of IL tribological behaviour research, modelling the elasticity of metallic plates plays a secondary role, we have selected a simplified model in which plate atoms interact strongly with each other if they belong to the same plate, i.e., $\epsilon_{pp} = 120$ kCal/mol, as opposed, to a very weak interaction between the different plates $\epsilon_{top/bottom} = 0.03$ kCal/mol. Furthermore, even though the typical engineering systems are often metallic, our initial

coarse grain MD study of liquid dynamics according to the applied conditions justified the implementation of a simpler solid system which does not feature substrate polarisation. Finally, it is possible that the actual surfaces might feature carbon coatings or depositions, in which case the surface polarisation can be of secondary importance.

The starting configuration for our MD simulations was obtained via a relaxation process. In order to obtain a stable and reproducible initial configuration, the relaxation was performed through a stepwise increase of absolute ion charge at steps of $\Delta|q_i| = e/10$, $i=A, C$. Each time the charge of the ions was increased, a minimisation of the system's energy through conjugated gradient method was performed. In this way, the system characteristics were gradually converted from pure LJ to a Coulomb interaction dominated system through a series of stable configurations.

As we are aiming at understanding the lubricant behaviour at mesoscopic conditions observed in a ring-liner system, we have attempted to include in our MD model the potential IL pressurisation that can occur due to the liquid flow resistance, as well as the variable pressure arising from the reacting gas in the combustion chamber. Inserting gas molecules directly in the simulation for this purpose would require a reduction of the time step due to higher thermal velocities of the gas. In turn, the computational cost would increase significantly making simulations impossible to run in realistic computational time. Therefore, in order to understand the effect of external pressure on the IL behaviour, we have applied a repulsive force between the topmost rigid solid layer and the IL particles in the form of a truncated and shifted LJ potential. Two cases with cut-off distances at 15 Å and 4 Å above the outermost top plate layer were studied so that the IL inside the confinement gap would remain outside the influence zone of this mechanistic force. By appropriate selection of the LJ parameters for this potential, the resulting external pressures applied on the unconfined surface of the IL were 120 kPa and 250 kPa, respectively.

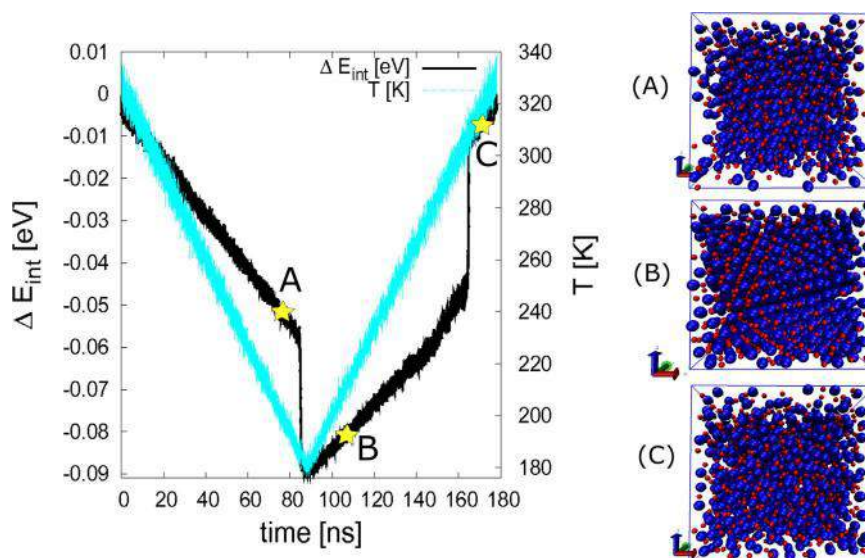


Fig. 2. (Left): Bulk internal energy change and temperature of the ionic liquid as a function of simulation time. (Right) Snapshots of ion arrangement at liquid (A), (C) and solid (B) state.

3. Probing ionic liquid's internal structure behaviour

3.1. Solidification and melting of bulk ionic liquid

In order to confirm that the IL used in our MD simulations remains in a liquid state for the conditions of interest, its liquid–solid and solid–liquid phase transitions were initially studied. A bulk IL configuration was prepared by placing the same number of cations and anions $N_c = N_a = 1000$ into a 3D periodic box, with pressure kept constant at 100 kPa. Phase transitions were then achieved via the application of linear ramping to the temperature, in a similar approach to the calculations performed in Ref. [21].

Starting from an initial temperature $T_1 = 330$ K where the IL is in liquid state, the temperature was decreased linearly down to $T_2 = 180$ K. The absolute rate of temperature change was: $|dT/dt| = 1.67$ K ns⁻¹. A liquid–solid phase transition was observed during the IL cooling. After reaching $T_2 = 180$ K, the temperature was increased back to the initial value of 330 K. This heating process caused with its turn a solid–liquid phase transition. In Fig. 2 the IL internal energy change ΔE_{int} and temperature T are shown as functions of time t . The temperature profile follows the applied conditions and its superimposition to internal energy change allows the observation of the dynamic behaviour of the liquid. By plotting the averaged internal energy change of the IL against its temperature in Fig. 3, the hysteresis behaviour in the solidification–melting cycle is clearly observed, while the phase transition locations can be clearly defined. It can be seen that during the cooling process, the internal energy of IL linearly decreases until the temperature reaches $T_{ls} = 190$ K, at which point a sharp drop is observed. This indicates a first order thermal phase transition (liquid–solid). During the heating process, a similar sharp jump of energy is observed at $T_{sl} = 305$ K which corresponds to an opposite phase transition (solid–liquid). The obtained results are in a good agreement with Ref. [21] and confirm that the IL is behaving as a liquid for temperatures higher than 310 K, under atmospheric pressure conditions. In the rest of our calculations a temperature value of $T=330$ K was applied, in order to allow a liquid state that is combined with local solidification under elevated contact pressure conditions.

3.2. Ionic liquid structure in thin film

The confinement has a profound influence on the structure of ILs in thin films [20,26,32]. The confining surfaces can induce ordering of the

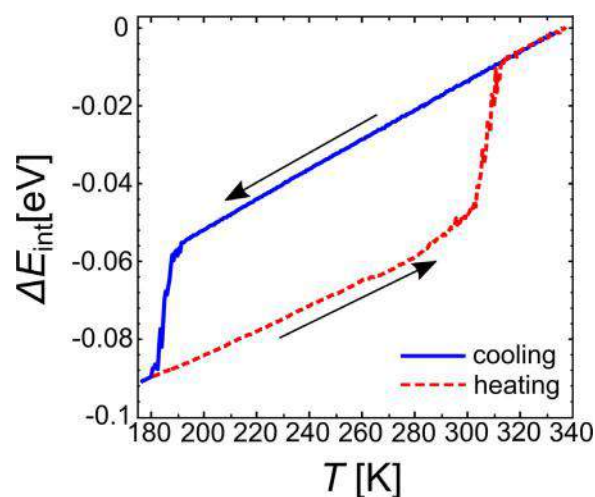


Fig. 3. Bulk internal energy change of the ionic liquid as a function of temperature. The internal energy was calculated by averaging on segments of $\Delta T = 0.5$ K.

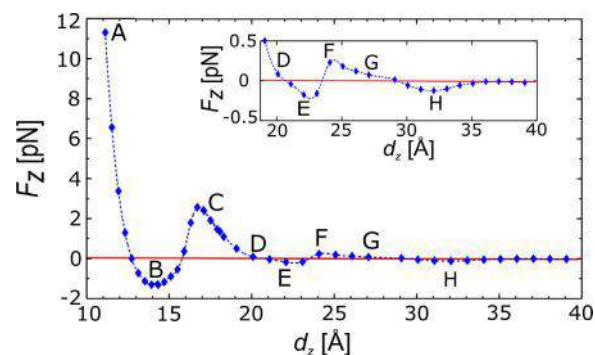


Fig. 4. Dependence of normal force F_z on plate-to-plate distance d_z . Eight characteristic points {A, B, C, D, E, F, G, H} with corresponding interplate distances $d_z = \{11, 14, 17, 20, 22, 24, 27, 32\}$ Å are marked on the $F_z(d_z)$ curve. The horizontal solid line denotes $F_z=0$ pN. The dashed line connects the points obtained from the simulation and serves as a visual guide.

particles in their vicinity. The resulting structure and forces are a result of the interplay between the limited volume and the particles which fill the space. In Fig. 4, the force–distance characteristic of our system is

presented. The solid horizontal line denotes the zero normal force level (i.e., $F_z=0$). A non-monotonous behaviour of the normal force F_z acting on the top plate can be observed as the plate-to-plate distance is changing. This distance corresponds to the gap between the plates where the IL is under confinement. The points (d_z , F_z) were obtained through our simulations, while the dashed line serves as a visual guide. It can be seen that the normal force strongly depends on the inter-plate distance and that it also becomes negative in certain regions. This can be translated as the IL striving to reduce the plate-to-plate distance due to adhesion phenomena. These changes of the normal force are correlated with the extraction and inclusion of IL layers into the gap, as already observed experimentally, cf. Ref. [20]. During the performed simulations, the cationic-anionic layers were squeezed out in pairs, in order to keep the system locally neutral, as observed in experimental studies [20,26,32–34].

Concerning the realisation of the simulations presented in Fig. 4, the inter-plate gap was modified in the following manner: the top plate was displaced towards the bottom one with a constant velocity $v_z=5$ m/s. For $d_z < 17$ Å the velocity was reduced to $v_z=1$ m/s. At each calculation point shown in Fig. 4, the top plate was kept fixed for a period of time $t_{static} = 50$ ps, during which period the average value of the normal force was calculated. The process was repeated until a distance $d_{z,min} = 11$ Å was reached.

In order to understand the dynamic evolution of our system, snapshots of the system from the MD simulations corresponding to several characteristic points in the $F_z(d_z)$ curve were selected and studied in more detail. Fig. 5 shows the configuration and ion density distribution along the z -direction for eight characteristic points {A, B, C, D, E, F, G, H}, corresponding to plate-to-plate distances $d_z = \{11, 14, 17, 20, 22, 24, 27, 32\}$ Å respectively. The ions are deliberately depicted smaller than their LJ radii in order to allow a direct observation of the layering. The position of the atomic centres of the innermost atomic layers of the top and bottom plate are indicated in Fig. 5 as z_T and z_B respectively. As the bottom plate was fixed, z_B remains constant while z_T changes with the top plate displacement.

A general feature observed under all conditions was the fact that the cations always formed the layer closest to the bottom plate. The reason is the smaller size of the cations ($\sigma_{CC} = 5$ Å) compared to the anion species ($\sigma_{AA} = 10$ Å). Following this, a second layer was induced by the first one and populated only by anions. The distance between the first and the second layer from the bottom is in the range of 1–2.5 Å, meaning that while the centres of mass of the particles are in different layers, the layers themselves overlap as their distance is smaller than the particle diameters. In the rest of this section, the changes in the number of layers as the inter-plate gap is reduced will be presented and correlated with the changes in the normal force F_z which is acting on the top plate.

For the minimum simulated plate-to-plate distance $d_z=11$ Å, shown in Fig. 5(A) we can observe a pronounced peak in the anion density distribution close to the bottom plate which is aligned with a well-defined anionic layer inside the gap. The anion peak is marked with the “1CU” annotation. In the case of cations, there are two peaks attached below and above the anionic peak. This situation corresponds to the formation of two incomplete cationic layers inside the gap. With increasing plate-to-plate distance d_z the normal force F_z is decreasing, with a sign change of F_z at $d_z=12.7$ Å. In the range 12.7 Å $< d_z < 15.7$ Å the normal force remains negative. This means that the IL is pulling the plates together, since the ions strive to reduce their interlayer distance, as well as the distance between themselves and the plate atoms. Such behaviour is typically observed in systems exhibiting layering transition, already seen in systems of both neutral molecules [2] and ILs [20]. With further increase of d_z the force becomes positive again, and reaches a local maximum at the point (C) in Fig. 4. At this point we observe a change in the number of anion layers confined in the gap from one to two, as shown in Fig. 5(C).

In Fig. 5(C), the plate-to-plate distance is $d_z=17$ Å and the two bottom peaks of the anion/cation density distribution, denoted by “1CU” and “2C”, are inside the gap. A third smaller anion/cation density peak, denoted by “2U” in Fig. 5(C), is the result of the ordering initiated at the bottom plate's surface and is actually outside the confinement gap. The vertical distance between the peaks “2C” and “2U” is approximately 3.5 Å and corresponds to the effect of the compression of the IL from the top plate. Further increase of the plate-to-plate distance results in a continuous decrease of the normal force without a sign change as the positions of peaks “2C” and “2U” become aligned, cf. Fig. 5(D) for a distance $d_z=20$ Å. Further increase of the inter-plate distance results once more in a reversal of the sign of the normal force (i.e., $F_z < 0$ for 21 Å $< d_z < 23.5$ Å). At the mid point between the plates a broad maximum of cation density distribution can then be observed, see Fig. 5(E). The cations, as smaller particles, have a tendency to fill the space between the more stable anionic layers. When the anions also start to form a third layer at the midpoint between the two plates the corresponding cationic peak of density becomes sharper and the normal force becomes positive again, see Fig. 5(F). In this case the cations can form a layer more easily while the anions remain scattered. This is the opposite behaviour to the one typically observed, where the larger anions tend to order more strongly due to the excluded volume effect [35]. From Fig. 5(F) to Fig. 5(G) an interesting transition can be observed, during which the single well resolved cation peak disappears and a less pronounced cation–anion pair peak takes its place. Finally in Fig. 5(H) at $d_z=32$ Å, we observe the clear formation of three anion and four cation peaks.

Considering engineering applications, the steep rise of the normal force at small plate-to-plate distances, i.e., $d_z < 14$ Å can be beneficial for protecting against solid-solid contact and consequent wear. On the other hand, there is also a strongly decreasing trend of maximal normal force which can be sustained by the system as the number of ion layers confined between the plates increases, i.e., for two cation layers the maximal force $F_{z,max} = 3$ pN, while for three it is $F_{z,max} = 0.25$ pN. In our model, the Lennard-Jones interaction between the plates and the ions is ten times stronger than between the ions themselves. The ion layers closest to the plates are therefore more stable than the layers in the midpoint of the gap (see Fig. 5(F)). As a result, the three layer system becomes less dense, and can build up a lower normal force compared to the two layer system (in Fig. 5(C)).

4. Friction simulations

Following the detailed study of the static system, we turn our focus to dynamic conditions, where there is a relative motion between the plates in x direction and as a result frictional forces can be observed. The dynamics of the plates impact the IL and result in an overall longitudinal force acting on each solid body. In order to evaluate the trends of specific friction we have performed simulations at different plate velocities and at two interplate distances. The simulations have been performed for a broad range of top plate velocities $v_x = 0.1, 0.2, 0.5, 1, 2, 5,$ and 10 m/s, with the bottom plate kept fixed. We have compared cases with different external pressures applied on the IL $p_{ext} = 0, 120$ and 250 kPa and two distinct plate distances $d_z=17$ and 27 Å. The simulations were performed as follows: Points (C) and (G) in Fig. 5 were chosen as the starting configurations. The simulations ran until the top plate had covered a distance of $d_x=50$ Å in x direction. Therefore cases with lower velocities required increased total time. The forces acting on the top plate were monitored, as shown in Fig. 6 for a randomly chosen case. It was observed that the normal force remained roughly the same after the onset of the simulation. Steady-state conditions were assumed following a displacement of $d_x=10$ Å, and then average values were calculated using the statistics until the completion of the simulation.

The results for the specific friction are shown as a function of sliding velocity in Fig. 7. The specific friction $\langle F_x \rangle / \langle F_z \rangle$ is defined as the ratio of

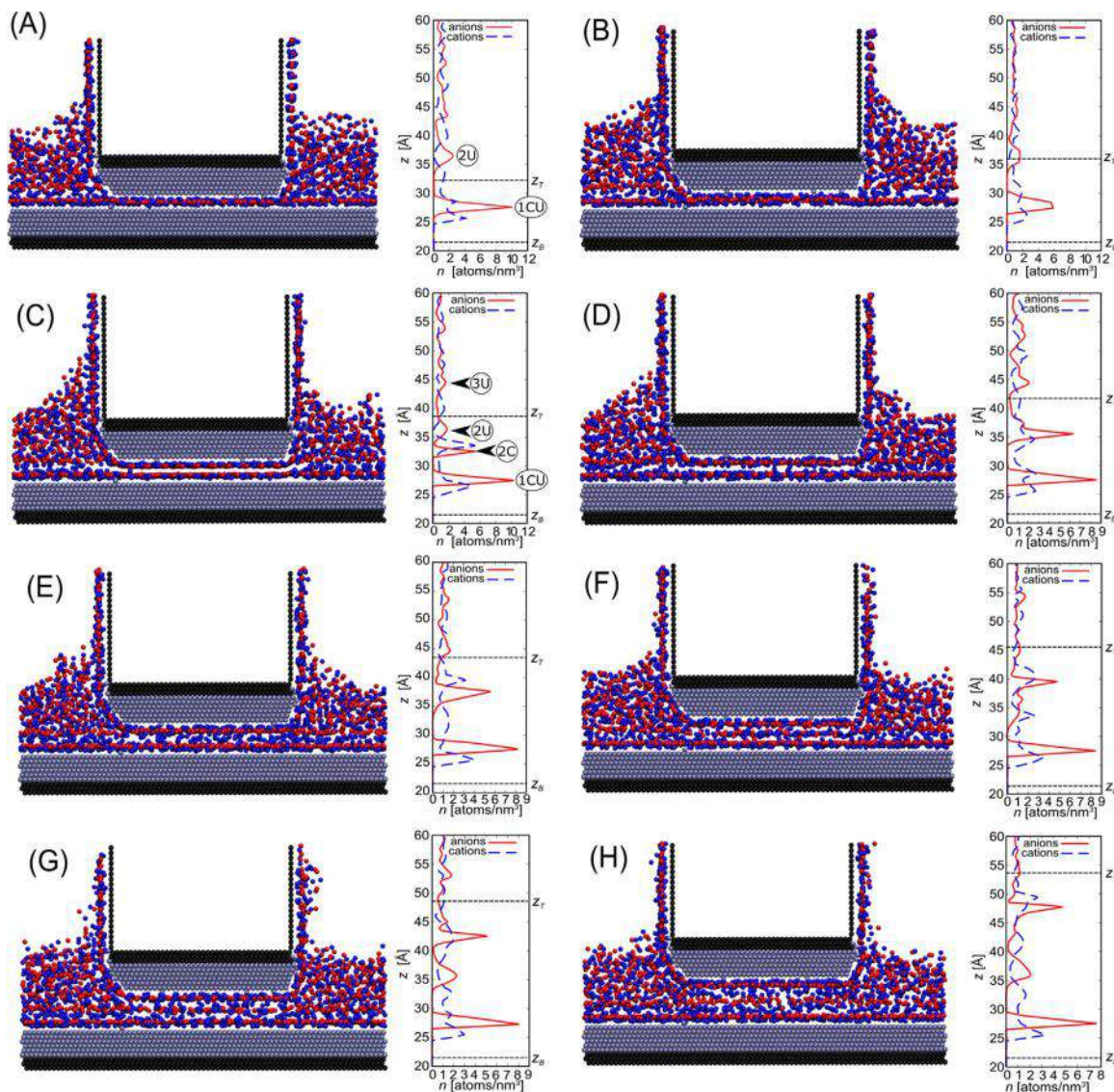


Fig. 5. Snapshots of system configurations at points {A, B, C, D, E, F, G, H} from Fig. 4 and corresponding density distribution of anions/cations along the z-axis. The position of the atomic centres of the innermost layer of the top and bottom plate is denoted by z_T and z_B , respectively. The bottom plate is fixed and $z_B = 21$ Å. The ions are deliberately depicted smaller than their LJ radii in order to allow a direct observation of the layering. In Figures (A) and (C) the annotations indicate the anion layer vertical order from the bottom (1, 2, 3) and the lateral placement: (C)onfined and (U)nconfined.

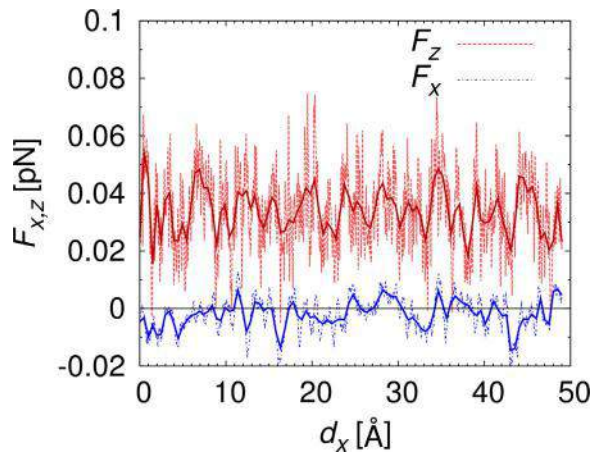


Fig. 6. Temporal evolution of total normal and axial forces acting on sliding surface for plate-to-plate distance $d_z = 27$ Å and top plate axial velocity $v_x = 10$ m/s. Dashed lines show the raw numerical data which are smoothed using the solid lines for a clearer identification of temporal trends.

the time averaged frictional and normal force F_x and F_z respectively and is different to the Coulomb friction coefficient $\mu = \partial F_x / \partial F_z$. In our simulated cases we have observed either a weak or a logarithmic dependence of specific friction on velocity. The numerical values were fitted to a linear function of the form $\langle F_x \rangle / \langle F_z \rangle = a \log(v_x / v_{ref}) + b$, where $v_{ref} = 1$ m/s. The coefficients a, b obtained from the simulation data are listed in Table 2. A reasonable fit to the linear regression curve can be observed for most cases. In the case of $p_{ext} = 120$ kPa, the system is potentially in a transition between the two significantly different cases of zero and high pressure, which can explain the poorer quality of the fit to the linear curve. The logarithmic dependence indicates typical elasto-hydrodynamic lubrication conditions [36]. On the other hand, the weak dependence of specific friction on velocity has also been observed in previous studies of IL lubrication, cf. Refs. [5,24].

4.1. Impact of ionic liquid confinement gap

The influence of plate-to-plate distance on specific friction was initially analysed, while the applied external pressure on the IL p_{ext} was kept equal to zero. In contrast to previous studies of IL lubrication

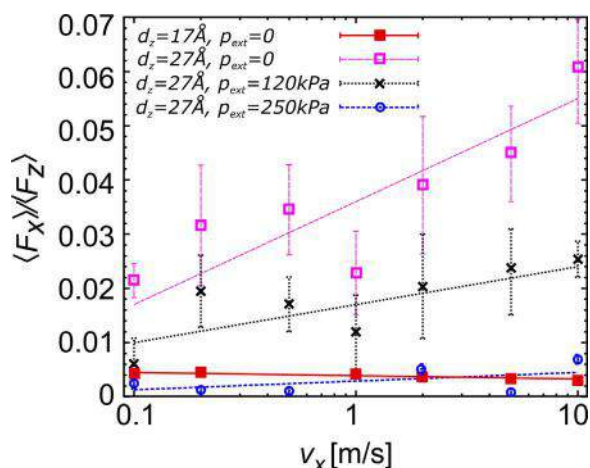


Fig. 7. Dependence of specific friction $\langle F_x \rangle / \langle F_z \rangle$ on velocity at external pressures $p_{\text{ext}} = 0$, 120 and 250 kPa and inter-plate distances $d_z = 17$ and 27 \AA . The error bars represent the standard deviation of the average values obtained from the simulation data. The curves showing the specific friction trends were obtained by linear regression and the corresponding parameters are listed in Table 2.

Table 2

Results for the coefficients a, b in the relation $\langle F_x \rangle / \langle F_z \rangle = a \log(v_x/v_{\text{ref}}) + b$, where $v_{\text{ref}} = 1 \text{ m/s}$. The results were obtained using the least-squares method.

Case	a	b	R^2
(A) $d_z = 17 \text{ \AA}, p_{\text{ext}} = 0 \text{ kPa}$	-0.0006(2)	0.0039(2)	0.63
(B) $d_z = 27 \text{ \AA}, p_{\text{ext}} = 0 \text{ kPa}$	0.016(5)	0.036(3)	0.72
(C) $d_z = 27 \text{ \AA}, p_{\text{ext}} = 120 \text{ kPa}$	0.007(2)	0.017(2)	0.26
(D) $d_z = 27 \text{ \AA}, p_{\text{ext}} = 250 \text{ kPa}$	0.002(1)	0.003(1)	0.62

[5,24], our system showed a strong crystalline order induced by confinement. The normal force was roughly ten times higher in the case of the smaller plate-to-plate distance, i.e., for $d_z = 17 \text{ \AA}$ compared to $d_z = 27 \text{ \AA}$. On the other hand, the lateral force F_x remained at similar levels, therefore leading to a sharp decrease of the specific friction values. At the same time, the weaker confinement and the smaller normal force for $d_z = 27 \text{ \AA}$ resulted in a steeper slope of the curve $\langle F_x \rangle / \langle F_z \rangle$.

In order to understand the potential correlation of the IL structure with the arising frictional forces, the confinement zone was observed in detail using Fig. 8, where a side view (left side) and top view (right side) of the system is shown. In the top view, the system is shown with the solid and IL particles above the upper plate plane removed. In this plot the ions are depicted with their corresponding LJ radii in order to achieve a realistic visualisation of the structure. The anions form a locally cubic structure, cf. right panel Fig. 8(A), while the crystal direction of the cubic structure is indicated with dashed lines. If we look into the structure of the IL in the confinement zone, Fig. 8(A) and (B), we can observe a single, well resolved crystal structure in the case of $d_z = 17 \text{ \AA}$, while in the case of $d_z = 27 \text{ \AA}$ some defects are present. It can also be observed that outside the gap, the IL remains in a disordered, liquid state.

Further clarification can be attained by plotting the ion density distribution profiles inside and outside the gap in Figs. 9(A) and (B). It can be observed that at the plate-to-plate distance $d_z = 17 \text{ \AA}$, both cation and anion peaks of density distribution function inside the gap are narrow and sharp. In addition, both the anion and cation peaks in each paired layer are located at approximately the same z location. These findings confirm that under these conditions the IL is in a crystalline, “solid-like” state with minimum disorder. In the case of a wider gap $d_z = 27 \text{ \AA}$ the anion peaks next to the walls remain narrow, with a third broader one appearing in the centre. The cation arrangement is more dispersed, with double peaks appearing above and below each anion

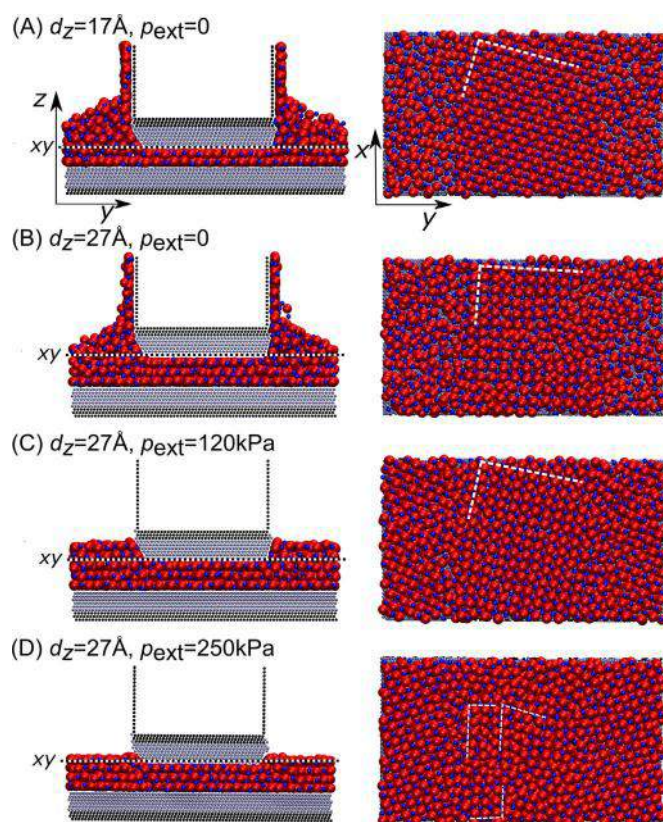


Fig. 8. Side (yz) and top (xy) views of snapshots from four separate friction simulations. The top views correspond to the planes marked with dashed lines in the side views and do not include the solid and IL particles above the upper plate plane. The ions are depicted according to their LJ radii in order to visualise the crystalline structures. The dashed lines in the top views denote the crystal direction of self-formed cubic structures.

peak. These statistics indicate a more layered, less strictly ordered state. The difference in the extent of confinement induced crystallisation is a probable reason for the observed steep slope of specific friction since the observed defects can interact more strongly with the upper plate at higher velocities and contribute to the increase of friction force. Our observations show some similarity to the behaviour previously seen in Lennard-Jones systems where systems at pressures above a certain critical value and at sufficiently low velocities exhibited such behaviour. In these studies, cf. Ref. [8], the shape of fluid molecule was identified as the main parameter that controls crystallisation through the promotion or prevention of internal ordering.

4.2. Impact of ionic liquid pressurisation

In addition to the impact of different confinement gaps, the effect of IL pressurisation was studied, while the inter-plate distance was kept constant. More specifically, a gap of $d_z = 27 \text{ \AA}$ was used, while different pressures $p_{\text{ext}} = 0, 120$ and 250 kPa were applied, using the approach described in Section 2.2.

Through observation of Fig. 9(B)–(D), it can be seen that the application of external pressure prevents the wetting of the side walls of the top plate and leads to a distinct crystallisation of the unconfined IL. On the other hand, the ion density profiles inside the confinement zone are moderately influenced.

The friction results for increasing values of applied pressure are consistent with the observations in the previous subsection, with specific friction decreasing as the order of the IL increases. It can be seen that for high external pressure, i.e., $p_{\text{ext}} = 250 \text{ kPa}$, the slope of the specific friction curve almost vanishes.

Fig. 8(C) shows that for $p_{\text{ext}} = 120 \text{ kPa}$ the local cubic structure

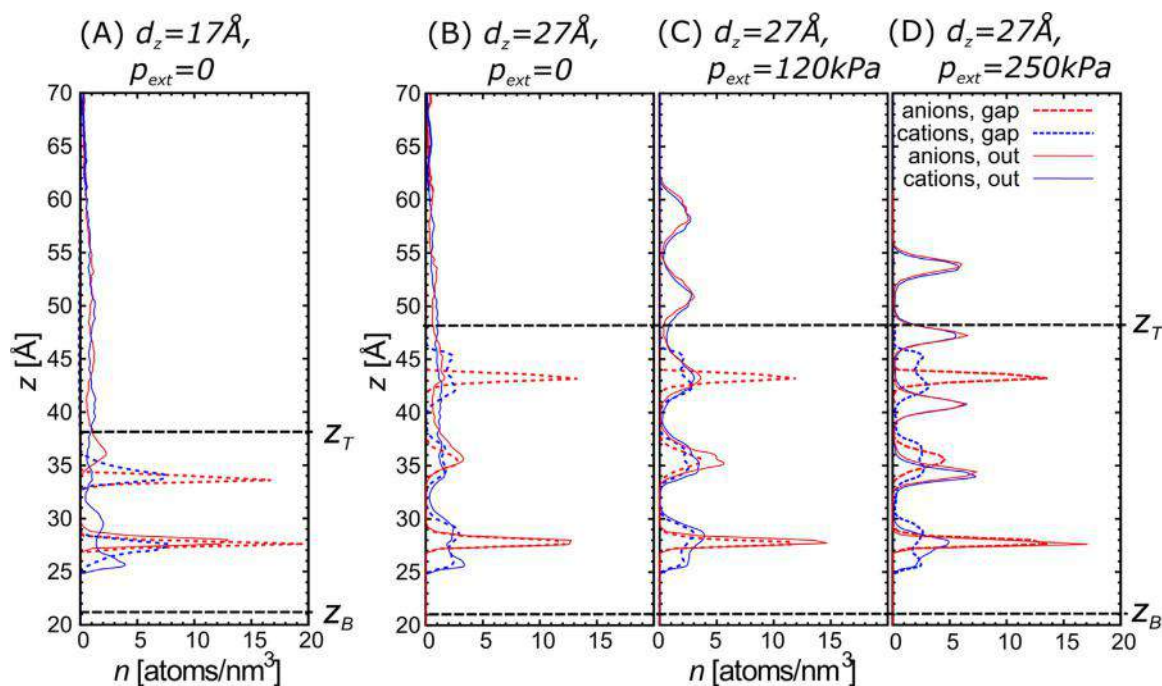


Fig. 9. Density distributions of ions along the z -axis inside (dashed lines) and outside (solid lines) the confinement zone between the solid plates for configurations shown in Fig. 8. The position of the atomic centres of the innermost layer of the top and bottom plate is denoted with z_T and z_B , respectively. Bottom plate is fixed with $z_B = 21$ Å.

induced by confinement between the plates served as a nucleus for further crystallisation between the plates and a well ordered single crystallite was formed in this region. Outside the confinement zone another crystallite was formed with a different orientation. Further increase of external pressure to $p_{\text{ext}} = 250$ kPa forced the IL in the void space to crystallise, while at the same time the IL in the confinement zone was converted to a number of smaller crystallites, cf. Fig. 8(D) and 9(D).

The reported results show a dual nature of IL lubrication, with EHL characteristics at low to medium pressures and confinement gaps that allow more than two distinct anion/cation pair layers to form. At higher pressures and smaller distances which can be translated as mixed lubrication conditions the IL is transformed to a solid-like body, while specific friction decreases to low values which are independent of the sliding velocity. This behaviour can be beneficial in engineering applications such as the piston ring–cylinder liner system, where it can be assumed that the IL crystallisation can potentially aid in preventing the solid contact between the surfaces, along with the associated high friction and wear.

5. Conclusions

In the current study we have implemented a MD simulation setup in order to study the behaviour of model ionic liquids confined between plates which are in close proximity while being in relative motion. Our MD setup was developed in a way that allows the meso–scopic study of the lubrication processes in automotive applications such as the piston ring – cylinder liner interaction inside the internal combustion engine. More specifically, our geometry was selected in order to allow a variable lubricant confinement gap combined with a varying lubricant quantity in the gap, while avoiding the squeeze-out of the lubricant into vacuum. Odd-number layering and near-wall solidification was observed between the solid plates, similar to published experimental findings. Our friction simulations have uncovered an interesting behaviour of ILs, with a logarithmic dependence of specific friction on velocity hinting at elasto-hydrodynamic lubrication at low loads. This behaviour completely changed under more critical conditions of high load, with specific friction decreasing to lower values and becoming independent of

sliding velocity. This behaviour was strongly correlated with the internal structure of the IL and can provide guidance for implementing lubrication concepts that can lead to friction reduction in internal combustion engines.

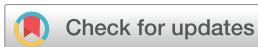
Acknowledgements

The work of I.S. and M.D. was supported in part by the Serbian Ministry of Education, Science and Technological Development under Project No. OI171017 and by COST Action MP1303. Numerical simulations were run on both the HPC facilities of the Advanced Technology Division in Toyota Motor Europe and the PARADOX supercomputing facility at the Scientific Computing Laboratory of the Institute of Physics Belgrade.

References

- [1] K. Holmberg, P. Andersson, A. Erdemir, Global energy consumption due to friction in passenger cars, *Tribol Int* 47 (2012) 221–234. <http://dx.doi.org/10.1016/j.triboint.2011.11.022>.
- [2] B. Bhushan, J.N. Israelachvili, U. Landman, Nanotribology: friction, wear and lubrication at the atomic scale, *Nature* 374 (6523) (1995) 607–616. <http://dx.doi.org/10.1038/374607a0>.
- [3] S.-J. Heo, S.B. Sinnott, D.W. Brenner, J.A. Harrison, Computational modeling of nanometer-scale tribology, in: B. Bhushan (Ed.) *Nanotribology and nanomechanics: an introduction*, Springer, Berlin, Heidelberg, 2005, pp. 623–691. http://dx.doi.org/10.1007/3-540-28248-3_13.
- [4] S. Loehe, C. Matta, C. Minfray, T. Le Mogne, J.-M. Martin, R. Iovine, Y. Obara, R. Miura, A. Miyamoto, Mixed lubrication with C18 fatty acids: effect of unsaturation, *Tribol Lett* 53 (1) (2014) 319–328. <http://dx.doi.org/10.1007/s11249-013-0270-3>.
- [5] A.C.F. Mendonça, A.A.H. Pádua, P. Malfreyt, Nonequilibrium molecular simulations of new ionic lubricants at metallic surfaces: prediction of the friction, *J Chem Theory Comput* 9 (3) (2013) 1600–1610. <http://dx.doi.org/10.1021/ct3008827>.
- [6] Heyes DM, Smith ER, Dini D, Spikes HA, Zaki TA. Pressure dependence of confined liquid behavior subjected to boundary-driven shear. *J. Chem. Phys.* Vol. 136 (13). (<http://dx.doi.org/10.1063/1.3698601>).
- [7] C. Gattinoni, D.M. Heyes, C.D. Lorenz, D. Dini, Traction and nonequilibrium phase behavior of confined sheared liquids at high pressure, *Phys Rev E* 88 (2013) 052406. <http://dx.doi.org/10.1103/PhysRevE.88.052406>.
- [8] L. Martinie, P. Vergne, Lubrication at extreme conditions: a discussion about the limiting shear stress concept, *Tribology Lett* 63 (2) (2016) 21. <http://dx.doi.org/10.1007/s11249-016-0709-4>.
- [9] N. Voeltzel, A. Giuliani, N. Fillot, P. Vergne, L. Joly, Nanolubrication by ionic

- liquids: molecular dynamics simulations reveal an anomalous effective rheology, *Phys Chem Chem Phys* 17 (2015) 23226–23235. <http://dx.doi.org/10.1039/C5CP03134F>.
- [10] J. Gao, W.D. Luedtke, D. Gourdon, M. Ruths, J.N. Israelachvili, U. Landman, Frictional forces and Amontons' law: from the molecular to the macroscopic scale, *J Phys Chem B* 108 (11) (2004) 3410–3425. <http://dx.doi.org/10.1021/jp036362l>.
- [11] M.O. Robbins, M.H. Müser, Computer simulations of friction, lubrication, and wear, in: B. Bhushan (Ed.) *Modern tribology handbook*, two volume set, mechanics & materials Science, CRC Press, Boca Roton, 2000. <http://dx.doi.org/10.1201/9780849377877.ch20>.
- [12] R.E. Rudd, J.Q. Broughton, Coarse-grained molecular dynamics and the atomic limit of finite elements, *Phys Rev B* 58 (1998) R5893–R5896. <http://dx.doi.org/10.1103/PhysRevB.58.R5893>.
- [13] Y. Wang, W. Jiang, T. Yan, G.A. Voth, Understanding ionic liquids through atomistic and coarse-grained molecular dynamics simulations, *Acc Chem Res* 40 (11) (2007) 1193–1199. <http://dx.doi.org/10.1021/ar700160p>.
- [14] M.-D. Bermúdez, A.-E. Jiménez, J. Sanes, F.-J. Carrión, Ionic liquids as advanced lubricant fluids, *Molecules* 14 (8) (2009) 2888–2908. <http://dx.doi.org/10.3390/molecules14082888>.
- [15] K. Mistry, M.F. Fox, M. Priest, Lubrication of an electroplated nickel matrix silicon carbide coated eutectic aluminium-silicon alloy automotive cylinder bore with an ionic liquid as a lubricant additive, *Proc Inst Mech Eng, Part J: J Eng Tribol* 223 (3) (2009) 563–569. <http://dx.doi.org/10.1243/13506501JET562>.
- [16] J. Qu, D.G. Bansal, B. Yu, J.Y. Howe, H. Luo, S. Dai, H. Li, P.J. Blau, B.G. Bunting, G. Mordukhovich, D.J. Smolenski, Antwear performance and mechanism of an oil-miscible ionic liquid as a lubricant additive, *ACS Appl Mater Interfaces* 4 (2) (2012) 997–1002. <http://dx.doi.org/10.1021/am201646k>.
- [17] J. Qu, P.J. Blau, S. Dai, H. Luo, H.M. Meyer, Ionic liquids as novel lubricants and additives for diesel engine applications, *Tribology Lett* 35 (3) (2009) 181–189. <http://dx.doi.org/10.1007/s11249-009-9447-1>.
- [18] O.Y. Fajardo, F. Bresme, A.A. Kornyshev, M. Urbakh, Electrotunable friction with ionic liquid lubricants: how important is the molecular structure of the ions?, *J Phys Chem Lett* 6 (20) (2015) 3998–4004. <http://dx.doi.org/10.1021/acs.jpclett.5b01802>.
- [19] Fajardo O, Bresme F, Kornyshev A, Urbakh M. Electrotunable lubricity with ionic liquid nanoscale films. *Scientific reports* 5. <http://dx.doi.org/10.1038/srep07698>.
- [20] A.E. Somers, P.C. Howlett, D.R. MacFarlane, M. Forsyth, A review of ionic liquid lubricants, *Lubricants* 1 (1) (2013) 3. <http://dx.doi.org/10.3390/lubricants1010003>.
- [21] Capozza R, Vanossi A, Benassi A, Tosatti E. Squeezeout phenomena and boundary layer formation of a model ionic liquid under confinement and charging. *J. Chem. Phys.* Vol. 142 (6). <http://dx.doi.org/10.1063/1.4907747>.
- [22] F. Varnik, L. Bocquet, J.-L. Barrat, L. Berthier, Shear localization in a model glass, *Phys Rev Lett* 90 (2003) 095702. <http://dx.doi.org/10.1103/PhysRevLett.90.095702>.
- [23] A.V. Mokshin, J.-L. Barrat, Shear-induced crystallization of an amorphous system, *Phys Rev E* 77 (2008) 021505. <http://dx.doi.org/10.1103/PhysRevE.77.021505>.
- [24] F. Federici Canova, H. Matsubara, M. Mizukami, K. Kurihara, A.L. Shluger, Shear dynamics of nanoconfined ionic liquids, *Phys Chem Chem Phys* 16 (2014) 8247–8256. <http://dx.doi.org/10.1039/C4CP00005F>.
- [25] S. Plimpton, Fast parallel algorithms for short-range molecular dynamics, *J Comput Phys* 117 (1) (1995) 1–19. <http://dx.doi.org/10.1006/jcph.1995.1039>.
- [26] J. Gao, W.D. Luedtke, U. Landman, Layering transitions and dynamics of confined liquid films, *Phys Rev Lett* 79 (1997) 705–708. <http://dx.doi.org/10.1103/PhysRevLett.79.705>.
- [27] D.J. Hardy, J.E. Stone, K. Schulten, Multilevel summation of electrostatic potentials using graphics processing units, *Parallel Comput* 35 (3) (2009) 164–177. <http://dx.doi.org/10.1016/j.parco.2008.12.005>.
- [28] M.S. Daw, M.I. Baskes, Embedded-atom method: derivation and application to impurities, surfaces, and other defects in metals, *Phys Rev B* 29 (12) (1984) 6443. <http://dx.doi.org/10.1103/PhysRevB.29.6443>.
- [29] I. Stankovic, S. Hess, M. Kröger, Structural changes and viscoplastic behavior of a generic embedded-atom model metal in steady shear flow, *Phys Rev E* 69 (2) (2004) 021509. <http://dx.doi.org/10.1103/PhysRevE.69.021509>.
- [30] A. Gubbels-Elzas, B.J. Thijse, Ionic motion during field-assisted oxidation of aluminium studied by molecular dynamics simulations, *Comput Mater Sci* 90 (2014) 196–202. <http://dx.doi.org/10.1016/j.commatsci.2014.03.062>.
- [31] F. Iori, S. Corni, Including image charge effects in the molecular dynamics simulations of molecules on metal surfaces, *J Comput Chem* 29 (10) (2008) 1656–1666. <http://dx.doi.org/10.1002/jcc.20928>.
- [32] S. Perkin, Ionic liquids in confined geometries, *Phys Chem Chem Phys* 14 (2012) 5052–5062. <http://dx.doi.org/10.1039/C2CP23814D>.
- [33] R. Hayes, N. Borisenko, M.K. Tam, P.C. Howlett, F. Endres, R. Atkin, Double layer structure of ionic liquids at the Au(111) electrode interface: an atomic force microscopy investigation, *J Phys Chem C* 115 (14) (2011) 6855–6863. <http://dx.doi.org/10.1021/jp200544b>.
- [34] A.M. Smith, K.R. Lovelock, N.N. Gosvami, T. Welton, S. Perkin, Quantized friction across ionic liquid thin films, *Phys Chem Chem Phys* 15 (37) (2013) 15317–15320. <http://dx.doi.org/10.1039/C3CP52779D>.
- [35] P.D. Kaplan, J.L. Rouke, A.G. Yodh, D.J. Pine, Entropically driven surface phase separation in binary colloidal mixtures, *Phys Rev Lett* 72 (4) (1994) 582–585. <http://dx.doi.org/10.1103/PhysRevLett.72.582>.
- [36] S. Bair, L. Martinie, P. Vergne, Classical EHL versus quantitative EHL: a perspective part II – super-arrhenius piezoviscosity, an essential component of elastohydrodynamic friction missing from classical EHL, *Tribol Lett* 63 (3) (2016) 37. <http://dx.doi.org/10.1007/s11249-016-0725-4>.



Cite this: *Phys. Chem. Chem. Phys.*,
2019, 21, 4375

Molecular dynamics investigation of the influence of the shape of the cation on the structure and lubrication properties of ionic liquids†

Miljan Dašić, ^a Igor Stanković ^{*a} and Konstantinos Gkagkas ^b

We present a theoretical study of the influence of the molecular geometry of the cation on the response of ionic liquids (ILs) to confinement and mechanical strain. The so-called tailed model includes a large spherical anion and asymmetric cation consisting of a charged head and a neutral tail. Despite its simplicity, this model recovers a wide range of structures seen in ILs: a simple cubic lattice for small tails, a liquid-like state for symmetric cation–tail dimers, and a molecular layer structure for dimers with large tails. A common feature of all investigated model ILs is the formation of a fixed (stable) layer of cations along solid plates. We observe a single anionic layer for small gap widths, a double anionic layer for intermediate ones, and tail-to-tail layer formation for wide gaps. The normal force evolution with gap size can be related to the layer formed inside the gap. The low hysteretic losses during the linear cyclic motion suggest the presence of strong slip inside the gap. In our model the specific friction is low and the friction force decreases with tail size.

Received 30th November 2018,
Accepted 23rd January 2019

DOI: 10.1039/c8cp07364c

rsc.li/pccp

1 Introduction

Ionic liquids (ILs) are two-component systems composed of large asymmetric and irregularly shaped organic cations and anions. The feature of irregularity is important as it effectively prevents low-temperature ordering and crystallisation. Therefore, ILs are usually in the melted or glassy state. The physical properties of ILs like negligible vapour pressure, high-temperature stability, and high ionic conductivity and also a great variety of ILs and their mixtures highlight them as potentially relevant to lubrication.^{1,2} A large number of variations in IL composition are possible, estimated at the order of magnitude of 10^{18} different ILs.³ From their variety stems the possibility of tuning their physicochemical properties which can affect lubrication such as viscosity, polarity, surface reactivity by varying their atomic composition, and the cation–anion combination. Hence, it would be advantageous if we could deduce general relations between the molecular structure and anti-wear and lubrication properties of ILs.

Since 2001, when ionic liquids were first considered for lubrication applications,⁴ there has been a large number of experimental studies in that direction. It has been observed that

the alkyl chain length of the cations affects the IL's viscosity,¹ melting point¹ and pressure–viscosity coefficients.⁵ Related specifically to lubrication, Dold *et al.*³ and Minami⁶ explored the impact of the cationic alkyl chain's length on the tribological properties of ILs. ILs considered in those references have the same cation but different anions (symmetric hexafluorophosphate $[\text{PF}_6]^-$ and asymmetric bis(trifluoromethylsulfonyl)imide $[\text{Tf}_2\text{N}]^-$, respectively). Still, while Minami observed that the coefficient of friction (COF) decreases from 0.25 to 0.15 with the increase of alkyl chain length $n_C = 2$ to 12 (n_C is the number of carbon atoms), Dold *et al.* observed that the COF increases from 0.025 to 0.1. The IL's wetting properties are also sensitive to its molecular geometry. ILs exhibit different wetting behaviours depending on the anion size:^{7–9} from the absence of wetting to partial or complete wetting. A well-studied IL, $[\text{BMIM}]^+[\text{PF}_6]^-$, exhibits full wetting at the interface with mica substrates.^{7,8} In contrast, $[\text{BMIM}]^+[\text{TFSI}]^-$ shows partial wetting on mica.^{8,9} In these examples, the ILs have the same cation and different anions.

An important observation about the structure of confined ILs is their arrangement into positively and negatively charged ionic layers and adsorption onto solid surfaces.^{10,11} These ionic adsorption layers should reduce friction and prevent wear, especially in the case of boundary lubrication.¹⁰ The wear is reduced primarily in two ways: *via* high load-carrying capability and self-healing of adsorbed IL layers. Still, these two processes seem conflicting with each other since high load-carrying capability requires strong adsorption of the lubricant to the surface, while self-healing requires high mobility.¹² Understanding the

^a Scientific Computing Laboratory, Center for the Study of Complex Systems, Institute of Physics Belgrade, University of Belgrade, Pregrevice 118, 11080 Belgrade, Serbia. E-mail: igor.stankovic@ipb.ac.rs

^b Advanced Technology Division, Toyota Motor Europe NV/SA, Technical Center, Hoge Wei 33B, 1930 Zaventem, Belgium

† Electronic supplementary information (ESI) available. See DOI: 10.1039/c8cp07364c

driving forces between them requires relating the molecular structure and flow properties of confined ILs. Kamimura *et al.*¹³ evaluated the tribological properties of different ionic liquids using a pendulum and ball on disk tribo testers. They considered ILs consisting of imidazolium cations with different alkyl chain lengths and $[\text{TF}_2\text{N}]^-$ anions as lubricants. Their main observation is that the increment of alkyl chain length can reduce the friction and wear of sliding pairs in the elastohydrodynamic lubrication (EHL) regime as a consequence of the increased viscosity. Generally, the conclusion is that longer alkyl chains lead to better tribological performance. Related to the impact of alkyl chain length on the structure of ILs, Perkin *et al.*¹⁴ experimentally achieved the formation of tail-to-tail bilayers of cations when their alkyl chain length was large, in case of confinement between solid surfaces. Their observations are in accordance with other experimental investigations of IL lubricants.^{15–17} In this work, we have obtained similar configurations *via* numerical simulations of ILs confined between two solid plates, where tail-to-tail formation in the middle of the interplate gap is visible.

In this theoretical study, we apply a coarse grained Molecular Dynamics (MD) simulation setup consisting of two solid plates and an IL placed between them. Our simulation setup also includes lateral reservoirs into which the IL can dynamically expand.¹⁸ The focus of our study is on the systematic investigation of the flow properties and lubrication mechanisms of ionic liquids modelled with a generic coarse grained model which considers a variable shape of the cation. We investigate the impact of cationic tail size on the structural and tribological properties of ILs *via* molecular dynamics simulations. Such an idea is meaningful since previous theoretical studies have pointed out that confinement modifies the behaviour of ILs, and despite their good wetting nature, slip is present at the plates.¹⁹ Coulombic interactions in ILs induce long-range ordering,^{19–21} which in turn can influence their lubrication response. Recently, there have been substantial modelling efforts towards the investigation of ILs as lubricants.^{22–24} Coarse grained approaches, being less computationally expensive, have an advantage for reaching the length- and time-scales that can be of relevance to the systems of industrial interest. Previously, coarse grained MD simulations^{25–31} were used to study thin lubricant films subjected to shearing between solid plates.

We outline the content of this paper: the Model section describes the interactions taken into account and the MD simulation setup. The focus of the Bulk ionic liquids section is first on obtaining the relaxed structures and then on calculating the viscosity coefficients of bulk ionic liquids. In the following Confined ionic liquids section we present and discuss the static and dynamic behaviours of confined ionic liquids. This section also presents the results of the friction behaviour of confined ILs. We present the overview of contributions in the Discussion section followed by the Conclusion.

2 Model

In this study, we have applied a generic coarse grained IL model, introduced in ref. 24. In this model, the anion is represented as a

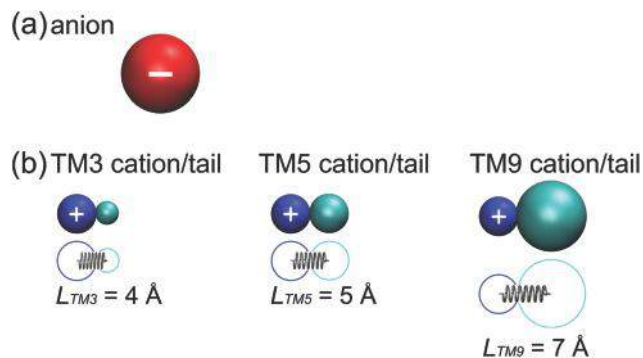


Fig. 1 Schematic representations of (a) anion and (b) cation molecules in a TM. The anion is represented by a spherical particle with a diameter $\sigma_A = 10 \text{ \AA}$. The cation molecule consists of a charged head with a diameter $\sigma_C = 5 \text{ \AA}$ and a neutral tail. In order to be more concise, we refer just to the cationic head as the cation. The cation and its tail are connected using a spring with length $L = (\sigma_C + \sigma_T)/2$. The size of the tail has been varied and (a) TM3, (b) TM5 and (c) TM9 ionic liquids have tail diameters of 3, 5 and 9 Å, respectively. The molecular asymmetry is a feature of real ionic liquids and the chosen parameters resemble $[\text{BMIM}]^+[\text{PF}_6]^-$ IL properties, *cf.* ref. 22 and 23.

negatively charged large-sized spherical particle, while the cation is a dimer consisting of a positively charged small-sized spherical particle (*i.e.* cationic head), and a neutral spherical particle (tail) attached to the corresponding cationic head *via* an elastic spring, see Fig. 1. Since the cationic tail is the principal feature of the model used in this paper, we will refer to it as a tail model (TM). The asymmetry of the cation leads to amorphous (glassy) states for realistic values of interaction parameters (*e.g.*, for hydrocarbons), in contrast to the simplest coarse-grained model of an IL known as a salt-like model (SM), where both cations and anions are spherical. The SM has already been exploited in previous studies.^{18,22,24,32} Despite its obvious advantage of simplicity, in order to avoid crystallization, the SM relies on a very weak non-bonded Lennard-Jones interaction, which makes any comparison with real ILs only qualitative. In addition, the SM cannot account for molecular asymmetry featured in real ILs. Nevertheless, the SM has been proven to be quite useful for the development of the simulation methodology, as it reduces computational complexity and enables faster equilibration (*e.g.*, for obtaining static force–distance characteristics as in ref. 18). More complex extensions of TM coarse grained models can involve several tails of different sizes, like in ref. 22. For simplicity reasons, we restrict our considerations in this study to a single neutral tail of variable size. Although a whole cationic dimer is an entity which actually represents a cation, in order to be more concise we refer just to the cationic head as the cation.

2.1 Interaction model

In cation–tail dimers an elastic spring connects cations and neutral tails, enabling the tail's freedom of moving independently from its cation, since their connection is not rigid, *cf.* Fig. 1. Interatomic interactions taken into consideration in our MD simulations are: (i) non-bonded Lennard-Jones (LJ) and

Coulombic electrostatic interactions and (ii) bonded interaction (an elastic spring potential in cation–tail pairs):

$$V_{\alpha\beta}(r_{ij}) = 4\epsilon_{\alpha\beta} \left[\left(\frac{\sigma_{\alpha\beta}}{r_{ij}} \right)^{12} - \left(\frac{\sigma_{\alpha\beta}}{r_{ij}} \right)^6 \right] + \frac{1}{4\pi\epsilon_0\epsilon_r} \frac{q_i q_j}{r_{ij}}, \quad (1)$$

where $i, j = 1, \dots, N$ are particle indices, and N is the total number of particles. Particles can be of different types $\alpha, \beta = A, C, T, P$, which refer to anions, cations, tails, and solid plate atoms, respectively. Interaction of tails (*i.e.*, at least one of the indices $\alpha, \beta = T$) with all other atom types, including tails themselves, is implemented using a purely repulsive potential. The ionic liquid is electro-neutral, *i.e.*, the numbers of cations and anions are the same. All MD simulations in this study were performed using the LAMMPS software.³³ More details are provided in the ESI.†

2.2 Model parameters

In this study we have fixed the diameters of the cationic heads and anions at $\sigma_C = 5 \text{ \AA}$ and $\sigma_A = 10 \text{ \AA}$, respectively. Such a choice respects the asymmetry that exists in ILs and it is consistent with other models, as well as, for example, the [BMIM]⁺[PF₆][−] ionic liquid, *cf.* ref. 18 and 22–24. The solid plate atoms have a diameter of $\sigma_P = 3 \text{ \AA}$. We have taken into consideration three different tailed-models of the IL depending on the tail size, which is defined by its Lennard-Jones σ_T parameter: a small-tail cationic dimer (*i.e.*, TM3 with $\sigma_T = 3 \text{ \AA}$), a symmetric cationic dimer (*i.e.*, TM5 with $\sigma_T = \sigma_C = 5 \text{ \AA}$) and a large-tail cationic dimer (*i.e.*, TM9 with $\sigma_T = 9 \text{ \AA}$), see Fig. 1. Drawing a comparison with the experiment in ref. 3 and 6, the TM IL mimics a folded alkyl chain and the radius of the sphere is related to the gyration radius of the chains. Depending on the length of the alkyl chain, the sphere has a smaller or larger radius. Thus, the size of a sphere which represents a neutral tail in TM ILs does not compare directly with the alkyl chain length. However, we can make a qualitative analogy. While the representation of the alkyl chain as a neutral LJ sphere does not include all the microscopic level features, we will show that the three selected radii, *i.e.*, $\sigma_T = \{3, 5, 9\} \text{ \AA}$, result in clear differences in the bulk properties of the ILs and their lubrication response.

Each cation–tail pair is connected *via* an elastic spring defined by the next two parameters: elastic constant $K = 80 \text{ kcal mol}^{-1} \text{ \AA}^{-2}$ and equilibrium length of the spring $L = (\sigma_C + \sigma_T)/2$. To account for the dielectric screening, the dielectric constant is set to $\epsilon_r = 2$ as in ref. 18, 23 and 24. The strength of the LJ interactions between different charged parts of ions ($\alpha, \beta = A, C$) is $\epsilon_{\alpha\beta} = 1.1 \text{ kcal mol}^{-1}$. The LJ parameters are chosen to compare well with one of the most widely studied ionic liquids, [BMIM]⁺[PF₆][−], *cf.* ref. 22 and 23. The charges of ions are set to elementary: $q_C = +e$ and $q_A = -e$, where $e = 1.6 \times 10^{-19} \text{ C}$. The tails interact with all other particle types repulsively. The strength of the ion–substrate interaction was tuned to ensure complete wetting, $\epsilon_{\alpha P} = 5.3 \text{ kcal mol}^{-1}$, where $\alpha = A, C, T$.‡ All the values of the $\{\epsilon_{\alpha\beta}, \sigma_{\alpha\beta}\}$ parameters used in our

‡ Only when the strength of the ion–substrate LJ interaction equals the strength of the inter-ionic LJ interaction, partial wetting is observed, *i.e.*, $\epsilon_{\alpha P} = 1.1 \text{ kcal mol}^{-1}$, as reported in the ESI.†

simulations are listed in the ESI.† The cross-interaction parameters are calculated using Lorentz–Berthelot mixing rules.

3 Bulk ionic liquids

3.1 Bulk structure

An initial configuration for a bulk ionic liquid was obtained by a random placement of ions ($N_C = N_A = 1000$) into a cubic simulation box with periodic boundary conditions in all three directions. The simulation box volume was chosen to ensure that the resulting pressure after the relaxation of the IL structure is comparable to the one experienced by a thin confined IL film studied in the following section of this paper. In the case of the present system the pressure is $p \approx 10 \text{ MPa}$, which corresponds to a normal force of 1 nN acting on a surface of 10^4 \AA^2 . Relaxation of the internal energy and pressure for the three TM ILs is presented in detail in the ESI.†

Fig. 2 presents the *xy* cross-sectional snapshots of bulk IL configurations at the end of relaxation simulations, again for (a) TM3, (b) TM5 and (c) TM9. These results have clearly revealed a strong dependence of the IL's structure on the tail size. It can be observed that (i) small tails in TM3 lead to cubic crystalline arrangement of ions, (ii) symmetric cationic dimers in TM5 enable a liquid-like state of the IL, and (iii) large tails in TM9 dictate ordering in the way that ions form layers with tails in-between.

These results are in agreement with experimental observations of the relationship between the length of the alkyl chain and the structure of a bulk IL.³⁴ When the cation alkyl chain is short, the Coulombic forces are dominant, enabling order. We observe this kind of result with TM3. Alkyl chains must be long enough in order to suppress the Coulombic interactions, *e.g.* the number of C atoms $n_C \approx 12$, which corresponds to the tail length of $(n_C - 1) \cdot 1.53 \text{ \AA} = 16.83 \text{ \AA}$, taking into account that a C–C bond has a length of 1.53 \AA . The suppression of Coulombic interactions results in the absence of order, as we obtain with TM5, *cf.* Fig. 2(b). However, the tail should not be too large since large tails tend to arrange into a separate layer. This leads to a reappearance of layered structural ordering, like in the case of TM9, *cf.* Fig. 2(c). This layering can take place even when the cohesive interaction between the tails is absent, since in our TM IL the pair-interaction of tails with all other particles is repulsive.

3.2 Bulk IL viscosity characteristics

We have calculated the viscosity using non-equilibrium (NEMD) simulations of the three TM IL systems in a box with periodic boundary conditions in all three directions under different shear rates. Since in bulk simulations the whole simulation box is sheared, the shape of the box changes. Therefore, we use the so-called SLLD thermostat^{35,36} (more details are provided in the ESI.†). For each value of $\dot{\gamma}$ in the range $0.01\text{--}10 \text{ ns}^{-1}$, we have calculated the average shear stress from three stress tensor components: $\tau = (\tau_{xy} + \tau_{xz} + \tau_{yz})/3$. The average shear stress τ and shear rate $\dot{\gamma}$ are related by

$$\tau = \eta \cdot \dot{\gamma}^\alpha, \quad (2)$$

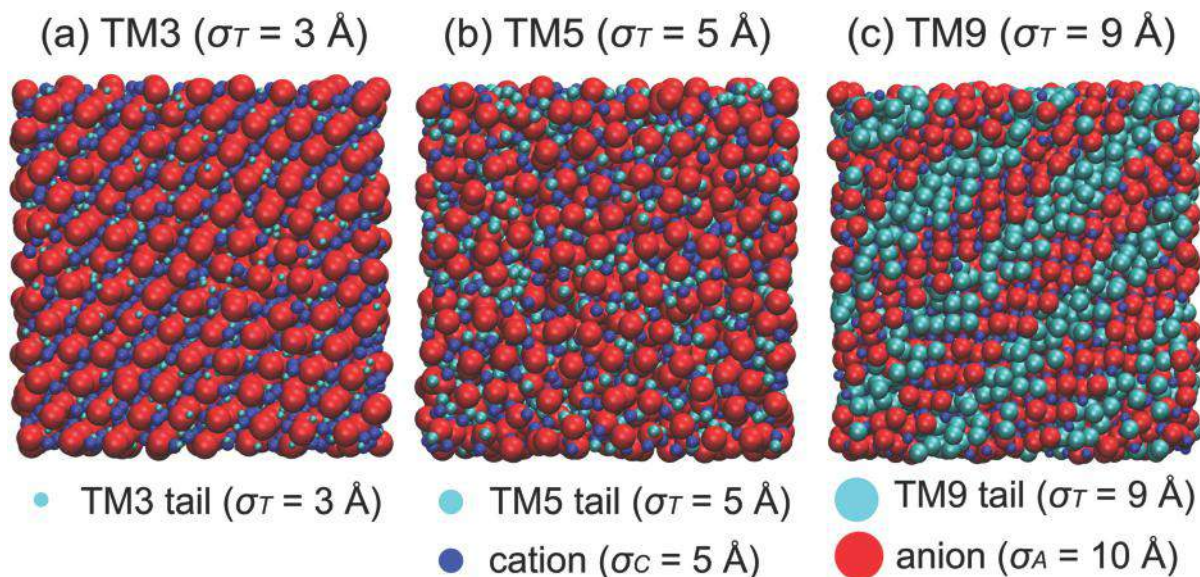


Fig. 2 Configuration snapshots of bulk (a) TM3, (b) TM5 and (c) TM9 ionic liquids, with tail diameters of 3, 5 and 9 Å, respectively. We may notice that each configuration snapshot represents a different state, *i.e.* the TM3 bulk IL crystallizes into a tilted simple cubic crystal structure, oriented along the face diagonal; the TM5 bulk IL is in a liquid state; the TM9 bulk IL crystallizes into crystal planes with alternating ionic-tail layers, oriented along the face diagonal as well.

where η is the generalised viscosity coefficient and α is an exponent. In addition to the NEMD method of simulation box shearing, we have also calculated the zero shear rate viscosity η^{GK} using the Green–Kubo (GK) relation for the three model ILs, as the integral of the stress tensor auto-correlation functions, see ref. 37 and 38.

In Fig. 3 we present the dependence of the average shear stress τ on the shear rate $\dot{\gamma}$ for the TM3, TM5 and TM9 bulk ILs. We notice that the average shear stress remains within the same order of magnitude in the TM3 and TM9 systems, although the shear rate changes by four orders of magnitude. As a result, the corresponding values of the exponent α are low, *i.e.* $\alpha_{\text{TM3}} = 0.15 \pm 0.02$ and $\alpha_{\text{TM9}} = 0.12 \pm 0.04$. The bulk ILs in

the case of TM3 and TM9 are ordered. The presence of order results also in high values of their Green–Kubo viscosities, *i.e.* $\eta_{\text{TM3}}^{\text{GK}} = 4.72$ mPa s and $\eta_{\text{TM9}}^{\text{GK}} = 1.67$ mPa s. In contrast to that, we observe a more than two orders of magnitude change in the average stress tensor component in the case of symmetric cations and a liquid-like bulk structure (TM5). We have obtained $\alpha_{\text{TM5}} = 0.8 \pm 0.1$, which is relatively close to a Newtonian viscous fluid, *i.e.*, $\alpha = 1$. The viscosities determined *via* shearing simulations and *via* the GK relation in the case of TM5 are different; however, they are of the same order of magnitude: $\eta_{\text{TM5}} = 0.1435$ mPa s and $\eta_{\text{TM5}}^{\text{GK}} = 0.6144$ mPa s.

4 Confined ionic liquids

For the study of ILs under confinement, we use the MD simulation setup of ILs under confinement shown in Fig. 4. The ionic liquid is placed between two solid plates: a bottom plate which is continuous in two dimensions (in the xy -plane) and a top plate which is infinite in one dimension (along the x -axis) and features lateral reservoirs in the other, *i.e.*, along the y -axis. This design allows long-range ordering of the ILs on the surface while at the same time creating quasi-micro-canonical conditions inside the interplate gap. We use this setup throughout the paper in order to investigate both the static and dynamic behaviours of the confined IL, as well as its lubrication performance. We keep the simulation setup geometry fixed, and we change the IL. Additional implementation details can be found in the ESI.†

4.1 Equilibrium behaviour of confined ionic liquids

Confinement induces layering in IL thin films.^{18,39} In order to understand how an interplay between layering and the

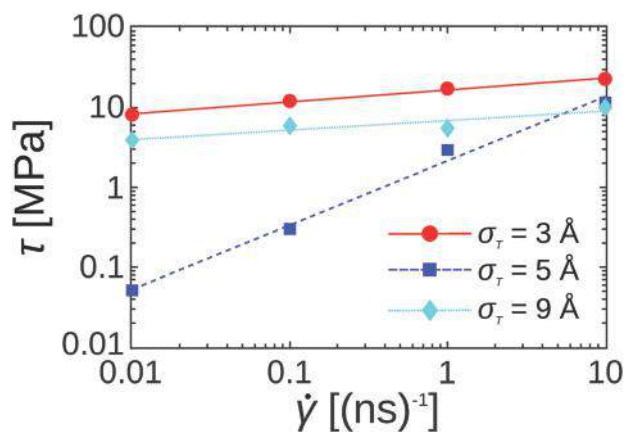


Fig. 3 Average shear stress τ as a function of shear rate $\dot{\gamma}$ of the TM3, TM5 and TM9 bulk ILs. We have conducted shear simulations for the shear rates in a range of four orders of magnitude ($\dot{\gamma} = 0.01$ – 10 ns⁻¹). The lines are obtained by fitting the points with eqn (2).

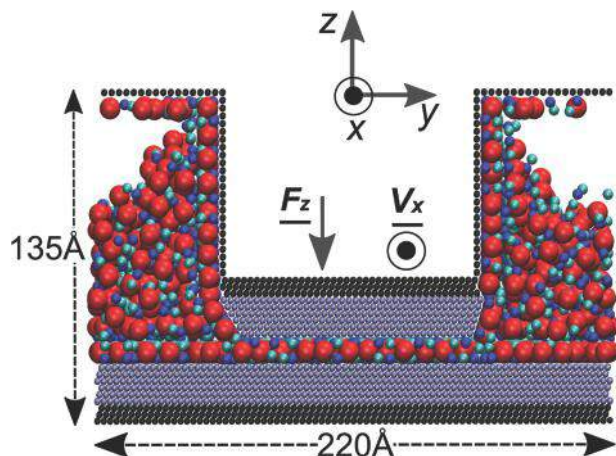


Fig. 4 Schematic of the simulation setup shown as a yz cross-section. The dimensions of the system along the y and z axes, together with the directions of the imposed normal load F_z and lateral velocity V_x , are noted. The total system length in the x direction is 125 \AA . There are two solid plates at the top and bottom of the system (more details on the simulation configuration are given in the ESI[†]). The different regions have different colours. The ionic liquid is composed of equal numbers of cation–tail pairs and anions (particles can be visually distinguished: cations – blue spheres, tails – cyan spheres, and anions – red spheres).

molecular geometry of ILs alters the load bearing capability of the thin films, we calculate the quasi-static force–distance characteristics. We follow the evolution of the normal load F_z acting on the top plate as a function of interplate distance d_z . To ensure static conditions, the interplate distance is changed through a series of alternating steps, called move and stay, related to the movement of the top plate and subsequent relaxation of the IL structure, respectively. We describe in detail the simulation procedure in the ESI.[†] The results for the force–distance characteristics of the three TM ILs are presented in Fig. 5, where three different markers correspond to the three IL models. The normal force F_z strongly and non-monotonically depends on the distance d_z . These changes in the normal force F_z are correlated with the squeezing in and out of cation/anion layer pairs into the gap, as already observed experimentally⁴⁰ and theoretically.¹⁸ The normal force becomes negative ($F_z < 0$) only in the case of small tails (TM3). The negative values are a result of the IL trying to reduce the plate-to-plate distance due to the adhesion forces inside the IL. The increasing tail size seems to reduce the effect of adhesion: for large tails (TM9) the normal force at the minimum is close to zero, while for symmetric cation molecules (TM5) it becomes positive ($F_z = 2 \text{ pN}$).

For all three curves corresponding to the three TM ILs we can identify three characteristic ranges of the plate-to-plate distance d_z : the initial segment ($11 \text{ \AA} \leq d_z \leq 13.8 \text{ \AA}$) characterized by a monotonic and steep decrease of the normal force F_z ; interval I ($13.8 \text{ \AA} \leq d_z \leq 19.8 \text{ \AA}$) characterized by the presence of local minima and maxima peaks of the normal force F_z , and interval II and beyond ($d_z \geq 19.8 \text{ \AA}$) characterized by a continuous and gentle decrease of the normal force F_z , where in all three cases the normal force practically becomes zero when $d_z > 32 \text{ \AA}$.

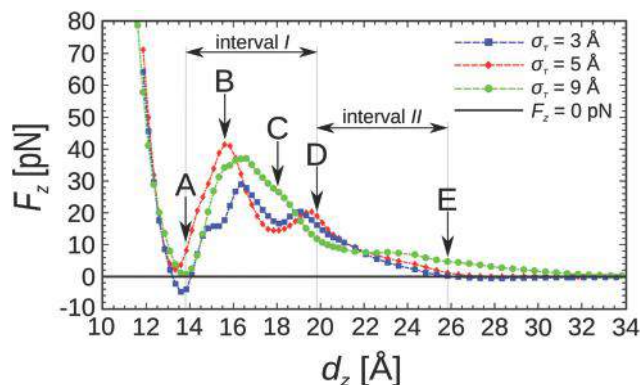


Fig. 5 Dependence of normal force F_z on plate-to-plate distance d_z . Five characteristic points denoted {A, B, C, D, E} with the corresponding interplate distances $d_z = 13.8, 15.5, 18.0, 19.8,$ and 25.8 \AA , respectively, are marked in the figure. They are chosen in the way that: point A is located in the proximity of a local minimum for all three cases; point B corresponds to a local maximum for TM5; point C is located in the proximity of a local minimum for TM3 and TM5; point D is located in the proximity of a local maximum for TM3 and TM5; and point E is chosen according to the condition $\overline{DE} = \overline{AD}$. For reference, the black horizontal line denotes $F_z = 0$. The lines connecting points (averages of normal force) serve as visual guides.

We will briefly describe the segments of the $F_z(d_z)$ curves, pointing out similarities and differences between the different IL models. In the initial segment, *i.e.*, for small gaps $d_z < 13 \text{ \AA}$, the normal force F_z is practically the same for all three systems, meaning that it does not depend on the tail size. The steep increase of the normal force with compression in the range $d_z < 13 \text{ \AA}$ is a sign of a very high resistance of the single anionic layer left in the gap to squeeze out. On the other hand, at large gap values (*i.e.*, $d_z > 32 \text{ \AA}$), the normal loads F_z in all three TM ILs are similar and small. We can conclude that at large gaps there is a low resistance of the IL to the gap changes. Significant differences in the force–distance curves depending on the tail size exist only in interval I, *i.e.*, $13.8 \text{ \AA} \leq d_z \leq 19.8 \text{ \AA}$. In the case of TM3, the $F_z(d_z)$ characteristic curve has two local minima and maxima and one saddle point; in TM5 there are two local minima and maxima; and for TM9, there is one local minimum and maximum.

4.1.1 IL layer structure inside the gap. In Fig. 6 we show the ionic density distribution along the z axis for the three IL models, at points A to E, *i.e.*, $d_z = \{13.8, 15.5, 18.0, 19.8, 25.8\} \text{ \AA}$. A common feature of all investigated IL models is the formation of fixed cationic layers along the whole length of the solid plates (top and bottom). The fixed layers and their stability are a result of strong LJ interactions between the plates and ions. In general, the smallest particles form the first layer next to the plates: for TM3 these particles are tail particles (which are part of the cation–tail pair), while for TM5 and TM9 these particles are the cations. The consecutive layers are formed inside the interplate gap *via* combined volume exclusion and Coulombic interactions, and their ordering is consistent with the fixed layers. As a result, tails migrate to the plates in TM3, mix with the cationic layer when the cation–tail dimer is symmetric in TM5, and finally mix into the anionic layer when they are large in TM9.

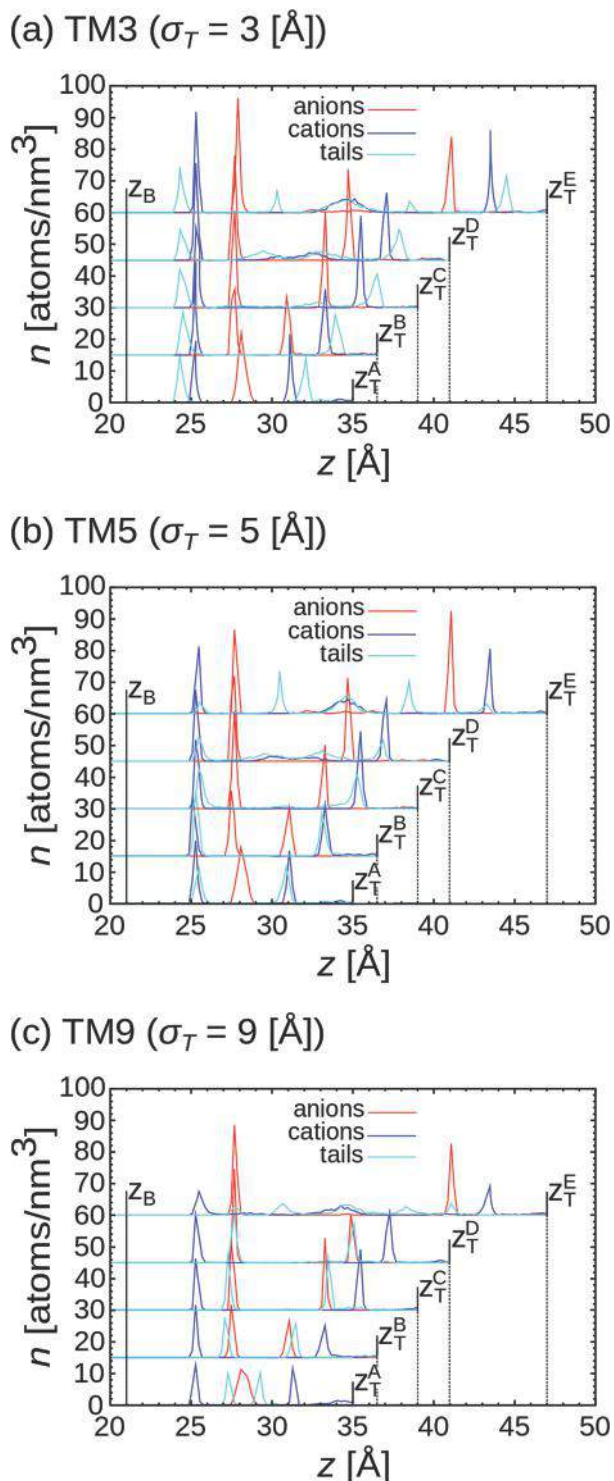


Fig. 6 Ionic density distribution of ions inside the interplate gap of (a) TM3, (b) TM5 and (c) TM9 in characteristic points {A, B, C, D, E} selected in the static force–distance characteristics presented in Fig. 5. The positions of the atomic centres of the innermost atomic layers of the (moving) top and (fixed) bottom plates are labeled z_T^{A-E} and z_B , respectively. The five characteristic points, denoted {A, B, C, D, E}, have the corresponding interplate distances $d_z = z_T - z_B = 13.8, 15.5, 18.0, 19.8,$ and 25.8 Å, respectively.

Since Coulombic interactions cause the layering with alternating charge signs, layers of anions always separate the cation layers.

We focus on analysing the changes in the segment between points A and D, *i.e.*, interval I. The normal force F_z changes rapidly and non-monotonically with d_z in interval I, *cf.* Fig. 5. For the minimum of F_z in the vicinity of point A, *i.e.*, for plate-to-plate distance $d_z^A = 13.8$ Å, we can observe a well-defined anionic layer in Fig. 6 (the corresponding snapshots of configurations are given in the ESI†). The most interesting change takes place during the A \rightarrow B transition when the single layer of anions is split into two layers, *cf.* Fig. 6. As a result, the normal force F_z increases and reaches a local maximum in the proximity of point B, *i.e.*, for plate-to-plate distance $d_z^B = 15.5$ Å. We observe that additional anion–cation pairs are pulled inside the gap in Fig. 7. We also observe that the two anionic layers in Fig. 6 for point B and the one for point A have the same maximum number density. As we increase d_z further, the number of anionic layers confined inside the gap remains unchanged and the normal load F_z decreases slowly. At the same time, the number of ions inside the gap steadily increases with gap width. Nevertheless, this increase is not sufficient to keep the density of the IL inside the gap constant (*cf.* Fig. 7). Looking into the changes in the spatial distribution of the IL components, as more cation–anion pairs are pulled into the gap (going from A \rightarrow E), we observe a steady increase of the concentration of anions in the layer next to the bottom plate. In the case of TM5 we have an increase from $n_{TM5}^A = 18$ atoms per nm^3 to $n_{TM5}^D = 27$ atoms per nm^3 , *cf.* Fig. 6. When we further look at configuration snapshots for TM3 and TM5, a formation of additional layers inside the gap is visible, between points C and D. This can also be clearly observed in Fig. 6 and results in a smaller maximum around $d_z = 19$ Å, in Fig. 5. We can conclude that the normal force–plate distance characteristics are not correlated with the number density of the IL molecules inside the gap, but with the layer formation as seen in Fig. 6.

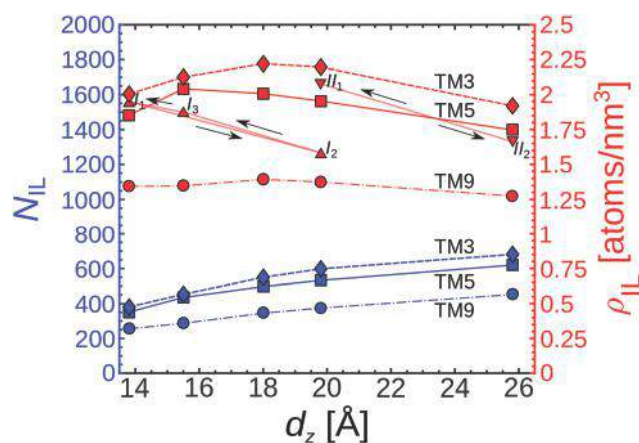


Fig. 7 Evolution of the number of confined ionic liquid (IL) molecules (bottom curves) and density (top curves) inside the gap with gap width d_z for TM3, TM5 and TM9 at characteristic points {A, B, C, D, E} selected from the static force–distance characteristics (Fig. 5). The corresponding axes for the number of IL molecules and the density are given on the left and right sides, respectively. The densities at characteristic points for the dynamic cases (intervals I and II) are also given, *i.e.*, $I_{1,2,3}$ and $II_{1,2}$. The five characteristic points denoted {A, B, C, D, E} in the static and $I_{1,2,3}$ and $II_{1,2}$ dynamic cases have the same corresponding interplate distances $d_z = 13.8, 15.5, 18.0, 19.8,$ and 25.8 Å, respectively.

As the interplate distance d_z increases further, from point D to E, we notice additional cations in the middle of the gap and the formation of a third cationic layer in all three systems. We can make an interesting observation: for all three models the tails in the middle of the confinement are grouped into three regions: one overlapping with cations at $z = 34$ Å and two located between the cationic and anionic layers, *i.e.*, $z = 30$ and 38 Å, *cf.* in Fig. 6. This outcome is reminiscent of the findings from ref. 14, where the authors have experimentally obtained the formation of the tail-to-tail bilayer of cationic dimers in case the alkyl chain length is oversized.

4.1.2 IL crystallinity: the influence of the gap. We show the xy cross-sectional snapshots in Fig. 8 in order to observe the IL's in-plane structure at the cross-section just below the top plate. We mark the boundaries of the top plate spatial region with the vertical dashed lines. The central area of the panels in the figure corresponds to the interplate gap region and it represents a half of the total cross-section's width in the y direction, while the remaining area corresponds to the lateral reservoirs. The solid lines mark the orientation of crystal grains in those areas, where we can observe the presence of structural ordering. In the case of TM3, we observe the presence of partial triangular ordering only at point B when the structure is the most compressed. We do not notice any crystallization for symmetric

dimers (TM5), which confirms that the symmetric tail prevents ordering both under confinement and in the bulk. Contrary to the previous two cases, we observe crystallization for all configurations with the large tail (TM9). Additionally, we observe changes in the type of crystalline structure. While in the lateral reservoirs a triangular lattice arrangement is always present, depending on the amount of compression we observe triangular lattice arrangements at points A and D and square lattice arrangements at points B and C. Even more surprisingly, the order is lost when the tail-to-tail bilayer is formed at point E.

4.2 Cyclic extension and compression of confined ILs

The top plate was moved between the two limiting points of intervals I ($d_z^A \leq d_z \leq d_z^D$) and II ($d_z^D \leq d_z \leq d_z^E$). We investigated the dynamic behaviour of the confined IL thin film during the cyclic movement of the top plate along the z axis, *i.e.*, the interplate gap was periodically extended (extension half-cycle) and compressed (compression half-cycle). We investigated our system at three velocities $V_z = \{0.1, 1, 10\}$ m s⁻¹, but we did not observe any velocity dependent differences in the system behaviour. The confined ionic liquid lubricant responds to the cyclic movement of the top plate with a hysteresis in normal force $F_z(d_z)$ shown in Fig. 9. We present the detailed results of TM5's dynamic behaviour in panels (a) and (c) of Fig. 9. Also, in panels (b) and (d) of the same figure, we present together the smooth average cycles of our three IL models (TM3, TM5, and TM9).

4.2.1 Narrow gap: normal force hysteresis. We will now discuss in detail the response of TM5 to the cyclic motion of the top plate, in interval I shown in Fig. 9(a). Ten compression-extension cycles are shown (thin lines) with an average cycle superimposed on them (thick line). We identify three points of interest: $\{I_1, I_2, I_3\}$, *i.e.*, the two terminal points of the cycle and the point with the maximal normal force, respectively. These three points also correspond to points $\{A, D, B\}$, respectively, in the quasi-static characteristics shown in Fig. 5. Point I_3 corresponds to the maximum of normal force F_z both in the cyclic compression cycle and in the static characteristics of TM5, which makes the comparison more straightforward.

The normal force F_z decreases down to a value close to zero during the extension half of the $I_1 \rightarrow I_2$ cycle. The anion-cation pairs are pulled into the gap from the lateral reservoirs as the gap is extended and at point I_2 an additional anionic layer is fully formed inside the gap. Actually, instead of the two fixed layers of cations which shared one anionic layer, we obtain two separate anionic layers. The total number of ions pulled in is about 60 atoms or 0.22 atoms per (nm² ns) at 1 m s⁻¹ plate linear speed. In the first part of the compression half-cycle, $I_2 \rightarrow I_3$, the ions are compressed and the density and the normal force F_z increase. Somewhat surprisingly, we observe that an equal number of ions flow out, while the normal force increases, *i.e.*, $I_2 \rightarrow I_3$ and during its sharp decrease, $I_3 \rightarrow I_1$ (*cf.* Fig. 7). The sharp decrease of the normal force F_z in the $I_3 \rightarrow I_1$ segment is therefore a result of two processes: out-flow of the ions from the gap and the collapse of the anionic double layer and its rearrangement into a single anionic layer. The resulting

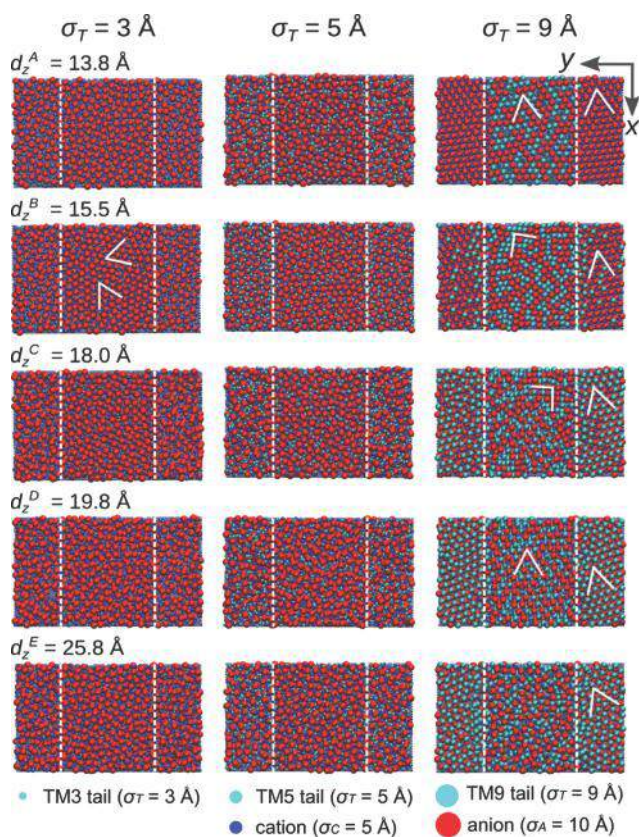


Fig. 8 Configuration snapshots (xy cross section) of TM3, TM5 and TM9 at five characteristic points $\{A, B, C, D, E\}$. The five characteristic points, denoted $\{A, B, C, D, E\}$, have the corresponding interplate distances $d_z = 13.8, 15.5, 18.0, 19.8,$ and 25.8 Å, respectively (see also Fig. 5).

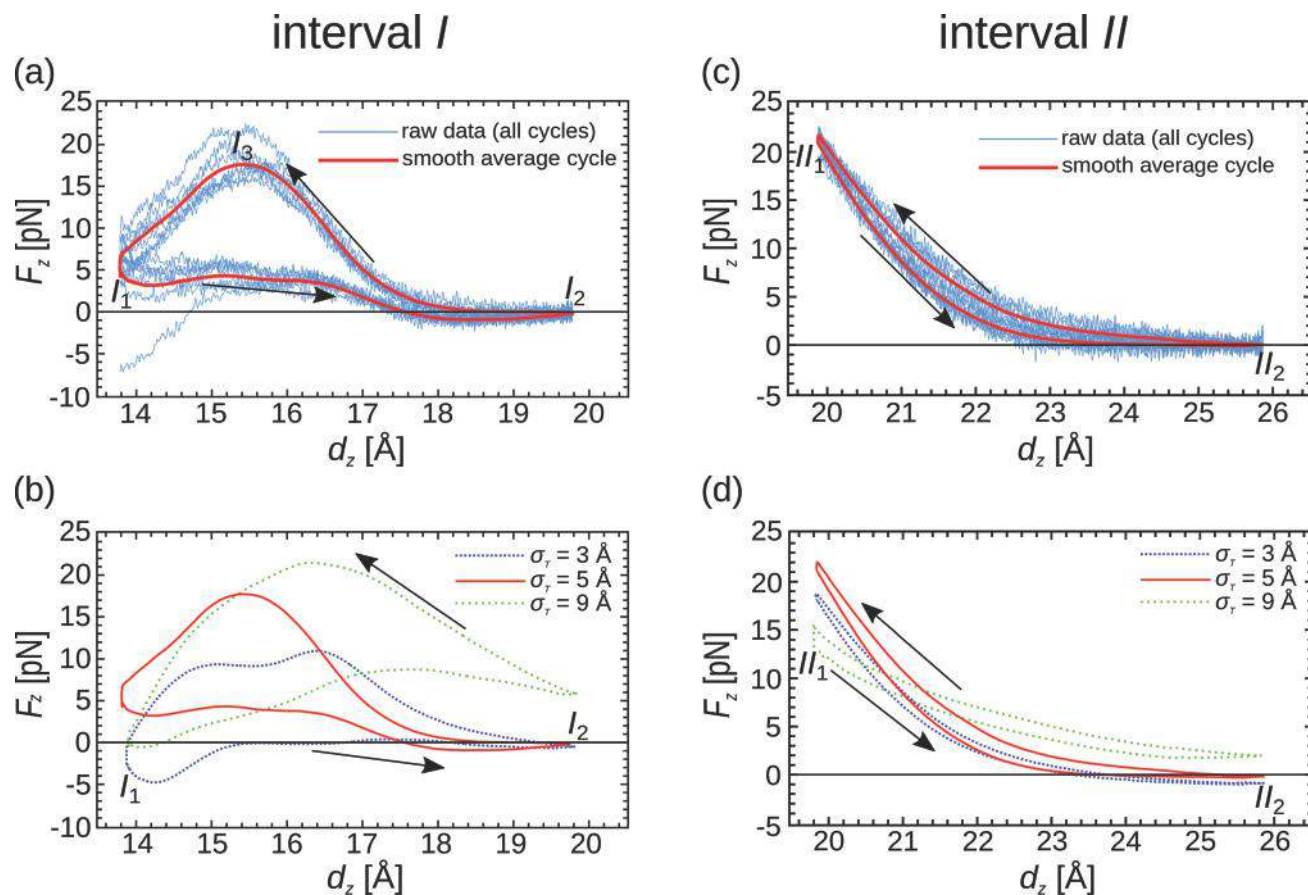


Fig. 9 The results of dynamic extension–compression cycles are shown for intervals I and II. In panels (a) and (c) we present dynamic $F_z(d_z)$ characteristics in the case of TM5 for intervals I and II, respectively; thin lines represent the hystereses of ten dynamic cycles, and the solid line on top of them is the smooth average hysteresis. There is also a solid horizontal line which corresponds to $F_z = 0$. In (a) points I_1 , I_2 , and I_3 denote representative points: I_1 – starting point, I_2 – ending point, I_3 – global maximum of the $F_z(d_z)$ curve. In (c) points II_1 and II_2 denote representative points: II_1 – starting point and II_2 – ending point. The arrows show the direction of hysteresis (extension $I/II_1 \rightarrow I/II_2$ followed by compression $I/II_2 \rightarrow I/II_1$). In panels (b) and (d) we show together the smooth average hystereses $F_z(d_z)$ of our three TMs, for intervals I and II, respectively. The starting and ending points and arrows are denoted, analogous to panels (a) and (c).

final density $\rho_{\text{IL}}^{\text{dyn}} = 1.95$ atoms per nm^3 of the system is slightly higher than in the static case $\rho_{\text{IL}}^{\text{stat}} = 1.85$ atoms per nm^3 , cf. Fig. 7. The value of the normal force F_z at point I_1 is similar, i.e., $F_z = 4$ pN, in both the static and dynamic cases.

In Fig. 9(b), we observe that each one of the three investigated ionic liquids (TM3, TM5, and TM9) exhibits different behaviour in the average $F_z(d_z)$ cycle during the extension and compression half-cycles. First, at the onset of the extension half-cycle, i.e. at point I_1 , the normal force F_z has a positive value for symmetric cations (TM5), it is close to zero for large tails (TM9), and it is negative for small tails (TM3). Somewhat surprisingly, the normal force increases for both TM ILs with asymmetric cations (TM3/TM9), while it decreases for symmetric cations (TM5). The reason for this behaviour is the strong interaction of the fixed layers of ions adjacent to the plates with the plate particles. This interaction drives as many ions inside the gap as possible, resulting in the non-intuitive behaviour of the normal force due to the interplay of density and intra-IL LJ interactions. During the compression half-cycle for all three ILs the maximal normal force sustained was about

50% smaller than that in the quasi-static case, i.e., for TM5 the maximal force is $F_z^{\text{max}} = 17$ pN in the dynamic case and $F_z^{\text{max}} = 40$ pN in the static case (see Fig. 5 and 9(b)). This observation indicates that the top plate's motion prevents the IL from filling the gap. We can also conclude that the mechanical response is mainly due to the rearrangement of the fixed layer and that the mobility of the IL molecules is too low to significantly increase the normal force resisting the compression. If we analyse the rate of mass transfer outside of the gap, we conclude that there is a substantial slip, which results in a lower normal force. Without slip at a velocity $V_z = 1$ m s^{-1} , the normal force calculated based on the bulk viscosity coefficient would be roughly two orders of magnitude higher.

4.2.2 Wide gap: monotonic force–distance characteristics. The expansion–compression force–inter-plate distance characteristics for interval II in the case of TM5 are given in Fig. 9(c). The difference from the quasi-static extension/compression in Fig. 5 is the monotonic behaviour during the strike. The quasi-static characteristics in interval II featured local minima and maxima in the case of TM3 and TM5. In the dynamic case, there are only

two characteristic points (starting and ending points) $\{II_1, II_2\}$ and a monotonically changing normal force between them. In the extension half-cycle there is a continuous decrease of the normal force F_z followed by its continuous increase in the compression half-cycle. The difference between the cycles in the normal force is small. In the dynamic characteristics of interval II the layer structure is similar to that of the static case, *i.e.*, two fixed layers stay-in-place and the tail double layer is formed during the extension half-cycle (the configuration snapshots are given in the ESI†). In contrast to interval I, the formation of the additional layer of tails is not a result of the ions flowing from the lateral reservoirs into the gap. The density inside the gap is 10% higher in the dynamic case and a few atoms (less than 30) are displaced during the cycle. We should note that the gap is also 50% larger in interval I compared to interval II; therefore, the decrease in density is even less striking. Actually, the cyclic motion has a tendency to increase the density inside the gap. Since there is no large displacement of the ions in and out of the gap in interval II, there is also no maximum of the normal force F_z , similar to the one we have seen in the case of interval I, *cf.* Fig. 9(a). In order to make comparisons of different TM ionic liquid models, in Fig. 9(d) we show together the $F_z(d_z)$ average cycle dynamic characteristics of all three IL models (TM3, TM5, TM9) for interval II. Compared to interval I, the tail size does not have such a pronounced impact on $F_z(d_z)$ hysteresis curves in interval II.

4.2.3 Energy losses due to cyclic expansion–compression.

At this point, we would like to quantify how the processes arising during the dynamic cyclic movement of the top plate contribute to energy losses. We calculate the area covered during the extension–compression cycle (*i.e.*, the area inside the $F_z(d_z)$ hysteresis). This area is equivalent to the work invested per average dynamic cycle, *i.e.*, the hysteretic energy losses. We show the dependence of the energy losses on the tail size for both intervals I and II in Fig. 10. We observe a clear tendency of the increase of the invested work per dynamic cycle, with the increase of the tail diameter. This is primarily due to the larger volume occupied by the tails, resulting in larger normal forces

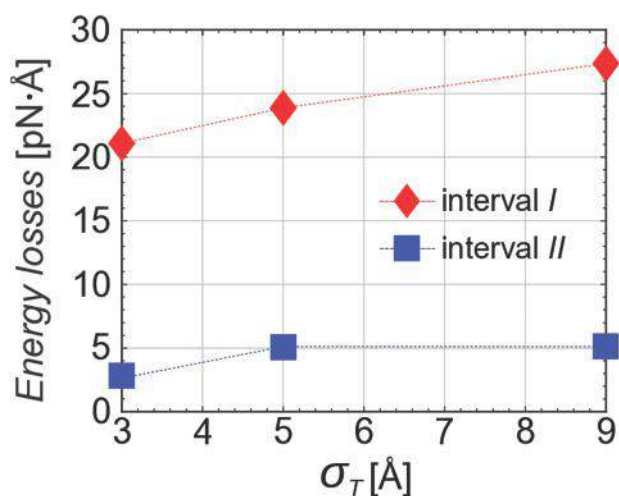


Fig. 10 Energy losses per average cycle as a function of the tail size for intervals I and II of dynamic extension–compression cycles.

resisting compression. There is a striking difference in the amount of invested work between the two intervals I and II (*e.g.* 27 pN Å for interval I of TM9 compared to 5 pN Å for interval II of TM9). This difference is proportional to the maximal normal force, which is sustained by the systems in the two intervals (*cf.* Fig. 5).

4.3 Tribological behaviour of confined ionic liquids

We have conducted static and dynamic characteristic analysis of the three generic IL models, focusing on the influence of their molecular structure on their anti-wear performance. In order to obtain a full picture, it is crucial to determine the IL's friction behaviour under different shear conditions. In this section we apply a relative motion between the plates by moving the top plate along the x -axis (see Fig. 4) and we observe the resulting frictional force (also along the x -axis, *i.e.*, F_x). We have performed two types of friction simulations: (i) at a constant top plate's velocity $V_x = 2 \text{ m s}^{-1}$, the simulations are performed at different fixed values of the gap: $d_z = 12 \text{ Å}$ to 25.5 Å ; and (ii) at a fixed gap $d_z = 15 \text{ Å}$ the top plate's lateral velocity takes five different values: $V_x = \{0.1, 0.3, 1.0, 3.0, 10.0\} \text{ m s}^{-1}$. In all friction simulations, the total distance covered by the top plate was $\Delta_x = 100 \text{ Å}$ in the x direction.

The dependence of the time-averaged frictional force $\langle F_x \rangle$ on the interplate gap d_z for the three IL models is shown in Fig. 11. The points obtained in the simulations are shown as markers. Linear fits through these points are provided as visual guides. For TM3, we observe a decrease of the frictional force $\langle F_x \rangle$ with the size of the gap. On the other hand, the frictional force weakly depends on the interplate gap width in the case of TM5 and TM9 ILs. Both the TM3 and TM9 ILs have high zero shear-rate (Green–Kubo) bulk viscosities correlated with the extent of their ordering, *i.e.*, $\eta_{\text{TM3}}^{\text{GK}} > \eta_{\text{TM9}}^{\text{GK}} > \eta_{\text{TM5}}^{\text{GK}}$. When comparing their

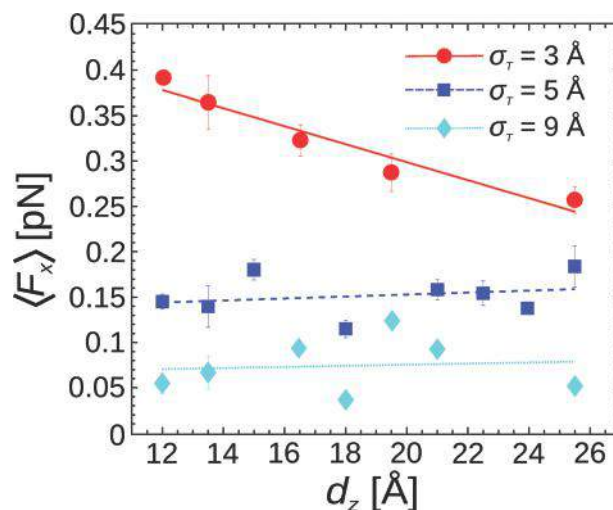


Fig. 11 Average frictional force $\langle F_x \rangle$ acting on the top plate as a function of the plate-to-plate distance d_z for confined TM3, TM5 and TM9 ionic liquid lubricants. In the case of TM3 there is a clear linear dependence showing the decrease of frictional force intensity with gap increase, while in the case of TM5 and TM9 the frictional force is practically constant and does not depend on the gap.

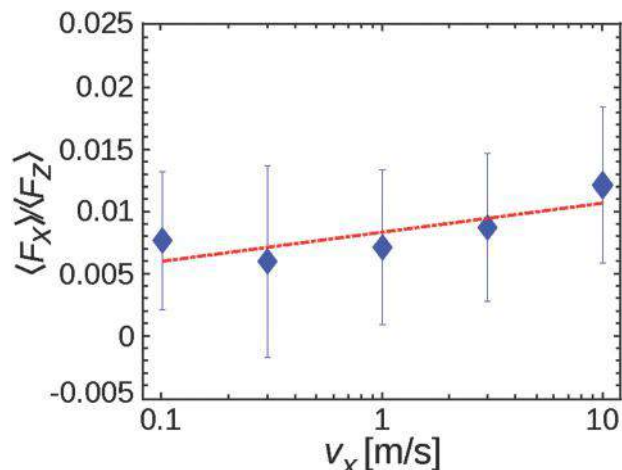


Fig. 12 Specific friction $\frac{\langle F_x \rangle}{\langle F_z \rangle}$ dependence on the top plate's lateral velocity v_x in the case of TM5.

tribological performances in a thin film, we can conclude that there is no correlation since the TM5 IL has the highest average frictional force. In Fig. 12, we show the dependence of the specific friction $\langle F_x \rangle / \langle F_z \rangle$ on the top plate's lateral velocity v_x in the case of TM5. We obtain specific friction values of the order $\langle F_x \rangle / \langle F_z \rangle \approx 0.01$, which are comparable to the results of Dold *et al.*³ for symmetric $[\text{PF}_6]^-$ anions. We also observe a similar tendency of decreasing friction force with respect to tail size, as reported in the same ref. 3.

The specific friction $\langle F_x \rangle / \langle F_z \rangle$ is defined as the ratio of the time averaged frictional $\langle F_x \rangle$ to normal $\langle F_z \rangle$ force and it is different from the Coulombic friction coefficient $\mu = \partial F_x / \partial F_z$. Consistently with our previous results for model ionic liquids, we have observed a logarithmic dependence of the specific friction on the lateral velocity, *cf.* ref. 18. The numerical values are fitted to a linear function of the form $\langle F_x \rangle / \langle F_z \rangle = a \log(v_x / v_{\text{ref}}) + b$, where $v_{\text{ref}} = 1 \text{ m s}^{-1}$. The coefficients of the linear fit took the following values: $a = 0.001$ and $b = 0.008$. A reasonable fit to the linear regression curve can be observed. The logarithmic dependence indicates typical elastohydrodynamic lubrication (EHL) conditions.⁴¹

5 Discussion

Ionic liquids interact *via* long-ranged Coulombic forces and their models require high-performance computational resources. This opens a question of the minimal model needed to capture the properties of the molecular processes governing lubrication mechanisms and the macroscopic performance relevant for engineering applications. In this paper, we investigate a generic tailed-model (TM) of ionic liquids (ILs), which includes an asymmetric cation consisting of a positively charged head and a neutral tail of variable size and a large spherical negatively charged anion. We observe that, though simple, this model results in striking differences in the equilibrium IL bulk structure governed by the tail size relative to the cationic head: (i) a simple cubic lattice for small tails, (ii) a liquid-like state for

symmetric cation–tail dimers, and (iii) a molecular layer structure for large tails.

We have investigated the influence of the molecular structure of a cation dimer on the response of three ILs to confinement and mechanical strain using molecular dynamics simulations. The properties of the three IL models are compared in and out of equilibrium. We have related the evolution of the normal force with inter-plate distance to the changes in the number and structure of the confined IL layers. We find that the density inside the gap has a secondary effect on the evolution of the normal force. We observe that symmetric molecules offset intra-IL adhesion due to the ordering of the IL. As a result, the thin layer of symmetric IL molecules exhibits non-negative normal force independent of the gap width. In analogy to the experimental observations, a tail-to-tail bilayer is formed for wide gaps in all three investigated model ILs. A mutual feature of all the investigated model ILs is the formation of fixed (stable) layers of cations along the solid plates. The fixed layer formation is a result of strong LJ interaction between the plates and ions. A consequence of the fixed layer stability is a steep increase of the normal force at small interplate gaps. The steep increase of the normal force is an effect useful for preventing solid–solid contact and the accompanying wear. The tails attached to the cations in the fixed layer migrate with increasing tail size. Small tails form the first layer next to the plates. For symmetric molecules the tails form a mixed layer with cations, while large tails form a mixed layer with anions.

We have explored the dynamic behaviour of IL thin films under cyclic extension–compression movements of the top plate. Two intervals of the interplate distances are investigated: a narrow gap interval, where the anionic layer is split into two, and a wide gap interval, where a tail-to-tail layer is formed. For the narrow gap interval, we observe a significant flow of ions during the cyclic motion of the top plate. A sharp decrease of the normal force at the final stage of compression is not only a consequence of the density change due to the flow, but is also a result of merging of the two anionic layers that repel each other by the electrostatic Coulomb forces into a single one. The mobility of ions in/out of the gap is driven by their interaction with plates, *i.e.*, filling of the fixed layers. As a result, for the narrow gap, the number of ions that entered the gap is 50% smaller in the dynamic case than in the static case. This results in a smaller density inside the moving narrow gap. The difference between the dynamic and static cases for the wide gap was even more striking. The number of ions that entered the gap is 80% smaller in the dynamic case than in the static case. Surprisingly, in the wide gap the density is higher in the dynamic case due to the lack of mobility of ions. The invested work per average cycle increases with tail size for all three IL models. As one could expect, the invested work is higher for the narrow gap where the number of confined ions/ionic layers changes during the cycle. Nevertheless, the low hysteretic losses suggest the presence of strong slip inside the gap, facilitating in- and out-flow of ions in the gap. An increase of the tail size reduces the friction force in our model. Depending on the tail size, the friction force decreases with increasing gap for small tails and it increases for large tails.

6 Conclusion

Understanding the interplay between the different processes taking place in thin lubricant films is important due to the conflicting demands imposed on how IL lubricants should behave in dynamic confinement. On the one hand, a high load-carrying capability requires strong adsorption of the lubricant to the surface, while, on the other hand, fast self-healing and low friction require high mobility/low viscosity. Our results confirm that the behaviour of ILs in confinement can be unrelated to their bulk behaviour, and therefore, it should be possible to achieve simultaneously, typically conflicting, low friction and good anti-wear performance. A search for optimal IL lubricants, using either synthesis and test methods or state-of-the-art computer-aided molecular design methods,⁴² should take into account the micro-scale properties of lubricating thin films (*e.g.*, normal force *vs.* number of layers characteristics), in which the effects of molecular-level processes are more pronounced. Directing the optimisation efforts towards the micro-scale would enable a better differentiation of the qualities of different ionic liquids.

Conflicts of interest

There are no conflicts to declare.

Acknowledgements

M. D. and I. S. acknowledge the support of the Ministry of Education, Science and Technological Development of the Republic of Serbia under Project No. OI171017 and the support of COST Action MP1303. All computer simulations were performed on the PARADOX supercomputing facility at the Scientific Computing Laboratory of the Institute of Physics Belgrade, University of Belgrade, Serbia.

References

- 1 F. Zhou, Y. Liang and W. Liu, *Chem. Soc. Rev.*, 2009, **38**, 2590–2599.
- 2 R. Hayes, G. G. Warr and R. Atkin, *Phys. Chem. Chem. Phys.*, 2010, **12**, 1709–1723.
- 3 C. Dold, T. Amann and A. Kailer, *Lubr. Sci.*, 2013, **4**, 251–268.
- 4 W. Liu, C. Ye, Y. Chen, Z. Ou and D. Sun, *Tribol. Int.*, 2002, **35**, 503–509.
- 5 A. Pensado, M. Comunas and J. Fernández, *Tribol. Lett.*, 2008, **31**, 107–118.
- 6 I. Minami, *Molecules*, 2009, **14**, 2286–2305.
- 7 I. Bou-Malham and L. Bureau, *Soft Matter*, 2010, **6**, 4062–4065.
- 8 D. A. Beattie, R. M. Espinosa-Marzal, T. T. Ho, M. N. Popescu, J. Ralston, C. J. Richard, P. M. Sellapperumage and M. Krasowska, *J. Phys. Chem. C*, 2013, **117**, 23676–23684.
- 9 Z. Wang and C. Priest, *Langmuir*, 2013, **29**, 11344–11353.
- 10 A. M. Smith, K. R. Lovelock, N. N. Gosvami, T. Welton and S. Perkin, *Phys. Chem. Chem. Phys.*, 2013, **15**, 15317–15320.
- 11 A. E. Somers, P. C. Howlett, D. R. MacFarlane and M. Forsyth, *Lubricants*, 2013, **1**, 3.
- 12 B. Bhushan, J. N. Israelachvili and U. Landman, *Nature*, 1995, **374**, 607–616.
- 13 H. Kamimura, T. Chiba, T. Kubo, H. Nanao, I. Minami and S. Mori, *Jpn. J. Tribol.*, 2006, **51**, 675–687.
- 14 S. Perkin, L. Crowhurst, H. Niedermeyer, T. Welton, A. M. Smith and N. N. Gosvami, *Chem. Commun.*, 2011, **47**, 6572–6574.
- 15 H. Wang, Q. Lu, C. Ye, W. Liu and Z. Cui, *Wear*, 2004, **256**, 44–48.
- 16 A. Jiménez, M. Bermudez, P. Iglesias, F. Carrión and G. Martínez-Nicolás, *Wear*, 2006, **260**, 766–782.
- 17 Z. Mu, F. Zhou, S. Zhang, Y. Liang and W. Liu, *Tribol. Int.*, 2005, **38**, 725–731.
- 18 K. Gkagkas, V. Ponnuchamy, M. Dašić and I. Stanković, *Tribol. Int.*, 2017, **113**, 83–91.
- 19 N. Voeltzel, A. Giuliani, N. Fillot, P. Vergne and L. Joly, *Phys. Chem. Chem. Phys.*, 2015, **17**, 23226–23235.
- 20 A. C. F. Mendonça, A. A. H. Pádua and P. Malfreyt, *J. Chem. Theory Comput.*, 2013, **9**, 1600–1610.
- 21 F. Federici Canova, H. Matsubara, M. Mizukami, K. Kurihara and A. L. Shluger, *Phys. Chem. Chem. Phys.*, 2014, **16**, 8247–8256.
- 22 O. Y. Fajardo, F. Bresme, A. A. Kornyshev and M. Urbakh, *J. Phys. Lett.*, 2015, **6**, 3998–4004.
- 23 O. Y. Fajardo, F. Bresme, A. A. Kornyshev and M. Urbakh, *Sci. Rep.*, 2015, **5**, 7698 EP.
- 24 R. Capozza, A. Vanossi, A. Benassi and E. Tosatti, *J. Chem. Phys.*, 2015, **142**, 064707.
- 25 J. Gao, W. D. Luedtke, D. Gourdon, M. Ruths, J. N. Israelachvili and U. Landman, *J. Phys. Chem. B*, 2004, **108**, 3410–3425.
- 26 M. O. Robbins and M. H. Müser, in *Modern Tribology Handbook, Two Volume Set*, ed. B. Bhushan, CRC Press, 2000.
- 27 R. E. Rudd and J. Q. Broughton, *Phys. Rev. B: Condens. Matter Mater. Phys.*, 1998, **58**, R5893–R5896.
- 28 Y. Wang, W. Jiang, T. Yan and G. A. Voth, *Acc. Chem. Res.*, 2007, **40**, 1193–1199.
- 29 D. M. Heyes, E. R. Smith, D. Dini, H. A. Spikes and T. A. Zaki, *J. Chem. Phys.*, 2012, **136**, 134705.
- 30 C. Gattinoni, D. M. Heyes, C. D. Lorenz and D. Dini, *Phys. Rev. E: Stat., Nonlinear, Soft Matter Phys.*, 2013, **88**, 052406.
- 31 L. Martinie and P. Vergne, *Tribol. Lett.*, 2016, **63**, 21.
- 32 M. Dašić, I. Stanković and K. Gkagkas, *Eur. Phys. J. E: Soft Matter Biol. Phys.*, 2018, **41**, 130.
- 33 S. Plimpton, *J. Comput. Phys.*, 1995, **117**, 1–19.
- 34 R. Hayes, G. G. Warr and R. Atkin, *Chem. Rev.*, 2015, **115**, 6357–6426.
- 35 D. J. Evans and G. Morriss, *Phys. Rev. A: At., Mol., Opt. Phys.*, 1984, **30**, 1528.

- 36 P. J. Davis and B. Todd, *J. Chem. Phys.*, 2006, **124**, 194103.
- 37 M. S. Green, *J. Chem. Phys.*, 1954, **22**, 398–413.
- 38 R. Kubo, *J. Phys. Soc. Jpn.*, 1957, **12**, 570–586.
- 39 S. Perkin, *Phys. Chem. Chem. Phys.*, 2012, **14**, 5052–5062.
- 40 R. Hayes, N. Borisenko, M. K. Tam, P. C. Howlett, F. Endres and R. Atkin, *J. Phys. Chem. C*, 2011, **115**, 6855–6863.
- 41 S. Bair, L. Martinie and P. Vergne, *Tribol. Lett.*, 2016, **63**, 37.
- 42 K. Padaszyński and U. Domańska, *J. Chem. Inf. Model.*, 2014, **54**, 1311–1324.

Influence of confinement on flow and lubrication properties of a salt model ionic liquid investigated with molecular dynamics^{*}

Miljan Dašić^{1,a}, Igor Stanković^{1,b}, and Konstantinos Gkagkas²

¹ Scientific Computing Laboratory, Center for the Study of Complex Systems, Institute of Physics Belgrade, University of Belgrade, Pregrevica 118, 11080 Belgrade, Serbia

² Advanced Technology Division, Toyota Motor Europe NV/SA, Technical Center, Hoge Wei 33B, 1930 Zaventem, Belgium

Received 27 April 2018 and Received in final form 18 September 2018

Published online: 2 November 2018

© EDP Sciences / Società Italiana di Fisica / Springer-Verlag GmbH Germany, part of Springer Nature, 2018

Abstract. We present a molecular dynamics study of the effects of confinement on the lubrication and flow properties of ionic liquids. We use a coarse-grained salt model description of ionic liquid as a lubricant confined between finite solid plates and subjected to two dynamic regimes: shear and cyclic loading. The impact of confinement on the ion arrangement and mechanical response of the system has been studied in detail and compared to static and bulk properties. The results have revealed that the wall slip has a profound influence on the force built-up as a response to mechanical deformation and that at the same time in the dynamic regime interaction with the walls represents a principal driving force governing the behaviour of ionic liquid in the gap. We also observe a transition from a dense liquid to an ordered and potentially solidified state of the ionic liquid taking place under variable normal loads and under shear.

1 Introduction

In this work, the lubricating ability and flow properties of salt model ionic liquids (ILs) containing salt-like spherical cations and anions are studied. ILs are molten salts typically consisting of large-size organic cations and anions. The thermochemical stability, negligible vapor pressure, viscosity, wetting performance and other physicochemical properties of ILs are important factors contributing to the interest in their research for lubricant applications [1, 2]. In addition, their properties can be modified by an applied voltage using confining charged surfaces in order to build up an electric field across the nanoscale film. The applied potential can affect the structure of IL layers and lead to externally controllable lubricating properties [3–5]. There is also a significant flexibility in tuning the physical and chemical properties of ILs which can affect lubrication such as viscosity, polarity and surface reactivity, by varying their atomic composition as well as the cation-anion combination. The thermal stability and negligible vapor pressure of ILs enable their usage at a high temperature.

Regarding the ability of ionic liquids to dynamically penetrate between surfaces, *i.e.* wetting, sometimes it is considered that a low contact angle of the lubricant indicates the affinity between the liquid and the surface, since the liquid is more likely to stay in the area in which it was initially placed. It is also expected that a lubricant is going to penetrate into small-gap components. However, the effect of wettability of the ionic liquids is not understood well. The wetting of plate surfaces such as mica is known to be partial by at least some ILs [6, 7]. Lubrication necessarily involves intimate molecular features of the liquid-solid plate interface, related with those mechanisms determining the ionic liquid's wetting of the plate. When ILs are used as lubricants, their ions are ordered into layers and adsorbed onto surfaces [8]. These adsorption layers can reduce friction and wear, particularly in the case of boundary lubrication [8].

An important observation is that ILs confined between surfaces feature alternating positive and negative ionic layers, with an interlayer separation corresponding to the ion pair size [9, 10]. However, determining the structure of ILs during flow and the mechanism of nanoscopic friction with ILs as lubricants, poses a great scientific challenge, and so far a few studies in this direction have been performed [3]. ILs involve long-range Coulombic interactions inducing long-range order on far greater scales than the IL itself [11–13]. Recent studies of

^{*} Contribution to the Topical Issue “Flowing Matter, Problems and Applications”, edited by Federico Toschi, Ignacio Pagonabarraga Mora, Nuno Araujo, Marcello Sega.

^a e-mail: mdasic@ipb.ac.rs

^b e-mail: igor.stankovic@ipb.ac.rs

IL lubricants [3–5, 10] have shown that if the molecules interact via non-bonded potentials (Lennard-Jones and Coulombic potential), this can capture all main physical attributes of the IL-lubricated nanotribological system. Therefore, molecular-scale simulations can provide important insights which are necessary for understanding the differences in the flow behaviour between bulk and confined liquid lubricants and the mechanisms behind, such as boundary layers formation in case of shearing and/or applied normal load.

For this study, we utilize our previously developed coarse-grained molecular dynamics (MD) simulation setup consisting of two solid plates, and an ionic liquid lubricant placed between them [10]. The motivation for the chosen values of relevant model parameters (*i.e.*, velocities, pressures, temperatures, time duration of simulations) comes from potential applications of ILs as lubricants in automotive industry. Under typical operation of internal combustion engines, the conditions inside the combustion chamber vary significantly. Temperature can range from 300 K to the values higher than 2000 K, while pressure ranges from atmospheric to the values higher than 10 MPa [14]. The piston reciprocates with a sinusoidal velocity variation with speeds varying from zero to over 20 m/s, with a typical speed being around 1 m/s. The time required for one revolution of the engine is of the order of 10^{-2} s, while the total distance travelled by the piston over this period is of the order of 0.2 m. Such scales are typically modelled using continuum mechanics simulations. However, such simulations cannot provide the physical insight which is necessary for understanding the molecule-dependent processes that affect the tribological phenomena. Therefore, we have implemented a coarse-grained MD simulation setup which can, *inter alia*, provide useful insights to lubrication mechanisms of piston ring-cylinder liner contact in automotive engines.

The determination and design of new applicable lubricants require the understanding of both general and specific behaviours of liquids when exposed to nanoscale confinement, shearing and normal load. In this study our focus is on determining the general features of ILs as nanoscale lubricants. Hence, we have chosen the model of a generic IL which is simple in order to provide a wide perspective of the relevant mechanisms governing the IL lubrication principles.

This paper is organized as follows: sect. 2 introduces the model and MD simulation setup of the solids and lubricants used, while the motivation for the choices made is provided. In sect. 3 the structure and viscosity characteristics of the bulk ionic liquid are presented. Section 4 deals with the static and dynamic behaviour of confined IL. It also presents the results of confined IL's shear behaviour. Section 5 includes an overview of the principal observations and conclusions.

2 Model

The model used in this work is a coarse-grained model of IL which has already been exploited in previous stud-

ies [3–5, 10] and it is known as SM model (salt-like model). It is a charged Lennard-Jones system consisting of cations and anions. There are two types of interatomic interactions in our system and both of them are non-bonded: Lennard-Jones (LJ) potential and Coulombic electrostatic potential. In the current work we are comparing bulk and confined IL properties. Therefore, there are three different atom types taken into consideration: i) cations, ii) anions and iii) solid plate atoms. Between all types of atoms we apply the full LJ 12-6 potential, with the addition of the Coulombic electrostatic potential for the interactions between ions. In our system the cations and the anions are charged particles, while the solid plate atoms are electroneutral. Accordingly, we have implemented a LJ 12-6 potential combined with a Coulombic electrostatic potential:

$$V(r_{ij}) = 4\epsilon_{ij} \left[\left(\frac{\sigma_{ij}}{r_{ij}} \right)^{12} - \left(\frac{\sigma_{ij}}{r_{ij}} \right)^6 \right] + \frac{1}{4\pi\epsilon_0\epsilon_r} \frac{q_i q_j}{r_{ij}}. \quad (1)$$

Parameters $\{\epsilon_{ij}, \sigma_{ij}\}$ define the LJ potential between different types of particles: $i, j = A, C, P$ which refer to anions, cations and solid plate atoms, respectively. The diameter of cations and anions is set to $\sigma_{CC} = 5 \text{ \AA}$ and $\sigma_{AA} = 10 \text{ \AA}$, respectively. The mass of cations and anions is $m_C = 130 \text{ g/mol}$ and $m_A = 290 \text{ g/mol}$, respectively. The asymmetry of ion sizes is typical in many experimentally explored systems and the parameters have already been explored in the literature, cf. refs. [5, 10]. The atoms of the solid plates have a diameter of $\sigma_{PP} = 3 \text{ \AA}$. The mass of the solid plate atoms is $m_P = 65 \text{ g/mol}$. The LJ potential has a short-range impact, since it vanishes rapidly as the distance increases $\propto r^{-6}$, while the Coulombic potential has a long-range impact, $\propto 1/r$. To handle long-range interactions, we have used a multi-level summation method (MSM) [15], since it scales well with the number of ions and allows the use of mixed periodic (in x and y directions) and non-periodic (in z -direction) boundary conditions, which are present in our simulation setup with confined IL. On the other hand, in our simulation setup with bulk IL, periodic boundary conditions are applied in all three directions ($\{x, y, z\}$). Ions are modelled as coarse-grained particles, the charge of which is set equal to elementary: $q_C = +e$ and $q_A = -e$, *i.e.*, $e = 1.6 \cdot 10^{-19} \text{ C}$. The dielectric constant is set to $\epsilon_r = 2$ to account for the dielectric screening, as in refs. [4, 5, 10].

In this study, modelling the elasticity of metallic plates plays a secondary role (central role belongs to the lateral and normal forces created by the lubricant). Therefore, we have selected a simplified model in which plate atoms interact strongly with each other if they belong to the same plate, *i.e.*, $\epsilon_{PP} = 120 \text{ kCal/mol}$, as opposed, to a very weak interaction between the different plates $\epsilon_{\text{top/bottom}} = 0.03 \text{ kCal/mol}$. The parameter ϵ_{PP} is so strong in order to ensure that the initial configuration of the solid bodies will basically remain unchanged (apart from high frequency oscillations). Furthermore, even though typical engineering systems are often metallic, our initial coarse-grained MD studies of liquid behaviour according to the

Table 1. List of LJ parameters used in simulations.

Pair ij	ϵ_{ij} (kCal/mol)	σ_{ij} (Å)
CC	0.03	5
AA	0.03	10
CA	0.03	7.5
PC	0.3	4
PA	0.3	6.5
PP	120	3

applied conditions justified the implementation of a simpler solid system which does not feature substrate polarization, cf. ref. [10]. Finally, it is possible that the actual surfaces might feature carbon coatings or depositions, in which case the surface polarization can be of secondary importance.

In table 1 we are presenting the values of $\{\epsilon_{ij}, \sigma_{ij}\}$ parameters used in our model. Arithmetic mixing rules for the LJ parameters are applied: $\epsilon_{ij} = \sqrt{\epsilon_i \cdot \epsilon_j}$, $\sigma_{ij} = (\sigma_i + \sigma_j)/2$.

3 Bulk ionic liquid

All MD simulations in this study were performed using the LAMMPS software [16]. The bulk ionic liquid is implemented by randomly placing a chosen number of ions ($N_C = N_A = 1000$) into a 3D simulation box that is periodic in all three directions. In order to make the bulk IL comparable with its confined counterpart, we have chosen a simulation box volume which enables the pressure experienced by the confined IL. More specifically, for the present system, the pressure is $p \approx 1$ MPa. The Nose-Hoover NVT thermostat was used to control the temperature and was set to $T = 330$ K. The system was relaxed for $t_{\text{tot}} = 3 \cdot 10^7$ fs until the internal energy had converged and the pressure had approached the desired value. The simulation timestep was $dt = 0.5$ fs. We have obtained pressure stabilization at $\langle p \rangle = 1.1$ MPa with a side length of the cubic simulation box at $L = 99$ Å. The energy relaxed to a value of $\langle E_{\text{int}} \rangle = 0.7597$ kCal/mol. The molar and mass density of the bulk IL is $\rho_n = 3400$ mol/m³ and $\rho_m = 719$ kg/m³, respectively.

We have calculated the viscosity in two ways: using the Green-Kubo relation since the viscosity of a system can be represented as an integral of the autocorrelation function [17], and using non-equilibrium molecular dynamics simulations with different shear strains.

In the non-equilibrium shearing simulations, the bulk IL is placed into a triclinic (non-orthogonal) simulation box with periodic boundary conditions applied in all three directions. Due to the deformation of the simulation box, every point in the box has an additional velocity component (a so-called *streaming velocity*). In order to prevent the streaming velocity from affecting the thermal kinetic energy, we use the so-called *SLLOD* thermostat [18, 19]. The *SLLOD* thermostat accounts for the streaming veloc-

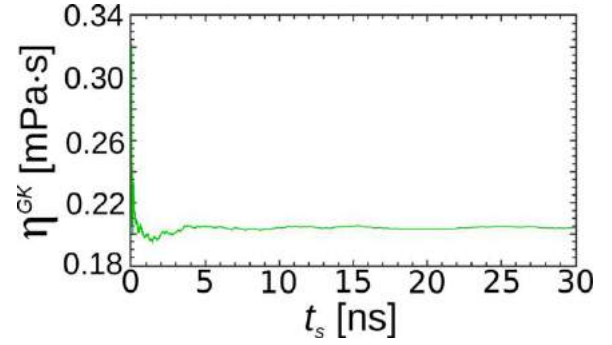


Fig. 1. Dependence of the Green-Kubo (GK) viscosity coefficient η^{GK} on the simulation time t_s in the case of the bulk ionic liquid. The time needed to obtain the viscosity coefficient is around $t_{\text{rel}} = 5$ ns.

ity which depends on an atom's position within the simulation box and it needs to be accounted for controlling the temperature.

Controlled shearing of the simulation box results in a stress acting on IL, which is quantified via the stress tensor. The relation between the stress tensor τ_{ij} components and the shear rate $\dot{\gamma}_{ij}$ of the corresponding shear strain ϵ_{ij} , with coefficient of viscosity η_{ij} as a proportionality constant is $\tau_{ij} = \eta_{ij} \cdot \dot{\gamma}_{ij}$, where $ij = \{xy, xz, yz\}$. We have applied three independent shear strains ($\epsilon_{xy}, \epsilon_{xz}, \epsilon_{yz}$). For each of them we have calculated its corresponding stress tensor component ($\tau_{xy}, \tau_{xz}, \tau_{yz}$). All shear strains were the same: $\epsilon_{xy} = \epsilon_{xz} = \epsilon_{yz} = \epsilon = 1$ leading to the shear rate of $\dot{\gamma} = \epsilon \cdot \frac{1}{t_{\text{tot}}} = \frac{1}{t_{\text{tot}}}$, where t_{tot} is the total simulation time of the shearing simulations. We have performed simulations at four orders of magnitude of the total simulation time: $t_{\text{tot}} = \{0.1, 1, 10, 100\}$ ns, and thus at four orders of magnitude of the corresponding shear rate. In this way we wanted to check the quality of our relaxation procedure and if there are shear rate dependence changes in the system. We have iterated the shearing simulations (at a shearing velocity of 1 m/s) using the output of the previous run as the input of the next run, obtaining higher strains (up to a strain of 5). We did not observe a strain dependence in the response of the system, meaning that the result is unaffected if the strain is further increased.

In fig. 1, we show the time relaxation of the Green-Kubo viscosity coefficient, which stabilizes around $\eta^{\text{GK}} = 0.2039$ mPa · s. The configuration snapshot of the bulk IL at the end of the simulation (cf. fig. 2) shows that the ions remain randomly positioned, like they were at the start of simulation, which indicates the liquid state of the bulk ionic liquid. The simulations for all three shear strains give similar values of stress components, and resulting values are shown in fig. 3. The points $\{\dot{\gamma}, \tau\}$ were obtained via shearing simulations and the solid line was obtained according to $\tau = \eta^{\text{GK}} \cdot \dot{\gamma}$, where η^{GK} was obtained via the Green-Kubo relation. Hence, we conclude that the results of shearing simulations are in agreement with the results of the relaxation simulation and therefore there are no changes in the bulk system which are shear rate dependent.

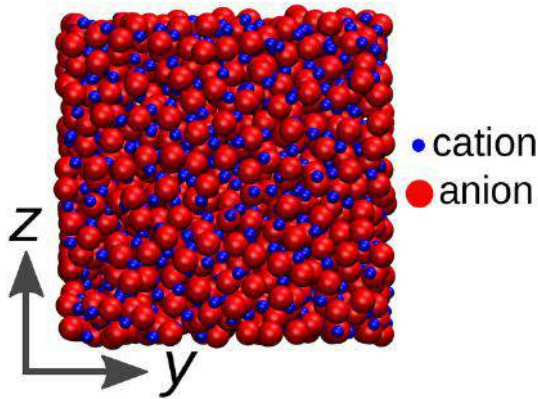


Fig. 2. Configuration snapshot (yz cross-section) of a bulk IL at the end of relaxation simulation. Cations are represented as smaller blue spheres and anions as larger red spheres.

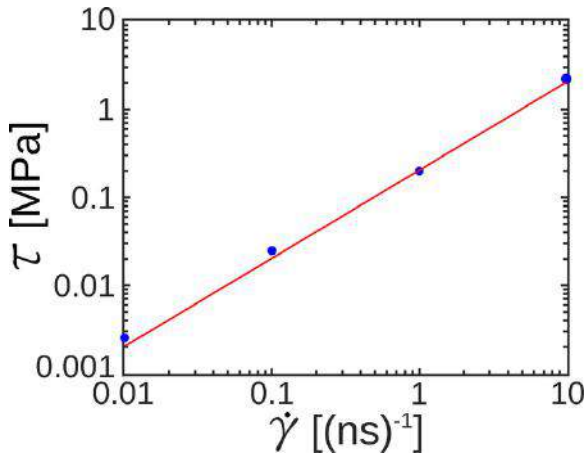


Fig. 3. Average stress tensor component τ as a function of the shear rate $\dot{\gamma}$ of a bulk SM ionic liquid. We have conducted shearing simulations on four orders of magnitude of the shear rate $\dot{\gamma}$, therefore with three orders of magnitude span, which is followed by three orders of magnitude span of τ . Points are obtained via shearing simulations and the solid line is obtained according to $\tau = \eta^{\text{GK}} \cdot \dot{\gamma}$, where η^{GK} is obtained via the Green-Kubo relation.

4 Confined ionic liquid

In order to study the properties of our ionic liquid under confinement, we use a setup consisting of two solid plates (so-called Top and Bottom plates) and ionic liquid lubricant placed between them. Such simulation setup has been introduced and described in detail in our previous paper [10], hence at this point we will describe it briefly. The geometry is shown as a schematic in fig. 4(a) together with the number of the coarse-grained particles used. In fig. 4(b) we show a configuration snapshot of our system in yz cross-section. By implementing such a geometry we have attempted to achieve a realistic particle squeeze-out behaviour with the formation of two lateral lubricant regions in a similar manner to the simulations of Capozza *et al.* [5]. For the description of the solid surfaces we have combined rigid layers of particles moving as a single entity on which the external force or motion is imposed, de-

noted by “Top Action” and “Bottom Action” in fig. 4(a), with thermalized layers, denoted by “Top Thermo” and “Bottom Thermo” in which particles vibrate thermally at $T = 330$ K. The particles in the Top and Bottom action layers are moved as rigid bodies and particles in the thermo layers are allowed to move thermally. In this way, we prevent a progressive deformation of the plates during the cyclic movement. The thermo layers only vibrate thermally since a strong LJ interaction holds them together. The ionic liquid is neutral in total, so the total number of cations and anions is the same: $N_C = N_A = N_{\text{IL}}/2$. In the present simulations the total number of IL atoms is $N_{\text{IL}} = 2500$.

The plates are driven along the x -direction at a constant velocity V_x , as shown in fig. 4(a). The solid plates are made up of nine atomic layers at a FCC (111) lattice arrangement. Periodic boundary conditions are applied in the x and y directions, while the simulation box is kept fixed in the z -direction. The Bottom plate can therefore be considered to be infinite, while the Top plate is surrounded by the lateral reservoirs, in which the lubricant can freely expand. The lateral reservoirs are implemented as a mechanistic way for allowing the lubricant to be dynamically squeezed in or out as an external load or velocity is applied. The number of lubricant molecules effectively confined inside the gap can dynamically change depending on the loading conditions. This is important for exploring the possible states of a mechanical system of particles that is being maintained in thermodynamic equilibrium (thermal and chemical) with a lubricant reservoir (*i.e.*, void spaces in tribological system). The nano-tribological system is open in the sense that it can exchange energy and particles, realizing an effectively grand-canonical situation [20, 21].

We have shown that our bulk IL is a Newtonian fluid: the validity of the $\tau = \eta^{\text{GK}} \cdot \dot{\gamma}$ relation over the whole range of shearing rate $\dot{\gamma}$ supports that fact. Our model does not assume the nature of the viscous response of IL. Only based on simulation results we conclude that the bulk salt model (SM) IL behaves as a Newtonian fluid. For a different choice of parameters one could obtain power law or solid-like behaviour. On the other hand, confinement has a profound influence on the structure of ILs in thin films [9, 10, 20, 22], therefore when the same IL is confined it does not behave as a Newtonian fluid, as we will show in the rest of the paper.

The confining surfaces can induce ordering of the particles in their vicinity. We have used simulations to obtain the static force-distance characteristic [10]. In order to determine a reliable static force-distance characteristic, at each calculation point we have to ensure the system is in equilibrium. Concerning the realization of those simulations the interplate gap is modified in the following manner: the gap is increased or decreased (*i.e.*, the Top-Bottom plate distance is changed) with a constant velocity $V_z = 5$ m/s for a *move* period of time $t_{\text{move}} = 20$ ps; thereafter, we apply conjugated gradient minimization on the ions in order to minimize their internal energy and relax them after the *move* period. As the energy minimization is performed, the ions take positions which ensure their

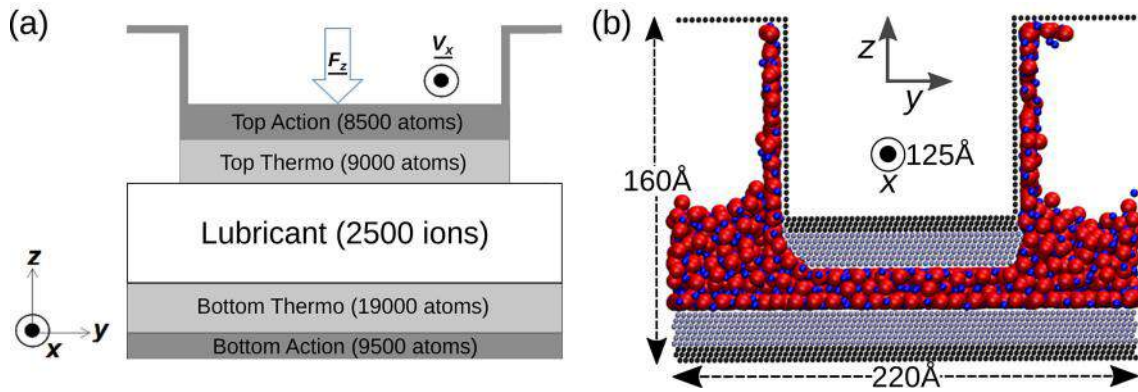


Fig. 4. (a) Schematic of the simulation setup shown as yz cross-section. There are two solid plates at the top and bottom of the system (*i.e.* Top and Bottom plates, names are chosen according to their position along the z -axis), consisting of two regions: at the outermost ones the particles are moving as a single entity (Top/Bottom Action) and at the innermost ones the particles are thermalized at a controlled temperature (Top/Bottom Thermo). The thermalized layers are in direct contact with the lubricant while the action layers are used to impose external velocity and/or force to the solid plates. (b) Front (yz) view with respect to the shear direction. A typical simulation configuration and key dimensions of the geometry are given. The solid plates are made up of FCC (111) atomic layers. The ionic liquid is composed of an equal number of cations and anions (cations: smaller blue spheres; anions: larger red spheres).

minimal internal energy and the Top plate stays fixed for a *stay* period of time $t_{stay} = 50$ ps, during which period the average value of the normal force is calculated; that value is presented as a simulation point in $F_z(d_z)$ static characteristic, cf. fig. 5. In order to avoid systematic errors due to the initial position or direction, the plate movement is performed in different directions and from different initial configurations, hence fig. 5 shows the averaged values of several realizations.

4.1 Equilibrium behaviour of confined ionic liquid

A non-monotonous behaviour of the normal force F_z acting on the Top plate can be observed in fig. 5 as the plate-to-plate distance changes from one point at which system is equilibrated to another, using the previously described procedure. The points (d_z, F_z) have been obtained through our simulations, while the dashed line serves as a visual guide. It can be seen that the normal force strongly depends on the interplate distance. The presence of negative values of normal force F_z can be understood as the IL trying to reduce the plate-to-plate distance due to adhesion phenomena. These changes of the normal force are correlated with the extraction and inclusion of IL layers into the gap, as already observed experimentally, cf. ref. [9]. During the performed stationary state simulations, the cationic-anionic layers were squeezed out in pairs, in order to keep the system locally neutral, as observed in experimental studies [8, 9, 20, 22, 23].

There is a strongly decreasing trend of the maximal normal force which can be sustained by the system as the number of ionic layers confined between the plates increases, *i.e.*, for the two ionic layers the maximal force $F_{z,\max}^I = 3$ pN, while for the three ionic layers it is $F_{z,\max}^{II} = 0.25$ pN. In our model, the Lennard-Jones interaction between the plates and the ions is ten times stronger than between the ions themselves. The ionic lay-

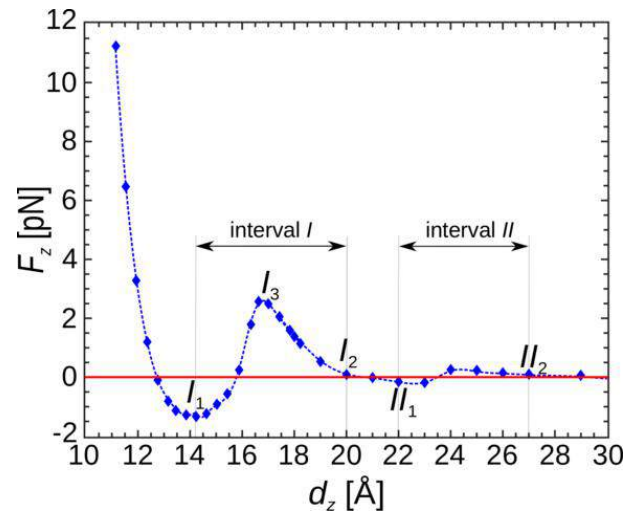


Fig. 5. Dependence of the normal force F_z acting on the Top plate on the plate-to-plate distance d_z . Five characteristic points $\{I_1, I_2, I_3, II_1, II_2\}$ with corresponding interplate distances $d_z \approx \{14, 20, 17, 22, 27\}$ Å are marked on the $F_z(d_z)$ curve. Also, the two characteristic intervals of d_z are labeled, where the interval I is bounded by the points I_1 and I_2 , while the interval II is bounded by the points II_1 and II_2 . The horizontal solid line denotes $F_z = 0$ pN. The dashed line connects the points obtained from the simulation and serves as a visual guide.

ers closest to the plates are therefore more stable than the layers in the midpoint of the gap (interval II). As a result, the three-layer system becomes less dense and can build up a lower normal force compared to the two-layer system. We have selected two intervals of interest for the interplate distance which capture the presence of local maxima and subsequent minima of the normal force F_z accompanied with the compression of IL. This corresponds to the expulsion of a cation-anion layer pair from the gap.

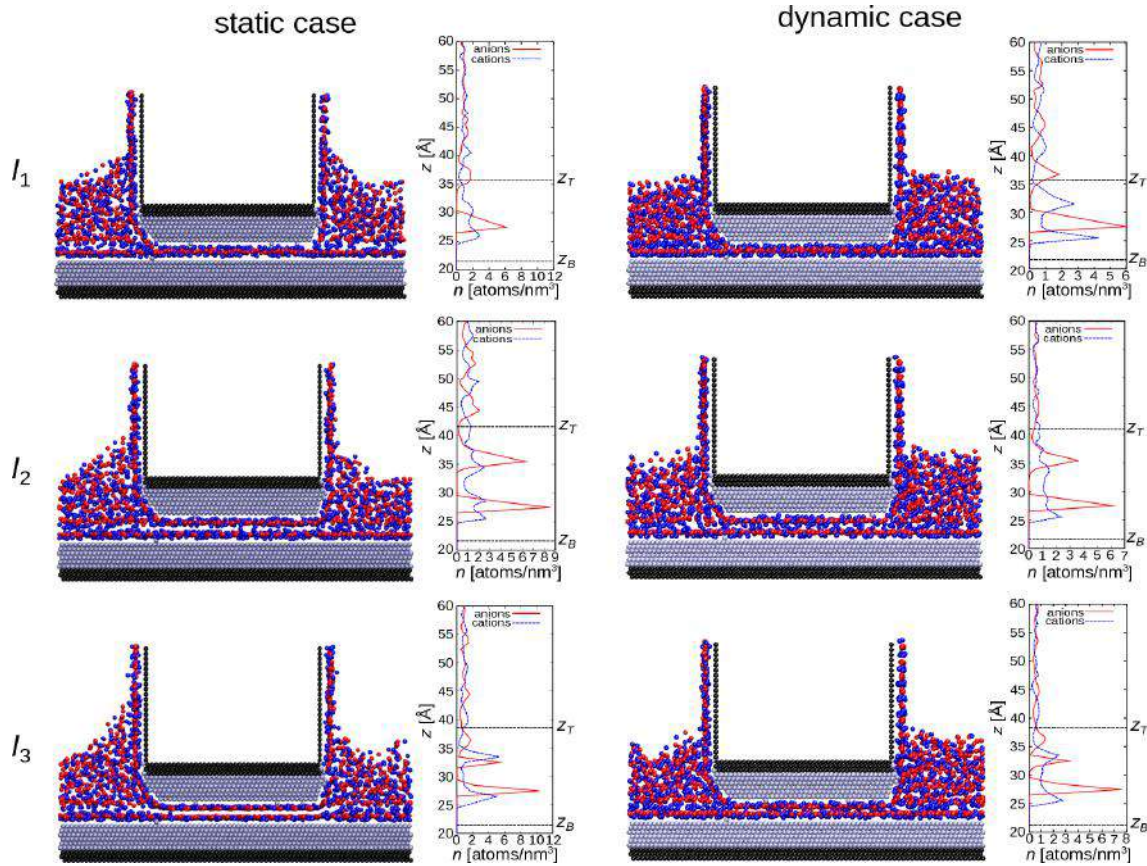


Fig. 6. Configuration snapshots (yz cross-section) accompanied with ionic density distribution along the z -direction in three representative points of the interval I : $\{I_1, I_2, I_3\}$. Left panels correspond to the static case of Top plate's movement, while right panels correspond to the dynamic case of Top plate's movement.

The intervals are: $d_z^I = [14.2, 20]$ Å, $d_z^{II} = [22, 27]$ Å, and they are labeled as I and II , respectively. In order to understand the changes of the system configurations and to correlate them with the changes of the interplate distance, snapshots of the system from the MD simulations corresponding to several characteristic points of the intervals I and II have been selected and studied in more detail: $I_{1,2}$, $II_{1,2}$ which correspond to the limits of the intervals, and the local maximum of the interval I , labeled as I_3 .

The left vertical panel of fig. 6 shows the system configuration in the yz cross-section and the ionic density distribution along the z -direction obtained in the equilibrium force-distance simulations for the three characteristic points of the interval I : $\{I_1, I_2, I_3\}$, corresponding to plate-to-plate distances $d_z = \{14.2, 20, 17.2\}$ Å, respectively. In fig. 7 the left vertical panels show analogous results for the two characteristic points of the interval II : $\{II_1, II_2\}$, corresponding to plate-to-plate distances $d_z = \{22, 27\}$ Å, respectively. The ions are depicted smaller than their LJ radii in order to allow a direct observation of the layering. The positions of the atomic centres of the innermost atomic layers of the Top and Bottom plates are labeled in figs. 6 and 7 as z_T and z_B respectively. As the Bottom plate is kept fixed during the whole simulation, z_B remains constant while z_T changes with the Top plate displacement. A general feature observed under

all conditions was the formation of cationic layer close to the plates. The reason is the smaller size of the cations ($\sigma_{CC} = 5$ Å) compared to the anions ($\sigma_{AA} = 10$ Å). Following, the second layer gets induced by the first one (due to Coulombic interaction) and it is populated by anions. The distance between the first and the second layer from the bottom is in the range of 1–2.5 Å, meaning that while the centres of mass of the particles are in different layers, the layers themselves overlap as their distance is smaller than the particle diameters.

From fig. 7 we observe that the anionic monolayer thickness is roughly 7 Å and corresponds to $10/\sqrt{2}$ Å, *i.e.*, the anions are placed in the centers of the squares formed by the cations of the neighboring layers (the diameter of an anion is 10 Å). In addition to the yz cross-section configuration snapshots together with the ionic density distribution along the z -axis, shown in the left panels of figs. 6 and 7 for the cases of intervals I and II , respectively, we have prepared the xy cross-section configuration snapshots, shown in the left panels of figs. 8 and 9.

4.2 Cyclic compression of confined ionic liquid

We have investigated the dynamic behaviour of the IL during a periodic linear movement of the Top plate along

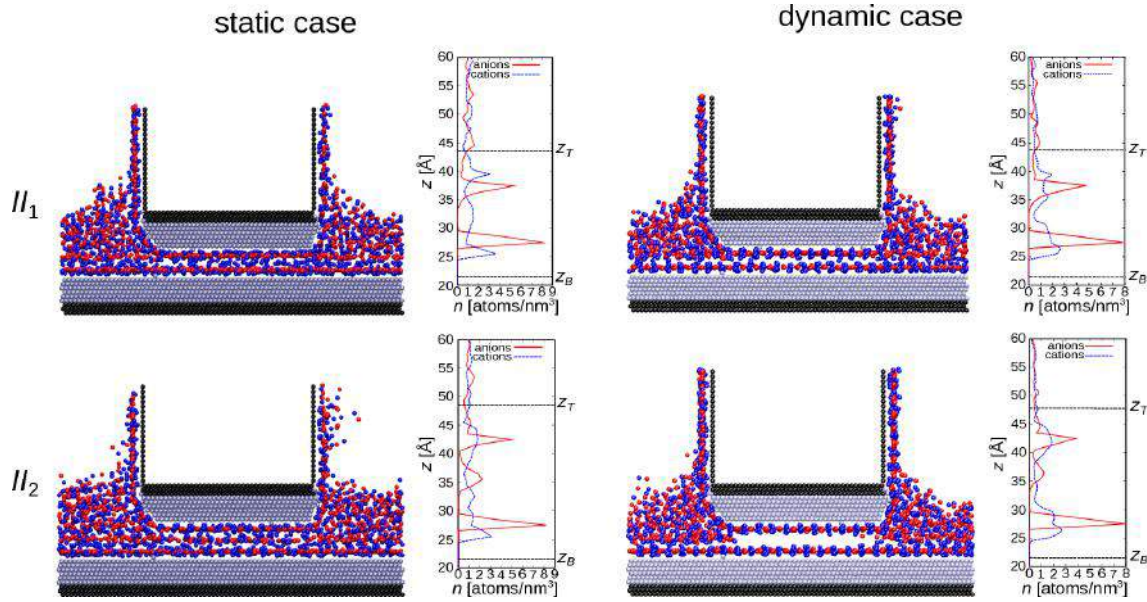


Fig. 7. Configuration snapshots (yz cross-section) accompanied with ionic density distribution along the z -direction in two representative points of the interval II : $\{II_1, II_2\}$. Left panels correspond to the static case of Top plate’s movement, while right panels correspond to the dynamic case of Top plate’s movement.

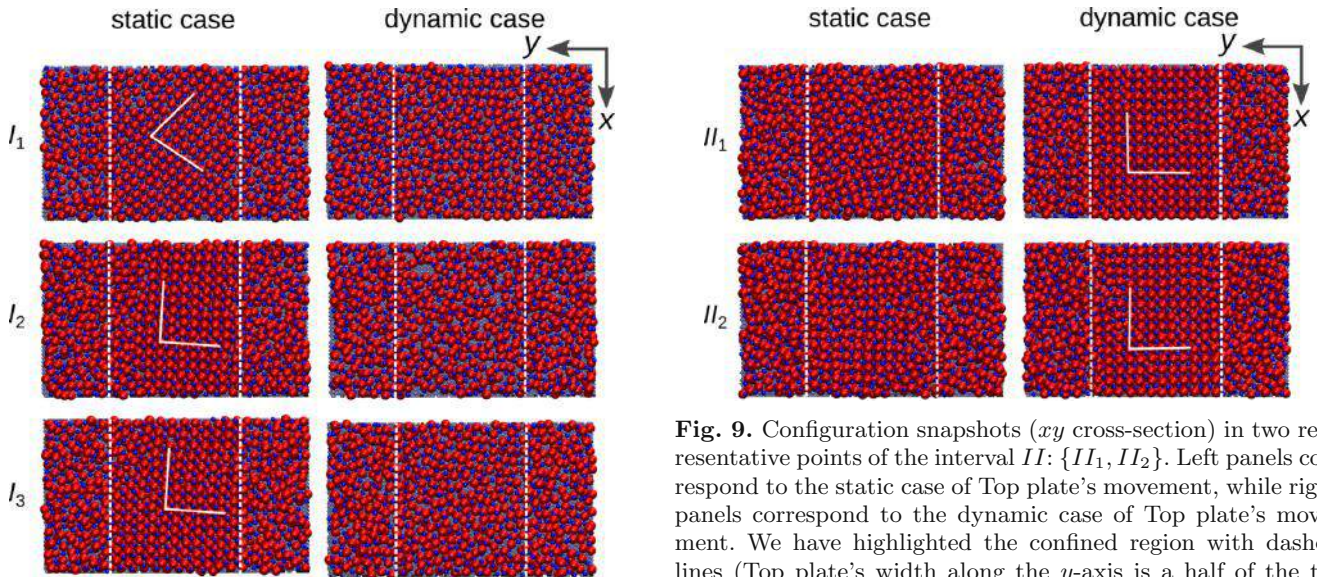


Fig. 8. Configuration snapshots (xy cross-section) in three representative points of the interval I : $\{I_1, I_2, I_3\}$. Left panels correspond to the static case of Top plate’s movement, while right panels correspond to the dynamic case of Top plate’s movement. We have highlighted the confined region with dashed lines (Top plate’s width along the y -axis is a half of the total system’s width) and also we have sketched crystallization patterns with solid lines. Periodic boundary conditions are applied in the x and y directions, while simulation box, which is cubic, is kept fixed in the z -direction.

Fig. 9. Configuration snapshots (xy cross-section) in two representative points of the interval II : $\{II_1, II_2\}$. Left panels correspond to the static case of Top plate’s movement, while right panels correspond to the dynamic case of Top plate’s movement. We have highlighted the confined region with dashed lines (Top plate’s width along the y -axis is a half of the total system’s width) and also we have sketched crystallization patterns with solid lines.

the z -axis, between the two limiting points of the intervals I and II . The space between the solid plates was in this way periodically expanded and compressed. Periodic movements of the Top plate were performed at three

constant velocities $V_z = \{0.1, 1, 10\}$ m/s but no velocity-dependent differences in the system behaviour were observed. We have performed ten cycles in order to determine how much the cycles differ and to determine a statistically reliable average cycle. The confined ionic liquid lubricant responds to the cyclic movement with a hysteresis in the normal force $F_z(d_z)$ as shown in fig. 10. We present both raw data of all cycles (thin solid lines) and a smooth average cycle (thick solid line). In the case of interval I there are three points of interest $\{I_1, I_2, I_3\}$, corresponding to the points noted in fig. 5. Points I_1 and I_2 are the starting and ending point, respectively, and the point I_3

corresponds to the maximum of the normal force F_z in the smooth average cycle. We observe that between each two of those points there are clear tendencies in the average cycle of the normal force $F_z(d_z)$. First, in the segment $I_1 \rightarrow I_2$, *i.e.* in the extension half of the cycle, there is a continuous increase of the normal force F_z from negative values up to the value around zero in point I_2 . In point I_1 there is one anionic layer confined in the gap and normal force F_z has a negative value. With the dynamic increase of the gap ions are pulled in from lateral reservoirs into the gap. In point I_2 an additional cationic-anionic layer pair is fully formed in the gap, hence increasing the number of confined anionic layers to two. Next, there is the segment $I_2 \rightarrow I_3$ where the ions are compressed within the gap, which is consistent with the continuous increase of normal force F_z . In this segment, the normal force F_z takes positive values meaning that the ionic liquid shows resistance to the compression but does not flow out. After that, in segment $I_3 \rightarrow I_1$ there is a sharp decrease of normal force F_z which is correlated with the squeezing-out of the additional cationic-anionic layer taken in from the lateral reservoirs during the extension half-cycle. During the compression half-cycle there is a return to the initial state I_1 , where the gap contains one compact anionic layer.

We should note that the distributions of cations and anions in the dynamic case for interval I bear close resemblance. Let us now discuss the changes in the number of confined ionic layers as a function of the interplate distance and correlate them with the changes in the normal force F_z acting on the Top plate: in the range $d_z = [11, 14.2] \text{ \AA}$ the normal force F_z acting on the Top plate has a steep decrease, reaching the minimum at point I_1 . For the point I_1 at $d_z = 14.2 \text{ \AA}$, cf. fig. 6, we can observe a pronounced peak in the anion density distribution which is aligned with a well-defined anionic layer inside the gap. In the case of cations, there are two peaks attached below and above the anionic peak. This situation corresponds to the formation of two incomplete cationic layers inside the gap. The value of normal force F_z is negative and in point I_1 it has the deepest minimum when considering the whole $F_z(d_z)$ characteristic. With increasing plate-to-plate distance d_z the normal force F_z is increasing, with a sign change of the normal force F_z around $d_z = 15.7 \text{ \AA}$ in the equilibrium case and $d_z = 17.8 \text{ \AA}$ in the dynamic case, cf. figs. 5 and 10(a), respectively. This means that before this point the IL is pulling the plates together, since the ions strive to reduce their interlayer distance. After this point, for $F_z > 0$, enough ions are pulled inside the gap and the IL now pushes the plates apart. Such behaviour is typically observed in systems exhibiting layering transition, already seen in systems of both neutral molecules [24] and ILs [9]. With reversing into compression in fig. 10(a), the normal force F_z reaches a local maximum in the point I_3 at $d_z = 17.2 \text{ \AA}$. This is actually the location of the maximum in the equilibrium case as well. With the further decrease of d_z beyond the point I_3 there is a continuous decrease of the normal force up to the distance $d_z = 14.2 \text{ \AA}$ as IL starts flowing out of the gap. Still, one should note that there are two differences between the two systems: i) the sign of the normal force in

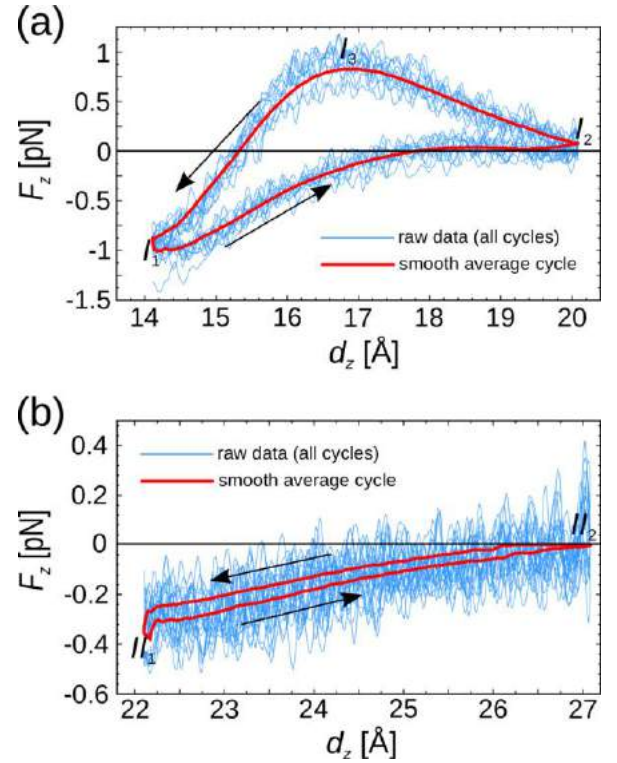


Fig. 10. This figure presents the results of dynamic extension-compression cycles in the intervals I and II . In panel (a) we present dynamic $F_z(d_z)$ characteristic in the interval I : thin lines represent the hystereses of ten dynamic cycles, the solid line on top of them is the smooth average hysteresis. There is also a solid horizontal line which corresponds to $F_z = 0$. Panel (b) is analogous to the panel (a), just it presents the results in the interval II .

point I_2 and ii) the magnitude of the normal force at local maximum I_3 . In the case of cyclic (dynamic) movement of the plates, the normal force is positive $F_z > 0$, *i.e.* the IL keeps pulling apart the plates at point I_2 and the maximum of the normal force in the point I_3 ($F_z^{dyn} = 1 \text{ pN}$) is lower than in the equilibrium case ($F_z^{eq} = 3 \text{ pN}$). Both observations indicate that the plate's motion is preventing the ionic liquid to fully fill the void space of the gap. Also, there is a substantial slip during the ejection of IL from the gap, which results in a lower normal force. Otherwise, if no slip would be present the maximum normal force at velocity $V_z = 1 \text{ m/s}$ should be about two orders of magnitude higher based on the bulk viscosity coefficient calculated in the previous section.

Partial filling of the gap due to the motion of the walls is even better observable in the results for the interval II . While the equilibrium characteristic has a local maximum, cf. fig. 5, in the dynamic case there are only two characteristic points (starting and ending point $\{II_1, II_2\}$) and a monotonously increasing normal force between them. At point II_1 at $d_z = 22 \text{ \AA}$ in the static case, we notice that at the midpoint between the plates there is a broad maximum of the cation density distribution, see fig. 7. In the static case we notice that, similar to the transition from one to two anionic layers within the interval I ,

there is a transition from two to three anionic layers within the interval II , which happens in proximity of the point $d_z = 24 \text{ \AA}$. At point II_2 we notice two sharp anionic layers in the proximity of the plates and the third anionic layer which is broader, less sharp and positioned in the middle of the interplate gap, cf. fig. 7. In the dynamic case the number of layers remains the same in the interval II , they just get separated during the extension; and a creation of additional ionic layers by the ions flowing from the lateral reservoirs into the gap does not take place, cf. fig. 7.

We can conclude that in a confined system with strong interaction between the walls and the IL, the major driving force that pulls IL into the gap between the plates is the interaction with the wall atoms rather than the inter-IL interactions. In order to visualize what happens in the vicinity of the plates, we are presenting snapshots of xy cross-section configurations in the intervals I and II , check figs. 8 and 9, respectively. Even on a cursory look, one sees that the phase behaviour of the confined IL is complex: in fig. 8, we observe a salt-like ordering taking place in all representative points $\{I_1, I_2, I_3\}$ of the equilibrium configurations. In the dynamic case the IL exhibits some level of ordering for a small gap (I_1) and it is amorphous in the other two points. On the other hand, in fig. 9 there was no movement of the IL in and out of the gap and the IL formed a two-dimensional square crystal $\{II_1, II_2\}$ on both surfaces during the dynamic case. In the equilibrium configurations, there are probably enough ions in the gap that allow the IL to obtain its liquid-like character.

At this point, we would like to quantify how could the processes described above contribute to the energy losses. If two macroscopically smooth surfaces come into contact, initially they only touch at a few of these asperity points. A motion of two bodies in contact lubricated by an ionic liquid would involve the generation of new contacts and the separation of the existing ones. Ionic liquids are characterized by strong Coulombic interactions between the particles. By calculating the area covered within the average cycle of the $F_z(d_z)$ curves in fig. 10, we calculate the amount of work invested per average dynamic cycle, *i.e.*, the hysteretic energy losses. There is a big difference in the amount of invested work in the two intervals: $3.5236 \text{ pN} \cdot \text{\AA}$ for the interval I compared to $0.2844 \text{ pN} \cdot \text{\AA}$ for the interval II , where the vertical displacement of the Top plate in the two intervals is roughly the same ($\Delta d_z \approx 5 \text{ \AA}$). This is consistent with a strongly decreasing trend of the maximal normal force which can be sustained by the system as the number of ionic layers confined between the plates increases, *i.e.* for the two ionic layers the maximal normal force $F_{z,\text{max}}^I = 3 \text{ pN}$, while for the three ionic layers it is $F_{z,\text{max}}^{II} = 0.25 \text{ pN}$, corresponding to the two maxima of the equilibrium force-distance characteristic in fig. 5.

4.3 Shear behaviour of confined ionic liquid

In order to study the behaviour of our confined IL under shearing, we apply a relative motion between the plates along the x -direction. The Bottom plate is kept

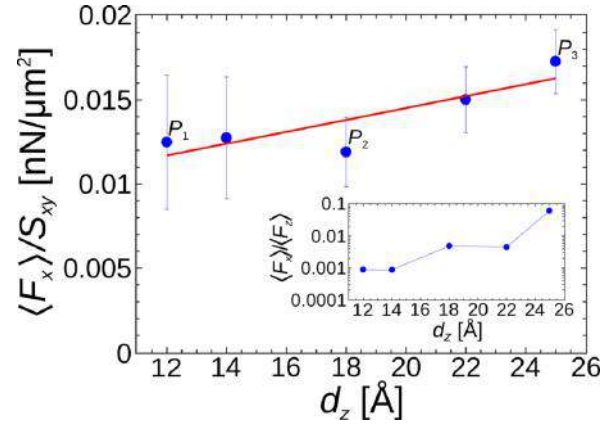


Fig. 11. Dependence of the frictional force divided by the contact area of the Top plate with IL lubricant $\langle F_x \rangle / S_{xy}$ on the interplate distance d_z . The three representative points $\{P_1, P_2, P_3\}$ are marked. Points obtained in simulations are shown as circle markers, accompanied with errors along the y -axis. Linear fit through those points is shown as a solid line. In the inset dependence of specific friction $\langle F_x \rangle / \langle F_z \rangle$ on the interplate distance d_z is shown, with y -axis in log scale. Simulation points are shown as circle markers, while the dashed line serves as a visual guide.

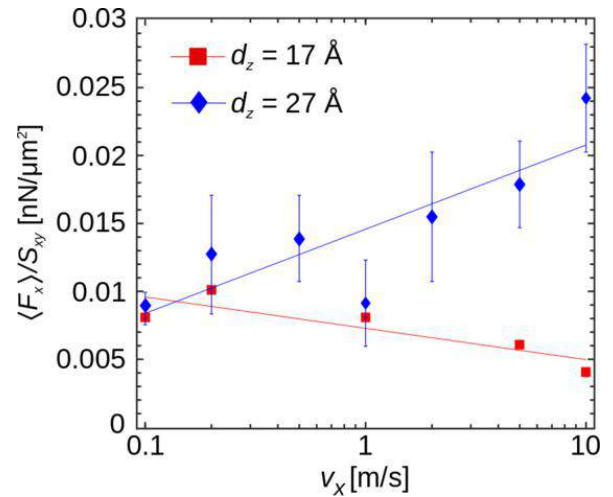


Fig. 12. Dependence of the frictional force divided by the contact area of the Top plate with IL lubricant $\langle F_x \rangle / S_{xy}$ on the Top plate's lateral velocity $V_x = 0.1\text{--}10 \text{ m/s}$. The error bars represent the standard deviation of the average values obtained from the simulation data. The lines showing the friction trends are obtained by linear regression.

fixed and a constant velocity V_x is imposed on the Top plate. We are interested in establishing how does the lateral (frictional) force F_x depend on the confinement gap $d_z = \{12, 14, 18, 22, 25\} \text{ \AA}$.

In fig. 11 we are showing the dependence of the time averaged frictional force divided by the contact area of the Top plate and the IL lubricant, *i.e.* $\langle F_x \rangle / S_{xy}$ on the interplate distance d_z . We observe a linear increase of the frictional force per contact area with the increase of the interplate distance, with a slope of $4 \text{ nN}/\mu\text{m}^3$. In the in-

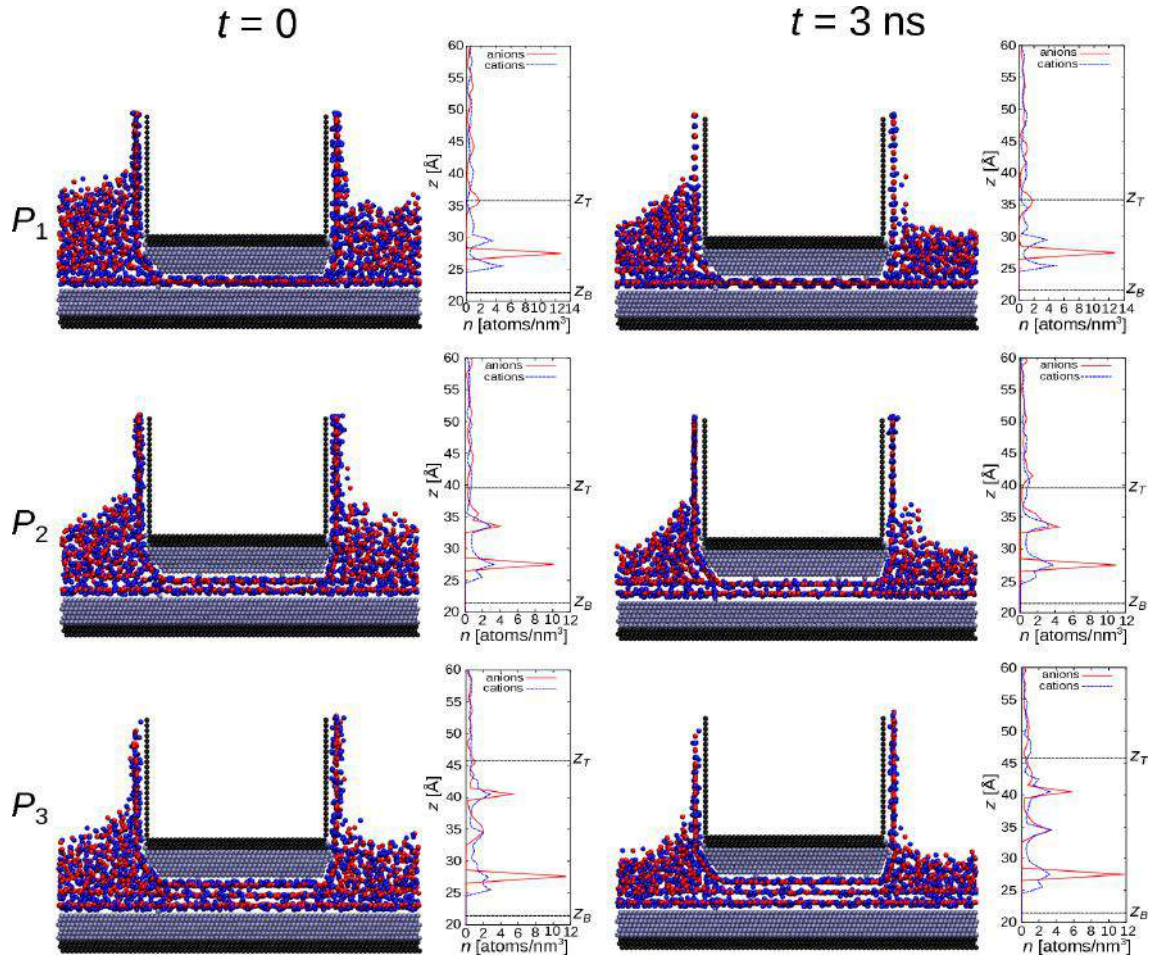


Fig. 13. Configuration snapshots (yz cross-section) accompanied with ionic density distribution along the z -direction in three representative points $\{P_1, P_2, P_3\}$. Left panels correspond to the start of friction simulations $t = 0$, while right panels correspond to the end of friction simulations $t = 3 \text{ ns}$. Top plate's lateral velocity is set to $V_x = 2 \text{ m/s}$, the total simulation time is $t_{\text{tot}} = 3 \text{ ns}$, hence all friction simulations have run until the Top plate had covered a distance of $d_x = V_x \cdot t_{\text{tot}} = 60 \text{ \AA}$ along the x -direction.

set of fig. 11, we are showing the dependence of specific friction defined as the ratio of the time averaged frictional and normal force $\langle F_x \rangle / \langle F_z \rangle$ on the interplate distance d_z . By comparing fig. 11 with the results for the bulk liquid in fig. 3 we observe that there is no correlation with the lubricant viscosity (*i.e.*, otherwise frictional force would be three orders of magnitude higher). This leads us to the assumption that our pressurized systems, whether they form a crystalline lattice or not, do not lie in a typical hydrodynamic regime and operate under full slip conditions in which the ionic liquid moves together with one of the walls. As there is no solid-solid contact between the two surfaces, but lubrication through very thin, highly viscous films which are solid-like, mixed or dry lubrication are the two potential regimes that can describe the observed conditions. A parametric study on different shearing velocities $V_x = 0.1\text{--}10 \text{ m/s}$ at two wall separations $d_z = 17, 27 \text{ \AA}$ provides additional information for the characterization of the tribological regime of our system. In fig. 12 one can observe a logarithmic (weak) dependence of the frictional force per contact area on lateral velocity of the Top plate's

movement which is consistent with the observations of previous studies of IL lubrication, cf. refs. [11, 13].

From fig. 11 we have selected three representative points with $d_z = \{12, 18, 25\} \text{ \AA}$ labeled as $\{P_1, P_2, P_3\}$, respectively. We provide an overview of the yz configuration cross-sections together with ionic density distributions along the z -axis (cf. fig. 13) at the simulation onset $t = 0$ and after $t = 3 \text{ ns}$. In the panels of fig. 14 we have highlighted the confined region with dashed lines (the Top plate's width along the y -axis is a half of the total system's width) and we have also sketched crystallization patterns with solid lines. In figs. 13 and 14 we show initial configurations at the input of friction simulations, together with the final configurations obtained after the friction simulations. We observe that any initial crystallization is not lost due to the lateral motion of the Top plate, but only slightly modified due to the motion, which suggests that the lateral movement does not alter the ordering. This is a significant finding since the longitudinal movement does alter the local order (it destroys the crystal structure for small gaps and induces it in larger ones).

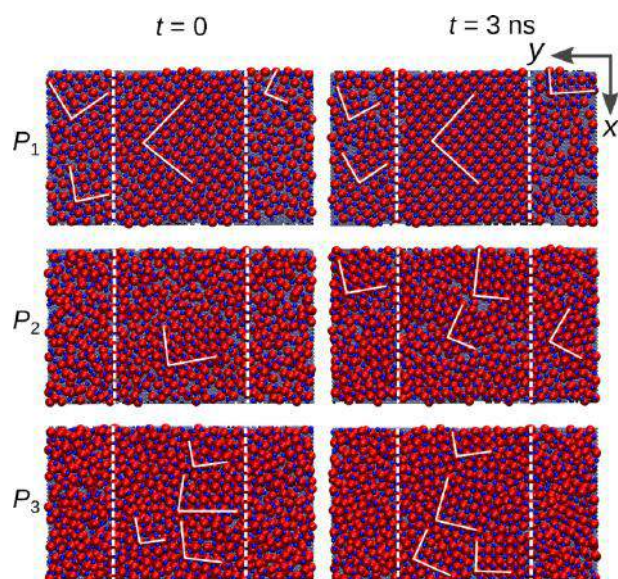


Fig. 14. Configuration snapshots (xy cross-section) in three representative points $\{P_1, P_2, P_3\}$. Left panels correspond to the start of friction simulations $t = 0$, while right panels correspond to the end of friction simulations $t = 3$ ns. We have highlighted the confined region with dashed lines (Top plate's width along the y -axis is a half of the total system's width) and also we have sketched crystallization patterns with solid lines. Top plate's lateral velocity is set to $V_x = 2$ m/s, the total simulation time is $t_{\text{tot}} = 3$ ns, hence all friction simulations have run until the Top plate had covered a distance of $d_x = V_x \cdot t_{\text{tot}} = 60$ Å along the x -direction.

5 Conclusions

In the current work we have used a molecular dynamics simulation setup in order to study the response of a model ionic liquid to imposed mechanical deformation. The properties of bulk and confined ionic liquid have been investigated under both static and dynamic conditions. First, we have shown that the Green-Kubo viscosity coefficient fits the shearing simulation results of our bulk salt model ionic liquid, indicating its liquid state. Our simulation results have shown the significant impact of the confinement and interaction with the walls on the ionic liquid response to mechanical deformation. The force-distance hysteresis surface under cyclic loading is smaller than one would expect considering only the viscosity value of the liquid. The simulations have also shown the transition from a liquid to a highly dense and ordered, potentially solidified state of the IL taking place under variable normal load and under shear. The wall slip has a profound influence on all the forces which arise as a response to the mechanical deformation. We also observe that the interaction of the IL with the walls represents a principal driving force for all processes observed in the dynamic regime for a range of studied velocities. If sufficient time is allowed for the system to reach equilibrium, inter-ionic interactions pull more ionic liquid inside the confinement gap.

Ionic liquids feature strong long-ranged Coulombic forces and their models require significant computational

effort. Coarse-grained models, such as the salt model implemented in the current study, are useful for bridging the gap between the molecular processes that control the lubrication phenomena and the macroscopic performance in engineering applications. The implementation of simplified models that describe fundamental physicochemical phenomena at a reduced computational cost can provide deep insights which shed light onto the mechanisms and processes that can render ILs as potentially interesting lubricant candidates.

The work of MD and IS was supported in part by the Serbian Ministry of Education, Science and Technological Development under Project No. OI171017 and by COST Action MP1305. Numerical simulations were run on the PARADOX supercomputing facility at the Scientific Computing Laboratory of the Institute of Physics Belgrade.

Author contribution statement

KG and IS designed the study. MD and IS performed the simulations. They also wrote the paper with inputs from KG.

References

1. F. Zhou, Y. Liang, W. Liu, Chem. Soc. Rev. **38**, 2590 (2009).
2. R. Hayes, G.G. Warr, R. Atkin, Phys. Chem. Chem. Phys. **12**, 1709 (2010).
3. O.Y. Fajardo, F. Bresme, A.A. Kornyshev, M. Urbakh, J. Phys. Chem. Lett. **6**, 3998 (2015).
4. O. Fajardo, F. Bresme, A. Kornyshev, M. Urbakh, Sci. Rep. **5**, 7698 (2015).
5. R. Capozza, A. Vanossi, A. Benassi, E. Tosatti, J. Chem. Phys. **142**, 064707 (2015).
6. Z. Wang, C. Priest, Langmuir **29**, 11344 (2013).
7. D.A. Beattie, R.M. Espinosa-Marzal, T.T. Ho, M.N. Popescu, J. Ralston, C.J. Richard, P.M. Sellapperumage, M. Krasowska, J. Phys. Chem. C **117**, 23676 (2013).
8. A.M. Smith, K.R. Lovelock, N.N. Gosvami, T. Welton, S. Perkin, Phys. Chem. Chem. Phys. **15**, 15317 (2013).
9. A.E. Somers, P.C. Howlett, D.R. MacFarlane, M. Forsyth, Lubricants **1**, 3 (2013).
10. K. Gkagkas, V. Ponnuchamy, M. Dasic, I. Stankovic, Tribol. Int. **113**, 83 (2017).
11. A.C.F. Mendonça, A.A.H. Pádua, P. Malfreyt, J. Chem. Theory Comput. **9**, 1600 (2013).
12. N. Voeltzel, A. Giuliani, N. Fillot, P. Vergne, L. Joly, Phys. Chem. Chem. Phys. **17**, 23226 (2015).
13. F. Federici Canova, H. Matsubara, M. Mizukami, K. Kurihara, A.L. Shluger, Phys. Chem. Chem. Phys. **16**, 8247 (2014).
14. K. Holmberg, P. Andersson, A. Erdemir, Tribol. Int. **47**, 221 (2012).
15. D.J. Hardy, J.E. Stone, K. Schulten, Parallel Comput. **35**, 164 (2009).
16. S. Plimpton, J. Comput. Phys. **117**, 1 (1995).
17. S. Viscardy, J. Servantie, P. Gaspard, J. Chem. Phys. **126**, 184512 (2007).
18. D.J. Evans, G. Morriss, Phys. Rev. A **30**, 1528 (1984).
19. P.J. Davis, B. Todd, J. Chem. Phys. **124**, 194103 (2006).

20. J. Gao, W.D. Luedtke, U. Landman, *Phys. Rev. Lett.* **79**, 705 (1997).
21. J. Gao, W.D. Luedtke, D. Gourdon, M. Ruths, J.N. Israelachvili, U. Landman, *J. Phys. Chem. B* **108**, 3410 (2004).
22. S. Perkin, *Phys. Chem. Chem. Phys.* **14**, 5052 (2012).
23. R. Hayes, N. Borisenko, M.K. Tam, P.C. Howlett, F. Endres, R. Atkin, *J. Phys. Chem. C* **115**, 6855 (2011).
24. B. Bhushan, J.N. Israelachvili, U. Landman, *Nature* **374**, 607 (1995).

Ultrafast carrier dynamics in QD semiconductor optical amplifiers

(numerical simulations and pump-probe experiment)

Miljan Dašić

Student of the first level studies
Faculty of electrical engineering
Belgrade, Serbia
miljandasic@yahoo.com

Abstract— The aim of this project is to examine relevant carrier (electrons/holes/photons) dynamics of a Quantum Dot Semiconductor Optical Amplifier (QD SOA) using pump-probe experiment and programming numerical simulations of a QD SOA. The speed of the carrier dynamics in a QD SOA is ultrafast because the transitions happen at picosecond timescale. We assume Auger dominated and phonon assisted mechanisms. Greater importance of Auger processes was obtained, which is a common result in the literature [3], [8]. Standard transitions between energy levels of a QD were used with the addition of the direct transition between Wetting Layer and Ground State. Pump-probe experiment has been performed. The gain and phase dynamics were time resolved for different currents. Three-exponential fit of those results was done and the timescales were extracted as functions of the current.

Key words-Quantum Dot; Semiconductor optical amplifier; carriers; dynamics; pump-probe

I. INTRODUCTION

Understanding of the ultrafast dynamics of semiconductor materials is extremely important in order to develop and improve next generation photonic sources. Ultrafast pump-probe measurements have been used to experimentally investigate the gain and phase recovery dynamics of QD SOAs - [1], [2], [3]. Main part of a QD SOA is optical cavity (active region) that is made between p-type and n-type layers. Essentially this device is a P-N junction because the band structure of an inverse populated P-N junction is the best structure for stimulated emission of light. In order to achieve the inverse population a SOA is pumped by injected current. The amplification happens by stimulated emission. The gain G of an QD SOA is its most important parameter. It is defined as the ratio of output over input power. A QD SOA consists of a large number of Quantum Dots grown in the Wetting Layer which is made of Quantum Wells. A simple Quantum Mechanical model of a QD would be a potential pit with finite height, therefore the energy levels possible into QD are discrete and depend on the depth of that potential pit, which means they depend on the size of a QD. Because of that, we use energy broadening in the model. Carrier dynamics includes radiative and non-radiative recombinations. In radiative recombinations, electron-hole pair is recombined with the presence of a photon which can be emitted or absorbed. In nonradiative

recombinations, photons are not present. Main radiative processes are spontaneous emission, amplified emission and absorption. Nonradiative processes are phonon assisted and Auger mediated recombinations. The transition between two states can be either a capture or an escape. If a carrier goes from higher level to lower, it is called capture and the transition from lower to higher energy level is an escape.

II. MODEL

The carriers we are dealing with are electrons in the conduction band (CB) and holes in the valence band (VB). Photons are created in recombine processes between electrons and holes from corresponding energy levels. We assume the existence of three different energy states for both CB and VB. The energy lowest is Ground State(GS), Excited State(ES) is higher energy state of excited carriers and Wetting layer(WL) corresponds to the reservoir of particles which is pumped by the current that supplies the power to the device.

A real QD SOA device is built of a huge number of quantum dots. Therefore, we divide GS and ES energy levels into ensembles of quantum dots with given energy and WL is one constant energy level, similar to Moreno et al[7]. This division gives us a model of a device consisting of different quantum dots, with different sizes and potential barriers and also leads to inhomogenous broadening of the emitted photons. The energy range of the simulation is between 0.919 and 1.18 eV. NumberSteps is the number of pieces that we are using. It was shown that resolution of 150 pieces is enough for good accuracy. Energy step is calculated as:

$$E_{step} = \frac{E_{max} - E_{min}}{NumberSteps}$$

The meaning of the broadening shown in Figure 1. is that the device should give that shape of the spectrum as the output, therefore we set the resolutions for each energy piece. The distribution is Gaussian with a full width half maximum (FWHM) of 35 meV for both GS and ES, like in [7]. We have chosen the peaks of the emission: $\lambda_{GS} = 1300nm$ and $\lambda_{ES} = 1165nm$

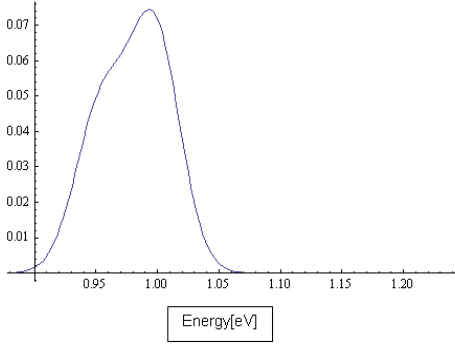


Figure 1. Inhomogeneous broadening of the GS and ES

The resolution of k-th part of the GS is calculated as a ratio of those two integrals of Gaussian distribution. The value of resolution is between 0 and 1 because it measures the ratio of integration over E_{step} interval around given energy divided by the integration over full energy scan.

$$resGS(k) = \frac{\int_{E_{GS}(k)-E_{step}/2}^{E_{GS}(k)+E_{step}/2} e^{-\frac{(x-E_{GSpeak})^2}{2\sigma^2}} dx}{\int_{E_{min}}^{E_{max}} e^{-\frac{(x-E_{GSpeak})^2}{2\sigma^2}} dx}$$

For the ES it is similar and the ratio of those two integrals is multiplied by 1.5. The Lorentzian function is used to describe that emission does not happen only for certain energy difference, but it can happen between k-th and j-th piece with the probability given by narrow Lorentzian distribution, meaning that photons of k-th energy can be produced after k-th and j-th piece recombine.

$$L(k)(y) = \frac{\Gamma}{\pi[\Gamma^2 + (E_{GS}(k) - E_{GS}(y))^2]}$$

where Γ is factor of homogenous broadening: $\Gamma = 7.5$ meV.

As usual in this area, the heart of the model are ratio equations. The ratio equations in this project are similar to those in [7] and [8] meaning that electron and hole equations are like in [8] and photon equations are like in [7] with the difference that in our model both Auger and phonon assisted processes are included. Also, a direct transition between WL and GS is added as additional connection between the levels that was not considered in [7] and [8]. The carrier dynamics equations are considered separately for electrons, holes and photons, but they are all coupled. Basically, we are solving 1 equation for electron WL, 1 for hole WL, NumberSteps*6 (for electron and hole GS and ES and for GS and ES photons) which means 902 coupled differential equations in total. GS photons are photons got in the radiative recombinations between the ground states of CB and VB, and ES photons are got in the processes between the excited states of CB and VB.

The GS photons equation (for ES photons it is similar) for i-th energy slice is:

$$\frac{\partial Pg(i)}{\partial t} = \frac{2\beta}{NumberSteps} \sum_{k=1}^{NumberSteps} \frac{res(k) \cdot hNg(k) \cdot eNg(k)}{\tau_r} + 2bPg(i) \sum_{k=1}^{NumberSteps} L(k)(i) \cdot res(k) \cdot (hNg(k) + eNg(k) - 1) - \frac{Pg(i)}{\tau_\phi}$$

Equation for WL of electrons and holes:

$$\begin{aligned} \frac{\partial Nw}{\partial t} = & J - \sum_{k=1}^{NumberSteps} \frac{res(k) \cdot Nw^\alpha \cdot (2 - Ne(k))}{\tau we} + \sum_{k=1}^{NumberSteps} \frac{Ne(k)^\alpha}{\tau EW(k)} \\ & + \sum_{k=1}^{NumberSteps} \frac{Ng(k)^\alpha}{\tau GW(k)} - \sum_{k=1}^{NumberSteps} \frac{res(k) \cdot Nw^\alpha \cdot (1 - Ng(k))}{\tau wg} \\ & - \left(\frac{1}{\tau} + \frac{1}{\tau nr} \right) \cdot Nw \cdot Nw^* \end{aligned}$$

where res(k) corresponds to resES(k) or resGS(k) and Nw^* means the opposite carrier's WL density.

The electron/hole equation for i-th energy slice of ES (for GS it is similar) is

$$\begin{aligned} \frac{\partial Ne(i)}{\partial t} = & \frac{Nw^\alpha \cdot (2 - Ne(i))}{\tau we} - \frac{Ne^\alpha(i) \cdot Nw}{\tau EW[i]} - \frac{Ne^\alpha(i) \cdot (1 - Ng(i))}{\tau eg} + \frac{Ng^\alpha(i) \cdot (2 - Ne(i))}{\tau GE[i]} \\ & b(Ne(i) + Ne^*(i) - 1) \sum_{k=1}^{NumberSteps} L(k)(i) \cdot res(k) \cdot Pe(k) - \left(\frac{1}{\tau} + \frac{1}{\tau nr} \right) Ne(i) \cdot Ne^*(i) \end{aligned}$$

where Nw , Ne and Ng are the normalized carrier densities of the WL, ES and GS, respectively. Photon populations of GS and ES are Pg and Pe , respectively. The index (i) or (k) counts the number of i-th or k-th energy slice. In the program there is (t) index which means a function of time, but we skip it here. Important feature of the rate equation models is that the dynamics of the capture/escape processes can be expressed using the parameter α which can take the integer values 1 or 2 depending on the dominant process we want to include into the model equations. The parameterization for the capture/escape terms is like in[8]:

$\alpha = 1$ corresponds to phonon assisted process and $\alpha = 2$ corresponds to an Auger mediated process. In Auger processes there is a collision of two carriers, therefore density is squared. Terms $(1 - Ng)$ and $(2 - Ne)$ are Pauli blocking factors, meaning that maximal value of normalized densities of carriers in GS and ES are limited to 1 and 2, respectively. The ES is two times more dense, therefore we use factor 2. The physical interpretation is that saturation of GS ($Ng = 1$) stops further fill of GS and because of that, term $(1 - Ng)$ in the capture processes to GS becomes zero, so further filling is blocked because GS is already full. This type of blocking factor is not used for the WL

because it has constantly being refilled by the current J , so Nw can take arbitrary high value. A serious numerical model has to include huge number of parameters in order to describe the system better. Using form τ_{ab} we represent the carrier lifetime due to the transition from energy level a to energy level b . Those parameters are of great importance because the essence of the whole simulation is to calculate the time response of the QD SOA, solving the system of coupled equations in time domain. Every process that happens has its average lifetime, for electrons and for holes separately. It is possible to get fine results only by using appropriate values for those time parameters. For example, carrier lifetime of 10 ps means that in average 10 picoseconds will go until that carrier performs the transition. We assume that capture times are constant and using formula

$$\tau_{esc} = \tau_{cap} e^{\frac{\Delta E}{k_B T}}$$

we calculate the escape times.

III. SIMULATION

Presented model is implemented in Mathematica. First part of the code consists of the constants, parameters and the calculations for the broadening (Gaussian integrals and Lorentzian function). After that, equations are written and all initial conditions set to zero. The system of the equations is solved using NDSolve (StiffnessSwitching Method).

The gain temporal changes of an QD SOA are of the key importance for its performance, so we examine it, in the simulation and using pump-probe experiment. In the simulation, gain is calculated using photon populations.

IV. PUMP-PROBE EXPERIMENT

A. General idea

Pump-probe measurements are used to obtain information on ultrafast phenomena. The general principle goes like this. A sample gets hit by a pump beam, which causes a perturbation in the sample. After an adjustable time delay that is controlled using time delay stage, a probe pulse hits the sample and its transmission is measured. By measuring the probe signal as a function of the time delay, it is possible to obtain information on the decay of the pump generated excitation. The temporal resolution of the experiment is limited only by the pulse duration, so we need the laser that generates ultrashort pulses.

Pump pulse is used to provide initial depletion of the amplifier, Non-equilibrium carrier distribution results in changed transmittance (gain/absorption and refractive index), which are affecting following probe pulse, changing its amplitude and phase. Carriers returning then to equilibrium state are affected by different radiative and non-radiative processes such as phonon or Auger assisted recombination. Such processes affect recovered time traces, so by proper choice of experimental conditions it is possible to pinpoint processes governing dynamics in the device.

Detection part of the system has to be also more complicated as the pump and probe beams cannot be spatially separated. In simplest case they can be cross-polarized, but due to the strong anisotropy of QD's this type of measurement won't provide full information on the carrier relaxation. In addition both beams have often the same wavelength and intensity of probe pulses is very low, on the level of few 100's of nW. The solution is provided by heterodyne probe detection, based on a fact that overlapping two waves with high frequencies f_1 and f_2 will produce a beating signal with a small frequency Δf equal to the difference of frequencies of original waves.

Heterodyning is commonly used in many types of detection systems as it allows detecting weak, high frequency signals using slow detectors of average sensitivity – most common example is a radio. Usually one of the signals is produced by local oscillator (LO) of known frequency and the other has external source e.g. in case of radio it is input amplifier, or laser beam passing through the tested device.

These two signals are in our case reference and probe pulses, whose frequencies are shifted by $f_1=79\text{MHz}$ and $f_2=80\text{MHz}$, respectively. As amplitude and phase between reference pulses are stable, both amplitude and phase of the beating signal depend only on the probe beam. Characterization of this beating signal provides information about device gain and refractive index properties in function of delay between pump and probe pulses.

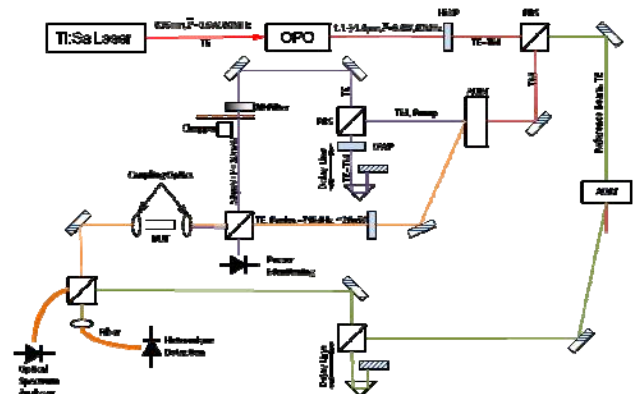


Figure 2. Pump-probe optics schematic

B. Technical details about the experiment

Power of the pump and probe beam (before coupling to the waveguide) was 500 μW and 20 μW . Pump probe always has higher power because it perturbs the system and probe is used for collecting the data about that perturbation. We have used Single Color (SC) pump-probe which means that central wavelength of both pump and probe is 1.3 μm . Bandwidth of the spectrum had Full Width Half Maximum (FWHM) of 20 nm. Pulse duration was 300 fs which is related to the time resolution of the experiment. Pump and probe beam had the same Transverse Electric (TE) polarization. The experiment was done at the room temperature (sensor was stable showing $\sim 20^\circ\text{C}$). In pump-probe experiments it is possible to pump and probe both GS and ES. We have used pumping and probing of GS only.

The main difficulties in the pump-probe and in device characterization were to align every mirror and optical element proper and to couple enough amount of light into the Single Mode Fiber (SMF) in order to perform spectrum analysis or some other measurement.

V. RESULTS AND DISCUSSION

A. Characterization of the device

The QD SOA device we were using in the experiments has sample number: QD DO1421, It comes from Innolume company. We got the layer of numerous devices and then the devices were extracted by the employees in fabrication labs. First of all, the device was mounted and put on the optical bench. It was connected to the current source and optical-current characteristic was measured using a powermeter. In the Figure 3. optical-current characteristic of three different QD SOAs grown on the same layer is given.

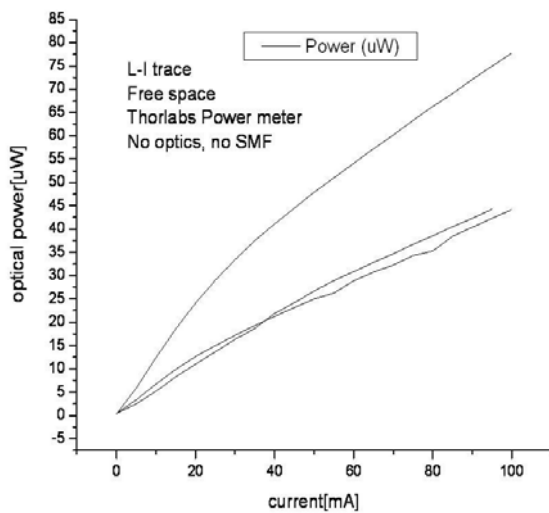


Figure 3. Optical-current characteristic of the SOA-s

There is no treshhold current which means that the devices are not lasers, they act as amplifiers. After we confirmed the devices are amplifiers, the spectrum analysis was performed. For 10mA we notice that only the GS emits and on 100mA GS is higher but on currents > 100mA, it will go to saturation and the ES starts to rise.

B. One single QD SOA simulation

The simulation of a single QD SOA by solving the model equations has given fine results. The curves are smooth and stable. After turning on the device, steady state is achieved after some time. Steady state means that the carrier densities and photon populations are constant. The time required to achieve steady state extracted from the simulation results is about 20 to 50 picoseconds. It is in a good agreement with the times from the experiment. In the experiment, we first measure the optical-current characteristic to prove that the device is a SOA, and after that, using pump-probe gain and phase recovery are got. The same procedure is in the simulation. First we plot optical-

current characteristic which is normalised number of photons (P_g and P_e) as a function of current. In a for loop we change the current and solve the equations for every current. The photons number is taken at $\text{phoTime}=20\text{ps}$ because that is the time when solutions become stable. We got the saturation of GS emission which happens in the experiment as we can see the saturation of GS on spectrum diagrams. The ES emission increases with the increase of the current and the curve looks similar to those in Figure 3.

The time plots of GS and ES gains were got. We can notice two different regimes – absorption and gain regime, as reported in [3]. The absorption regime happens on low current when inverse population is not achieved. GS absorption was got for simulation current of $J=0.5$ and ES absorption was got for $J=0.9$. The gain regime happens on high current when inverse population is achieved. Both GS and ES gain regimes were got for $J=5$. Comparing the values of GS and ES photons populations in absorption and gain regime, we can conclude that ES is affected by the current changes stronger than GS.

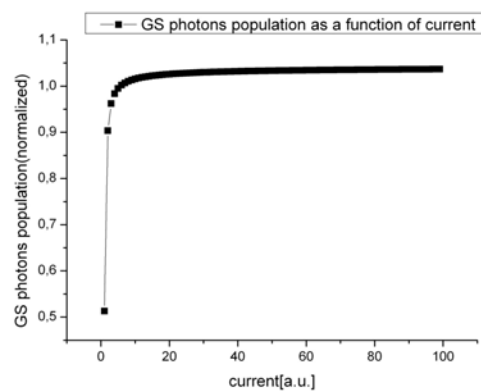


Figure 4. GS photons optical-current characteristic

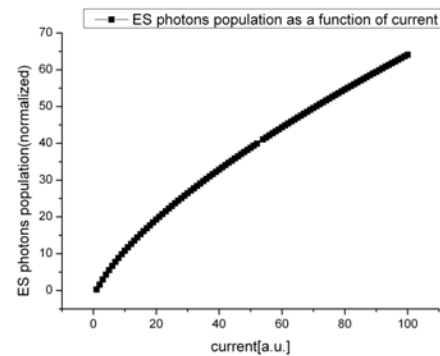


Figure 5. ES photons optical-current characteristic

In Figures 6. and 7. ES photons population is shown with Auger processes and without them, respectively. Without Auger processes we didn't get steady state in 50ps time range which means that the device is not stable. When we include Auger processes, ES photons population goes to steady state after $\sim 20\text{ps}$ which is reasonable time.

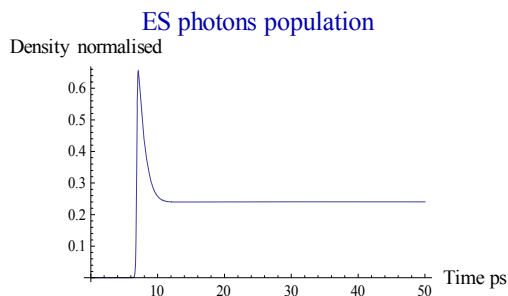


Figure 6. ES photons population time resolved (Auger included)

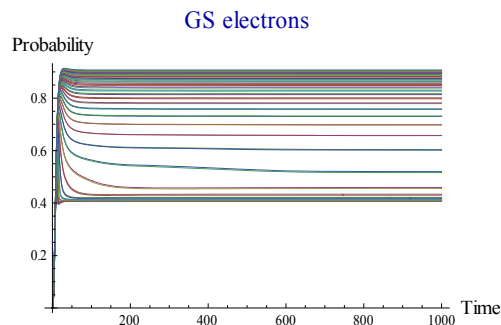


Figure 9. GS electron occupation time resolved (without WL \leftrightarrow GS)

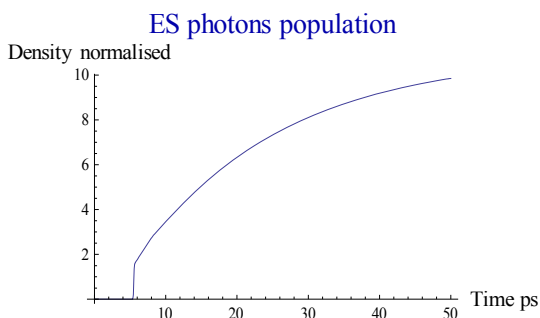


Figure 7. ES photons time resolved (Auger excluded)

C. Ensembles of Quantum Dots on different energies

The results of the simulation that considers different energy levels and broadening of the light are shown. The comparison of the results with direct transition WL \leftrightarrow GS and without that transition is made. We were using different timescales, 200ps for the simulation with WL \leftrightarrow GS and 1000 ps for the simulation without that transition because it was expected to get faster response with additional process. As we can see in those plots, additional process does not make a big difference in both the stable values and times needed for achieving stable response. The only difference is that results with WL \leftrightarrow GS are more compact for GS electrons and holes, meaning that time resolved carrier densities for different energy levels within GS more converge to one curve than in the model without additional transition where divergence of the results is higher. More expected result is to get divergence because different energy levels should have different densities of carriers because escape lifetimes directly depend on the energy differences between the levels.

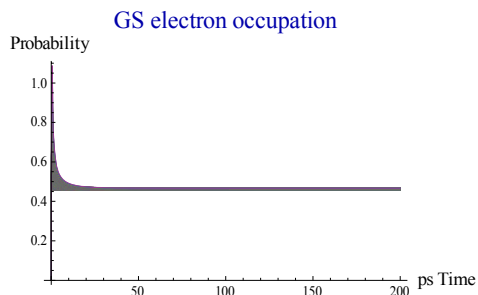


Figure 8. GS electron occupation time resolved (with WL \leftrightarrow GS)

D. Results of the pump-probe experiment

In the pump-probe experiment time delay between pump and probe beam is changing and the gain and phase are measured as functions of the time delay. This gives us the time recovery of the device. Depending on the current that is injected into the device, there are two different regimes – absorption and gain.

The absorption regime plot is given for 10mA and gain regime plot is given for 50mA.

On the lower current inverse population is not achieved. When pump beam enters the cavity of the device it gets absorbed. An electron from the VB absorbs a photon of the pump beam and goes to the CB leaving a hole in the VB. This leads to higher number of relevant carriers in both bands. When the probe beam arrives after the time delay we set, there are conditions for the emission and gain increases, recovers to the constant level in the steady state. On the other side, in the gain regime inverse population is achieved because of the higher current. When the pump beam arrives the gain instantaneously increases because the conditions for the stimulated emission are already satisfied. As the time delay increases, gain changes decrease because the probe beam sees lower inverse population due to the emission that goes all the time. After some amount of time device goes to steady state and gain changes keep being constant when time delay increases. It is obvious that recovery time in the absorption regime is higher than in the gain regime. It indicates that absorption processes are the slowest component in the ultrafast carrier dynamics.

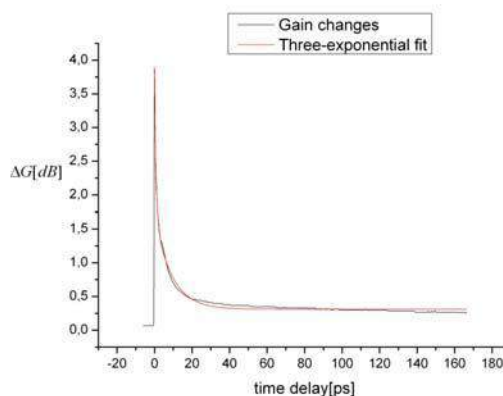


Figure 10. Gain changes on 50 mA

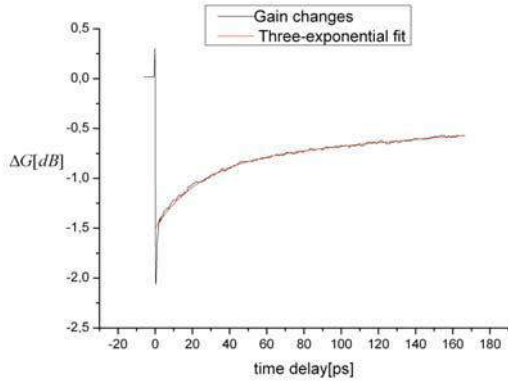


Figure 11. Gain changes on 10 mA

The three-exponential decay fit is performed using Origin's fitting tool and ExpDecay3 function. It reads:

$$y = y_0 + A_1 e^{-\frac{x-x_0}{t_1}} + A_2 e^{-\frac{x-x_0}{t_2}} + A_3 e^{-\frac{x-x_0}{t_3}}$$

where A1, A2 and A3 are the amplitudes of exponential decay components and t1, t2 and t3 are time constants in those exponential decays. The three exponential fit indicates that there are three components of carrier dynamics in a QD SOA – ultrafast, medium and slow.

VI. CONCLUSIONS AND FURTHER WORK

Pump-probe measurements of gain and phase recoveries of a QD SOA have been performed. The fitting with three-exponential decay is successful and three different timescales are extracted and plotted as a function of current. The plots are similar to the results in [8]. Removing of the Auger processes from the model equations causes slower response and the solutions that do not correspond to the experimental results, therefore we have concluded that they affect the dynamics strongly. Adding the direct transition $WL \leftrightarrow GS$ does not make a big difference in the solutions and for GS it leads to lower divergence of the results, therefore there are not advantages in adding that process to the model equations.

Results of single QD SOA simulations have shown good agreement with the experimental results which means that it is possible to use the ratio equations from this project to model a QD SOA.

When the broadening was introduced, the simulation has become complicated. The main problem is that we need to use large number of parameters with unknown values, so estimations have to be made. All of the model equations are coupled and changing of one parameter (carrier lifetime for a certain process or energy level) strongly affects the solution of the system. In the experiment we extracted three different timescales but it is impossible to connect them to every particular time parameter in the model.

Spectrum plots of carrier densities and photon populations as functions of wavelength have been made but they were not good enough, so there is a huge space of improving the simulation in order to achieve better spectrum characteristics of the light emitted by the QD SOA.

ACKNOWLEDGEMENTS

I am very thankful to my PhD student mentor Jaroslaw Pulka for his support in the programming in Mathematica and explaining me the model I was using. Also I would like to say many thanks to my supervisor Dr Tomasz Piwonski for his help and explanations about the pump-probe experiment and in general, about the lab work. The UREKA program 2011 funded by Science Fundation Ireland has given me a great chance to experience real scientific work at high class institute, which Tyndall National Institute in Cork (Ireland) definitely is, and I am very thankful for that.

REFERENCES

- [1] P. Borri, S. Schneider, W. Langbein, and D. Bimberg, "Ultrafast carrier dynamics in InGaAs quantum dot materials and devices," *J. Opt. A: Pure Appl. Opt.*, vol. **8**, pp. S33–S46, 2006.
- [2] S. Dommers, V. V. Temnov, U. Woggon, J. Gomis, J. Martinez-Pastor, M. Laemmlin, and D. Bimberg, "Complete ground state gain recovery after ultrashort double pulses in quantum dot based semiconductor optical amplifier," *Appl. Phys. Lett.*, vol. **90**, no. 033508, 2007.
- [3] I. O'Driscoll, T. Piwonski, C.-F. Schlessner, J. Houlihan, G. Huyet, and R. J. Manning, "Electron and hole dynamics of InAs/GaAs quantum dot semiconductor optical amplifiers," *Appl. Phys. Lett.*, vol. **91**, no. 071111, 2007.
- [4] Piwonski, T., O'Driscoll, I., Houlihan, J., Huyet, G., Manning, R., Uskov, A.: "Carrier capture dynamics of InAs/GaAs quantum dots". *Appl. Phys. Lett.* **90**(12), 122108 (2007)
- [5] Rossetti, M., Markus, A., Fiore, A., Occhi, L., Vélez, C.: "Quantum dot superluminescent diodes emitting at 1.3 μm". *IEEE Photonics Technol. Lett.* **17**(3), 540–542 (2005)
- [6] Saito H., Nishi, K., Kamei, A., Sugou, S.: "Low chirp observed in directly modulated quantum dot lasers". *IEEE Photonics Technol. Lett.* **12**(10), 1298–1300 (2000)
- [7] Moreno P., Rossetti M., Deveaud-Plédran B., Fiore A.: "Modeling of gain and phase dynamics in quantum dot amplifiers", *Opt Quant Electron* (2008) **40**:217–226 DOI 10.1007/s11082-008-9219-4
- [8] Ian O'Driscoll PhD thesis
- [9] Kim J., Meuer C., Bimberg D., Eisenstein G.: "Numerical Simulation of Temporal and Spectral Variation of Gain and Phase Recovery in Quantum-Dot Semiconductor Optical Amplifiers", *IEEE Journal Of Quantum Electronics*, Vol. 46, No. 3, MARCH 2010

Minimum Drop-Loss Design of Microphotonic Microring-Resonator Channel Add-Drop Filters

Miljan Dašić and Miloš A. Popović, *Member, IEEE*

Abstract—Microring-resonator filters have important applications as filtering elements in microphotonic circuits. In this paper, we address the question of optimum design of resonator-based add-drop filters in the presence of finite losses, and show that symmetric coupling provides the optimum design. This conclusion contravenes previous work on this subject, and the oft-cited critically coupled resonator case. While the minimum bandwidth of a resonant filter is ultimately limited by intrinsic losses, i.e. the intrinsic Q , we show that the symmetric design can approach twice as narrow a linewidth as a critically coupled design for the same losses, in principle. We present a coupled-mode theory (CMT) model, and a complete electromagnetic device design example based on finite-difference time-domain field simulations which validates our conclusions.

Index Terms—Microring resonators, channel add-drop filters, coupled mode theory, filter synthesis, power splitters.

I. INTRODUCTION

INTEGRATED silicon based photonics has many promising applications in optical telecommunications, optoelectronics and optical signal processing [1]–[4]. The integration of silicon photonics and electronic circuits offers the prospect of low energy devices, circuits and systems for applications including on-chip and processor-to-memory interconnects [3], [4], as well as photonic analog-to-digital converters [5]. Other applications include nonlinear and quantum optical devices for applications in quantum information and computing [6].

An important photonic device, and one of the earliest concepts realized in integrated photonics, is the resonant channel add-drop filter. Microring resonators are particularly well suited for add-drop filter applications [7], [8] because of their traveling wave structure that allows for a natural separation of the four ports (in, through, drop, add in Fig. 1), without the use of circulators. Detailed techniques have been worked out for synthesizing standard Butterworth, Chebyshev [1], [9], and more advanced [10] filter responses.

These filter synthesis techniques have primarily dealt with lossless structures. However, radiation and scattering losses are not insubstantial in strong-confinement photonics, with typical losses of 2-3 dB/cm [4] and radiation Q 's on the order of 250,000 in silicon, and higher in some other material systems. Regardless of the magnitude of the loss, it begins to play a major role for narrow enough bandwidth filters, when the total

M. Dašić and M.A. Popović are with the Department of Electrical, Computer and Energy Engineering, University of Colorado Boulder, Engineering Center, Room ECEE1B55, 425 UCB, Boulder, CO 80309-0425, United States of America, E-mail: miljandasic@yahoo.com, milos.popovic@colorado.edu.

M. Dašić is also with the Department of Physical Electronics, Faculty of Electrical Engineering, University of Belgrade, Kralja Aleksandra 73, 11000 Beograd, Serbia.

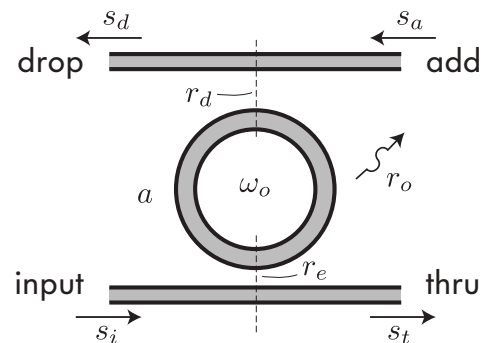


Fig. 1. Schematic of a single microring-resonator add-drop filter showing the parameters used in the CMT model.

Q approaches the loss Q , Q_o . Therefore it is of interest to investigate the optimal design of filters in the presence of loss.

Some prior work has already addressed this issue in photonics [11], and considerably more in circuit and microwave theory. Here, we show that the design of single-microring filters that provides minimum loss calls for symmetric coupling to the input and drop bus. This is in contradiction with the critically coupled design claimed to provide optimum transmission e.g. by Vörckel *et al.* [12] explicitly, and often assumed optimal in other work (e.g. [13]).

II. COUPLING OF MODES IN TIME (CMT) MODEL

Coupled-mode theory in time (CMT) provides a simple model that affords all of the necessary physics of the resonant add-drop filter problem, including resonance, loss and coupling to ports. The system of equations that describes a single-resonator filter excited by a monochromatic input wave $s_i(t)$ at angular frequency ω is [1], [2]

$$\begin{aligned} \frac{d}{dt}a(t) &= j\omega a(t) = (j\omega_o - r)a(t) - j\sqrt{2r_e}s_i(t) \\ s_t(t) &= s_i(t) - j\sqrt{2r_e}a(t) \\ s_d(t) &= -j\sqrt{2r_d}a(t) \end{aligned} \quad (1)$$

where $|a|^2$ is the energy amplitude of the ring resonant mode, and s_i , s_t , and s_d are the power-normalized amplitudes of input, through and drop port waves [2] (Fig. 1). With input wave s_i incident, some excitation is picked up by the resonator, and the remaining field propagates on to the through port. It then interferes with the light leaving the resonator in the through port and is carried away by through-port wave s_t . The energy stored in the resonator is $|a|^2$ and according to Eq. (1) the energy amplitude $a(t)$ decays at the total rate r ,

comprising a decay rate describing external coupling to the input port, r_e , the drop port, r_d , and a loss mechanism, r_o :

$$r = r_e + r_d + r_o \quad (2)$$

The decay rates are related to decay time constants as $r_i = 1/\tau_i$, for $i \in \{e, d, o\}$. Since τ is a field time constant, the associated photon lifetime ($1/e$ -intensity time) is $\tau/2$.

The drop-port response of the device is found from Eq. (1),

$$\left| \frac{s_d}{s_i} \right|^2 = \frac{4r_e r_d}{(\omega - \omega_o)^2 + r^2} \quad (3)$$

The response is Lorentzian, with a 3dB (full width at half maximum, FWHM) bandwidth of $\delta\omega_{3dB} = 2r$.

Unlike a full scattering model using transfer matrices [2], [14], the CMT model treats only given resonances (here, ω_o) of the ring and does not include geometry information that would reveal properties such as the free spectral range (FSR).

III. OPTIMAL AND CRITICAL COUPLING

Given a certain loss Q , Q_o , and corresponding loss rate $r_o = \omega_o/(2Q_o)$, our objective is to find the optimum choice of ring-waveguide couplings r_e, r_d in order to maximize on-resonance efficiency of transmission to the drop port, $|s_d/s_i|^2$. The CMT model, because of its simplicity, lends itself to closed-form analytical synthesis.

To find the optimum solution, we first note that the transmission efficiency, see Eq. (3), not surprisingly decreases with increasing loss, r_o . On the other hand, increasing r_e and r_d with a fixed r_o increases transmission, but also bandwidth, thus providing lower loss for a *different* filter. Therefore, we must ask for the best design of a fixed bandwidth. This was neglected in Ref. [12], and is the cause of its erroneous claim that critical coupling provides the minimum drop loss. Fixing bandwidth means fixing total rate r , according to $\delta\omega_{3dB} = 2r$, and together with a fixed loss, r_o , leaves only one undetermined degree of freedom, since from Eq. (2), $r_d = r - r_e - r_o$. Maximizing with respect to the remaining (input) coupling rate r_e , gives the optimal couplings for maximum drop port transmission

$$r_e = r_d = \frac{r - r_o}{2} \quad (4)$$

It is instructive to compare this solution to the critical coupling solution of the same bandwidth [1], [13] which leads to

$$r_e = r_d + r_o = \frac{r}{2} \quad (5)$$

A comparison of the transmission efficiency of the optimal (symmetric) and critical-coupling designs is given in Fig. 2, showing that the symmetric design is indeed optimal for maximizing dropped on-resonant power. We define normalized bandwidth $\alpha \equiv \Delta\omega_{3dB}/\Delta\omega_o$ as the ratio of total bandwidth $2r$ to intrinsic (loss limited) bandwidth $2r_o$. Substitution of Eqs. (4,5) into (3) yields the efficiency of the symmetric and critically coupled designs for various relative bandwidths α :

$$\left| \frac{s_d}{s_i} \right|^2 = \left(1 - \frac{1}{\alpha} \right)^2 \quad (6)$$

$$\left| \frac{s_d}{s_i} \right|^2 = 1 - \frac{2}{\alpha} \quad (7)$$

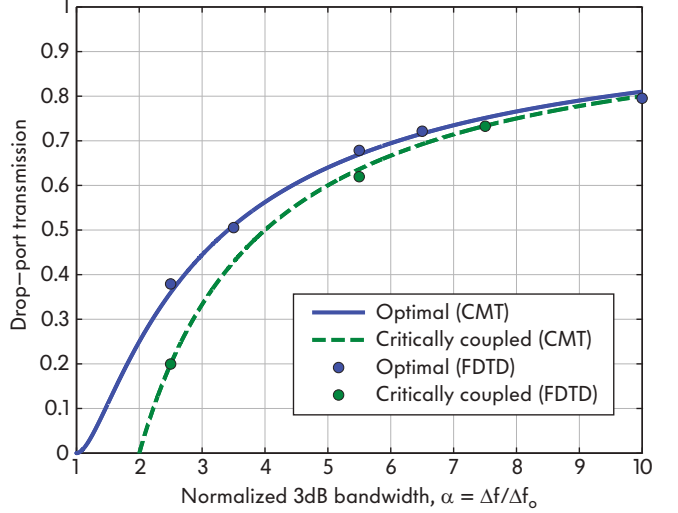


Fig. 2. Minimizing the impact of loss on a single filter stage: comparison of symmetric (optimal) and critically coupled single-ring filter designs for different normalized bandwidths, α (ratio of total bandwidth to loss-limited, intrinsic bandwidth).

This comparison is useful in the design process to determine the narrowest bandwidth that supports a desired transmission to the drop port, or the maximum transmission achievable at a certain bandwidth, given known linear losses. Fig. 2 and Eqs. (4–5) show that the optimum symmetric design has a minimum bandwidth limit of Δf_o , while the critically coupled design has a minimum bandwidth of $2\Delta f_o$. In the limit of a large relative bandwidth α , the loss plays a negligible role and the two solutions can be verified to be equal by a first-order Taylor series expansion in α^{-1} of Eqs. (4–5). For 3dB transmission, the symmetric case can reach $\alpha = \sqrt{2}/(\sqrt{2} - 1) \approx 3.412$ times the intrinsic linewidth, while the critically coupled case is limited to $\alpha = 4$ intrinsic linewidths, a difference of $\sim 20\%$.

IV. ELECTROMAGNETIC DESIGN

We next verify these results on a hypothetical lossy device design, via full-wave finite-difference time-domain (FDTD) numerical simulations [15]. We first use numerical simulations to design the example filter and relate the physical geometry to CMT variables such as r_e, r_d and r_o , and then verify the total device performance against the CMT model by simulating the entire device's response using FDTD. Without loss of generality, we consider a two-dimensional (2D) model in TE polarization, because all relevant physics is in the plane. The theory applies, however, to arbitrary resonator type (microring, photonic crystal cavity, etc.), in 2D (e.g. toy models) or 3D (real devices), and for arbitrary choices of excitation mode (e.g. polarization) and loss mechanism. In our example, we consider bending loss as the source of loss, but the approach treats equally absorption, roughness-induced scattering, etc.

Fig. 1 shows the geometry of the device. First, the bus and ring waveguide widths are chosen to be the widest that still give single mode slab operation in the $1.55 \mu\text{m}$ wavelength range. For core and cladding indices $n_{co} = 3.5$ and $n_{cl} =$

1.45, the waveguide width is $w_g = 0.24 \mu\text{m}$. The microring resonator radius is chosen next, purposefully small enough to result in substantial radiation losses, so that we can test our design approach for filters with lossy resonant elements. A circularly bent waveguide is known to produce radiation loss due to bending that exponentially increases with decreasing radius [16]. We use a two-dimensional mode solver for bent slab waveguides [17] to find a radius for which the radiation Q , $Q_o \approx 1,000$. This amounts to selecting a radius at which the real part of the propagation constant forms an integer number of wavelengths in one round trip at 1550 nm, and the imaginary part of the propagation constant yields the losses, and the target loss Q ($Q_o \approx k_o(d\beta_R/dk_o)/(2\beta_I)$). This radiation Q , Q_o , determines the minimum possible 3 dB linewidth known as the intrinsic linewidth, $\Delta f_o = f_o/Q_o$, due to decay rate r_o . The closest radius to a Q_o of 1,000 and 1550nm resonance is an outer radius of $R_o = 0.78 \mu\text{m}$.

Next we choose the gaps that correspond to calculated coupling rates r_e, r_d in the presence of loss, r_o . The evanescent field that exists in the cladding is responsible for coupling between the bus waveguide and the ring waveguide. The fraction of power coupled to the ring normalized to the input bus power is termed the power coupling coefficient, k^2 . Since the evanescent field decays exponentially far from the core, larger gaps between the bus and the ring lead to smaller coupling coefficients as [2], [14]

$$k^2(g) \approx k_o^2 e^{-\gamma(g-g_o)}. \quad (8)$$

where $k_o \equiv k(g_o)$. In high-index-contrast, strong-confinement structures, this dependence deviates from purely exponential dependence, but rigorous FDTD simulations provide the exact relationship between the coupling coefficients and the bus-ring gap. Hence, to capture the data in a physically consistent model, we take the log of k^2 vs. gap, which is nearly linear and fit it to a low-order polynomial to account for higher-order effects captured in the full-wave simulation [8]

$$\ln k^2(g) = p_3 + p_2 g + p_1 g^2. \quad (9)$$

From this type of fit, the coupling geometry of the device can be chosen to obtain desired r_e, r_d . Finally, for a given loss Q , Q_o (i.e. r_o), we use FDTD simulations to simulate the full device design to confirm the analytic solutions obtained using the CMT model and Eqs. (4–5) in both the optimal and critically coupled case. We give one design example in this paper, for $\alpha = 2.5$. From the chosen microring cavity design, and corresponding radiation loss r_o , we obtain total bandwidth $2r = 2r_o\alpha$, and the corresponding r_e and r_d for the symmetric and critical designs. To connect the power coupling coefficient to the CMT model, we use the first-order correspondence [1]

$$k_i^2 \approx \frac{2r_i}{\Delta f_{\text{FSR}}} \quad \text{for } i \in \{e, d\} \quad (10)$$

where the FSR is $\Delta f_{\text{FSR}} \equiv \frac{c}{2\pi R n_g}$, c is the speed of light in vacuum and $n_g \approx 3.62$ is the ring group index found in modesolver simulations. Using Eq. (9), the coupling gaps are

$$g_i = \frac{-p_2 - \sqrt{p_2^2 - 4p_1(p_3 - \ln k_i^2)}}{2p_1} \quad \text{for } i \in \{e, d\} \quad (11)$$

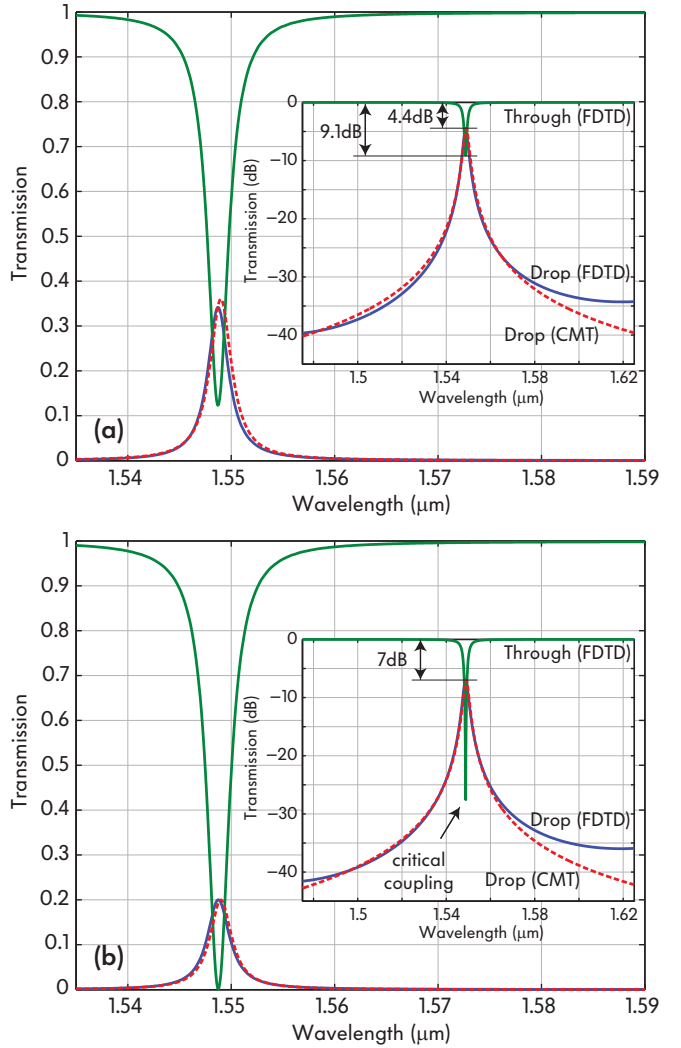


Fig. 3. Spectra of through and drop ports calculated in FDTD simulations and drop port calculated using the CMT model for a) optimally coupled and b) critically coupled microring resonator channel add-drop filters on $\alpha = 2.5$. A good matching of the analytic CMT solution with numerically simulated FDTD is observable. The insets are showing spectra on dB scale.

In Fig. 3, spectral responses resulting from FDTD simulations are shown for optimal and critically coupled filters for $\alpha = 2.5$. Overlapping the data is the CMT model of the target design, showing very good matching. CMT and FDTD spectra significantly differ only at far off-resonant detuning, where drop port transmission is less than -30 dB. The reason for this disagreement is that the CMT model here has included only one resonance, while a physical microring cavity has a finite FSR and repeating resonances. Hence, the FDTD drop response levels off on the left (shorter wavelength side) and right (longer wavelength side) because it is about to rise into another peak one FSR away. The left and right sides of the FDTD response are unequal because dispersion results in the FSR becoming smaller with increasing wavelength. We have verified that equally good agreement can be obtained for other values of the normalized bandwidth α . The on-resonant drop loss is plotted (points) alongside the analytic response (lines) in Fig. 2 and confirms the analytic model of the optimum

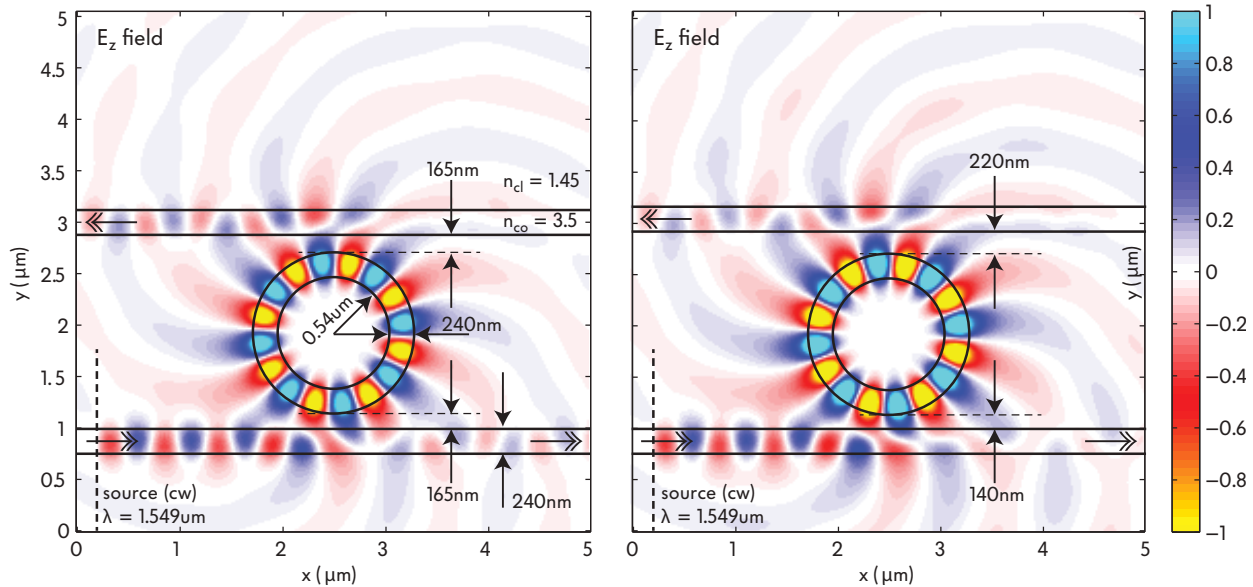


Fig. 4. Numerical FDTD simulations of symmetrically (on the left), i.e. optimally, and critically (on the right) coupled microring resonator channel add-drop filters showing the electric field propagation in the structures. Geometrical parameters are also provided. This is a snapshot under continuous-wave excitation on-resonance and it shows that more power is dropped for optimally coupled device.

symmetric and critical designs, respectively.

Figure 4 shows field snapshots of FDTD simulations of the $\alpha = 2.5$ designs whose spectra are in Fig. 3. While pulsed excitation was used to obtain full spectral response data in a single simulation, the snapshots are taken in the steady state with continuous-wave excitation at the resonant wavelength, for simpler interpretation. Fields are shown with excitation amplitudes on the same scale. More power is seen dropped by the symmetric design in Fig. 4(a) even though the critical case has less through-port transmission (it also radiates more). The guided fields look ‘wobbly’ because of the significant presence of radial radiation from the ring in the total field. An additional interesting observation is the larger steady-state field enhancement in the critically-coupled cavity in Fig. 4(b) even though both have the same total Q (r). This is because the input coupling r_e is stronger for the critically coupled case. Hence, the symmetric design is not only more efficient but also less sensitive to nonlinear resonance shifting and nonlinear loss due to Kerr nonlinearity and two-photon absorption.

V. CONCLUSION

We showed that the optimum design of a drop filter, in the context of minimizing on-resonance insertion loss, is a design with a symmetric coupling configuration. A CMT model shows that the symmetric design approaches a 2-fold narrower loss-limited bandwidth, and allows 20% narrower passbands for 3 dB insertion loss. We constructed an example geometry using mode solver and FDTD simulations of a microring cavity and directional couplers, and verified that the complete device has the CMT-predicted response from full-wave simulations of the entire device. We also noted that the symmetric design is in addition more robust to nonlinearities.

ACKNOWLEDGMENT

We thank M.T. Wade for comments on the manuscript.

REFERENCES

- [1] B. E. Little, S. T. Chu, H. A. Haus, J. Foresi and J.-P. Laine, “Microring Resonator Channel Dropping Filters”, *J. Lightwave Technol.*, vol. 15, No. 6, June 1997.
- [2] H. A. Haus, “Waves and Fields in Optoelectronics”, Englewood Cliffs, NJ: Prentice-Hall, 1984.
- [3] J. S. Orcutt *et al.*, “An Open Foundry Platform for High-Performance Electronic-Photonic Integration”, *Optics Express* 20, 12222 (2012).
- [4] F. Xia, L. Sekaric and Y. Vlasov, “Ultracompact optical buffers on a silicon chip”, *Nature Photonics* 1, 65 - 71 (2007).
- [5] A. Khilo *et al.*, “Photonic ADCs: Overcoming the Electronic Jitter Bottleneck,” *Optics Express* 20, pp. 4454-4469 (2012).
- [6] S. Clemmen, K. Phan Huy, *et al.*, “Continuous wave photon pair generation in silicon-on-insulator waveguides and ring resonators”, *Opt. Express* 17, 16558-16570 (2009).
- [7] B. E. Little *et al.*, “Ultra-compact Si-SiO₂ microring resonator optical channel dropping filters”, *IEEE Photon. Technol. Lett.*, v. 10, Apr. 1998.
- [8] M. A. Popović, “Multistage high-order microring-resonator add-drop filters”, *Optics Letters*, vol. 31, no. 17, pp. 2571, September 2006.
- [9] B. E. Little and S.T. Chu, “Toward very large-scale integrated photonics”, *Optics and Photonics News*, Nov 2000.
- [10] M. A. Popović, “Sharply-defined optical filters and dispersionless delay lines based on loop-coupled resonators and “negative” coupling”, in *Proc. Conference on Lasers and Electro-Optics (CLEO)*, Washington DC, May 6-11, 2007, paper CThP6.
- [11] M. A. Popović, “Optical coupled-resonator filters with asymmetric coupling”, U.S. Patent 7,292,751 (2003; 2007).
- [12] A. Vörckel *et al.*, “Asymmetrically Coupled Silicon-On-Insulator Microring Resonators for Compact Add-Drop Multiplexers”, *IEEE Photon. Technol. Lett.*, vol. 15, no. 7, July 2003.
- [13] C. Manolatu *et al.*, “Coupling of Modes Analysis of Resonant Channel Add-Drop Filters”, *IEEE J. Quantum Electron.*, vol. 35, no. 9, Sep 1999.
- [14] A. Yariv and P. Yeh, “*Photonics: Optical Electronics in Modern Communications*”, Oxford University Press (New York/Oxford), 2007.
- [15] A. Taflov and S. C. Hagness, “*Computational Electrodynamics: The Finite-Difference Time-Domain Method*”, 3rd ed., Artech House (2005).
- [16] M. Heiblum and J. Harris, “Analysis of curved optical waveguides by conformal transformation”, *IEEE J. Quant. Electron.* **QE-11**, p. 75, 1975.
- [17] M. Popović, “Complex-frequency leaky mode computations using PML boundary layers for dielectric resonant structures,” in *Proc. Integrated Photonics Research 2003*, Washington, DC, June 17, 2003.

Comparison of Transfer Matrix (T-matrix) and Coupling of Modes in Time (CMT) Models of Coupled Microring Resonator Filters

Miljan Dašić

Student of the first level studies

Faculty of Electrical Engineering, University of Belgrade,
Belgrade, Serbia

miljandasic@yahoo.com

Abstract—The aim of this paper is to use theoretical models of coupled microring resonator filter to show its operation and to apply those calculations in order to maximize drop port power. Coupled microring resonators are one of fundamental elements in photonic devices. They have good resonator characteristics useful for filter applications, because arbitrary -3dB bandwidth and FSR(Free Spectral Range) are easily designed. Theoretical models include T-matrix (Transfer Matrix) and CMT (Coupling of Modes in Time). A comparison of those models is shown. CMT model is applied in optimization of transmission to the drop port.

Key words-model; transfer matrix; coupling of modes in time; microring; resonator; filters;

I. INTRODUCTION

INTEGRATED silicon based photonics has many promising applications in optical telecommunications, optoelectronics and optical signal processing [1]–[4]. The integration of silicon photonics and electronic circuits offers the prospect of low energy devices, circuits and systems for applications including on-chip and processor-to-memory interconnects [3], [4], as well as photonic analog-to-digital converters [5]. Other applications include nonlinear and quantum devices for applications in quantum information and computing [6]. An important photonic device, and one of the earliest concepts realized in integrated photonics, is the resonant channel add-drop filter. Microring resonators are particularly well suited for add-drop filter applications [7], [8] because of their traveling wave structure that allows for a natural separation of the four ports (in, through, drop, add).

II. TRANSFER MATRIX MODEL

In the Fig. 1. schematic drawing of a ring resonator coupled to two bus waveguides is shown. In transfer matrix model we have two linear systems. First one has optical signal amplitude inputs of a_1 and a_2 , and outputs of b_1 and b_2 . It represents coupling of the first bus to the ring with

coupling coefficient of k_i , while the other linear system represents coupling of the second bus to the ring with

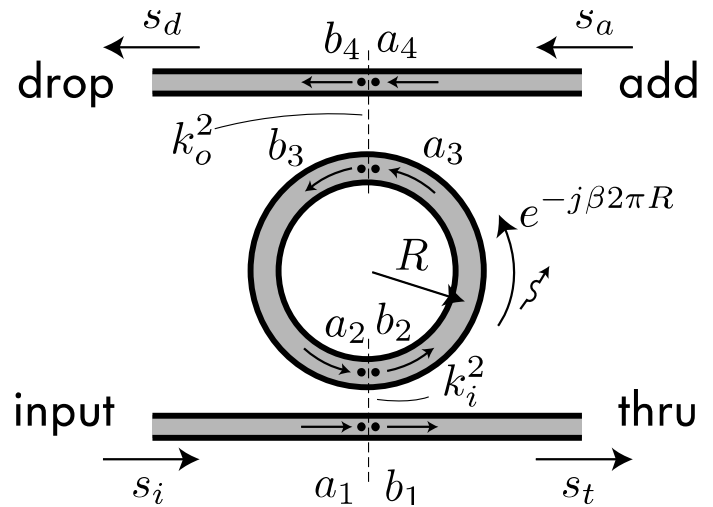


Fig. 1. Schematic of a microring-resonator add-drop filter showing the parameters used in the T matrix model

coupling coefficient of k_0 , where optical amplitude inputs are a_3 and a_4 while outputs are b_3 and b_4 . In transfer matrix model we want to solve next matrix equation

$$\begin{pmatrix} b_4 \\ b_1 \end{pmatrix} = \bar{\bar{T}} \times \begin{pmatrix} a_4 \\ a_1 \end{pmatrix} = \begin{pmatrix} T_{11} & T_{12} \\ T_{21} & T_{22} \end{pmatrix} \times \begin{pmatrix} a_4 \\ a_1 \end{pmatrix} \quad (1)$$

Optical signals a_1 and a_2 are coming from input ports, b_1 leaves the system at through port and optical signal b_4 leaves the system at drop port. The goal is to determine transfer matrix $\bar{\bar{T}}$. We solve it using next three matrix equations. First two stand for the linear systems that model couplings of the buses to the ring while third one is about the phase constraint for the signals propagating in the microring resonator [2], [9].

$$\begin{pmatrix} b_1 \\ b_2 \end{pmatrix} = \overset{=}{t} \times \begin{pmatrix} a_1 \\ a_2 \end{pmatrix} = \begin{pmatrix} \sqrt{1-k_i} - j\sqrt{k_i} \\ -j\sqrt{k_i}\sqrt{1-k_i} \end{pmatrix} \times \begin{pmatrix} a_1 \\ a_2 \end{pmatrix} \quad (2)$$

$$\begin{pmatrix} b_3 \\ b_4 \end{pmatrix} = \overset{=}{\tau} \times \begin{pmatrix} a_3 \\ a_4 \end{pmatrix} = \begin{pmatrix} \sqrt{1-k_o} - j\sqrt{k_o} \\ -j\sqrt{k_o}\sqrt{1-k_o} \end{pmatrix} \times \begin{pmatrix} a_3 \\ a_4 \end{pmatrix} \quad (3)$$

$$\begin{pmatrix} a_3 \\ a_2 \end{pmatrix} = \begin{pmatrix} e^{-j\beta\pi R} 0 \\ 0 \quad e^{-j\beta\pi R} \end{pmatrix} \times \begin{pmatrix} b_2 \\ b_3 \end{pmatrix} \quad (4)$$

In Eq. 4 j is imaginary one, $\beta\pi R$ is the product of propagation constant and half of the circumference of the ring and term R is inner radius of the ring. The expression for beta is

$$\beta = n_g \times \frac{2\pi}{\lambda} \quad (5)$$

where n_g is group refractive index. We use notation:

$$\overset{=}{t} = \begin{pmatrix} t_{11} & t_{12} \\ t_{21} & t_{22} \end{pmatrix} \quad (6)$$

$$\overset{=}{\tau} = \begin{pmatrix} \tau_{11} & \tau_{12} \\ \tau_{21} & \tau_{22} \end{pmatrix}$$

When matrix equations are written in developed form, we obtain

$$\begin{aligned} b_1 &= t_{11}a_1 + t_{12}a_2 \\ b_2 &= t_{21}a_1 + t_{22}a_2 \\ b_3 &= \tau_{11}a_3 + \tau_{12}a_4 \\ b_4 &= \tau_{21}a_3 + \tau_{22}a_4 \end{aligned} \quad (7)$$

Together with the phase constraints

$$\begin{aligned} a_3 &= b_2 \times e^{-j\beta\pi R} \\ a_2 &= b_3 \times e^{-j\beta\pi R} \end{aligned} \quad (8)$$

The algorithm is to solve Eq. 7.4 for a_3 and to obtain b_2 in terms of a_4 and b_4 using Eq. 8.1. Then plug in a_3 to Eq. 7.3 which leads to an expression of b_3 in terms of (a_4, b_4) . We were using Eq. 8.1, Eq. 7.3 and Eq. 7.4. In similar way using Eq. 8.2, Eq. 7.1 and Eq. 7.2 we solve a_2 and b_2 in terms of (a_1, b_1) . Then we have to combine expressions obtained by this separate solvings using

constraint equations (Eq. 8.1 and Eq. 8.2) which leads to this solution

$$\begin{aligned} b_4 &= T_{11}a_4 + T_{12}a_1 \\ b_1 &= T_{21}a_4 + T_{22}a_1 \end{aligned} \quad (9)$$

like in Eq. 1, where expressions for transfer matrix elements are

$$T_{11} = \frac{\tau_{22} + e^{-j2\beta\pi R} t_{22} (\tau_{12}\tau_{21} - \tau_{11}\tau_{22})}{(1 - e^{-j2\beta\pi R} \tau_{11}t_{22})}$$

$$T_{12} = \frac{e^{-j\beta\pi R} \tau_{21}t_{21}}{(1 - e^{-j2\beta\pi R} \tau_{11}t_{22})} \quad (10)$$

$$T_{21} = \frac{e^{-j\beta\pi R} t_{12}\tau_{12}}{(1 - e^{-j2\beta\pi R} \tau_{11}t_{22})}$$

$$T_{22} = \frac{t_{11} + e^{-j2\beta\pi R} \tau_{11} (t_{12}t_{21} - t_{11}t_{22})}{(1 - e^{-j2\beta\pi R} \tau_{11}t_{22})}$$

Here T_{12} represents normalized drop port power and T_{22} represents normalized through port power. Now we apply those expressions from Eq. 10 to calculate spectral response of a filter made of two bus waveguides that are coupled to the microring-resonator. We have chosen free spectral range of 2 THz and -3dB bandwidth of 40 GHz. It is known that free spectral range of a microring-resonator is determined by ring's radius [2].

$$FSR = \frac{c}{2\pi R n_g} \Rightarrow R = \frac{c}{2\pi n_g FSR} \quad (11)$$

Taking the Eq. 12 from reference [1] and using

$$\lambda = \frac{c}{f} \Rightarrow |d\lambda| = \frac{c}{f^2} df \quad (12)$$

gives us the relation for -3dB bandwidth

$$\pi \cdot \Delta f_{-3dB} = k^2 \cdot 2FSR \quad (13)$$

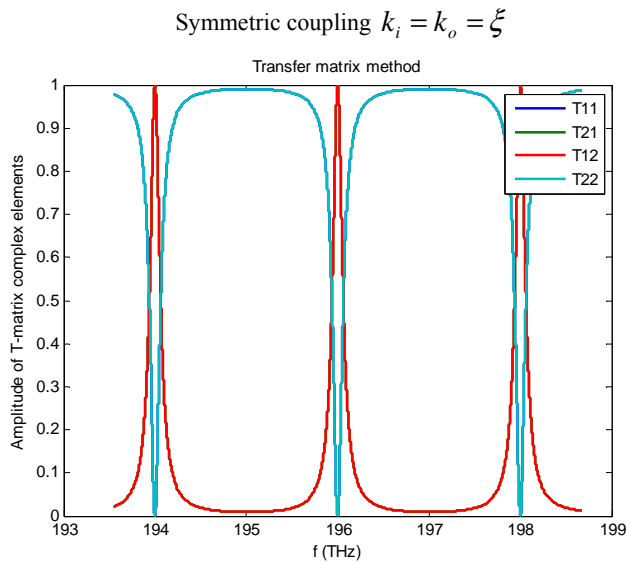
Therefore we define normalized coupling

$$\xi = \sqrt{\frac{\pi \times \Delta f_{-3dB}}{2FSR}} \quad (14)$$

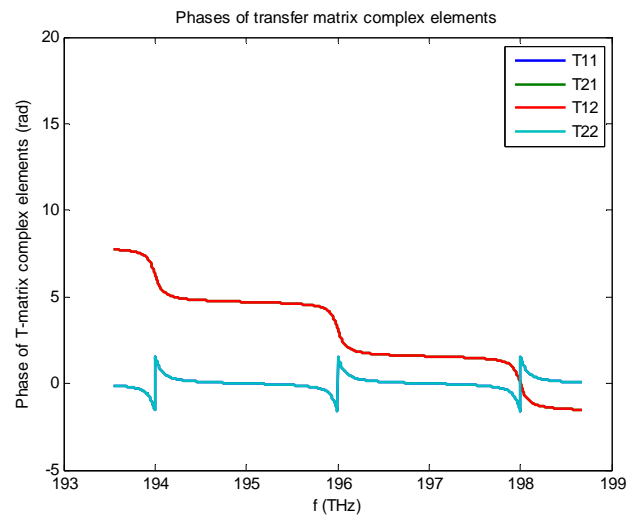
Delay in group time is calculated using this formula

$$t_g = -\frac{1}{2\pi} \frac{d\Phi}{df} \quad (15)$$

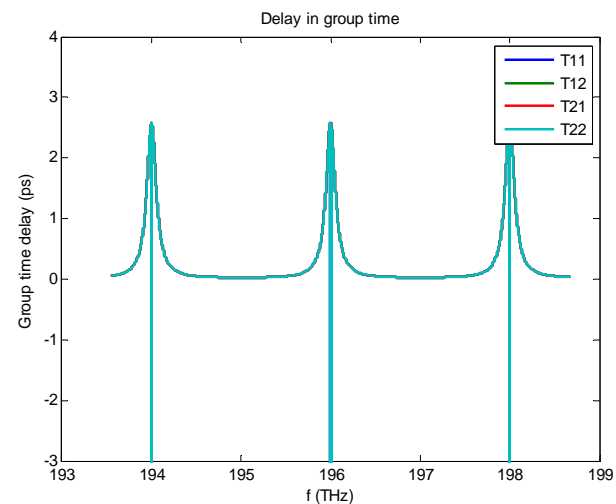
where Φ is the phase and f is the frequency.



(a)

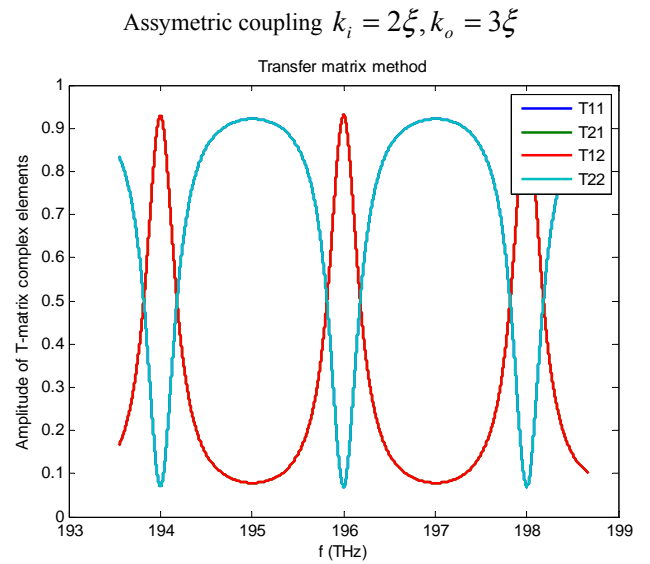


(b)

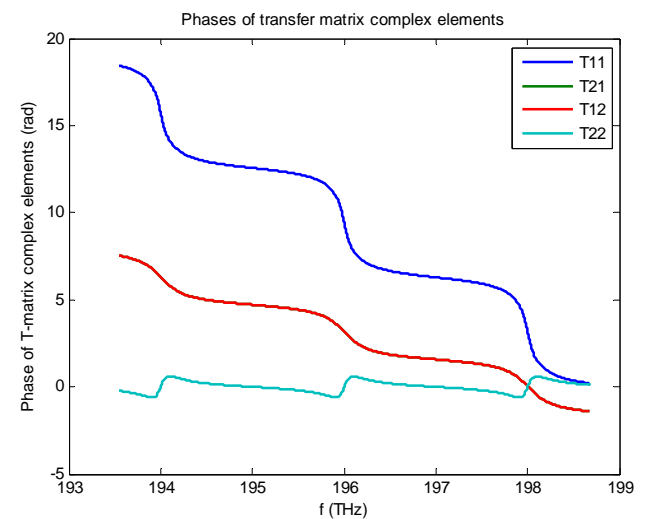


(c)

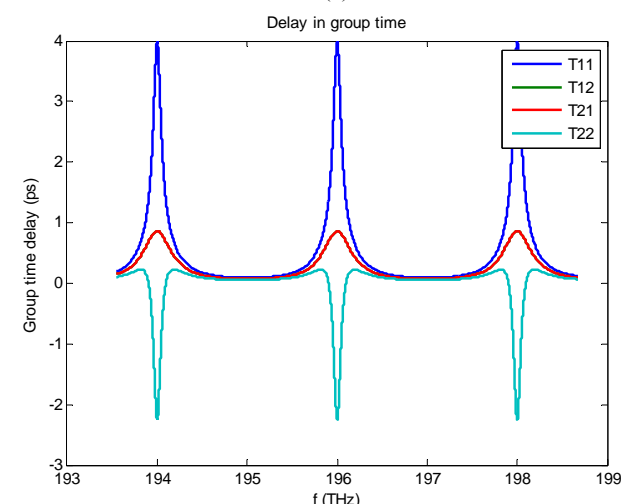
Fig. 2. Frequency spectra of T-matrix elements' amplitude, phase and group time delay - (a), (b), (c)



(a)



(b)



(c)

Fig. 3. Frequency spectra of T-matrix elements' amplitude, phase and group time delay - (a), (b), (c)

In Fig. 2 and Fig. 3 frequency spectra of T-matrix elements' amplitude, phase and group time delay are given, in symmetric and chosen asymmetric case, respectively. We can notice that symmetric coupling affords 100% transmission to the drop port. In the phase and group time delay plots we can notice differentiation of the bus lines, caused by the asymmetric coupling.

III. COUPLING OF MODES IN TIME (CMT) MODEL

Coupled-mode theory in time (CMT) provides a simple model that affords all necessary physics of the resonant add-drop filter problem, including resonance, loss and coupling to input and output ports [1,2,6]. The system of equations that describes a single-resonator filter excited by a monochromatic input wave at angular frequency ω is

$$\begin{aligned} \frac{d}{dt} a(t) &= j\omega a(t) = (j\omega_0 - r)a(t) - j\sqrt{2r_e} s_i(t) \\ s_i(t) &= s_i(t) - j\sqrt{2r_e} a(t) \\ s_d(t) &= -j\sqrt{2r_d} a(t) \end{aligned} \quad (16)$$

where $a(t)$ is energy amplitude of the ring resonant mode, s_i , s_s , s_d , are the power-normalized amplitudes of input, through and drop port waves [2]. With input wave s_i incident, some excitation is picked up by the resonator, and the remaining field interferes with that leaving the resonator in the through port and is carried away by through-port wave s_t . The energy stored in the resonator is $|a(t)|^2$ and according to Eqs. (16) the energy amplitude $a(t)$ decays at a total rate r , comprising decay rates describing external coupling to the input port, r_e , to the drop port, r_d , and to loss mechanisms, r_o :

$$r = r_e + r_d + r_o \quad (17)$$

The coupling rates r_e and r_d are determined in the evanescent-coupling geometry in Fig. 8 by the size of the ring-waveguide coupling gaps [1,9]. The decay rates are related to decay time constants as $r_i = 1/\tau_i$, for $i = \{e, d, o\}$. Since τ is a field time constant, the associated photon lifetime of the resonant cavity (which measures decay of intensity) is $\tau/2$.

The through-port and drop-port responses of the device can be found from Eqs. (16) as

$$\left| \frac{s_t}{s_i} \right|^2 = \frac{(\omega - \omega_0)^2 + (r_0 + r_d - r_e)^2}{(\omega - \omega_0)^2 + (r_0 + r_d + r_e)^2} \quad (18)$$

$$\left| \frac{s_d}{s_i} \right|^2 = \frac{4r_e r_d}{(\omega - \omega_0)^2 + r^2} \quad (19)$$

The drop-port response is Lorentzian, with a full 3dB bandwidth $\Delta\omega_{3dB} = 2r$.

Unlike a full scattering model (T matrix model) using transfer matrices, the CMT model addresses only one resonant mode of the ring and does not include geometry information that can define a free spectral range (FSR).

Resonant frequencies are determined by the resonant condition

$$f_m = m \frac{c}{2\pi R n_{eff}} \quad (20)$$

where c is the speed of light in vacuum, R is the ring resonator radius, and n_{eff} is the (frequency dependent) effective index of the guided mode. The FSR is given by

$$\Delta f_{FSR} = \frac{c}{2\pi R n_g} \quad (21)$$

where n_g is group effective index of the guided mode.

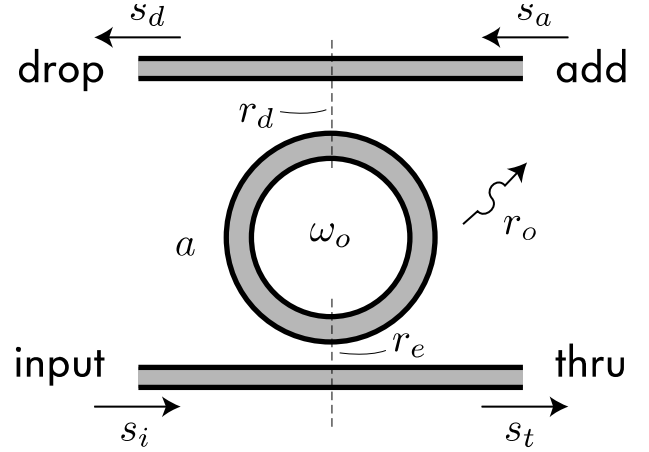


Fig. 4. Schematic of a single microring-resonator add-drop filter showing the parameters used in the CMT model.

IV. CORRESPONDENCE OF CMT AND T-MATRIX MODELS

We have derived T-matrix and CMT models of coupled microring resonator filters. Now we will compare those models. In Fig. 5 we show wavelength spectra of amplitude in linear and db scale. The task is to connect coupling coefficients k_i, k_o from T-matrix model with decay rates r_e, r_d . There is a direct relation [1]

$$r_m = 2k_n^2 \times FSR \quad (22)$$

for $m = \{e, d\}$ and $n = \{i, o\}$. Using normalized couplings from Eq. (14) we obtain expression for decay rates as

$$r = \pi \cdot \Delta f_{-3dB} \quad (23)$$

We are showing the results of comparison for symmetric coupling, with zero losses. One disadvantage of T-matrix model is that it does not model losses while CMT model includes losses. On the other side, T-matrix shows free spectral range and multiple resonances while CMT model has only one resonant wavelength. In Fig. 5(b) we can

notice that deviation of CMT Lorentzian from T-matrix trace is bigger on dB scale than on linear scale in Fig.5 (a).

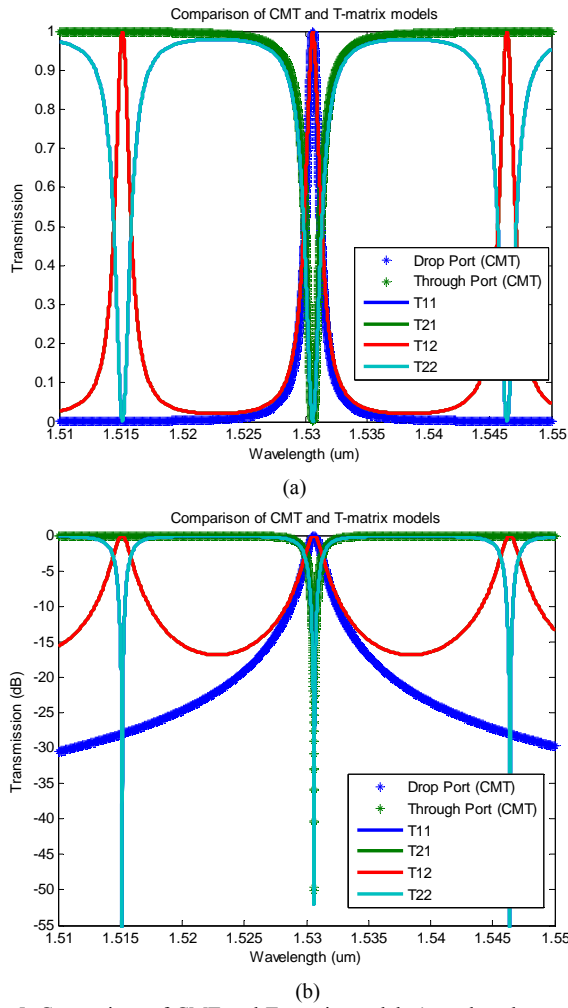


Fig. 5. Comparison of CMT and T-matrix models (wavelength spectra of amplitude) linear (a) and dB scale (b)

V. OPTIMAL AND CRITICAL COUPLING

We apply CMT model in order to optimize drop port transmission. Fixing the bandwidth means fixing the total rate r , according to Eq. (17) and, together with a fixed loss rate, there is only one degree of freedom left. Taking the first derivative of Eq. (19) in respect to r_e and setting this to zero gives

$$r_e = r_d = \frac{r - r_0}{2} \quad (24)$$

From setting Eq. (18) to zero on-resonance, we derive the couplings of critically coupled filter

$$r_e = r_d + r_0 \quad (25)$$

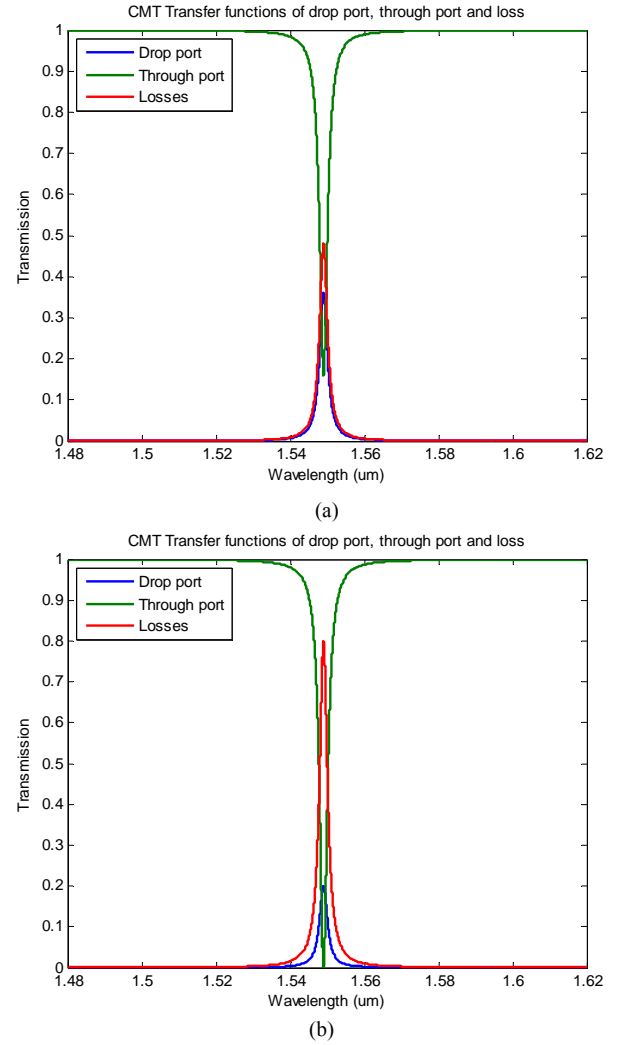


Fig. 6. CMT transmission (drop port, through port and losses) in optimally and critically coupled filters – (a), (b)

In Fig. 6 transmission spectra of through and drop port is given for optimally and critically coupled filters. A comparison of the transmission efficiency of the optimal symmetric [Eq. (24)] and critical coupling [Eq. (25)] designs is given in Fig. 7, showing that the symmetric design is indeed optimal for maximizing dropped on-resonant power. We define a normalized bandwidth, α , by normalizing the 3dB bandwidth Δf_{3dB} by the intrinsic linewidth Δf_o due to the loss rate r_o , i.e. loss Q, Q_o . Substitution of the solutions of Eq. (24) and Eq. (25) into Eq. (19) provides the normalized efficiency of the symmetric and critically coupled designs given in Eq. (26).

$$\left| \frac{s_d}{s_i} \right|_{optimal}^2 = \left(1 - \frac{1}{\alpha} \right)^2 \quad (26)$$

$$\left| \frac{s_d}{s_i} \right|_{critical}^2 = 1 - \frac{2}{\alpha}$$

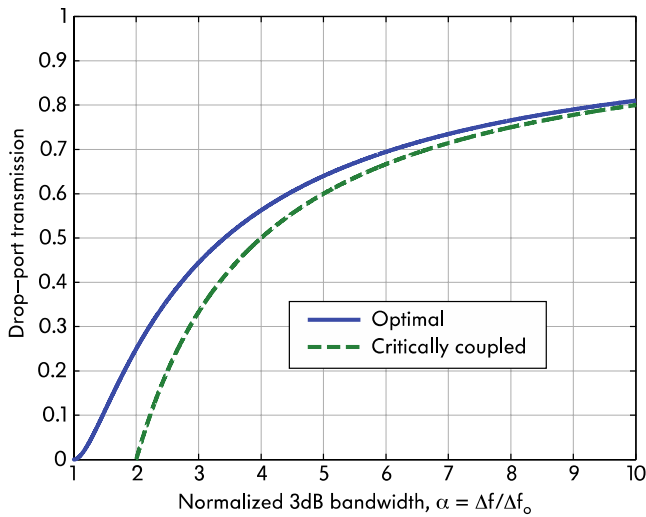


Fig. 7. Minimizing the impact of loss on a single filter stage: comparison of symmetric (optimal) and critically coupled single-ring filter designs for different normalized bandwidths, (ratio of total bandwidth to loss-limited, intrinsic bandwidth). Ref. [12]

TABLE I
MINIMUM NORMALIZED BANDWIDTH FOR 3DB DROP-PORT POWER

Symmetric coupling	Critical coupling
$\frac{\sqrt{2}}{\sqrt{2}-1} \approx 3,412$	4

VI. CONCLUSION

Transfer matrix model of a photonic microring-resonator channel add-drop filter has been solved and applied to design a filter with chosen free spectral range (FSR) and -3dB bandwidth (Δf_{3dB}). The results of those calculations are given for symmetric and asymmetric coupling. CMT model was solved and applied in order to maximize drop port power of a single ring filter. We have determined how to choose optimal couplings and then compared this to the case of critical coupling. This comparison is useful in the design process to determine the narrowest bandwidth that supports a desired transmission to the drop port, or the maximum transmission achievable at a certain bandwidth, given known linear losses. Fig. 7 and Eqs. (26) show that the optimum symmetric design has a minimum bandwidth limit of Δf_0 , while the critically coupled design has a minimum bandwidth of $2\Delta f_0$. In the limit of a large bandwidth α , the loss plays a negligible role and the two solutions can be verified by a first-order Taylor series expansion of Eqs. (26) to be equal.

ACKNOWLEDGEMENT

Author is very thankful for all the support of professor Miloš A. Popović, who was the supervisor of the research presented in this paper. First of all, he gave me a great opportunity to work as a research intern in his Nanophotonic Systems Laboratory at Electrical, Computer and Energy Engineering Department, University of Colorado Boulder, United States of America. His ideas and comments guided me through this research. Many thanks to all the people from our group - Savvy, Chris, Kareem, Mark, Cale, Jeff and Yangyang whose support and help made my work more efficient.

REFERENCES

- [1] B. E. Little, S. T. Chu, H. A. Haus, J. Foresi and J.-P. Laine, "Microring Resonator Channel Dropping Filters", *Journal of Lightwave Technology*, June 1997, vol. 15, No. 6
- [2] H. A. Haus, "Waves and Fields in Optoelectronics", Englewood Cliffs, NJ: Prentice-Hall, 1984.
- [3] J.S. Orcutt, B. Moss, C. Sun, J. Leu, M. Georgas, J. Shainline, E. Zraggen, H. Li, J. Sun, M. Weaver, S. Urosevic, M.A. Popovic, R.J. Ram and V.M. Stojanovic, "An Open Foundry Platform for High-Performance Electronic-Photonic Integration", *Optics Express* 20, 12222-12232 (2012).
- [4] H. A. Haus and Y. Lai, "Narrow-band optical channel-dropping filter", *Journal of Lightwave Technol.* Jan. 1992., vol. 10
- [5] A. Khilo et al., "Photonic ADCs: Overcoming the Electronic Jitter Bottleneck", *Optics Express* 20, pp. 4454-4469 (2012).
- [6] S. Clemmen, K. Phan Huy, et al., "Continuous wave photon pair generation in silicon-on-insulator waveguides and ring resonators", *Optics Express* 17, 16558-16570 (2009).
- [7] B. E. Little, J. S. Foresi, G. Steinmeyer, E. R. Thoen, S. T. Chu, H. A. Haus, E. P. Ippen, L. C. Kimerling, and W. Greene, "Ultra-compact Si - SiO₂ microring resonator optical channel dropping filters", *IEEE Photon. Technol. Lett.*, vol. 10, pp. 549-551, Apr. 1998.
- [8] C. Manolatou, M. J. Khan, Shanhui Fan, Pierre R. Villeneuve, H. A. Haus, *Life Fellow, IEEE*, and J. D. Joannopoulos, "Coupling of Modes Analysis of Resonant Channel Add-Drop Filters", *IEEE Journal of Quantum Electronics*, vol. 35, no. 9, September 1999.
- [9] A. Yariv and P. Yeh, "Photonics - Optical Electronics in Modern Communications", New York Oxford, Oxford University Press, 2007.
- [10] Andreas Vörckel, Mathias Mönster, Wolfgang Henschel, Peter Haring Bolivar, and Heinrich Kurz, "Asymmetrically Coupled Silicon-On-Insulator Microring Resonators for Compact Add-Drop Multiplexers", *IEEE Photonics Technology Letters*, vol. 15, no. 7, July 2003
- [11] M.A. Popović, "Sharply-defined optical filters and dispersionless delay lines based on loop-coupled resonators and 'negative' coupling," in Conference on Lasers and Electro-Optics(CLEO), 2007
- [12] M. Dašić and M.A. Popović, "Minimum Drop Loss Design of Microphotonic Microring Resonator Channel Add-Drop Filters", Telecommunications Forum (TELFOR) 2012, Belgrade, Serbia

Calculation of Magnetic Field and Supercurrent Distributions of Type-II Superconductors in the Mixed State using Modified London Model

Miljan Dašić

Student of the master studies
Faculty of Electrical Engineering, University of Belgrade
Belgrade, Serbia
miljandasic@yahoo.com

Abstract—Calculation of magnetic field and supercurrent distribution has been performed, using modified London model. We have written a simulation in MATLAB that calculates a mixed state of type-II superconductors. Starting point of the calculations was magnetic field distribution. Supercurrent distribution was obtained from the magnetic field distribution, according to the Ampere's law. It has been shown that it is possible to extract the vortex-core size from the profile of supercurrent distribution. Dependence of the vortex-core size upon the cutoff parameter is provided. Two basic cases of the vortex lattice (VL) have been used – square and triangular lattice.

Key words-superconductors; type-II; mixed state; London model; vortex lattice (VL); vortex-core size; simulation; MATLAB

I. INTRODUCTION

Superconductivity (SC) is a physical phenomenon characterized by vanishing of the electric resistivity in different materials and alloys when they are cooled down below a certain temperature, known as the critical temperature (T_c). Beside the stepwise decrease of the specific electric resistivity to zero, it was observed that a superconductor pushes out the magnetic flux, when placed in an external magnetic field. This appearance is called Meissner effect. The explanation is that *surface supercurrents* are induced and their magnetic field cancels out the external magnetic field. Inside the superconductors, electric field is $E = \rho J = 0$ (since $\rho = 0$), therefore only surface currents can exist. Under the condition $T < T_c$, there is a surface supercurrent whose magnetic field completely cancels out external magnetic field, under the condition that external magnetic field is smaller than the *critical field* ($H < H_c$). The value of critical field depends on the temperature. It decreases from its maximum value $H_c(0)$ to the zero value at critical temperature ($H_c(T_c) = 0$). When one places already cooled superconductor ($T < T_c$) in a magnetic field bigger than critical field at that temperature ($H > H_c(T)$), material loses SC characteristics and Meissner effect does not happen. In principle, one can define superconductivity as a characteristic behaviour of a given material. SC exists in a certain space of parameters, like $H(T)$ defined by the values of magnetic field H and temperature T .

There are two possible cases, depending exclusively on the kind of the SC material. In type-I superconductors, when $H = H_c(T)$, whole sample returns to a *normal state*, when magnetic induction B completely penetrates into the sample. In type-II superconductors, when $H < H_{c1}(T)$, where H_{c1} is the lower critical field, magnetic induction does not penetrate into the sample and this is called – *superconducting state*. When $H > H_{c2}(T)$, where H_{c2} is the upper critical field, sample returns to a normal state, with full penetration of the magnetic induction. Under the condition $H_{c1}(T) < H < H_{c2}(T)$, there is a partial penetration of magnetic induction into the sample. Regular microscopic structure with alternate placements of normal and superconducting areas settles, this is known as the *mixed state*. In the mixed state magnetic induction enters the sample partly, as magnetic vortex lines. Alexei Abrikosov won a Nobel prize in physics for his prediction about the mixed state. He predicted that some materials could preserve SC in strong magnetic fields by allowing the external magnetic field to penetrate the sample as a periodic arrangement of quantized flux lines, this is a vortex lattice (VL) [1].

The basis of Abrikosov's model of the mixed state is phenomenological Ginzburg-Landau (GL) theory. The structure of the VL is, within the GL theory, characterized by the two fundamental length scales. Those are *magnetic field penetration depth* - λ and *coherence length* - ξ . The first phenomenological theory of superconductivity was London theory. A major triumph of the equations of this theory is their ability to explain the Meissner effect. Their equation shows that magnetic induction in the superconductor decays exponentially with the distance from the surface. It means that a superconductor in Meissner state is not ideal because magnetic induction penetrates into the sample on the length scale of λ – London penetration depth. One way of explaining the other parameter, coherence length, is that it defines the length scale over which the transition between normal and SC areas in the mixed state happens. There are different experimental techniques that investigate the mixed state of type-II superconductors. One of the most powerful among them is the muon spin rotation technique.

Muon spin rotation is an experimental technique used to measure local magnetic fields inside the sample. It can probe

magnetic induction in the bulk of a superconductor in a vortex lattice state [3]. Those measurements can determine the vortex-core size.

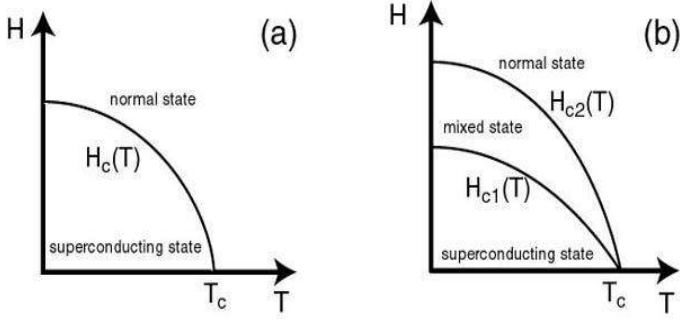


Figure 1. $H_c(T)$ characteristic for type-I and type-II superconductors

II. LONDON MODEL

There are different models for the description of magnetic field distribution of the mixed state in type-II superconductors. The aim of those models is to extract data from muon spin rotation experiments. The difference between the models is in their ability to take into account various effects which can be measured in the experiments. In phenomenological London model, magnetic field for a perfect flux-line lattice (FLL) [3] is

$$\vec{h}_L(\vec{r}) = \vec{e}_z \frac{\Phi_0}{S} \sum_{\vec{G}} \frac{e^{i\vec{G}\cdot\vec{r}}}{1 + \lambda^2 G^2} \quad (1)$$

where the sum goes over the reciprocal lattice vectors \vec{G} of the FLL. Here Φ_0 is a flux quantum with its normalized value of 2π . Parameter S is the area of the vortex lattice unit cell. Vector \vec{r} is the radius vector in the xy plane, it determines the position of the point in which magnetic field is calculated. Parameter λ is the penetration depth in the Meissner state. In reference [5] the temperature dependence of λ is given in the Eq. 2. However, we are dealing with a simplified model that does not account for the temperature dependence, so parameter λ has a fixed normalized value.

III. MODIFIED LONDON MODEL

London model used for the analysis of the experimental data does not account for the spatial dependence of the order parameter and it breaks down at distances on the order of coherence length from the vortex core center, $B(r)$ diverges. To correct this, the sum over \vec{G} can be truncated by multiplying each term in Eq. 1 by a cutoff function $F(G)$, where G is the module of \vec{G} . One important fact is that the adequate form of $F(G)$ depends on the precise spatial dependence of the order parameter in the vortex core, which in general depends on temperature and magnetic field. Modified London model has the analytical expression for $F(G)$ in the form of a smooth Gaussian cutoff factor [3]

$$F(G) = \exp(-\alpha G^2 \xi_h^2) \quad (2)$$

Magnetic field distribution in modified London model is given as

$$\vec{h}_L(\vec{r}) = \vec{e}_z \frac{\Phi_0}{S} \sum_{\vec{G}} \exp(-\alpha G^2 \xi_h^2) \frac{e^{i\vec{G}\cdot\vec{r}}}{1 + \lambda^2 G^2} \quad (3)$$

Brandt determined the values of α by solving Ginzburg-Landau (GL) equations [5]. Furthermore, Laiho et al. have shown that α is temperature dependent [2]. They have determined the temperature and magnetic field dependences of the cutoff function used in the modified London model. These calculations show that the London model with the proper cutoff function provides a reasonable description of the magnetic field distribution of the FLL in type-II superconductors.

IV. VORTEX LATTICE CONFIGURATION

Before the calculation of magnetic field, shape of the vortex lattice has to be fixed. The shape of the VL is determined by the unit vectors [4]

$$\begin{aligned} \vec{r}_1 &= (a, 0, 0) \\ \vec{r}_2 &= (a \cos \theta_L, a \sin \theta_L, 0) \\ \vec{r}_3 &= (0, 0, 1) \end{aligned} \quad (4)$$

where a is the lattice constant

$$a = \sqrt{\frac{\Phi_0}{H}}$$

The range for H is $0 < H < 1$. The lattice characteristic angle θ_L is the angle between \vec{r}_1 and \vec{r}_2 . Two basic shapes are considered in this paper: square lattice ($\theta_L = 90^\circ$) and triangular lattice ($\theta_L = 60^\circ$). By introducing reciprocal unit vectors

$$\begin{aligned} \vec{k}_1 &= 2\pi \frac{\vec{r}_2 \times \vec{r}_3}{S} \\ \vec{k}_2 &= 2\pi \frac{\vec{r}_3 \times \vec{r}_1}{S} \end{aligned} \quad (5)$$

that define reciprocal lattice vector \vec{G} , where n and m are integers

$$\vec{G}(n, m) = -n\vec{k}_1 + m\vec{k}_2 \quad (6)$$

Area of the vortex unit cell is calculated as

$$S = \vec{r}_1 \cdot (\vec{r}_2 \times \vec{r}_3) \quad (7)$$

The sum over reciprocal lattice vector \vec{G} is symmetric.

It means that integers (n,m) take the values from the interval

$$-l \leq \{n, m\} \leq l \quad (8)$$

Value of l is determined under the cutoff condition [5],

$$|\vec{G}_{\max}| \approx \frac{2\pi}{\xi_h} \quad (9)$$

From the Eq. 6 we obtain the value of G

$$|\vec{G}| = \sqrt{(mk_{2x} - nk_{1x})^2 + (mk_{2y} - nk_{1y})^2} \quad (10)$$

A. Square lattice

In the case of square lattice, Eq. 10 simplifies to

$$|\vec{G}| = \sqrt{(nk_{1x})^2 + (mk_{2y})^2} \quad (11)$$

Since $k_{1x} = k_{2y}$ and $n_{\max} = m_{\max} = l$, we obtain

$$|\vec{G}|_{\max} = l\sqrt{2}k_{1x} \quad (12)$$

Combining Eq. 9 and Eq. 12 gives us

$$l = \frac{2\pi}{\sqrt{2}\xi_h k_{1x}} \quad (13)$$

According to Eq. 5, $k_{1x} = \frac{2\pi}{a}$, therefore Eq. 13 becomes

$$l = \frac{a}{\sqrt{2}\xi_h} \quad (14)$$

B. Triangular lattice

In the case of triangular lattice, Eq. 10 simplifies to

$$|\vec{G}| = \sqrt{(nk_{1x})^2 + (mk_{2y} - nk_{1y})^2} \quad (15)$$

Maximum value of G is

$$|\vec{G}|_{\max} = l\sqrt{(k_{1x})^2 + (k_{2y} + |k_{1y}|)^2} \quad (16)$$

Combining Eq. 9 and Eq. 16, gives us

$$l = \frac{2\pi}{\xi_h \sqrt{(k_{1x})^2 + (k_{2y} + |k_{1y}|)^2}} \quad (17)$$

According to Eq. 5, $k_{1x} = \frac{2\pi}{a}$, $k_{1y} = -\frac{2\pi}{a\sqrt{3}}k_{2y} = \frac{4\pi}{a\sqrt{3}}$

$$l = \frac{\sqrt{3}a}{2\xi_h} \quad (18)$$

V. CURRENT DISTRIBUTION

Magnetic field distribution over a chosen xy mesh has been calculated, according to Eq. 3. Next parameter of a type-II superconductor we want to calculate is the vortex-core size. One of possible ways for defining a vortex-core size is provided in [6]. It is defined from the supercurrent density near the vortex center. At the vortex center supercurrent density is equal to zero, since that part of the superconductive material is not in SC state. The absolute value of supercurrent density reaches its maximum value at the distance R_0 from the vortex center. This distance is the vortex-core size. When there is an analytical expression for the magnetic field, current distribution is easily calculated. According to the Ampere's law (IV Maxwell's equation)

$$\vec{J}(\vec{r}) = \vec{\nabla} \times \vec{h}(\vec{r}) \quad (19)$$

Magnetic field points along the z -direction. By solving the determinant that corresponds to the vector product from Eq. 19, the expression for current distribution is obtained

$$\vec{J}(\vec{r}) = \vec{e}_x \frac{\partial h(\vec{r})}{\partial y} - \vec{e}_y \frac{\partial h(\vec{r})}{\partial x} \quad (20)$$

Let us calculate the x and y components of the current:

$$\frac{\partial h(\vec{r})}{\partial \varepsilon} = i \frac{\Phi_0}{S} \sum_{\vec{G}} \frac{F(\vec{G}) e^{i\vec{G}\cdot\vec{r}}}{1 + \lambda^2 G^2} G_{\varepsilon}, \varepsilon = \{x, y\} \quad (21)$$

Intensity of the current in a given point of the xy mesh is

$$J(\vec{r}) = \sqrt{J_x(\vec{r})^2 + J_y(\vec{r})^2} \quad (22)$$

VI. RESULTS

Magnetic field and current distribution of modified London mode have been calculated, in the cases of square and triangular vortex lattices. We show the results for $\xi_h = 0.18$. Furthermore, the values of vortex-core size have been extracted from the profile of the current distribution. Dependence of vortex-core size upon the cutoff parameter has been found.

A. Square lattice

In Fig. 2 and Fig. 3 top view and side view of magnetic field distribution in square lattice case are shown, respectively.

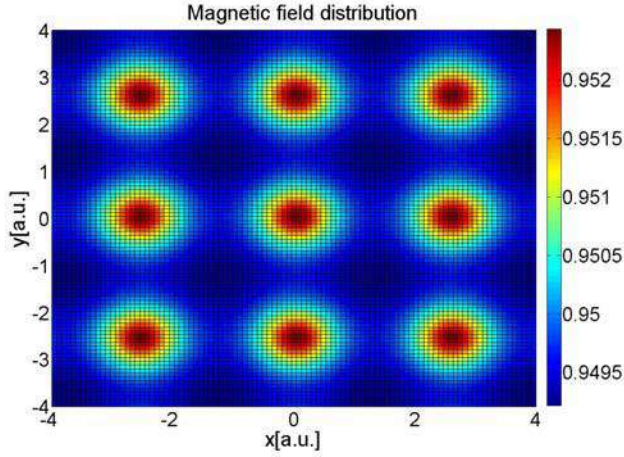


Figure 2. Top view of magnetic field distribution (square lattice)

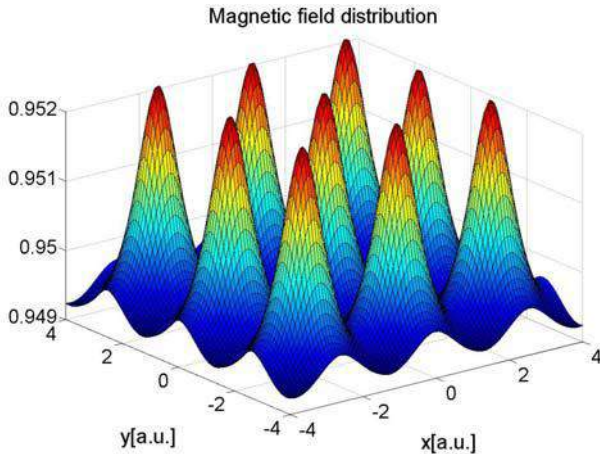


Figure 3. Side view of magnetic field distribution (square lattice)

It is confirmed that the lattice constant extracted from Fig. 2 is equal to the lattice constant given in the simulation. In Fig. 3 we can observe that magnetic field has maximum value in the core center and symmetrically drops down around the core center. In Fig. 4 and Fig. 5 top view and side view of current distribution are shown.

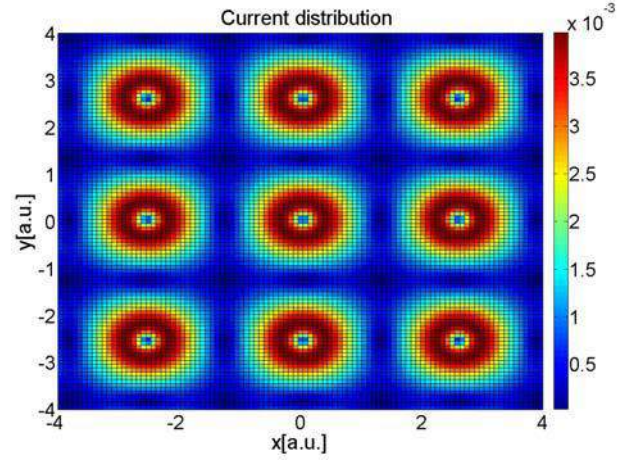


Figure 4. Top view of current distribution (square lattice)

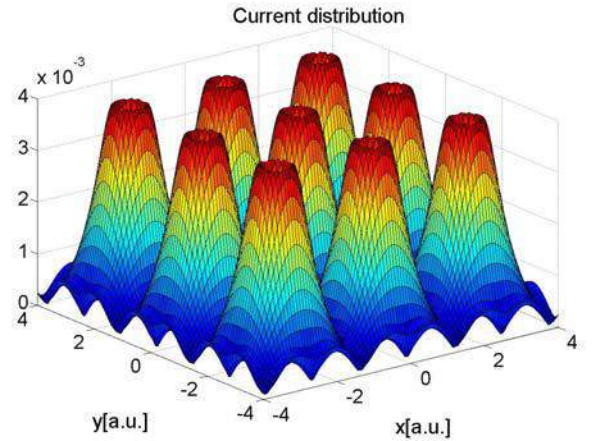


Figure 5. Side view of current distribution (square lattice)

One can notice the square lattice in Fig. 4, with the proper lattice constant. In Fig. 5 one can observe that current has minimum value in the core center and symmetrically rises up around the core center, in “volcano-like” shape.

B. Triangular lattice

Fig. 6 and Fig. 7 top view and side view of magnetic field distribution in triangular lattice case are shown, respectively. One can notice the triangular lattice in Fig. 6, with the lattice constant equal to the lattice constant calculated in the simulation. In Fig. 7 one can observe that magnetic field has maximum value in the core center and symmetrically drops down around the core center.

In Fig. 8 and Fig. 9 top and side view of current distribution are presented. Similar to the square lattice case, current has

minimum value in the core center, and rises up symmetrically around the core center.

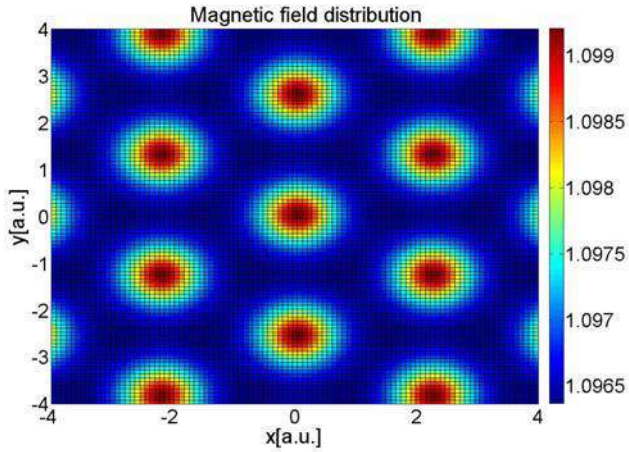


Figure 6. Top view of magnetic field distribution (triangular lattice)

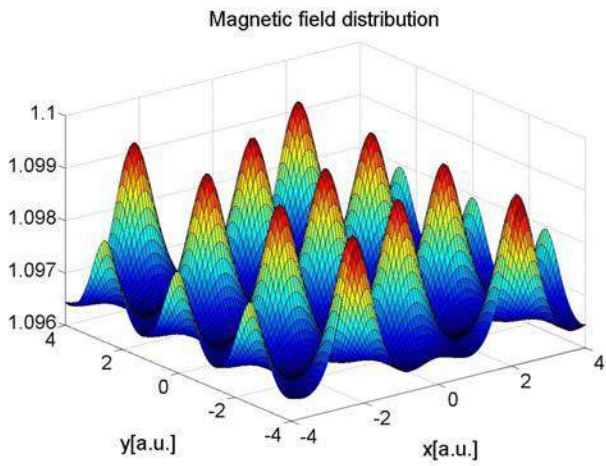


Figure 7. Side view of magnetic field distribution (triangular lattice)

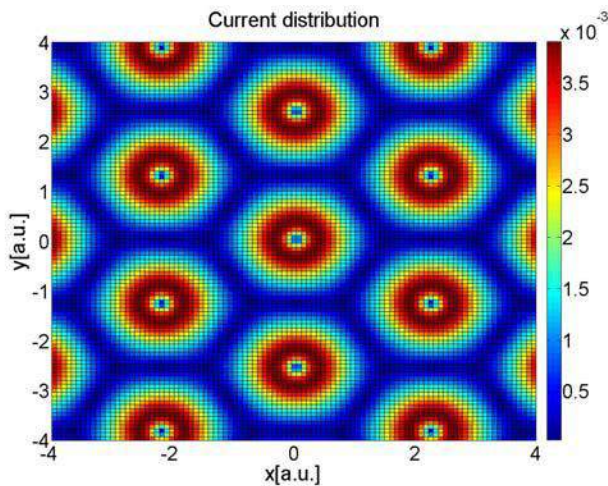


Figure 8. Top view of current distribution (triangular lattice)

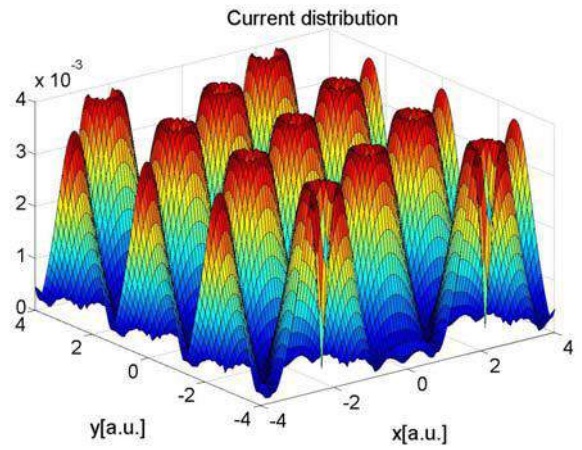


Figure 9. Side view of current distribution (triangular lattice)

Now when we have the current distribution, next step is to plot its profile and extract the vortex-core size. As stated in [6] (Fig. 6 (b)) vortex core size is the distance from the vortex centre at which supercurrent density has maximum value. In Fig. 10 profile of the supercurrent distribution is presented, for $\zeta_h = 0.18$.

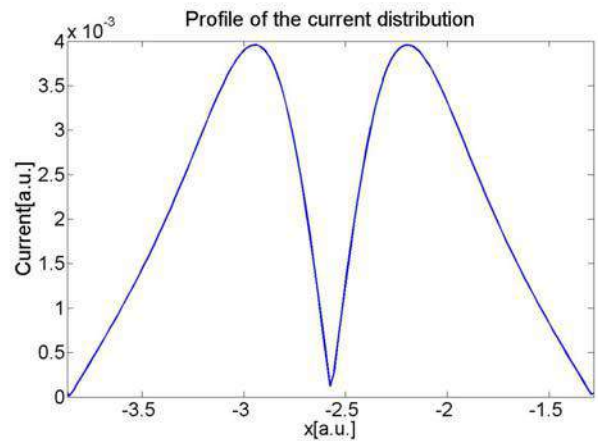


Figure 10. Profile of the current distribution ($\zeta_h = 0.18$)

The vortex-core size does not depend on the lattice shape, for one value of ζ_h it is the same for both lattices. The profile along x -axis is presented, it is the same along y -axis, due to symmetry. The xy mesh includes three vortex cores along both axes. This plot has been obtained by observing one arbitrary chosen vortex core. In Fig. 11 the dependence of vortex-core size on the cutoff parameter is shown.

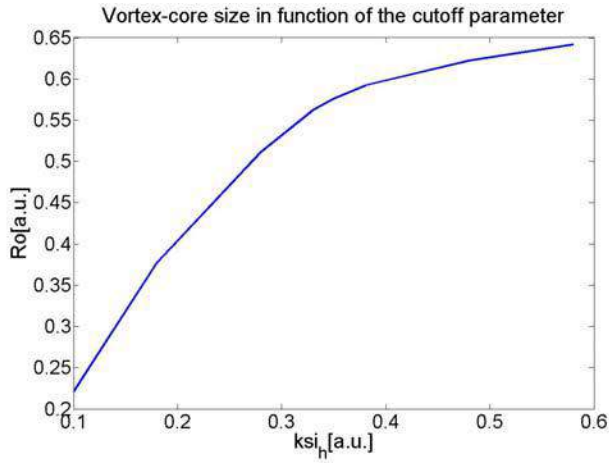


Figure 11. Vortex-core size in function of the cutoff parameter

VII. CONCLUSION

Magnetic field and supercurrent distribution have been calculated according to the modified London model. The results have met expectations, meaning that the lattice shape with proper lattice constant has been obtained. Distributions correspond to the mixed state of a type-II superconductor. Vortex-core size has been obtained from the profile of the supercurrent distribution. Plot of the vortex-core size versus cutoff parameter shows that they are on the same order of magnitude and that an increase of the cutoff parameter causes the increase of the vortex-core size. Future work may include the analysis and application of the models that include temperature dependence, which will allow comparison and matching of the calculations with experimental results.

ACKNOWLEDGEMENT

I would like to say many thanks to Mr. Dragan Vukićević, the director of IAESTE Serbia, who found for me this great internship at Lappeenranta University of Technology, Finland.

Many thanks to prof. Erkki Lähderanta for accepting me as a trainee in the Laboratory of Physics at Lappeenranta University of Technology (LUT), Lappeenranta, Finland.

I am very thankful to my mentor, dr Ivan Zakharchuk, for the ideas related to my research and for very useful discussions.

REFERENCES

- [1] A. A. Abrikosov, "On the magnetic properties of Superconductors of the Second Group", *Soviet Phys.*, 1957, *JETP* 5 1174.
- [2] R. Laiho, M. Safonchik, and K. B. Traito, "Quasiclassical approach to nonlocal generalized London equation in the mixed state of s-wave superconductors", *Phys. Rev. B*, 2007, 75 174524.
- [3] J. E. Sonier, J. H. Brewer, and R. F. Kiefl, " μ SR studies of the vortex state in type-II superconductors", *Rev. Mod. Phys.*, Jul 2000, vol. 72, pp. 769-811.
- [4] M. Ichioka, A. Hasegawa, and K. Machida, "Field dependence of the vortex structure in d-wave and s-wave superconductors", *Phys. Rev. B*, April 1999, vol. 59, pp. 8902-8915.
- [5] P. Belova, M. Safonchik, K. B. Traito, and E. Lähderanta, "Cutoff parameter and the field distribution in the mixed state of iron pnictides with S_{\pm} and S_{++} pairing symmetries", *Phys. Rev. B*, 2011, vol. 83, pp. 104518-1 – 104518-5.
- [6] J. E. Sonier, "Muon spin rotation studies of electronic excitations and magnetism in the vortex cores of superconductors", *Rep. Prog. Phys.*, 2007., vol. 70, 1717-1755.

Calculation of Geometrical Packing and Binding Energy of Self-Assembled Magnetic Tubular Structures

Miljan Dašić

Student of the the doctoral studies
Faculty of Physics, University of Belgrade
Institute of physics Belgrade
mdasic@ipb.ac.rs

Abstract—This paper is dealing with tubular structures composed through the self-assembly of magnetic hard spheres, in a given geometric confinement. Since the structures are tubes, geometric confinement is a cylinder with a given radius (confinement radius). Interaction of interest is magnetic dipole-dipole interaction, therefore a detailed analysis of it is provided. Next step is formation of the structures. We are analyzing infinitely long tubes, therefore an efficient method (Lekner method) for summing the dipole-dipole interactions of 1D periodical systems (periodical along one direction, the z-axis) is implemented in MATLAB. One of the main goals is determination of energetically favoured configurations, so a comparison of the tubes' energy has been done.

Key words-calculations; geometrical packing; binding energy; magnetic; tubes; MATLAB

I. INTRODUCTION

Self-assembly of magnetic particles is an interesting and relevant research topic which investigates the ways of forming regular structures composed of magnetic particles, in a fixed geometric confinement. Interaction between each two particles is magnetic dipole-dipole interaction [1]. What is a magnetic particle? It is a hard sphere which is a magnet (it has magnetic dipole moment). Why is this topic attractive? First of all, it is relevant from the theoretical point of view, since the dipole-dipole interaction is a long-ranged ($\sim 1/r^3$, r is the distance) and unisotropic interaction. Applications of magnetic structures are numerous, especially in nanoelectronics and biotechnology. For example, in nanotechnology, mixtures of self-assembled magnetic particles can lead to the formation of very strong magnets [2,3]. Interaction between magnetic planar layers can lead to 3D structures with a great potential for the microfabrication of electronic devices [4]. Ground states of microstructures in ferrofluid monolayers, in which the interaction is magnetic dipole-dipole interaction, have been investigated [5]. In the paper [6] self-assembled magnetic structures with minimal energy (ground state) have been found. It has been shown that as the number of particles, N , increases, the dimensionality of the ground state structures increases as well. For a small number of particles ($N = \{2, 3\}$), a chain is the ground state. For ($3 < N < 14$), a chain closes into a ring. In

the end, for a sufficiently big number of particles ($N > 13$) ground state is obtained via ring stacking. There is a clear transition with the increase of N , since a chain is 1D, a ring is 2D and stacked rings is a 3D structure. The subject of this paper is investigation of 3D structures (infinitely long tubes) formed via ring stacking into tubes. In the first part of this paper, a detailed analysis of the magnetic dipole-dipole interaction is performed, in order to better understand self-assembly of magnetic particles. There are two specific geometrical packings of the rings into tubes (square and triangular), leading to so called, AA and AB tubes. Our goal is to form a certain structure and calculate its binding energy, which is a result of the dipole-dipole interactions of each pair of particles that are building it. Once a structure is built geometrically, its dipole orientation (also called magnetization) should be defined. We have introduced three different magnetizations (ST/MT/ZZ magnetization) and compared their impact on the energy. Also, for a fixed magnetization, a scan over a wide range of confinement radii has been done, in order to understand how does the energy change when the confinement radius increases. When the confinement radius goes to infinity, then a convergence to corresponding lattice plane happens [6], which confirms the accuracy of the implemented summation method.

II. MAGNETIC DIPOLE-DIPOLE INTERACTION

Interaction for modelling the self-assembly of hard magnetic spheres is magnetic dipole-dipole interaction. It occurs between two particles with magnetic moments \mathbf{m}_1 and \mathbf{m}_2 . Potential energy of this interaction has the form:

$$U_{dd}(\vec{r}_{12}) = C \left[\frac{(\vec{m}_1 \cdot \vec{m}_2)}{r^3} - 3 \frac{(\vec{m}_1 \cdot \vec{r}_{12})(\vec{m}_2 \cdot \vec{r}_{12})}{r^5} \right] \quad (1)$$

In the above equation, constant C is:

$$C = \frac{\mu_0}{4\pi} = 10^{-7} \left[\frac{H}{m} \right] \quad (2)$$

and the position vector connecting the two particles is $\mathbf{r}_{12} = \mathbf{r}_1 - \mathbf{r}_2$. Distance between the particles is the moduo of this vector and we note it as r . Let us assume that magnetic moments belong to the same plane. In such a case, they have two components, one normal to the direction of \mathbf{r}_{12} , \mathbf{m}_n and the other one parallel to it, \mathbf{m}_p . It leads to the expression for the potential energy:

$$U_{dd} = C \left[\frac{(m_{1n}m_{2n} + m_{1p}m_{2p})}{r^3} - 3 \frac{m_{1p}m_{2p}r^2}{r^5} \right] \quad (3)$$

$$\Rightarrow U_{dd} = C \frac{m_{1n}m_{2n} - 2m_{1p}m_{2p}}{r^3}$$

In the next figure, a sketch of the two dipoles that we are analyzing is shown.

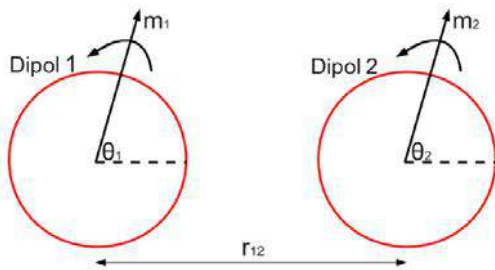


Figure 1. A sketch of two dipoles interacting via magnetic dipole-dipole interaction

Potential of their interaction has been derived. Let us normalize the values of the variables in it:

$$C = 1, |\vec{m}_1| = |\vec{m}_2| = 1, \vec{r}_1 = [000], \vec{r}_2 = [010] \quad (4)$$

Vectors \mathbf{m}_1 and \mathbf{m}_2 form the angles θ_1 and θ_2 with the direction of vector \mathbf{r}_{12} . Let us write:

$$\begin{aligned} m_p &= m \cos \theta \\ m_n &= m \sin \theta \end{aligned} \quad (5)$$

There is a compact expression for the potential:

$$U_{dd} = C \frac{m_1 m_2 \sin \theta_1 \sin \theta_2 - 2m_1 m_2 \cos \theta_1 \cos \theta_2}{r^3} \quad (6)$$

Let us test how does the potential depend on the mutual orientation of the dipoles. We are scanning the angle θ_1 in 1000 points over the full range,, and angle θ_2 takes selected values. In Fig. 2 the potential depending on the mutual dipole orientation is shown. Potential has a minimum when the

dipoles are parallel to vector \mathbf{r}_{12} and they point to the same direction. It has a maximum when the dipoles have opposite directions, parallel to vector \mathbf{r}_{12} . The same stands if the dipoles are normal to vector \mathbf{r}_{12} , just the absolute values of the potential are smaller. Stars indicate the higher absolute value minimum and maximum, while triangles indicate lower absolute value minimum and maximum.

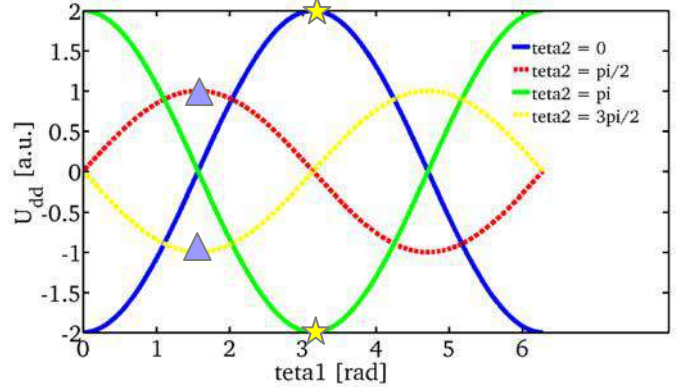


Figure 2. Potential of the dipole-dipole interaction depending on the dipole orientation

From the previous analysis, we have learned that two dipole orientations are of interest: parallel and normal to the vector \mathbf{r}_{12} . Distance was kept fixed and the dipole orientation was being changed. Now, we will keep the orientation fixed, but the distance will be changing.

In Fig. 3 a sketch of two dipoles parallel to the position vector \mathbf{r}_{12} is shown. This system corresponds to the minimum marked with a star in Fig. 2.

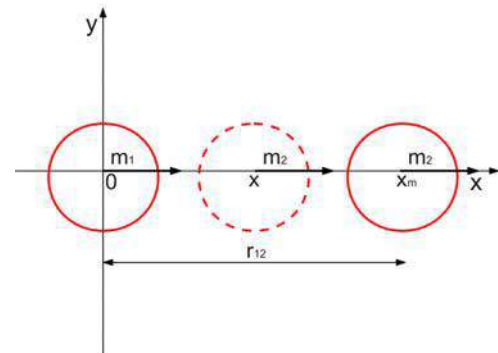


Figure 3. A sketch of two dipoles parallel to the position vector

In Fig. 4 dependence of potential on distance is shown. Obviously, absolute value of interaction potential decreases as the distance increases. This is an example of attraction between two dipoles. In Fig. 5 a sketch of two dipoles normal to the position vector \mathbf{r}_{12} is shown. This system corresponds to the maximum marked with a triangle in Fig. 2.

In Fig. 6 dependence of potential on distance is shown. The same remark applies here, absolute value of interaction potential decreases as the distance increases. This is an example of repulsion between two dipoles.

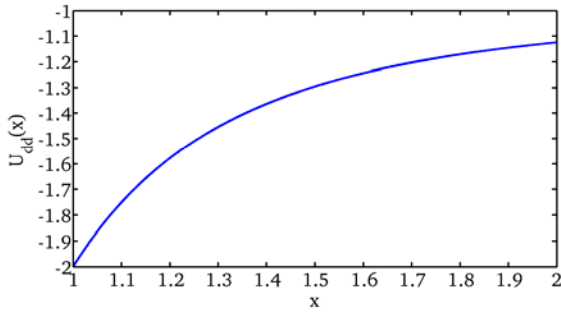


Figure 4. Dependence of the interaction potential on the position of dipole 2

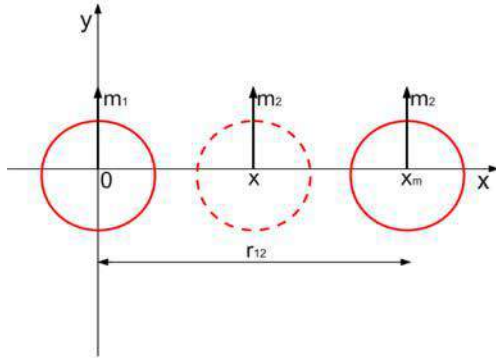


Figure 5. A sketch of two dipoles normal to the position vector

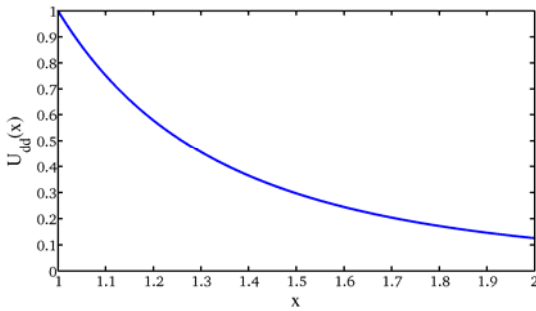


Figure 6. Dependence of the interaction potential on the position of dipole 2

This was the analysis of two systems of interest based on the general picture presented in Fig. 2. On the other side, from the Eq. 3, we can conclude that for a specific dipole orientation, interaction potential will be equal to zero [7]. We came up with a sketch shown in Fig. 7, in order to find out how does the system look like when this is the case. In Fig. 8 dependence of potential on distance is shown. When the angle is equal to the magic angle, potential is equal to zero. From the Eq. 3 we can derive what should be the angle α which causes the dipole-dipole interaction potential to be equal to zero.

$$\begin{aligned}
 m_{1n}m_{2n} - 2m_{1p}m_{2p} &= 0 \\
 \Leftrightarrow \sin^2 \alpha - 2 \cos^2 \alpha &= 0 \\
 \Leftrightarrow \alpha &= \arccos\left(\frac{1}{\sqrt{3}}\right) = 54.74^\circ
 \end{aligned}
 \tag{7}$$

Angle $\alpha = 54.74^\circ$ is the magic angle, interaction potential goes through the zero value at the x-coordinate (see Fig. 8) which corresponds to this angle. For this system, there is a switch of potential's sign, so there are both, attraction and repulsion between two dipoles.

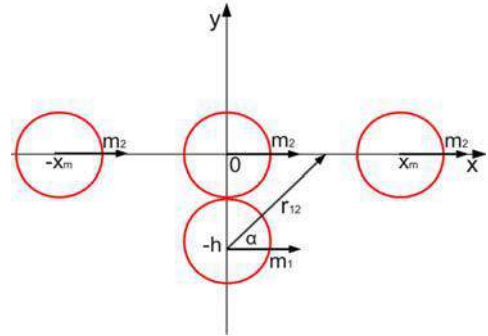


Figure 7. An illustration of the magic angle in the dipole-dipole interactions

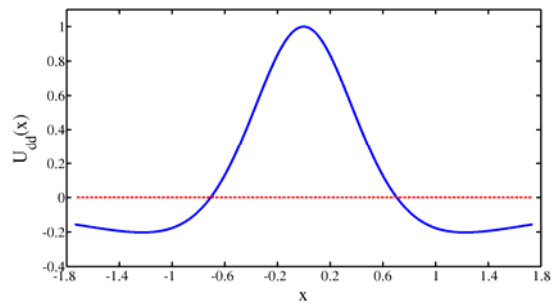


Figure 8. Dependence of the interaction potential on the position of dipole 2

III. CALCULATION OF THE BINDING ENERGY

In this chapter, a method for calculating the binding energy of a tubular structure is provided. Since we are analyzing infinitely long tubes, an efficient method for summing the dipole-dipole interactions of 1D periodical structures (periodical along one direction, the z-axis) had to be found. There are two well known and widely applied methods for this type of calculations, those are Ewald sums and Lekner method. Ewald sums are usually used for 2D periodical systems, while Lekner summation method converges faster in the 1D case, therefore we decided to implement Lekner method. The key feature of Lekner method is the choice of a periodic cell. It is a part of the infinite structure which is being replicated. Since we are dealing with tubes, one has to define its cell which is being replicated along the tube's axis (z – axis). Energy of an infinitely long tube is calculated as a sum of the self and cross energy. In next

expressions, we are dividing by N , since the energy is defined per particle, which allows a comparison of different structures with different number of particles in a cell.

Self energy represents the interaction energy of a selected particle in a cell, with all of its copies in the other cells. Total self energy is got as a sum over all particles in a cell, where number of particles in one cell is equal to N .

Self energy is given as [8]:

$$E_{self} = \frac{1}{L_z^3} \frac{\sum_{i=1}^N (1 - 3m_{z_i}^2) \zeta(3)}{N} \quad (8)$$

Cross energy represents the interaction energy of a selected particle in a cell, with all other particles of the same cell and with all their copies in the other cells. Total cross energy is got as a sum over all particles in a cell, $i = \{1, N\}$, $j = \{1, N\}$ [8]:

$$E_{cross} = \frac{\sum_{i \neq j} U_{cross}(\vec{r}_i, \vec{r}_j, \vec{m}_i, \vec{m}_j, L_z)}{N} \quad (9)$$

In the above equation, the cross energy is got as a sum of cross potentials of pairs of particles (i, j). Cross potential is defined as a sum of four sums. In those sums a modified Bessel function of the second kind, zero and first order, K_0 and K_1 appears, respectively. In the following text, those sums are presented.

$$U_{cross}(\vec{r}_i, \vec{r}_j, \vec{m}_i, \vec{m}_j, L_z) = \sum_{i=1}^4 S_i \quad (10)$$

Method for calculation of the binding energy of 1D infinitely long periodic structures is presented briefly. Goal of this paper is geometric formation and calculation of the binding energy of structures with minimal energy. Since the dipole orientation dictates the interaction potential, energy minimization means finding the optimal dipole orientation.

$$\begin{aligned} S_1 &= \frac{-8\pi}{L_z^2} \left[\frac{2(\vec{m}_{\rho_i} \cdot \vec{\rho})(\vec{m}_{\rho_j} \cdot \vec{\rho})}{\rho^3} - \frac{\vec{m}_{\rho_i} \cdot \vec{m}_{\rho_j}}{\rho} \right] \times \\ &\times \sum_{k=1}^{+\infty} k \cos(k\eta_z) K_1(k\eta_\rho) \\ S_2 &= \frac{-16\pi^2}{L_z^3} \left[\frac{(\vec{m}_{\rho_i} \cdot \vec{\rho})(\vec{m}_{\rho_j} \cdot \vec{\rho})}{\rho^2} - m_{z_i} m_{z_j} \right] \times \\ &\times \sum_{k=1}^{+\infty} k^2 \cos(k\eta_z) K_0(k\eta_\rho) \\ S_3 &= \frac{2}{L_z} \left[\frac{2(\vec{m}_{\rho_i} \cdot \vec{\rho})(\vec{m}_{\rho_j} \cdot \vec{\rho})}{\rho^4} - \frac{\vec{m}_{\rho_i} \cdot \vec{m}_{\rho_j}}{\rho^2} \right] \\ S_4 &= \frac{-16\pi^2}{L_z^3} \frac{(\vec{m}_{\rho_i} \cdot \vec{\rho})m_{z_i} + (\vec{m}_{\rho_j} \cdot \vec{\rho})m_{z_j}}{\rho} \times \\ &\times \sum_{k=1}^{k=+\infty} k^2 \sin(k\eta_z) K_1(k\eta_\rho) \end{aligned} \quad (11)$$

IV. GEOMETRIC FORMATION OF THE STRUCTURES

In this paper we are analyzing tubes composed of magnetic particles. A specific configuration of a tube is defined by the geometry and the dipole orientation. There are two possible tube's geometries depending on the ring stacking. If the rings are stacked one on top of each other, those are AA tubes. Otherwise, if the rings are stacked in the way that there is one particle in the upper ring between two particles in the lower ring, those are AB tubes. There are only two ways of ring stacking, but there is a huge number of different dipole orientations. We took both stackings, and three well-defined dipole orientations. Those dipole orientations are called: single-thread (ST), multi-thread (MT) and ZZ dipole orientation. ST means that dipoles follow one thread that is tangential to the contour of the tube. MT means that dipoles follow multi threads of which the tube is composed, while ZZ means that all the dipoles are parallel to the z-axis. We have analyzed all three chosen dipole orientations for AA and AB tubes. When calculating binding energy of an infinite periodic structure using Lekner method, the key task is to define the periodic cell. In an AA tube, a cell is one ring. In an AB tube, a cell is composed of two rings. Normalization of the system includes dimension and energy scales. The diameter of every particle is $d = 1$. The distance between two particles is calculated from centre to centre, which means that the distance between two touching particles is equal to 1. On the other side, it is very convenient to introduce energy scale, so the energy is not defined in joules or electronvolts, but rather in arbitrary units [a. u.]. Energy scale is defined via repulsive potential of two touching dipoles standing side by side. The dipole moment is also normalized so that the length of dipole moment vector is equal to 1. Now we will explain geometric formation of the structures. For a tube, the basis is a ring composed of magnetic particles. In Fig. 9 the cross-section of a tube is presented.

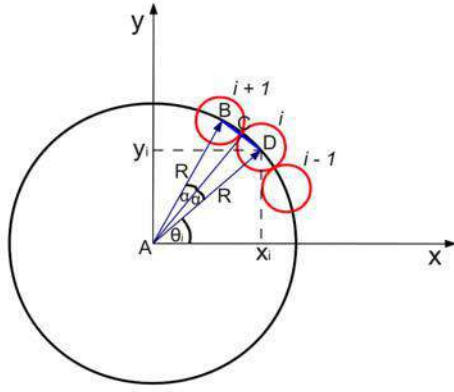


Figure 9. A sketch of the tube's cross-section

A ring is composed of N touching particles. Angular distance between two successive particles is $\Delta\theta = \frac{2\pi}{N}$ for an arbitrary chosen i -th particle, its angular position in respect to the positive x -semiaxis is $\theta_i = i \frac{2\pi}{N}$. Let us look at the triangle

ABC in Fig. 9. Since the distance between touching particles is equal to 1, then $BC = 1/2$. There are relations:

$$\begin{aligned} \sin \alpha &= \frac{1}{2R} \\ 2\alpha &= 2 \frac{\pi}{N} \Rightarrow \alpha = \frac{\pi}{N} \end{aligned} \quad (12)$$

Therefore, the relation between ring's radius and number of particles is:

$$R = \frac{1}{2\sin(\pi/N)} \quad (13)$$

A. Formation of AA tubes

In AA tubes, a periodic cell is one ring. Next array of equations defines coordinates of the particles, $i = \{1, N\}$.

$$\begin{aligned} x_i &= \frac{1}{2\sin(\pi/N)} \cos\left(i \frac{2\pi}{N}\right) \\ y_i &= \frac{1}{2\sin(\pi/N)} \sin\left(i \frac{2\pi}{N}\right) \\ z_i &= 0 \end{aligned} \quad (14)$$

Dipole moments are defined in the next way, $i = \{1, N\}$.

$$\begin{aligned} \mu_{x_i} &= \cos\left(i \frac{2\pi}{N} + \frac{\pi}{2}\right) \\ \mu_{y_i} &= \sin\left(i \frac{2\pi}{N} + \frac{\pi}{2}\right) \\ \mu_{z_i} &= 0 \end{aligned} \quad (15)$$

In the case of AA tubes, period along the z -axis is $Lz = 1$.

B. Formation of AB tubes

In AB tubes, periodic cell is a pair of rings. There are two arrays of equations, one for the lower ring, and another one for the upper ring. For the lower ring, coordinates of the particles are defined like in the case of AA tubes. There was a problem defining the z -coordinates of upper ring particles, which was solved using the definition of the distance between touching particles. Let us look at two arbitrary chosen particles in the lower ring (particles A and B) and one particle in the upper ring (particle C), which is placed between them. As it stands $AC = BC = 1$, from this condition we can derive how much are the upper ring particles displaced compared to the lower ring particles, along the z direction:

$$\Delta z = \sqrt{1 - (x_A - x_C)^2 - (y_A - y_C)^2} \quad (16)$$

In the upper ring, coordinates of the particles are those:

$$\begin{aligned} x_i &= \frac{1}{2\sin(\pi/N)} \cos\left(i \frac{2\pi}{N} + \frac{\pi}{N}\right) \\ y_i &= \frac{1}{2\sin(\pi/N)} \sin\left(i \frac{2\pi}{N} + \frac{\pi}{N}\right) \\ z_i &= \Delta z \end{aligned} \quad (17)$$

In this case, period along the z -axis is $Lz = 2 \Delta z$.

V. RESULTS OF THE STRUCTURE AND ENERGY CALCULATIONS

In this chapter, results of the structure and energy calculations are presented. In Fig. 10, a geometry of one tube configuration is shown, obtained via MATLAB calculations. We are showing how does the tube (AA tube) look like in a side and in a top view.

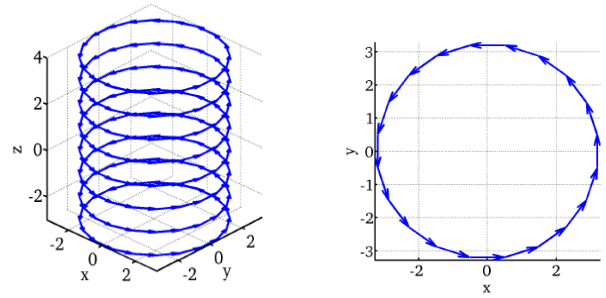


Figure 10. A side and a top view of an AA tube

In Fig. 11 and Fig. 12, dependence of binding energy on the confinement radius for AA and AB tubes is shown, including three different magnetizations.

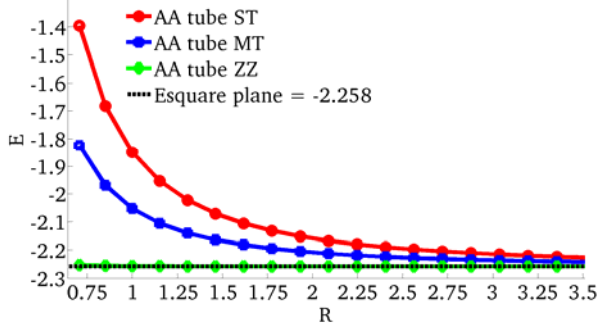


Figure 11. Energy in function of the confinement radius for different magnetizations (AA tube)

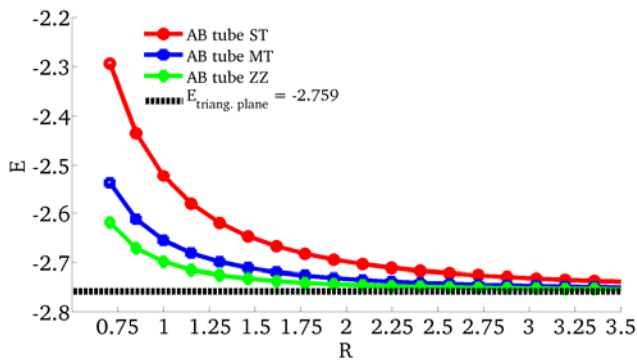


Figure 12. Energy in function of the confinement radius for different magnetizations (AB tube)

It is clear that for a fixed packing geometry (AA or AB), binding energy decreases as the magnetization changes from ST and MT into ZZ. Tubes with ZZ dipole orientation have minimal binding energy, and therefore they are the most stable tube configurations. When the confinement radius goes to the infinity, energy of all differently oriented tubes (ST/MT/ZZ) converges into the energy of an infinite plane. Energy of a square lattice plane is $E_{\text{square}} = -2.258$, all AA tubes converge into a square lattice plane. Energy of a triangular lattice plane

is $E_{\text{triangular}} = -2.759$, all AB tubes converge into a triangular lattice plane.

VI. CONCLUSION

We have developed MATLAB simulations which form tubular structures composed of magnetic particles and calculate its binding energy. Both AA and AB ring stackings, including three different magnetizations, have been investigated.

From the results, we conclude that all those tube configurations are stable, since their binding energy is negative. For a fixed packing geometry (AA or AB), binding energy decreases as magnetization changes in the way: ST - MT - ZZ. For a fixed magnetization, AB tubes have lower energy than AA tubes. Since AB tubes are more densely packed than AA tubes, we may say that bigger packing density implies lower binding energy and more stable structures.

ACKNOWLEDGEMENT

I am thankful to dr Igor Stanković, my mentor from the Institute of physics at University of Belgrade, for the ideas, discussions and help in programming the simulations.

I am also thankful to my colleagues from the research group, for the help and support.

REFERENCES

- [1] G. M. Whitesides and B. Grzybowski, "Self-Assembly at All Scales", *Science*, Vol. 225, No. 29, 2002.
- [2] D. J. Sellmayer, "Strong magnets by self-assembly", *Nature*, Vol. 420, No. 28, 2002.
- [3] H. Zeng et al., *Nature*, Vol. 420, No. 395, 2002.
- [4] M. Boncheva et al., *Proc. Natl. Acad. Sci., USA* 102, 3924, 2005.
- [5] T. A. Prokopieva, V. A. Danilov, S. Kantorovich and C. Holm, "Ground state structures in ferrofluid monolayers", *Phys. Rev. E*, 80, 031404, 2009.
- [6] R. Messina, L. A. Khalil and I. Stankovic, "Self-assembly of magnetic balls: From chains to tubes", *Phys. Rev. E*, 89, 011202(R), 2014.
- [7] L. Kocbach and S. Lubbad, "Geometrical simplification of the dipole-dipole interaction formula", *Physics Education*, Vol. 45, Issue 4, 2010.
- [8] A. Grzybowski and A. Brodka, "Lekner type method for summing the dipole-dipole interactions", *Molecular Physics*, Vol 101, No. 8, 2003.

Theoretical and Experimental Study of Helices Composed of Spherical Dipoles

Miljan Dašić^a, Igor Stanković^a

^aScientific Computing Laboratory, Institute of Physics Belgrade, University of Belgrade

Abstract. Tubular and cylindrical lattices are principal structural elements in biological systems. They give rise to structures, such as bacterial flagella and microtubules, which are essential building blocks of cells. The complexity of the structures formed by the particles with dipole-dipole interaction is a result of the interplay between anisotropic near-field interaction and long-range influence of the global geometry of the structure. Subject of this paper is the investigation of infinite 3D structures, i. e. tubes and helices. We will show that tubes are in terms of structure, actually a subset of helices. There is an endless number of different helical configurations. Nevertheless, densely packed structures exist in a number of well defined points in parameter space. We observe a structural similarity of, so called, Z-tubes, with the structures in typical experimental images of microtubules. These tubes can be decomposed into chains which are analogous to biological filaments, of which microtubules are made of. We present a way of geometric generation of densely packed helical structures composed of hard spheres. Later on, we show how to assign dipole moments to the particles making up those structures, in order to obtain dipole orientations which follow the geometry. Experimental study has proved that structures with such dipole orientations are stable.

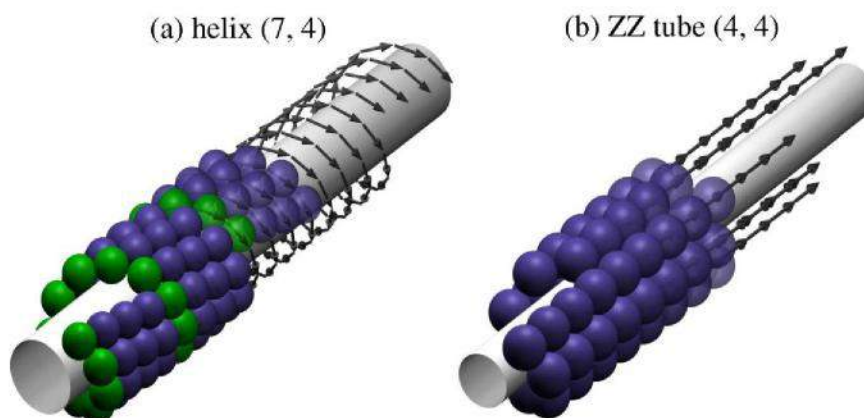


FIGURE 1. Illustration of one representative four-stranded helix (i. e. having ST dipole orientation) (a) and one representative ZZ tube (b).

10TH LIQUID MATTER CONFERENCE
LJUBLJANA SLOVENIA JULY 17-21 2017

This is to certify that

Miljan Dašić

presented a poster at the

10th LIQUID MATTER CONFERENCE

17-21 July 2017, Ljubljana, Slovenia

Igor Muševič



Chair of the 10th Liquid Matter Conference



CERTIFICATE OF ATTENDANCE

To Whom It May Concern:

On behalf of the Organizing Committee, I am pleased to inform that Miljan Dasic has attended the 7th Iberian Meeting on Rheology - IBEREO 2019, held in Porto on 4th-6th September 2019, and presented the work entitled "Molecular dynamics investigation of the flow and tribological properties of a salt model ionic liquid under confinement and imposed mechanical deformations" as a poster.

Porto 6th of September 2019.

Francisco José Galindo Rosales

(Member of the Organizing Committee)

A handwritten signature in blue ink, consisting of several overlapping loops and a long horizontal stroke.

UNIVERSITY OF BELGRADE

FACULTY OF PHYSICS

Miljan Dašić

**MODELING THE BEHAVIOUR OF
CONFINED DIPOLAR AND IONIC
SYSTEMS**

Doctoral dissertation

Belgrade, 2019

УНИВЕРЗИТЕТ У БЕОГРАДУ

ФИЗИЧКИ ФАКУЛТЕТ

Миљан Дашић

**МОДЕЛОВАЊЕ ПОНАШАЊА
ПРОСТОРНО ОГРАНИЧЕНИХ
ДИПОЛНИХ И ЈОНСКИХ СИСТЕМА**

Докторска дисертација

Београд, 2019

Thesis advisor, Committee member:

Dr. Igor Stanković

Associate Research Professor

Institute of Physics Belgrade

University of Belgrade

Committee member:

Prof. Dr. Đorđe Spasojević

Professor

Faculty of Physics

University of Belgrade

Committee member:

Prof. Dr. Milan Knežević

Professor

Faculty of Physics

University of Belgrade

Date of the defense: 23.9.2019.

Посвећујем ову докторску тезу својој породици,
оцу Драгану, мајци Смиљи и брату Стефану,
са искреном и јаком жељом да кући Дашића вазда буде на понос.

Acknowledgments

This doctoral thesis was done in Scientific Computing Laboratory (SCL) which is a part of the Center for the Study of Complex Systems at the Institute of Physics Belgrade (IPB), University of Belgrade, under the supervision of Dr. Igor Stanković. I would like to thank my mentor for all the help and guidance during my master and doctoral studies. I am thankful to him for introducing me into interesting areas of computational physics, related to the modeling of dipolar and ionic systems. Also, thanks to his support, I got accepted as an intern in a renowned company of Toyota Motor Europe (TME) in Zaventem (Belgium). During my six-month TME internship I had a great opportunity to gain valuable industrial experience and to understand the role of a researcher in a company. Besides of his careful guidance and support of my step into industrial research, I have received many valuable advices about a good scientific practice from my mentor. The most important lesson I have learned from him is the right attitude when facing a tough, but still doable, scientific problem: we should not ask ourselves are we able to solve it, just how are we going to do it.

I am thankful to Dr. Konstantinos Gkagkas, Expert in Material Design Division of Toyota Motor Europe in Belgium, my supervisor in TME, for introducing me into industrial research environment and guiding me during the internship. Besides that, I am very thankful to Dr. Gkagkas for our fruitful collaboration which continued for several years after the internship completion.

For interesting discussions and fruitful collaboration on a bilateral Serbian-French project, I would like to thank Dr. René Messina, Professor of Physics at Université de Lorraine in France.

The years spent at SCL office will stay in a nice memory with me thanks to my colleagues. I am grateful to all of them for the pleasant and friendly working atmosphere.

I would like to thank Dr. Antun Balaž, the head of SCL, for accepting me as a member of this reputable laboratory. I am thankful for the support that I have been receiving from him all those years.

I thank Dr. Aleksandar Bogojević, the director of IPB, for giving me the opportunity to work at IPB.

During my doctoral studies, I was taking active participation in the Petnica Science Center (PSC) seminars of physics for several years, as a lecturer and as a mentor on yearly projects. It was my sincere pleasure to be a mentor of talented high school students on their research projects in physics and to guide them in their first steps into science. I enjoyed seeing the joy for research of those high school students, who reminded me of myself in their age, since I used to be a participant of the same seminar back in the days when I was a high school student. It is an interesting fact worth of mentioning, that my mentor on two of my PSC projects was Dr. Aleksandar Bogojević and that I had a great opportunity to come in contact with SCL back in those days. That first sparkle of interest in numerical simulations in physics which was lighted up then still glows and it attracted me to SCL for my master and doctoral studies, after completing undergraduate studies of physical electronics at the Faculty of Electrical Engineering, University of Belgrade. The results of my mentorship on PSC physics seminars are three completed yearly projects, presented at the annual conferences called "A step into science", which were held in Petnica (municipality of Valjevo, Serbia). The reports of those projects in a form of scientific paper have been published in "Petničke sveske". Happiness of my PSC students coming from the successful completion of their projects made me happy as well and inspired my own research efforts.

I am also thankful to all my friends and relatives whose support and love mean a lot to me. Especially, I would like to mention my friends, members of the Society of Gusle Players "Serdar Janko Vukotić" from Belgrade, with whom I share interest for epic poetry and singing to the accompaniment of the gusle (a single-stringed traditional musical instrument). Sincerely thanks for all the memorable hours that we have spent listening to the sounds of our favourite musical instrument.

Finally, I am infinitely thankful to my family, father Dragan, mother Smilja and brother Stefan, for their unconditional love, understanding and support.

I acknowledge financial support of the Ministry of Education, Science and Technological Development of the Republic of Serbia under Project No. OI171017, the

support from the bilateral Serbian-French PHC Pavle Savić 2014/15 Grant 32135NJ and the support received under COST Actions MP1303 - Understanding and Controlling Nano and Mesoscale Friction and MP1305 - Flowing matter. Numerical simulations were run on the PARADOX supercomputing facility at the Scientific Computing Laboratory of the Institute of Physics Belgrade, University of Belgrade, Serbia.

Modeling the behaviour of confined dipolar and ionic systems

Abstract

In this doctoral thesis confined dipolar and ionic systems have been modelled and investigated, namely dipolar tubes and helices composed of dipolar hard spheres and ionic liquids. Mutual for those systems is the fact that their structure and behaviour are dominated by long-range interactions, i.e., dipole-dipole interaction in case of dipolar systems and Coulombic interaction in case of ionic systems. The feature of pronounced ordering of formed configurations and possibility of manipulating them via externally applied fields (magnetic/electric field in case of magnetic/electric dipoles and electric field in case of ions) attract attention of condensed matter physics.

The first part of this doctoral thesis, which is dedicated to dipolar systems, is dealing with the investigation of the structure and cohesive energy in tubes and helices composed of dipolar hard spheres. A complex dependence of cohesive energy on surface packing fraction and dipole moment orientation has been observed. In case that single-thread helices are considered, the lowest cohesive energy is achieved at the highest surface packing fraction. Besides that, an interesting non-monotonic behaviour of the cohesive energy as a function of the surface packing fraction has been obtained. In case of multi-thread helices, a new phase, showing remarkably lower cohesive energy, has been determined. This phase is referred to as *ZZ* tube and it consists of threads following the confining cylinder's axis, labeled as the z axis, in terms of both spatial and dipole moment orientation. Actually, in case of *ZZ* tubes dipolar hard spheres are arranged into a local triangular lattice, with densely packed threads following the z axis.

In the scope of this doctoral thesis dipolar configurations under the condition of cylindrical confinement are considered, meaning that dipolar spheres are placed on a confining cylinder. First question which arises is what are the possible configurations, since there is an interplay between the two components, i.e., positioning

and dipole moment orientation of the particles. For a fixed geometry, only certain dipole moment orientations lead to stable configurations. The above mentioned two components can be treated as independent variables, while dependent variable is the cohesive energy emerging from the dipole-dipole interactions. Accordingly, geometry is kept fixed, while dipole moment orientation is varied and the dependence of cohesive energy on dipole moment orientation is determined. In an analogous way, dipole moment orientation is kept fixed, while geometry is varied, i.e., the radius of confining cylinder, leading to the dependence of cohesive energy on geometry. Besides the cohesive energy, some other dependent variables are considered, like the total polarization of a dipolar configuration. Except from the theoretical relevance, dipolar tubes and helices represent *model systems* which might be useful for other scientific areas. Modeling of dipolar tubes and helices might provide better understanding of certain biological structures (for example, microtubules) or macromolecules (protein folding is dominated by electric dipole-dipole interactions). Due to the mechanical flexibility of dipolar structures and possibilities of manipulating them by external electric or magnetic fields, they might be useful in the synthesis of electronic devices.

In the second part of this doctoral thesis, which is dedicated to ionic systems, a molecular dynamics (*MD*) based modeling approach for simulating mesoscopic phenomena related to lubrication with ionic liquid (*IL*) lubricants has been developed. In that approach, geometry of the system allows a variable confinement gap between solid plates and consequently a varying amount of lubricant in the gap. A coarse grain *MD* description of: (i) *IL* lubricant, which can expand into lateral reservoirs, and (ii) *FCC* (111) structured solid plates has been employed. Namely, two models of *IL*: (a) the salt-like model (*SM*) and (b) the tailed model (*TM*) have been implemented. In case of (a) *SM* model, *IL* consists of spherical cations and anions, while in case of (b) *TM* model, a neutral spherical tail is attached to the cation via an elastic spring. Three relevant *TM* models have been examined by varying the size of neutral tail. The effects of confinement on flow and lubrication properties of *SM* and *TM* ionic liquids, that were subjected to dynamic regimes of cyclic loading and shearing, have been investigated. The impact of confinement on ionic arrangement

and mechanical response of *SM* and *TM* ionic liquids has been studied in detail and compared to bulk properties. In case of *TM* models the influence of the molecular geometry of the cation on the response of *IL* to confinement and imposed mechanical deformations (normal load, cyclic loading and shearing) has been investigated. Although it is simple, *TM* model recovers a wide range of structures seen in bulk *ILs*: simple cubic lattice for small tails, liquid-like state for symmetric cation-tail dimers, and layering for large tails. The dependence of normal force on interplate gap can be related to ionic layering inside the gap. In investigated *TM* models of *IL*, specific friction is low and friction force decreases with neutral tail size. As a concluding remark, it has been found that the size of neutral tail from cation-tail dimer has a huge impact on structure and tribological behaviour of confined ionic liquids.

Ionic liquids are composed of large asymmetric and irregularly shaped organic cations and anions. Irregularity effectively prevents low-temperature ordering and crystallization of *ILs*, hence they are usually in the melted or glassy state. Physical properties of *ILs*: negligible vapour pressure, high-temperature stability, high ionic conductivity, chemical stability and possibility of external control, make them relevant to various applications. Modeling of ionic liquids is an interesting problem from the theoretical point of view due to their ordering and possibility of manipulating them via external electric fields. On the other side, ionic liquids are high quality lubricants used for friction reduction and wear prevention and modeling of *ILs* gives an insight about their industrial applications.

Keywords: dipolar hard spheres, tubes, helices, Lekner summation, ionic liquids, tribological behaviour, molecular dynamics

Scientific field: Physics

Research area: Condensed matter physics

UDC number: 538.9

Моделовање понашања просторно ограничених диполних и јонских система

Сажетак

У овој докторској тези моделовани су и испитани просторно ограничени диполни и јонски системи, тачније диполне тубе и хеликси састављени од диполних чврстих сфера и јонске течности. Заједничко за ове системе је чињеница да су им структура и понашање претежно одређени дугодометним интеракцијама, дипол-диполном интеракцијом у случају диполних система, односно Кулоновом интеракцијом у случају јонских система. Одлика наглашеног структурног уређивања формираних конфигурација и могућност манипулације њима преко екстерно примењених поља (магнетно/електрично поље у случају магнетних/електричних дипола, односно електрично поље у случају јона) привлаче пажњу са аспекта физике кондензоване материје.

Први део ове докторске тезе, који је посвећен диполним системима, бави се истраживањем структуре и кохезионе енергије у тубама и хеликсима који су састављени од диполних чврстих сфера. Добијена је комплексна зависност кохезионе енергије од површинске густине паковања и оријентације диполних момената. У случају једноструко намотаних хеликса, најнижа кохезиона енергија постигнута је при највишој површинској густини паковања. Поред тога, добијена је занимљива немонотона зависност кохезионе енергије од површинске густине паковања. У случају вишеструко намотаних хеликса откривена је нова фаза, која показује приметно нижу кохезиону енергију. Ова фаза названа је ZZ туба, а састоји се од нити које прате осу конфинирајућег цилиндра, означену као z оса, у смислу просторне и оријентације диполних момената. Заправо, у случају ZZ туба диполне чврсте сфере су уређене у локално троугаону решетку, са густо пакованим нитима које су паралелне са z осом.

У оквиру ове докторске тезе разматране су диполне конфигурације при услову цилиндричног просторног конфинирања, што значи да су диполне сфере постављене на конфинирајући цилиндар. Прво питање које се поставља јесте

које су могуће конфигурације, са обзиром да постоји преплитање две компоненте, просторног позиционирања и оријентације диполних момената честица. За фиксирану геометрију, само одређене оријентације диполних момената доводе до стабилних конфигурација. Поменуте две компоненте могу се третирати као независне променљиве, а зависна променљива је кохезиона енергија услед дипол-диполних интеракција. Према томе, геометрија је фиксирана, а диполна оријентација се варира и одређује се зависност кохезионе енергије од оријентације диполних момената. На аналоган начин, диполна оријентација је фиксирана, а геометрија се варира, рецимо радијус конфинирајућег цилиндра, што доводи до зависности кохезионе енергије од геометрије. Осим кохезионе енергије, разматране су и друге зависне променљиве, као што је укупна поларизација диполне конфигурације. Поред теоријског значаја, диполне тубе и хеликси представљају *моделне системе* који могу бити корисни у другим научним областима. Моделовање диполних туба и хеликса може пружити боље разумевање одређених биолошких структура (на пример, микротубула) или макромолекула (савијање протеина доминантно је одређено електричним дипол-диполним интеракцијама). Услед механичке флексибилности диполних структура и могућности за манипулацију њима преко екстерних магнетних или електричних поља, дате структуре могу бити корисне у синтези електронских уређаја.

У другом делу ове докторске тезе, који је посвећен јонским системима, развијен је приступ у моделовању на бази молекуларне динамике (*MD*) за симулирање мезоскопских феномена повезаних са подмазивањем јонским течностима. У том приступу, геометрија система омогућава променљиви конфинирајући процеп између чврстих плоча и последично променљиву количину подмазивача у процесу. Примењен је опис на бази *MD* укрупњавања скала: (i) јонске течности као подмазивача који се може проширити у латералне резевоаре и (ii) *FCC* (111) структурираних чврстих плоча. Наиме, имплементирана су два модела јонске течности: (a) модел на бази соли (*SM*) и (b) модел са репом (*TM*). У случају (a) *SM* модела јонска течност се састоји од сферичних катиона и аниона, док је у случају (b) *TM* модела неутрални сферични

реп везан за катион еластичном опругом. Испитана су три релевантна *ТМ* модела варирањем величине неутралног репа. Истражени су ефекти конфинирања на протицање и подмазивачке особине *SM* и *ТМ* јонских течности које су изложене динамичким режимима цикличног пуњења и смицања. Утицај конфинирања на уређивање јона и на механички одзив *SM* и *ТМ* јонских течности детаљно је проучен и упоређен са особинама датих јонских течности у балку. У случају *ТМ* модела испитан је утицај молекуларне геометрије катиона на одзив јонске течности при конфинирању и при задатим механичким деформацијама (нормална сила, циклично пуњење и смицање). Иако једноставан, *ТМ* модел реконструира широки опсег структура виђених код балк јонских течности: једноставна кубична решетка за мале репове, течно стање за симетричне катион-реп димере и уређивање у слојеве за велике репове. Зависност нормалне силе од величине процепа између чврстих плоча може се повезати са уређивањем јона у слојеве унутар процепа. У испитаним *ТМ* моделима јонске течности, специфично трење је мало, а сила трења опада са порастом величине неутралног репа. Као закључна напомена може се навести да је установљено да величина неутралног репа из катион-реп димера има велики утицај на структуру и триболошко понашање конфинираних јонских течности.

Јонске течности су састављене од великих асиметричних органских катиона и аниона неправилног облика. Неправилност облика спречава уређивање на ниским температурама и кристализацију јонских течности, тако да су јонске течности углавном у топљеном или стакластом стању. Физичке особине јонских течности: занемарљив притисак паре, високотемпературна стабилност, висока јонска проводљивост, хемијска стабилност и могућност екстерне контроле чине их релевантним за различите примене. Моделовање јонских течности је интересантан проблем са теоријског становишта услед структурног уређивања и могућности за манипулацију јонским течностима преко екстерних електричних поља. Са друге стране, јонске течности су високо квалитетни подмазивачи који се користе за смањење трења и спречавање хабања, а моделовање јонских течности даје увид о њиховим индустријским применама.

Кључне речи: диполне чврсте сфере, тубе, хеликси, Лекнер сумирање, јонске течности, триболошко понашање, молекуларна динамика

Научна област: Физика

Област истраживања: Физика кондензоване материје

УДК број: 538.9

Contents

1	Introduction	1
1.1	General overview	1
1.2	Confined dipolar systems	2
1.2.1	Outline of the research on cylindrically confined dipolar systems	5
1.3	Motivation for the research of ionic liquids	7
1.3.1	Salt model of ionic liquid	10
1.3.2	Tailed model of ionic liquid	11
1.3.3	Outline of the research on model ionic liquids	13
2	Confined dipolar systems	15
2.1	Geometry of helices and tubes composed of hard spheres	15
2.1.1	Geometry of helices	15
2.1.1.1	Geometry of single-thread helices	15
2.1.1.2	Order parameters for single-thread helices	18
2.1.1.3	Geometry of multi-thread helices	21
2.1.2	Tubes as sub-sets of helices	25
2.2	Dipole moments	26
2.2.1	Dipolar interaction model	26
2.2.2	Relevant dipole moment orientations	27
2.3	Methods	30
2.3.1	Methods for summing the dipole-dipole interactions of infinite periodic structures	30
2.3.1.1	Overview of available methods	30
2.3.1.2	Selection of the proper method	31

2.3.1.3	Application of the derived Lekner-type method in case of infinite 1D periodic dipolar structures	32
2.3.2	Energy minimization method for obtaining ground state dipole orientation of dipolar structures	33
2.4	Degeneracy in 2D triangular and square lattice and properties of tubes	36
2.4.1	Ground state of 2D triangular and square lattice	36
2.4.2	Degeneracy break-up with curvature in case of AA and AB tubes	39
2.5	Cohesive energy-packing relations in dipolar helices	40
2.5.1	Compression of a single-thread helix	41
2.5.2	From square to triangular arrangement of a single-thread helix	43
2.5.2.1	Looking for the ground state	46
2.5.3	Cohesive energy of multi-thread helices at high surface packing fraction	47
3	Ionic liquids	51
3.1	Methods	51
3.1.1	Molecular Dynamics method	51
3.1.1.1	The Lennard-Jones potential	54
3.1.1.2	Thermodynamic properties	55
3.1.1.3	Analysis of the key components of a typical molecular dynamics simulation	56
3.1.2	<i>LAMMPS</i> code for molecular dynamics	63
3.1.2.1	Multi-level summation method for summing long-range Coulombic interactions	64
3.2	Simulation setup and models of ionic liquid	65
3.2.1	Simulation setup	65
3.2.2	Models of ionic liquid	68
3.2.2.1	Salt model of ionic liquid	68
3.2.2.2	Tailed model of ionic liquid	71
3.3	Bulk ionic liquid	75

3.3.1	Bulk salt model of ionic liquid	76
3.3.1.1	Solidification and melting of bulk salt model of ionic liquid	76
3.3.1.2	Relaxation simulations	77
3.3.1.3	Viscosity characteristics	78
3.3.1.4	Wetting properties	81
3.3.2	Bulk tailed models of ionic liquid	84
3.3.2.1	Relaxation simulations	84
3.3.2.2	Viscosity characteristics	88
3.3.2.3	Wetting properties	89
3.4	Confined ionic liquid	90
3.4.1	Confined salt model of ionic liquid	92
3.4.1.1	Static force-distance characteristic	92
3.4.1.2	Dynamic force-distance characteristic	99
3.4.1.3	Tribological behaviour of confined salt model of ionic liquid	105
3.4.2	Confined tailed models of ionic liquid	116
3.4.2.1	Static force-distance characteristic	117
3.4.2.2	Dynamic force-distance characteristic	129
3.4.2.3	Tribological behaviour of confined tailed models of ionic liquid	135
4	Conclusions	138
4.1	Confined dipolar systems	138
4.2	Ionic liquids	139
4.2.1	Salt model of ionic liquid	139
4.2.2	Tailed models of ionic liquid	141
A	Lekner-type summation method for 1D periodic dipolar structures	144
A.1	Total interaction energy in the selected Lekner-type method	144
A.2	Derivation of the expression for the self energy	146
A.3	Derivation of the expression for the cross energy	147

B Conjugate gradient method	171
Bibliography	178

Chapter 1 Introduction

1.1 General overview

In this doctoral thesis there are two research topics involving systems with long-range interactions, namely structures composed of dipolar hard spheres and ionic liquids. Investigation of dipolar hard spheres is directed towards exploring the cohesive energy-packing relations, while investigation of ionic liquids is dedicated to determining the structure, flow properties and tribological behaviour of confined ionic liquids. In a higher instance the topics share two important aspects which unify them: long-range interactions and accentuated self-assembly behaviour. Both dipole-dipole interaction in dipolar systems and Coulombic interaction in ionic systems are long-ranged. An interaction $V(r)$ depending on the distance between the interacting particles r as $V(r) \propto r^{-p}$ is considered to be *long-range interaction* if it meets the condition: $p \leq n_d$, where n_d is the dimensionality of the system. In case of the dipole-dipole interaction, which has the same functional form (up to a constant) for magnetic and electric dipoles, it stands $V_{dd} \propto r^{-3}$, while in case of Coulombic interaction $V_{Clb} \propto r^{-1}$. In case of a $3D$ system, i.e., $n_d = 3$, both of the mentioned interactions meet the criterion of being long-range interactions. Another mutual feature of both of those systems is accentuated self-assembly under the conditions of spatial confinement. Dipolar hard spheres self-assemble into tubes and helices on a confining cylinder. It is possible to obtain ordering of ionic liquid into regular cationic-anionic layers, starting from a random arrangement of ions, in case that ionic liquid is placed into a gap between two solid surfaces. A common consequence of long-range interactions is ordering of the particles on length scales which are much longer than the size of the particles itself. One might expect that the na-

ture of long-range interactions combined with the conditions of spatial confinement should lead to the emerging of ordered and stable structures. The systems that have been investigated in this thesis are $3D$ and they are also infinite: (i) tubular and helical dipolar structures are $1D$ infinite and periodic, (ii) ionic liquid is $2D$ infinite. Besides the self-assembly under conditions of spatial confinement, mutual for both systems is rich behaviour in terms of state and phase transitions.

1.2 Confined dipolar systems

Particles with permanent dipole moment are known for outstanding self-assembly properties [1–3]. Self-assembly of hard dipolar spheres is an active research topic dedicated to the investigation of the mechanisms by which ordered dipolar structures form. To be more precise, we are focused on the self-assembly of spatially confined dipolar systems. Spatial confinement imposes formation of specific structures, e.g., cylindrical confinement imposes self-assembly of particles into tubular and helical structures. Interaction of each pair of dipolar particles is the dipole-dipole interaction, which is described by the same term (up to a constant) in case of both magnetic and electric dipoles. Therefore, we consider structures composed of dipolar hard spheres in a general case. Depending on given examples in nature or technology, we compare considered structures with building elements composed of particles with permanent magnetic or electric dipole moment. Self-assembly of dipolar particles and a large number of different ways for their application have always been attracting interest due to a spontaneous transition from disordered into ordered state. This topic is attractive because it is relevant from theoretical point of view since dipole-dipole interaction is a long-range and anisotropic interaction which leads to the complexity of structures formed via dipole-dipole interaction. Besides that, examples of dipolar structures in nature and technology are numerous, especially in biology and some areas of nanotechnology.

Generally speaking from the aspects of geometry and without the need for the presence of dipole-dipole interaction in given examples, tubular and helical structures are basic structural elements in many biological systems. Those structures are

important building blocks of cells. Illustrative examples include bacterial flagella [4] and microtubules [5, 6]. Additional examples of tubular and helical structures can be found in various materials with specific building blocks, which can be: coiled carbon nanotubes [7], DNA molecule [8], nanoparticles [9], amphiphilic molecules [10–12]. In biology there is an example of magnetotactic bacteria whose dynamics is especially sensitive under external magnetic field, so that microstructures formed by those bacteria can be manipulated via application of external magnetic field [13].

Another example of the importance of dipole-dipole interaction in biology is the formation of proteins. All processes in protein formation, i.e., folding of individual aminoacids into a secondary structure and later-on formation of tertiary and quaternary structures, depend on electric dipole-dipole interactions [14, 15]. Formation of erythrocytes, which have a vital importance for human health, is realized through several steps. Each of those steps includes electric dipole-dipole interactions. Any kind of mutation which harms the dipole-dipole interaction suppresses proper formation of erythrocytes, which as a response disables their capability of transporting oxygen in the blood system.

In nanotechnology self-assembly of binary mixtures of magnetic nanoparticles can lead to the synthesis of very strong magnets [16]. Interaction between magnetic planar layers can enable formation of $3D$ structures with a great potential of applications in microfabrication of electronic devices [17]. Ground states of microstructures in ferrofluid monolayers, in which the interaction between magnetic particles is the dipole-dipole interaction, have been studied in detail [18].

In the following text an overview of the accomplishments in experimental and numerical studies of helical structures' formation is given. Self-assembly of cubic magnetic nanoparticles [19] and colloidal magnetic clusters [20] into helical structures has been accomplished experimentally, without the need for the pre-existing templates. Another result following this research line tells that hard spherical particles confined inside narrow cylinders spontaneously group themselves into helical structures. This has been achieved both via numerical simulations [21, 22] and experimentally [23]. Hard spheres with a permanent dipole moment can be utilized as a model for describing more complex helical molecular structures [24] and

microtubules [25, 26].

The overview of the topic related to the self-assembly of dipolar particles should mention the pioneering theoretical work of Jacobs and Beans [27] followed by the work of De Gennes and Pincus [28]. Those works have provided the insight into the microstructure of self-assembled spatially free spherical dipoles. More recently, ground states of self-assembled magnetic structures have been thoroughly investigated via numerical simulations [29]. The results of that paper have shown that for the number of particles $N \geq 14$ ground state is obtained via ring stacking into tubes. In the experimental work [30] mechanical properties of the chains, rings and tubes composed of ferromagnetic hard spheres of macroscopic dimensions (e.g., diameter of particles is 6 mm) have been investigated. Besides that, the authors of that work have provided an illustrative example which shows a spontaneous wrapping of a straight chain into a tube. A general scientific problem of understanding the mechanisms via which the building blocks, i.e. dipolar hard spheres, self-assemble into structures and gain functionality is demanding and has a wide scientific importance [31–34].

In this thesis one of the two directions of research is dedicated to the modeling of confined dipolar systems. By confinement we assume cylindrical confinement, i.e., dipolar hard spheres are constrained to compose a configuration on top of an imagined cylinder, at a cylinder's prescribed radius. Following this problem definition, we systematically investigate long tubes and helices. The tubes are formed via ring stacking, i.e., by periodical repeating of an unit cell containing a ring along an axis. The helices are formed by rolling of one or multiple threads on a cylindrical confinement surface. In terms of geometry, rolling is very much like 1D crystal formation, which is conducted by replicating a patch of dipolar spheres on a cylindrical confinement surface along the helix backbone. There is an endless number of different helical configurations, but we point out that the densely packed structures exist at well-defined points in parameter space.

In Reference [35], very much in analogy to carbon nanotubes (*CNTs*), it was shown that densely packed helices are defined by two numbers: lattice patch dimensions n_1, n_2 . The lattice patch dimension n_1 is an integer which counts the number

of spheres in one full turn around the confining cylinder and it is directly related to the radius of a helix. An increase of n_1 corresponds to the increase of the radius of a helix. On the other side, the lattice patch dimension n_2 is an integer which counts the number of threads building up the helix and equivalently it counts the number of spheres along the confining cylinder's surface between two consecutive helix turns. Realizing the fact that helix formation is dictated by those two preferential directions, i.e., turns around the cylinder's surface (related to n_1) and threads along the cylinder's surface (related to n_2), we have decided to assign to the particles dipole moments following those two preferential directions. We have defined \vec{a}_1 and \vec{a}_2 dipole moment orientations. In both of them the dipole moment of a certain sphere points to its consecutive sphere, where in the first case consecutive spheres compose turns around the confining cylinder, while in the second case they follow the threads along the cylinder's surface. Besides those two dipole moment orientations assigned according to the geometrical features of helices, we have performed energy minimization in order to obtain dipole moment orientation which corresponds to the ground state and that type of dipole moment orientation is called *ground state dipole moment orientation*. We show that pairs (n_1, n_2) represent the two numbers of threads which can generate geometrically the same densely packed helices, however those helices are energetically completely different depending on the type of their dipole moment orientation. We should mention that densely packed tubes are basically sub-classes of helices (similar to armchair and zig-zag *CNTs*) for special cases of the values of lattice patch dimensions n_1, n_2 .

1.2.1 Outline of the research on cylindrically confined dipolar systems

The goal of the study of confined dipolar systems, i.e., dipolar tubes and helices, is to address the intimate link between the microstructure and cohesive energy. In order to do so, it was necessary to precisely define the geometry, establish dipole moment orientations and appropriately calculate cohesive energy. The research dealing with confined dipolar systems (except for the parts related to introduction and

conclusions) is placed in the chapter *Confined dipolar systems*, which consists of five sections. In the section *Geometry of helices and tubes composed of hard spheres* the geometry is explained in details. Next, the dipolar interaction model is introduced and a link between the dipole distribution and the microstructure is established in the section *Dipole moments*. Speaking in terms of cohesive energy, since the dipolar hard spheres interact via two interaction potentials: potential of hard spheres and dipole-dipole interaction potential, an appropriate method for summing the dipole-dipole interactions should be implemented. Once that task is realized, an efficient energy minimization method for determining the ground state of dipolar structures should be introduced. In the section *Methods* the Lekner-type method for summing the dipole-dipole interactions which we have implemented for calculating the cohesive energy of considered dipolar structures is presented. Besides that, the method for obtaining the ground state dipole moment orientation of a given dipolar structure is presented as well. At that point, after the geometry, dipole moments and method for treating long-range dipole-dipole interactions are established, it is possible to switch the focus to configuration-cohesive energy relations. Namely, in the section *Degeneracy in 2D triangular and square lattice and properties of tubes* it is shown that triangular and square lattices of dipolar hard spheres possess degeneracy in terms of cohesive energy, which breaks-up with curvature in case of *AA* and *AB* tubes. In the following section *Cohesive energy-packing relations in dipolar helices* starting from the simplest case corresponding to a single-thread helix, the relationship between the surface packing and the resulting macroscopic properties, such as cohesive energy or overall polarization, is discussed. Then, the more complex situation of multi-thread helices with densely packed constitutive particles is addressed. There, the degree of alignment (especially in the ground state) between dipole moment orientation and helix axis is analyzed. In the section *Confined dipolar systems* of the chapter *Conclusions*, the conclusions and possible connections of the investigated model system with some real systems, namely with biological microtubules, are given.

1.3 Motivation for the research of ionic liquids

Tribology is the name of a multidisciplinary scientific area which is related to the phenomena of friction, lubrication and wear. In tribology, the knowledge and competences of physics, chemistry and high performance computing are overlapped and combined [36]. Term nanotribology is related to the specific branch of tribology which studies the phenomena of friction, lubrication and wear at the nanoscale. Scientific discipline of computational nanotribology has been well-established in the last couple of decades [36, 37]. Powerful computational resources enable application of the methods of computational nanotribology in the cases of increasing complexity.

There are numerous systems which are of interest in the field of computational nanotribology, however we have focused on ionic liquids. They are a promising candidate for the applications as a high quality lubricant, especially in automotive industry. Bearing that in mind, our investigation in the framework of this topic is directed towards the understanding of physical properties of ionic liquids related to the friction, lubrication and wear phenomena. After gaining a relevant expertise, we might realize the potential of using ionic liquids as a lubricant in automotive industry. Let us start the considerations with this, in a certain way surprising fact, that approximately one-third of the fuel energy in a passenger car is consumed by friction [38]. Therefore, understanding of the lubrication mechanisms in an automotive vehicle's engine is highly important. Numerical simulations at the molecular scale can provide insights which are necessary for understanding the mechanisms governing the system's behaviour, such as structural changes in the lubricant layers during shearing and normal load application, as well as the interaction between the lubricant and solid surfaces. In recent studies of the nanoscopic friction phenomenon, based on the Molecular Dynamics (*MD*) method, ionic liquids are considered as a lubricant [39]. The width of lubricating films of just a few molecular layers is relevant for suppressing wear and achieving low friction [40–43]. In 2001, for the first time it was published that ionic liquids have a great potential as lubricants. Since then, they attract attention in the field of tribology due to their remarkable characteristics relevant for lubrication and wear prevention, when compared to conventional

lubricating oils which are generally used. The number of publications dealing with ionic liquids is constantly increasing, in both forms of journal articles and industrial patents. Therefore, there is a wide interest for this topic from both fundamental and industrial aspects [44].

In industrial applications, there are considerations of using ionic liquids as a neat lubricant and as an additive [45–47]. Significant improvements in friction and wear reduction have been achieved experimentally [46]. Namely, in Reference [46] the authors have achieved coefficient of friction reduction for 60% and wear reduction for three orders of magnitude. They have added and mixed certain ionic liquids with synthetic lubricating oils.

Understanding and description of nanoscopic friction in ionic liquids, as well as their structure under imposed conditions, represents a challenging scientific problem and so far there have been just a couple of studies in this direction, e.g., References [48, 49]. Detailed studies of *ILs* at the nanoscale using the methods of computational physics provide a wider perspective as compared to experimental studies where the investigation is restricted to certain *ILs* which possess certain values of relevant physical parameters. On the other side, in simulations *ILs* are considered in a generic way and it is possible to explore a wide range of parameter values. Practically, it means that simulations enable the design of favourable characteristics of *ILs*, and later-on it is possible to experimentally synthesize certain *ILs*, based on the simulated ones.

In this thesis one of the two directions of research is dedicated to the modeling of confined ionic systems, namely ionic liquids (*ILs*). In order to better understand the structure and behaviour of confined ionic liquids, we investigate the same ionic liquids in the bulk state, as well. We have started from the basis, by implementing and studying the simplest *IL* model which includes a positively charged spherical cation and a negatively charged spherical anion, i.e., *SM* (salt-like model). This was followed by the implementation and investigation of a more realistic *IL* model which includes a positively charged spherical head connected by an elastic spring with a neutral spherical tail and a negatively charged spherical anion, i.e., *TM* (tailed model). Our interest in modeling ionic liquids comes from its scientific im-

portance. However, we bear in mind potential applications of *ILs* as high quality lubricants, hence we guide our research towards exploring *IL* lubricating properties. Simulation setup with two solid plates between which *IL* is confined, is designed with the aspirations of probing *IL* lubricating abilities. To enclose this exposé, in this section we provide general introduction into ionic liquids, which is followed by the introduction into *SM* and *TM* model based studies, respectively.

Ionic liquids are two-component systems composed of large asymmetric and irregularly shaped organic cations and anions. The feature of irregularity is important as it is effectively preventing low-temperature ordering and crystallization. Therefore, *ILs* are usually in the melted or glassy state. Physical properties of *ILs* like negligible vapour pressure, high-temperature stability, high ionic conductivity and also a great variety of *ILs* and their mixtures highlight them as potentially relevant to lubrication [44, 50]. In addition, their properties can be modified by an applied voltage using confining charged surfaces in order to build-up an electric field across the nanoscale film. The applied potential can affect the structure of *IL* layers and lead to externally controllable lubricating properties [49, 51, 52].

A large number of variations in *IL* composition is possible, estimated at the order of magnitude of 10^{18} different *ILs* [53]. From their variety stems the possibility of tuning their physicochemical properties which can affect lubrication such as viscosity, polarity, surface reactivity by varying their atomic composition, as well as the cation-anion combination. Hence, it would be advantageous if we could deduce the general relations between the molecular structure and the anti-wear and lubrication properties of *ILs*.

Previous work employing Lennard-Jones fluids has provided insights into the complete dynamic diagram of confined liquids, including wall slip, shear banding and solid friction. In terms of fluid complexity these studies have mainly employed monomolecular systems, and only a few authors have considered mixtures of molecules [54, 55]. In addition to inherently being a mixture of cation and anion molecules, *ILs* involve long-range Coulombic interactions inducing long-range order on far greater scales than the *IL* itself [39, 43, 56]. Detailed investigation of *ILs* as lubricants at the nanoscale is therefore essential for exploring the potentials of implementing

them in lubrication systems.

Our specific goal, related to industrial applications of *IL* lubricants, is to achieve a representation of the tribological system which is relevant to automotive power-train applications. As approximately 45% of the engine friction losses occur in the piston assembly [38], our initial target is to mimic the conditions observed in the piston ring–cylinder liner contact, in terms of pressure, temperature and shear rates. In addition, in order to be able to achieve length– and time– scales that can be of relevance to the real–life systems, it is necessary to apply appropriate simulation methodologies, such as the use of coarse grain molecular dynamics [57–60].

1.3.1 Salt model of ionic liquid

The focus of our study employing the *SM* ionic liquid, which contains salt–like spherical cations and anions, is on investigating lubricating ability and flow properties of *ILs*. Regarding the ability of ionic liquids to dynamically penetrate between surfaces, i.e. wetting, sometimes it is considered that a low contact angle of the lubricant indicates the affinity between the liquid and the surface, since the liquid is more likely to stay in the area in which it was initially placed. It is also expected that a lubricant is going to penetrate into small–gap components. However, the effect of wettability of the ionic liquids is not understood well. The wetting of plate surfaces such as mica is known to be partial by at least some *ILs* [61, 62]. Lubrication necessarily involves intimate molecular features of the liquid–solid plate interface, related with those mechanisms determining the ionic liquid’s wetting of the plate. When *ILs* are used as lubricants and, as such, confined between solid plates, their ions are ordered into layers and adsorbed onto surfaces [63]. These adsorption layers can reduce friction and wear, particularly in the case of boundary lubrication [63].

Recent studies of *IL* lubricants [49, 51, 52, 64] have shown that if the molecules interact via non–bonded potentials (Lennard–Jones and Coulombic potential), this can capture all main physical attributes of the *IL*–lubricated nanotribological system. Therefore, molecular–scale simulations can provide important insights which are necessary for understanding the differences in flow behaviour between bulk and confined liquid lubricants and the mechanisms behind, such as boundary layers for-

mation in case of shearing and/or applied normal load.

We utilize our coarse grain *MD* simulation setup consisting of two solid plates and an ionic liquid lubricant placed between them [64]. The motivation for the chosen values of relevant model parameters (i.e. velocities, pressures, temperatures, time duration of simulations) comes from potential applications of *ILs* as lubricants in automotive industry. Under typical operation of internal combustion engines, the conditions inside the combustion chamber vary significantly. Temperature can range from 300 K to the values higher than 2000 K, while pressure ranges from atmospheric to the values higher than 10 MPa [38]. The piston reciprocates with a sinusoidal velocity variation with speeds varying from zero to over 20 m/s, with a typical velocity being around 1 m/s. The time required for one revolution of the engine is of the order of 10^{-2} s, while the total distance travelled by the piston over this period is of the order of 0.2 m. Such scales are typically modeled using continuum mechanics simulations. However, such simulations cannot provide the physical insight which is necessary for understanding the molecule-dependent processes that affect the tribological phenomena. Therefore, we have implemented a coarse grain *MD* simulation setup which can, inter alia, provide useful insights into lubrication mechanisms of piston ring–cylinder liner contact in automotive engines. Our simulation setup consists of two solid plates and an *IL* placed between them. It also includes lateral reservoirs into which the *IL* can dynamically expand.

The determination and design of new applicable lubricants require understanding of both general and specific behaviour of liquids when exposed to nanoscale confinement, shearing and normal load. In accordance with those facts, our focus is on determining general features of *ILs* as nanoscale lubricants. Hence, we have chosen the model of a generic *IL* which is simple in order to provide a wide perspective of relevant mechanisms governing the *IL* lubrication principles.

1.3.2 Tailed model of ionic liquid

Since 2001., when ionic liquids were first considered for lubrication applications [65], there has been a large number of experimental studies in that direction. It has been observed that the alkyl chain length of the cations affects the *IL* viscosity [44],

melting point [44] and pressure-viscosity coefficients [66]. Related specifically to lubrication, References [53, 67] explored the impact of cationic alkyl chain's length on the tribological properties of *ILs*. *ILs* considered in those references have the same cations but different anions: symmetric hexafluorophosphate $[PF_6]^-$ and asymmetric bis(trifluoromethylsulfonyl) imide $[Tf_2N]^-$, respectively. Still, while the authors of Reference [67] observed that the coefficient of friction (*COF*) decreases from 0.25 to 0.15 with the increase of alkyl chain length $n_C = 2$ to 12 (n_C is the number of carbon atoms), the authors of Reference [53] observed that the *COF* increases from 0.025 to 0.1. The *ILs* wetting properties are also sensitive to its molecular geometry. *ILs* change wetting behaviour depending on the anion size [61, 62, 68]: from the absence of wetting to partial or complete wetting. A well-studied *IL* $[BMIM]^+[PF_6]^-$ exhibits full wetting at the interface with mica substrates [62, 68]. On contrary, $[BMIM]^+[TFSI]^-$ shows partial wetting on mica [61, 62]. In these examples, *ILs* have the same cation and different anions.

An important observation about the structure of confined *ILs* is their arrangement into positively and negatively charged ionic layers and adsorption onto solid surfaces [63, 69]. These ionic adsorption layers should reduce friction and prevent wear, especially in the case of boundary lubrication [63]. The wear is reduced primarily in two ways: via high load-carrying capability and self-healing of adsorbed *IL* layers. Still, these two processes seem conflicting with each other since high load-carrying capability requires strong adsorption of the lubricant to the surface while self-healing requires high mobility [36]. Understanding the driving forces between them requires relating the molecular structure and flow properties of confined *IL*. In Reference [70] the authors have evaluated tribological properties of different ionic liquids by pendulum and ball on disk tribo testers. They have considered *ILs* consisting of imidazolium cations with different alkyl chain length and $[Tf_2N]^-$ anion as lubricants. Their main observation is that the increment of alkyl chain length can reduce friction and wear of sliding pairs in the elastohydrodynamic lubrication regime (EHL) as a consequence of increased viscosity. Generally, the conclusion is that longer alkyl chains lead to better tribological performance. Related to the impact of alkyl chain length on the structure of *ILs*, in Reference [71] the authors have experi-

mentally obtained the formation of tail-to-tail bilayers of cations if their alkyl chain length is large, in case of confinement between solid surfaces. Their observations are in accordance with other experimental investigations of *IL* lubricants [72–74]. It is worth of mentioning that we have obtained similar configurations via numerical simulations of *ILs* confined between two solid plates, where tail-to-tail formation in the middle of the interplate gap is visible.

The focus of our *TM* model based study is on the systematic investigation of the flow properties and lubrication mechanisms of ionic liquids modeled with a generic coarse grain model which considers a variable shape of the cation. We investigate the impact of cationic tail size on the structural and tribological properties of *ILs* via *MD* simulations. Such an idea is meaningful since previous theoretical studies have pointed out that confinement modifies the behaviour of *ILs* and despite the good wetting nature, the slip is present at the plates [43]. Coulombic interactions in *ILs* induce long-range ordering [39, 43, 56], which in turn can influence their lubrication response. Previously, coarse grain *MD* simulations [40–42, 57–60] were used to study thin lubricant films subjected to the shearing between solid plates.

1.3.3 Outline of the research on model ionic liquids

The research dealing with ionic systems (except for the parts related to introduction and conclusions) is presented in chapter *Ionic liquids*, which consists of four sections. Let us present them briefly in the following text. A method of choice for studying the structure and lubrication characteristics of ionic liquids at the nanoscale, in the framework of this doctoral thesis, is Molecular Dynamics (*MD*) method. Accordingly, in section *Methods* *MD* method and *LAMMPS* code for molecular dynamics are introduced. This is followed by section *Simulation setup and models of ionic liquid* which describes the *SM* and *TM* models of ionic liquid in detail, as well as the implemented *MD* simulation setup. The focus of *Bulk ionic liquid* section is first on obtaining the relaxed structure and then on calculating the viscosity coefficient of bulk *SM* and *TM* ionic liquids. In the following *Confined ionic liquid* section, static and dynamic behaviour of confined *SM* and *TM* ionic liquids are presented and discussed. This section also presents the results of confined *ILs* tribological

behaviour. In chapter *Conclusions*, section *Ionic liquids*, conclusions and prospects of future directions in the investigation of *ILs* from both, theoretical and industrial aspects, are given.

Chapter 2 Confined dipolar systems

2.1 Geometry of helices and tubes composed of hard spheres

2.1.1 Geometry of helices

2.1.1.1 Geometry of single-thread helices

In the framework of this study, helices are composed of hard spherical particles and they are confined to a cylinder's surface, i.e., the helices are formed by rolling threads of hard spherical particles on the cylindrical surface of radius R_{cyl} [75]. Geometrical parameters that define a single helix are: the azimuthal angular shift Γ between the centers of two successive particles and the radius of the helix $R = R_{cyl} + d/2$, where d stands for the hard sphere diameter, see Figure 2.1. The radius R physically represents the distance of the closest approach between cylinder axis and center of the spherical particle. The Cartesian coordinates of particle i in a single helix are calculated as:

$$\begin{aligned}x_i &= R \cos(i\Gamma), \\y_i &= R \sin(i\Gamma), \\z_i &= i\Delta z,\end{aligned}\tag{2.1}$$

where $i \in \mathbb{Z}$ and assuming that one particle is at $(x, y, z) = (R, 0, 0)$. The distance between the centers of each two successive particles along the helix axis is labelled as Δz , see Figure 2.1. When constructing a helix, its radius R and azimuthal angular distance Γ have to be chosen in a way which ensures non-overlapping of hard spheres. The non-overlapping constraint is expressed for any two particles i, j

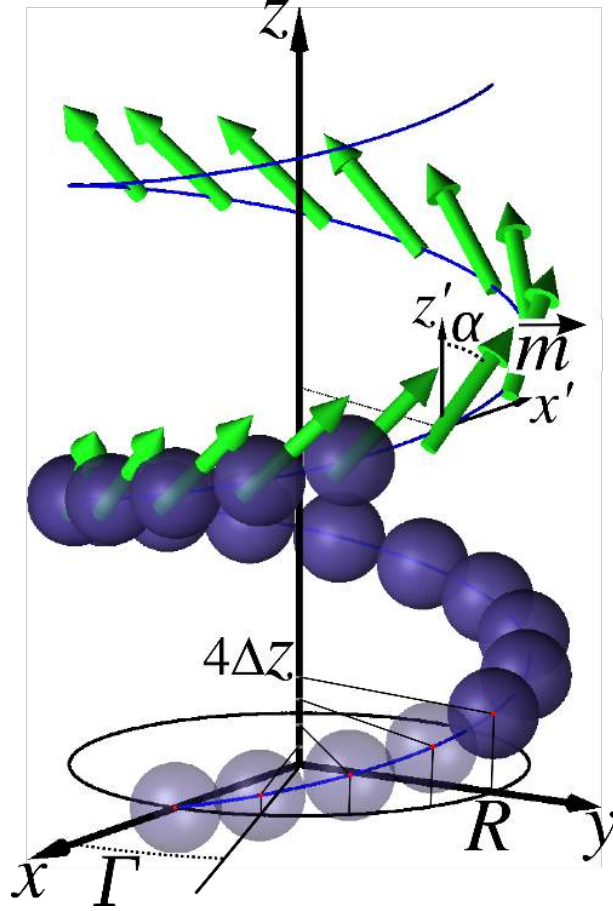


Figure 2.1: Illustration of a single thread helix with relevant geometrical parameters ($R, \Gamma, \Delta z$) labelled. The black bold line connecting spherical particle centers represents backbone of the helix. In upper part of the figure, the azimuthal dipole moment orientation α is defined in a local coordinate system with its origin corresponding to the particle center. The z' axis is parallel to the cylinder axis.

as $|\vec{r}_{ij}| \geq d$. Since the helix thread is connected everywhere, any two successive particles are touching. Starting from Equation 2.1 we can obtain Δz as a function of other two variables, i.e., as a function of R and Γ . Let us write down Equation 2.1 taking the values of the index $i = 1, 2$: $x_1 = R \cos \Gamma, y_1 = R \sin \Gamma, z_1 = \Delta z; x_2 = R \cos(2\Gamma), y_2 = R \sin(2\Gamma), z_2 = 2\Delta z$. Distance between the centers of those two successive spheres is equal to the sphere diameter d , hence it stands:

$$d = \sqrt{(x_2 - x_1)^2 + (y_2 - y_1)^2 + (z_2 - z_1)^2}. \quad (2.2)$$

2. Confined dipolar systems

Taking the relations: $x_2 - x_1 = R(\cos 2\Gamma - \cos \Gamma)$, $y_2 - y_1 = R(\sin 2\Gamma - \sin \Gamma)$, $z_2 - z_1 = \Delta z$, and replacing them into Equation 2.2 we obtain:

$$d^2 = R^2 (\cos 2\Gamma - \cos \Gamma)^2 + R^2 (\sin 2\Gamma - \sin \Gamma)^2 + \Delta z^2. \quad (2.3)$$

From Equation 2.3 we obtain:

$$\begin{aligned} d^2 = R^2 & (\cos^2 2\Gamma - 2 \cos 2\Gamma \cos \Gamma + \cos^2 \Gamma + \sin^2 2\Gamma \\ & - 2 \sin 2\Gamma \sin \Gamma + \sin^2 \Gamma) + \Delta z^2. \end{aligned} \quad (2.4)$$

Bearing in mind the relations of trigonometry: $\sin^2 x + \cos^2 x = 1$, $\sin 2x = 2 \sin x \cos x$, $\cos 2x = \cos^2 x - \sin^2 x$, we obtain:

$$d^2 = 2R^2 (1 - \cos \Gamma) + \Delta z^2. \quad (2.5)$$

Rearrangement of the previous equation leads to the relation expressing Δz as a function of R and Γ :

$$\Delta z = \sqrt{d^2 + 2(\cos \Gamma - 1)R^2}. \quad (2.6)$$

Thereby, variables Δz , R and Γ are not independent. Clearly, with decreasing Δz (i.e., increasing Γ) helices become more compact. Because of the connectivity, every particle in a helix has at least two neighbors, i.e., the coordination number, n_c , is always greater or equal than two ($n_c \geq 2$). We define *coordination number of a helix* as the number of neighbors each particle has, with the exception in case of particles at helix ends, since they have less neighbors. The highest packing density of the particles for prescribed helix radius R will be achieved when successive helix turns touch. In this situation of touching turns, the coordination number n_c can be either four or six. Therefore, in general, $n_c \in \{2, 4, 6\}$, where the case $n_c = 2$ corresponds to non-touching turns. Based on the coordination number n_c , we can classify helices as follows (see Figure 2.2(a)-(c)). Examples of helices with two neighbors $n_c = 2$ and four neighbors $n_c = 4$ at a prescribed cylindrical confinement, e.g., $R/d = 1.78$, are sketched in Figure 2.2(a) and (b), respectively. For a number of well-defined

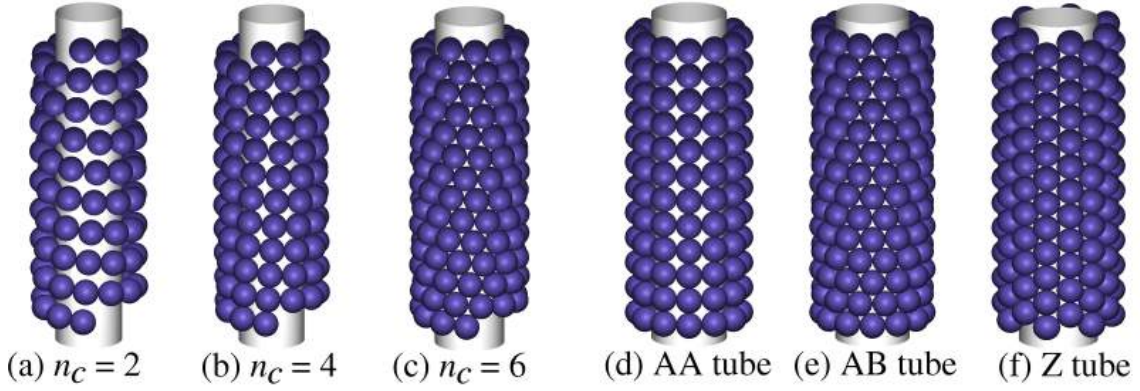


Figure 2.2: Illustration of different classes of helices, based on coordination number $n_c = \{2, 4, 6\}$. (a) Helix with non-touching turns ($n_c = 2$). (b) Helix with touching turns ($n_c = 4$). (c) Densely packed helix ($n_c = 6$). The other panels illustrate, the so called, (d) *AA*, (e) *AB*, and (f) *Z* tubes. The tubes can be created by strict axial stacking of unit rings. For *AA* and *AB* tubes unit rings are flat, whereas, for *Z* tubes the unit ring has a 'zig-zag' shape. The radii of *AA* and *AB* tubes are the same $R/d = 1.93$.

radii, as discussed in details in the coming sections, densely packed helices with six neighbors ($n_c = 6$) can be formed, see Figure 2.2(c). In the following sections of this chapter, we will also investigate stacked rings forming the so-called tubes, also depicted in Figure 2.2(d)-(f).

2.1.1.2 Order parameters for single-thread helices

The surface packing fraction is defined as the ratio of the area $S = \pi d^2/4$ covered by one particle and the area available for one particle S_{avail} , in an unrolled configuration:

$$\eta = S/S_{\text{avail}}. \quad (2.7)$$

Since the distance along the z axis between successive particles is Δz , by parameterization of the helix backbone we obtain for arc length covered by one particle $L_1 = [(\Gamma R)^2 + (\Delta z)^2]^{1/2}$. The available area per particle is $S_{\text{avail}} = (2\pi/\Gamma)\Delta z L_1$.

2. Confined dipolar systems

Following the definition of the surface packing density we obtain:

$$\eta = \frac{d^2}{8\Delta z R}. \quad (2.8)$$

For comparison we are going also to derive packing fraction for the tubes:

- The surface packing fraction of AA tubes is given by:

$$\eta_{AA} = N_{\text{ring}} d / 8R_{AA}, \quad (2.9)$$

for an AA tube with N_{ring} particles per ring and the confinement radius $R_{AA}/d = 1/[2 \sin(\pi/N_{\text{ring}})]$, see Figure 2.2(d) for a microstructure with $R_{AA}/d = 1.93$.

- Similarly, for AB tubes, the packing fraction is:

$$\eta_{AB} = N_{\text{ring}} d^2 / 8R_{AB} \Delta z_{AB}, \quad (2.10)$$

with $R_{AB} = R_{AA}$. Here, the elevation Δz_{AB} between two consecutive rings is:

$$\Delta z_{AB} = (d/2) \sqrt{2 + 2 \cos(\pi/N) - \cos^2(\pi/N)}. \quad (2.11)$$

- For Z tubes, the packing fraction is:

$$\eta_Z = N_{\text{ring}} d / 8R_Z, \quad (2.12)$$

with confinement radius $R_Z/d = \sqrt{3}/[4 \sin(\pi/N_{\text{ring}})]$.

To further characterize the helical microstructures, we introduce an additional geometrical order parameter ξ which is valid for $n_c = 4$ and 6. This order parameter connects an individual reference particle 0 located at \vec{r}_0 in the helix with its two neighbors: its immediate successive particle 1 in the turn ($\vec{r}_{01} = \vec{r}_1 - \vec{r}_0$) and a neighboring particle 2 from the next turn ($\vec{r}_{02} = \vec{r}_2 - \vec{r}_0$), see Figure 2.3(a). The

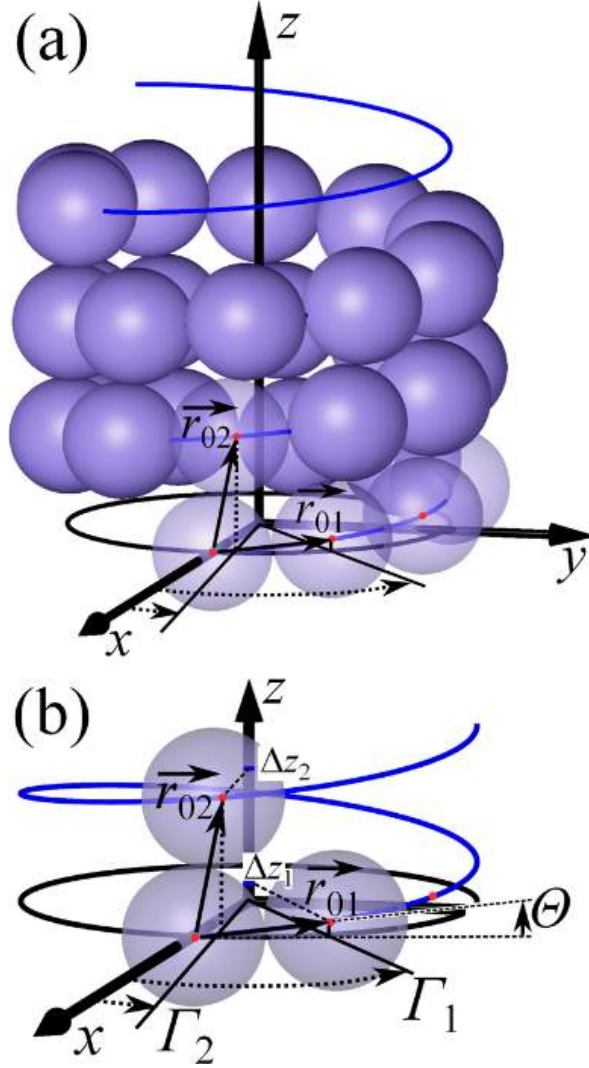


Figure 2.3: (a) Illustration of a helix made of hard spheres, helix backbone (solid line), and the vectors connecting a reference particle 0 located at $(x, y, z) = (R, 0, 0)$ with its neighbours: an immediate successive particle 1 in the turn located at (\vec{r}_{01}) and a neighbouring particle 2 from the next thread turn at (\vec{r}_{02}) . (b) Overview of the principal geometrical parameters of $n_c = 4, 6$ helices: elevation angle Θ and azimuthal angular shifts Γ_1 and Γ_2 (see Equation 2.17). The corresponding elevation distances of successive particles along helix axes $\Delta z_{1,2}$ (see Equation 2.20) are also given for two possible rolling of the same helix configuration.

angular coordination order parameter is conveniently defined as:

$$\xi = 2 \frac{|\vec{r}_{01} \cdot \vec{r}_{02}|}{d^2}. \quad (2.13)$$

In the two limiting cases, the angular coordination order parameter has values:

$\xi_{\min} = 0$, for a locally square lattices on a cylinder (e.g., AA tubes, check Figure 2.2(d)) and $\xi_{\max} = 1$, for a locally triangular lattice (e.g. AB tubes, check Figure 2.2(e)). In all other cases, the value of the angular coordination order parameter ξ is between those two extreme values, i.e., $0 \leq \xi \leq 1$.

2.1.1.3 Geometry of multi-thread helices

The densely packed helices ($n_c = 6$) can be created, in analogy with carbon nanotubes, by rolling a ribbon of a triangular lattice on a cylinder surface [35]. We deal with cylindrical geometry, infinite in one direction. We can generate these helical structures by periodical reproduction of a curved patch (unit cell) along the helical line with spanning vectors (\vec{a}_1, \vec{a}_2) . This curved unit cell has n_1 particles along the \vec{a}_1 direction and n_2 particles in the \vec{a}_2 direction. The values n_1 and n_2 can be seen as the two possible widths of the ribbon generating the same helical structure.

Since we deal with hard spheres and we aim to build very dense structures, the parameter space $(R, \Delta z, n_1, n_2)$ is significantly restricted. We are going to find out that only two of these parameters are independent. There exists a relationship linking the elevation angle $\Theta = \arcsin(\Delta z/d)$ and the confinement radius R , see Reference [35]. Bearing in mind that for any pair (n_1, n_2) or equivalently (n_2, n_1) , we have a unique corresponding structure with $n_c = 6$, one arrives at the following two independent equations:

$$\Theta(n_1, n_2) = \arctan \left(\frac{\sqrt{3}n_2}{2n_1 + n_2} \right) \quad (2.14)$$

and

$$\begin{aligned} \pi = & n_1 \arcsin \left[\left(\frac{d}{4R} \right) \frac{2n_1 + n_2}{\sqrt{n_1^2 + n_2^2 + n_1 n_2}} \right] \\ & + n_2 \arcsin \left[\left(\frac{d}{4R} \right) \frac{2n_2 + n_1}{\sqrt{n_1^2 + n_2^2 + n_1 n_2}} \right]. \end{aligned} \quad (2.15)$$

We have solved those two equations in Mathematica software package [76] and obtained the sets $(\Theta, R/d)$ shown in Figure 2.4. For each value of R there are two

2. Confined dipolar systems

different values of Θ , symmetric around $\Theta = 30^\circ$, which correspond to lattice constant pairs (n_1, n_2) and (n_2, n_1) , respectively. The (n_1, n_2) pairs are actually identical structures with opposite chirality [77]. The six-fold rotational symmetry of the lattice restricts $\Theta \in [0^\circ, 60^\circ]$.

We now look into properties of (n_1, n_2) pairs in order to characterize the multi-thread structure of six neighbor helices ($n_c = 6$). First, we identify the link between $n_c = 6$ -tubes and the (n_1, n_2) pair values. The pairs $(0, n_2)$ and $(n_1, 0)$ leading to $\Theta = 60^\circ$ and 0° , respectively, represent AB tubes, check Figure 2.4. The pairs with $n_1 = n_2$ corresponding to $\Theta = 30^\circ$ lead to Z tubes that are characterized by constitutive straight filaments parallel to the Z tube axis, see Figure 2.2(f). The curve with $n_1 = 1$ (with $n_2 \geq 3$) corresponds to a single helix, $n_1 = 2$ (with $n_2 \geq 3$) corresponds to a double helix, $n_1 = 3$ (for any $n_2 \geq 4$) corresponds to a triple helix, and more generally an n_1 -helical structure is obtained when $n_2 \geq n_1 + 1$. We employ Cartesian coordinates to express positions of particles in an n -helix similarly to the single helix case, using two indices, $i \in Z$ and $j = \{1, n\}$:

$$\begin{aligned} x_{i+jn} &= R \sin(i\Gamma_1 + j\Gamma_2), \\ y_{i+jn} &= R \cos(i\Gamma_1 + j\Gamma_2), \\ z_{i+jn} &= i\Delta z_1 + j\Delta z_2. \end{aligned} \tag{2.16}$$

In Equation 2.16, Γ_1 represents the azimuthal angular shift between each two consecutive particles along a given thread and Γ_2 is the angular shift between threads, i.e., densely packed directions in a superstructure, see Figure 2.3(b). The azimuthal angle Γ_1 is merely provided by :

$$\Gamma_1 = \arccos \left[1 - \left(\frac{d}{\sqrt{2}R} \cos \Theta \right)^2 \right]. \tag{2.17}$$

The angular shift Γ_2 between threads is more delicate to derive. Knowing that starting from the reference particle it is possible to reach the same particle position following two paths along threads (in \vec{a}_1 - or \vec{a}_2 -direction), one can arrive at a relation

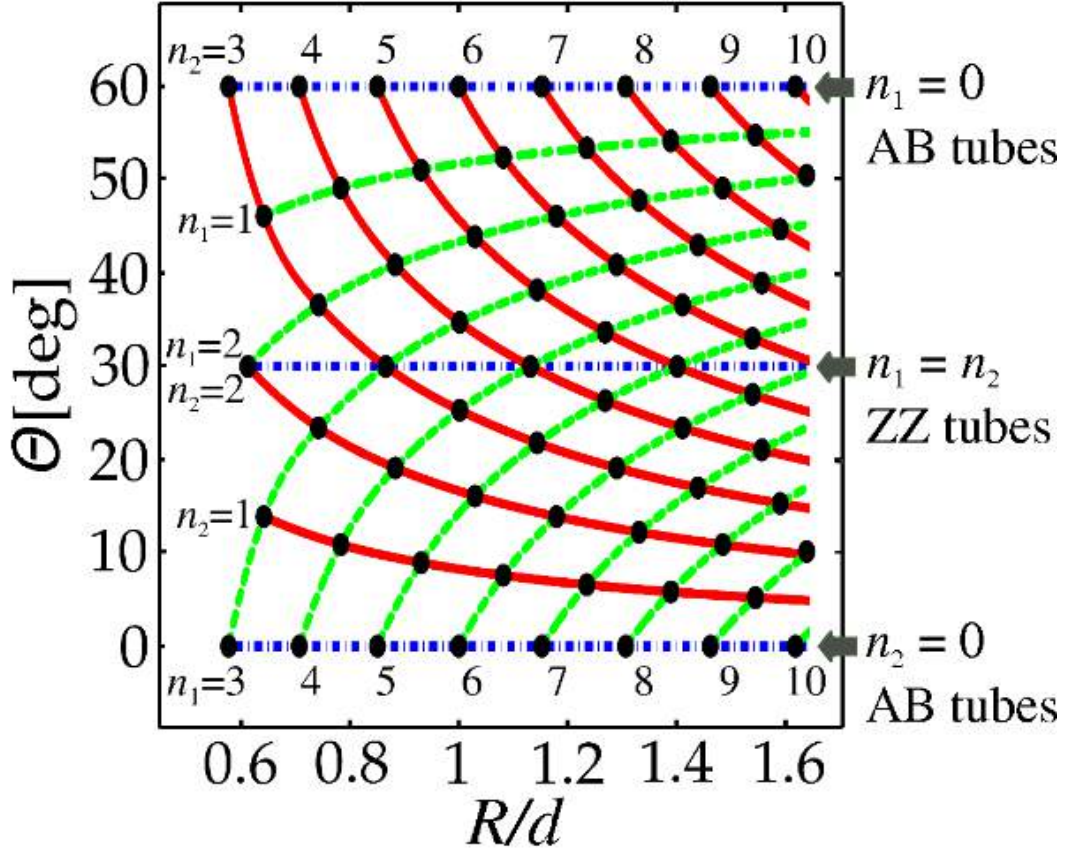


Figure 2.4: State diagram in the $(\Theta, R/d)$ -plane showing possible unit cells characterized by (n_1, n_2) pairs. Solid lines represent unit cells with n_2 fixed, and the dashed ones represent unit cells with n_1 fixed. The three horizontal lines (dot-dashed) correspond to tubes.

linking Γ_1 and Γ_2 :

$$2\pi = (n_1 + n_2)\Gamma_1 - n_2\Gamma_2. \quad (2.18)$$

The dependence of angle parameters Γ_1 and Γ_2 on the reduced helix radius R/d is displayed in Figure 2.5, for $\Theta < 30^\circ$ in the single helix ($n_2 = 1, n_1 \geq 4$), the double helix ($n_2 = 2, n_1 \geq n_2$) and the quadruple helix ($n_2 = 4, n_1 \geq n_2$). In our notation, multi-thread helices are named after the smallest unit patch particle dimension, i.e., the smallest number of generating threads. As the helix radius R/d increases, the value of Γ_1 monotonically decreases, since additional particles are added to a turn. The angular parameter Γ_2 monotonically decreases only for $n_2 = 1$. The scenario becomes qualitatively different at $n_2 \geq 2$ where non-monotonic behavior is found, see Figure 2.5. This feature can be rationalized as follows. The smallest compatible

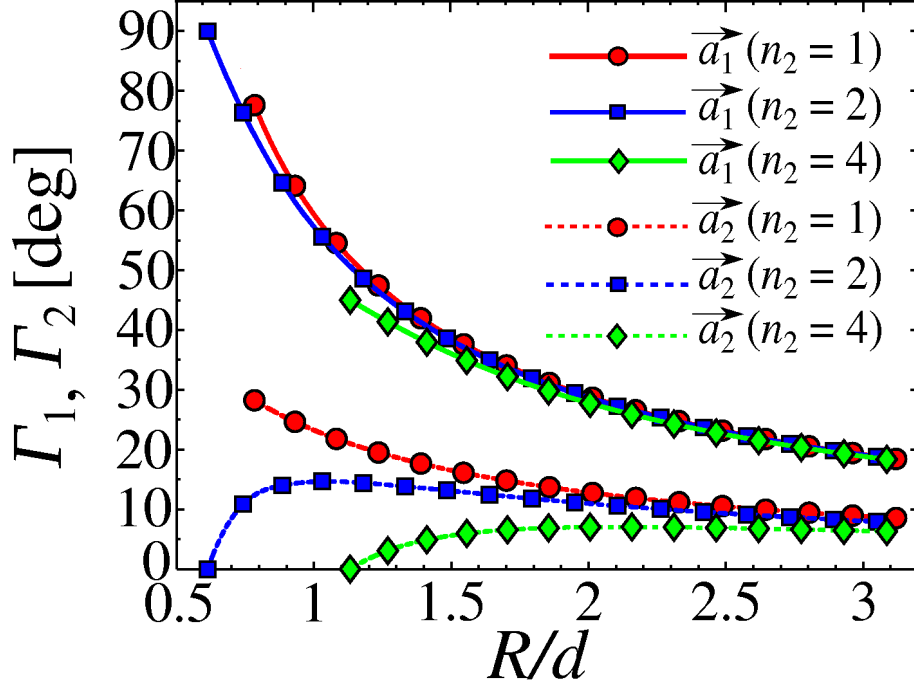


Figure 2.5: Dependence of azimuthal angular shift parameters Γ_1, Γ_2 coming from corresponding spanning vectors \vec{a}_1, \vec{a}_2 , respectively, on reduced helix radius R/d , for single thread ($n_2 = 1$), double thread ($n_2 = 2$), and four-thread ($n_2 = 4$) helices.

radii R with $n_2 \geq 2$ and $\Theta < 30^\circ$, are obtained when $n_1 = n_2$ (check Figure 2.4) corresponding to Z tubes where $\Gamma_2 = 0$. Besides that, Γ_2 tends to zero for vanishing cylinder curvature ($R/d \rightarrow \infty$). These are the reasons why the profile of $\Gamma_2(R/d)$ is non-monotonic when $n_2 \geq 2$. The surface packing fraction of densely packed multiple helices is simply obtained by multiplying the surface packing fraction of a single helix with the number of threads n_2 ($\eta_{multi} = n_2\eta$, see Equation 2.8):

$$\eta_{multi} = n_2 \frac{d^2}{8\Delta z_1 R}, \quad (2.19)$$

where the elevation distance Δz_1 (shown in Figure 2.3(b)) is given by:

$$\Delta z_1 = \sqrt{d^2 - 4R^2 \sin^2 \left(\frac{\Gamma_1}{2} \right)}. \quad (2.20)$$

The calculated surface packing fraction of single ($n_2 = 1$), double ($n_2 = 2$), and quadruple ($n_2 = 4$) helices is shown in Figure 2.6. At a given confinement curvature (fixed R/d), adding threads results in higher surface packing fraction, see Figure 2.6.

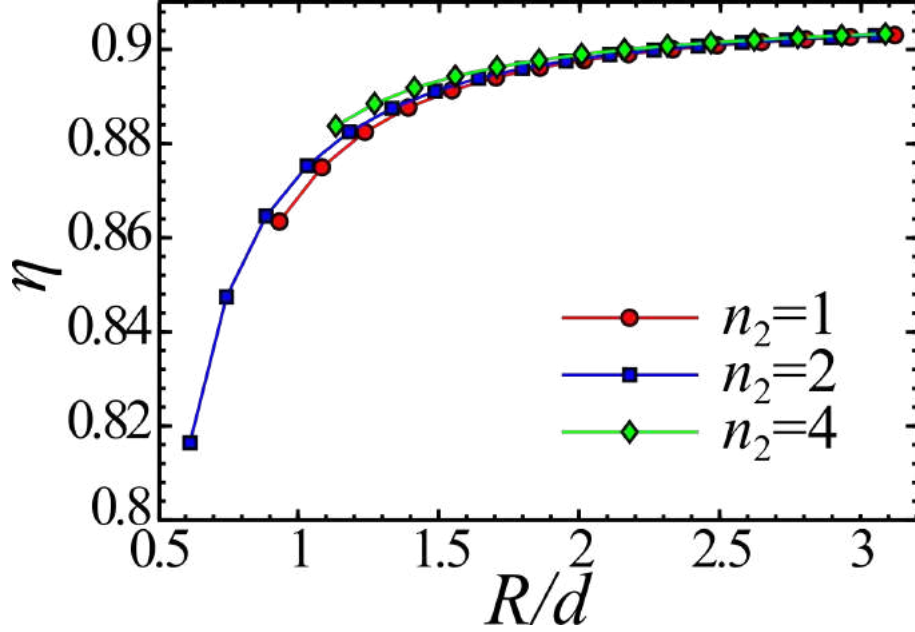


Figure 2.6: Surface fraction η , see Equation 2.19 as a function of reduced helix radius R/d for single thread ($n_2 = 1$), double thread ($n_2 = 2$), and four-thread ($n_2 = 4$) helices.

2.1.2 Tubes as sub-sets of helices

We refer to tubes made by stacking of rings. In *AA* tubes all constitutive rings are exactly aligned, see Figure 2.2(d), and in *AB* tubes every ring is shifted for half of the particle's diameter, in respect to its preceding ring, see Figure 2.2(e). Alternatively, *AA* or *AB* tubes could be generated by rolling of square or triangular lattices on cylindrical confinement, respectively.

Particle i -positions in *AA* tubes are calculated as:

$$\begin{aligned}
 x_i &= R \cos(2\pi i/N), \\
 y_i &= R \sin(2\pi i/N), \\
 z_i &= \lfloor i/N \rfloor d,
 \end{aligned} \tag{2.21}$$

where $\lfloor x \rfloor$ is the greatest integer function and gives the largest integer less than or equal to x , while N is the number of particles in a constitutive ring. To simplify discussion, we refer to N also as *curvature* since there is a correspondence with the tube's geometrical curvature $R/d = 1/2 \sin(\pi/N)$, e.g., we obtain $R/d = \sqrt{2}/(\sqrt{3} -$

1) ≈ 1.3 for $N = 8$ ring.

One of the ways to obtain AB tubes is stacking of a pair of two successive rings. Total number of particles in the tube N_{tube} is a multiple of the number of particles in the ring N and the number of rings N_{rings} , i.e., $N_{\text{tube}} = N_{\text{rings}} \cdot N$.

In both rings particle positions are calculated based on their index $i = 1, N_{\text{tube}}$:

$$\begin{aligned} x_i &= R \cos(2\pi i/N + \theta_i), \\ y_i &= R \sin(2\pi i/N + \theta_i), \\ z_i &= \lfloor i/N \rfloor \Delta z, \end{aligned} \tag{2.22}$$

where θ_i is angular displacement of rings:

$$\theta_i = \pi \bmod (\lfloor i/N \rfloor, 2)/N \tag{2.23}$$

and the displacement between successive rings along AB tube's axis is:

$$\Delta z = \sqrt{d^2 - 2R^2[1 - \cos(\pi/N)]}. \tag{2.24}$$

We have already explained when discussing the Figure 2.4 that densely packed tubes, i.e. AB and Z tubes, can be seen as sub-classes of helices. Bearing this in mind, in addition to stacking of the rings, we point out that the tubes can be created by rolling a ribbon with square or triangular lattice on a cylindrical surface. In fact, every ordered tubular structure can be generated by reproduction of a curved unit cell along helical lines defined through curved spanning vectors in analogy to crystals in two dimensions. This curved unit cell has n_1 and n_2 particles along two spanning directions \vec{a}_1 and \vec{a}_2 , respectively.

2.2 Dipole moments

2.2.1 Dipolar interaction model

We have explained the geometry of helices and tubes composed of hard spheres in section 2.1 of this chapter. In this section we want to address the situation where the

constitutive particles are dipolar. Each particle carries an identical dipole moment in magnitude, $m = |\vec{m}_i|$, where $\vec{m}_i = (m_i^x, m_i^y, m_i^z)$ defines the dipole moment of a particle i , see also Figure 2.1 in section 2.1. The potential energy of interaction $U(\vec{r}_{ij})$ between two point-like dipoles whose centers are located at \vec{r}_i and \vec{r}_j can be written as:

$$U(\vec{r}_{ij}) = C \frac{1}{r_{ij}^3} \left[\vec{m}_i \cdot \vec{m}_j - 3 \frac{(\vec{m}_i \cdot \vec{r}_{ij})(\vec{m}_j \cdot \vec{r}_{ij})}{r_{ij}^2} \right], \quad (2.25)$$

for $r_{ij} \geq d$ or ∞ otherwise, where C represents a constant that depends on the intervening medium, and $r_{ij} = |\vec{r}_{ij}| = |\vec{r}_j - \vec{r}_i|$. It is convenient to introduce the energy scale defined by $U_{\uparrow\uparrow} \equiv Cm^2/d^3$ that physically represents the repulsive potential value for two parallel dipoles at contact standing side by side, as clearly suggested by the notation. Therefore, the total potential energy of interaction in a given structure U_{tot} is given by:

$$U_{\text{tot}} = \sum_{\substack{i,j \\ i>j}} U(\vec{r}_{ij}). \quad (2.26)$$

One can then define the reduced potential energy of interaction u (per particle) of N magnetic spheres. It reads $u = U_{\text{tot}} / (U_{\uparrow\uparrow}N)$, which will be referred to as the cohesive energy. Since we are dealing with infinitely long structures (in one direction), we shall consider only periodic structures in that direction, so this imposed condition greatly facilitates the calculation of the cohesive energy. Our method of choice is the Lekner-type summation method for systems with periodicity in one direction which we have presented in section 2.3. The central feature in Lekner-type methods is the choice of the periodic cell. For structures with coordination number $n_c = 2, 4$ we can always find helical parameters with a finite number of particles in the unit cell. The periodicity is achieved by imposing a condition on the angular shift parameter Γ that a helix has to make an integer number of turns within the unit cell.

2.2.2 Relevant dipole moment orientations

Taking into account the symmetry of helices it is intuitive to assume dipole moments following helix threads. In order to have dipole moments tangential to the helical

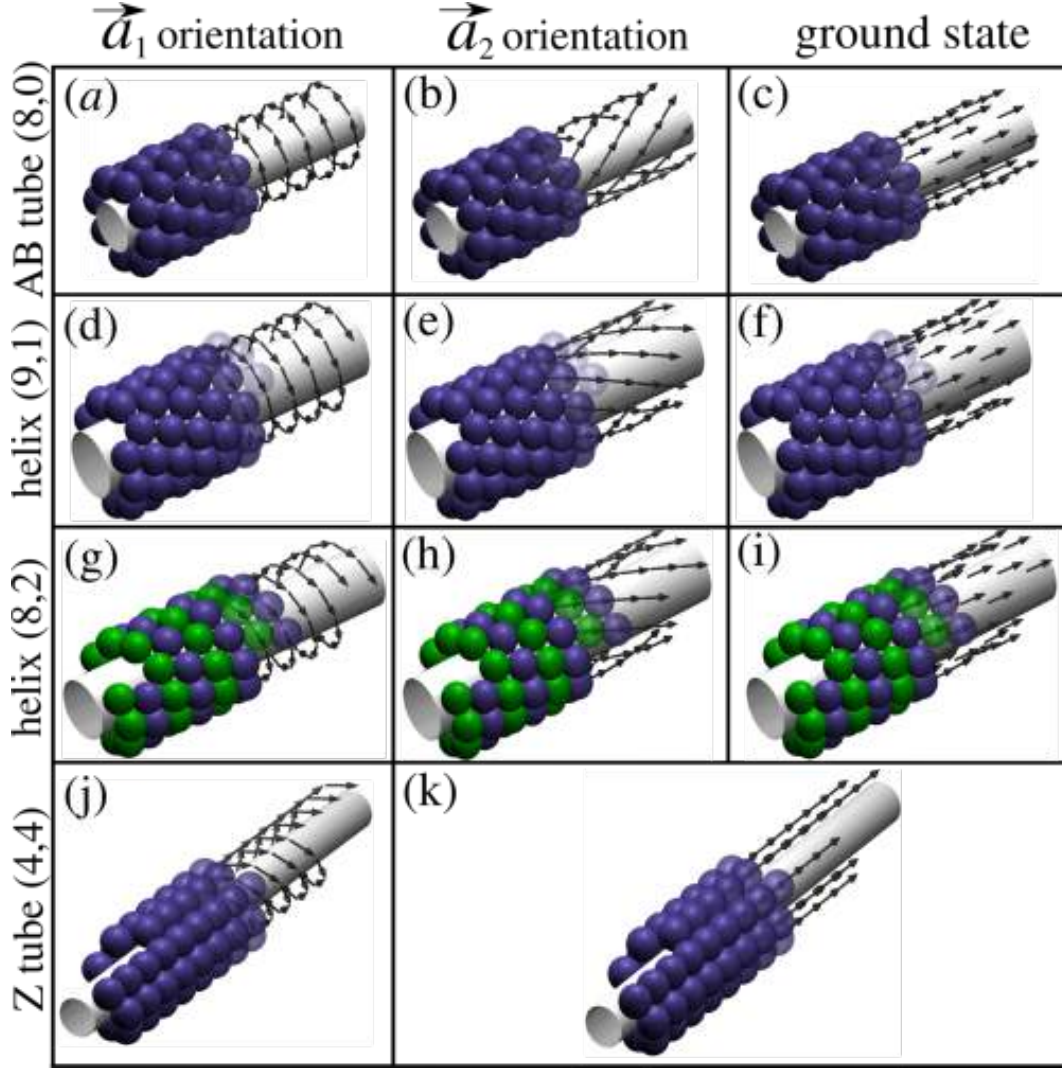


Figure 2.7: The representative structures including dipole moment distributions are displayed. For AB tube with patch parameters $(n_1, n_2) = (8, 0)$ dipole distributions which correspond to spanning unit cell vectors (a) \vec{a}_1 (oblique to cylinder's axis), (b) \vec{a}_2 (closer to cylinder's axes), as well as, (c) ground state dipole distribution. For single thread helix $(n_1, n_2) = (9, 1)$ dipole distributions which correspond to (d) \vec{a}_1 and (e) \vec{a}_2 (closer to helix axes) spanning vectors, as well as, (f) ground state dipole distribution. For double thread helix $(n_1, n_2) = (8, 2)$ dipole distributions which correspond to (g) \vec{a}_1 , (h) \vec{a}_2 (closer to helix axes) spanning vectors, and (i) ground state dipole distribution. In case of Z tube (j) \vec{a}_1 and (k) \vec{a}_2 dipole distributions are shown. Ground state of Z tube follows \vec{a}_2 dipole distribution (parallel to cylinder's axis).

backbone, we introduce two components of dipole moments. The parallel component with respect to the helix axis (we have chosen to orient a helix along the z direction)

is given by:

$$m^z = m\Delta z/d, \quad (2.27)$$

and the orthogonal one is given by:

$$|\vec{m}^{xy}| = m\sqrt{1 - (\Delta z/d)^2}. \quad (2.28)$$

Hence, the dipole moment of a particle i in the single thread helix reads:

$$\begin{aligned} m_i^x &= -m^{xy} \sin(i\Gamma), \\ m_i^y &= m^{xy} \cos(i\Gamma), \\ m_i^z &= m_z. \end{aligned} \quad (2.29)$$

In the multi-thread case, the Cartesian dipole moment components are given by:

$$\begin{aligned} m_{ij}^x &= -m^{xy} \sin(i\Gamma_1 + j\Gamma_2), \\ m_{ij}^y &= m^{xy} \cos(i\Gamma_1 + j\Gamma_2), \\ m_{ij}^z &= m\Delta z/d, \end{aligned} \quad (2.30)$$

where $i \in Z$ is the internal particle label within a thread and $j = \{1, n_2\}$ stands for the thread's label. In dense helices ($n_c = 4, 6$) dipole moments can follow two directions \vec{a}_1 and \vec{a}_2 .

In general, the dipole moments do not have to follow helix threads. In order to find the dipole moment orientation that ensures minimal cohesive energy, we perform minimization of the cohesive energy using a constrained minimization algorithm which we have presented in section 2.3.

We have considered three relevant dipole moment orientations: \vec{a}_1 and \vec{a}_2 orientations which are defined by the helix threads and the ground state dipole moment orientation, which is determined via cohesive energy minimization procedure. In Figure 2.7, representative dipole moment distributions are shown.

2.3 Methods

In this chapter we present the methods applied in the study of confined dipolar systems. We have carefully and in details derived the Lekner-type summation method for summing the dipole–dipole interactions in $1D$ periodic dipolar systems, check appendix A. In subsection 2.3.1 we present the overview of available methods for summing the dipole-dipole interactions of infinite periodic structures, followed by our selection of the proper method and the final expressions of the Lekner-type method that we have implemented. Next, we describe the energy minimization method which we have used for determining the ground state dipole orientation of our dipolar structures.

2.3.1 Methods for summing the dipole-dipole interactions of infinite periodic structures

2.3.1.1 Overview of available methods

Energy of a dipolar structure with finite number of particles can be calculated via direct summation of potential energies of the dipole-dipole interaction (DDI) of every pair of particles. On the other hand, we might be interested in calculating the energy of infinite periodic dipolar structures. As DDI is a long-range interaction, a proper approach is needed. We present a brief overview of available numerical techniques for summing the long-range interactions of spatially periodic structures.

In case of $3D$ periodic structures a standard method of choice for summing the long-range interactions is the Ewald method [78]. Besides the periodicity in all three spatial dimensions, there are three-dimensional systems having the periodicity in one or two dimensions, let us note them as $1D$ and $2D$ periodic systems. Hence, those are $3D$ systems possessing the periodicity along one- or two- dimensions. Ewald type methods for these kinds of periodic systems have been established [79–84]. For example, a $2D$ Ewald method for the electrostatic [79–81] and dipole-dipole interactions [79, 80] has been developed. Such a method computes properly the long range DDI , however its disadvantage is the bad scaling of computational time

with the number of dipoles N (i.e., it scales $\propto N^2$). A computationally more efficient method for summing DDI in a $2D$ periodic system has been presented in [82]. It represents a modification of the previously mentioned computationally inefficient $2D$ Ewald method since its computational time scales $\propto N$. A mutual feature of Ewald type methods [79–81] is the need for an arbitrary convergence parameter necessary for the control of the accuracy of summations. Convergence parameter is a numerical factor related to computation and without physical interpretations. The modified $2D$ Ewald method [82, 83] requires one additional parameter, while the modified $1D$ Ewald method requires even two additional parameters [84].

Summation techniques which avoid the usage of convergence parameters are advantageous, leading to both the reduction of complexity and computational time. For example, such a method for summing long-range Coulombic interactions in periodic systems has been originally introduced by Lekner [85]. Since it opened a new direction in the field of long-range interaction summations, this type of approach has been known under the term *Lekner summation*. Modifications and improvements based on Lekner’s work [85] led to the development of *Lekner-type* methods [86–88]. In Lekner-type methods [85–88] the forces are calculated first and the interaction energy is obtained by integrating the force expressions. On the other side, an approach has been introduced in which the expression for the interaction energy is directly derived [89, 90]. In the next two References [89, 90] Coulombic interaction is considered, while in Reference [91] the approach is applied to the DDI .

To conclude our overview, there are several Ewald type [78–84] and Lekner-type [85–88] methods for summing both Coulombic and dipole-dipole interactions in all possible cases of periodicity of the system (i.e., $1D$, $2D$ or $3D$ periodic systems).

2.3.1.2 Selection of the proper method

We are interested in calculating the energy of infinite $1D$ periodic dipolar tubes and helices. We have arbitrary chosen to orient them along the z axis, so they are periodic along this direction. According to that we have chosen the Lekner-type method for summing the DDI of $1D$ periodic systems, presented in [91].

Let us explain the key features of this method. An infinite dipolar structure is

represented by its elementary cell which is periodically replicated along the z axis. Interaction energy of a structure (i.e., structure's cohesive energy) is determined as a sum of *self energy* E_{self} and *cross energy* E_{cross} , which are calculated based on the elementary cell of that structure. Elementary cell is infinitely replicated along the z axis in both directions, hence we might speak about the particles in the cell and about their images in the replicas of the cell. Knowing this, we define the self energy as a sum of the interactions of a given particle from the elementary cell with all its images. On the other side, the cross energy includes interactions of a given particle with all other particles belonging to the elementary cell and with all their images.

In Reference [91] the authors consider the *DDI* which decays with the distance between the dipoles $\propto r^{-3}$, hence the expressions for the self and cross energy are derived for this type of long-range interaction. Our opinion was that it might be useful to round-up the derivation and come up with the expressions for the self and cross energy in function of parameter s which is defined by setting that the *DDI* decays with the distance $\propto r^{-2s}$. Once we accomplish this and derive closed-form expressions in function of s , we can simply set $s = 3/2$ and obtain the final expressions for the self and cross energy in case of *DDI*.

2.3.1.3 Application of the derived Lekner-type method in case of infinite 1D periodic dipolar structures

We have derived the expressions which define the self energy E_{self} and cross energy E_{cross} in a Lekner type method for summing the *DDI* in case of 1D periodic structures. Since our investigation considers 1D periodic infinite dipolar helices, this method is appropriate for calculating their cohesive energy. We can state that the cohesive energy of a dipolar structure corresponds to the potential energy of *DDI* between the hard dipolar spheres which the structure is composed of. In every structure we should determine its periodic cell and within this cell we should calculate the self and cross energy. Expression for the self energy A.10 is the same in case of any periodic cell. On the other hand, we should carefully choose the expression for the cross energy depending whether the condition $\vec{\rho}_{ij} \neq 0$ does or does not apply, the indices i and j can take any value from the range $\overline{1, N}$, where N is the total

2. Confined dipolar systems

number of particles in the periodic cell. As in case of infinite dipolar tubes and helices the elementary cell of every structure fulfills the condition $\vec{\rho}_{ij} \neq 0$, we take the expression A.120 for the cross energy. Hence, the total energy of an infinite dipolar tube or helix, where N is the total number of particles in its periodic cell, is computed using the next expression:

$$\begin{aligned}
E_{\text{tot}} = E_{\text{cross}} + E_{\text{self}} &= \frac{1}{2} \sum_{i=1}^N \sum_{j=1, j \neq i}^N \left\{ -\frac{8\pi}{L_z^2} \left[\frac{2(\vec{\mu}_i^\rho \cdot \vec{\rho}_{ij})(\vec{\mu}_j^\rho \cdot \vec{\rho}_{ij})}{\rho_{ij}^3} - \frac{(\vec{\mu}_i^\rho \cdot \vec{\mu}_j^\rho)}{\rho_{ij}} \right] \right. \\
&\times \sum_{k=1}^{+\infty} k \cos(k\eta_{ij}^z) K_1(k\eta_{ij}^\rho) \\
&- \frac{16\pi^2}{L_z^3} \left[\frac{(\vec{\mu}_i^\rho \cdot \vec{\rho}_{ij})\mu_j^z + (\vec{\mu}_j^\rho \cdot \vec{\rho}_{ij})\mu_i^z}{\rho_{ij}} \right] \\
&\times \sum_{k=1}^{+\infty} k^2 \sin(k\eta_{ij}^z) K_1(k\eta_{ij}^\rho) \\
&- \frac{16\pi^2}{L_z^3} \left[\frac{(\vec{\mu}_i^\rho \cdot \vec{\rho}_{ij})(\vec{\mu}_j^\rho \cdot \vec{\rho}_{ij})}{\rho_{ij}^2} - \mu_i^z \mu_j^z \right] \\
&\times \sum_{k=1}^{+\infty} k^2 \cos(k\eta_{ij}^z) K_0(k\eta_{ij}^\rho) \\
&\left. - \frac{2}{L_z} \left[\frac{2(\vec{\mu}_i^\rho \cdot \vec{\rho}_{ij})(\vec{\mu}_j^\rho \cdot \vec{\rho}_{ij})}{\rho_{ij}^4} - \frac{(\vec{\mu}_i^\rho \cdot \vec{\mu}_j^\rho)}{\rho_{ij}^2} \right] \right\} \\
&+ \frac{1}{L_z^3} \sum_{i=1}^N \left[|\vec{\mu}_i^\rho|^2 - 2(\mu_i^z)^2 \right] \zeta(3). \tag{2.31}
\end{aligned}$$

Cohesive energy of a dipolar structure is defined per particle, hence we just have to divide E_{tot} by the number of particles in the periodic cell:

$$E_{\text{cohesive}} = E_{\text{tot}}/N. \tag{2.32}$$

2.3.2 Energy minimization method for obtaining ground state dipole orientation of dipolar structures

In dipolar structures' analysis an obvious question which arises is related to the determination of the dipole moment orientation of a structure. By this term *dipole moment orientation* we consider a logical and meaningful rule of orienting the dipole

moment of each particle. We have deduced that dipole orientations which follow the thread structure (i.e., \vec{a}_1 and \vec{a}_2 dipole orientation) are relevant, since there is a tight relation between the geometry of a dipolar structure and a favourable dipole orientation. Dipolar structures which we consider are spatially $3D$ structures, however with a $1D$ periodicity along the z direction. Hence, there are two threads a structure is made of: a circular thread (leading to \vec{a}_1 dipole orientation) and a slanted thread (leading to \vec{a}_2 dipole orientation). We have asked ourselves how would an optimal dipole orientation look like, i.e., a dipole orientation which minimizes the cohesive energy of a structure. Besides that, we should in general determine dipole orientations which allow a negative cohesive energy: $E_{\text{cohesive}} < 0$, i.e., realistically possible configuration of dipolar spheres. To do so, we perform minimization of cohesive energy using a constrained minimization algorithm [29, 92], namely the *fmincon* minimization procedure from *Matlab* software package [93]. The name of the *fmincon* procedure has been constructed according to its purpose which is *function minimization under constraints*. Minimization procedure *fmincon* [93] finds a minimum of a constrained nonlinear multivariable function. Its mathematical definition is given as:

$\min f(x)$ over x under the constraints:

$$c(x) \leq 0, c_{\text{eq}}(x) = 0, A \cdot x \leq b, A_{\text{eq}} \cdot x = b_{\text{eq}}, lb \leq x \leq ub,$$

where b and b_{eq} are vectors, A and A_{eq} are matrices, $c(x)$ and $c_{\text{eq}}(x)$ are functions which return vectors, $f(x)$ is a function being minimized which returns a scalar value. The argument x over which minimization is performed can be a vector or a matrix, lb and ub are the lower and upper boundaries for the argument x , respectively, hence they are the same data type as x , i.e., a vector or a matrix. A dipolar structure has a given fixed geometry which is not subjected to minimization, hence the particles stay in place during the minimization. Their dipole moments $\vec{\mu}_i$ are subjected to minimization. A randomly oriented dipole moment is assigned to every particle of a dipolar structure, defined in the spherical coordinate system using two angles: θ and φ . Those angles are standard coordinates of a spherical coordinate

2. Confined dipolar systems

system. Each particle i is assigned with a randomly oriented dipole moment, where $\theta_i \in [0, \pi]$ and $\varphi_i \in [0, 2\pi]$. Mathematically speaking, we can write down the previous considerations (bearing in mind that $\text{rand}(1)$ returns a random real number in the range $[0, 1]$) as:

$$\begin{aligned}\theta_i &= \pi \cdot \text{rand}(1), \\ \varphi_i &= 2\pi \cdot \text{rand}(1).\end{aligned}\tag{2.33}$$

The dipole moment of i -th particle, i.e., $\vec{\mu}_i = (\mu_i^x, \mu_i^y, \mu_i^z)$ in spherical coordinate system is:

$$\begin{aligned}\mu_i^x &= \sin(\theta_i) \cos(\varphi_i), \\ \mu_i^y &= \sin(\theta_i) \sin(\varphi_i), \\ \mu_i^z &= \cos(\theta_i),\end{aligned}\tag{2.34}$$

where $i = \overline{1, N}$, with N being the total number of particles in a dipolar structure.

The function which we minimize is the cohesive energy of a given dipolar structure, i.e., $f = E_{\text{cohesive}}$ and the argument $x = \theta_1, \theta_2, \dots, \theta_N; \varphi_1, \varphi_2, \dots, \varphi_N$. The lower and upper boundaries are: $lb = 0, 0, \dots, 0; 0, 0, \dots, 0$ and $ub = \pi, \pi, \dots, \pi; 2\pi, 2\pi, \dots, 2\pi$, respectively. We have determined two important features emerging from energy minimization computations employing the *fmincon* procedure [93]:

- (i) dipole moments are tangential to the confining cylinder's surface, and
- (ii) component of a dipole moment in the z -axis direction m_z of a given dipolar structure is identical for all particles.

We have found that under some circumstances the dipole moment orientations alternate, i.e., we have obtained the antiferromagnetic-like coupling between the neighbouring threads. This actually occurs with any AA tube. Similar behaviour is reported for some moderately dense $n_c = 4$ -helical structures. Therefore, we need just one angular parameter to characterize the dipole moment orientation. We choose the dipole moment angular parameter, $\alpha \in [-\pi, \pi]$, relative to the z axis, see

Figure 2.1. Doing so we arrive at:

$$\begin{aligned}
 m_{ij}^x &= -m \sin(\alpha) \sin(i\Gamma_1 + j\Gamma_2), \\
 m_{ij}^y &= m \sin(\alpha) \cos(i\Gamma_1 + j\Gamma_2), \\
 m_{ij}^z &= m \cos(\alpha),
 \end{aligned}
 \tag{2.35}$$

where the indices i and j have the same meaning as in Equation 2.30. Consequently, the angular parameter α is most of the time a unique variable, at prescribed helical structures, entering into the energy minimization procedure. Obtaining an optimal dipole orientation which leads to the minimal cohesive energy of a certain dipolar structure, in other words obtaining *ground state dipole orientation*, comes down to determining the right value of the angular parameter α . In general, except for some cases where we have obtained the antiferromagnetic-like dipole orientation, dipole moments of all particles are parallel, building the same angle α with the z axis direction.

To sum up, we have started with the most general case of each particle having an independent and randomly oriented dipole moment. Application of the *fmincon* minimization procedure [93] significantly narrowed down the diversity of possible dipole orientations, leading to just one scalar parameter α determining the ground state dipole orientation. This is a significant finding, meaning that for obtaining the ground state dipole orientation of a dipolar structure we do not need computationally demanding *fmincon* procedure [93] anymore. Just a simple direct search over the range of α , using a reasonable precision (i.e., $\alpha \in [-\pi, \pi]$ with a step of 10^{-3}), solves our optimization problem.

2.4 Degeneracy in 2D triangular and square lattice and properties of tubes

2.4.1 Ground state of 2D triangular and square lattice

First, we investigate the dependence of ground state energy on dipole moment orientation. All dipoles in triangular lattice are parallel and allowed to rotate only

2. Confined dipolar systems

around a fixed axis orthogonal to the plane, see Figure 2.8(a). There is a continuous ground state for any in-plane angle θ with cohesive energy value $u_{AB} \simeq -2.7586$, which is the cohesive energy of an infinite triangular two dimensional lattice. This value is defined as [94, 95]:

$$u_{AB} = -2\zeta(3) + 16\pi^2 \sum_{k=1}^{+\infty} \sum_{l=1}^{+\infty} \cos(kl\pi) K_0(kl\sqrt{3}\pi). \quad (2.36)$$

For an infinite square two dimensional lattice, similarly, there is a continuous degeneracy of its ground state, described in Figure 2.8(b)-(c). A continuous state, in this case, involves a unit cell of four particles. The moments in a unit cell are synchronously coupled and in our notation take directions θ , $\pi - \theta$, $\pi + \theta$, and $-\theta$, in anti-clockwise direction in Figure 2.8(b). The ground states found are obviously antiferromagnetic, with the total dipole moment within the cell conserved and equal to zero. The most striking is the so-called *vortex state* for $\theta = \pi/4$ with a fully enclosed circulation of the magnetic dipole moment within the unit cell. The ground state cohesive energy value is $u_{AA} \simeq -2.5494$, which is the cohesive energy of an infinite square two dimensional lattice. This value is defined as [94, 95]:

$$u_{AA} = -2\zeta(3) + 16\pi^2 \sum_{k=1}^{+\infty} \sum_{l=0}^{+\infty} k^2 \{K_0[4k(l+1)\pi] - K_0[2k(2l+1)\pi]\}. \quad (2.37)$$

We will use the calculated ground state energy value as an absolute point for comparison of energies of different states in tubes with square or triangular lattice structure.

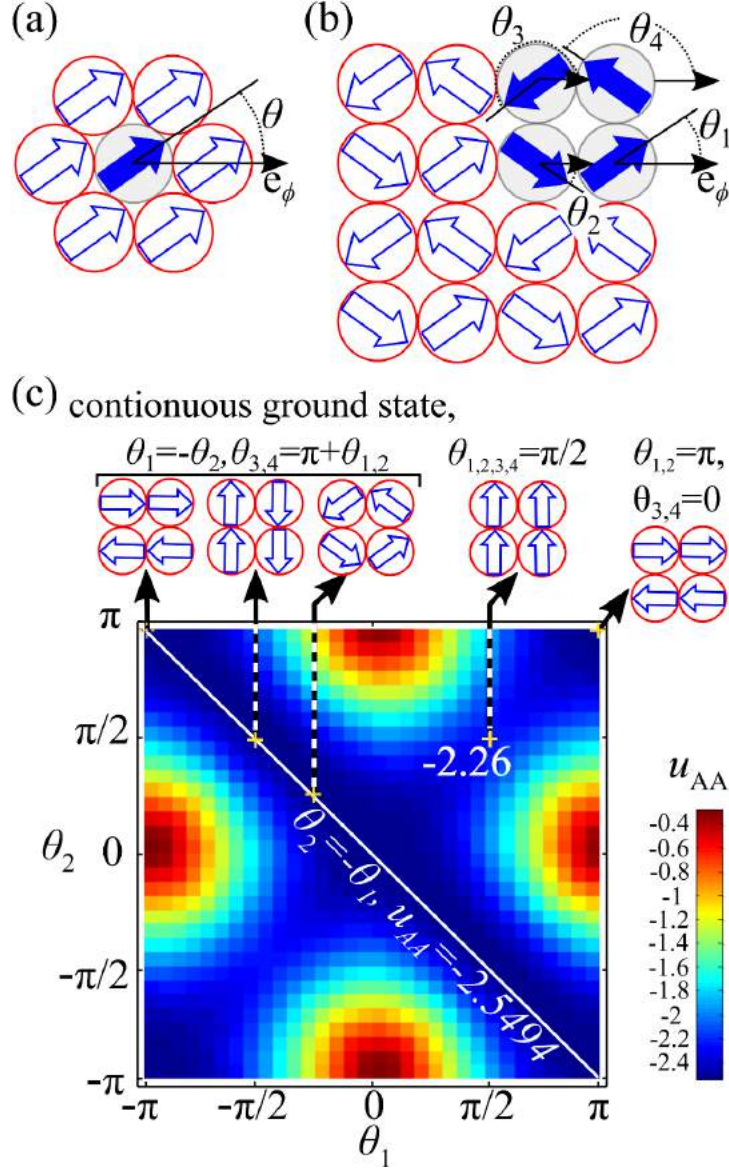


Figure 2.8: Visualization of degenerate states in infinite (a) triangular and (b) square lattice, i.e., AB and AA packings, respectively. The dipoles are depicted as arrows located in the center of the spheres. In case of triangular lattice the unit cell consists of a single particle (as noted in panel (a) of this figure) and in case of square lattice it consists of four particles (as noted in panel (b) of this figure). (c) Energy landscape for square lattice is shown with respect to two θ_1 and θ_2 out of four magnetic moments in the unit cell. Other two moments were oriented so the energy of the system is minimal. One can observe a flat valley of degenerate ground state, $\theta_2 = -\theta_1$, with energy $u_{AA} \simeq -2.5494$. The saddle point which represents square plane with uniform dipole moment orientation with energy $u_{AA}^{\text{sd}} = -2.26$ is also marked. The curves are drawn through the discrete points and they are smooth. The results are in principle scale independent.

2.4.2 Degeneracy break-up with curvature in case of AA and AB tubes

Wrapping of the plane around the confinement cylinder will make the system quasi one-dimensional and break the degeneracy [96]. We will discuss repercussions of the degeneracy breakup on cohesive energy for different dipole moment orientations. We analyze the degeneracy breakup in infinite tubes: according to tube's cylindrical geometry, we represent the dipole moment of the i -th particle in cylindrical coordinates like:

$$\vec{m}_i = m_{i\phi}\vec{e}_\phi + m_{iz}\vec{e}_z, \quad (2.38)$$

with constraints $m^2 = m_{i\phi}^2 + m_{iz}^2$ ($i = 1, \dots, N$). The parallel component with respect to tube's axis is given by m_z and the orthogonal component is m_ϕ (i.e., m_ϕ is tangential to cylinder's circumference). In Figure 2.9, we follow the dependence of energy on angular parameter θ , $m_{iz} = m \sin(\theta)$. We find that axial dipole moment orientation (i.e., $\theta = \pi/2$) represents the ground state for both AA and AB tubes while circular orientation (i.e., $\theta = 0$) is the most unfavorable, as seen in Figure 2.9.

Between circular and axial dipole moment orientation (i.e., for the range $0 < \theta < \pi/2$), we observe a continuous decrease of cohesive energy with increasing axial alignment of dipole moment orientation. These transition states we call *vortex* in case of square AA tubes and *helical* in case of triangular AB tubes, e.g., $\theta = \pi/4$ in Figures 2.9(a) and (b), respectively. The cohesive energy of different configurations in Figure 2.9 converges to a continuously degenerate state with increasing curvature N following the next power law (see inset in Figure 2.9):

$$u^N - u^\infty \sim N^{-2}. \quad (2.39)$$

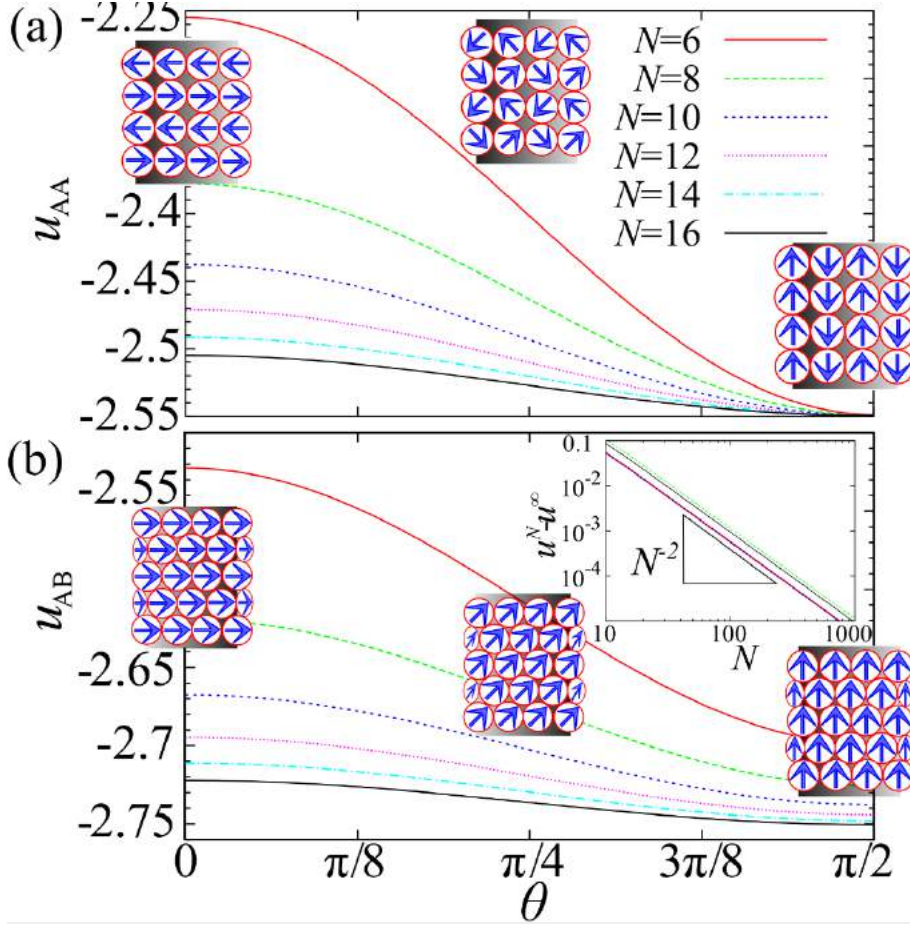


Figure 2.9: Cohesive energy spectrum of configurations for dipole orientations in Figure 2.8 on a curved surface of the infinitely long tube for (a) square AA and (b) triangular AB tubes. Breaking of degeneracy with respect to angle θ due to the curvature, i.e., proportional to the number of particles in the constitutive ring N , is shown. The axial dipole moment orientation corresponds to $\theta = \pi/2$. The inset shows convergence of cohesive energies for $\theta = 0$ and $\theta = \pi/4$ to the infinite two dimensional planar value u (for square lattice $u_{AA} = -2.5494$ and for triangular lattice $u_{AB} = -2.7586$).

2.5 Cohesive energy-packing relations in dipolar helices

We have described geometry of helices and tubes composed of hard spheres in section 2.1. In the following section 2.5 we have introduced dipolar interaction model and three relevant dipole moment orientations. Setting up the geometry and dipole moments represents a preparation for the key considerations which are dedicated to the investigation of cohesive energy-configuration relations of dipolar helices (and

dipolar tubes, as their sub-classes). A dipolar configuration is determined by the next two components: (i) structure by means of geometry (how are the hard spheres positioned spatially) and (ii) dipole moment orientation (how are the dipole moments of those hard spheres oriented). Two dipolar configurations can be identical in structure, but can have different dipole moment orientation, and vice versa they can have a different structure and the same dipole moment orientation. In this chapter we present our findings about the relations of both configurational components with cohesive energy in case of dipolar configurations under investigation.

2.5.1 Compression of a single-thread helix

A simple way to deform a helix is to compress (or extend) it along its axis, i.e., the z -direction, while ensuring the dipole moments follow the thread. Compression of a helix results in a continuous increase of its surface packing fraction η . Figure 2.10 shows the dependence of cohesive energy u_R on the surface packing fraction η for a single helix with reduced radius ($R/d \simeq 1.7$, chosen in the vicinity of $n_c = 6$ point). Recalling geometrical considerations in section 2.1 the increase of the azimuthal angular shift Γ at prescribed curvature results in a continuous decrease of Δz and in a compression of a helix. The compression process begins with a fully extended helix (i.e., $\eta \rightarrow d/8R \approx 0.073$) where the chain stands up with $\Delta z/d = 1$, and the cohesive energy of an infinite chain is $u \simeq -2.404$ [29]. The compression ends when two successive turns of the helix touch, i.e., the coordination number of particles in the helix changes from $n_c = 2$ to $n_c = 4$. We also address the minimal energy of the helix with respect to the dipole moment orientation (i.e., not necessarily prescribed by tangentially following the helix). From Figure 2.10, we observe that $u_R = u_R(\eta)$ is non-monotonic. We can identify two regimes: (i) At small packing fraction up to $\eta \leq 0.4$ (with no touching turns), the compression of the helix requires energy input and therefore cohesive energy increases. The reason for this is that two distant consecutive turns of the helix experience weaker attraction upon increasing η . (ii) In the regime of high $\eta \geq 0.4$ where successive turns are allowed to be close or even touching, the cohesive energy starts to decrease as η increases, i.e., the helix would compress on its own without the input of energy. This is a consequence of

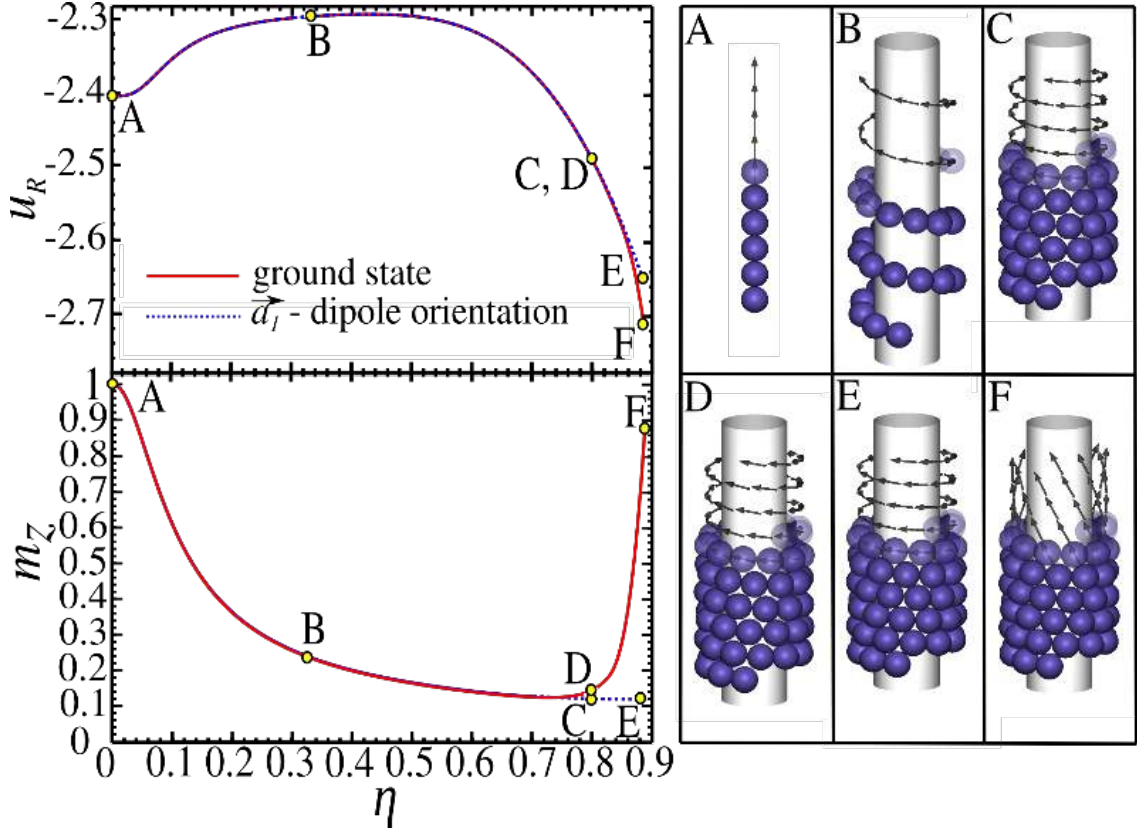


Figure 2.10: Compression of single thread helix on a cylindrical confinement with fixed radius ($R/d \simeq 1.7$). Dependence of cohesion energy (upper left panel) and axial component of the dipole moment (lower left panel) on packing fraction is shown for two characteristic dipole moment orientations: one that follows the thread structure, i.e., spanning vector \vec{d}_1 , and ground state dipole moment orientation obtained by full energy minimization (check subsection 2.3.2 of section 2.3). The illustrations of characteristic structures and corresponding dipole moment orientations are provided as well, in the panels on the right side.

enhanced attraction caused by the discreteness of the constitutive dipolar spheres, see Reference [97]. The overall polarization order parameter $\langle m_z \rangle$ is also analyzed in Figure 2.10. During most of the course of the helix compression, see Figure 2.10, a dipole moment orientation following the helix corresponds to the ground state structure up to $\eta \approx 0.8$, check points C and D in Figure 2.10 (the details of ground state calculations are presented in section 2.3). Only for very high packing fractions, i.e., $\eta > 0.8$, the helix direction is accompanied by a significant reduction in cohesive energy (see points E and F in Figure 2.10). The highest difference in $\langle m_z \rangle$

occurs for $\eta \approx 0.887$, where $n_c = 4$ helix with touching turns is formed, and the energy difference is $u_R^E - u_R^F \simeq 0.06$. Corresponding values of axial dipole moment component m_z for points E and F are $m_z^E \simeq 0.12$, $m_z^F \simeq 0.88$, respectively.

2.5.2 From square to triangular arrangement of a single-thread helix

The crucial question which we ask about dipolar helices and tubes is: how does their cohesive energy depend on structural changes and especially on curvature (quantified by the helix radius R). With increasing curvature the structure changes from the triangular to square arrangement and vice versa through a continuous series of rhombic configurations. We study first in detail systems with dipole moments following the spanning vector that are most oblique to helix axes, see Figure 2.7(d). For the sake of comparison with tubes (AA/AB tubes), we also chose dipole moments that are building vortices along the rings, check Fig 2.7(a). Motivation for that choice stems from a previous study [29], where it has been shown that finite AB tubular systems are energetically favorable, see Figure 2.7(a) (dipole moment orientation is perpendicular to the tube's axis).

The surface packing fraction η (Equation 2.8), the angular coordination order parameter ξ (Equation 2.13), and the cohesive energy per particle u_R (Equation 2.26), are plotted versus the reduced helix radius R/d in Figure 2.11. Actually, the energy and structural properties change in an oscillatory quasi-periodic manner and they are enveloped from both sides with the properties of AA and AB tubes, see Figure 2.11. In Figure 2.12 behavior of these observables is depicted within one period ($R/d \in [2.09, 2.26]$, which has been chosen arbitrary). In one period, the number of particles (n) in a constitutive ring of (AA/AB) tubes is increased for one, i.e., from n -ring to $n+1$ -ring. Within this period, the order parameter changes from $\xi = 0$, i.e., square arrangement, to $\xi = 1$, i.e., triangular arrangement, via a continuous rhombic transformation, see Figure 2.12(a). The radii of densely packed helices are roughly in the middle between two corresponding (AB/AA) tube radii, see Figure 2.12(a). This is a result of the radial constraint and excluded volume.

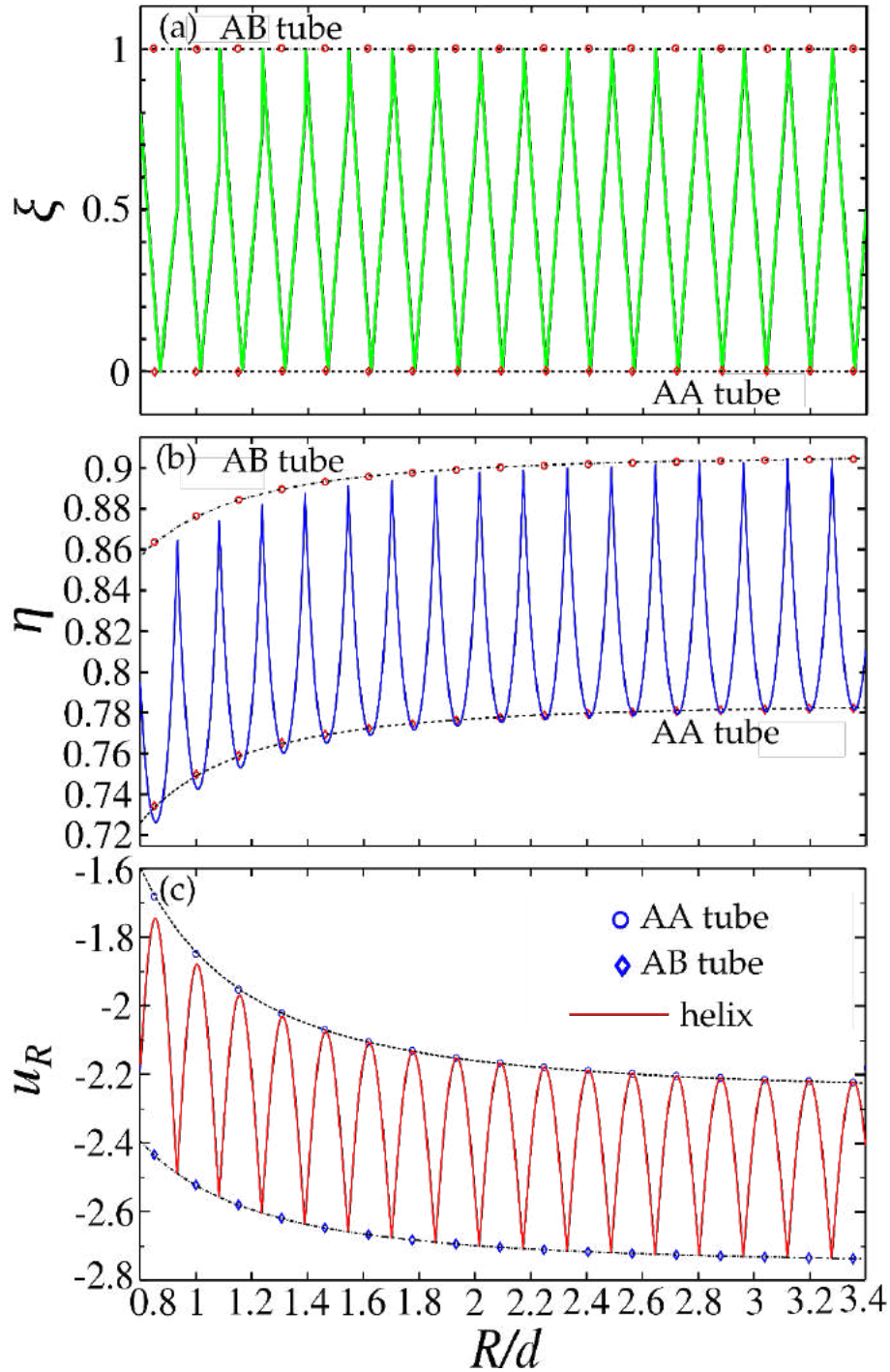


Figure 2.11: Dependence of (a) angular coordination order parameter ξ , (b) packing density η and (c) cohesive energy u_R on helix radius R/d , for \vec{a}_1 dipole orientation. *AA* and *AB* tube points are clearly indicated, they bracket the parameter values of helices, like a kind of envelopes (solid and dashed lines connecting the tube points are power law fits).

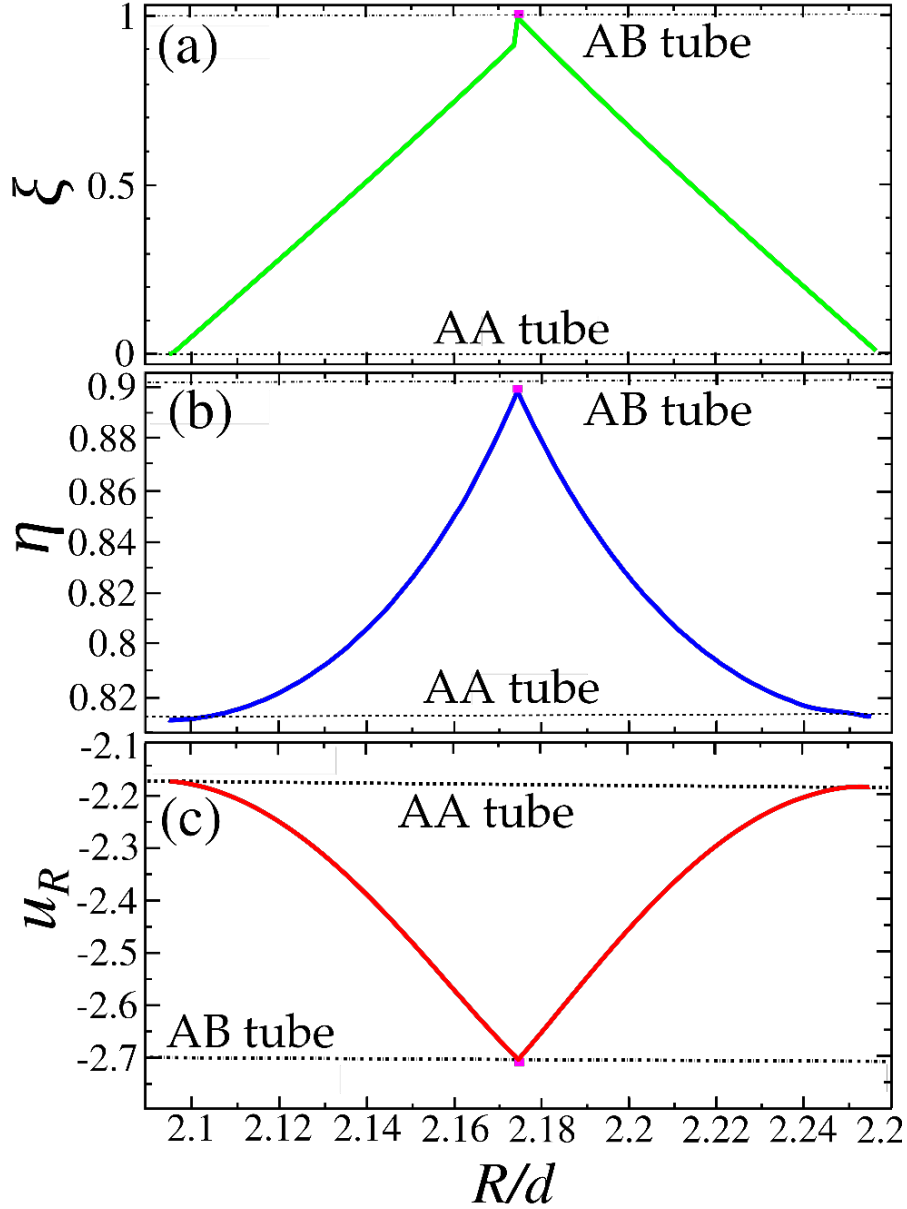


Figure 2.12: Dependence of (a) angular coordination order parameter ξ , (b) packing density η and (c) cohesive energy u_R on helix radius R/d , for a segment in vicinity of $R_{(13,1)}/d = 2.17$ of Figure 2.11. AA and AB tubes are represented with discrete points since they can be formed only with a fixed number of particles in a ring, the fitted (power law) curves serve only as a guide to the eye.

Though in a single thread helical structure we cannot close rings in the plane perpendicular to the cylinder axis, one can nevertheless realize a full 360° helix turn with roughly $n + 1/2$ particles. We observe discontinuity and strong asymmetry of

the angular coordination order parameter ξ at the mid-period ($R_{(13,1)}/d \approx 2.17$), see Figure 2.12(a). This is due to a change of the number of lateral threads n_2 , see Figure 2.7(e), at the mid period going from $n_2 = 9$ to $n_2 = 10$, see Figure 2.12(a). With decreasing curvature, the surface packing fraction increases globally, see Figure 2.11(b). We observe oscillatory behavior as the system continuously evolves from the square to triangular arrangement and vice versa. The AA and AB tubes still roughly bound the values taken by the surface packing fraction. At the helix radius $R/d > 3.4$, see Figure 2.11(b), we are already within 3% of the asymptotic expected values in the planar case. In contrast to the angular coordination parameter ξ , the surface packing fraction η is continuous everywhere, compare Figures 2.12(a) and (b). Moreover, at the mid-period the η value is slightly (and systematically, see Figure 2.11(b)) above the interpolated value stemming from AB tubes (see Figure 2.12(b)). In Figure 2.11(b) and (c), it can be clearly seen that the profiles of energy oscillations u_R and the surface packing fraction η are anti-correlated. The mid-period values u_R coincide with interpolated values stemming from AB tube radii (confirmed by Figures 2.11(c) and 2.12(c)).

2.5.2.1 Looking for the ground state

At this point, we would like to discuss mechanisms which govern the minimal energy dipole moment orientation near the mid-period transition point (more details about implementation are provided in section 2.3). There are three privileged directions in a helix: two which follow helix spanning vectors (determined by \vec{a}_1, \vec{a}_2) and the third one which is the direction of the helix axis. These privileged directions come into play in two competing mechanisms: (i) The first mechanism is typically dictated by first neighbor interactions which favor dipole moments following the thread directions. (ii) The distant-neighbor interactions favor the distribution of dipole moments parallel to the helix axis. We can justify these two mechanisms as follows. It is well known for a small finite system that rings are formed with dipole moments building vortices, see Reference [29]. When a helix turn is projected along the z -axis, the resulting figure is highly reminiscent of the vortex discussed above. The head to tail configuration is favored at long distances, explaining the second advocated

mechanism. The abrupt change in dipole orientation in the direction of the axis $\langle m_z \rangle$, seen in Fig 2.13(b), is correlated with the discontinuous change in the angular coordination order parameter ξ in the vicinity of transition, see Figure 2.12(a). At the mid-period point $R_{(13,1)}/d = 2.17$ dipole orientation in the direction of the axis $\langle m_z \rangle$ is close to one, but not exactly one, see Figure 2.13. For the sake of comparison with tubes (AA/AB tubes), we choose dipole moments that are parallel with the helix axis, see Figure 2.7(c). The fact that the system is able to relax its dipole moment orientation to the ground state results in more dependence of energy on confinement curvature around the mid-point. The degree of asymmetry of u_R is stronger around the transition point, see Figure 2.13(b), than in the excited state in Figure 2.12(c). The ground state calculations confirm the high stability of AB tubes (see Figure 2.12(c)).

2.5.3 Cohesive energy of multi-thread helices at high surface packing fraction

In this part, we consider the high surface packing fraction regime with $n_c = 6$. Some representative structures including dipole moment streamlines are displayed in Figure 2.7. The streamlines following spanning unit cell vectors \vec{a}_1 (oblique to the helix axis) and \vec{a}_2 (more aligned to the helix axis) are also shown. It is possible to polarize the helix by a homogeneous external field parallel to its axis. For symmetry reasons, a reversal of the external field should result in the reversal of the dipole orientation. In the case of magnetic dipoles, it should also be possible to polarize the system to follow \vec{a}_1 and \vec{a}_2 spanning vectors by combination of a curling magnetic field of electric current flowing through the confining cylinder and the homogeneous external magnetic field parallel to its axis. Dipole moment distributions in the ground states are also indicated for comparison in Figure 2.7. In analogy with the study of a single helix case, we start analysis with a dipole moment distribution prescribed by tangentiality with thread backbone. In Figure 2.14, cohesive energy for the \vec{a}_1 -generated dipole moment distribution is shown for different helical structures. The cohesive energy in a planar triangular lattice, $u_\infty \simeq -2.759$, represents the energy

value which will be reached asymptotically ($R/d \rightarrow +\infty$) for all considered structures. As already found for AB tubes in Reference [29], cohesive energy exhibits the scaling law of the form $u_R - u_\infty \sim R^{-2}$, see Figure 2.14. The cohesive energies of all three helices and AB tubes are weakly dependent on the number of threads for \vec{a}_1 -generated dipole moment distribution. This is in accordance with surface packing fraction behavior reported in Figure 2.6. A comparison with the azimuthal angular shift parameter Γ_1 , see Figure 2.5, and the corresponding cohesive energy (for \vec{a}_1 -generated dipole moment distribution) clearly reveals a correlation between these two quantities. In Figure 2.15, cohesive energy for \vec{a}_2 -generated dipole moment distribution is compared with ground state energy for different number of threads. There exists an analogous correlation (as discussed for \vec{a}_2 -dipole distribution) between the azimuthal shift Γ_2 and the resulting cohesive energy, compare Figures 2.5 and 2.15. The smallest compatible radius R for multi thread helices ($n_2 = 2, 4$) is obtained for ZZ tubes ($n_1 = n_2$). In Figure 2.15, the corresponding radii read $R_{(2,2)}/d = 0.61$ and $R_{(4,4)}/d = 1.13$. In this case the \vec{a}_2 and ground state dipole moment orientations are the same, see Figure 2.7(k). Strikingly, ZZ tube ground states converge very fast to the expected planar value u_∞ at the smallest accessible radii, i.e., the largest curvature, within less than 1% of the planar case, see Figure 2.15 for $R_{(2,2)}/d = 0.61$. A structural similarity of ZZ tubes, with typical experimental images of microtubules is striking, see Figure 2.7(k). ZZ tubes can be created by closing the rectangular strip on a cylinder. We should notice the structural characteristic of ZZ tubes' decomposition into chains which are analogous to filaments in microtubules.

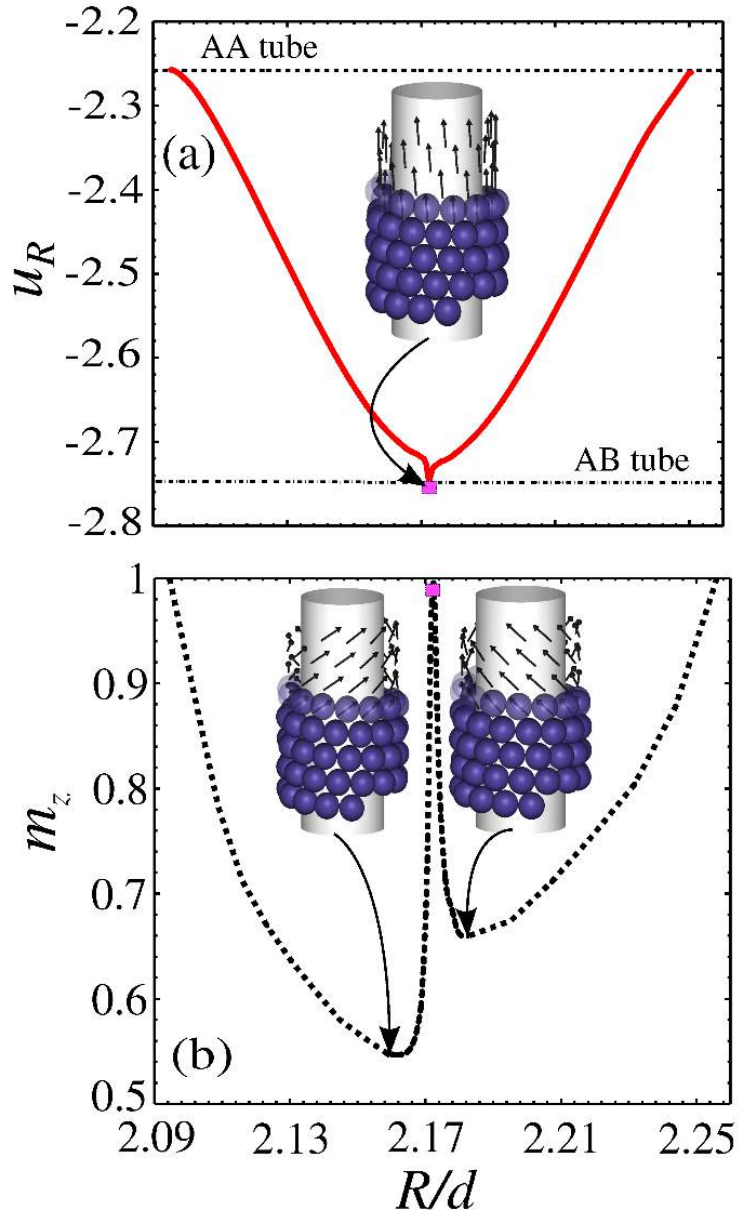


Figure 2.13: Dependence of (a) cohesive energy, and (b) polarization in the direction of z axis m_z on helix radius R/d (in the ground state), for a chosen segment of Figure 2.11. AA and AB tubes are represented with discrete points since they can be formed only with a fixed number of particles in a ring, the fitted (power law) curves serve only as a guide to the eye. The point which represents the dense helix with $(n_1, n_2) = (13, 1)$ and $R_{(13,1)}/d = 2.17$, is marked with a rectangle.

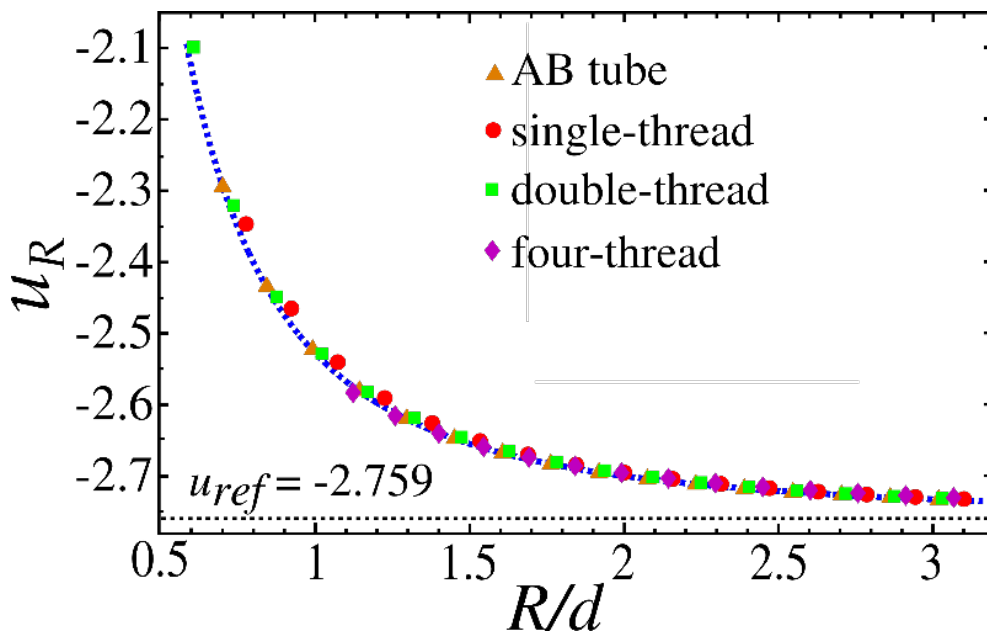


Figure 2.14: Dependence of cohesive energy u_R on helix radius R/d , for different families of helices having $\{1, 2, 4\}$ threads, and AB tubes, with \vec{a}_1 dipole orientation.

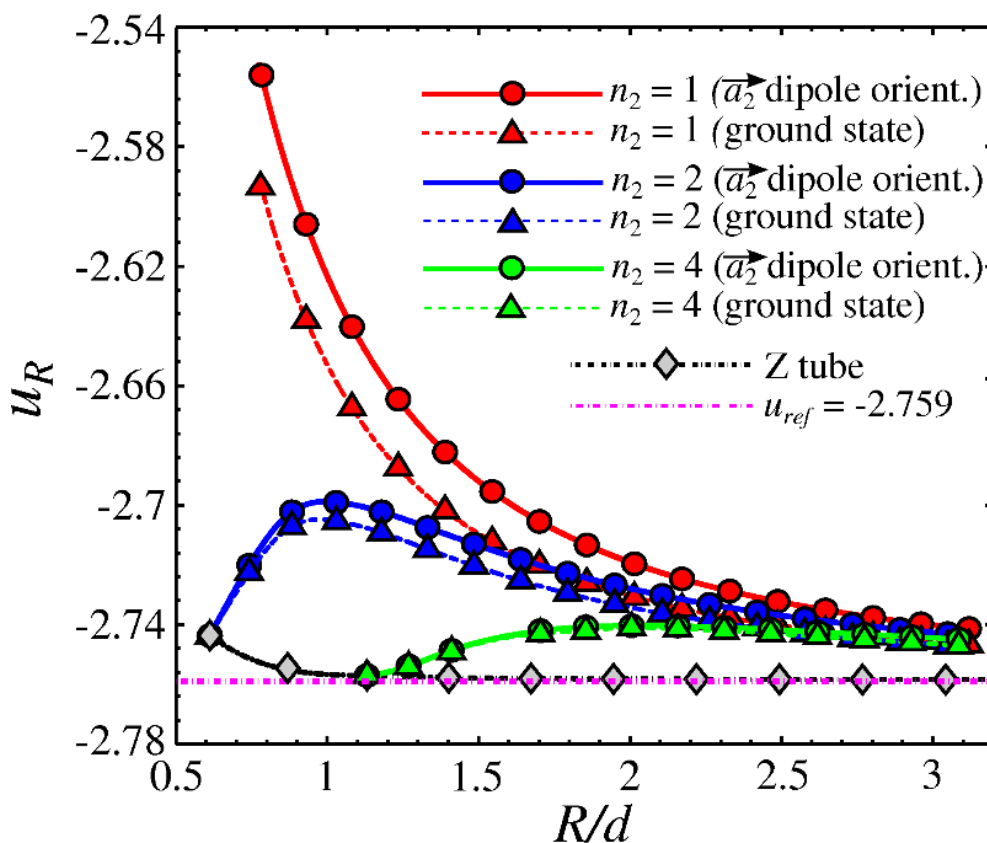


Figure 2.15: Dependence of cohesive energy u_R on helix radius R/d , for different families of helices having $\{1, 2, 4\}$ threads, and AB tubes, with \vec{a}_2 and optimized dipole moment orientation.

Chapter 3 Ionic liquids

3.1 Methods

In this section we present the methods applied in the study of ionic systems. First we explain the basics of the molecular dynamics (*MD*) method. Next, we give a short overview of the *LAMMPS* code for *MD* simulations, since all *MD* simulations presented in this thesis were performed using the *LAMMPS* software package [98].

3.1.1 Molecular Dynamics method

Molecular dynamics (*MD*) represents a simulation technique which generates trajectories of a system of N particles by numerical time integration of Newton's classical mechanics equations of motion [99]. An *MD* simulation is defined by: the interaction potential by which the particles interact, initial conditions (IC) and boundary conditions (BC). Let us consider a system of N particles (check Figure 3.1) in a volume V . The Newton's equations of motion for the system of N particles are:

$$m \frac{d^2 \vec{r}_i}{dt^2} = \vec{F}_i(\vec{r}_1, \vec{r}_2, \dots, \vec{r}_N), i = 1, \dots, N, \quad (3.1)$$

where \vec{r}_i are the position vectors and \vec{F}_i are the forces acting on the particles of a system. It is often case in *MD* simulations that the forces can be derived from interaction potential functions $U(\vec{r}_1, \vec{r}_2, \dots, \vec{r}_N)$, representing the potential energy of the system:

$$\vec{F}_i(\vec{r}_1, \vec{r}_2, \dots, \vec{r}_N) = -\nabla_{\vec{r}_i} U(\vec{r}_1, \vec{r}_2, \dots, \vec{r}_N). \quad (3.2)$$

Equation 3.2 is consistent with the conservation of the total energy. We might define mechanical energy of the system as: $E = K + U$, where kinetic energy is defined as:

$$K = \sum_{i=1}^N \frac{1}{2} m_i \left(\frac{d\vec{r}_i}{dt} \right)^2, \quad (3.3)$$

and potential energy is defined as:

$$U = U(\vec{r}^N(t)), \quad (3.4)$$

where $\vec{r}^N(t)$ denotes position vectors of all N particles in the system. We emphasize that E should be a conserved quantity, if the system is isolated. The potential of an isolated system (no external forces present) can be written in the simplest case as a sum of pairwise interactions:

$$U = \sum_{i=1}^N \sum_{j>i}^N u(r_{ij}), \quad (3.5)$$

where $\vec{r}_{ij} = \vec{r}_i - \vec{r}_j$, $r_{ij} = |\vec{r}_{ij}|$ and $i > j$ eliminates the double counting of the particle pairs. Practically it means that the forces acting on the particles are resultants of the forces coming from the individual interactions with the rest of the particles:

$$\vec{F}_i = \sum_{j \neq i}^N \vec{f}_{ij}, \quad \vec{f}_{ij} = -\frac{du(r_{ij})}{dr_{ij}} \cdot \frac{\vec{r}_{ij}}{r_{ij}}. \quad (3.6)$$

According to the Newton's third law it stands: $\vec{f}_{ji} = -\vec{f}_{ij}$. Computational effort of solving the equations of motion 3.1 is proportional to N^2 and is mostly related to the force computations. Accordingly, to speed-up the computations it is desirable to express the forces analytically. In order to further more reduce the computational effort, it is a standard practice in *MD* simulations to cut off the potential at some limiting distance, i.e., we neglect the potential if the distance between two interacting atoms is $r_{ij} > r_{cut}$, where r_{cut} is reasonably chosen. For example, in case of the Lennard-Jones potential (standard potential in *MD* simulations) usually it is set that $r_{cut} = 2.5 \cdot \sigma$, where σ determines the length scale.

In principle, we might treat an *MD* simulation as a numerical experiment [100], hence the methodology is practically the same like in a real experiment, as we can see in the schematic of a typical *MD* simulation in Figure 3.2.

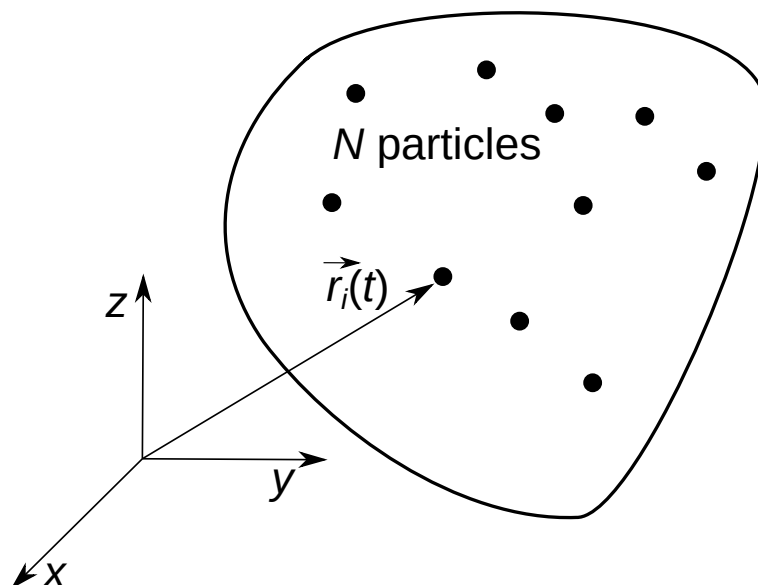


Figure 3.1: Illustration of an *MD* system with N particles.

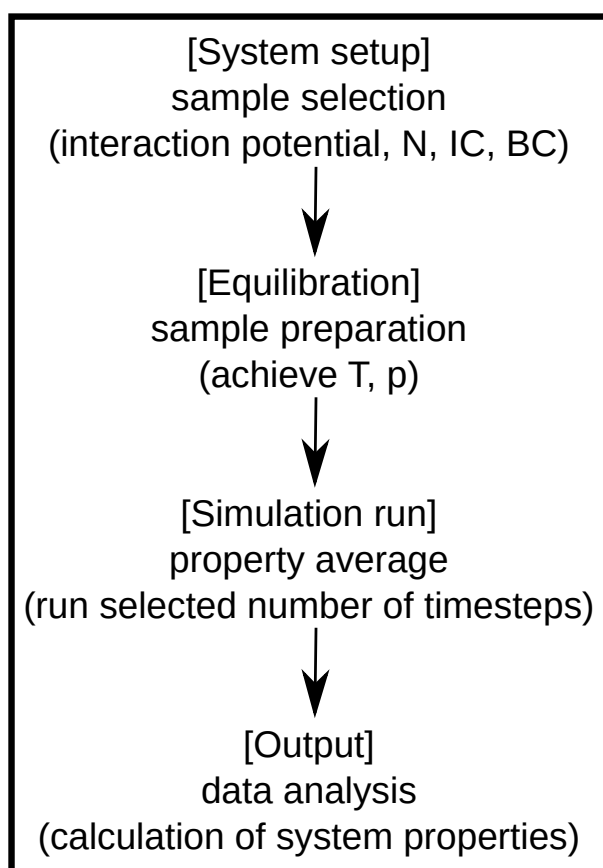


Figure 3.2: Basic schematic of an *MD* simulation.

In the first step we should setup the system, which means: selecting a proper interaction potential, choosing the number of particles in the system and setting up

their properties (shape, mass, charge), defining initial and boundary conditions. The subsequent step, after the system setup has been done, is the system equilibration which means achievement of desired temperature and pressure (macroscopic properties which depend on the microstate of the system). After the system setup and equilibration are done, simulation is run a given number of simulation steps and averaged characteristics are calculated (for example, radial distribution function $g(r)$). In the end, output data is analyzed and based on that, the desired quantities are computed. Besides equilibrium *MD* simulations, there are non-equilibrium molecular dynamics (*NEMD*) simulations. For example, a system is exposed to perturbation or high external forces and its response is analyzed, like in simulations of mechanical deformations. We have used *NEMD* simulations in the way that shearing of the simulation box (mechanical deformation) was imposed, and by analyzing bulk *IL's* response to the imposed shearing, we have determined *IL's* viscosity coefficient. There are five key components of *MD* simulations and those are: (i) initial conditions (IC), (ii) boundary conditions (BC), (iii) force computation, (iv) integrator and (v) computation of system's characteristics.

3.1.1.1 The Lennard-Jones potential

The most common pair potential for describing the interaction of van der Waals systems is the Lennard-Jones potential (*LJ* potential), given by the formula:

$$U^{LJ}(r_{ij}) = 4\epsilon \left[\left(\frac{\sigma}{r_{ij}} \right)^{12} - \left(\frac{\sigma}{r_{ij}} \right)^6 \right], \quad (3.7)$$

where r_{ij} is the distance between the atoms i and j . The ϵ parameter defines the strength of the *LJ* interaction and the σ parameter defines the length scale. *LJ* potential is strongly repulsive at short distances, it crosses zero at $r_{ij} = \sigma$, i.e., $U^{LJ}(r_{ij} = \sigma) = 0$. *LJ* potential reaches its minimum $U^{LJ}(r_m) = -\epsilon$ at $r_m = 2^{1/6}\sigma \approx 1.1225\sigma$ and it has an attractive tail at long distances. Values of the parameters $\{\epsilon, \sigma\}$ are chosen to model physical properties of a real system. For example, *LJ* potential was initially proposed to model liquid argon. Let us now analyze the two terms from the square brackets of Equation 3.7. The term

$\propto r_{ij}^{-12}$ dominates at short distances and it models the repulsion due to the non-bonded overlap of electronic orbitals. It might have an arbitrary form meaning that other exponents or even other functional forms are possible. However, we should think about minimizing the computational effort, hence in most cases this form with $\left(\frac{\sigma}{r_{ij}}\right)^{12}$ is fine. The term $\propto r_{ij}^{-6}$ dominates at long distances and models the van der Waals forces caused by the dipole-dipole interactions due to the fluctuation of dipoles. These weak forces are responsible for the bonding character of systems like rare gases, such as argon or krypton. The interaction force due to the interaction via LJ potential, see Equation 3.7 is:

$$\vec{f}_{ij} = \frac{48\epsilon}{r_{ij}^2} \left[\left(\frac{\sigma}{r_{ij}}\right)^{12} - \frac{1}{2} \left(\frac{\sigma}{r_{ij}}\right)^6 \right] \vec{r}_{ij}. \quad (3.8)$$

As the force is expressed analytically, this is advantageous in terms of the reduction of computational effort.

3.1.1.2 Thermodynamic properties

Key thermodynamic properties of an MD system are the temperature and pressure. Temperature of the system might be introduced via mean kinetic energy of the system:

$$\frac{1}{2N} \sum_{i=1}^N m_i \left(\frac{d\vec{r}_i}{dt}\right)^2 = \frac{3}{2} k_B T \Rightarrow T = \frac{1}{3Nk_B} \sum_{i=1}^N m_i \left(\frac{d\vec{r}_i}{dt}\right)^2. \quad (3.9)$$

By expressing the temperature T in function of the kinetic energy K we obtain the next relation:

$$T = \frac{2K}{3Nk_B}. \quad (3.10)$$

In case that we consider the temperature T and the density ρ as independent variables, we might express the energy of the system E and the pressure p . These quantities link the microscopic and macroscopic level and can be easily measured in an MD simulation. We should mention that in an MD simulation usually the energy is conserved, while the temperature fluctuates, hence the average temperature

$\langle T \rangle$ should be used instead of T . Pressure is defined by the formula:

$$pV = Nk_B T + \frac{1}{3} \left\langle \sum_{i=1}^N \vec{r}_i \cdot \vec{F}_i \right\rangle. \quad (3.11)$$

In case of a pair potential this formula is:

$$pV = Nk_B T + \frac{1}{3} \left\langle \sum_{i<j}^N \vec{r}_{ij} \cdot \vec{f}_{ij} \right\rangle. \quad (3.12)$$

Bearing in mind the relation 3.10 between the temperature T and the kinetic energy K , we express the pressure p as:

$$p = \frac{\rho}{3N} \left\langle 2K + \sum_{i<j}^N \vec{r}_{ij} \cdot \vec{f}_{ij} \right\rangle. \quad (3.13)$$

Contrary to the total energy $E_{\text{tot}} = K + U$ which should be conserved during a simulation, the temperature and the pressure fluctuate and should be averaged over a chosen number of timesteps.

3.1.1.3 Analysis of the key components of a typical molecular dynamics simulation

In the following text we briefly analyze the key components of a typical *MD* simulation, which include: (i) initial conditions (IC), (ii) boundary conditions (BC), (iii) force computation, (iv) integrator and ensemble and (v) computation of system's characteristics [99].

(i) Initial conditions (IC)

As Newton's equations of motion are ordinary differential equations of the second order, initial conditions are defined as:

$$\vec{r}^{2N}(t=0) = \vec{r}^{2N(0)}; \quad \frac{d\vec{r}^{2N}}{dt}(t=0) = \frac{d\vec{r}^{2N(0)}}{dt}. \quad (3.14)$$

Generating of IC is simple for ordered systems like crystals, but in case of amorphous solids or for polymer chains it should be treated carefully. Setting the IC is important

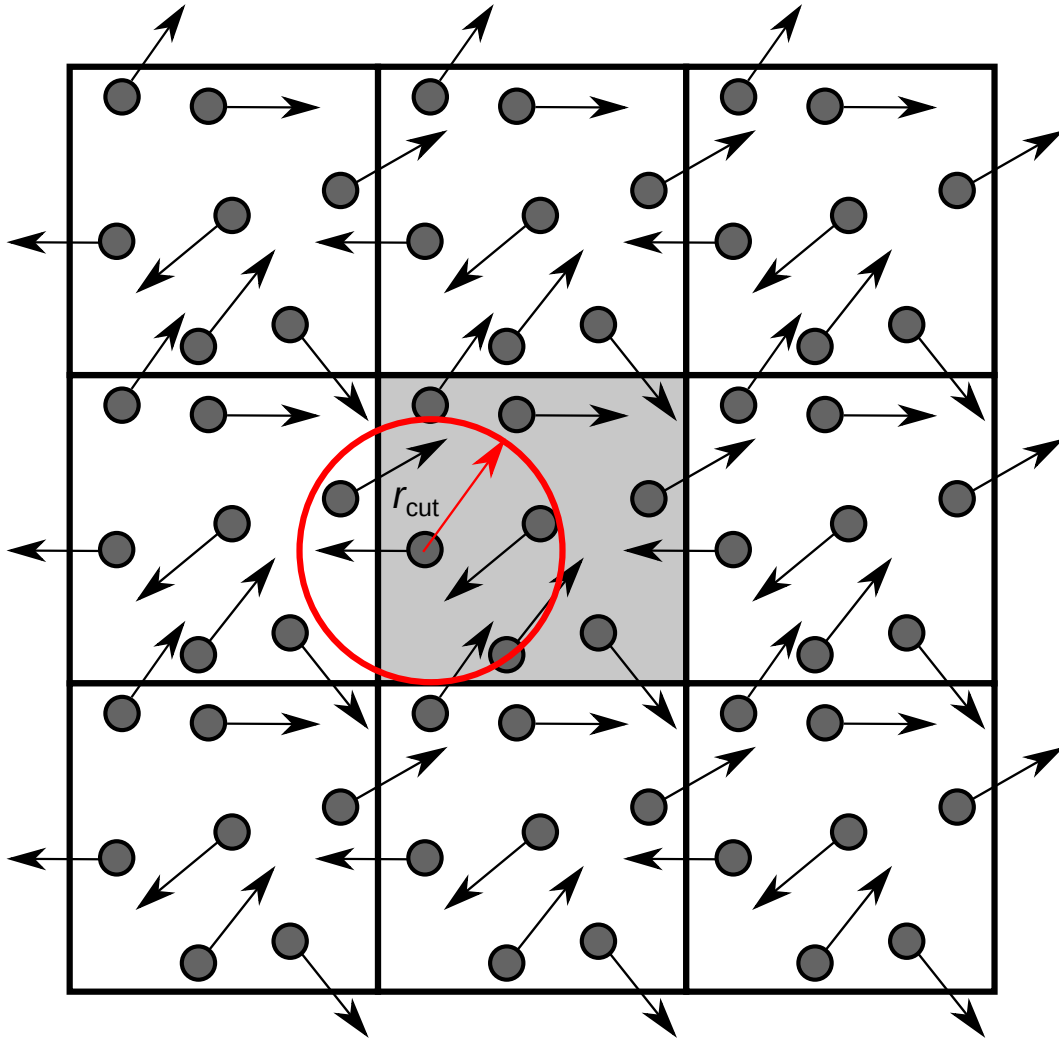


Figure 3.3: Illustration of periodic boundary conditions (*PBC*). Trajectories of only the atoms in the central cell, also known as supercell (square filled with gray) are explicitly followed. The supercell is infinitely replicated in a given $2D$ or $3D$ space. In this figure we show an example of a $2D$ system with periodic boundaries in both directions in a plane. An atom (let us label it as referent atom) from the supercell interacts with other atoms from the supercell, as well as with the atoms from neighbouring copies of the supercell, under the condition that their distance from the referent atom is within the cutoff radius. Interaction is neglected in case the distance is larger than the cutoff radius.

because often it causes errors. For example, if the particles are positioned too close at the beginning of a simulation, the forces between them get too high.

Related to assignment of initial velocities, it should be taken into account that each independent degree of freedom should carry kinetic energy of $k_B T/2$. Such

a condition can be met by taking initial velocities from the Maxwell-Boltzmann distribution.

(ii) **Boundary conditions (BC)**

The behaviour of finite systems is quite different from the behaviour of infinite systems. The number of particles for simulating bulk properties of macroscopic systems has an important role, unless we simulate clusters of atoms in which case the number of constituents is well-defined. No matter how large the simulated system is, the number of particles N is negligible as compared to the number of particles contained in a macroscopic system (at the order of 10^{21} to 10^{23}). In case of macroscopic systems just a small fraction of the particles are located close to the boundaries (walls of the container in which the system is placed). In case of a typical liquid with the order of magnitude of $N = 10^{21}$ particles, the number of particles in the vicinity of the walls is at the order of $N^{2/3} = 10^{14}$, which means that 1 out of 10^7 is a surface particle. Therefore, in systems like liquids the fraction of particles in the vicinity of the walls is negligible. In modern *MD* simulations the typical number of particles which can be handled is at the order of 10^6 particles. In such a system, the fraction of the surface particles is more significant and the behaviour of the system is very impacted by the surface effects. An efficient solution for solving the finite-size problem and for minimizing the surface effects is the application of periodic boundary conditions. When periodic boundary conditions are applied the particles are enclosed in the simulation box, which is replicated to infinity by translation in all three directions $\{x, y, z\}$ completely filling the space. When a particle enters or leaves the simulation box, an image particle leaves or enters the simulation box, hence the number of particles is kept constant. Accordingly, the surface effects are suppressed. Summing up the previous discussion, we note that there are two types of boundary conditions: isolated (*IBC*) and periodic (*PBC*) boundary conditions (for the illustration of *PBC* check Figure 3.3). *IBC* are suitable for the analysis of clusters and molecules, while *PBC* are suitable for the analysis of bulk materials. There are mixed boundary conditions as well, where the system is periodic along one or two dimensions, but not in all three dimensions. In case of *PBC* a system of particles is surrounded by vacuum, those particles interact between each other and

do not interact with anything outside the system, except in case that some external force is introduced.

(iii) **Force computation**

Equation of motion for the i -th particle can be written as [99]:

$$m_i \frac{d^2 \vec{r}_i}{dt^2} = - \sum_{j \neq i} \frac{\partial U(r_i - r_j)}{\partial (r_i - r_j)}, i = 1, \dots, N. \quad (3.15)$$

Computation of the right-hand side of the above equation is the key step which consumes the most computational time in *MD* simulations, so the efficiency of that computation is of crucial importance. For long-range Coulombic interaction there are special algorithms which break it into two terms: one term represents short-range interaction and the other term represents smooth interaction, like a field. Both of those terms can be computed efficiently in different ways. When *PBC* are applied, movement of particles within the basic cell is monitored and the basic cell is surrounded by its periodic copies. A consequence of the application of *PBC* is that each particle i in the simulation box interacts not only with the other particles in the box, but with their images also. This means that the number of interacting pairs is very large. However, this obstacle is usually overcome by setting a cutoff distance, since the interaction of two particles separated by a distance larger than the chosen r_{cut} is neglected. There is the term *minimum image criterion* which claims that among all images of a particle we should consider only the closest ones and neglect the others.

(iv) **Integrator and ensemble**

Newton's equations of motion represent a set of ordinary differential equations of the second order, which can be very nonlinear. Transforming them into ordinary differential equations of the first order in $6N$ -dimensional space $\{\vec{r}^N, \vec{v}^N\}$, general numeric algorithms for solving ordinary differential equations can be applied, such as Runge-Kutta method. However, general numeric algorithms are rarely applied in *MD* simulations, because the existence of Hamiltonian enables more accurate integration algorithms, such as predictor-corrector integrator. There are three main ensembles: micro-canonical, canonical and grand-canonical ensemble. They are dis-

tinguished based on the distribution of initial conditions. When the system is defined by a certain ensemble, it should strictly follow equations of motion, with conserved mechanical energy. Ensemble and integrator are often grouped since there is a class of methods which generate desired ensemble under time integration. In a micro-canonical (NVE) ensemble, system is isolated from the changes in the number of particles (N), volume (V) and energy (E). It corresponds to an adiabatic process in which there is no heat exchange. Micro-canonical MD trajectory can be seen as exchange of potential and kinetic energy, under the condition that the total energy is conserved. In a canonical (NVT) ensemble, the number of particles (N), volume (V) and temperature (T) are conserved. Canonical ensemble is often called constant temperature molecular dynamics ($CTMD$). In NVT ensemble the energy of endothermic and exothermic processes is exchanged with a thermostat. There is a large number of thermostat algorithms which add or remove energy keeping temperature constant. It is not easy to obtain canonical distribution of spatial arrangement and velocities using thermostat algorithms. A wide and relevant topic is which thermostat should be chosen and how its parameters should be set, how does that depend on the system size, how to choose the timestep and integrator. Grand-canonical ensemble represents possible states of a system of particles which is kept in thermodynamic equilibrium (thermal and chemical) with a reservoir. System is considered to be open, in a sense that it can exchange the energy and particles with a reservoir and accordingly, possible states of a system differ in terms of total energy and total number of particles. Volume is the same in all possible states of a system. Thermodynamic variables of a grand-canonical system are chemical potential and temperature. It is called (μVT ensemble, since each of those three quantities is an ensemble constant. There are two main classes of MD integrators: (i) low-order integrators like leapfrog, Verlet, velocity Verlet which is characterized by easy implementation and stability, and (ii) predictor-corrector integrators which are characterized by high accuracy for large timesteps.

- Examples of integrators

We present common integrators in MD simulations, namely: (i) The Leapfrog algorithm, (ii) The Verlet algorithm and (iii) The Velocity Verlet algorithm. In

all three examples the integration of Newton's equations of motion is done with a small timestep δt . In the following text index i is used for an i -th particle where $i = 1, \dots, N$, where N is the total number of particles in the system. Its position, velocity and acceleration are labeled as $\vec{r}_i, \vec{V}_i = \frac{d\vec{r}_i}{dt}, \vec{a}_i = \frac{d^2\vec{r}_i}{dt^2}$, respectively.

(i) The Leapfrog algorithm

In the Leapfrog algorithm the velocities are first computed at the time moment $t + \frac{\delta t}{2}$ and these are used to compute the positions \vec{r}_i , at the time moment $t + \delta t$:

$$\vec{r}_i(t + \delta t) = \vec{r}_i(t) + \vec{V}_i\left(t + \frac{\delta t}{2}\right) \delta t. \quad (3.16)$$

In this way, the velocities leap over the positions, then the positions leap over the velocities:

$$\vec{V}_i\left(t + \frac{\delta t}{2}\right) = \vec{V}_i\left(t - \frac{\delta t}{2}\right) + \vec{a}_i(t) \delta t. \quad (3.17)$$

The advantage of this algorithm is that the velocities are explicitly calculated. However, the disadvantage is that the velocities are not calculated at the same time moment as the positions. The velocities at the time moment t can be computed as:

$$\vec{V}_i(t) = \frac{1}{2} \left[\vec{V}_i\left(t - \frac{\delta t}{2}\right) + \vec{V}_i\left(t + \frac{\delta t}{2}\right) \right]. \quad (3.18)$$

(ii) The Verlet algorithm

New positions and velocities of particles are computed after every timestep. Position of a particle i in time moment $t + \delta t$ can be computed via Taylor expansion over degrees of timestep δt :

$$\vec{r}_i(t + \delta t) = \vec{r}_i(t) + \delta t \frac{d\vec{r}_i}{dt}(t) + \frac{1}{2} \delta t^2 \frac{d^2\vec{r}_i}{dt^2}(t) + \frac{1}{6} \delta t^3 \frac{d^3\vec{r}_i}{dt^3}(t) + \dots \quad (3.19)$$

In a similar way, position of particle i in previous timestep can be written as:

$$\vec{r}_i(t - \delta t) = \vec{r}_i(t) - \delta t \frac{d\vec{r}_i}{dt}(t) + \frac{1}{2} \delta t^2 \frac{d^2\vec{r}_i}{dt^2}(t) - \frac{1}{6} \delta t^3 \frac{d^3\vec{r}_i}{dt^3}(t) + \dots \quad (3.20)$$

Summing of previous two equations leads to the expression which determines posi-

tion of particle i in time moment $t + \delta t$

$$\vec{r}_i(t + \delta t) = 2\vec{r}_i(t) - \vec{r}_i(t - \delta t) + \delta t^2 \frac{d^2 \vec{r}_i}{dt^2}(t) + O(\delta t^4). \quad (3.21)$$

This integrator is called Verlet algorithm, as we can see from Equation 3.21 it uses positions and accelerations at time moment t and positions at time moment $t - \delta t$ to compute new positions at time $t + \Delta t$. The Verlet algorithm does not use explicit velocities. There are two main advantages of the Verlet algorithm: (i) its straightforwardness, and (ii) reasonable storage requirements. The disadvantage is the algorithm's moderate precision. Acceleration of particle i is determined from Newton's equation of motion:

$$\frac{d^2 \vec{r}_i}{dt^2} = -\frac{1}{m_i} \sum_{j \neq i} \frac{\partial U(r_i - r_j)}{\partial (r_i - r_j)}. \quad (3.22)$$

Position of a particle is computed with precision of δt^4 as it is noted with $O(\delta t^4)$. Velocity of particle i in time moment t can be determined from its positions in time moments $t + \delta t$ and $t - \delta t$ with precision of $O(\delta t^3)$, by subtracting the equation for $\vec{r}_i(t - \delta t)$ from the equation for $\vec{r}_i(t + \delta t)$:

$$\frac{d\vec{r}_i}{dt} = \frac{\vec{r}_i(t + \delta t) - \vec{r}_i(t - \delta t)}{2\delta t} + O(\delta t^3). \quad (3.23)$$

Positions and velocities of all particles in a system are computed in each step of MD simulation, producing complete time evolution of the system. In order for this time evolution to be of high accuracy, integration timestep δt should be much shorter than the shortest characteristic time of the system. Simple Verlet integrator is used for systems with constant number of particles, constant volume and constant total energy, which is micro-canonical (NVE) ensemble.

(iii) The Velocity Verlet algorithm

In the Velocity Verlet algorithm, positions, velocities and accelerations at time moment t are used for computing position at time moment $t + \delta t$:

$$\vec{r}_i(t + \delta t) = \vec{r}_i(t) + \vec{V}_i(t) \delta t + \frac{1}{2} \vec{a}_i(t) \delta t^2. \quad (3.24)$$

For computing velocity at time moment $t + \delta t$, velocity at time moment t and acceleration at time moments t and $t + \delta t$ are used:

$$\vec{V}_i(t + \delta t) = \vec{V}_i(t) + \frac{1}{2} [\vec{a}_i(t) + \vec{a}_i(t + \delta t)] \delta t. \quad (3.25)$$

(v) **Computation of system's characteristics**

A big advantage of *MD* simulations is their applicability at the level of classical atoms. All characteristics which are well defined in classical and statistical mechanics can be computed. The two main problems to be taken into account when performing *MD* simulations, are accuracy and efficiency. System's characteristics can be roughly divided into four categories:

- (1) Structural characteristics, for example radial distribution function
- (2) State equation, for example phase diagrams, static response like coefficient of thermal expansion
- (3) Transport characteristics, for example viscosity, thermal conductivity, diffusivity
- (4) Non-equilibrium response - for example plastic deformation

Physical quantity $\langle A \rangle$ is determined as mean value of its values $A(t)$ in time moments t during a long time interval (large number n of *MD* steps) after initial relaxation during long enough time (with relaxation time t_0) [99]:

$$\langle A \rangle = \frac{1}{n} \sum_{j=1}^n A(t_0 + j\delta t). \quad (3.26)$$

If simulation is long enough so that the system can achieve equilibrium state (if simulation is much longer than all relaxation times), this time averaging of quantity $\langle A \rangle$ is equivalent to the ensemble averaging.

3.1.2 *LAMMPS* code for molecular dynamics

An usual algorithm for developing *MD* simulations can be roughly divided into next subsequent steps:

- (i) geometric formation of the simulation setup
- (ii) definition of the atom types and their attributes (e.g., shape, mass, charge)

(iii) definition of the interactions between all atom types

(iv) implementation of the model and *MD* simulation of a certain physical phenomenon, (e.g., in our case we simulate effects related to nanoscopic tribological behaviour of ionic liquids)

(v) storage of the relevant data and its analysis with the goal of obtaining results
LAMMPS (Large-scale Atomic/Molecular Massively Parallel Simulator) is a well-known and widely used *MD* code [98]. Development of *MD* simulations in *LAMMPS* code can be roughly divided into three subsequent phases:

(a) pre-processing, which includes points (i), (ii), (iii) from the above list

(b) processing, actually this is *MD* simulation which corresponds to the point (iv) from the above list and

(c) post-processing, which corresponds to the point (v) from the above list

Processing is done via development of *LAMMPS* scripts, while for pre- and post-processing we write codes in C programming language. *MD* simulations are computationally highly demanding since we work with systems that contain tens of thousands of atoms. The key advantage of *LAMMPS* is parallelization, which means that *LAMMPS* codes can be run on a supercomputer. We write Linux bash scripts for submitting simulations to the supercomputer, as well as for the efficient manipulation with the output files. For visualization we use *VMD* (Visual Molecular Dynamics) software package [101].

3.1.2.1 Multi-level summation method for summing long-range Coulombic interactions

Long-range Coulombic interactions are treated in *LAMMPS* with methods that work in the inverse k -space [102–104]. In our *LAMMPS* simulations we apply the Multi-level summation (*MSM*) method which maps the charge of atoms onto a 3D mesh and uses hierarchy of several levels of coarse-graining of the mesh on which it directly computes Coulombic interaction. Competitive methods to *MSM* method for summing Coulombic interactions are Ewald and Particle Particle Particle Mesh (*PPPM*) methods, but they can be applied in case of a 3D simulation just if periodic boundary conditions are present along all three directions. On the other

side, *MSM* method can be applied in case of a 3D simulation without restrictions related to periodic boundary conditions, i.e., it can be applied for non-periodic as well as for mixed periodic and non-periodic boundary conditions. When we work with bulk *ILs*, our system is periodic in all three directions. On the other side, in case of confined *ILs*, our system is periodic along the x and y directions and it is fixed along the z direction. Actually, we might state that our system with confined *IL* includes mixed periodic (along two directions) and non-periodic (along one direction) boundary conditions, hence *MSM* method is adequate for treating long-range Coulombic interactions in our simulations.

3.2 Simulation setup and models of ionic liquid

3.2.1 Simulation setup

We have developed our simulation setup bearing in mind lubrication role of *IL*, hence it consists of two solid plates and *IL* which is confined between them and also present in the lateral reservoirs. Schematic of simulation setup together with configuration snapshots in three cross-sections, i.e., xz, yz, xy cross-sections which are exported from the *VMD* (Visual Molecular Dynamics program [101]) is shown in Figure 3.4 in case of *SM* model and in Figure 3.5 in case of *TM* model (e.g., diameter of neutral tail is arbitrary chosen to be the same as the diameter of cationic head). Schematic in simulation setup figures (i.e., Figures 3.4 and 3.5) indicates the number of particles used and the imposed normal load F_z and lateral velocity V_x . In *VMD* configuration snapshots dimensions of the system along the three axes, i.e., x, y, z , are noted. The simulation setup was loosely inspired by previously published research by others [39, 49, 51, 52]. By implementing such a geometry we have attempted to achieve:

- (i) a realistic particle squeeze-out behaviour with the formation of two lateral lubricant regions (in a similar manner to the simulations of Capozza et al. [52]) and
- (ii) a system that allows the lubricant to be externally pressurized.

For the description of the solid surfaces we have combined rigid layers of particles moving as a single entity on which the external force or motion is imposed, denoted

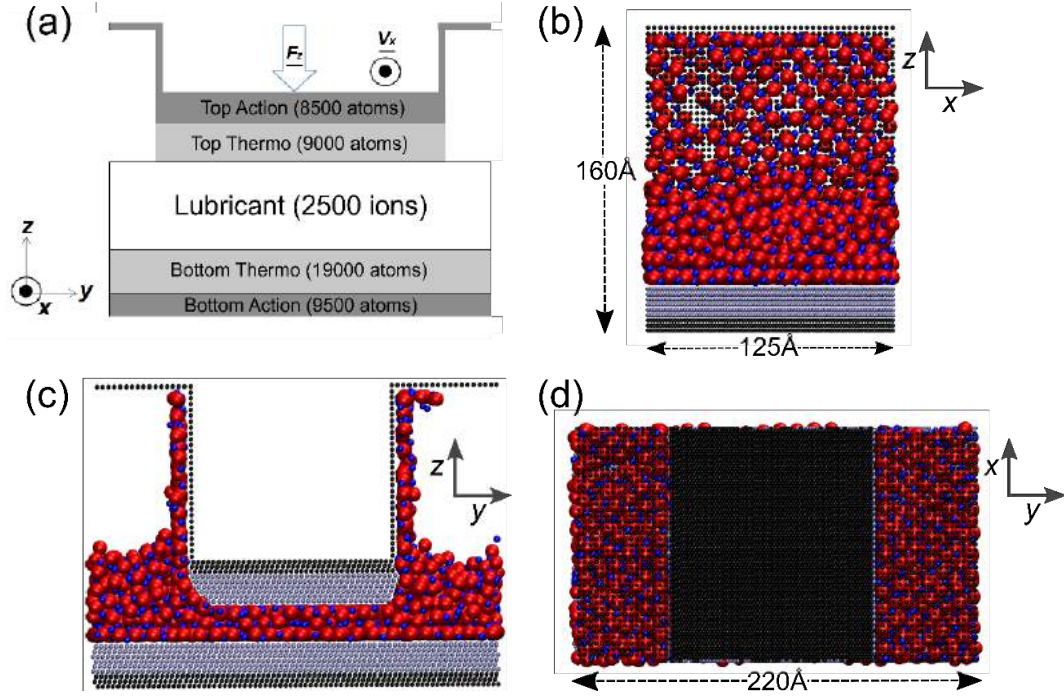


Figure 3.4: (a) Schematic of the simulation setup shown as yz cross-section. There are two solid plates at the top and bottom of the system, consisting of two regions: at the outermost ones the particles are moving as a single entity (Top/Bottom Action) and at the innermost ones the particles are at a controlled temperature (Top/Bottom Thermo). The thermalized layers are in direct contact with the lubricant while the action layers are used to impose external velocity and/or force to the solid plates. (b)-(d) Side views of the typical simulation configuration and key dimensions of the geometry. (b) Side (xz) view with respect to the shear direction. (c) Front (yz) view in the direction of the Top plate motion. (d) Top (xy) view of the system. The solid plates are made up of FCC (111) atomic layers. The ionic liquid is composed of an equal number of cations (blue spheres) and anions (red spheres).

by "Top Action" and "Bottom Action" in Figures 3.4 and 3.5 (a), with thermalized layers (denoted by "Top Thermo" and "Bottom Thermo") in which particles vibrate thermally at $T = 330$ K.

The Nose-Hoover NVT thermostat is used to control the temperature. As in previous MD simulations [43, 49, 51, 52, 56], under similar operating conditions, the details of the adopted dissipation scheme are not expected to change the essence of the system response on mechanical deformation. The relaxation time of the Nose-Hoover NVT thermostat for the lubricant and the solids is 200 fs (check Reference [43]). The plates were treated as rigid bodies, with the lower one being fixed

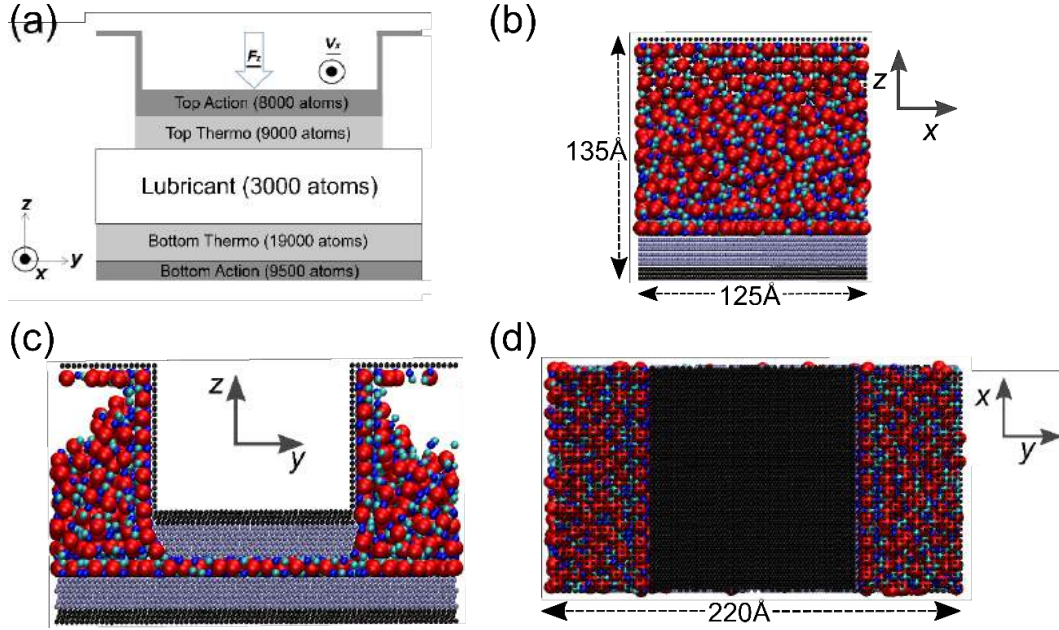


Figure 3.5: Schematic of the simulation setup shown as yz cross-section. Dimensions of the system along the y and z axes, together with the directions of the imposed normal load F_z and lateral velocity V_x are noted. The total system length in the x direction is 125 Å. There are two solid plates at the top and bottom of the system. Ionic liquid is composed of an equal number of cation–tail pairs and anions (cations: blue spheres; tails: cyan spheres; anions: red spheres). (a) Schematic of the simulation setup presented as yz cross-section, showing the number of atoms in each region. (b) Side (xz) view of the system showing the dimensions along the x and z direction. (c) Side (yz) view of the system. (d) Top (xy) view of the system showing the dimension along the y direction.

and the upper one subjected to a force oriented along the z direction, i.e., normal load F_z , as shown in Figures 3.4 and 3.5 (a) and driven along the x direction at a constant velocity V_x . The solid plates were made up of densely packed atomic layers at a FCC (111) lattice arrangement. Periodic boundary conditions were applied in the x and y directions. The Bottom plate can therefore be considered to be infinite, while the Top plate is surrounded by vacuum pockets on its sides, the so called lateral reservoirs, in which the lubricant can freely expand. The lateral reservoirs were implemented as a mechanistic way for allowing the lubricant to be dynamically squeezed in or out as an external load or velocity is applied, or due to local fluctuations during the simulation progression. At the same time, the lubricant remains an infinite continuous body in the x and y directions, similar to the conditions

observed in a real tribological system from a mesoscopic point of view. This is especially important if the system experiences partial or complete crystallization under compression, check Figure 3.29 in section 3.4. While the total number of considered lubricant molecules is constant, the finite upper plate width and the resulting free space enable the particles to be squeezed-out into the lateral reservoirs. The number of lubricant molecules effectively confined inside the gap can therefore dynamically change depending on the loading conditions. This is important for exploring the possible states of a mechanical system of particles that is being maintained in thermodynamic equilibrium (thermal and chemical) with a lubricant reservoir (i.e., void spaces in tribological system). The nanotribological system is open in the sense that it can exchange energy and particles, realizing an effectively grand-canonical situation, check Figures 3.4 and 3.5 (c) and Reference [105].

3.2.2 Models of ionic liquid

In this subsection we present implementation details about the modeled solid plates and *IL* lubricants in case of *SM* and *TM* models of ionic liquid, respectively.

3.2.2.1 Salt model of ionic liquid

The model used in this work is a coarse-grained model of *IL* which has already been exploited in previous studies [49, 51, 52, 64] and it is known as *SM* model (salt-like model). It is a charged Lennard–Jones system consisting of cations and anions. There are two types of interatomic interactions in our system and both of them are non-bonded: Lennard–Jones (*LJ*) potential and Coulombic electrostatic potential. In the current work we are comparing bulk and confined *IL* properties. Therefore, there are three different atom types taken into consideration: (*i*) cations, (*ii*) anions and (*iii*) solid plate atoms. The solid plates consist of nine densely packed layers in a *FCC* (111) lattice arrangement. Between all types of atoms we apply full *LJ* 12-6 potential, with the addition of Coulombic electrostatic potential for the interactions between ions. In our system the cations and the anions are charged particles, while the solid plate atoms are electroneutral. Accordingly, we have implemented a *LJ*

12-6 potential combined with Coulombic electrostatic potential:

$$V_{\alpha\beta}(r_{ij}) = 4\epsilon_{\alpha\beta} \left[\left(\frac{\sigma_{\alpha\beta}}{r_{ij}} \right)^{12} - \left(\frac{\sigma_{\alpha\beta}}{r_{ij}} \right)^6 \right] + \frac{1}{4\pi\epsilon_0\epsilon_r} \frac{q_i q_j}{r_{ij}}, \quad (3.27)$$

where $i, j = 1, \dots, N$ are particle indices, and N is the total number of particles. Parameters $\{\epsilon_{\alpha\beta}, \sigma_{\alpha\beta}\}$ define the LJ potential between different types of particles: $\alpha, \beta \in \{A, C, P\}$ which refer to anions, cations and solid plate atoms, respectively. The diameter of cations and anions is set to $\sigma_{CC} = 5 \text{ \AA}$ and $\sigma_{AA} = 10 \text{ \AA}$, respectively. The mass of cations and anions is $m_C = 130 \text{ g/mol}$ and $m_A = 290 \text{ g/mol}$, respectively. The asymmetry of ion sizes is typical in many experimentally explored systems and the parameters have already been explored in literature, check Reference [52, 64]. The atoms of the solid plates have a diameter of $\sigma_{PP} = 3 \text{ \AA}$. The mass of the solid plate atoms is $m_P = 65 \text{ g/mol}$. The LJ potential has a short-range impact, since it vanishes rapidly as the distance increases $\propto r^{-6}$, while the Coulombic potential has a long-range impact, $\propto 1/r$. To handle long-range interactions, we have used a multi-level summation method (MSM) [104], since it scales well with the number of ions and allows the use of mixed periodic (in x and y directions) and non-periodic (in z direction) boundary conditions, which are present in our simulation setup with confined IL . On the other hand, in our simulation setup with bulk IL , periodic boundary conditions are applied in all three directions ($\{x, y, z\}$). Ions are modeled as coarse grain particles, the charge of which is set equal to elementary: $q_C = +e$ and $q_A = -e$, i.e., $e = 1.6 \cdot 10^{-19} \text{ C}$. The dielectric constant is set to $\epsilon_r = 2$ to account for the dielectric screening, as in Refs. [51, 52, 64].

In engineering applications, the lubricant molecules typically interact with metal surfaces. Computationally efficient many-body potentials such as embedded atom method (EAM) potential [106, 107] can be applied for the description of such solids. Such schemes have been employed extensively for modeling a wide range of systems including metals [107] and metal-metal oxide interfaces [108]. In addition, in order to account for the induced charges on the metallic conductor surface by the ions, the Drude-rod model developed by Iori and Corni [109] which consists of the addition of an embedded dipole into each metal atom, thus rendering it polarizable, has been

applied in previous studies [39]. In this study, modeling the elasticity of metallic plates plays a secondary role (central role belongs to *IL* lubricant). Therefore, we have selected a simplified model in which plate atoms interact strongly with each other if they belong to the same plate, i.e., $\epsilon_{PP} = 120$ kCal/mol, as opposed, to a very weak interaction between the different plates $\epsilon_{\text{top/bottom}} = 0.03$ kCal/mol. The parameter ϵ_{PP} is so strong in order to ensure that the initial configuration of the solid bodies will basically remain unchanged (apart from high frequency oscillations). Furthermore, even though typical engineering systems are often metallic, our initial coarse grained *MD* studies of liquid behaviour according to the applied conditions justified the implementation of a simpler solid system which does not feature substrate polarization, check Reference [64]. Finally, it is possible that the actual surfaces might feature carbon coatings or depositions, in which case the surface polarization can be of secondary importance. In the Table 3.1 we present the values of $\{\epsilon_{\alpha\beta}, \sigma_{\alpha\beta}\}$ parameters used in our model. Cross-interaction parameters are calculated by Lorentz-Berthold mixing rules: $\epsilon_{\alpha\beta} = \sqrt{\epsilon_{\alpha} \cdot \epsilon_{\beta}}$ and $\sigma_{\alpha\beta} = (\sigma_{\alpha} + \sigma_{\beta})/2$. The starting configuration for our *MD* simulations was obtained via a relaxation process. In order to obtain a stable and reproducible initial configuration, the relaxation was performed through a step-wise increase of absolute ion charge at steps of $\Delta|q_i| = e/10$, $i = \{A, C\}$. Each time the charge of the ions was increased, a minimization of the system's energy through conjugated gradient method was performed. In this way, the system characteristics were gradually converted from pure *LJ* to a Coulomb interaction dominated system through a series of stable configurations. As we are aiming at understanding the lubricant behaviour at mesoscopic conditions observed in a ring-liner system, we have attempted to include in our *MD* model the potential *IL* pressurization that can occur due to the liquid flow resistance, as well as the variable pressure arising from the reacting gas in the combustion chamber. Inserting gas molecules directly in the simulation for this purpose would require a reduction of the time step due to higher thermal velocities of the gas. In turn, the computational cost would increase significantly making simulations impossible to run in realistic computational time. Therefore, in order to understand the effect of external pressure on the *IL* behaviour, we have applied a repulsive force between

Table 3.1: List of LJ parameters of SM model of ionic liquid.

pair $\alpha\beta$	$\epsilon_{\alpha\beta}$ [kCal/mol]	$\sigma_{\alpha\beta}$ [Å]
CC	0.03	5
AA	0.03	10
CA	0.03	7.5
PC	0.3	4
PA	0.3	6.5
PP	120	3

the topmost rigid solid layer and the IL particles in the form of a truncated and shifted LJ potential. Two cases with cut-off distances at 15 Å and 4 Å above the outermost Top plate layer were studied so that the IL inside the confinement gap would remain outside the influence zone of this mechanistic force. By appropriate selection of the LJ parameters for this potential, the resulting external pressures applied on the unconfined surface of the IL were 120 kPa and 250 kPa, respectively.

3.2.2.2 Tailed model of ionic liquid

In this study, we have applied a generic coarse grained IL model, introduced in Reference [52]. In this model, the anion is represented as a negatively charged large-sized spherical particle, while the cation is a dimer consisting of a positively charged small-sized spherical particle (i.e. cationic head), and a neutral spherical particle (tail) attached to the corresponding cationic head via an elastic spring, see Figure 3.6 and Reference [110]. Since the cationic tail is the principal feature of the model used in this paper, we will refer to it as tail model (TM). The asymmetry of the cation leads to amorphous (glassy) states for realistic values of interaction parameters (e.g., for hydrocarbons), in contrast to the simplest coarse-grained model of IL known as SM model (salt-like model), where both cations and anions are spherical. The SM model has already been exploited in previous studies [49, 52, 64, 111]. Despite an obvious advantage of simplicity, in order to avoid crystallization, the SM model relies on a very weak non-bonded Lennard-Jones interaction which makes any comparison with real IL only qualitative.

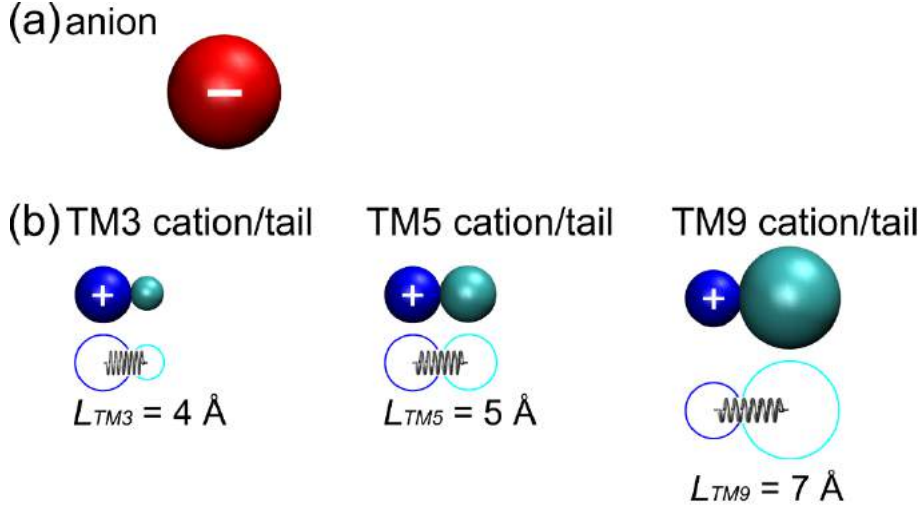


Figure 3.6: Schematic representation of (a) anion and (b) cation molecules in *TM* model. The anion is represented by a spherical particle with a diameter $\sigma_{AA} = 10 \text{ \AA}$. The cation molecule consists of a charged head with a diameter $\sigma_{CC} = 5 \text{ \AA}$ and a neutral tail. In order to be more concise, we refer just to cationic head as the cation. The cation and its tail are connected by a spring with length $L = (\sigma_C + \sigma_T)/2$. The size of the tail has been varied and (a) *TM3*, (b) *TM5* and (c) *TM9* ionic liquids have a tail diameter of 3, 5 and 9 \AA , respectively. The molecular asymmetry is a feature of real ionic liquids and chosen parameters resemble $[BMIM]^+ [PF_6]^-$ IL properties, check References [49, 51].

In addition, the *SM* model cannot account for molecular asymmetry featured in real *ILs*. Nevertheless, the *SM* model has been proven to be quite useful for the development of the simulation methodology, as it reduces computational complexity and enables faster equilibration (e.g., for obtaining static force-distance characteristics as in Reference [64]). More complex extensions of *TM* coarse grain models can involve several tails of different size, like in Reference [49]. For simplicity reasons, we restrain our considerations in this study to a single neutral tail of a variable size. Although a whole cationic dimer is an entity which actually represents a cation, in order to be more concise we refer just to cationic head as the cation. One might raise a question what are the reasons for the attaching of a neutral tail to a cation? First of all, real *ILs* usually include cations that consist of the cationic head (positively charged) and alkyl chain (neutral part of cation). Alkyl chains can have different lengths (different number of *C* atoms). Furthermore, the tail enhances the general

tendency of *ILs* to form a glass rather than a crystal at low temperatures [52]. As the previous studies have shown, the shape of *IL* molecules may affect their layering structure [49]. According to that, the central question which we address in this study is how does the tail size affect the structure, static and dynamic behaviour, as well as, lubrication properties of a generic *IL* represented via tailed-model.

- Interaction model

In the current work we are dealing with both bulk and confined *ILs*. Hence, in case of simulation setup with confined *ILs*, there are two solid plates consisting of solid plate atoms. To sum up, in total there are four different atom types taken into consideration:

(i) cations, (ii) tails, (iii) anions and (iv) solid plate atoms.

In cation-tail dimers an elastic spring connects cations and tails enabling the tail's freedom of moving independently from its cation, since their connection is not rigid. Interatomic interactions taken into consideration in our molecular dynamics simulations are:

(i) non-bonded interactions (Lennard-Jones (*LJ*) and Coulombic electrostatic potential) and

(ii) bonded interaction (elastic spring potential in cation-tail pairs). The next equation defines the interaction potential:

$$V_{\alpha\beta}(r_{ij}) = 4\epsilon_{\alpha\beta} \left[\left(\frac{\sigma_{\alpha\beta}}{r_{ij}} \right)^{12} - \left(\frac{\sigma_{\alpha\beta}}{r_{ij}} \right)^6 \right] + \frac{1}{4\pi\epsilon_0\epsilon_r} \frac{q_i q_j}{r_{ij}}, \quad (3.28)$$

where $i, j = 1, \dots, N$ are particle indices, and N is the total number of particles. Particles which comply to the interaction potential written in the above equation, i.e., Equation 3.28, can be of different types: $\alpha, \beta \in \{A, C, P\}$ which refer to anions, cations and solid plate atoms, respectively. On the other hand, interaction of tails with all other atom types, including tails themselves, is implemented using a purely repulsive potential, namely a shifted and cut *LJ* 12-6 potential. It means that full *LJ* 12-6 potential is shifted up for the value of potential well depth (ϵ) and cut at the distance corresponding to the potential well minimum ($r_{\text{cut}} = 2^{1/6}\sigma$). The next

equation defines the above mentioned interaction potential:

$$V_{\alpha\beta}(r_{ij}) = \epsilon_{\alpha\beta} + 4\epsilon_{\alpha\beta} \left[\left(\frac{\sigma_{\alpha\beta}}{r_{ij}} \right)^{12} - \left(\frac{\sigma_{\alpha\beta}}{r_{ij}} \right)^6 \right], r_{ij} \leq 2^{1/6} \sigma_{\alpha\beta} \quad (3.29)$$

and $V_{\alpha\beta}(r_{ij}) = 0, r_{ij} > 2^{1/6} \sigma_{\alpha\beta}$, where in Equation 3.29 at least one of indices $\alpha, \beta = T$ which refers to tails. The ionic liquid is electroneutral, i.e., the number of cations and anions is the same. The total number of ionic liquid molecules (cation–tail dimers and anions) is $N_{IL} = 3000$. Therefore, the total number of ions is $N_C = N_A = 1000$ and the number of tails is $N_T = N_C = 1000$.

- Model Parameters

In this study we have fixed the diameter of the cationic heads and anions to $\sigma_{CC} = 5 \text{ \AA}$ and $\sigma_{AA} = 10 \text{ \AA}$, respectively. Such choice respects the asymmetry that exists in *ILs* and it is consistent with other models, as well as, for example $[BMIM]^+ [PF_6]^-$ ionic liquid, check Reference [49, 51, 52, 64]. The solid plate atoms have a diameter of $\sigma_{PP} = 3 \text{ \AA}$. We have taken into consideration three different *TM* models of *IL* depending on the tail size which is defined as Lennard–Jones σ_{TT} parameter: small–tail cationic dimer (i.e., *TM3* model with $\sigma_{TT} = 3 \text{ \AA}$), symmetric cationic dimer (i.e., *TM5* model with $\sigma_{TT} = \sigma_{CC} = 5 \text{ \AA}$) and large–tail cationic dimer (i.e., *TM9* model with $\sigma_{TT} = 9 \text{ \AA}$). The values of the tail size are chosen to take into account their relation to the size of the cationic head which is $\sigma_{CC} = 5 \text{ \AA}$, hence our choice can be described as: tail size less–, equal to– and greater than– the size of cation.

Drawing a comparison with the experiment in Refs. [53, 67], the *TM IL* mimics a folded alkyl chain and the radius of the sphere is related to the gyration radius of the chains. Depending on the length of the alkyl chain, the sphere has a smaller or larger radius. Thus, the size of a sphere which represents a neutral tail in *TM ILs* does not compare directly with the alkyl chain length. However, we can make a qualitative analogy. While the representation of the alkyl chain as a neutral *LJ* sphere does not include all the microscopic level features, we will show that the three selected radii, i.e., $\sigma_{TT} = \{3, 5, 9\} \text{ \AA}$, result in clear differences of the bulk properties of *ILs* and their lubrication response. Each cation–tail pair is connected via identical elastic spring defined by the next two parameters: elastic constant

Table 3.2: List of LJ parameters of TM models of ionic liquid; the tail size is denoted by σ_{TT} since it is variable.

pair $\alpha\beta$	$\epsilon_{\alpha\beta}^{LJ}$ [kCal/mol]	$\sigma_{\alpha\beta}$ [Å]
CC	1.1	5
AA	1.1	10
TT	1.1	σ_{TT}
CA	1.1	7.5
CT	1.1	$(5 + \sigma_{TT})/2$
AT	1.1	$(10 + \sigma_{TT})/2$
PC	5.3	4
PA	5.3	6.5
PT	5.3	$(3 + \sigma_{TT})/2$
PP	120	3

$K = 80 \text{ kcal/mol}\text{\AA}^2$ and equilibrium length of the spring $l_0 = (\sigma_{CC} + \sigma_{TT})/2$. The strength of the LJ interactions between different charged parts of ions ($i, j = \{A, C\}$) is $\epsilon_{ij} = 1.1 \text{ kcal/mol}$. The LJ parameters are chosen to compare well with one of the most widely studied ionic liquids $[BMIM]^+ [PF_6]^-$, check Reference [49, 51]. The charge of ions is set to elementary: $q_C = +e$ and $q_A = -e$, where $e = 1.6 \cdot 10^{-19} \text{ C}$. The strength of the ion-substrate interaction was tuned to ensure complete wetting, $\epsilon_{\alpha P} = 5.3 \text{ kcal/mol}$, $\alpha \in \{A, C, T\}$. Only when the strength of ion-substrate LJ interaction $\epsilon_{\alpha P}$ equals the strength of inter-ionic LJ interaction $\epsilon_{\alpha\beta}$, partial wetting is observed, i.e., $\epsilon_{\alpha P} = 1.1 \text{ kcal/mol}$, where $\alpha, \beta \in \{A, C, T\}$ (more details about the wetting behaviour of TM ionic liquids are provided in section 3.3 in the subsection 3.3.2.3). In the table 3.2 we present the values of $\{\epsilon_{\alpha\beta}, \sigma_{\alpha\beta}\}$ parameters used in our models. Cross-interaction parameters are calculated by Lorentz-Berthold mixing rules: $\epsilon_{\alpha\beta} = \sqrt{\epsilon_{\alpha} \cdot \epsilon_{\beta}}$ and $\sigma_{\alpha\beta} = (\sigma_{\alpha} + \sigma_{\beta})/2$.

3.3 Bulk ionic liquid

The main focus of our research is oriented towards revealing the properties and behaviour of confined IL , since IL accomplishes its lubricating role when confined

between solid surfaces. The length scale of confinement we are interested in is expressed in nanometers, hence the nanoscale confinement affects the structure and behaviour of *IL*. In order to better understand the effects of nanoconfinement on *IL*, we should first understand the *IL* itself, which means that we should first characterize bulk *IL*. For this purpose we have relaxed bulk *IL* and determined its viscosity characteristics, as well as its wetting behaviour. This section is dedicated to our study of bulk *IL* in case of *SM* model (subsection 3.3.1) and in case of three representative *TM* models (subsection 3.3.2).

3.3.1 Bulk salt model of ionic liquid

3.3.1.1 Solidification and melting of bulk salt model of ionic liquid

In order to confirm that the *SM* modeled *IL* used in our *MD* simulations remains in a liquid state for the conditions of interest, its liquid–solid and solid–liquid phase transitions have been studied. The bulk ionic liquid was implemented by randomly placing a chosen number of ions ($N_C = N_A = 1000$) into a 3D simulation box that is periodic in all three directions, with pressure kept constant at 100 kPa. Phase transitions were then achieved via the application of linear ramping to the temperature, in a similar approach to the calculations performed in Reference [52]. Starting from an initial temperature $T_1 = 330$ K where the *IL* is in a liquid state, the temperature was decreased linearly down to $T_2 = 180$ K. The absolute rate of temperature change was: $|dT|/dt = 1.67 \text{ K ns}^{-1}$. A liquid–solid phase transition was observed during the *IL* cooling.

After reaching $T_2 = 180$ K, the temperature was increased back to the initial value of $T_1 = 330$ K. A solid–liquid phase transition was observed during this heating process. In Figure 3.7 the *IL* internal energy change ΔE_{int} and temperature T are shown as functions of time t . The temperature profile follows the applied conditions and its superimposition to internal energy change allows the observation of the dynamic behaviour of the liquid. By plotting the averaged internal energy change of the *IL* against its temperature in Figure 3.8, the hysteresis behaviour in the solidification–melting cycle is clearly observed, while the phase transition locations

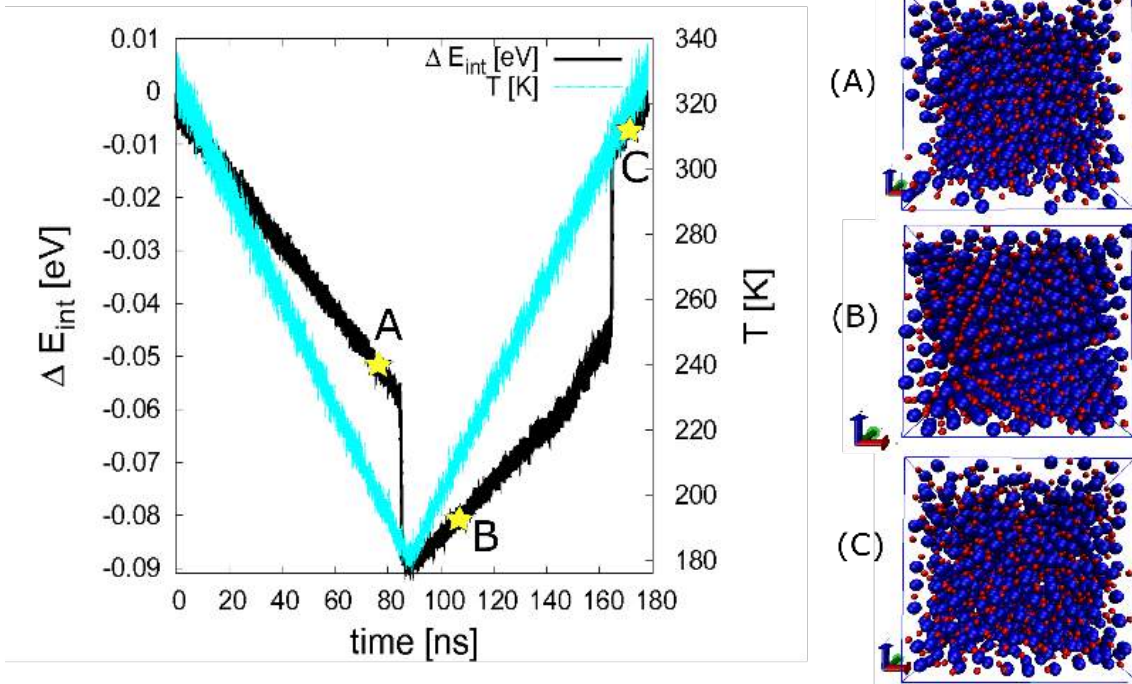


Figure 3.7: (Left panel): Bulk internal energy change and temperature of the ionic liquid as a function of simulation time. (Right panel) Snapshots of ion arrangement at liquid (A), (C) and solid (B) state.

can be clearly defined. It can be seen that during the cooling process, the internal energy of *IL* linearly decreases until the temperature reaches $T_{ls} = 190$ K, at which point a sharp drop is observed. This indicates a first order thermal phase transition (liquid–solid). During the heating process, a similar sharp jump of energy is observed at $T_{sl} = 305$ K which corresponds to an opposite phase transition (solid–liquid). The obtained results are in a good agreement with Reference [52] and confirm that the *IL* behaves as a liquid for temperatures higher than 310 K, under atmospheric pressure conditions. In the rest of our calculations a temperature value of $T = 330$ K was applied, in order to allow a liquid state that is combined with local solidification under elevated contact pressure conditions.

3.3.1.2 Relaxation simulations

We have revealed the solidification and melting phase transitions of bulk *SM* ionic liquid, under the condition of atmospheric pressure. The subsequent step was to

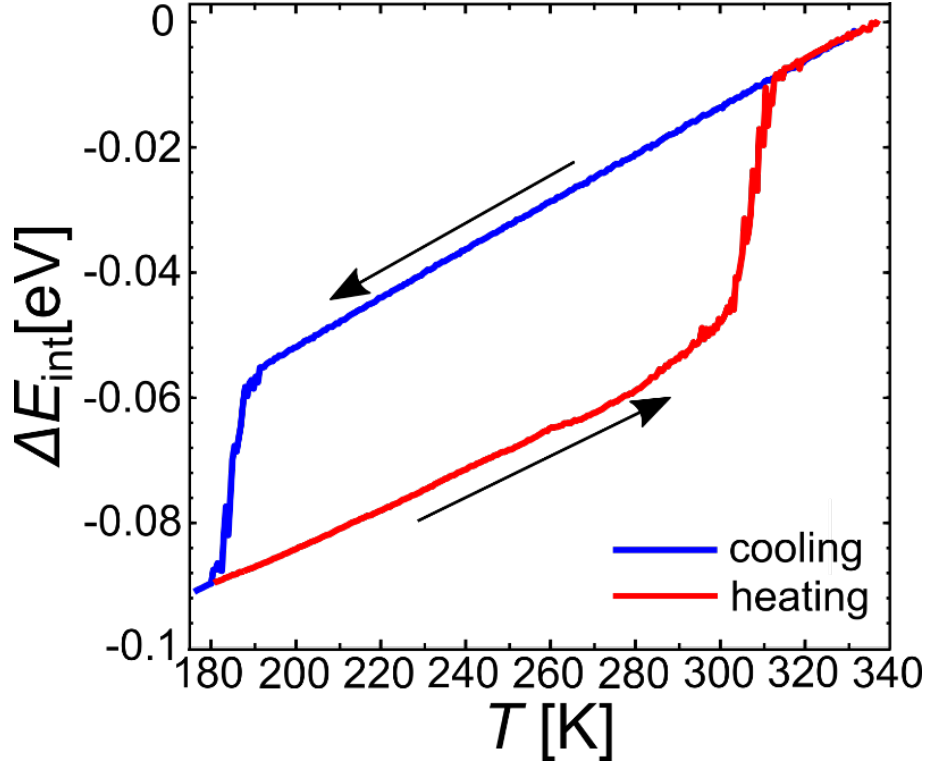


Figure 3.8: Bulk internal energy change of the ionic liquid as a function of temperature. The internal energy was calculated by averaging on segments of $\Delta T = 0.5K$.

make the bulk *IL* comparable with its confined counterpart and to do so we had to determine simulation box volume which enables the pressure experienced by the confined *IL*. More specifically, for the present system of bulk *SM* ionic liquid confined between the solid plates (c.f. Figure 3.4), the pressure was $p \approx 1$ MPa. The Nose–Hoover *NVT* thermostat was used to control the temperature and was set to $T = 330$ K. The system was relaxed for $t_{\text{tot}} = 3 \cdot 10^7$ fs until the internal energy had converged and the pressure had approached the desired value. The simulation timestep was $dt = 0.5$ fs. We have obtained pressure stabilization at $\langle p \rangle = 1.1$ MPa with a side length of the cubic simulation box at $L = 99$ Å. The energy relaxed to a value of $\langle E_{\text{int}} \rangle = 0.7597$ kCal/mol. The molar and mass density of the bulk *IL* was $\rho_n = 3400$ mol/m³ and $\rho_m = 719$ kg/m³ respectively.

3.3.1.3 Viscosity characteristics

We have calculated the viscosity in two ways: using the Green–Kubo relation since the viscosity of a system can be represented as an integral of the auto-correlation

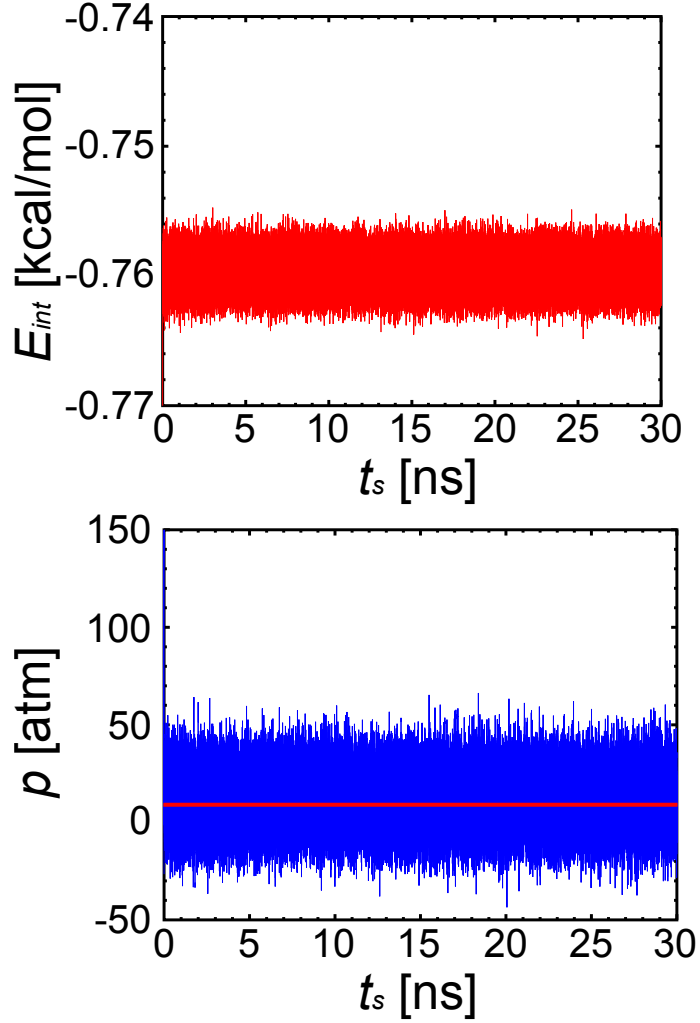


Figure 3.9: Dependences of internal energy E_{int} and pressure p on simulation time t_s in case of bulk *SM* ionic liquid. Solid line in $p(t_s)$ plot denotes the value of target pressure $p = 1$ MPa ($p \approx 10$ atm).

function [112], and using non-equilibrium molecular dynamics simulations with different shear strains.

In the non-equilibrium shearing simulations, the bulk *IL* is placed into a triclinic (non-orthogonal) simulation box with periodic boundary conditions applied in all three directions. Due to the deformation of the simulation box, every point in the box has an additional velocity component (a so called *streaming velocity*). In order to prevent the streaming velocity from affecting the thermal kinetic energy, we use the so-called *SLLOD* thermostat [113, 114]. The *SLLOD* thermostat accounts for the streaming velocity which depends on an atom's position within the simulation box

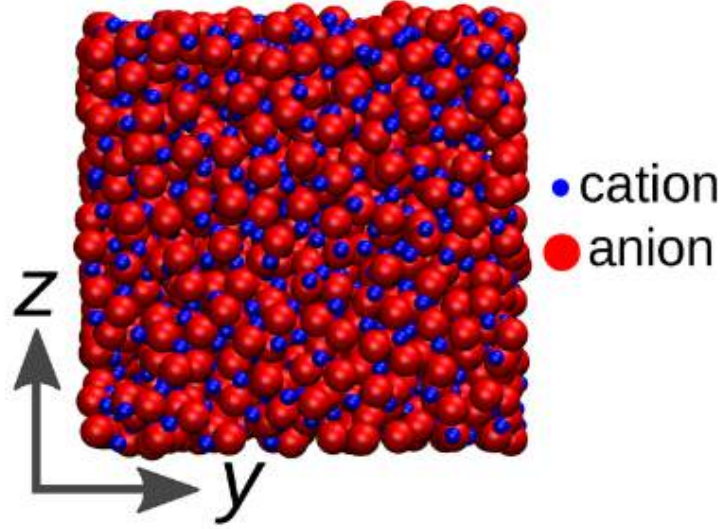


Figure 3.10: Configuration snapshot (yz cross-section) of a bulk IL at the end of relaxation simulation. Cations are represented as smaller blue spheres and anions as larger red spheres.

and it needs to be accounted for controlling the temperature. Controlled shearing of the simulation box results in a stress acting on IL , which is quantified via the stress tensor. The relation between the stress tensor components τ_{ij} and the shear rate $\dot{\gamma}_{ij}$ of corresponding shear strain ϵ_{ij} , with coefficient of viscosity η_{ij} as a proportionality constant is:

$$\tau_{ij} = \eta_{ij} \cdot \dot{\gamma}_{ij}, \quad (3.30)$$

where $ij = \{xy, xz, yz\}$. We have applied three independent shear strains ($\epsilon_{xy}, \epsilon_{xz}, \epsilon_{yz}$). For each of them we have calculated its corresponding stress tensor component ($\tau_{xy}, \tau_{xz}, \tau_{yz}$). All shear strains were the same, i.e., $\epsilon_{xy} = \epsilon_{xz} = \epsilon_{yz} = \epsilon = 1$ leading to the shear rate of:

$$\dot{\gamma} = \epsilon \cdot \frac{1}{t_{\text{tot}}} = \frac{1}{t_{\text{tot}}}, \quad (3.31)$$

where t_{tot} is the total simulation time of the shearing simulations. We have performed simulations at four orders of magnitude of the total simulation time: $t_{\text{tot}} = \{0.1, 1, 10, 100\}$ ns, and thus at four orders of magnitude of the corresponding shear rate. In this way we wanted to check the quality of our relaxation procedure and if there are shear rate dependence changes in the system. We have iterated the shearing simulations (at a shearing velocity of 1 m/s) using the output of the previous

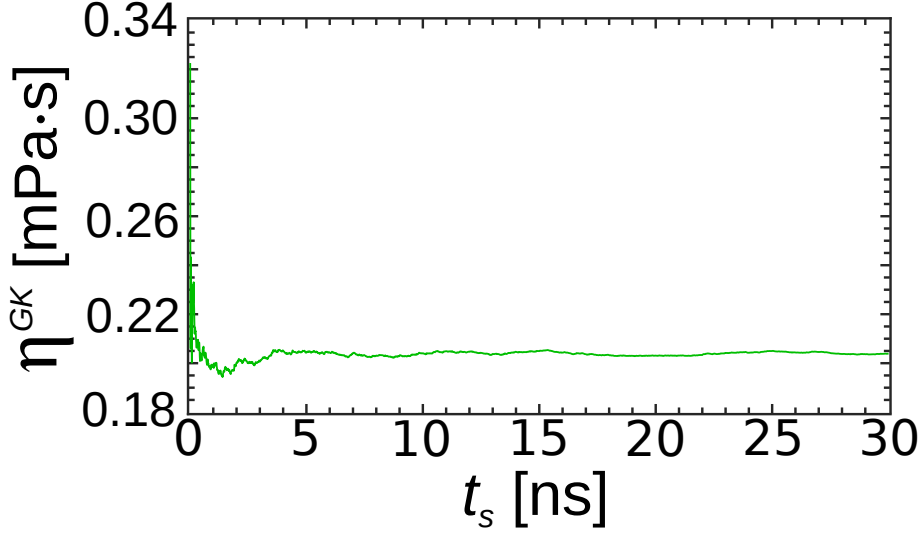


Figure 3.11: Dependence of Green–Kubo (GK) viscosity coefficient η^{GK} on simulation time t_s in case of bulk *SM* ionic liquid. The time needed to obtain the viscosity coefficient is around $t_{\text{rel}} = 5$ ns.

run as the input of the next run, obtaining higher strains (up to a strain of 5). We did not observe a strain dependence in the response of the system, meaning that the result is unaffected if the strain is further increased.

In Figure 3.11, we show the time relaxation of the Green–Kubo viscosity coefficient, which stabilizes around $\eta^{\text{GK}} = 0.2039$ mPa · s. The configuration snapshot of the bulk *IL* at the end of the simulation (check Figure 3.10) shows that the ions remain randomly positioned, like they were at the start of simulation, which indicates the liquid state of the bulk ionic liquid. The simulations for all three shear strains give similar values of stress components, and resulting values are shown in Figure 3.12. The points $\{\dot{\gamma}, \tau\}$ were obtained via shearing simulations and the solid line was obtained according to $\tau = \eta^{\text{GK}} \cdot \dot{\gamma}$, where η^{GK} was obtained via Green–Kubo relation. Hence, we conclude that the results of shearing simulations are in agreement with the results of relaxation simulation and therefore there are no changes in the bulk system which are shear rate dependent.

3.3.1.4 Wetting properties

Besides the necessary relaxation of bulk *IL* and determination of its viscosity characteristics, the liquid–solid interface should be well–known so that we can understand

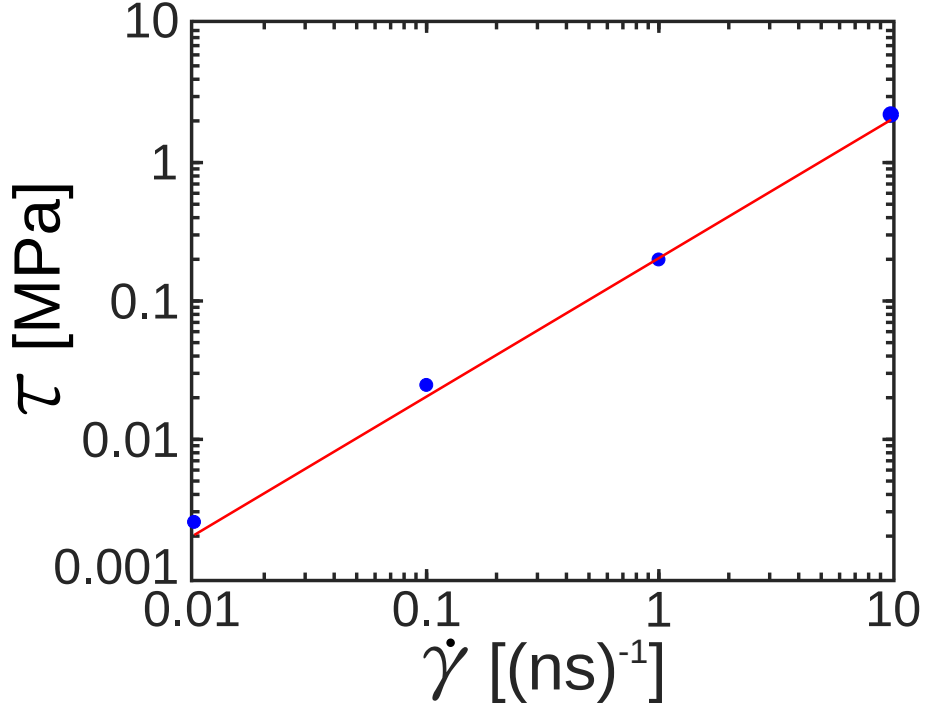


Figure 3.12: Average stress tensor component τ in function of the shear rate $\dot{\gamma}$ of a bulk *SM* ionic liquid. We have conducted shearing simulations on four orders of magnitude of the shear rate $\dot{\gamma}$, therefore with three orders of magnitude span, which is followed by three orders of magnitude span of τ . Points are obtained via shearing simulations and solid line is obtained according to: $\tau = \eta^{\text{GK}} \cdot \dot{\gamma}$, where η^{GK} is obtained via Green–Kubo relation.

the behaviour of liquids confined between solid plates. Accordingly, it is important to investigate the wetting properties of modeled *ILs*. For this purpose we examine the wetting properties of *SM* ionic liquid by placing an *IL* droplet consisting of $N_{\text{IL}} = 2000$ ions, i.e., $N_C = N_A = 1000$, above a neutral solid plate (where the term above means a higher z coordinate) which consists of one atomic layer in a *FCC* (111) lattice.

Wetting properties simulation consist of two parts: (1) movement of the solid plate at a constant velocity of $V_z = 1$ m/s towards the *IL* droplet, which promotes the contact of *IL* droplet with the plate. Due to the *LJ* interaction between the ions and solid plate atoms, the *IL* droplet starts covering the plate. The ending configuration of this part (1) simulation is used as the starting configuration of the part (2) simulation in which the solid plate rests and a long simulation time of $t_s = 5$ ns is given to the ionic liquid, so that it can spread over the plate. In the end

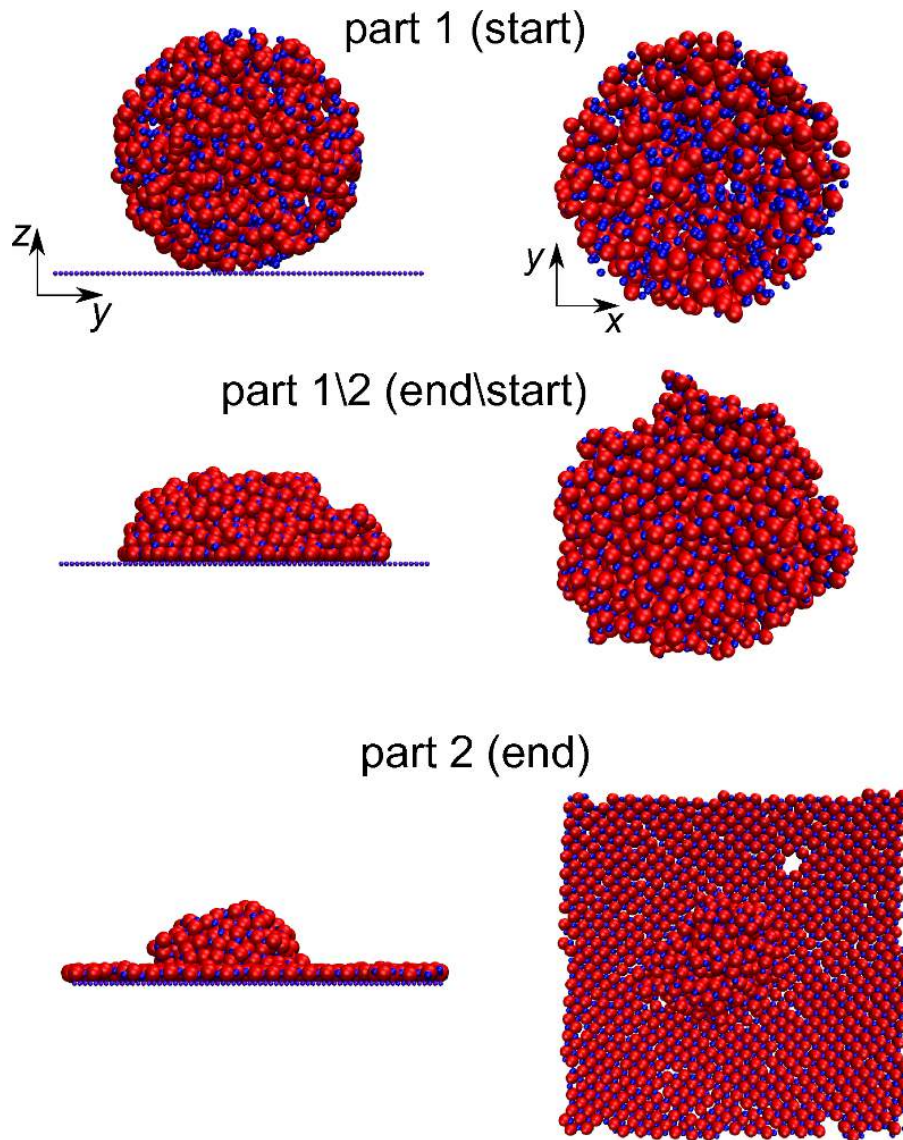


Figure 3.13: Results of wetting properties simulation in case of *SM* ionic liquid. Left panels show *yz* cross-section, while right panels show *xy* cross-section of the system consisting of an *SM* ionic liquid droplet and a solid plate.

of the part (2) simulation, the ionic liquid is placed on the solid plate in the way that it forms a cationic-anionic layer over the whole plate, with an amorphous droplet in the center of the plate. We might conclude that, for the value of the strength of ions-plate *LJ* interaction, i.e., $\epsilon_{\text{IP}} = 0.3$ kCal/mol, *SM* ionic liquid completely wets the given solid plate (*LJ* interaction parameters $\{\sigma_{\alpha\beta}, \epsilon_{\alpha\beta}\}$ are taken from Table 3.1 in subsection 3.2.2.1 of section 3.2). In Figure 3.13 we show the results of wetting properties simulation in three vertical panels: the top one shows the *yz* (in the left-

hand side of the panel) and xy (in the right-hand side of the panel) configuration of the system at the start of part (1) simulation. The middle panel shows the same two configurations of the system at the end of part (1) simulation, which is taken as the start of part (2) simulation. The bottom panel shows the same two configurations of the system at the end of part (2) simulation.

3.3.2 Bulk tailed models of ionic liquid

3.3.2.1 Relaxation simulations

In an analogous way like in the case of bulk SM ionic liquid, check subsection 3.3.1.2, we have performed relaxation simulations in case of three representative TM ionic liquids. An initial configuration for a bulk TM ionic liquid was obtained by a random placement of ions ($N_C = N_T = N_A = 1000$) into the simulation box (cube) with periodic boundary conditions in all three directions. We have chosen the simulation box volume which ensures, after the relaxation of the IL structure, the pressure comparable to the one experienced by confined IL . In case of the present system the pressure was $p \approx 10$ MPa, which corresponds to the normal force of 10^3 pN acting on a surface of 10^4 \AA^2 (see Figures 3.5 and 3.35). We provide implementation details related to the relaxation simulations: a Nose–Hoover NVT thermostat at $T = 330$ K is used to control the temperature; the system is relaxed for $t_{\text{tot}} = 3 \times 10^7$ fs until internal energy converges and pressure approaches the desired value of $p \approx 100$ atm; simulation timestep is $dt = 0.5$ fs.

Table 3.3: Overview of the results of relaxation simulations: σ_{TT} is the tail size, L is the side length of cubic simulation box, t_{rel} is the estimated relaxation time, $\langle p \rangle$ and $\langle E_{\text{int}} \rangle$ are the mean values of pressure and internal energy respectively, averaged over the time span $t_{\text{rel}} \leq t \leq t_{\text{tot}}$, where t_{tot} is the total simulation time.

σ_{TT} [\AA]	L [\AA]	t_{rel} [ns]	t_{tot} [ns]	$\langle p \rangle$ [atm]	$\langle E_{\text{int}} \rangle$ [kCal/mol]
3	104.5	11	30	95.31	-0.62
5	110	0	19	103.81	-0.57
9	129	20	30	118.21	-0.54

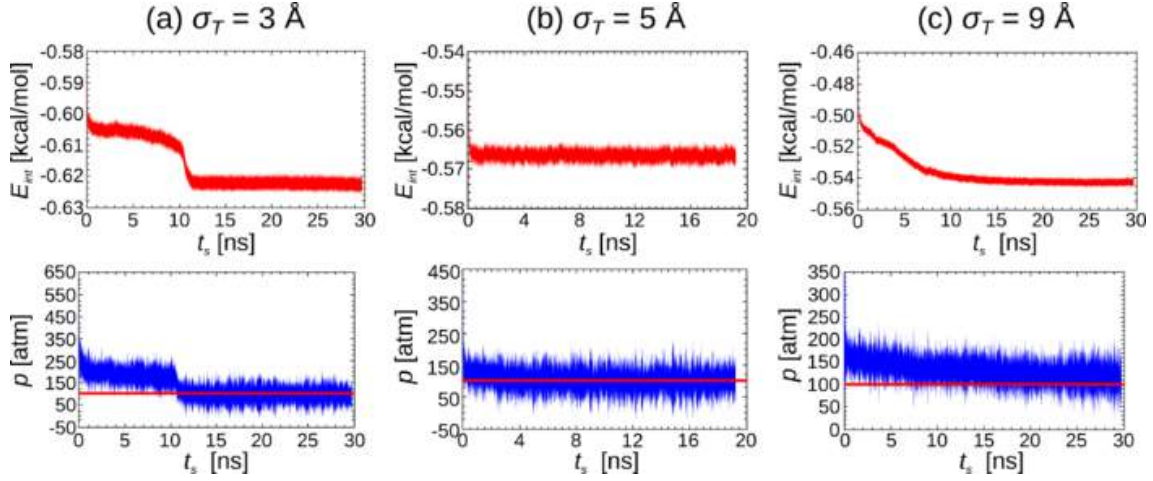


Figure 3.14: Dependences of internal energy E_{int} and pressure p on simulation time t_s in case of bulk (a) *TM3*, (b) *TM5* and (c) *TM9* ionic liquid. Solid lines in $p(t_s)$ plots denote the value of target pressure $p = 10$ MPa ($p \approx 100$ atm) in all cases.

In Table 3.3 we are showing the overview of the relevant parameters of relaxation simulations, for *TM3*, *TM5* and *TM9* bulk *IL*. In Figure 3.14 we are showing the dependences of bulk *IL*'s internal energy E_{int} and pressure p on simulation time t_s for bulk (a) *TM3*, (b) *TM5* and (c) *TM9* ionic liquid. Figure 3.15 presents the xy cross-section snapshots of bulk *IL* configurations at the end of relaxation simulations for (a) *TM3*, (b) *TM5* and (c) *TM9* model. Those results have clearly revealed a strong dependence of *IL*'s structure on the tail size. We have obtained three completely different outcomes of relaxation simulations in terms of internal energy and structure (check Figure 3.14), depending on the tail size.

- Tail significantly smaller than cation (*TM3* model)

We can notice three different segments (check Figure 3.14(a)) in the dependences of internal energy and pressure on simulation time. First, there is a smooth decrease of both parameters over the time interval of $t \leq 10$ ns. The first segment is followed by a sudden drop of E_{int} and p in the time interval $10 \leq t_s \leq 11$ ns. For $t_s \geq 11$ ns both system parameters remain stable in terms of their average values. Therefore, we might estimate the relaxation time as $t_{\text{rel}} \approx 11$ ns. Actually, the values of E_{int} and p are oscillating around their averages (a common result in *MD* simulations) which remain fixed in the time span $t_{\text{rel}} \leq t_s \leq t_{\text{tot}}$. Since the temperature is thermostated

at $T = 330$ K we might not speak about a phase transition, but those sharp drops of internal energy and pressure are a demonstration of a state transition. Structural changes consistently follow the changes in system parameters, hence there is a clear transition from initially randomly positioned atoms into an ordered structure. We might conclude that a small tail does not affect the cationic–anionic ordering into a cubic lattice, which arises due to Coulombic interaction. We should emphasize that the obtained cubic lattice is not an ordinary simple cubic lattice, but it is tilted. Ionic layers are oriented in the way that they follow the face diagonal of the cube. A conclusion is that *TM3* bulk *IL* does not stay in initially assigned liquid state during the relaxation process, but it leaves the relaxation process as an ordered structure (check Figure 3.15(a)).

- Tail of the same size like cation (i.e. symmetric cationic dimer, TM5 model)

Both system parameters E_{int} and p remain stable (check Figure 3.14(b)) and with practically the same average values throughout the whole simulation, indicating that a state transition does not happen. The structure of bulk *IL* remains the same during the simulation, which is consistent with the behaviour of those parameters. We can claim that relaxation of bulk *TM5* ionic liquid gives a liquid state as the outcome (check Figure 3.15(b)).

- Tail significantly larger than cation (TM9 model)

There is a continuous and smooth decrease of both E_{int} and p over a long time span $t_s \leq 20$ ns (check Figure 3.14(c)). Later during the relaxation simulation those parameters remain stable, hence we estimate the relaxation time in this case as $t_{\text{rel}} \approx 20$ ns. It is almost two times longer than the relaxation time of *TM3* model. Structural changes are consistent with system parameters' changes, hence we notice a clear state transition from initially randomly positioned atoms into an ordered structure (check Figure 3.15(c)). We can state that a large tail enables cationic-anionic ordering, which arises due to Coulombic interaction. All layers are oriented along the face diagonal of the cube and they are composed of alternating ionic and tail layers, namely ionic layers consisting of two cationic–anionic sublayers separated by tail layers consisting of two tail sublayers. Tail sublayers are organized

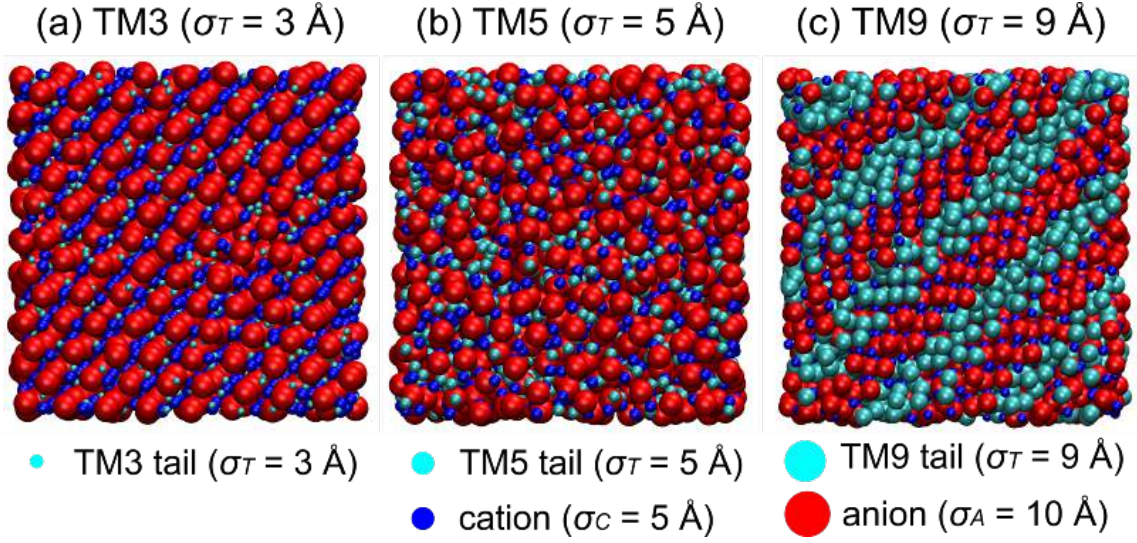


Figure 3.15: Configuration snapshots of bulk (a) *TM3*, (b) *TM5* and (c) *TM9* ionic liquid (i.e., with tail of diameter 3, 5 and 9 Å, respectively). We may notice that each configuration snapshot represents a different state, i.e. *TM3* bulk *IL* crystallizes into a tilted simple cubic crystal structure, oriented along the face diagonal; *TM5* bulk *IL* is in liquid state; *TM9* bulk *IL* crystallizes into crystal planes with alternating ionic–tail layers, oriented along the face diagonal as well.

in the way that the tails of cationic sublayers in successive ionic layers belong to the tail layer which separates those successive ionic layers. Simply said, the structure looks like this: ionic layer (consisting of two cationic–anionic sublayers) - tail layer (consisting of two tail sublayers) - ionic layer - tail layer and so on.

These observations are in agreement with Reference [115] in which the authors discuss the relationship between the length of alkyl chain and the structure of bulk *IL*. When the cationic alkyl chain is short Coulombic forces are dominant, enabling ordering. We observe this kind of result with *TM3* model. Alkyl chain must be long enough in order to suppress Coulombic interaction, e.g. number of *C* atoms $n_C \approx 12$, which corresponds to $(n_C - 1) \cdot 1.53 \text{ \AA} = 16.83 \text{ \AA}$ of tail length, taking into account that a *C-C* bond has a length of 1.53 Å. Suppressed Coulombic interaction suppresses lattice arrangement, as we obtain with *TM5* model. However, alkyl chain should not be too long since cohesive interactions increase with the length of non-polar groups. This leads to a reappearance of structural ordering, like in the case of *TM9* model.

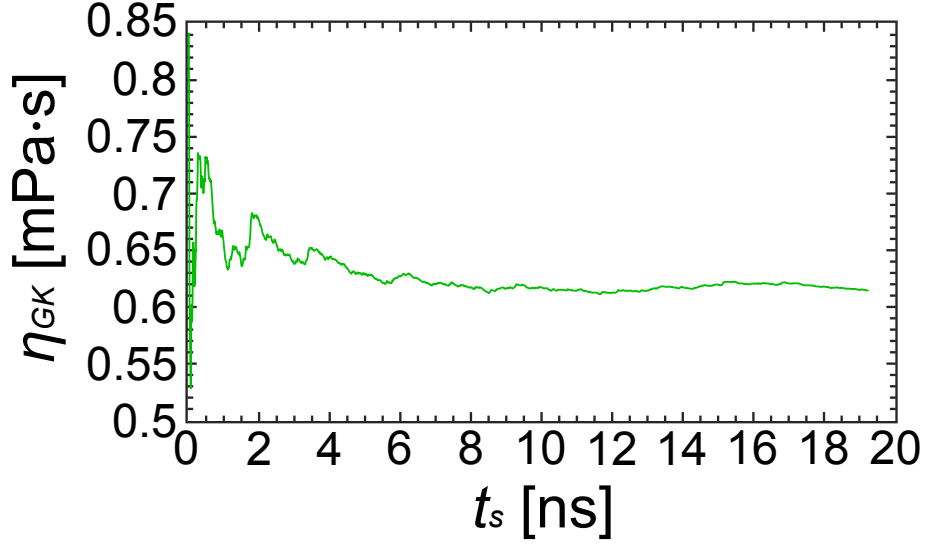


Figure 3.16: Dependence of Green–Kubo (GK) viscosity coefficient η^{GK} on simulation time t_s in case of bulk *TM5* ionic liquid. The time needed to obtain the viscosity coefficient is around $t_{\text{rel}} = 10$ ns.

3.3.2.2 Viscosity characteristics

In an analogous way like in the case of bulk *SM* ionic liquid, we have calculated the viscosity coefficient of bulk *TM* ionic liquids using non–equilibrium molecular dynamics (*NEMD*) simulations with different shear strains, taking configurations obtained by relaxation. For each value of the shear rate $\dot{\gamma}$ in the range $0.01 - 10 \text{ ns}^{-1}$, we calculate the average stress tensor component: $\tau = (\tau_{xy} + \tau_{xz} + \tau_{yz})/3$. The average stress tensor component τ and shear rate $\dot{\gamma}$ are connected by the relation:

$$\tau = \eta \cdot \dot{\gamma}^\alpha, \quad (3.32)$$

where η is a generalized viscosity coefficient and α is an exponent. Besides the *NEMD* method of simulation box shearing, we have also calculated the viscosity coefficient using Green-Kubo (*GK*) relation. In Figure 3.16, we show the time relaxation of the *GK* viscosity coefficient of bulk *TM5* ionic liquid, which stabilizes around $\eta^{\text{GK}} = 0.62 \text{ mPa}\cdot\text{s}$. In Figure 3.17 we present the dependence of the average stress tensor component τ on the shear rate $\dot{\gamma}$ for *TM3*, *TM5* and *TM9* bulk *IL*.

We notice that the average tensor component stays within the same order of magnitude in *TM3* and *TM9* cases, although the shear rate changes four orders

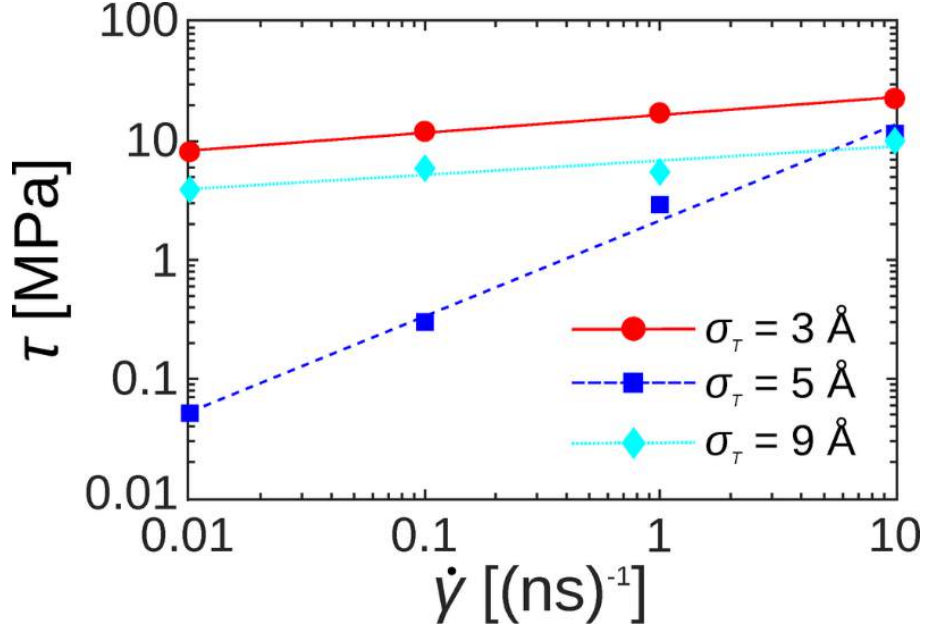


Figure 3.17: Average stress tensor component τ in function of shearing rate $\dot{\gamma}$ of *TM3*, *TM5* and *TM9* bulk *IL*. We have conducted shearing simulations with four orders of magnitude of the shearing rate ($\dot{\gamma} = 0.01 - 10 \text{ ns}^{-1}$). The lines are obtained by fitting the points with Equation 3.32.

of magnitude. Contrary to that, in case of *TM5* model there is a two orders of magnitude change of the average stress tensor component. We have obtained ordered bulk *IL* in case of *TM3* and *TM9* model, hence their values of α are low, i.e. $\alpha_{\text{TM3}} = 0.15 \pm 0.02$, $\alpha_{\text{TM9}} = 0.12 \pm 0.04$. We have obtained rather high values of their GK viscosity coefficients, i.e. $\eta_{\text{TM3}}^{\text{GK}} = 4.72 \text{ mPa} \cdot \text{s}$, $\eta_{\text{TM9}}^{\text{GK}} = 1.67 \text{ mPa} \cdot \text{s}$, which makes sense due to their ordered structure. In case of *TM5* model we have obtained $\alpha_{\text{TM5}} = 0.8 \pm 0.1$, which is fair enough close to the viscous fluid, i.e., $\alpha = 1$. This is in accordance with the liquid-like state of *TM5* model, as obtained in relaxation simulations, check Figure 3.15(b). Viscosity coefficients determined via shearing simulations and via GK method in case of *TM5* model are different, however they are of the same order of magnitude: $\eta_{\text{TM5}} = 0.1435 \text{ mPa} \cdot \text{s}$, $\eta_{\text{TM5}}^{\text{GK}} = 0.6144 \text{ mPa} \cdot \text{s}$.

3.3.2.3 Wetting properties

Analogously to the case of *SM* ionic liquid, we have determined the wetting properties of *TM* ionic liquids. The relaxed bulk *IL* obtained via relaxation simulations

represents the input of wetting simulations, i.e. a liquid droplet (with a cubic shape initially) is placed on a neutral solid plate which consists of one atomic layer in a *FCC* (111) lattice. The *LJ* interaction parameters take the values $\epsilon_{\text{II}} = 1.1$ kCal/mol and $\epsilon_{\text{IP}} = 5.3$ kCal/mol in all cases (i.e. for *TM3*, *TM5*¹ and *TM9* model) except in case of *TM5*² model where they are equal (i.e. $\epsilon_{\text{II}} = \epsilon_{\text{IP}} = 1.1$ kCal/mol), where ϵ_{II} , ϵ_{IP} correspond to ion–ion and ion–plate *LJ* interaction, respectively. The results of wetting simulations are presented in Figure 3.18. We have obtained partial wetting (to lower or higher extent) in all cases except in case of *TM5*² model in which practically there is no wetting. We notice that with the increase of the tail size σ_{TT} the wetting angle increases, i.e. partial wetting becomes weaker. The wetting process occurs in the way that a mixed cationic–anionic layer forms right next to the surface (a monolayer coating), and the rest of ions get "spilled" over this first layer. The tail size affects the quality of wetting. Neutral tails are responsible for the weakening of Coulombic interaction between the cations and anions. The formation of a monolayer coating is a mutual mechanism of wetting for every tail size, but the spilling of ions over that first layer becomes lower with the increase of the tail size. Comparison of *TM5*¹ and *TM5*² cases indicates that the strength of ϵ_{IP} parameter affects the wetting properties strongly. We have obtained a transition from partial to non–wetting behaviour when changing the value of ϵ_{IP} from 5.3 to 1.1 kCal/mol. This result is in agreement with Reference [49] where they conclude that the increase of *LJ* interaction between *IL* and substrate increases the quality of wetting.

3.4 Confined ionic liquid

We have learned about the characteristics of bulk *IL* and consequently prepared for exploring the confined *IL*, which is the main focus of our modeling of ionic liquids. This section is dedicated to the study of confined *IL* in case of *SM* model (subsection 3.4.1) and in case of three representative *TM* models (subsection 3.4.2). Each of those subsections includes three subsubsections, which are dealing with the static and dynamic force–distance characteristics of given *ILs*, as well as with their

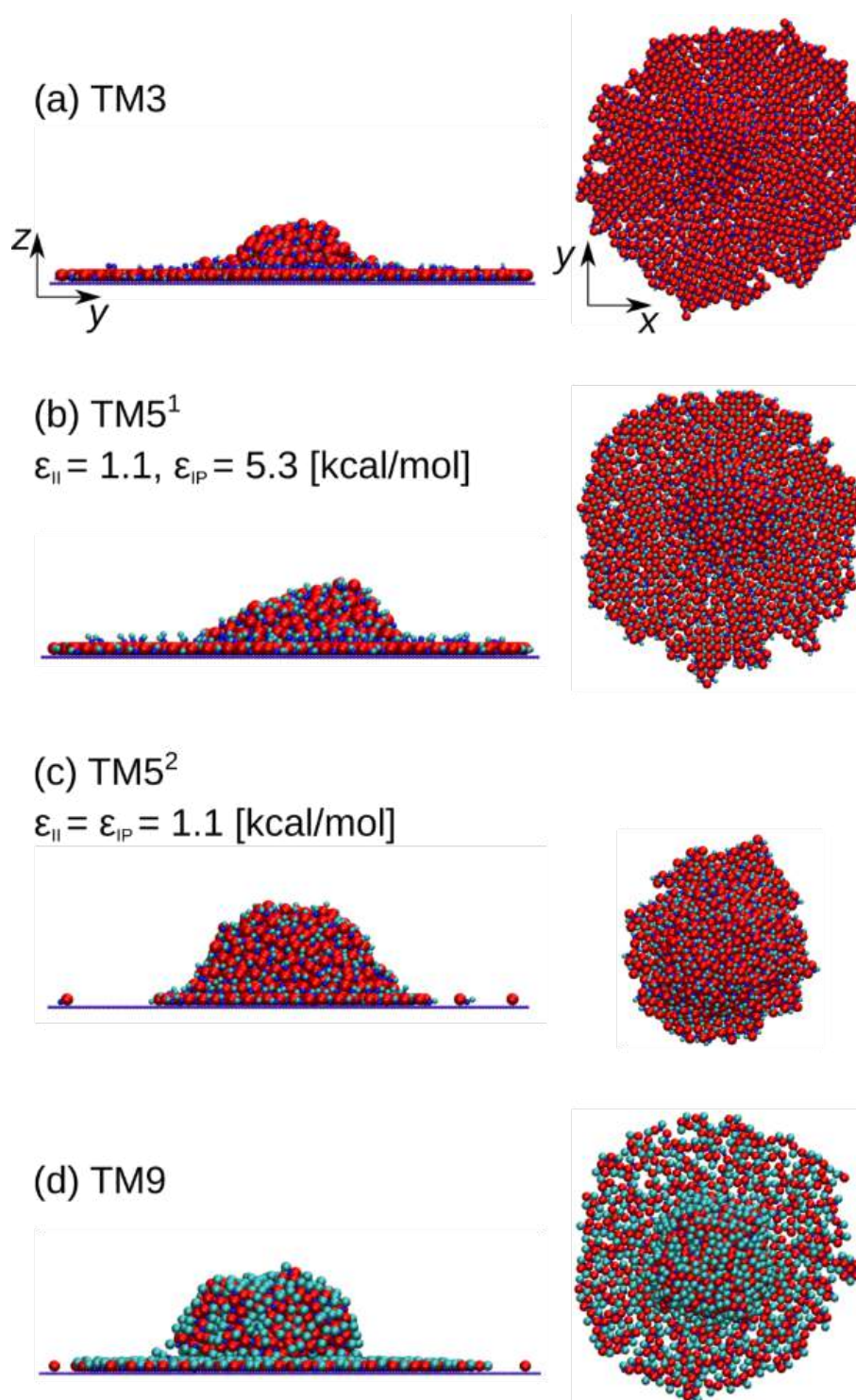


Figure 3.18: Wetting properties results in case of: (a) *TM3*, (b) *TM5*¹, (c) *TM5*² and (d) *TM9* model of *IL*. Left panels show *yz* cross-section of the system, while right panels show *xy* cross-section of the system.

tribological behaviour.

3.4.1 Confined salt model of ionic liquid

We have shown that our bulk *IL* is a Newtonian fluid: the validity of $\tau = \eta^{\text{GK}} \cdot \dot{\gamma}$ relation over the whole range of shearing rate $\dot{\gamma}$ supports that fact. Our model does not assume the nature of viscous response of *IL*. Only based on simulation results we conclude that bulk salt model (*SM*) *IL* behaves as a Newtonian fluid. For a different choice of parameters one could obtain power law or solid like behaviour. On the other hand, confinement strongly impacts the structure of *ILs* in thin films [64, 69, 105, 116], therefore when the same *IL* is confined it does not behave as a Newtonian fluid, as we will show in the rest of this section.

3.4.1.1 Static force-distance characteristic

The confinement has a profound influence on the structure of *ILs* in thin films [69, 105, 116]. The confining surfaces can induce ordering of the particles in their vicinity. The resulting structure and forces are a result of the interplay between the limited volume and the particles which fill the space.

We have used *MD* simulations to obtain the static force–distance characteristic. In order to determine a reliable static force–distance characteristic, at each calculation point we have to ensure that the system is in equilibrium. Concerning the realization of those simulations the interplate gap is modified in the following manner: the gap is increased or decreased (i.e., the Top–Bottom plate distance is changed) with a constant velocity $V_z = 5$ m/s for a *move* period of time $t_{\text{move}} = 20$ ps; thereafter, we apply conjugated gradient minimization on the ions in order to minimize their internal energy and relax them after the *move* period. As the energy minimization is performed, the ions take positions which ensure their minimal internal energy and the Top plate stays fixed for a *stay* period of time $t_{\text{stay}} = 50$ ps, during which period the average value of the normal force is calculated; that value is presented as a simulation point in $F_z(d_z)$ static characteristic, check Figures 3.19 and 3.21. The process was repeated until a distance $d_{z,\text{min}} = 11$ Å was reached. In order to avoid systematic errors due to the initial position or direction, the plate movement

is performed in different directions and from different initial configurations, hence Figures 3.19 and 3.21 show the averaged values of several realizations.

- Detailed analysis of the static force-distance characteristic

In Figure 3.19, the static force-distance characteristic of our system is presented. The red horizontal line denotes the zero normal force level (i.e., $F_z = 0$). A non-monotonous behaviour of the normal force F_z acting on the Top plate can be observed as the plate-to-plate distance is changing. This distance corresponds to the gap between the plates where the *IL* is under confinement. The points (d_z, F_z) have been obtained through our simulations, while the dashed line serves as a visual guide. It can be seen that the normal force strongly depends on the interplate distance. The presence of negative values of normal force F_z can be understood as the *IL* trying to reduce the plate-to-plate distance due to adhesion phenomena. These changes of the normal force are correlated with the extraction and inclusion of *IL* layers into the gap, as already observed experimentally, check Reference [69]. During the performed stationary state simulations, the cationic–anionic layers were squeezed out in pairs, in order to keep the system locally neutral, as observed in experimental studies [63, 69, 105, 116, 117]. In order to understand the structural evolution of our system, snapshots of the system from the *MD* simulations corresponding to several characteristic points in the $F_z(d_z)$ curve from Figure 3.19 were selected and studied in more detail. Figure 3.20 shows the configuration and ionic density distribution along the *z*–direction for eight characteristic points $\{A, B, C, D, E, F, G, H\}$, corresponding to plate-to-plate distances $d_z = \{11, 14, 17, 20, 22, 24, 27, 32\}$ Å respectively. The ions are deliberately depicted smaller than their *LJ* radii in order to allow a direct observation of the layering. The position of the atomic centers of the innermost atomic layers of the Top and Bottom plate are indicated in Figure 3.20 as z_T and z_B respectively. As the Bottom plate was fixed, z_B remains constant while z_T changes with the Top plate displacement.

A general feature observed under all conditions was the formation of cationic layer close to the plates. The reason for this is the smaller size of the cations ($\sigma_{CC} = 5\text{Å}$) compared to the anions ($\sigma_{AA} = 10\text{Å}$). Following this, the second layer gets induced by the first one (due to Coulombic interaction) and it is populated by

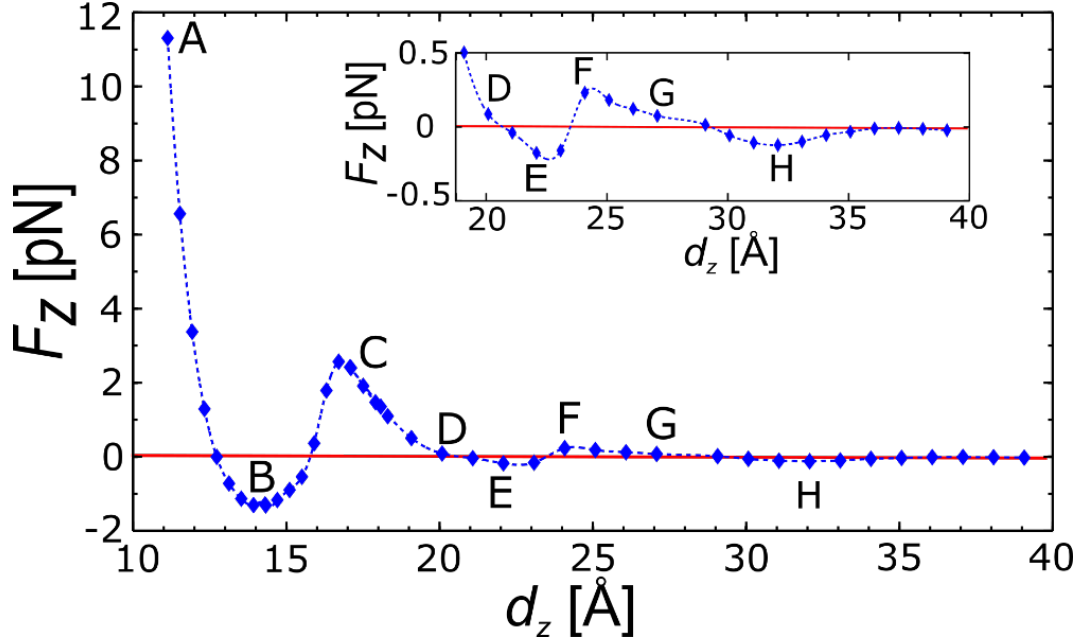


Figure 3.19: Dependence of normal force F_z on plate-to-plate distance d_z . Eight characteristic points $\{A, B, C, D, E, F, G, H\}$ with corresponding interplate distances $d_z = \{11, 14, 17, 20, 22, 24, 27, 32\}$ Å are marked on the $F_z(d_z)$ curve. The horizontal solid line denotes $F_z = 0$ pN. The dashed line connects the points obtained from the simulation and serves as a visual guide.

anions. The distance between the first and the second layer from the bottom is in the range of $1 - 2.5$ Å, meaning that while the centers of mass of the particles are in different layers, the layers themselves overlap as their distance is smaller than the particle diameters. From Figure 3.20 we observe that the anionic monolayer thickness is roughly 7 Å and corresponds to $10/\sqrt{2}$ Å, i.e., the anions are placed in the centers of the squares formed by the cations of the neighboring layers (the diameter of an anion is 10 Å). We will present the changes in the number of layers as the interplate gap is reduced and correlate them with the changes in the normal force F_z which is acting on the Top plate.

For the minimum simulated plate-to-plate distance $d_z = 11$ Å, shown in Figure 3.20(A) we can observe a pronounced peak in the anion density distribution close to the Bottom plate which is aligned with a well-defined anionic layer inside the gap. The anion peak is marked with the $1CU$ indication. In the case of cations, there are two peaks attached below and above the anionic peak. This situation

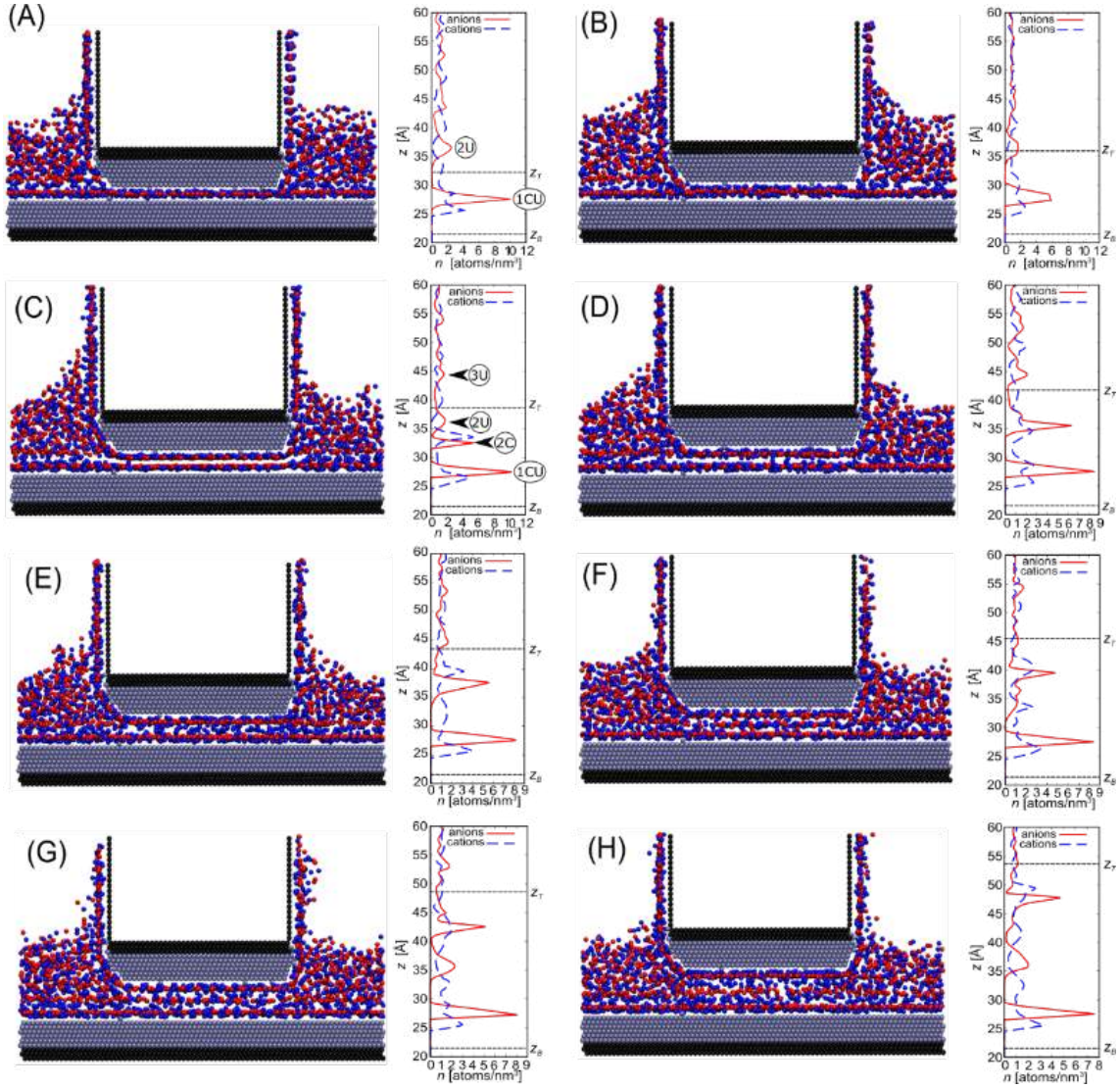


Figure 3.20: Snapshots of system configurations at points $\{A, B, C, D, E, F, G, H\}$ from Figure 3.19 and corresponding density distribution of cations/anions along the z axis. The position of the atomic centers of the innermost layer of the Top and Bottom plate is denoted by z_T and z_B , respectively. The Bottom plate is fixed and $z_B = 21 \text{ \AA}$. The ions are deliberately depicted smaller than their LJ radii in order to allow a direct observation of the layering. In Figures (A) and (C) the annotations indicate the anion layer vertical order from the bottom (1, 2, 3) and the lateral placement: (C)onfined and (U)ncconfined.

corresponds to the formation of two incomplete cationic layers inside the gap. With increasing plate-to-plate distance d_z the normal force F_z is decreasing, with a sign change of F_z at $d_z = 12.7 \text{ \AA}$. In the range $12.7 \text{ \AA} < d_z < 15.7 \text{ \AA}$ the normal force

remains negative. This means that the *IL* is pulling the plates together, since the ions strive to reduce their interlayer distance, as well as the distance between themselves and the plate atoms. Such behaviour is typically observed in systems exhibiting layering transition, already seen in systems of both neutral molecules [36] and *ILs* [69]. With further increase of d_z the force becomes positive again, and reaches a local maximum at the point (C) in Figure 3.19. At this point we observe a change in the number of anion layers confined in the gap from one to two, as shown in Figure 3.20(C). In Figure 3.20(C), the plate-to-plate distance is $d_z = 17 \text{ \AA}$ and the two bottom peaks of the anion/cation density distribution, denoted by $1CU$ and $2C$, are inside the gap. A third smaller anion/cation density peak, denoted by $2U$ in Figure 3.20(C), is the result of the ordering initiated at the Bottom plate's surface and is actually outside the confinement gap. The vertical distance between the peaks $2C$ and $2U$ is approximately 3.5 \AA and corresponds to the effect of the compression of the *IL* from the Top plate. Further increase of the plate-to-plate distance results in a continuous decrease of the normal force without a sign change as the positions of peaks $2C$ and $2U$ become aligned, check Figure 3.20(D) for a distance $d_z = 20 \text{ \AA}$. Further increase of the interplate distance results once more in a reversal of the sign of the normal force (i.e., $F_z < 0$ for $21 \text{ \AA} < d_z < 23.5 \text{ \AA}$). At the midpoint between the plates a broad maximum of cation density distribution can then be observed, see Figure 3.20(E). The cations, as smaller particles, have a tendency to fill the space between the more stable anionic layers. When the anions also start to form a third layer at the midpoint between the two plates the corresponding cationic peak of density becomes sharper and the normal force becomes positive again, see Figure 3.20(F). In this case the cations can form a layer more easily while the anions remain scattered. This is the opposite behaviour to the one typically observed, where the larger anions tend to order more strongly due to the excluded volume effect [118]. From Figure 3.20(F) to Figure 3.20(G) an interesting transition can be observed, during which the single well resolved cation peak disappears and a less pronounced cation–anion pair peak takes its place. Finally in Figure 3.20(H) at $d_z = 32 \text{ \AA}$, we observe the clear formation of three anion and four cation peaks. Considering engineering applications, the steep rise of the normal

force at small plate-to-plate distances, i.e., $d_z < 14 \text{ \AA}$ can be beneficial for protecting against solid-solid contact and consequent wear.

- Analysis of the static force-distance characteristic over intervals

There is a strongly decreasing trend of the maximal normal force which can be sustained by the system as the number of ionic layers confined between the plates increases, i.e., for the two ionic layers the maximal force $F_{z,max}^I = 3 \text{ pN}$, while for the three ionic layers it is $F_{z,max}^{II} = 0.25 \text{ pN}$. In our model, the Lennard-Jones interaction between the plates and the ions is ten times stronger than between the ions themselves. The ionic layers closest to the plates are therefore more stable than the layers in the midpoint of the gap (interval *II*). As a result, the three-layer system becomes less dense and can build up a lower normal force compared to the two-layer system.

We have selected two intervals of interest for the interplate distance which capture the presence of local maxima and subsequent minima of the normal force F_z accompanied with the compression of *IL*. This corresponds to the expulsion of a cation–anion layer pair from the gap. The intervals are: $d_z^I = [14.2, 20] \text{ \AA}$, $d_z^{II} = [22, 27] \text{ \AA}$, and they are labeled as *I* and *II* respectively. In order to understand the changes of the system configurations and to correlate them with the changes of the interplate distance, snapshots of the system from the *MD* simulations corresponding to several characteristic points of the intervals *I* and *II* have been selected and studied in more detail: $I_{1,2}$, $II_{1,2}$ which correspond to the limits of the intervals, and the local maximum of the interval *I*, labeled as I_3 .

The left vertical panel of Figure 3.22 shows the system configuration in the *yz* cross-section and the ionic density distribution along the *z*–direction obtained in the equilibrium force–distance simulations for the three characteristic points of the interval *I*: $\{I_1, I_2, I_3\}$, corresponding to the interplate distances $d_z = \{14.2, 20, 17.2\} \text{ \AA}$, respectively. In Figure 3.23 the left vertical panels show analogous results for the two characteristic points of the interval *II*: $\{II_1, II_2\}$, corresponding to the interplate distances $d_z = \{22, 27\} \text{ \AA}$, respectively. In addition to the *yz* cross-section configuration snapshots together with the ionic density distribution along the *z* axis, shown in the left panels of Figures 3.22 and 3.23 for the cases of intervals *I* and *II*, respec-

tively, we have prepared the xy cross-section configuration snapshots, shown in the left panels of Figures 3.24 and 3.25.

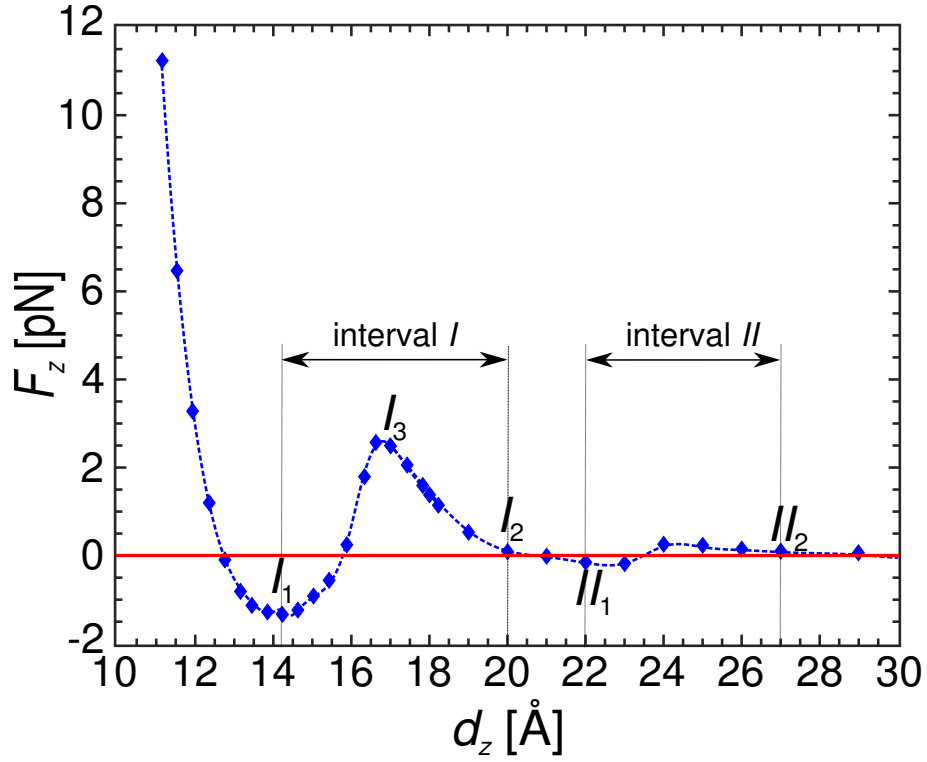


Figure 3.21: Dependence of normal force F_z acting on the Top plate on interplate distance d_z . Five characteristic points $\{I_1, I_2, I_3, II_1, II_2\}$ with corresponding interplate distances $d_z \approx \{14, 20, 17, 22, 27\}$ Å are marked on the $F_z(d_z)$ curve. Also, the two characteristic intervals of d_z are labeled, where the interval I is bounded by the points I_1 and I_2 , while the interval II is bounded by the points II_1 and II_2 . The horizontal solid line denotes $F_z = 0$ pN. The dashed line connects the points obtained from the simulation and serves as a visual guide.

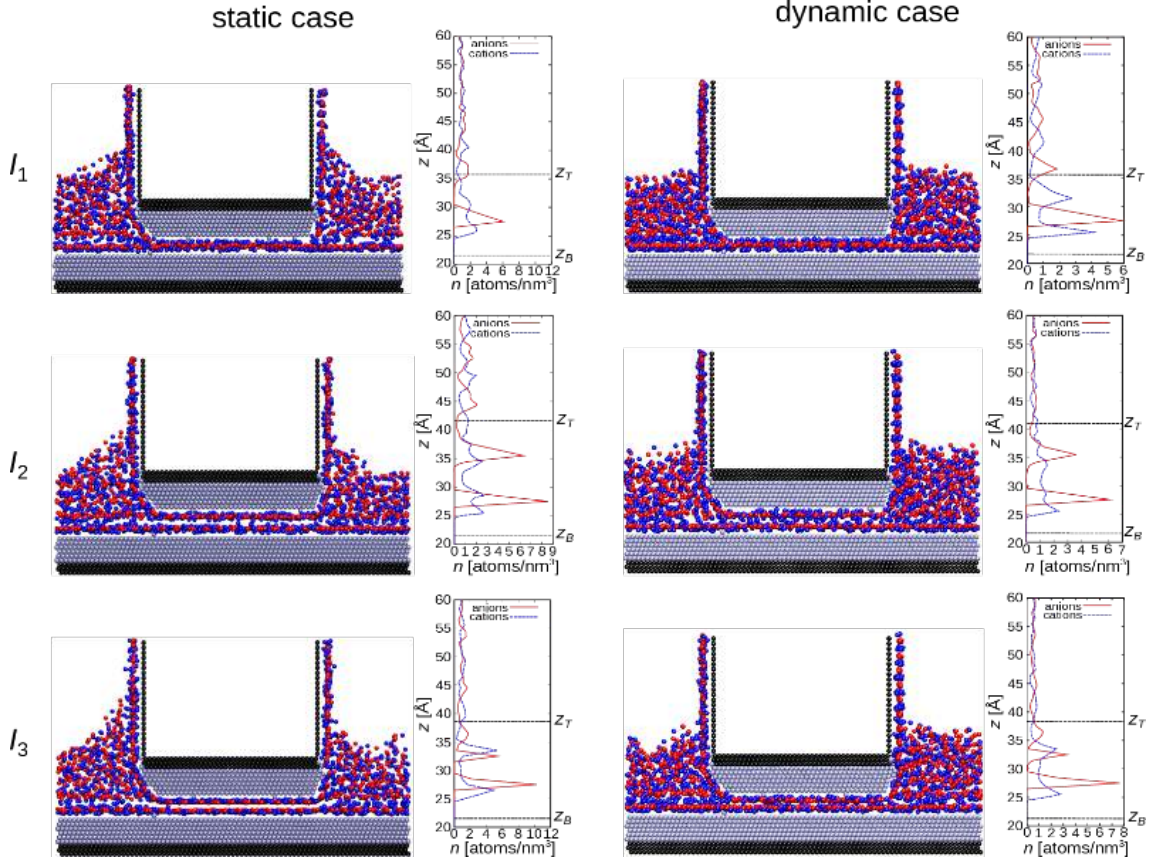


Figure 3.22: Configuration snapshots (yz cross-section) accompanied with ionic density distribution along the z direction in three representative points of the interval I : $\{I_1, I_2, I_3\}$. Left panels correspond to the static case of Top plate's movement, while right panels correspond to the dynamic case of Top plate's movement.

3.4.1.2 Dynamic force-distance characteristic

We have investigated the dynamic behaviour of the IL during a periodic linear movement of the Top plate along the z axis, between the two limiting points of the intervals I and II . The space between the solid plates was in this way periodically expanded and compressed. Periodic movements of the Top plate were performed at three constant velocities $V_z = \{0.1, 1, 10\}$ m/s but no velocity dependent differences in the system behaviour were observed. We have performed ten cycles in order to determine how much do the cycles differ and to determine a statistically reliable average cycle. The confined ionic liquid lubricant responds to the cyclic movement with a hysteresis in the normal force $F_z(d_z)$ as shown in Figure 3.26. We present

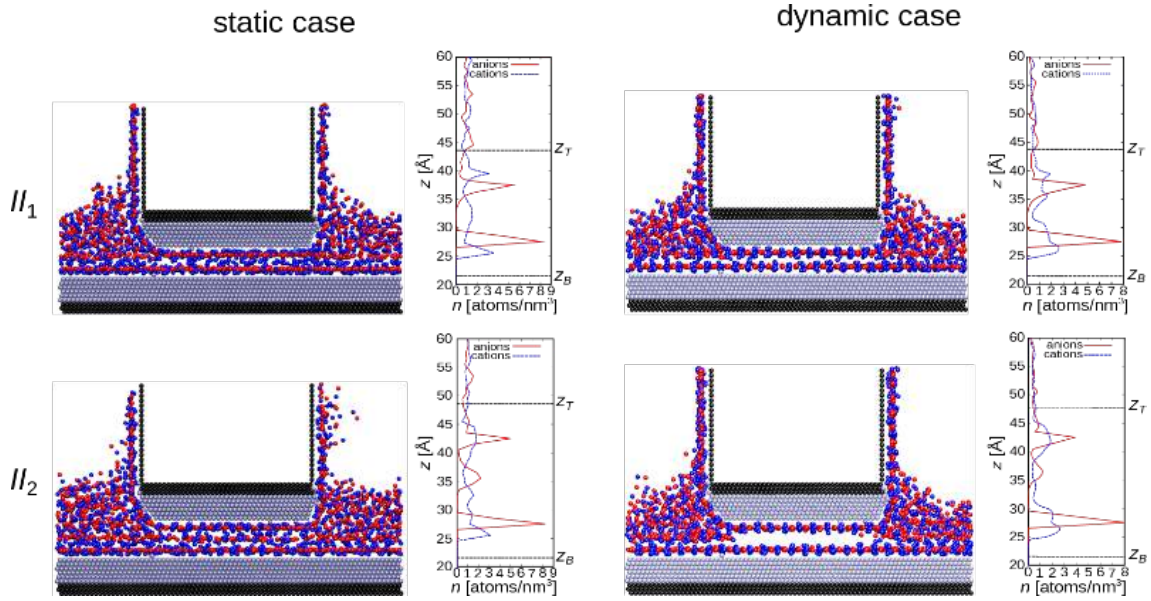


Figure 3.23: Configuration snapshots (yz cross-section) accompanied with ionic density distribution along the z direction in two representative points of the interval II : $\{II_1, II_2\}$. Left panels correspond to the static case of Top plate's movement, while right panels correspond to the dynamic case of Top plate's movement.

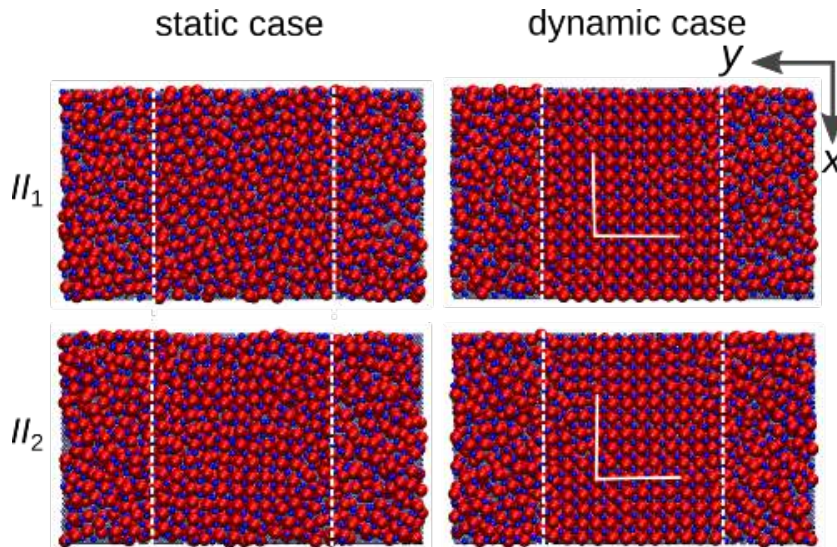


Figure 3.24: Configuration snapshots (xy cross-section) in two representative points of the interval II : $\{II_1, II_2\}$. Left panels correspond to the static case of Top plate's movement, while right panels correspond to the dynamic case of Top plate's movement. We have highlighted the confined region with dashed lines (Top plate's width along the y axis is a half of the total system's width) and also we have sketched crystallization patterns with solid lines.

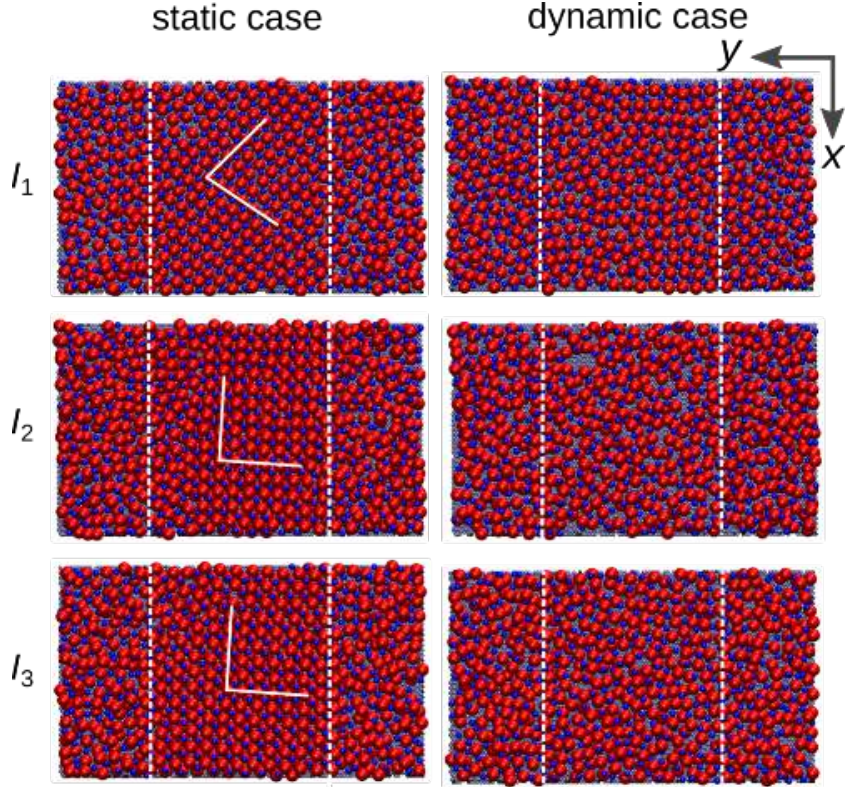


Figure 3.25: Configuration snapshots (xy cross-section) in three representative points of the interval I : $\{I_1, I_2, I_3\}$. Left panels correspond to the static case of Top plate's movement, while right panels correspond to the dynamic case of Top plate's movement. We have highlighted the confined region with dashed lines (Top plate's width along the y axis is a half of the total system's width) and also we have sketched crystallization patterns with solid lines. Periodic boundary conditions are applied in the x and y directions, while simulation box, which is cubic, is kept fixed in the z direction.

both the raw data of all cycles (thin solid lines) and a smooth average cycle (thick solid line). In the case of interval I there are three points of interest $\{I_1, I_2, I_3\}$, corresponding to the points noted in Figure 3.21. Points I_1 and I_2 are the starting and ending point respectively and the point I_3 corresponds to the maximum of the normal force F_z in the smooth average cycle. We observe that between each two of those points there are clear tendencies in the average cycle of the normal force as a function of the interplate distance $F_z(d_z)$. First, in the segment $I_1 \rightarrow I_2$, i.e., in the extension half of the cycle, there is a continuous increase of the normal force F_z from negative values up to the value around zero in point I_2 . In point I_1 there is one anionic layer confined in the gap and normal force F_z has a negative value. With the

dynamic increase of the gap ions are pulled-in from lateral reservoirs into the gap. In point I_2 an additional cationic-anionic layer pair is fully formed in the gap, hence increasing the number of confined anionic layers to two. Next, there is the segment $I_2 \rightarrow I_3$ where the ions are compressed within the gap, which is consistent with the continuous increase of the normal force F_z . In this segment, the normal force F_z takes positive values meaning that the ionic liquid shows resistance to the compression but does not flow out. After that, in segment $I_3 \rightarrow I_1$ there is a sharp decrease of the normal force F_z which is correlated with the squeezing-out of the additional cationic-anionic layer taken in from the lateral reservoirs during the extension half-cycle. During the compression half-cycle there is a return to the initial state I_1 , where the interplate gap contains one compact anionic layer. We should note that the distributions of cations and anions in the dynamic case for interval I bear close resemblance. Let us now discuss the changes in the number of confined ionic layers as a function of the interplate distance and correlate them with the changes in the normal force F_z acting on the Top plate: in the range $d_z = [11, 14.2]$ Å the normal force F_z acting on the Top plate has a steep decrease, reaching the minimum at point I_1 . For the point I_1 at $d_z = 14.2$ Å, check Figure 3.22, we can observe a pronounced peak in the anion density distribution which is aligned with a well-defined anionic layer inside the gap. In the case of cations, there are two peaks attached below and above the anionic peak. This situation corresponds to the formation of two incomplete cationic layers inside the gap. The value of normal force F_z is negative and in point I_1 it has the deepest minimum when considering the whole $F_z(d_z)$ characteristic. With increasing plate-to-plate distance d_z the normal force F_z is increasing, with a sign change of normal force F_z around $d_z = 15.7$ Å in the equilibrium case and $d_z = 17.8$ Å in the dynamic case, check Figures 3.21 and 3.26(a), respectively. This means that before this point the *IL* is pulling the plates together, since the ions strive to reduce their interlayer distance. After this point, for $F_z > 0$, enough ions are pulled inside the gap and the *IL* now pushes the plates apart. Such behaviour is typically observed in systems exhibiting layering transition, already seen in systems of both neutral molecules [36] and *ILs* [69]. With reversing into compression in Figure 3.26(a), the normal force F_z reaches a local maximum

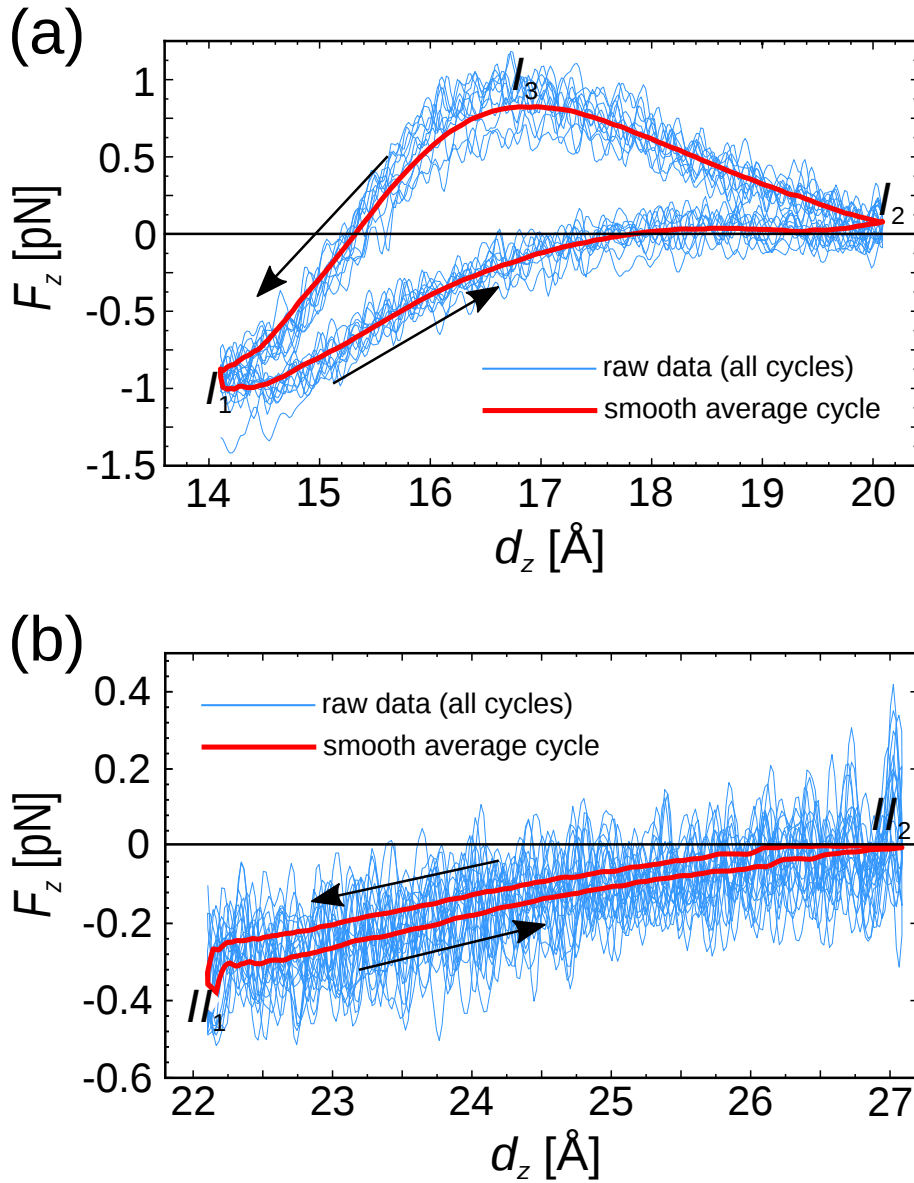


Figure 3.26: This figure presents the results of dynamic extension–compression cycles in the intervals I and II . In panel (a) we present dynamic $F_z(d_z)$ characteristic in the interval I : thin lines represent the hystereses of ten dynamic cycles, solid line on top of them is the smooth average hysteresis. There is also a solid horizontal line which corresponds to $F_z = 0$. Panel (b) is analogous to the panel (a), just it presents the results in the interval II .

in the point I_3 at $d_z = 17.2$ Å. This is actually the location of the maximum in the equilibrium case as well, check Figure 3.21. With the further decrease of d_z beyond the point I_3 there is a continuous decrease of the normal force up to the distance $d_z = 14.2$ Å as IL starts flowing out of the gap. Still, one should note that there

are two differences between the two systems:

- (i) the sign of the normal force in point I_2 and
- (ii) the magnitude of the normal force at local maximum I_3 .

In the case of cyclic (dynamic) movement of the plates, the normal force is positive $F_z > 0$, i.e. the IL keeps pulling apart the plates at point I_2 and the maximum of the normal force in the point I_3 ($F_z^{dyn} = 1$ pN) is lower than in the static case ($F_z^{stat} = 3$ pN). Both observations indicate that the plate's motion is preventing the ionic liquid to fully fill the void space of the gap. Also, there is a substantial slip during the ejection of IL from the gap, which results in a lower normal force. Otherwise, if no slip would be present the maximal normal force at velocity $V_z = 1$ m/s should be about two orders of magnitude higher based on the bulk viscosity coefficient calculated in section 3.3.

Partial filling of the gap due to the motion of the walls is even better observable in the results for the interval II . While the equilibrium characteristic has a local maximum, check Figure 3.21, in the dynamic case there are only two characteristic points (starting and ending point $\{II_1, II_2\}$) and a monotonously increasing normal force between them. At point II_1 at $d_z = 22$ Å in the static case, we notice that at the midpoint between the plates there is a broad maximum of the cation density distribution, see Figure 3.23. In the static case we notice that, similar to the transition from one to two anionic layers within the interval I , there is a transition from two to three anionic layers within the interval II , which happens in proximity of the point $d_z = 24$ Å. At point II_2 we notice two sharp anionic layers in the proximity of the plates and the third anionic layer which is broader, less sharp and positioned in the middle of the interplate gap, check Figure 3.23. In the dynamic case the number of layers remains the same in the interval II , they just get separated during the extension and a formation of additional ionic layers by the ions flowing from the lateral reservoirs into the gap does not take place, check Figure 3.23.

We can conclude that in a confined system with strong interaction between the walls and the IL , the major driving force that pulls IL into the gap between the plates is the interaction with the wall atoms rather than the inter- IL interactions. In order to visualize what happens in the vicinity of the plates, we are presenting

snapshots of xy cross-section configurations in the intervals I and II , check Figures 3.24 and 3.25, respectively. Even on a cursory look, one sees that the phase behaviour of the confined IL is complex: in Figure 3.24 there was no movement of the IL in and out of the gap and the IL formed a two-dimensional square crystal on both surfaces during the dynamic case. In the equilibrium configurations, there are probably enough ions in the gap that allow the IL to obtain its liquid-like character. On the other hand, in Figure 3.25, we observe a salt-like ordering taking place in all representative points $\{I_1, I_2, I_3\}$ of the static configurations. In the dynamic case the IL exhibits some level of ordering for a small gap (I_1) and it is amorphous in the other two points.

At this point, we would like to quantify how could the processes described above contribute to the energy losses. If two macroscopically smooth surfaces come into contact, initially they only touch at a few of these asperity points. A motion of two bodies in contact lubricated by an ionic liquid would involve the generation of new contacts and the separation of the existing ones. Ionic liquids are characterized by strong Coulombic interactions between the particles. By calculating the area covered within the average cycle of the $F_z(d_z)$ curves in Figure 3.26, we calculate the amount of work invested per average dynamic cycle, i.e., the hysteretic energy losses. There is a big difference in the amount of invested work in the two intervals: $3.5236 \text{ pN} \cdot \text{\AA}$ for the interval I compared to $0.2844 \text{ pN} \cdot \text{\AA}$ for the interval II , where the vertical displacement of the Top plate in the two intervals is roughly the same $\Delta d_z \approx 5 \text{ \AA}$. This is consistent with a strongly decreasing trend of the maximal normal force which can be sustained by the system as the number of ionic layers confined between the plates increases, i.e. for the two ionic layers the maximal normal force $F_{z,max}^I = 3 \text{ pN}$, while for the three ionic layers it is $F_{z,max}^{II} = 0.25 \text{ pN}$, corresponding to the two maxima of the static force-distance characteristic in Figure 3.21.

3.4.1.3 Tribological behaviour of confined salt model of ionic liquid

- Tribological behaviour under different conditions in terms of interplate gap and external pressure

Following the detailed study of the static and dynamic system, we turn our focus to

exploring tribological behaviour of confined *SM* ionic liquid under given conditions. Namely we impose a relative motion between the plates in the x -direction and as a result frictional forces can be observed. The dynamics of the plates impact the *IL* and result in an overall longitudinal force acting on each solid body. In order to evaluate the trends of specific friction we have performed simulations at different plate velocities and at two interplate distances. The simulations have been performed for a broad range of the Top plate velocities $V_x = \{0.1, 0.2, 0.5, 1, 2, 5, 10\}$ m/s, with the Bottom plate kept fixed. We have compared cases with different external pressures applied on the *IL*: $p_{\text{ext}} = \{0, 120, 250\}$ kPa and two different interplate distances $d_z = 17$ and 27 \AA . The simulations were performed as follows: Points (C) and (G) in Figure 3.20 were chosen as the starting configurations. The simulations ran until the Top plate had covered a distance of $d_x = 50 \text{ \AA}$ along the x -direction.

Table 3.4: Results for the coefficients a, b in the relation $\langle F_x \rangle / \langle F_z \rangle = a \log(V_x / V_{\text{ref}}) + b$, where $V_{\text{ref}} = 1$ m/s. The results were obtained using the least-squares method.

Case	a	b	R^2
(A) $d_z = 17 \text{ \AA}$, $p_{\text{ext}} = 0$ kPa	-0.0006(2)	0.0039(2)	0.63
(B) $d_z = 27 \text{ \AA}$, $p_{\text{ext}} = 0$ kPa	0.016(5)	0.036(3)	0.72
(C) $d_z = 27 \text{ \AA}$, $p_{\text{ext}} = 120$ kPa	0.007(2)	0.017(2)	0.26
(D) $d_z = 27 \text{ \AA}$, $p_{\text{ext}} = 250$ kPa	0.002(1)	0.003(1)	0.62

Therefore, the cases with lower velocities required an increased total time. The forces acting on the Top plate were monitored, as shown in Figure 3.27 for a randomly chosen case. It was observed that the normal force remained roughly the same after the onset of the simulation. Steady-state conditions were assumed following a displacement of $d_x = 10 \text{ \AA}$, and then average values were calculated using the statistics until the completion of the simulation. The results for the specific friction $\langle F_x \rangle / \langle F_z \rangle$ are shown as a function of the sliding velocity V_x in Figure 3.28. The specific friction $\langle F_x \rangle / \langle F_z \rangle$ is defined as the ratio of the time averaged frictional and normal force F_x and F_z respectively and is different to the Coulomb friction coefficient $\mu = \partial F_x / \partial F_z$. In our simulated cases we have observed either a weak or a logarithmic dependence of specific friction on velocity. The numerical values

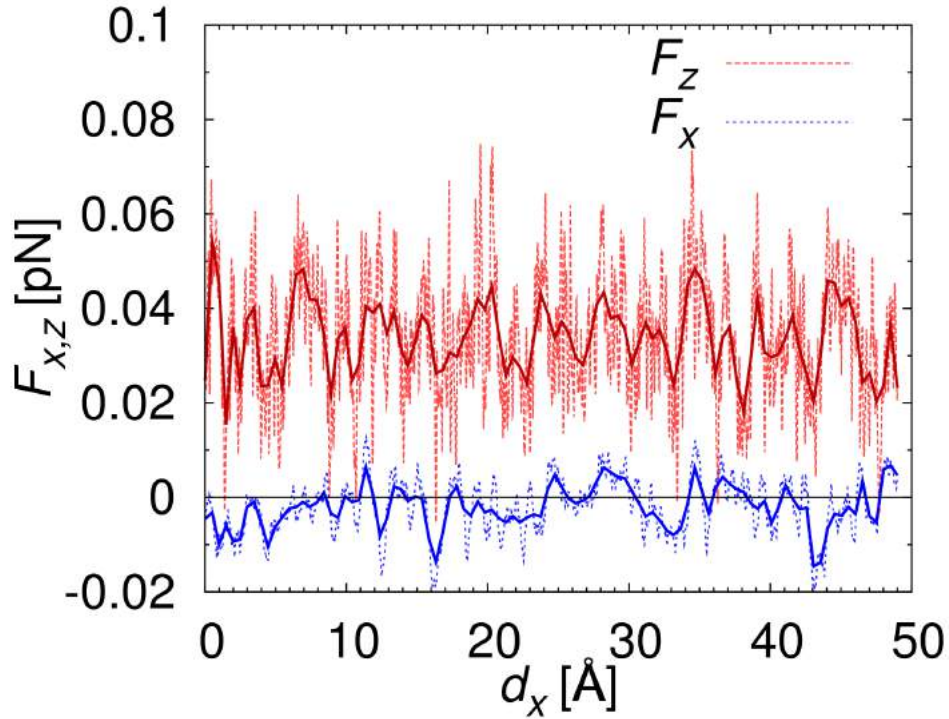


Figure 3.27: Temporal evolution of total normal and axial forces acting on sliding surface for the interplate distance $d_z = 27 \text{ \AA}$ and Top plate axial velocity $V_x = 10 \text{ m/s}$. Dashed lines show the raw numerical data which are smoothed using the solid lines for a clearer identification of trends.

were fitted to a linear function of the form $\langle F_x \rangle / \langle F_z \rangle = a \log(V_x / V_{ref}) + b$, where $V_{ref} = 1 \text{ m/s}$. The coefficients a, b obtained from the simulation data are listed in Table 3.4. A reasonable fit to the linear regression curve can be observed for most cases. In the case of $p_{ext} = 120 \text{ kPa}$, the system is potentially in a transition between the two significantly different cases of zero and high pressure, which can explain the poorer quality of the fit to the linear curve. The logarithmic dependence indicates typical elasto-hydrodynamic lubrication conditions [119]. On the other hand, the weak dependence of specific friction on velocity has also been observed in previous studies of *IL* lubrication, check Reference [39, 56].

- Impact of ionic liquid confinement gap and pressurization

The influence of the interplate distance on specific friction was initially analyzed, while the applied external pressure on the *IL* p_{ext} was kept equal to zero. In contrast

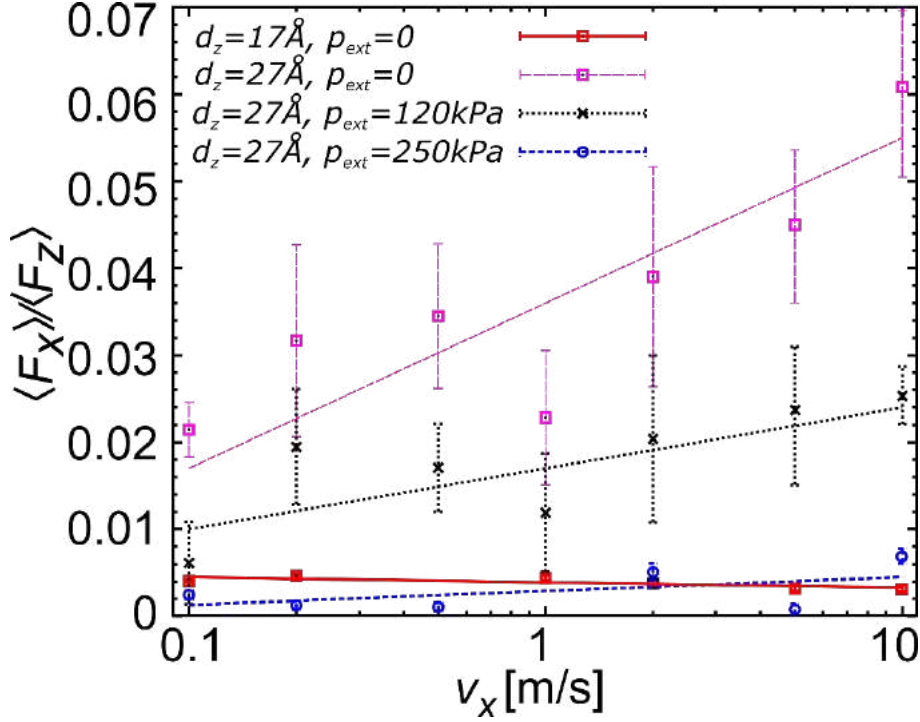


Figure 3.28: Dependence of specific friction $\langle F_x \rangle / \langle F_z \rangle$ on velocity V_x at external pressures $p_{ext} = \{0, 120, 250\}$ kPa and interplate distances $d_z = 17$ and 27 Å. The error bars represent the standard deviation of the average values obtained from the simulation data. The curves showing the specific friction trends were obtained by linear regression and the corresponding parameters are listed in Table 3.4.

to the previous studies of *IL* lubrication [39, 56], our system has shown a strong crystalline ordering induced by confinement. The normal force was roughly ten times higher in the case of the smaller interplate distance, i.e., for $d_z = 17$ Å compared to $d_z = 27$ Å. On the other hand, the lateral force F_x remained at similar levels, therefore leading to a sharp decrease of the specific friction values. At the same time, the weaker confinement and the smaller normal force for $d_z = 27$ Å resulted in a steeper slope of the curve $\langle F_x \rangle / \langle F_z \rangle$.

In order to understand the potential correlation of the *IL* structure with the arising frictional forces, the confinement zone was observed in detail using Figure 3.29, where a side view (left side) and top view (right side) of the system is shown. In the top view, the system is shown with the solid and *IL* particles above the upper plate's plane removed. In this plot the ions are depicted with their corresponding *LJ* radii in order to achieve a realistic visualization of the structure. The anions

form a locally cubic structure, check right panel Figure 3.29(A), while the crystal direction of the cubic structure is indicated with the dashed lines. If we look into the structure of the *IL* in the confinement zone, Figure 3.29(A) and (B), we can observe a single, well-resolved crystal structure in the case of $d_z = 17 \text{ \AA}$, while in the case of $d_z = 27 \text{ \AA}$ some defects are present. It can also be observed that outside the gap, the *IL* remains in a disordered, liquid state.

Further clarification can be attained by plotting the ionic density distribution profiles inside and outside the gap in Figures 3.30(A) and (B). It can be observed that at the plate-to-plate distance $d_z = 17 \text{ \AA}$, both cation and anion peaks of density distribution function inside the gap are narrow and sharp. In addition, both the anion and cation peaks in each paired layer are located at approximately the same z location. These findings confirm that under these conditions the *IL* is in a crystalline, "solid-like" state with minimum disorder. In the case of a wider gap $d_z = 27 \text{ \AA}$ the anion peaks next to the walls remain narrow, with a third broader one appearing in the center. The cation arrangement is more dispersed, with double peaks appearing above and below each anion peak. These statistics indicate a more layered, less strictly ordered state.

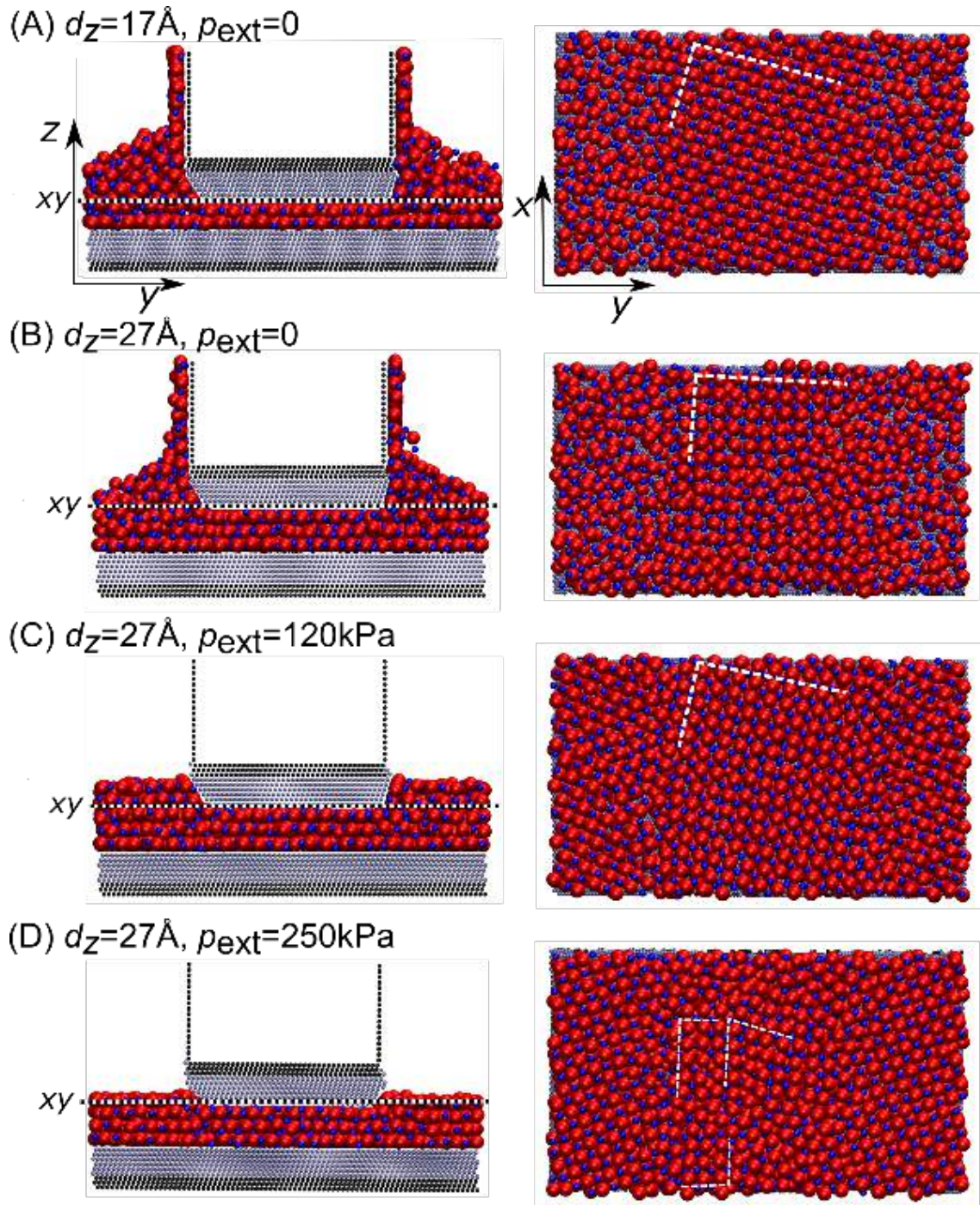


Figure 3.29: Side (yz) and top (xy) views of the snapshots from four separate friction simulations. The top views correspond to the planes marked with dashed lines in the side views and do not include the solid and IL particles above the upper plate plane. The ions are depicted according to their LJ radii in order to visualize the crystalline structures. The dashed lines in the top views denote the crystal direction of self-formed cubic structures.

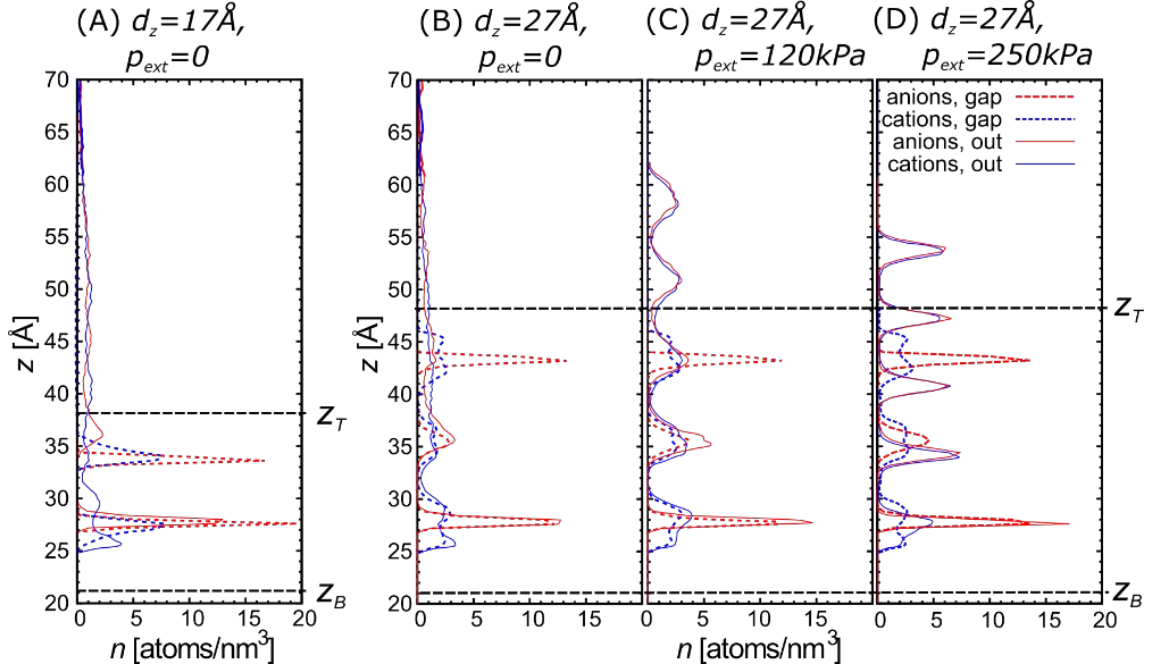


Figure 3.30: Density distributions of ions along the z axis inside (dashed lines) and outside (solid lines) the confinement zone between the solid plates for configurations shown in Figure 3.29. The position of the atomic centers of the innermost layer of the Top and Bottom plate is denoted with z_T and z_B , respectively. Bottom plate is fixed with $z_B = 21 \text{ \AA}$.

The difference in the extent of confinement-induced crystallization is a probable reason for the observed steep slope of specific friction since the observed defects can interact more strongly with the upper plate at higher velocities and contribute to the increase of friction force. Our observations show some similarity to the behaviour previously seen in Lennard-Jones systems where systems at pressures above a certain critical value and at sufficiently low velocities exhibited such behaviour. In these studies, check Reference [42], the shape of fluid molecule was identified as the main parameter that controls crystallization through the promotion or prevention of internal ordering.

In addition to the impact of different confinement gaps, the effect of IL pressurization was studied, while the interplate distance was kept constant. More specifically, a gap of $d_z = 27 \text{ \AA}$ was used, while different pressures $p_{ext} = \{0, 120, 250\}$ kPa were applied.

Through observation of Figure 3.30(B)-(D), it can be seen that the application of external pressure prevents the wetting of the side walls of the Top plate and leads to a distinct crystallization of the unconfined *IL*. On the other hand, the ion density profiles inside the confinement zone are moderately influenced.

Friction results for increasing values of applied pressure p_{ext} are consistent with the observations from Figure 3.28 with specific friction decreasing as the ordering of the *IL* increases. It can be seen that for high external pressure, i.e., $p_{ext} = 250$ kPa, the slope of the specific friction curve almost vanishes.

Figure 3.29(C) shows that for $p_{ext} = 120$ kPa the local cubic structure induced by confinement between the plates served as a nucleus for further crystallization between the plates and a well-ordered single crystallite was formed in this region. Outside the confinement zone another crystallite was formed with a different orientation. Further increase of external pressure to $p_{ext} = 250$ kPa forced the *IL* in the void space to crystallize, while at the same time the *IL* in the confinement zone was converted to a number of smaller crystallites, check Figures 3.29(D) and 3.30(D).

The reported results show a dual nature of *IL* lubrication, with EHL characteristics at low to medium pressures and confinement gaps that allow more than two distinct anion/cation pair layers to form. At higher pressures and smaller distances, which can be translated as mixed lubrication conditions, the *IL* is transformed into a solid-like body, while specific friction decreases to low values which are independent of the sliding velocity. This behaviour can be beneficial in engineering applications such as the piston ring–cylinder liner system, where it can be assumed that the *IL* crystallization can potentially help in preventing the solid contact between the solid surfaces, along with the associated high friction and wear.

- Shear behaviour of confined salt model of ionic liquid

In order to study the behaviour of our confined *SM* ionic liquid under shearing we apply a relative motion between the plates along the x direction. The Bottom plate is kept fixed and a constant velocity V_x is imposed on the Top plate. We are interested in establishing how does the lateral (frictional) force F_x depend on the confinement gap $d_z = \{12, 14, 16, 18, 22, 25\}$ Å. In Figure 3.31 we are showing the dependence of the time averaged frictional force divided by the contact area of the

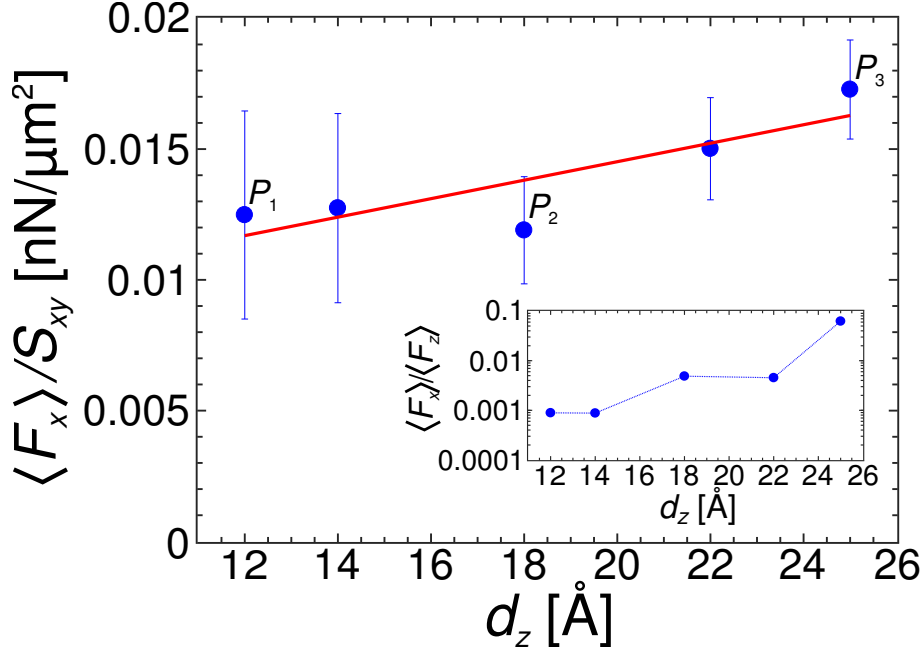


Figure 3.31: Dependence of the frictional force divided by the contact area of the Top plate with *IL* lubricant $\langle F_x \rangle / S_{xy}$ on the interplate distance d_z . The three representative points $\{P_1, P_2, P_3\}$ are marked. Points obtained in simulations are shown as circle markers, accompanied with errors along the y axis. Linear fit through those points is shown as a solid line. In the inset dependence of specific friction $\langle F_x \rangle / \langle F_z \rangle$ on the interplate distance d_z is shown, with y axis in log scale. Simulation points are shown as circle markers, while the dashed line serves as a visual guide.

Top plate and the *IL* lubricant, i.e. $\langle F_x \rangle / S_{xy}$ on the interplate distance d_z . We observe a linear increase of the frictional force per contact area with the increase of the interplate distance, with a slope of 4 nN/ μm^3 . In the inset of Figure 3.31, we are showing the dependence of specific friction defined as the ratio of the time averaged frictional and normal force $\langle F_x \rangle / \langle F_z \rangle$ on the interplate distance d_z . By comparing Figure 3.31 with the results for the bulk liquid in Figure 3.12 we observe that there is no correlation with the lubricant viscosity (i.e., otherwise frictional force would be three orders of magnitude higher). This leads us to the assumption that our pressurized systems, whether they form a crystalline lattice or not, do not lie in a typical hydrodynamic regime and operate under full slip conditions in which the ionic liquid moves together with one of the walls. As there is no solid–solid contact between the two surfaces, but lubrication through very thin, highly viscous films which are solid–like, mixed or dry lubrication are the two potential regimes

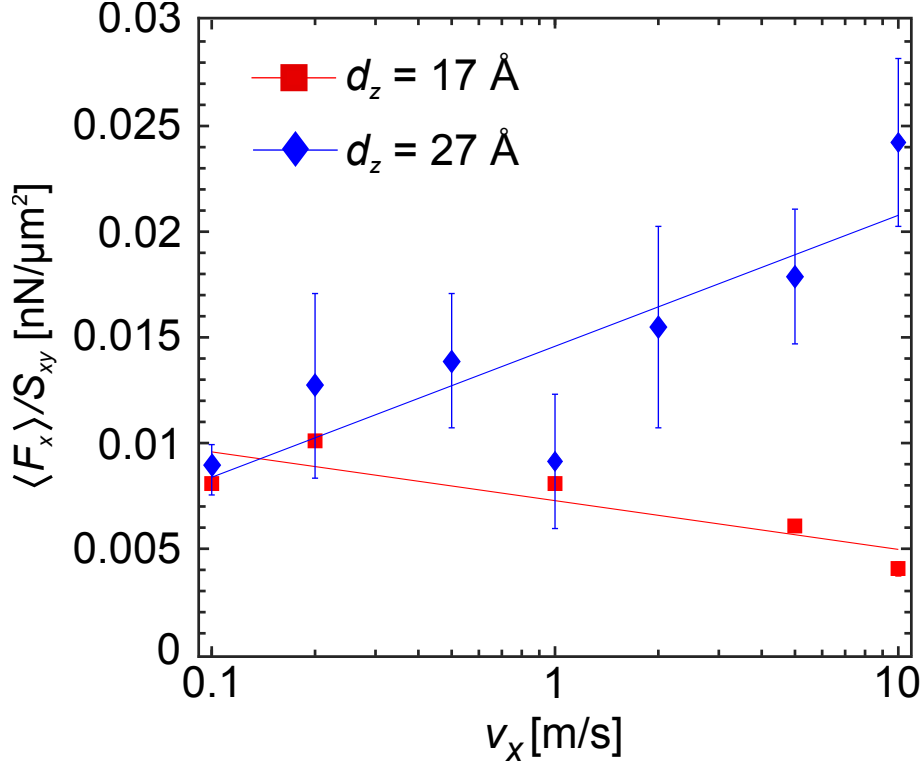


Figure 3.32: Dependence of the frictional force divided by the contact area of the Top plate with *IL* lubricant $\langle F_x \rangle / S_{xy}$ on the Top plate's lateral velocity $V_x = 0.1 - 10$ m/s. The error bars represent the standard deviation of the average values obtained from the simulation data. The lines showing the friction trends are obtained by linear regression.

that can describe the observed conditions. A parametric study on different shearing velocities $V_x = 0.1 - 10$ m/s at two wall separations $d_z = 17, 27 \text{ \AA}$ provides additional information for the characterization of the tribological regime of our system. In Figure 3.32 one can observe a logarithmic (weak) dependence of the frictional force per contact area on lateral velocity of the Top plate's movement, which is consistent with the observations of previous studies of *IL* lubrication, check Refs. [39, 56].

From Figure 3.31 we have selected three representative points with $d_z = \{12, 18, 25\} \text{ \AA}$ labeled as $\{P_1, P_2, P_3\}$ respectively. We provide an overview of the yz configuration cross-sections together with ionic density distributions along the z axis (check Figure 3.33) at the simulation onset $t = 0$ and after $t = 3$ ns. In the panels of Figure 3.34 we have highlighted the confined region with dashed lines (the Top plate's width along the y axis is half of the total system's width) and we have also

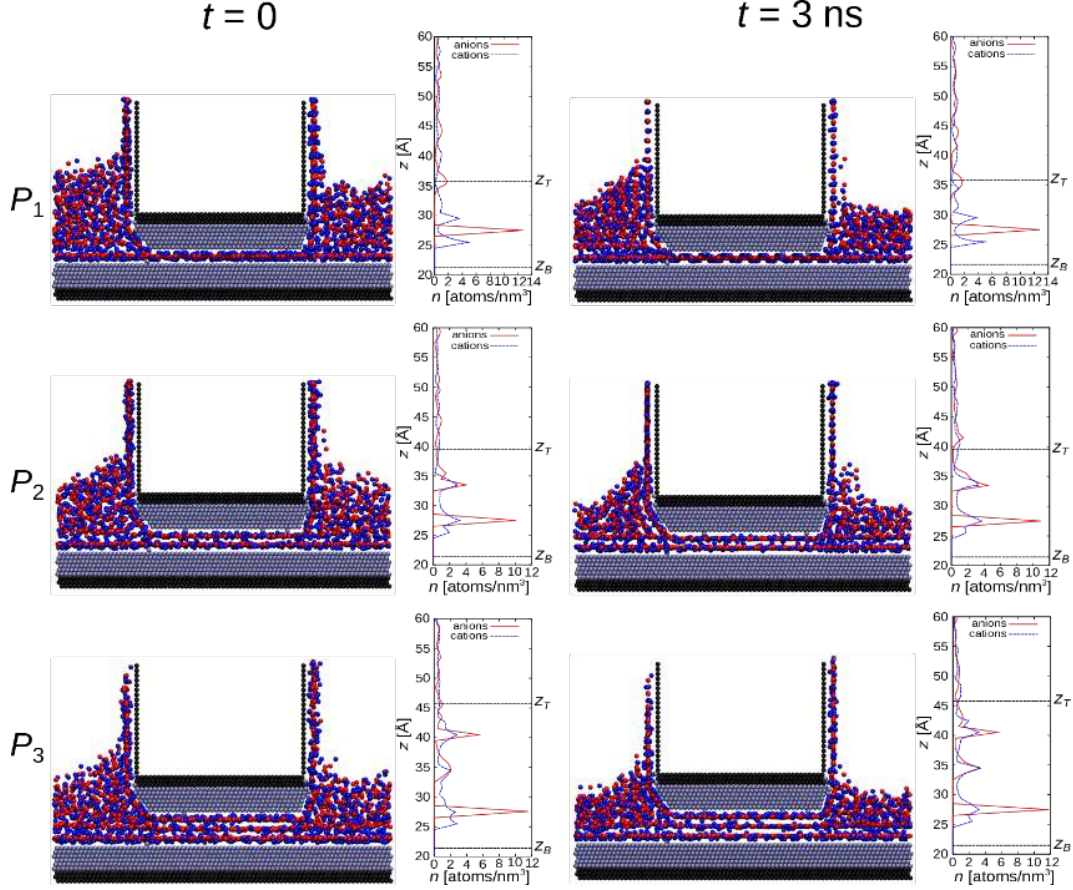


Figure 3.33: Configuration snapshots (yz cross-section) accompanied with ionic density distribution along the z direction in three representative points $\{P_1, P_2, P_3\}$. Left panels correspond to the start of friction simulations $t = 0$, while right panels correspond to the end of friction simulations $t = 3 \text{ ns}$. Top plate's lateral velocity is set to $V_x = 2 \text{ m/s}$, total simulation time is $t_{\text{tot}} = 3 \text{ ns}$, hence all friction simulations have run until the Top plate had covered a distance of $d_x = V_x \cdot t_{\text{tot}} = 60 \text{ \AA}$ along the x direction.

sketched crystallization patterns with solid lines. In Figures 3.33 and 3.34 we show initial configurations at the input of shearing simulations, together with the final configurations obtained after the shearing simulations. We observe that any initial crystallization is not lost due to the lateral motion of the Top plate, but only slightly modified due to the motion, which suggests that the lateral movement does not alter the ordering. This is a significant finding since the longitudinal movement, i.e., movement along the z -axis does alter the local ordering (it destroys the crystal structure in small gaps and induces it in larger ones).

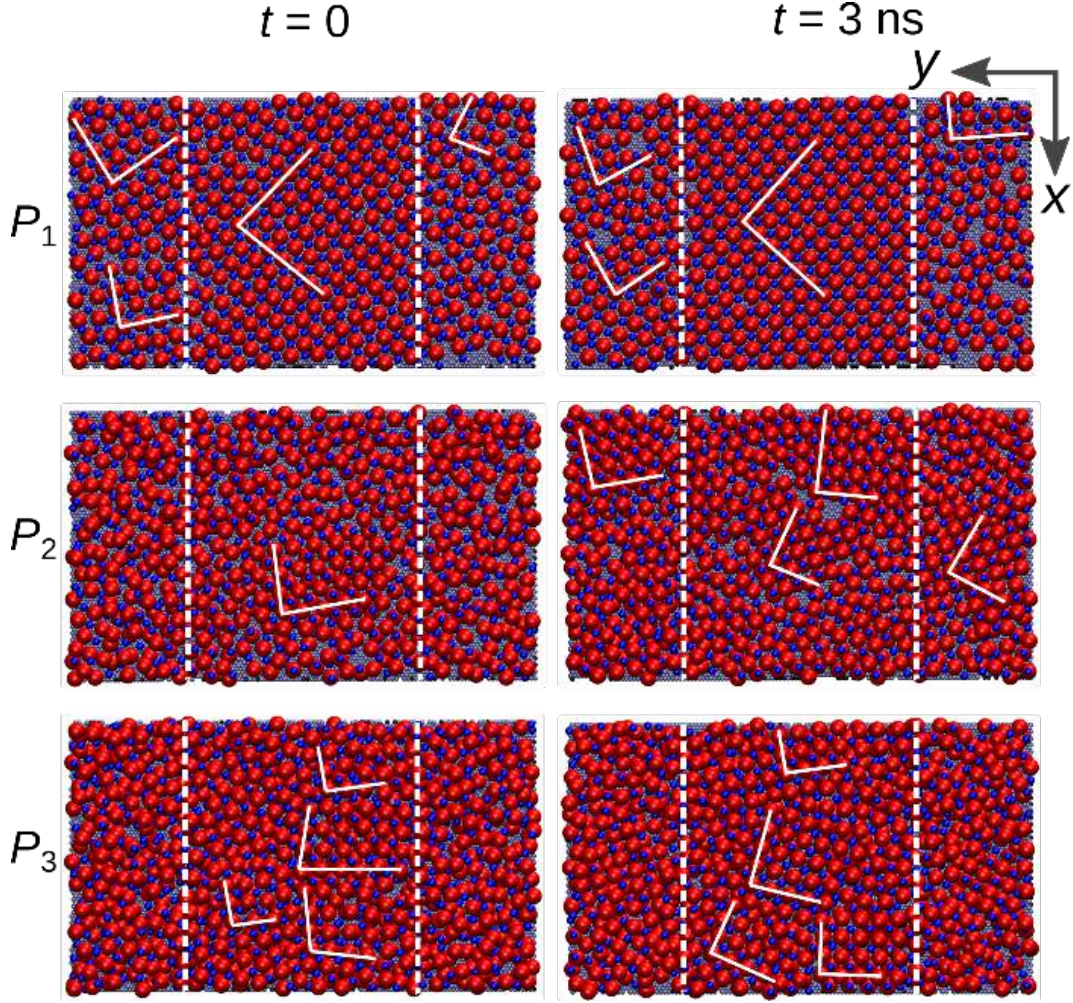


Figure 3.34: Configuration snapshots (xy cross-section) in three representative points $\{P_1, P_2, P_3\}$. Left panels correspond to the start of friction simulations $t = 0$, while right panels correspond to the end of friction simulations $t = 3$ ns. We have highlighted the confined region with dashed lines (Top plate's width along the y axis is a half of the total system's width) and also we have sketched crystallization patterns with solid lines. Top plate's lateral velocity is set to $V_x = 2$ m/s, total simulation time is $t_{\text{tot}} = 3$ ns, hence all friction simulations have run until the Top plate had covered a distance of $d_x = V_x \cdot t_{\text{tot}} = 60$ Å along the x direction.

3.4.2 Confined tailed models of ionic liquid

For the study of TM ionic liquids under confinement, we use the MD simulation setup of ILs under confinement shown in Figure 3.5 in section 3.2. We use that setup throughout this section in order to investigate both the static and dynamic behaviour of confined TM ionic liquids, as well as, their lubrication performance.

We keep the simulation setup geometry fixed, and we change the ionic liquid.

3.4.2.1 Static force-distance characteristic

Confinement induces layering in *IL* thin films [64, 116]. In order to understand how does an interplay between layering and molecular geometry of *TM* ionic liquids alter the load bearing capability of *IL* thin films, we calculate the quasi-static force-distance characteristic. We follow the evolution of the normal load F_z acting on the Top plate as a function of the interplate distance d_z . In order to ensure static conditions, the interplate distance is changed through a series of alternating steps, called *move* and *stay* steps, related to the movement of the Top plate and subsequent relaxation of the *IL* structure, respectively. We provide a detailed description of the procedure of modifying the interplate gap in the simulations of the static behaviour of confined ionic liquid: Top plate is moved along the z axis at a constant velocity $V_z = 5$ m/s for a period of time $t_{move} = 5$ ps; During the *move* period the elastic constant of cation–tail bonds takes its original value of $K = 80$ kCal/molÅ². After the transition regime happening during the *move* period finishes, we apply conjugate gradient (*CG*) minimization (for the details about *CG* minimization method check) on the ions, in order to minimize their internal energy and relax them after the *move* period. As the ion minimization procedure is done, ions take positions which ensure their minimal internal energy. In case of *SM* model of *IL*, ion minimization procedure performs fine, enabling well–relaxed *IL* [64]. However, we have noticed that in case of *TM* models of *IL*, due to a rather high value of the elastic constant of cation–tail bonds, ion minimization procedure does not perform fine. The key action of minimization procedure is the repositioning of the charged particles (i.e. cations and anions), since they interact strongly via Coulombic potential. Cations are bonded to neutral tails via bonds, hence they do not have that much freedom to rearrange during the minimization procedure, compared to anions. We have solved this problem by taking a low value of the elastic constant (i.e., 1% of its original value, $K^{min} = K/100 = 0.8$ kCal/molÅ²) during the ion minimization procedure. As the ion minimization procedure finishes, elastic constant K gradually increases and restores to the original value. This gradual increase is realized

via subsequent steps in which elastic constant takes the values from the next list: $K \in \{0.8, 2, 4, 10, 20, 40\}$ kCal/molÅ², where elastic constant takes each of the listed values for a period of time $\Delta t = 2.5$ ps. As the elastic constant gets restored to the original value, Top plate stays fixed for another $2\Delta t = 5$ ps during which period the average value of the normal force F_z is calculated and that value is presented as a simulation point in $F_z(d_z)$ static characteristic, i.e., in Figure 3.35. Hence, a *stay* period is made up of: ion minimization procedure with elastic constant $K^{min} = K/100$, the stepwise increase of K for $6\Delta t = 15$ ps and the calculation of the average value of the normal force F_z with the original elastic constant K for $2\Delta t = 5$ ps. In total, the time duration of the *stay* period is $t_{stay} = 20$ ps. In order to avoid a systematic error due to the initial position or direction, the Top plate movement is performed in different directions and from different initial configurations, hence Figure 3.35 shows the averages. The Top plate movement procedure consisting of *move* and *stay* periods is repeated until the distance $d_z^{min} = 11$ Å is reached.

The results for the force-distance characteristic of the three *TM ILs* are presented in Figure 3.35, where three different markers correspond to the three *IL* models. The normal force F_z strongly and non-monotonically depends on the distance d_z . These changes of the normal force F_z are correlated with the squeezing in and out of cation/anion layer pairs into the gap, as already observed experimentally [117] and theoretically [64]. The normal force becomes negative, i.e., $F_z < 0$ only in the case of small tails (*TM3*). The negative values are a result of the *IL* trying to reduce the plate-to-plate distance due to the adhesion forces inside of *IL*. The increasing tail size seems to reduce the effect of adhesion: for large tails (*TM9*) the normal force at the minimum is close to zero, while for symmetric cation molecule (*TM5*) it becomes positive, i.e., $F_z = 2$ pN. For all three curves corresponding to the three *TM* ionic liquids we can identify three characteristic ranges of the plate-to-plate distance d_z :

Segment(1): initial segment ($11 \text{ \AA} \leq d_z \leq 13.8 \text{ \AA}$) characterized by a monotonous and steep decrease of the normal force F_z

Segment(2): interval *I* ($13.8 \text{ \AA} \leq d_z \leq 19.8 \text{ \AA}$) characterized by the presence of local minima and maxima peaks of the normal force F_z , and

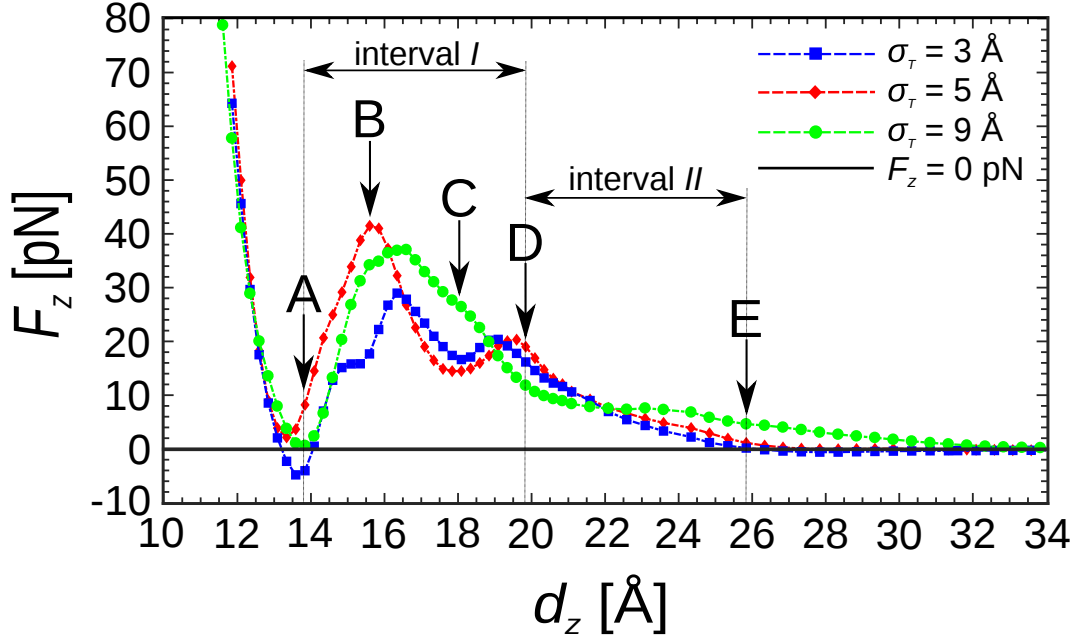


Figure 3.35: Dependence of normal force F_z on interplate distance d_z . Five characteristic points denoted with $\{A, B, C, D, E\}$ with corresponding interplate distances $d_z = 13.8, 15.5, 18.0, 19.8, 25.8$ Å, respectively, are marked in the figure. They are chosen in the way that: point A is located in the proximity of a local minimum for all three cases; point B corresponds to a local maximum for *TM5* model; point C is located in the proximity of a local minimum for *TM3* and *TM5* model; point D is located in the proximity of a local maximum for *TM3* and *TM5* model; point E is chosen according to the condition $\overline{DE} = \overline{AD}$. For reference, the black horizontal line denotes $F_z = 0$. The lines connecting points (averages of normal force) serve as visual guide.

Segment(3): interval *II* and beyond ($d_z \geq 19.8$ Å) characterized by a continuous and gentle decrease of the normal force F_z , where in all three cases the normal force practically becomes zero when $d_z > 32$ Å.

We will briefly describe the segments of $F_z(d_z)$ curves, pointing out similarities and differences between the different *IL* models. In the initial segment, (i.e., for small gaps $d_z < 13$ Å), the normal force F_z is practically the same for all three systems, meaning that it does not depend on the tail size. The steep rise of the normal force with compression in the range $d_z < 13$ Å is a sign of a very high resistance of the single anionic layer left in the gap to squeezing out. On the other hand, at large gap values (i.e., $d_z > 32$ Å), the normal load F_z in all three *TM* ionic liquids is similar and small. We can conclude that at large gaps there is a low resistance of *IL* to the

gap changes. Significant differences in the force-distance curves, depending on the tail size, exist only in the interval I , (i.e., $13.8 \text{ \AA} \leq d_z \leq 19.8 \text{ \AA}$). In the case of the *TM3* model, the $F_z(d_z)$ characteristic has two local minima and maxima and one saddle point, in the *TM5* model there are two local minima and maxima, and in the *TM9* model, there is one local minimum and maximum.

In the present setup, *IL* lubricant remains an infinite continuous body in x and y directions. However, there is a difference in *IL's* structure depending on the fact whether it is confined inside the gap between the Top and Bottom plate or it is located in the lateral reservoirs (LRs), see Figure 3.38. Ionic liquid confined inside the gap forms alternating cationic–anionic layers, while ionic layering in LRs is less pronounced beyond first two layers, see Figure 3.38. Besides that, from Figure 3.38, we notice that in all three systems the layer closest to the solid plates is formed by cation–tail dimmers. We might label the layers formed alongside the solid plates as fixed layers, since they always form first. Inside the interplate gap ionic ordering is dictated according to the layers formed next to the solid plates:

- (i) Bottom plate - cation–tail layer - anionic layer, looking from the bottom,
- (ii) Top plate - cation–tail layer - anionic layer, looking from the top, where bottom and top correspond to the position along the z axis.

In Figures 3.36 and 3.37 we present 5×3 panels of configuration snapshots for 5 chosen characteristic points of 3 *TM* models. The atoms are depicted keeping the ratios of their sizes.

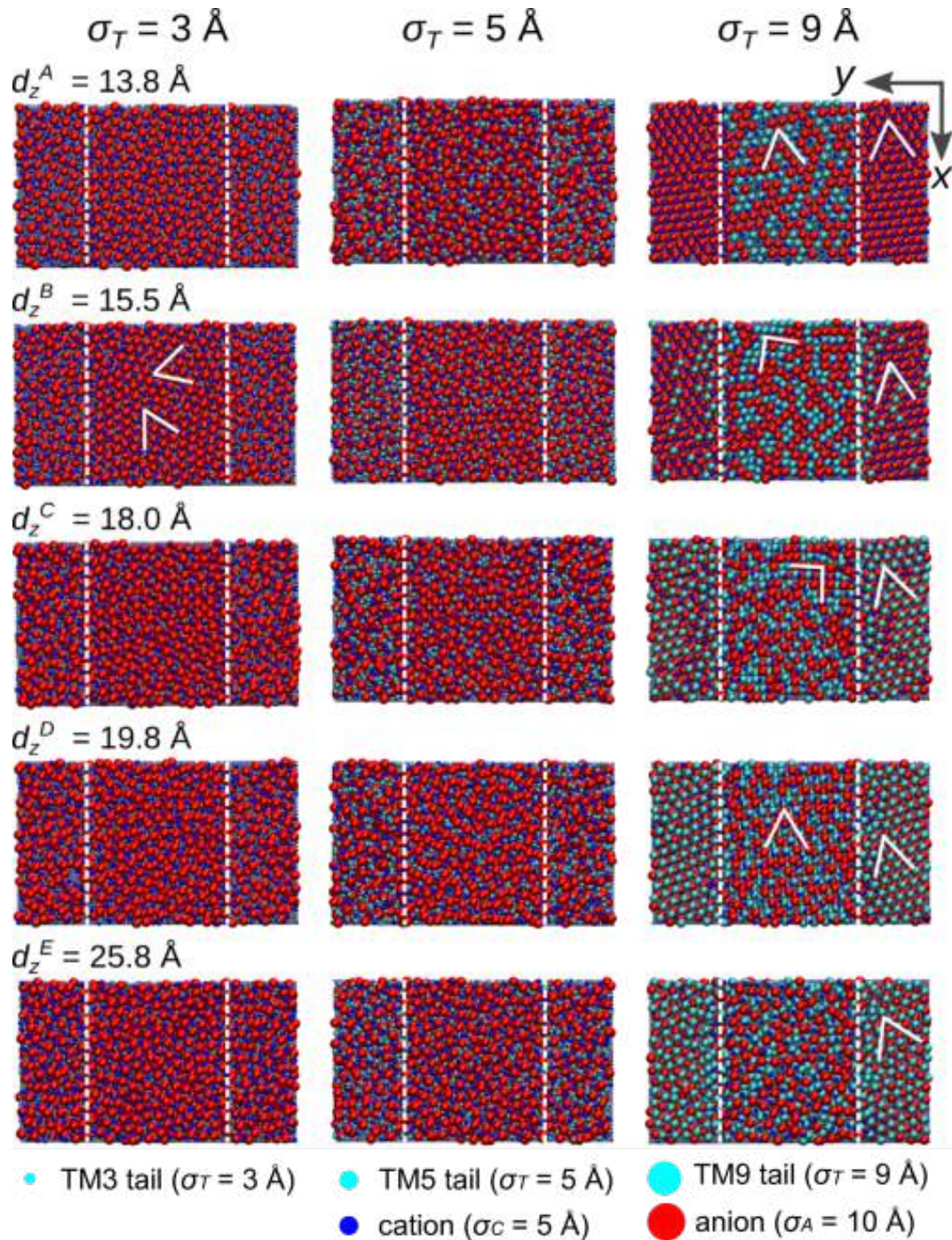


Figure 3.36: Configuration snapshots (xy cross section) of *TM3*, *TM5* and *TM9* models in five characteristic points $\{A, B, C, D, E\}$. Five characteristic points, denoted with $\{A, B, C, D, E\}$, have corresponding interplate distances $d_z = \{13.8, 15.5, 18.0, 19.8, 25.8\} \text{ \AA}$, respectively (see also Figure 3.35).

- *IL* structure inside and outside the interplate gap

In Figure 3.39 we are showing the ionic density distribution along the z axis for

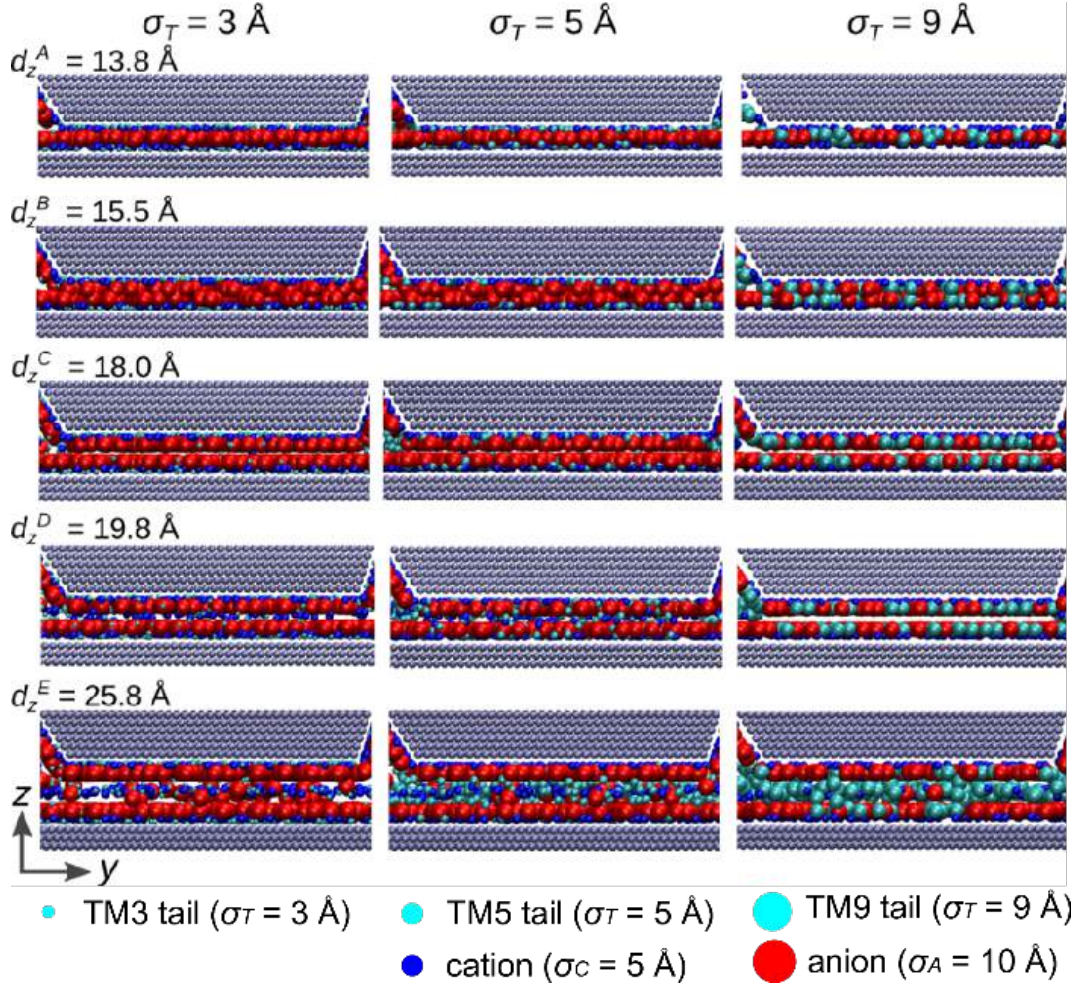


Figure 3.37: Configuration snapshots (yz cross section) of *TM3*, *TM5* and *TM9* models in five characteristic points $\{A, B, C, D, E\}$ (see also Figure 3.35). This figure presents the changes taking place in the confined ionic layers as the interplate distance changes in case of static force–distance simulations.

the three *IL* models, in points A to E, i.e., $d_z = \{13.8, 15.5, 18.0, 19.8, 25.8\} \text{ \AA}$. A common feature of all investigated *IL* models is the formation of *fixed* cationic layers along the whole length of the solid plates (Top and Bottom plate). The fixed layers and their stability are a result of strong *LJ* interactions between the plates and ions. In general, the smallest particles form the first layer next to the plates.

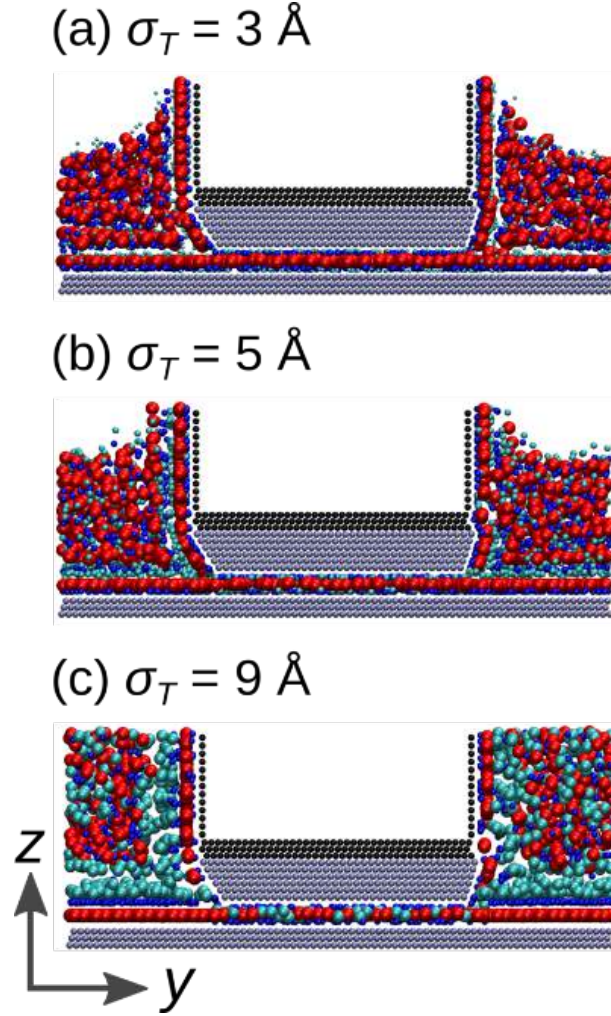


Figure 3.38: Configuration snapshots (yz cross section) of $TM3$, $TM5$ and $TM9$ models in a characteristic point A marked in Figure 3.35. This figure represents an illustration of ionic layering.

For $TM3$ the first layer to the plates is formed by the tail particles (which are part of the cation-tail pair), while for $TM5$ and $TM9$ models these particles are the cations. The consecutive layers are formed inside the interplate gap via combined volume exclusion and Coulombic interactions and their ordering is consistent with the fixed layers. As a result, tails migrate to the plates in $TM3$ model, they mix with the cationic layer when cation-tail dimer is symmetric in $TM5$ model, and finally they mix into the anionic layer when they are large in $TM9$ model. Since Coulombic interactions cause the layering with alternating charge sign, anionic layers always separate cationic layers. We focus on analyzing the changes in the segment between the points A and D , i.e., the interval I . The normal force F_z

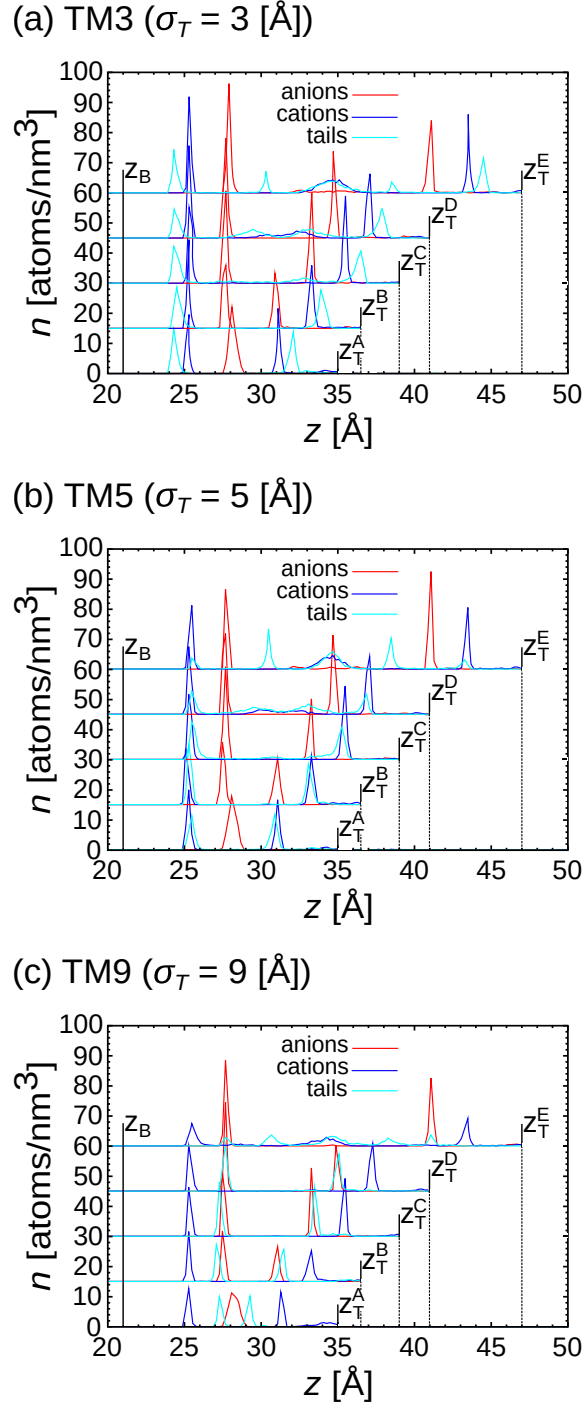


Figure 3.39: Ionic density distribution of ions inside the interplate gap of (a) $TM3$, (b) $TM5$ and (c) $TM9$ models in characteristic points $\{A, B, C, D, E\}$ taken from the static force–distance characteristic presented in Figure 3.35. The positions of the atomic centers of the innermost atomic layers of the (moving) Top and the (fixed) Bottom plate are labeled as z_T^{A-E} and z_B , respectively.

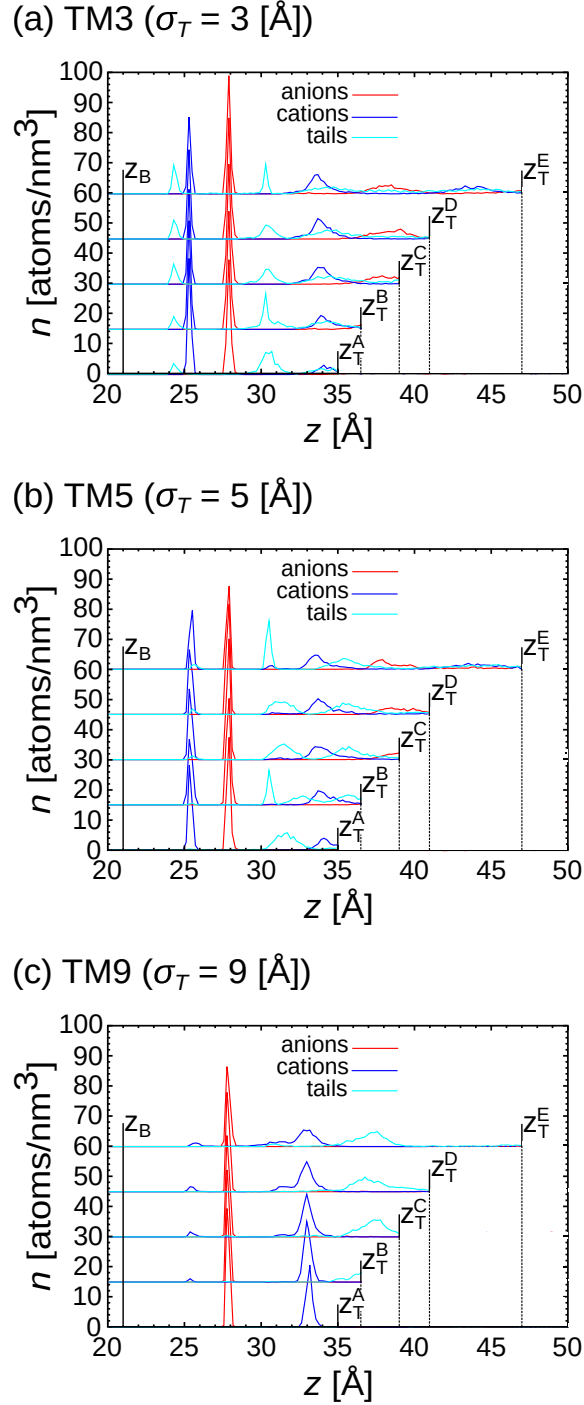


Figure 3.40: Ionic density distribution of ions outside the interplate gap of (a) $TM3$, (b) $TM5$ and (c) $TM9$ models in characteristic points $\{A, B, C, D, E\}$ taken from the static force–distance characteristic presented in Figure 3.35. The positions of the atomic centers of the innermost atomic layers of the (moving) Top and the (fixed) Bottom plate are labeled as z_T^{A-E} and z_B , respectively.

changes rapidly and non-monotonically with the interplate distance d_z in the interval I , check Figure 3.35. For the minimum of F_z in the vicinity of point A, i.e., for the interplate distance $d_z^A = 13.8 \text{ \AA}$, we can observe a well-defined anionic layer in Figure 3.39. The most interesting change takes place during the transition A \rightarrow B when the single layer of anions is split into two layers, check Figure 3.39. As a result, the normal force F_z increases and reaches a local maximum in the proximity of point B, i.e., for plate-to-plate distance $d_z^B = 15.5 \text{ \AA}$. We observe that additional anion-cation pairs are pulled inside the gap in Figure 3.41. We also observe that the two anionic layers in Figure 3.39 for point B and the one for point A have the same maximum number density. As we increase d_z further, the number of anionic layers confined inside the gap remains unchanged and the normal load drops slowly. At the same time, the number of ions inside the gap steadily increases with the gap width. Nevertheless, this increase is not sufficient to keep the density of IL inside of the gap constant (check Figure 3.41). Looking into the changes in the spatial distribution of IL components, as more cation-anion pairs are pulled into the gap (going from A \rightarrow E), we observe a steady increase of the concentration of anions in the layer next to the Bottom plate. In the case of $TM5$ model we have an increase from $n_{TM5}^A = 18 \text{ atoms/nm}^3$ to $n_{TM5}^D = 27 \text{ atoms/nm}^3$, check Figure 3.39. When we further look at configuration snapshots for $TM3$ and $TM5$ model, a formation of additional layers inside the gap is visible, between the points C and D. This can also be clearly observed in Figure 3.39 and results in smaller maximum around $d_z = 19 \text{ \AA}$, in Figure 3.35. We can conclude that the form of the normal force-plate distance characteristic is not correlated with the number density of the IL molecules inside the gap, but the layer formation seen in Figure 3.39. As the interplate distance d_z increases further, from point D to E, we notice additional cations in the middle of the gap and formation of a third cationic layer in all three systems. We can make an interesting observation that for all three models the tails in the middle of the confinement are grouped in three regions: with cations at $z = 34 \text{ \AA}$, and in the middle between cationic and anionic layers, i.e., $z = 30, 38 \text{ \AA}$, check in Figure 3.39. This outcome is reminiscent of the findings from Reference [71] where the authors have experimentally obtained the formation of the tail-to-tail bilayer of cationic

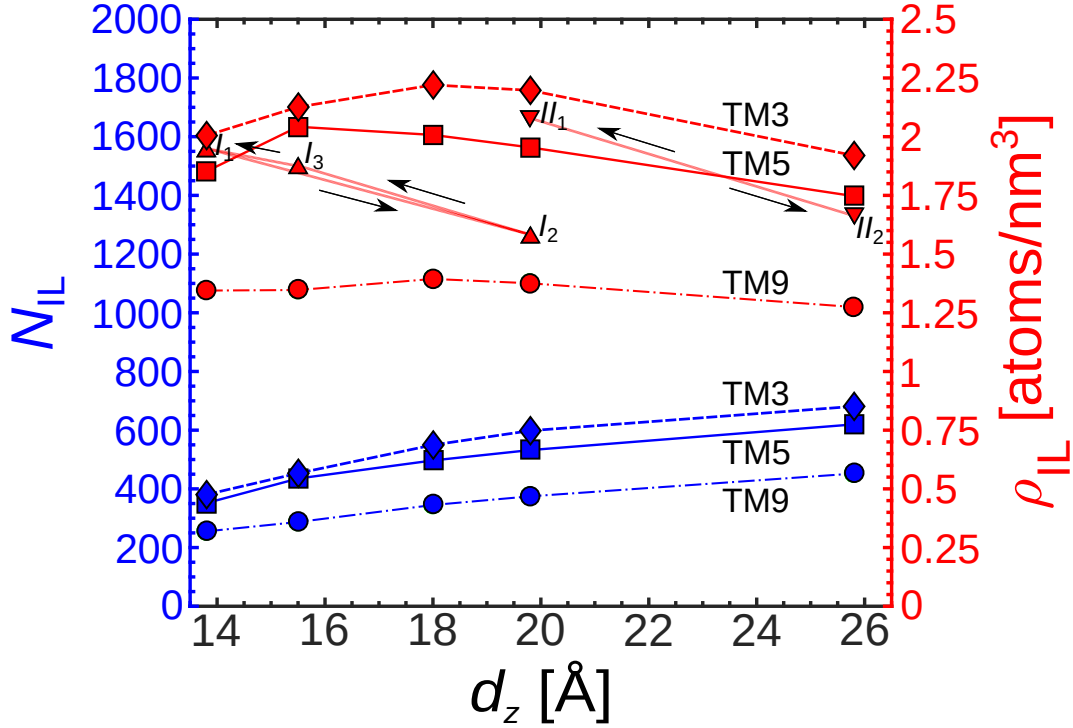


Figure 3.41: Evolution of the number of confined ionic liquid (IL) molecules (bottom curves) and density (top curves) inside the gap with gap width d_z for $TM3$, $TM5$ and $TM9$ models in characteristic points $\{A, B, C, D, E\}$ selected from the static force–distance characteristic (Figure 3.35). The corresponding axes for the number of IL molecules and the density are given on the left and right side, respectively. The densities at characteristic points for the dynamic cases (intervals I, II) of $TM5$ model are also given, i.e., $I_{1,2,3}$ and $II_{1,2}$, for the purpose of comparison with the static case of $TM5$ model.

dimers in case the alkyl chain length is oversized. In Figure 3.42 we present how do the number of confined IL molecules and density depend on the interplate distance d_z in dynamic cases for $TM3$, $TM5$ and $TM9$ models. In all three TM models, we notice the same tendencies for both N_{IL} and ρ_{IL} dependences on d_z .

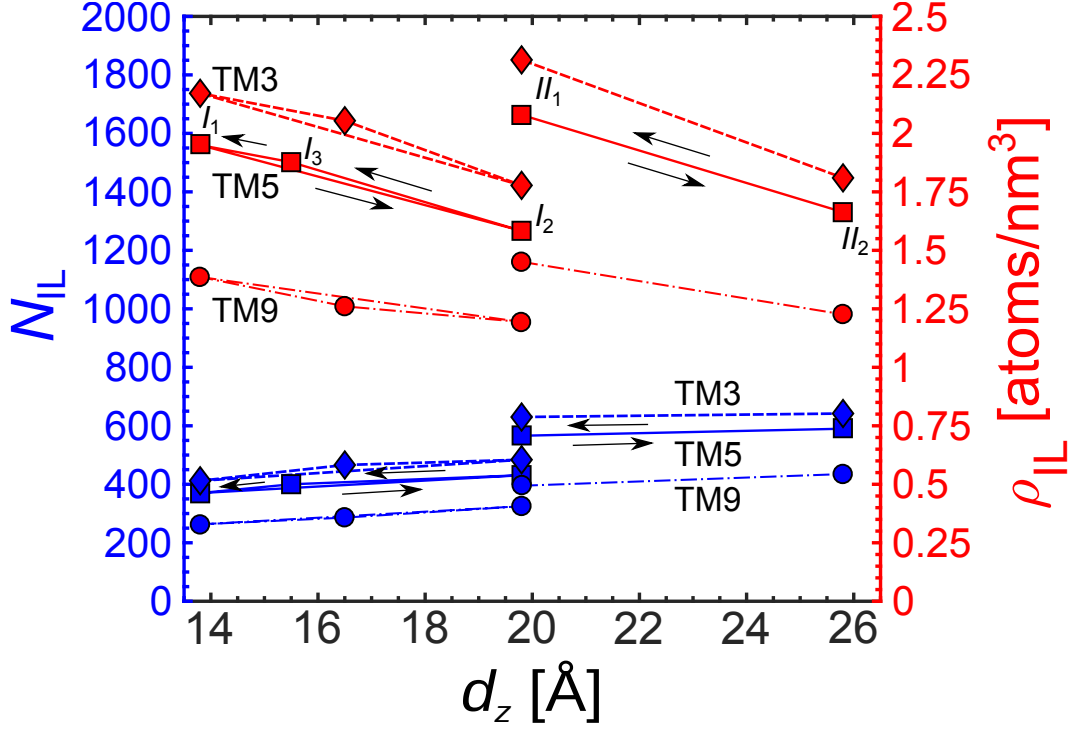


Figure 3.42: Evolution of the number of confined ionic liquid (IL) molecules (bottom curves) and density (top curves) inside the gap with gap width d_z for $TM3$, $TM5$ and $TM9$ models for the dynamic cases (intervals I, II), i.e., $I_{1,2,3}$ and $II_{1,2}$. The corresponding axes for the number of IL molecules and the density are given on the left and right side, respectively.

- IL crystallinity: influence of the gap

We show the xy cross-section snapshots in Figure 3.36 in order to observe the IL 's in-plane structure at the cross-section just below the Top plate. We mark the boundaries of the Top plate spatial region with the vertical dashed lines. The central area of the panels in Figure 3.36 corresponds to the interplate gap region and it represents a half of the total cross-section's width in the y direction, while the remaining area corresponds to the lateral reservoirs. The solid lines mark the orientation of crystal grains in those areas, where we can observe the presence of structural ordering. In the case of $TM3$ model, we observe the presence of partial triangular ordering only at point B when the structure is the most compressed. We do not notice any crystallization for symmetric dimers ($TM5$ model), which confirms that the symmetric tail prevents ordering both under confinement and in the bulk. Contrary to the previous two cases, we observe crystallization for all configurations

with the large tail (*TM9* model). Additionally, we observe changes in the type of crystalline structure. While in the lateral reservoirs a triangular lattice arrangement is always present, depending on the amount of compression we observe triangular lattice arrangements in points A and D and square lattice arrangements in points B and C. Even more surprisingly, the order is lost when the tail-to-tail bilayer is formed in point E.

3.4.2.2 Dynamic force-distance characteristic

The Top plate was moved between the two limiting points of the intervals *I* ($d_z^A \leq d_z \leq d_z^D$) and *II* ($d_z^D \leq d_z \leq d_z^E$). We have investigated the dynamic behaviour of the confined *IL* thin film during the cyclic movement of the Top plate along the z axis, i.e., the interplate gap was periodically extended (*extension* half-cycle) and compressed (*compression* half-cycle). We have investigated our system at three velocities $V_z = \{0.1, 1, 10\}$ m/s, but we did not observe any velocity dependent differences in the system behaviour. The confined ionic liquid lubricant responds to the cyclic movement of the Top plate with a hysteresis in normal force $F_z(d_z)$ shown in Figure 3.43. We present the detailed results of the *TM5* model dynamic behaviour in (a) and (c) panels of Figure 3.43. Also, in (b) and (d) panels of the same figure, we present together smooth average cycles of our three *IL* models (*TM3*, *TM5*, and *TM9*).

- Narrow gap (interval *I*): normal force hysteresis

We will now discuss in detail the response of the *TM5* model to the cyclic motion of the Top plate, in the interval *I* shown in Figure 3.43(a). Ten cycles of compression-extension are shown (thin lines) with an *average* cycle superimposed on them (thick line). We identify three points of interest: $\{I_1, I_2, I_3\}$, i.e., the two terminal points of the cycle and the point with the maximal normal force, respectively. These three points also correspond to the points $\{A, D, B\}$ respectively, in the static characteristics shown in Figure 3.35. Point I_3 corresponds to the maximum of normal force F_z both in the cyclic compression cycle and in the static characteristic of *TM5* model, which makes the comparison more straightforward.

The normal force F_z decreases down to a value close to zero during the *extension*

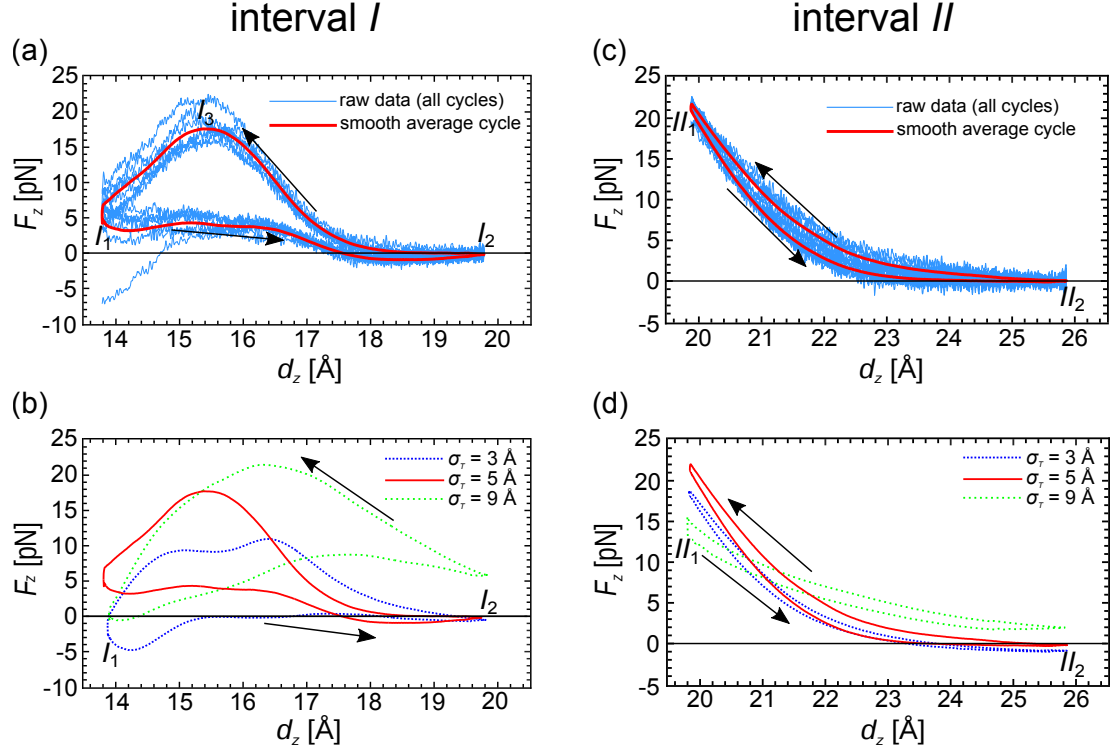


Figure 3.43: The results of dynamic extension–compression cycles are shown for the intervals I and II . In the panels (a) and (c) we present dynamic $F_z(d_z)$ characteristic in case of $TM5$ model, for the intervals I and II , respectively; thin lines represent the hystereses of ten dynamic cycles, solid line on top of them is the smooth average hysteresis. There is also a solid horizontal line which corresponds to $F_z = 0$. In (a) points I_1 , I_2 , I_3 denote representative points: I_1 - starting point, I_2 - ending point, I_3 - global maximum of the $F_z(d_z)$ curve. In (c) points II_1 and II_2 denote representative points: II_1 - starting point and II_2 - ending point. The arrows show the direction of hysteresis (extension $I/II_1 \rightarrow I/II_2$ followed by compression $I/II_2 \rightarrow I/II_1$). In the panels (b) and (d) we show together smooth average hystereses $F_z(d_z)$ of our three TM ionic liquids, for the intervals I and II , respectively. Starting and ending points and arrows are denoted, analogous to the panels (a) and (c).

half of the cycle $I_1 \rightarrow I_2$. The anion-cation pairs are pulled into the gap from the lateral reservoirs as the gap is extended and at point I_2 an additional anionic layer is fully formed inside the gap. Actually, instead of the two fixed layers of cations which share one anionic layer, we obtain two separate anionic layers. The total number of ions pulled in is about 60 atoms or 0.22 atoms/(nm²ns) at 1 m/s plate linear speed. In the first part of the compression half-cycle, $I_2 \rightarrow I_3$, the ions are compressed and the density and the normal force F_z increase. Somewhat surprisingly, we observe that

an equal number of ions flows out while the normal force increases, i.e., $I_2 \rightarrow I_3$ and during its sharp drop $I_3 \rightarrow I_1$ (check Figure 3.41). The sharp decrease of the normal force F_z in the segment $I_3 \rightarrow I_1$ is therefore a result of two processes: out-flow of the ions from the gap and the collapse of the anionic double layer and its rearrangement into a single anionic layer. The resulting final density $\rho_{IL}^{dyn} = 1.95$ atoms/nm³ of the system is slightly higher than in the static case $\rho_{IL}^{stat} = 1.85$ atoms/nm³, check Figure 3.41. The value of the normal force F_z at point I_1 is similar, i.e., $F_z = 4$ pN in both static and dynamic case.

In Figure 3.43(b), we observe that each one of the three investigated ionic liquids (*TM3*, *TM5*, and *TM9*) exhibits different behaviour in the average $F_z(d_z)$ cycle during the extension and compression half-cycle. First, at the onset of the extension half-cycle, i.e. in the point I_1 , the normal force F_z has a positive value for symmetric cations (*TM5* model), it is close to zero for large tails (*TM9* model), and it is negative for small tails (*TM3* model). Somewhat surprisingly, the normal force increases for both *TM ILS* with asymmetric cations (*TM3/TM9* models) while it decreases for symmetric cation (*TM5* model). The reason for this behaviour is the strong interaction of the fixed layers of ions adjacent to the plates with the plate particles. This interaction drives as many ions inside the gap as possible, resulting in the non-intuitive behaviour of the normal force due to an interplay of density and intra-*IL LJ* interactions. During the compression half-cycle for all three *ILs* the maximal normal force sustained was about 50% smaller than in the quasi-static case, i.e., for *TM5* model the maximal force is $F_z^{max} = 17$ pN in the dynamic case and $F_z^{max} = 40$ pN in the static case (see Figures 3.43(b) and 3.35). This observation indicates that the Top plate's motion prevents the *IL* to fill the gap. We can also conclude that the mechanical response is mainly due to a rearrangement of the fixed layer and that the mobility of the *IL* molecules is too low to significantly increase the normal force resisting to the compression. If we analyze the rate of mass transfer outside of the gap, we conclude that there is a substantial slip, which results in a lower normal force. Without slip at a velocity $V_z = 1$ m/s, the normal force calculated based on the bulk viscosity coefficient would be roughly two orders of magnitude higher. Figure 3.44 shows configurations snapshots accompanied with

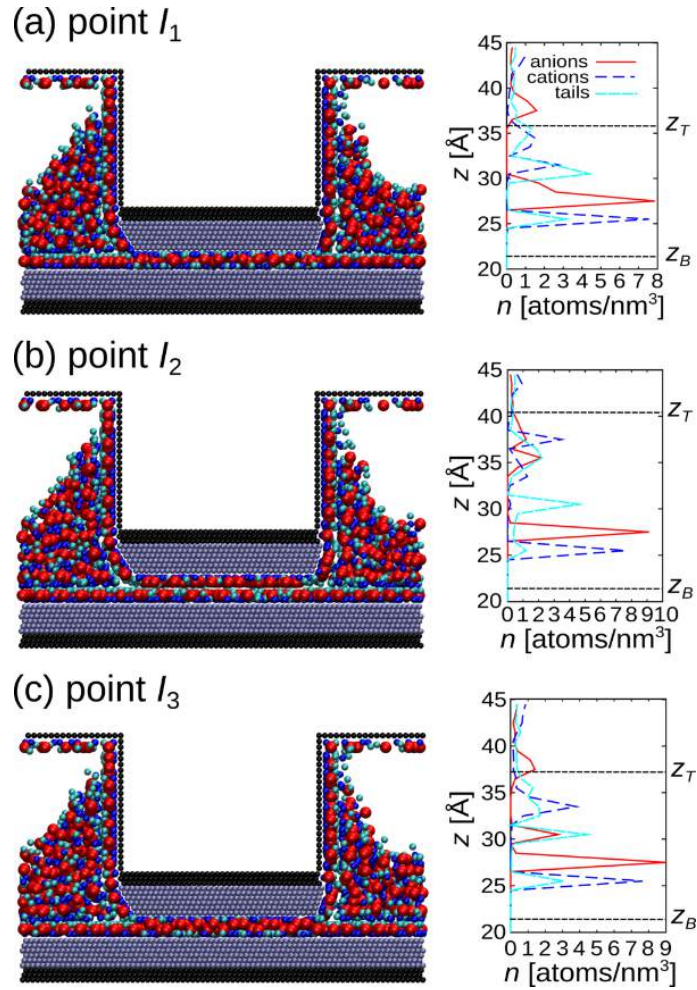


Figure 3.44: Configuration snapshots accompanied with ionic density distribution along the z direction in the three characteristic points (I_1 , I_2 , I_3) from the panel (a) of Figure 3.43.

the ionic density distribution along the z direction, for the interval I of dynamic cycle of $TM5$ modeled ionic liquid. In the point I_1 there is one compact anionic layer leading to a rather low positive value of the normal force F_z . In the *extension* half-cycle ions from the LRs get taken into the gap. This leads to the formation of another compact anionic layer, which means that from one compact anionic layer at the starting point I_1 , we arrive at two compact anionic layers at the ending point I_2 . In the return *compression* half-cycle, those extra ions get pushed back into the LRs, leading to the reduction of the number of compact anionic layers confined inside the gap to one.

- **Wide gap (interval II): monotonic force-distance characteristics**

The extension-compression force-distance characteristic for the interval II in case of $TM5$ model is given in Figure 3.43(c). The difference from the quasi-static extension/compression in Figure 3.35 is the monotonic behaviour during the cycle. The quasi-static characteristics in the interval II featured local minima and maxima in the case of $TM3$ and $TM5$ models. In the dynamic case, there are only two characteristic points (starting and ending point II_1 and II_2 , respectively and a monotonically changing normal force between them. In the *extension* half-cycle there is a continuous decrease of the normal force F_z followed by its continuous increase in the *compression* half-cycle. The difference in the normal force between the cycles is small. In the dynamic characteristic of the interval II the layer structure is similar to the static case, i.e., two fixed layers stay-in-place and the tail double layer is formed during the extension half-cycle (check Figure 3.45). In contrast to the interval I , the formation of the additional layer of tails is not a result of the ions flowing from the lateral reservoirs into the gap. The density inside the gap is 10% higher in the dynamic case and a few atoms (less than 30) are displaced during the cycle. We should note that the gap is also 50% larger in the interval I compared to the interval II , therefore the drop in density is even less striking. Actually, the cyclic motion has a tendency to increase the density inside the gap. Since there is no large displacement of the ions in and out of the gap in the interval II , there is also no maximum of the normal force F_z , similar to the one we have seen in the case of the interval I , check Figure 3.43(a). In order to make comparisons of different TM ionic liquid models, in Figure 3.43(d) we show together $F_z(d_z)$ average cycle dynamic characteristics of all three TM models of ionic liquid (i.e., $TM3$, $TM5$, $TM9$ model) for the interval II . Compared to the interval I , the tail size does not have such a pronounced impact on $F_z(d_z)$ hysteresis curves in the interval II . Figure 3.45 shows configurations snapshots accompanied with the ionic density distribution along the z direction, for the interval II of dynamic cycles of $TM5$ model IL . In the point II_1 there are two compact anionic layers opposite to each other leading to a high positive value of the normal force F_z . In the *extension* half-cycle the fixed layers become separated, and a marginal number of cation-tail dimers diffuses from the lateral reservoirs (LRs) into the gap. However, another anionic layer does not form,

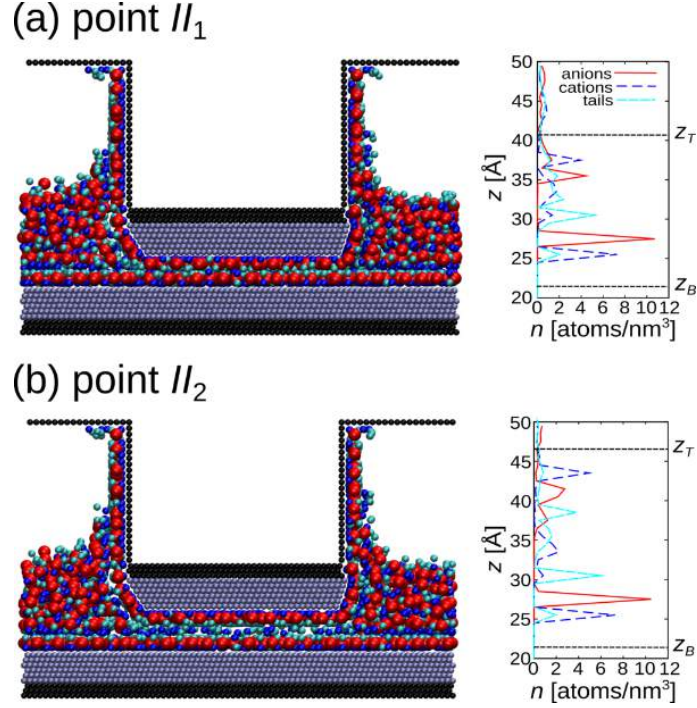


Figure 3.45: Configuration snapshots accompanied with ionic density distribution along the z direction in the two characteristic points (II_1 , II_2) from the panel (c) of Figure 3.43.

which means that from the two compact anionic layers with the cationic layer in-between at the starting point II_1 , we arrive at two separated layers in the ending point II_2 with the tail bi-layer in-between.

- Energy losses due to cyclic extension-compression

At this point, we would like to quantify how do the processes arising during the dynamic cyclic movement of the Top plate contribute to energy losses. We calculate the area covered during the extension-compression cycle (i.e., the area inside the $F_z(d_z)$ hysteresis). This area is equivalent to the work invested per average dynamic cycle, i.e., the hysteretic energy losses. We show the dependence of the energy losses on the tail size for both intervals I and II in Figure 3.46. We observe a clear tendency of the increase of the invested work per dynamic cycle, with the increase of the tail diameter. This is primarily due to the larger volume occupied by the tails resulting in larger normal forces resisting compression. There is a striking difference in the amount of invested work between the two intervals I and II (e.g. $27 \text{ pN} \cdot \text{Å}$ for the interval I of $TM9$ model compared to $5 \text{ pN} \cdot \text{Å}$ for the interval II of $TM9$ model).

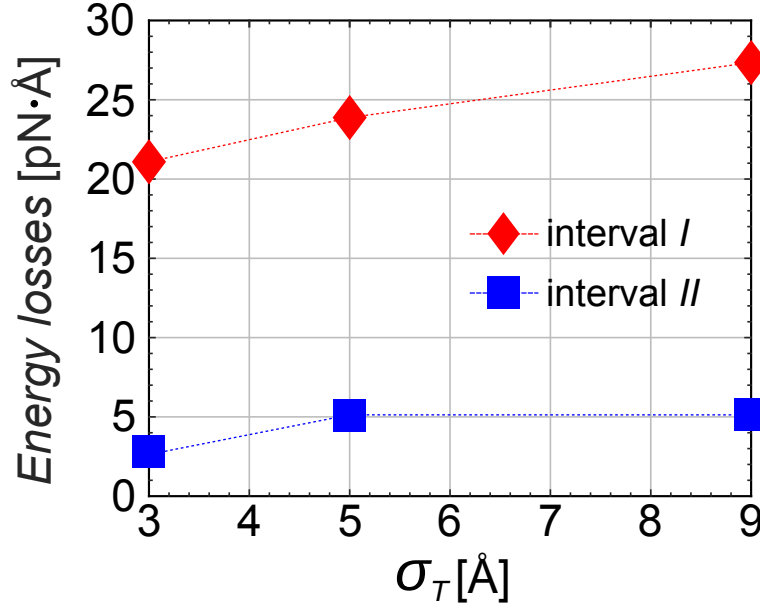


Figure 3.46: Energy losses per average cycle in function of the tail size, for intervals *I* and *II* of dynamic extension–compression cycles.

This difference is proportional to the maximal normal force which is sustained by the systems in the two intervals (check Figure 3.35).

3.4.2.3 Tribological behaviour of confined tailed models of ionic liquid

We have conducted static and dynamic characteristic analysis of the three generic *IL* models, focusing on the influence of their molecular structure on the anti-wear performance. In order to obtain a full picture, it is crucial to determine *IL*'s friction behaviour under different shear conditions. In this section we apply a relative motion between the plates by moving the Top plate along the x -axis (see Figure 3.5 from section 3.2) and we observe the resulting frictional force (also along the x -axis, i.e., F_x). We have performed two types of friction simulations:

- (i) at a constant Top plate's velocity $V_x = 2$ m/s, the simulations are performed at different fixed values of the gap: $d_z = 12$ Å to 25.5 Å, and
- (ii) at a fixed gap $d_z = 15$ Å Top plate's lateral velocity takes five different values: $V_x = \{0.1, 0.3, 1.0, 3.0, 10.0\}$ m/s.

In all friction simulations, the total distance covered by the Top plate was $\Delta_x = 100$ Å in the x direction. The dependence of the time-averaged frictional force $\langle F_x \rangle$

on the interplate gap d_z for the three *IL* models is shown in Figure 3.47. The points obtained in the simulations are shown as markers. Linear fits through these points are provided as visual guides. For the *TM3* model ionic liquid, we observe a decrease of the frictional force $\langle F_x \rangle$ with the size of the gap. On the other hand, the frictional force weakly depends on the gap width in case of *TM5* and *TM9* model ionic liquids. Both the *TM3* and *TM9* have high zero shear-rate (Green-Kubo) bulk viscosities correlated with extent of their ordering, i.e., $\eta_{TM3}^{GK} > \eta_{TM9}^{GK} > \eta_{TM5}^{GK}$. When comparing with their tribological performance in a thin film we can conclude that there is no correlation since the *TM5* ionic liquid has the highest average frictional force. In Figure 3.48, we show the dependence of specific friction $\langle F_x \rangle / \langle F_z \rangle$ on the Top plate's lateral velocity V_x in case of *TM5* model ionic liquid. We obtain specific friction values of the order $\langle F_x \rangle / \langle F_z \rangle \approx 0.01$ which are comparable to the result from Reference [53] for symmetric $[PF_6]^-$ anion. We observe also a similar tendency of decreasing friction force with respect to tail size, as reported in the same Reference [53]. The specific friction $\langle F_x \rangle / \langle F_z \rangle$ is defined as the ratio of the time averaged frictional $\langle F_x \rangle$ and normal $\langle F_z \rangle$ force and it is different from the Coulombic friction coefficient $\mu = \partial F_x / \partial F_z$. Consistently with our previous results for model ionic liquids, we have observed a logarithmic dependence of specific friction on the lateral velocity, check Reference [64]. The numerical values are fitted to a linear function of the form $\langle F_x \rangle / \langle F_z \rangle = a \log (V_x / V_{ref}) + b$, where $V_{ref} = 1$ m/s. The coefficients of the linear fit took those values: $a = 0.001, b = 0.008$. A reasonable fit to the linear regression curve can be observed. The logarithmic dependence indicates typical elastohydrodynamic lubrication (EHL) conditions [119].

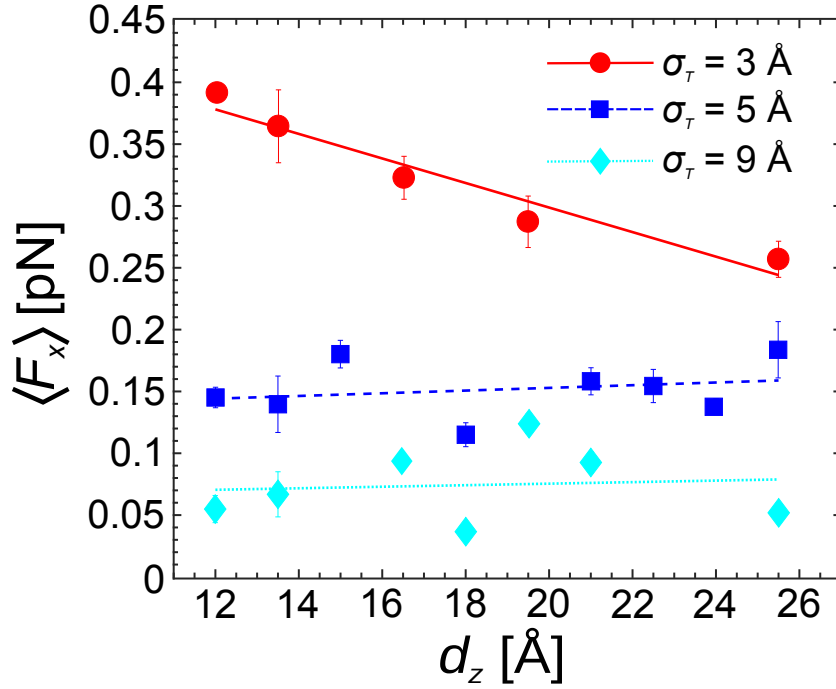


Figure 3.47: Average frictional force $\langle F_x \rangle$ acting on the Top plate as a function of the interplate distance d_z for confined *TM3*, *TM5* and *TM9* ionic liquid lubricant. In case of *TM3* model there is a clear linear dependence showing the decrease of frictional force intensity with the gap increase, while on the other side in case of *TM5* and *TM9* model frictional force is practically constant and does not depend on the gap.

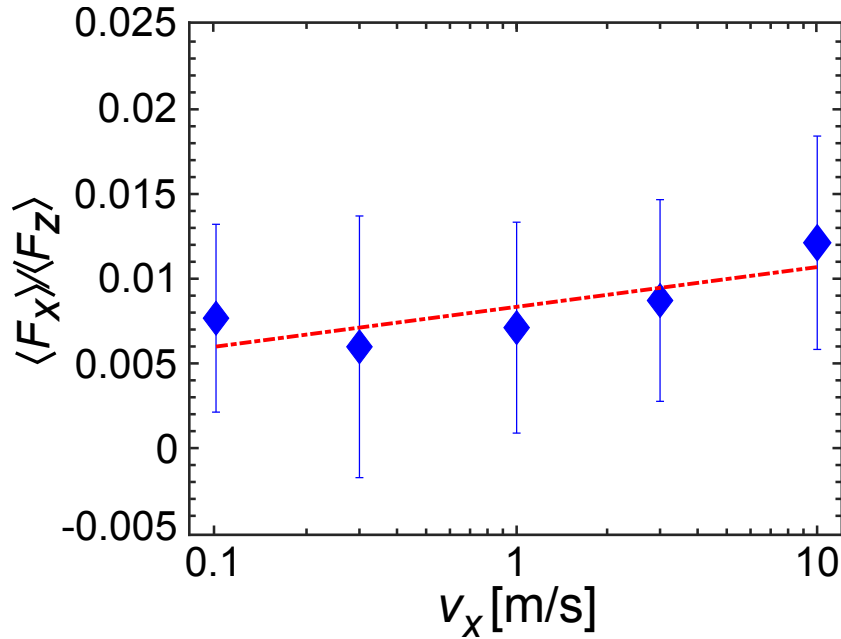


Figure 3.48: Specific friction $\frac{\langle F_x \rangle}{\langle F_z \rangle}$ dependence on Top plate's lateral velocity V_x in case of *TM5* model.

Chapter 4 Conclusions

In this doctoral thesis two research topics, related to dipolar and ionic systems, namely tubes and helices composed of dipolar hard spheres and ionic liquids, have been modeled and investigated. Pronounced ordering under the conditions of spatial confinement has been obtained in both systems. The ordering is a consequence of the dominant long-range interactions, i.e., dipole-dipole interaction in dipolar structures and Coulombic interaction in ionic liquids. In both systems long-range interactions have led to the ordering that spans the system. A rich phase behaviour, sensitive to: variations of packing in case of dipolar systems and particle shape in case of ionic systems, has been obtained.

4.1 Confined dipolar systems

A study about cohesive energy of helical and tubular structures composed of hard spheres with permanent dipole moments has been presented. Helices were created by replication of a particle or patch of particles on a confining cylindrical surface. Even for the most simple situation, namely the single thread helix, a non-trivial behaviour is found when monitoring the cohesive energy as a function of surface packing (i.e., axial compression).

In particular, a non-monotonic dependence of the cohesive energy on the packing fraction (or equivalently the amount of compression) as a result of a delicate interplay of dipole-dipole interactions and excluded volume effects can be observed. The lowest cohesive energy is achieved at the highest packing fraction with touching turns. In parallel, the polarization order parameter, i.e., the mean dipole moment per particle $\langle m_z \rangle$, also displays a striking non-monotonic behavior as a function of the extent of compression. In the regime of very high surface packing fraction with

local triangular arrangement compatible with certain cylinder radius R over particle diameter d ratio (R/d), a pronounced cohesive energy is found.

Accordingly, the polarization order parameter indicates a sharp change in the dipole moment orientation, which tends to be parallel to the helix axis. Finally, cohesive energies of dense multiple (i.e., double or quadruple) helices, as well as, AB and ZZ tubes made up of stacking rings that can also be seen as special multiple helices have been compared. A remarkable finding is the enhanced cohesive energy for the ZZ tube structure. The latter already emerges at strong substrate curvature with cohesive energies very close to that obtained at vanishing curvatures. In these ZZ tube structures, an alignment of the helix threads with its axis is a microstructural signature for this low cohesive energy. As a final note, it should be emphasized that the implemented model of dipolar tubes and helices mimics nicely the geometry and microstructure of biological microtubules. It could also provide a possible clue about the self-assembly mechanisms and cohesion within microtubular structures.

4.2 Ionic liquids

4.2.1 Salt model of ionic liquid

In the study conducted in this doctoral research an molecular dynamics (MD) simulation setup in order to study the behaviour of model ionic liquids (ILs) confined between plates which are in close proximity while being in relative motion has been implemented. In the framework of this doctoral thesis the MD setup was developed in a way that allows the mesoscopic study of the lubrication processes in automotive applications such as the piston ring–cylinder liner interaction inside the internal combustion engine. More specifically, the geometry was selected in order to allow a variable lubricant confinement gap combined with a varying lubricant quantity in the gap, while avoiding the squeeze-out of the lubricant into vacuum. Odd-number layering and near-wall solidification was observed between the solid plates, similar to published experimental findings. The friction simulations have uncovered an interesting behaviour of ILs , with a logarithmic dependence of specific friction on velocity hinting at elasto-hydrodynamic lubrication at low loads. This behaviour

completely changed under more critical conditions of high load, with specific friction decreasing to lower values and becoming independent of sliding velocity. This behaviour was strongly correlated with the internal structure of the *IL* and can provide guidance for implementing lubrication concepts that can lead to friction reduction in internal combustion engines.

Also, the implemented *MD* simulation setup has been used in order to study the response of a model ionic liquid to imposed mechanical deformation. The properties of bulk and confined ionic liquid have been investigated under both static and dynamic conditions. First, it has been shown that the Green–Kubo viscosity coefficient fits the shearing simulation results of the bulk salt model ionic liquid, indicating its liquid state. The simulation results have shown the significant impact of the confinement and interaction with the walls on the ionic liquid response to mechanical deformation. The force–distance hysteresis surface under cyclic loading is smaller than one would expect considering only the viscosity value of the liquid. The simulations have also shown the transition from a liquid to a highly dense and ordered, potentially solidified state of the *IL* taking place under variable normal load and under shear. The wall slip has a profound influence on all the forces which arise as a response to the mechanical deformation. It has also been observed that the interaction of the *IL* with the walls represents a principal driving force for all processes observed in the dynamic regime for a range of studied velocities. If sufficient time is allowed for the system to reach the equilibrium, inter–ionic interactions pull more ionic liquid inside the confinement gap.

Ionic liquids feature strong long–ranged Coulombic forces and their models require significant computational effort. Coarse grained models, such as the salt model implemented in the current study, are useful for bridging the gap between the molecular processes that control the lubrication phenomena and the macroscopic performance in engineering applications. The implementation of simplified models that describe fundamental physicochemical phenomena at a reduced computational cost can provide deep insights which shed light onto the mechanisms and processes that can render *ILs* as potentially interesting lubricant candidates.

4.2.2 Tailed models of ionic liquid

Since ionic liquids interact via long-ranged Coulombic forces and their models require high-performance computational resources, there rises a question of the minimal model needed to capture the properties of the molecular processes governing lubrication mechanisms and the macroscopic performance relevant for engineering applications. A generic tailed-model (*TM*) of ionic liquids which includes: an asymmetric cation consisting of a positively charged head and a neutral tail of variable size and a large spherical negatively charged anion has been investigated. It has been observed that, though simple, this model results in striking differences of the equilibrium *IL* bulk structure governed by the tail size relative to cationic head:

- (i) simple cubic lattice for the small tail,
- (ii) liquid-like state for symmetric cation-tail dimer, and
- (iii) molecular layer structure for the large tail.

The influence of the molecular structure of cation dimer on the response of the three representative ionic liquids to confinement and mechanical strain has been investigated using *MD* simulations. Properties of three *IL* models are compared in and out of equilibrium. The evolution of normal force with inter-plate distance has been related to the changes in the number and structure of the confined *IL* layers. It has been found that the density inside the gap has a secondary effect on the evolution of the normal force. It has been observed that symmetric molecule offsets intra-*IL* adhesion due to the ordering of *IL*. As a result, the thin layer of symmetric *IL* molecules exhibits non-negative normal force independent of the gap width. In analogy to the experimental observations, a tail-to-tail bilayer is formed for wide gaps in all three investigated model *ILs*. A mutual feature of all investigated model *ILs* is the formation of fixed (stable) layers of cations along the solid plates. The fixed layer formation is a result of strong LJ interaction between the plates and ions. A consequence of the fixed layer stability is a steep rise of the normal force at small interplate gaps. The steep rise of the normal force is an effect useful for preventing solid-solid contact and accompanying wear. The tails attached to the cations in the fixed layer migrate with increasing tail size. Small tails form the first layer next to

the plates. For symmetric molecules the tails form a mixed layer with cations, while large tails form a mixed layer with anions.

The dynamic behaviour of *IL* thin film under cyclic extension–compression movements of the Top plate has been explored. Two intervals of the interplate distances are investigated: narrow gap interval, where the anionic layer is split into two, and a wide gap interval where tail–to–tail layer is formed. For the narrow gap interval, a significant flow of ions during the cyclic motion of the Top plate has been observed. A sharp decrease of the normal force at the final stage of compression is not only a consequence of the density change due to the flow, but it is also a result of merging of two anionic layers that repel each-other by the electrostatic Coulombic forces into a single one. The mobility of ions in and out of the gap is driven by their interaction with plates, i.e., filling of the fixed layers. As a result, for the narrow gap, the number of ions that entered the gap is 50% smaller in the dynamic case than in the static case. This results in a smaller density inside the moving narrow gap. The difference between dynamic and static cases for the wide gap was even more striking, the number of ions that entered the gap is 80% smaller in the dynamic case than in the static case. Surprisingly, in wide gap the density is higher in dynamic case due to the lack of mobility of ions. The invested work per average cycle increases with the tail size increase for all three *IL* models. As one could expect, the invested work is higher for the narrow gap, where the number of confined ionic layers changes during the cycle. Nevertheless, the low hysteretic losses suggest the presence of strong slip inside the gap facilitating in– and out– flow of ions in the gap. An increase of the tail size reduces friction force in the implemented *TM* model of ionic liquid. Depending on the tail size, friction force decreases with increasing gap for small tails and it increases for large tails.

Understanding the interplay between the different processes taking place in thin lubricant films is important due to the conflicting demands imposed on how *IL* lubricant should behave in dynamic confinement. On the one hand, a high load-carrying capability requires strong adsorption of the lubricant to the surface, while on the other hand fast self-healing and low friction require high mobility/low viscosity. The obtained results confirm that the behaviour of *ILs* in confinement can

be unrelated to their bulk behaviour and therefore it should be possible to achieve simultaneously, typically conflicting, low friction and good anti-wear performance. A search for optimal *IL* lubricants, either using synthesis and test methods or state-of-the-art computer-based molecular design methods [120], should take into account the microscale properties of lubricating thin films (e.g., normal force vs. number of layers characteristics), in which the effects of molecular-level processes are more pronounced. Directing the optimization efforts to the microscale would enable us a better differentiation of the qualities of different ionic liquids.

Appendix A Lekner-type summation method for 1D periodic dipolar structures

A.1 Total interaction energy in the selected Lekner-type method

Let us consider N particles with i -th particle ($i = \overline{1, N}$) having a dipole moment $\vec{\mu}_i$. Its position is defined as $\vec{r}_i = (x_i, y_i, z_i)$. Position vector between dipoles i and j is given as $\vec{r}_{ij} = \vec{r}_i - \vec{r}_j$. We use the notation for the projection of the vectors \vec{r}_{ij} and $\vec{\mu}_i$ on the xy plane: $\vec{\rho}_{ij}$ and $\vec{\mu}_i^\rho$, respectively. Precisely speaking, $\vec{\rho}_{ij} = (x_{ij}, y_{ij}, 0)$ and $\vec{\mu}_i^\rho = (\mu_i^x, \mu_i^y, 0)$. Projection of the above mentioned vectors on the z axis is noted as: z_{ij} and μ_i^z .

This is the expression for the potential energy of the DDI between the dipole $\vec{\mu}_i$ positioned at \vec{r}_i and the dipole $\vec{\mu}_j$ positioned at \vec{r}_j :

$$u_{\text{dd}} = C \left[\frac{\vec{\mu}_i \cdot \vec{\mu}_j}{r_{ij}^3} - 3 \frac{(\vec{\mu}_i \cdot \vec{r}_{ij})(\vec{\mu}_j \cdot \vec{r}_{ij})}{r_{ij}^5} \right], \quad (\text{A.1})$$

where C represents a constant which depends on the intervening medium and for simplicity reasons we set $C = 1$ in the following derivations.

Knowing the interaction energy u_{dd} in case of a pair of dipoles i and j ($i, j = \overline{1, N}$) let us form the expression for the total interaction energy of the system whose elementary cell contains N dipoles. We take into account the fact $u_{\text{dd}} \propto r^{-2s}$ which replaces $u_{\text{dd}} \propto r^{-3}$:

$$E_{\text{dd}} = \frac{1}{2} \sum_{i,j=1}^N \sum_{m'} \left\{ \frac{\vec{\mu}_i \cdot \vec{\mu}_j}{[\rho_{ij}^2 + (z_{ij} + mL_z)^2]^s} - 3 \frac{[\vec{\mu}_i^\rho \cdot \vec{\rho}_{ij} + \mu_i^z (z_{ij} + mL_z)][\vec{\mu}_j^\rho \cdot \vec{\rho}_{ij} + \mu_j^z (z_{ij} + mL_z)]}{[\rho_{ij}^2 + (z_{ij} + mL_z)^2]^{s+1}} \right\}, \quad (\text{A.2})$$

where the quantity L_z has a physical meaning of length, i.e., it determines the periodicity of a structure along the z -direction. The elementary cell contains N particles and it is positioned in the way that for its each particle i stands $z_i \geq 0$ (i.e., the lower end of the elementary cell is placed at $z = 0$). The $1/2$ factor regulates the fact that we consider the interaction of each i, j pair twice, due to the double sum $\sum_{i,j=1}^N$. In each i, j pair the i -th particle belongs to the elementary cell, while the particle j can belong to the elementary cell or to the one of elementary cell's copies along the z axis. Hence, $m = 0$ corresponds to the elementary cell, while $m \neq 0$ counts the copies. This is why we define the distance between two dipoles along the z axis as: $z_{ij} + mL_z$. It is clear that m is an integer which counts how many periods along the z axis is a given copy shifted from the elementary cell. Summation index m is denoted as m' in Equation A.2 to mark the fact that for $m = 0$ the terms with $i = j$ are excluded, since the dipoles do not auto-interact. Let us define the lattice sums $\Psi_r(s)$ and $\Xi_{r,\xi}(s)$ for $\vec{r} \neq 0$ as:

$$\Psi_r(s) = \frac{1}{L_z^{2s}} \sum_m \left[\left(\frac{\rho}{L_z} \right)^2 + \left(\frac{z}{L_z} + m \right)^2 \right]^{-s}, \quad (\text{A.3})$$

$$\Xi_{r,\xi}(s) = \frac{e^{-i\vec{\xi}_\rho \cdot \vec{\rho}}}{L_z^{2s}} \sum_m \left[\left(\frac{\rho}{L_z} \right)^2 + \left(\frac{z}{L_z} + m \right)^2 \right]^{-s} e^{-i\xi_z(z+mL_z)}. \quad (\text{A.4})$$

By comparing Equations A.3 and A.4 we notice that $\Xi_{r,\xi}(s) = e^{-i\vec{\xi}_\rho \cdot \vec{\rho}} e^{-i\xi_z(z+mL_z)} \Psi_r(s)$. The terms $e^{-i\vec{\xi}_\rho \cdot \vec{\rho}}$ and $e^{-i\xi_z(z+mL_z)}$ are introduced in order to enable the conversion of real-space sums into reciprocal-space sums, in the further steps of derivation. Quantity $\vec{\xi}$ has the physical meaning of reciprocal length and it can be represented as: $\vec{\xi} = (\vec{\xi}_\rho, \xi_z)$, $\vec{\xi}_\rho = (\xi_x, \xi_y)$.

Using the lattice sums $\Psi_r(s)$ and $\Xi_{r,\xi}(s)$ we can rewrite Equation A.2 coming up with:

$$\begin{aligned} E_{\text{dd}} &= \frac{1}{2} \sum_{i=1}^N \sum_{j=1, j \neq i}^N [\vec{\mu}_i \cdot \vec{\mu}_j \Psi_{r_{ij}}(s) + 3(\vec{\mu}_i \cdot \nabla \xi)(\vec{\mu}_j \cdot \nabla \xi) \Xi_{r_{ij}, \xi}(s+1)|_{\xi=0}] \\ &\quad + \frac{1}{2} \sum_{i=1}^N [|\vec{\mu}_i|^2 - 3(\mu_i^z)^2] \Psi_0(s), \end{aligned} \quad (\text{A.5})$$

where the condition $\xi = 0$ ensures that the terms intentionally introduced in the definition of the lattice sum $\Xi_{r,\xi}(s)$ in Equation A.4 are $e^{-i\vec{\xi}_\rho \cdot \vec{\rho}} = 1$ and $e^{-i\xi_z(z+mL_z)} = 1$.

A.2 Derivation of the expression for the self energy

From the expression for the total energy of interaction in Equation A.5 we can extract the expression for the self energy:

$$\begin{aligned} E_{\text{self}}(s) &= \frac{1}{2} \sum_{i=1}^N \left[|\vec{\mu}_i|^2 - 3(\mu_i^z)^2 \right] \Psi_0(s), \\ \Rightarrow E_{\text{self}}(s) &= \frac{1}{2} \sum_{i=1}^N \left[|\vec{\mu}_i^\rho|^2 - 2(\mu_i^z)^2 \right] \Psi_0(s), \end{aligned} \quad (\text{A.6})$$

taking into account that: $|\vec{\mu}_i|^2 = |\vec{\mu}_i^\rho|^2 + (\mu_i^z)^2$.

From Equation A.3 we see that the lattice sum $\Psi_0(s)$ for $\vec{r} = 0$ is:

$$\Psi_0(s) = \frac{1}{L_z^{2s}} \sum_{m \neq 0} |m|^{-2s} = \frac{1}{L_z^{2s}} \left(\sum_{m=-\infty}^{-1} |m|^{-2s} + \sum_{m=+1}^{+\infty} |m|^{-2s} \right). \quad (\text{A.7})$$

A fact that: $\sum_{m=-\infty}^{-1} |m|^{-2s} = \sum_{m=+1}^{+\infty} |m|^{-2s}$, leads to the next form of Equation A.7:

$$\Psi_0(s) = \frac{2}{L_z^{2s}} \sum_{m=+1}^{+\infty} |m|^{-2s}. \quad (\text{A.8})$$

By replacing $\Psi_0(s)$ from Equation A.8 into Equation A.6 and according to the definition of the Riemann zeta function, $\zeta(s) = \sum_{m=+1}^{+\infty} m^{-s}$, we arrive to the general expression for the self energy $E_{\text{self}}(s)$:

$$E_{\text{self}}(s) = \frac{1}{L_z^{2s}} \sum_{i=1}^N \left[|\vec{\mu}_i^\rho|^2 - 2(\mu_i^z)^2 \right] \zeta(2s). \quad (\text{A.9})$$

By applying $s = 3/2$ we obtain the expression for the self energy in case of the DDI:

$$E_{\text{self}}\left(\frac{3}{2}\right) = \frac{1}{L_z^3} \sum_{i=1}^N \left[|\vec{\mu}_i^\rho|^2 - 2(\mu_i^z)^2 \right] \zeta(3), \quad (\text{A.10})$$

where $\zeta(3)$ is a numerical factor with the value of $\zeta(3) = 1.2020569031\dots$ [76].

A.3 Derivation of the expression for the cross energy

Let us start from the expression for the cross energy from Equation A.5:

$$E_{\text{cross}}(s) = \frac{1}{2} \sum_{i=1}^N \sum_{j=1, j \neq i}^N \left[\vec{\mu}_i \vec{\mu}_j \Psi_{\text{rij}}(s) + 3(\vec{\mu}_i \cdot \nabla_\xi)(\vec{\mu}_j \cdot \nabla_\xi) \Xi_{\text{rij}, \xi}(s+1)|_{\xi=0} \right]. \quad (\text{A.11})$$

There are the two lattice sums in Equation A.11 (i.e., $\Psi_r(s)$, $\Xi_{r,\xi}(s+1)$) which should be determined. We will calculate them following the procedure presented in [89] by using the integral representation of the Gamma function [121]:

$$a^{-s} = \frac{1}{\Gamma(s)} \int_{t=0}^{+\infty} t^{s-1} e^{-at} dt. \quad (\text{A.12})$$

In Equation A.3 we recognize that we might write down:

$$a = \left(\frac{\rho}{L_z} \right)^2 + \left(\frac{z}{L_z} + m \right)^2. \quad (\text{A.13})$$

According to this observation we can rewrite Equation A.3 as:

$$\Psi_r(s) = \frac{1}{L_z^{2s}} \sum_m a^{-s}. \quad (\text{A.14})$$

By replacing a in the right-hand side of Equation A.12 with the expression from Equation A.13 and keeping the left-hand side as a^{-s} we arrive at:

$$a^{-s} = \frac{1}{\Gamma(s)} \int_{t=0}^{+\infty} t^{s-1} e^{-\left[\left(\frac{\rho}{L_z} \right)^2 + \left(\frac{z}{L_z} + m \right)^2 \right] t} dt. \quad (\text{A.15})$$

Now we replace the factor a^{-s} in Equation A.14 with the right-hand side expression from Equation A.15:

$$\Psi_r(s) = \frac{1}{L_z^{2s}\Gamma(s)} \sum_m \int_{t=0}^{+\infty} t^{s-1} e^{-\left[\left(\frac{\rho}{L_z}\right)^2 + \left(\frac{z}{L_z} + m\right)^2\right]t} dt. \quad (\text{A.16})$$

In the next step we switch the order of the sum and integral and extract the summation over m inside the integral:

$$\Psi_r(s) = \frac{1}{L_z^{2s}\Gamma(s)} \int_{t=0}^{+\infty} t^{s-1} e^{-\left(\frac{\rho}{L_z}\right)^2 t} \sum_m e^{-\left(\frac{z}{L_z} + m\right)^2 t} dt. \quad (\text{A.17})$$

We use the general form of the Poisson summation formula [122], thus converting from the real-space summation to the reciprocal-space summation:

$$\sum_{m=-\infty}^{+\infty} e^{-\left(\frac{u+c}{L_0} + m\right)^2 t} = \left(\frac{\pi}{t}\right)^{\frac{1}{2}} \sum_{k=-\infty}^{+\infty} e^{i2\pi k \frac{u+c}{L_0}} e^{-\frac{\pi^2 k^2}{t}}. \quad (\text{A.18})$$

Looking at Equation A.17, we decide to write down those identities: $u + c = z$, $L_0 = L_z$. We apply the Poisson summation formula, taking into account the previously mentioned identities, therefore coming up with:

$$\sum_m e^{-\left(\frac{z}{L_z} + m\right)^2 t} = \left(\frac{\pi}{t}\right)^{\frac{1}{2}} \sum_{k=-\infty}^{+\infty} e^{i2\pi k \frac{z}{L_z}} e^{-\frac{\pi^2 k^2}{t}}. \quad (\text{A.19})$$

$$\begin{aligned} \Rightarrow \Psi_r(s) &= \frac{1}{L_z^{2s}\Gamma(s)} \int_{t=0}^{+\infty} t^{s-1} e^{-\left(\frac{\rho}{L_z}\right)^2 t} \left(\frac{\pi}{t}\right)^{\frac{1}{2}} \\ &\quad \times \left[\sum_{k=-\infty, k \neq 0}^{+\infty} e^{i2\pi k \frac{z}{L_z}} e^{-\frac{\pi^2 k^2}{t}} + 1 \right] dt. \end{aligned} \quad (\text{A.20})$$

At this point we switch the order of the sum and integral, hence the integral comes inside the sum over k :

$$\begin{aligned} \Psi_r(s) &= \frac{\pi^{1/2}}{L_z^{2s}\Gamma(s)} \sum_{k=-\infty, k \neq 0}^{+\infty} e^{i2\pi k \frac{z}{L_z}} \int_{t=0}^{+\infty} t^{s-3/2} e^{-(\frac{\rho}{L_z})^2 t} e^{-\frac{\pi^2 k^2}{t}} dt \\ &\quad + \frac{\pi^{1/2}}{L_z^{2s}\Gamma(s)} \int_{t=0}^{+\infty} t^{s-3/2} e^{-(\frac{\rho}{L_z})^2 t} dt. \end{aligned} \quad (\text{A.21})$$

From Equation A.21 we can extract the integral:

$$I = \int_{t=0}^{+\infty} t^{s-3/2} e^{-(\frac{\rho}{L_z})^2 t} e^{-\frac{\pi^2 k^2}{t}} dt. \quad (\text{A.22})$$

We have solved this integral in Mathematica software package [76]:

$$I = 2^{3/2-s} \left(\frac{L_z}{\rho}\right)^{s-1/2} (2\pi k)^{s-1/2} K_{s-1/2} \left(2\pi k \frac{\rho}{L_z}\right), \quad (\text{A.23})$$

where $K_n(u)$ is the modified Bessel function of the second kind [123].

This expression can be simplified in the following manner:

$$I = 2^{3/2-s} \left(2\pi k \frac{L_z}{\rho}\right)^{s-1/2} K_{s-1/2} \left(2\pi k \frac{\rho}{L_z}\right). \quad (\text{A.24})$$

By replacing the expression for the integral I from Equation A.24 to the sum in the first term in Equation A.21, we obtain:

$$\sum_{k=-\infty, k \neq 0}^{+\infty} e^{i2\pi k \frac{z}{L_z}} \left[2 \left(\pi k \frac{L_z}{\rho}\right)^{s-1/2} K_{s-1/2} \left(2\pi k \frac{\rho}{L_z}\right) \right] = \sum_{k=-\infty, k \neq 0}^{+\infty} e^{i2\pi k \frac{z}{L_z}} f(k). \quad (\text{A.25})$$

Applying the identity:

$$\cos\left(2\pi k \frac{z}{L_z}\right) = \frac{e^{i2\pi k \frac{z}{L_z}} + e^{-i2\pi k \frac{z}{L_z}}}{2}, \quad (\text{A.26})$$

we come up with the next expression:

$$\sum_{k=-\infty, k \neq 0}^{+\infty} e^{i2\pi k \frac{z}{L_z}} f(k) = \left(2 \sum_{k=1}^{+\infty} \cos\left(2\pi k \frac{z}{L_z}\right) f(k) \right). \quad (\text{A.27})$$

Hence, the first term of Equation A.21 is equal to:

$$\frac{\pi^{1/2}}{L_z^{2s}\Gamma(s)} \times 4 \sum_{k=1}^{+\infty} \cos\left(2\pi k \frac{z}{L_z}\right) \left(\pi k \frac{L_z}{\rho}\right)^{s-1/2} K_{s-1/2}\left(2\pi k \frac{\rho}{L_z}\right).$$

So far we have computed the first term in Equation A.21 for $k \neq 0$ and now we should compute the second term which corresponds to $k = 0$, which means that we should compute the integral:

$$II = \int_{t=0}^{+\infty} t^{s-3/2} e^{-\left(\frac{\rho}{L_z}\right)^2 t} dt. \quad (\text{A.28})$$

We notice that Equation A.12 which represents the integral representation of the Gamma function can be a good starting point for this. Setting the exponent to $s - 1/2$ instead of s gives us:

$$a^{-(s-1/2)} = \frac{1}{\Gamma(s-1/2)} \int_{t=0}^{+\infty} t^{s-3/2} e^{-at} dt, \quad (\text{A.29})$$

$$\Rightarrow a^{-(s-1/2)} \Gamma(s-1/2) = \int_{t=0}^{+\infty} t^{s-3/2} e^{-at} dt. \quad (\text{A.30})$$

By comparing the right-hand side of Equations A.30 and A.28 we conclude that we can say $a = \left(\frac{\rho}{L_z}\right)^2$ which enables the solution of the integral II :

$$II = a^{-(s-1/2)} \Gamma(s-1/2). \quad (\text{A.31})$$

Hence, the second term of Equation A.21 is equal to $\frac{\pi^{1/2}}{L_z^{2s}\Gamma(s)} \left(\frac{\rho}{L_z}\right)^{1-2s} \Gamma\left(s - \frac{1}{2}\right)$.

Finally, the expression for the lattice sum $\Psi_r(s)$ is:

$$\begin{aligned} \Psi_r(s) &= \frac{4\pi^{1/2}}{L_z^{2s}\Gamma(s)} \sum_{k=1}^{+\infty} \left(\cos\left(2\pi k \frac{z}{L_z}\right) \left(\frac{\pi^2 k^2 L_z^2}{\rho^2}\right)^{s/2-1/4} K_{s-1/2}\left(2\pi k \frac{\rho}{L_z}\right) \right) \\ &\quad + \frac{\pi^{1/2}}{L_z^{2s}\Gamma(s)} \left(\frac{\rho}{L_z}\right)^{1-2s} \Gamma\left(s - \frac{1}{2}\right). \end{aligned} \quad (\text{A.32})$$

The other unknown lattice sum from Equation A.11 is $\Xi_{r,\xi}(s)$. Let us apply a procedure analogous to the previous derivation of the unknown lattice sum $\Psi_r(s)$.

In the first step, using the integral representation of the Gamma function from Equation A.12 and the definition of the parameter a as in Equation A.13 we obtain:

$$\Xi_{r,\xi}(s) = \frac{e^{-i\vec{\xi}_\rho \cdot \vec{\rho}}}{L_z^{2s}\Gamma(s)} \sum_m e^{-i\xi_z(z+mL_z)} \int_{t=0}^{+\infty} t^{s-1} e^{-\left[\left(\frac{\rho}{L_z}\right)^2 + \left(\frac{z}{L_z} + m\right)^2\right]t} dt. \quad (\text{A.33})$$

Now we use the complete Poisson summation formula from Equation A.18 ($\xi_z \neq 0$) which leads to:

$$\Xi_{r,\xi}(s) = \frac{e^{-i\vec{\xi}_\rho \cdot \vec{\rho}} \pi^{1/2}}{L_z^{2s}\Gamma(s)} \int_{t=0}^{+\infty} t^{s-3/2} e^{-\left(\frac{\rho}{L_z}\right)^2 t} \sum_{k=-\infty}^{+\infty} e^{i2\pi k \frac{z}{L_z}} e^{-\frac{(2\pi k + \xi_z L_z)^2}{4t}} dt. \quad (\text{A.34})$$

By placing the sum in front of the integral (which is the same step like in Equation A.21) we obtain:

$$\Xi_{r,\xi}(s) = \frac{e^{-i\vec{\xi}_\rho \cdot \vec{\rho}} \pi^{1/2}}{L_z^{2s}\Gamma(s)} \sum_{k=-\infty}^{+\infty} e^{i2\pi k \frac{z}{L_z}} \int_{t=0}^{+\infty} t^{s-3/2} e^{-\left(\frac{\rho}{L_z}\right)^2 t} e^{-\frac{(2\pi k + \xi_z L_z)^2}{4t}} dt. \quad (\text{A.35})$$

In the expression for $\Xi_{r,\xi}(s)$ in Equation A.35 we have encountered the same integral I like in Equation A.22. By replacing its solution from Equation A.23 into Equation A.35 we obtain the final expression for the lattice sum $\Xi_{r,\xi}(s)$:

$$\begin{aligned} \Xi_{r,\xi}(s) &= \frac{e^{-i\vec{\xi}_\rho \cdot \vec{\rho}} \pi^{1/2}}{L_z^{2s}\Gamma(s)} \sum_{k=-\infty}^{+\infty} e^{i2\pi k \frac{z}{L_z}} 2^{3/2-s} \left(\frac{L_z}{\rho}\right)^{s-1/2} \\ &\quad \times (2\pi k + \xi_z L_z)^{s-1/2} K_{s-1/2} \left(|2\pi k + \xi_z L_z| \frac{\rho}{L_z} \right). \end{aligned} \quad (\text{A.36})$$

Simplification of the previous expression leads to:

$$\begin{aligned} \Xi_{r,\xi}(s) &= \frac{2\pi^{1/2} e^{-i\vec{\xi}_\rho \cdot \vec{\rho}}}{L_z^{2s}\Gamma(s)} \sum_{k=-\infty}^{+\infty} e^{i2\pi k \frac{z}{L_z}} \left(\frac{(\xi_z L_z + 2\pi k)^2 L_z^2}{4\rho^2} \right)^{s/2-1/4} \\ &\quad \times K_{s-1/2} \left(|\xi_z L_z + 2\pi k| \frac{\rho}{L_z} \right). \end{aligned} \quad (\text{A.37})$$

Now, as we have derived the general expression for the lattice sum $\Xi_{r,\xi}(s)$, we can proceed to the derivation of the general expression for the cross energy from Equation A.11. The next step is the application of the operator:

$$(\vec{\mu}_i \cdot \nabla_\xi)(\vec{\mu}_j \cdot \nabla_\xi),$$

where due to the simplicity reasons we introduce the variables: $\eta^z = \frac{2\pi z}{L_z}$ and $\eta^\rho = \frac{2\pi\rho}{L_z}$. We first apply the next scalar product:

$$(\vec{\mu}_j \cdot \nabla_\xi) = \left(\mu_j^x \frac{\partial}{\partial \xi_x} + \mu_j^y \frac{\partial}{\partial \xi_y} + \mu_j^z \frac{\partial}{\partial \xi_z} \right). \quad (\text{A.38})$$

We can introduce the substitution $A = \frac{2\pi^{1/2}}{L_z^{2s}\Gamma(s)}$ and label the part of the function $\Xi_{r,\xi}(s)$ that depends just on ξ_z as $F(\xi_z)$:

$$\Xi_{r,\xi}(s) = A e^{-i(\xi_x x + \xi_y y)} F(\xi_z), \quad (\text{A.39})$$

$$\begin{aligned} F(\xi_z) &= \sum_{k=-\infty}^{+\infty} e^{i2\pi k \frac{z}{L_z}} \left(\frac{(\xi_z L_z + 2\pi k)^2 L_z^2}{4\rho^2} \right)^{s/2-1/4} \\ &\quad \times K_{s-1/2} \left(|\xi_z L_z + 2\pi k| \frac{\rho}{L_z} \right). \end{aligned} \quad (\text{A.40})$$

Application of the operator $(\vec{\mu}_j \cdot \nabla_\xi)$ on $\Xi_{r,\xi}(s)$ gives:

$$(i) \quad \mu_j^x \frac{\partial}{\partial \xi_x} \Xi_{r,\xi}(s) = \mu_j^x (-ix) A e^{-i(\xi_x x + \xi_y y)} F(\xi_z). \quad (\text{A.41})$$

$$(ii) \quad \mu_j^y \frac{\partial}{\partial \xi_y} \Xi_{r,\xi}(s) = \mu_j^y (-iy) A e^{-i(\xi_x x + \xi_y y)} F(\xi_z). \quad (\text{A.42})$$

(iii)

$$\begin{aligned}
 \mu_j^z \frac{\partial}{\partial \xi_z} \Xi_{r,\xi}(s) &= \mu_j^z A e^{-i\vec{\xi}_\rho \cdot \vec{\rho}} \sum_{k=-\infty}^{+\infty} e^{ik\eta z} \\
 &\times \left[\left(\frac{L_z}{2\rho} \right)^{(2s-1)/2} \left(\frac{2s-1}{2} \right) (\xi_z L_z + 2\pi k)^{(2s-3)/2} L_z K_{s-1/2}(\alpha) \right. \\
 &\left. + \left(\frac{(\xi_z L_z + 2\pi k) L_z}{2\rho} \right)^{(2s-1)/2} \rho \frac{\partial K_{s-1/2}(\alpha)}{\partial \alpha} \right]. \tag{A.43}
 \end{aligned}$$

In the previous equation, due to the simplicity of the further analysis, the argument of the modified Bessel functions $K_{s-1/2}$ is labeled as α :

$$|\xi_z L_z + 2\pi k| \frac{\rho}{L_z} = \alpha.$$

In order to obtain the full expression for $(\vec{\mu}_j \cdot \nabla_\xi) \Xi_{r,\xi}(s)$, let us make a summation of all three components computed in the previous equations. Prior to obtaining the final expression it is convenient to write down the terms that correspond to the x, y components separately from the terms that correspond to the z component:

$$P_{xy} = (-i) (\mu_j^x x + \mu_j^y y) \left(\frac{(\xi_z L_z + 2\pi k) L_z}{2\rho} \right)^{(2s-1)/2} K_{s-1/2}(\alpha),$$

$$\begin{aligned}
 P_z &= \mu_j^z \left[\left(\frac{L_z}{2\rho} \right)^{(2s-1)/2} \left(\frac{2s-1}{2} \right) (\xi_z L_z + 2\pi k)^{(2s-3)/2} L_z K_{s-1/2}(\alpha) \right. \\
 &\left. + \left(\frac{(\xi_z L_z + 2\pi k) L_z}{2\rho} \right)^{(2s-1)/2} \rho \frac{\partial K_{s-1/2}(\alpha)}{\partial \alpha} \right].
 \end{aligned}$$

The application of the scalar product $(\vec{\mu}_j \cdot \nabla_\xi)$ on the lattice sum $\Xi_{r,\xi}(s)$ gives:

$$(\vec{\mu}_j \cdot \nabla_\xi) \Xi_{r,\xi}(s) = A e^{-i\vec{\xi}_\rho \cdot \vec{\rho}} \sum_{k=-\infty}^{+\infty} e^{ik\eta z} (P_{xy} + P_z). \tag{A.44}$$

Bearing in mind the practical importance of simplifying the forthcoming computations, let us repeat the definition of α and introduce another two variables, β and

γ :

$$\alpha = |\xi_z L_z + 2\pi k| \frac{\rho}{L_z},$$

$$\beta = (\xi_z L_z + 2\pi k) \frac{L_z}{2\rho},$$

$$\gamma = \xi_z L_z + 2\pi k.$$

The expression in Equation A.44 can be represented as a sum of three independent terms, and each of those terms will be treated separately:

Term C_1

$$C_1 = (-i) \vec{\mu}_j^{\rho} \cdot \vec{\rho} A e^{-i\vec{\xi}_\rho \cdot \vec{\rho}} \sum_{k=-\infty}^{+\infty} e^{ik\eta z} \beta^{(2s-1)/2} K_{s-1/2}(\alpha), \quad (\text{A.45})$$

Term C_2

$$C_2 = A e^{-i\vec{\xi}_\rho \cdot \vec{\rho}} \mu_j^z \sum_{k=-\infty}^{+\infty} e^{ik\eta z} \left(\frac{L_z}{2\rho} \right)^{(2s-1)/2} \left(\frac{2s-1}{2} \right) \gamma^{(2s-3)/2} L_z K_{s-1/2}(\alpha), \quad (\text{A.46})$$

Term C_3

$$C_3 = A e^{-i\vec{\xi}_\rho \cdot \vec{\rho}} \mu_j^z \sum_{k=-\infty}^{+\infty} e^{ik\eta z} \beta^{(2s-1)/2} \rho \frac{\partial K_{s-1/2}(\alpha)}{\partial \alpha}. \quad (\text{A.47})$$

The next step is the application of the scalar product

$$\vec{\mu}_i \cdot \vec{\nabla}_\xi = \mu_i^x \frac{\partial}{\partial \xi_x} + \mu_i^y \frac{\partial}{\partial \xi_y} + \mu_i^z \frac{\partial}{\partial \xi_z}$$

on Equation A.44, which produces new terms.

In the mentioned scalar product there are three independent operators which act on each of the three terms $\{C_1, C_2, C_3\}$, hence producing nine new terms, numerated as C_{ij} , with $i \in \{1, 2, 3\}$, $j \in \{1, 2, 3\}$.

In the next equation we write down the term C_{11} :

Term C_{11}

$$C_{11} = \mu_i^x \frac{\partial}{\partial \xi_x} \left[(-i) \vec{\mu}_j^{\lambda \rho} \cdot \vec{\rho} A e^{-i \vec{\xi}_\rho \cdot \vec{\rho}} \sum_{k=-\infty}^{+\infty} e^{ik\eta^z} \beta^{(2s-1)/2} K_{s-1/2}(\alpha) \right]. \quad (\text{A.48})$$

Since it stands

$$\frac{\partial}{\partial \xi_x} e^{-i \vec{\xi}_\rho \cdot \vec{\rho}} = (-ix) e^{-i \vec{\xi}_\rho \cdot \vec{\rho}}, \quad (\text{A.49})$$

the final expression for the term C_{11} becomes

$$C_{11} = -x \mu_i^x \vec{\mu}_j^{\lambda \rho} \cdot \vec{\rho} A e^{-i \vec{\xi}_\rho \cdot \vec{\rho}} \sum_{k=-\infty}^{+\infty} e^{ik\eta^z} \beta^{(2s-1)/2} K_{s-1/2}(\alpha). \quad (\text{A.50})$$

In the next equation we write down the term C_{21} :

Term C_{21}

$$C_{21} = \mu_i^y \frac{\partial}{\partial \xi_y} \left[(-i) \vec{\mu}_j^{\lambda \rho} \cdot \vec{\rho} A e^{-i \vec{\xi}_\rho \cdot \vec{\rho}} \sum_{k=-\infty}^{+\infty} e^{ik\eta^z} \beta^{(2s-1)/2} K_{s-1/2}(\alpha) \right]. \quad (\text{A.51})$$

Since it stands

$$\frac{\partial}{\partial \xi_y} e^{-i \vec{\xi}_\rho \cdot \vec{\rho}} = (-iy) e^{-i \vec{\xi}_\rho \cdot \vec{\rho}}, \quad (\text{A.52})$$

the final expression for the term C_{21} becomes

$$C_{21} = -y \mu_i^y \vec{\mu}_j^{\lambda \rho} \cdot \vec{\rho} A e^{-i \vec{\xi}_\rho \cdot \vec{\rho}} \sum_{k=-\infty}^{+\infty} e^{ik\eta^z} \beta^{(2s-1)/2} K_{s-1/2}(\alpha). \quad (\text{A.53})$$

In the next equation we write down the term C_{12} :

Term C_{12}

$$C_{12} = \mu_i^x \frac{\partial}{\partial \xi_x} A e^{-i \vec{\xi}_\rho \cdot \vec{\rho}} \mu_j^z \sum_{k=-\infty}^{+\infty} e^{ik\eta^z} \left(\frac{L_z}{2\rho} \right)^{(2s-1)/2} \left(\frac{2s-1}{2} \right) \times \gamma^{(2s-3)/2} L_z K_{s-1/2}(\alpha). \quad (\text{A.54})$$

Taking into account Equation A.49 the final expression for the term C_{12} becomes:

$$\begin{aligned}
 C_{12} = & -ix\mu_i^x\mu_j^z A e^{-i\vec{\xi}_\rho \cdot \vec{\rho}} \sum_{k=-\infty}^{+\infty} e^{ik\eta z} \left(\frac{L_z}{2\rho}\right)^{(2s-1)/2} \left(\frac{2s-1}{2}\right) \\
 & \times \gamma^{(2s-3)/2} L_z K_{s-1/2}(\alpha).
 \end{aligned} \tag{A.55}$$

In the next equation we write down the term C_{22} :

Term C_{22}

$$C_{22} = \mu_i^y \frac{\partial}{\partial \xi_y} A e^{-i\vec{\xi}_\rho \cdot \vec{\rho}} \mu_j^z \sum_{k=-\infty}^{+\infty} e^{ik\eta z} \left(\frac{L_z}{2\rho} \right)^{(2s-1)/2} \left(\frac{2s-1}{2} \right) \times \gamma^{(2s-3)/2} L_z K_{s-1/2}(\alpha). \quad (\text{A.56})$$

Taking into account Equation A.52 the final expression for the term C_{22} becomes:

$$C_{22} = -iy\mu_i^y \mu_j^z A e^{-i\vec{\xi}_\rho \cdot \vec{\rho}} \sum_{k=-\infty}^{+\infty} e^{ik\eta z} \left(\frac{L_z}{2\rho} \right)^{(2s-1)/2} \left(\frac{2s-1}{2} \right) \times \gamma^{(2s-3)/2} L_z K_{s-1/2}(\alpha). \quad (\text{A.57})$$

In the next equation we write down the term C_{13} :

Term C_{13}

$$C_{13} = \mu_i^x \frac{\partial}{\partial \xi_x} \left[A e^{-i\vec{\xi}_\rho \cdot \vec{\rho}} \mu_j^z \sum_{k=-\infty}^{+\infty} e^{ik\eta z} \beta^{(2s-1)/2} \rho \frac{\partial K_{s-1/2}(\alpha)}{\partial \alpha} \right]. \quad (\text{A.58})$$

Taking into account Equation A.49 the final expression for the term C_{13} becomes:

$$C_{13} = -ix\mu_i^x \mu_j^z A e^{-i\vec{\xi}_\rho \cdot \vec{\rho}} \sum_{k=-\infty}^{+\infty} e^{ik\eta z} \beta^{(2s-1)/2} \rho \frac{\partial K_{s-1/2}(\alpha)}{\partial \alpha}. \quad (\text{A.59})$$

In the next equation we provide the term C_{23} :

Term C_{23}

$$C_{23} = \mu_i^y \frac{\partial}{\partial \xi_y} \left[A e^{-i\vec{\xi}_\rho \cdot \vec{\rho}} \mu_j^z \sum_{k=-\infty}^{+\infty} e^{ik\eta z} \beta^{(2s-1)/2} \rho \frac{\partial K_{s-1/2}(\alpha)}{\partial \alpha} \right]. \quad (\text{A.60})$$

Taking into account Equation A.52 the final expression for the term C_{23} becomes:

$$C_{23} = -iy\mu_i^y \mu_j^z A e^{-i\vec{\xi}_\rho \cdot \vec{\rho}} \sum_{k=-\infty}^{+\infty} e^{ik\eta z} \beta^{(2s-1)/2} \rho \frac{\partial K_{s-1/2}(\alpha)}{\partial \alpha}. \quad (\text{A.61})$$

In the next equation we provide the term C_{31} :

Term C_{31}

$$C_{31} = \mu_i^z \frac{\partial}{\partial \xi_z} \left[(-i) \vec{\mu}_j^{\rho} \cdot \vec{\rho} A e^{-i \vec{\xi}_\rho \cdot \vec{\rho}} \sum_{k=-\infty}^{+\infty} e^{ik\eta^z} \beta^{(2s-1)/2} K_{s-1/2}(\alpha) \right]. \quad (\text{A.62})$$

In the term C_{31} we encounter two constituents of the expression depending on ξ_z (i.e., $\beta^{(2s-1)/2}$ and $K_{s-1/2}(\alpha)$) and therefore we obtain two terms inside the square brackets, according to the product rule for derivatives:

$$\begin{aligned} C_{31} &= (-i) \vec{\mu}_j^{\rho} \cdot \vec{\rho} \mu_i^z A e^{-i \vec{\xi}_\rho \cdot \vec{\rho}} \\ &\quad \times \sum_{k=-\infty}^{+\infty} e^{ik\eta^z} \left[\frac{(2s-1)}{2} \beta^{(2s-3)/2} \frac{L_z^2}{2\rho} K_{s-1/2}(\alpha) \right. \\ &\quad \left. + \beta^{(2s-1)/2} \rho \frac{\partial K_{s-1/2}(\alpha)}{\partial \alpha} \right]. \end{aligned} \quad (\text{A.63})$$

In the next equation we write down the term C_{32} :

Term C_{32}

$$\begin{aligned} C_{32} &= \mu_i^z \frac{\partial}{\partial \xi_z} A e^{-i \vec{\xi}_\rho \cdot \vec{\rho}} \mu_j^z \sum_{k=-\infty}^{+\infty} e^{ik\eta^z} \left(\frac{L_z}{2\rho} \right)^{(2s-1)/2} \left(\frac{2s-1}{2} \right) \\ &\quad \times \gamma^{(2s-3)/2} L_z K_{s-1/2}(\alpha). \end{aligned} \quad (\text{A.64})$$

Similarly to the case of term C_{31} we obtain:

$$\begin{aligned} C_{32} &= \mu_i^z \mu_j^z A e^{-i \vec{\xi}_\rho \cdot \vec{\rho}} \left(\frac{L_z}{2\rho} \right)^{(2s-1)/2} L_z \left(\frac{2s-1}{2} \right) \\ &\quad \times \sum_{k=-\infty}^{+\infty} e^{ik\eta^z} \left[\left(\frac{2s-3}{2} \right) \gamma^{(2s-5)/2} L_z K_{s-1/2}(\alpha) \right. \\ &\quad \left. + \gamma^{(2s-3)/2} \rho \frac{\partial K_{s-1/2}(\alpha)}{\partial \alpha} \right]. \end{aligned} \quad (\text{A.65})$$

In the next equation we write down the term C_{33} :

Term C_{33}

$$C_{33} = \mu_i^z \frac{\partial}{\partial \xi_z} \left[A e^{-i\vec{\xi}_\rho \cdot \vec{\rho}} \mu_j^z \sum_{k=-\infty}^{+\infty} e^{ik\eta^z} \beta^{(2s-1)/2} \rho \frac{\partial K_{s-1/2}(\alpha)}{\partial \alpha} \right]. \quad (\text{A.66})$$

Similarly to the previous two terms we obtain:

$$\begin{aligned} C_{33} &= \mu_i^z \mu_j^z A e^{-i\vec{\xi}_\rho \cdot \vec{\rho}} \\ &\times \sum_{k=-\infty}^{+\infty} e^{ik\eta^z} \rho \left[\left(\frac{2s-1}{2} \right) \beta^{(2s-3)/2} \left(\frac{L_z^2}{2\rho} \right) \frac{\partial K_{s-1/2}(\alpha)}{\partial \alpha} \right. \\ &\left. + \beta^{(2s-1)/2} \rho \frac{\partial^2 K_{s-1/2}(\alpha)}{\partial \alpha^2} \right]. \end{aligned} \quad (\text{A.67})$$

As we have obtained all nine terms C_{ij} , $i, j \in \{1, 2, 3\}$, the next step is grouping them according to the mutual sum over k or mutual constituent terms.

Group 1

This group includes the sum $\sum_{k=-\infty}^{+\infty} e^{ik\eta^z} \beta^{(2s-1)/2} K_{s-1/2}(\alpha)$, hence $GR_1 = C_{11} + C_{21}$,

$$\begin{aligned} GR_1 &= -(\vec{\mu}_i^\rho \cdot \vec{\rho})(\vec{\mu}_j^\rho \cdot \vec{\rho}) A e^{-i\vec{\xi}_\rho \cdot \vec{\rho}} \\ &\times \sum_{k=-\infty}^{+\infty} e^{ik\eta^z} \beta^{(2s-1)/2} K_{s-1/2}(\alpha). \end{aligned} \quad (\text{A.68})$$

Group 2

This group includes the sum $\sum_{k=-\infty}^{+\infty} e^{ik\eta^z} \left(\frac{L_z}{2\rho} \right)^{(2s-1)/2} \left(\frac{2s-1}{2} \right) \gamma^{(2s-3)/2} L_z K_{s-1/2}(\alpha)$, hence $GR_2 = C_{12} + C_{22}$,

$$\begin{aligned} GR_2 &= (-i)(\vec{\mu}_i^\rho \cdot \vec{\rho}) \mu_j^z A e^{-i\vec{\xi}_\rho \cdot \vec{\rho}} \\ &\times \sum_{k=-\infty}^{+\infty} e^{ik\eta^z} \left(\frac{L_z}{2\rho} \right)^{(2s-1)/2} \left(\frac{2s-1}{2} \right) \gamma^{(2s-3)/2} L_z K_{s-1/2}(\alpha). \end{aligned} \quad (\text{A.69})$$

Group 3

This group includes the sum $\sum_{k=-\infty}^{+\infty} e^{ik\eta^z} \beta^{(2s-1)/2} \rho \frac{\partial K_{s-1/2}(\alpha)}{\partial \alpha}$, therefore $GR_3 = C_{13} +$

C_{23} ,

$$\begin{aligned}
 GR_3 &= (-i) (\vec{\mu}_i^\rho \cdot \vec{\rho}) \mu_j^z A e^{-i\vec{\xi}_\rho \cdot \vec{\rho}} \\
 &\times \sum_{k=-\infty}^{+\infty} e^{ik\eta z} \beta^{(2s-1)/2} \rho \frac{\partial K_{s-1/2}(\alpha)}{\partial \alpha}. \tag{A.70}
 \end{aligned}$$

Group 4

This group includes the mutual factor $\mu_i^z \mu_j^z$, therefore $GR_4 = C_{32} + C_{33}$,

$$\begin{aligned}
 GR_4 &= \mu_i^z \mu_j^z A e^{-i\vec{\xi}_\rho \cdot \vec{\rho}} \\
 &\times \sum_{k=-\infty}^{+\infty} e^{ik\eta z} \left\{ \left(\frac{L_z}{2\rho} \right)^{(2s-1)/2} \left(\frac{2s-1}{2} \right) \left(\frac{2s-2}{3} \right) \gamma^{(2s-5)/2} L_z^2 K_{s-1/2}(\alpha) \right. \\
 &+ \left(\frac{L_z}{2\rho} \right)^{(2s-1)/2} \left(\frac{2s-1}{2} \right) \gamma^{(2s-2)/3} L_z \rho \frac{\partial K_{s-1/2}(\alpha)}{\partial \alpha} \\
 &+ \rho \left(\frac{2s-1}{2} \right) \beta^{(2s-3)/2} \left(\frac{L_z^2}{2\rho} \right) \frac{\partial K_{s-1/2}(\alpha)}{\partial \alpha} \\
 &\left. + \beta^{(2s-1)/2} \rho^2 \frac{\partial^2 K_{s-1/2}(\alpha)}{\partial \alpha^2} \right\}. \tag{A.71}
 \end{aligned}$$

Group 5

This group includes the factor $(\vec{\mu}_j^\rho \cdot \vec{\rho}) \mu_i^z$, hence $GR_5 = C_{31}$,

$$\begin{aligned}
 GR_5 &= (-i) (\vec{\mu}_j^\rho \cdot \vec{\rho}) \mu_i^z A e^{-i\vec{\xi}_\rho \cdot \vec{\rho}} \\
 &\times \sum_{k=-\infty}^{+\infty} e^{ik\eta z} \left[\frac{(2s-1)}{2} \beta^{(2s-3)/2} \left(\frac{L_z^2}{2\rho} \right) K_{s-1/2}(\alpha) \right. \\
 &\left. + \beta^{(2s-1)/2} \rho \frac{\partial K_{s-1/2}(\alpha)}{\partial \alpha} \right]. \tag{A.72}
 \end{aligned}$$

At this point let us overview what have we realized up to this step, towards obtaining the expression for the cross energy from Equation A.11. We have derived the expression for $\Psi_r(s)$ and the expressions for $(\vec{\mu}_i \cdot \nabla_\xi)(\vec{\mu}_j \cdot \nabla_\xi) \Xi_{r,\xi}(s)$, written down as GR_i , $i = \overline{1,5}$, bearing in mind that $(\vec{\mu}_i \cdot \nabla_\xi)(\vec{\mu}_j \cdot \nabla_\xi) \Xi_{r,\xi}(s) = \sum_{i=1}^5 GR_i$. By applying $s = 3/2$ in Equation A.11 we obtain the expression for the cross energy in case of the DDI, hence we should compute the terms: $\vec{\mu}_i \vec{\mu}_j \Psi_{r_{ij}}(3/2)$ and $(\vec{\mu}_i \cdot \nabla_\xi)(\vec{\mu}_j \cdot \nabla_\xi) \Xi_{r_{ij},\xi}(5/2)|_{\xi=0}$. We proceed the derivations by determining the first term

in Equation A.11, i.e., $\vec{\mu}_i \vec{\mu}_j \Psi_{\text{rij}}(3/2)$:

$$\begin{aligned} \Psi_r(3/2) &= \frac{4\sqrt{\pi}}{L_z^3 \Gamma(3/2)} \sum_{k=1}^{+\infty} \cos(k\eta^z) \left(\frac{\pi k L_z}{\rho} \right) K_1(k\eta^\rho) \\ &\quad + \frac{\sqrt{\pi}}{L_z^3 \Gamma(3/2)} \left(\frac{\rho}{L_z} \right)^{-2} \Gamma(1). \end{aligned} \quad (\text{A.73})$$

Taking into account the facts that $\Gamma(3/2) = \frac{\sqrt{\pi}}{2}$, $\Gamma(1) = 1$ [76],

$$\Rightarrow \Psi_r(3/2) = \frac{8\pi}{L_z^2 \rho} \sum_{k=1}^{+\infty} k \cos(k\eta^z) K_1(k\eta^\rho) + \frac{2}{L_z \rho^2}. \quad (\text{A.74})$$

We might write the scalar product $\vec{\mu}_i \cdot \vec{\mu}_j$ as:

$$(\vec{\mu}_i^\rho, \mu_i^z) \cdot (\vec{\mu}_j^\rho, \mu_j^z) = \vec{\mu}_i^\rho \cdot \vec{\mu}_j^\rho + \mu_i^z \mu_j^z. \quad (\text{A.75})$$

$$\begin{aligned} \Rightarrow \vec{\mu}_i \vec{\mu}_j \Psi_{\text{rij}}(3/2) &= (\vec{\mu}_i^\rho \cdot \vec{\mu}_j^\rho + \mu_i^z \mu_j^z) \frac{8\pi}{L_z^2 \rho} \sum_{k=1}^{+\infty} k \cos(k\eta^z) K_1(k\eta^\rho) \\ &\quad + (\vec{\mu}_i^\rho \cdot \vec{\mu}_j^\rho + \mu_i^z \mu_j^z) \frac{2}{L_z \rho^2}. \end{aligned} \quad (\text{A.76})$$

We have obtained the first term in Equation A.11 and now we proceed the derivations by obtaining the second term, i.e., $3(\vec{\mu}_i \cdot \nabla_\xi)(\vec{\mu}_j \cdot \nabla_\xi) \Xi_{\text{rij},\xi}(5/2)|_{\xi=0}$. By taking $s = 5/2$ and setting $\xi = 0$ we come up with:

Group 1 ($s = 5/2$) $|_{\xi=0}$

$$\begin{aligned} GR_1(s = 5/2)|_{\xi=0} &= -(\vec{\mu}_i^\rho \cdot \vec{\rho})(\vec{\mu}_j^\rho \cdot \vec{\rho}) \frac{2}{3L_z^3 \rho^2} \\ &\quad \times \sum_{k=-\infty}^{+\infty} e^{ik\eta^z} 4\pi^2 k^2 K_2(k\eta^\rho). \end{aligned} \quad (\text{A.77})$$

Group 2 ($s = 5/2$) $|_{\xi=0}$

$$\begin{aligned}
 GR_2(s = 5/2)|_{\xi=0} &= (-i) (\vec{\mu}_i^\rho \cdot \vec{\rho}) \mu_j^z \frac{2}{3L_z^3 \rho^2} \\
 &\times \sum_{k=-\infty}^{+\infty} e^{ik\eta^z} 4\pi k L_z K_2(k\eta^\rho). \quad (\text{A.78})
 \end{aligned}$$

Group 3 ($s = 5/2$) $|_{\xi=0}$

$$\begin{aligned}
 GR_3(s = 5/2)|_{\xi=0} &= (-i) (\vec{\mu}_i^\rho \cdot \vec{\rho}) \mu_j^z \frac{2}{3L_z^3 \rho^2} \\
 &\times \sum_{k=-\infty}^{+\infty} e^{ik\eta^z} 4\pi^2 k^2 \rho \frac{\partial K_2(k\eta^\rho)}{\partial(k\eta^\rho)}. \quad (\text{A.79})
 \end{aligned}$$

Group 4 ($s = 5/2$) $|_{\xi=0}$

$$\begin{aligned}
 GR_4(s = 5/2)|_{\xi=0} &= \mu_i^z \mu_j^z \frac{2}{3L_z^3 \rho^2} \\
 &\times \sum_{k=-\infty}^{+\infty} e^{ik\eta^z} \left\{ \frac{1}{2^{-1}} L_z^2 K_2(k\eta^\rho) \right. \\
 &+ 4L_z \pi k \rho \frac{\partial K_2(k\eta^\rho)}{\partial(k\eta^\rho)} \\
 &+ 4\rho \pi k L_z \frac{\partial K_2(k\eta^\rho)}{\partial(k\eta^\rho)} \\
 &\left. + 4\pi^2 k^2 \rho^2 \frac{\partial^2 K_2(k\eta^\rho)}{\partial(k\eta^\rho)^2} \right\}. \quad (\text{A.80})
 \end{aligned}$$

Group 5 ($s = 5/2$) $|_{\xi=0}$

$$\begin{aligned}
 GR_5(s = 5/2)|_{\xi=0} &= (-i) (\vec{\mu}_j^\rho \cdot \vec{\rho}) \mu_i^z \frac{2}{3L_z^3 \rho^2} \\
 &\times \sum_{k=-\infty}^{+\infty} e^{ik\eta^z} \left[\frac{1}{4^{-1}} \pi k L_z K_2(k\eta^\rho) \right. \\
 &\left. + 4\pi^2 k^2 \rho \frac{\partial K_2(k\eta^\rho)}{\partial(k\eta^\rho)} \right]. \quad (\text{A.81})
 \end{aligned}$$

We notice that in all GR_i terms a modified Bessel function of the second kind with index 2, i.e., $K_2(u)$ figures, together with its first and second derivative. In order to simplify the above mentioned terms, we express $K_2(u)$, as well as its derivatives, in

function of $K_0(u)$ and $K_1(u)$. Let us remind about the recurrence relations which apply to the modified Bessel function of the second kind [123]:

$$\frac{2\nu}{u}F_\nu(u) = F_{\nu-1}(u) - F_{\nu+1}(u), \quad (\text{A.82})$$

and to its derivative [123]:

$$\frac{\partial F_\nu(u)}{\partial u} = F_{\nu-1}(u) - \frac{\nu}{u}F_\nu(u) = F_{\nu+1}(u) + \frac{\nu}{u}F_\nu(u), \quad (\text{A.83})$$

where $F_\nu(u) = e^{i\pi\nu}K_\nu(u)$.

Utilizing the above mentioned relations and knowing that $F_0(u) = K_0(u)$, $F_1(u) = -K_1(u)$, $F_2(u) = K_2(u)$ we come up with the expression for $K_2(u)$ in function of $K_0(u)$ and $K_1(u)$:

$$K_2(u) = K_0(u) + \frac{2}{u}K_1(u). \quad (\text{A.84})$$

For its first derivative we get:

$$\frac{\partial K_2(u)}{\partial u} = -K_1(u) - \frac{2}{u}K_2(u), \quad (\text{A.85})$$

where, replacing $K_2(u)$ from Equation A.84, we get:

$$\frac{\partial K_2(u)}{\partial u} = -\frac{2}{u}K_0(u) - K_1(u) - \frac{4}{u^2}K_1(u). \quad (\text{A.86})$$

The second derivative $\frac{\partial^2 K_2(u)}{\partial u^2}$ is computed straightforward by taking the first derivative of Equation A.86:

$$\begin{aligned} \frac{\partial^2 K_2(u)}{\partial u^2} &= -2 \left(-\frac{K_0(u)}{u^2} + \frac{1}{u} \frac{\partial K_0(u)}{\partial u} \right) - \frac{\partial K_1(u)}{\partial u} \\ &\quad - 4 \left(-\frac{2}{u^3}K_1(u) + \frac{1}{u^2} \frac{\partial K_1(u)}{\partial u} \right). \end{aligned} \quad (\text{A.87})$$

From the recurrence relation given in Equation A.83 we obtain:

$$\frac{\partial K_0(u)}{\partial u} = -K_1(u), \quad \frac{\partial K_1(u)}{\partial u} = -K_2(u) + \frac{1}{u}K_1(u), \quad (\text{A.88})$$

which together with Equation A.84 leads to the final expression for the second derivative $\frac{\partial^2 K_2(u)}{\partial u^2}$:

$$\frac{\partial^2 K_2(u)}{\partial u^2} = K_0(u) + \frac{6}{u^2} K_0(u) + \frac{3}{u} K_1(u) + \frac{12}{u^3} K_1(u). \quad (\text{A.89})$$

Now we replace $K_2(u)$, $\frac{\partial K_2(u)}{\partial u}$, $\frac{\partial^2 K_2(u)}{\partial u^2}$ (knowing that $u = k\eta^\rho$) in Equations A.77 to A.81, coming up with:

Group 1 ($s = 5/2$) $|_{\xi=0}$

$$\begin{aligned} GR_1(s = 5/2)|_{\xi=0} &= -(\vec{\mu}_i^\rho \cdot \vec{\rho})(\vec{\mu}_j^\rho \cdot \vec{\rho}) \frac{2}{3L_z^3 \rho^2} \\ &\times \sum_{k=-\infty}^{+\infty} e^{ik\eta^z} 4\pi^2 k^2 \left(K_0(k\eta^\rho) + \frac{2}{k\eta^\rho} K_1(k\eta^\rho) \right), \end{aligned} \quad (\text{A.90})$$

$$\begin{aligned} \Rightarrow GR_1(s = 5/2)|_{\xi=0} &= -(\vec{\mu}_i^\rho \cdot \vec{\rho})(\vec{\mu}_j^\rho \cdot \vec{\rho}) \left[\frac{8\pi^2}{3L_z^3 \rho^2} \times \sum_{k=-\infty}^{+\infty} k^2 e^{ik\eta^z} K_0(k\eta^\rho) \right. \\ &\left. + \frac{8\pi}{3L_z^2 \rho^3} \times \sum_{k=-\infty}^{+\infty} k e^{ik\eta^z} K_1(k\eta^\rho) \right]. \end{aligned} \quad (\text{A.91})$$

Group 2 ($s = 5/2$) $|_{\xi=0}$

$$\begin{aligned} GR_2(s = 5/2)|_{\xi=0} &= (-i)(\vec{\mu}_i^\rho \cdot \vec{\rho}) \mu_j^z \frac{2}{3L_z^3 \rho^2} \\ &\times \sum_{k=-\infty}^{+\infty} e^{ik\eta^z} 4\pi k L_z \left(K_0(k\eta^\rho) + \frac{2}{k\eta^\rho} K_1(k\eta^\rho) \right), \end{aligned} \quad (\text{A.92})$$

$$\begin{aligned} \Rightarrow GR_2(s = 5/2)|_{\xi=0} &= (-i)(\vec{\mu}_i^\rho \cdot \vec{\rho}) \mu_j^z \left[\frac{8\pi}{3L_z^2 \rho^2} \times \sum_{k=-\infty}^{+\infty} k e^{ik\eta^z} K_0(k\eta^\rho) \right. \\ &\left. + \frac{8}{3L_z \rho^3} \times \sum_{k=-\infty}^{+\infty} e^{ik\eta^z} K_1(k\eta^\rho) \right]. \end{aligned} \quad (\text{A.93})$$

Group 3 ($s = 5/2, \xi = 0$)

$$GR_3(s = 5/2)|_{\xi=0} = (-i)(\vec{\mu}_i^{\lambda\rho} \cdot \vec{\rho}) \mu_j^z \frac{2}{3L_z^3 \rho^2} \times \sum_{k=-\infty}^{+\infty} e^{ik\eta^z} 4\pi^2 k^2 \left(-\frac{2}{k\eta^\rho} K_0(k\eta^\rho) - K_1(k\eta^\rho) - \frac{4}{(k\eta^\rho)^2} K_1(k\eta^\rho) \right) \quad (\text{A.94})$$

$$\begin{aligned} \Rightarrow GR_3(s = 5/2)|_{\xi=0} &= (-i)(\vec{\mu}_i^{\lambda\rho} \cdot \vec{\rho}) \mu_j^z \left[-\frac{8\pi}{3L_z^2 \rho^2} \times \sum_{k=-\infty}^{+\infty} k e^{ik\eta^z} K_0(k\eta^\rho) \right. \\ &\quad - \frac{8\pi^2}{3L_z^3 \rho} \times \sum_{k=-\infty}^{+\infty} k^2 e^{ik\eta^z} K_1(k\eta^\rho) \\ &\quad \left. - \frac{8}{3L_z \rho^3} \times \sum_{k=-\infty}^{+\infty} e^{ik\eta^z} K_1(k\eta^\rho) \right]. \quad (\text{A.95}) \end{aligned}$$

Group 4 ($s = 5/2$) $|_{\xi=0}$

$$GR_4(s = 5/2)|_{\xi=0} = \mu_i^z \mu_j^z \frac{2}{3L_z^3 \rho^2} \times \sum_{k=-\infty}^{+\infty} e^{ik\eta^z} \times [2L_z^2 T_1 + 4L_z \pi k \rho T_2 + 4\rho \pi k L_z T_3 + 4\pi^2 k^2 \rho^2 T_4] \quad (\text{A.96})$$

where the terms T_1, T_2, T_3, T_4 are defined as:

$$T_1 = K_0(k\eta^\rho) + \frac{2}{k\eta^\rho} K_1(k\eta^\rho), \quad (\text{A.97})$$

$$T_2 = -\frac{2}{k\eta^\rho} K_0(k\eta^\rho) - K_1(k\eta^\rho) - \frac{4}{(k\eta^\rho)^2} K_1(k\eta^\rho), \quad (\text{A.98})$$

$$T_3 = -\frac{2}{k\eta^\rho} K_0(k\eta^\rho) - K_1(k\eta^\rho) - \frac{4}{(k\eta^\rho)^2} K_1(k\eta^\rho), \quad (\text{A.99})$$

$$T_4 = K_0(k\eta^\rho) + \frac{6}{(k\eta^\rho)^2} K_0(k\eta^\rho) + \frac{3}{k\eta^\rho} K_1(k\eta^\rho) + \frac{12}{(k\eta^\rho)^3} K_1(k\eta^\rho), \quad (\text{A.100})$$

respectively.

$$\begin{aligned} \Rightarrow GR_4(s = 5/2)|_{\xi=0} &= \mu_i^z \mu_j^z \left[-\frac{4\pi}{3L_z^2 \rho} \times \sum_{k=-\infty}^{+\infty} k e^{ik\eta^z} K_1(k\eta^\rho) \right. \\ &\quad \left. + \frac{8\pi^2}{3L_z^3} \times \sum_{k=-\infty}^{+\infty} k^2 e^{ik\eta^z} K_0(k\eta^\rho) \right]. \end{aligned} \quad (\text{A.101})$$

Group 5 ($s = 5/2$) $|_{\xi=0}$

$$\begin{aligned} GR_5(s = 5/2)|_{\xi=0} &= (-i) (\vec{\mu}_j^\rho \cdot \vec{\rho}) \mu_i^z \frac{2}{3L_z^3 \rho^2} \\ &\quad \times \sum_{k=-\infty}^{+\infty} e^{ik\eta^z} [4\pi k L_z R_1 + 4\pi^2 k^2 \rho R_2], \end{aligned} \quad (\text{A.102})$$

where the terms R_1, R_2 are defined as:

$$R_1 = K_0(k\eta^\rho) + \frac{2}{k\eta^\rho} K_1(k\eta^\rho), \quad (\text{A.103})$$

$$R_2 = -\frac{2}{k\eta^\rho} K_0(k\eta^\rho) - K_1(k\eta^\rho) - \frac{4}{(k\eta^\rho)^2} K_1(k\eta^\rho), \quad (\text{A.104})$$

respectively.

$$\Rightarrow GR_5(s = 5/2)|_{\xi=0} = (-i) (\vec{\mu}_j^\rho \cdot \vec{\rho}) \mu_i^z \left[-\frac{8\pi^2}{3L_z^3 \rho} \sum_{k=-\infty}^{+\infty} k^2 e^{ik\eta^z} K_1(k\eta^\rho) \right]. \quad (\text{A.105})$$

We can furthermore simplify the Equations A.90 to A.105 applying the relations:

$$e^{ik\eta^z} + e^{-ik\eta^z} = 2 \cos(k\eta^z), \quad e^{ik\eta^z} - e^{-ik\eta^z} = 2i \sin(k\eta^z), \quad (\text{A.106})$$

that allow us to switch from the $\sum_{k=-\infty}^{+\infty}$ summation to the $\sum_{k=1}^{+\infty}$ summation, where the case $k = 0$ should be considered separately. Accordingly, let us resolve the $k = 0$ case first:

$$(\vec{\mu}_i \cdot \nabla_\xi) (\vec{\mu}_j \cdot \nabla_\xi) \Xi_{r_{ij}, \xi}(5/2)|_{\xi=0, k=0} = \sum_{i=1}^5 GR_i(s = 5/2)|_{\xi=0, k=0}. \quad (\text{A.107})$$

Based on the next relations [123]:

$$u^2 K_1(u) \rightarrow 0, u^2 K_0(u) \rightarrow 0, u K_1(u) \rightarrow 1, \quad (\text{A.108})$$

which are valid when $k \rightarrow 0$, setting that $u = k\eta^\rho$ we obtain that:

$$\begin{aligned} \sum_{i=1}^5 GR_i(s=5/2)|_{\xi=0, k=0} &= -\frac{8\pi}{3L_z^2 \rho^3} \frac{L_z}{2\pi\rho} (\vec{\mu}_i^\rho \cdot \vec{\rho}) (\vec{\mu}_j^\rho \cdot \vec{\rho}) \\ &\quad - \frac{4\pi}{3L_z^2 \rho} \frac{L_z}{2\pi\rho} \mu_i^z \mu_j^z, \end{aligned} \quad (\text{A.109})$$

$$\Rightarrow \sum_{i=1}^5 GR_i(s=5/2)|_{\xi=0, k=0} = -\frac{4}{3L_z \rho^4} (\vec{\mu}_i^\rho \cdot \vec{\rho}) (\vec{\mu}_j^\rho \cdot \vec{\rho}) - \frac{2}{3L_z \rho^2} \mu_i^z \mu_j^z. \quad (\text{A.110})$$

Now we resolve the $k \neq 0$ case:

$$(\vec{\mu}_i^\rho \cdot \nabla_\xi)(\vec{\mu}_j^\rho \cdot \nabla_\xi) \Xi_{r_{ij}, \xi}(5/2)|_{\xi=0, k \neq 0} = \sum_{i=1}^5 GR_i(s=5/2)|_{\xi=0, k \neq 0}. \quad (\text{A.111})$$

Let us modify the expressions for $GR_i(s=5/2)|_{\xi=0}$ following the Equation A.106:

Group 1 ($s=5/2$) $|_{\xi=0, k \neq 0}$

$$\begin{aligned} GR_1(s=5/2)|_{\xi=0, k \neq 0} &= -(\vec{\mu}_i^\rho \cdot \vec{\rho}) (\vec{\mu}_j^\rho \cdot \vec{\rho}) \left[\frac{16\pi^2}{3L_z^3 \rho^2} \times \sum_{k=1}^{+\infty} k^2 \cos(k\eta^z) K_0(k\eta^\rho) \right. \\ &\quad \left. + \frac{16\pi}{3L_z^2 \rho^3} \times \sum_{k=1}^{+\infty} k \cos(k\eta^z) K_1(k\eta^\rho) \right]. \end{aligned} \quad (\text{A.112})$$

Group 2 ($s=5/2$) $|_{\xi=0, k \neq 0}$

$$\begin{aligned} GR_2(s=5/2)|_{\xi=0, k \neq 0} &= (\vec{\mu}_i^\rho \cdot \vec{\rho}) \mu_j^z \left[\frac{16\pi}{3L_z^2 \rho^2} \times \sum_{k=1}^{+\infty} k \sin(k\eta^z) K_0(k\eta^\rho) \right. \\ &\quad \left. + \frac{16}{3L_z \rho^3} \times \sum_{k=1}^{+\infty} \sin(k\eta^z) K_1(k\eta^\rho) \right]. \end{aligned} \quad (\text{A.113})$$

Group 3 ($s = 5/2$) $|_{\xi=0, k \neq 0}$

$$\begin{aligned}
 GR_3(s = 5/2) |_{\xi=0, k \neq 0} &= (\vec{\mu}_i^\rho \cdot \vec{\rho}) \mu_j^z \left[-\frac{16\pi}{3L_z^2 \rho^2} \times \sum_{k=1}^{+\infty} k \sin(k\eta^z) K_0(k\eta^\rho) \right. \\
 &\quad - \frac{16\pi^2}{3L_z^3 \rho} \times \sum_{k=1}^{+\infty} k^2 \sin(k\eta^z) K_1(k\eta^\rho) \\
 &\quad \left. - \frac{16}{3L_z \rho^3} \times \sum_{k=1}^{+\infty} \sin(k\eta^z) K_1(k\eta^\rho) \right]. \quad (\text{A.114})
 \end{aligned}$$

Group 4 ($s = 5/2$) $|_{\xi=0, k \neq 0}$

$$\begin{aligned}
 GR_4(s = 5/2) |_{\xi=0, k \neq 0} &= \mu_i^z \mu_j^z \left[-\frac{8\pi}{3L_z^2 \rho} \times \sum_{k=1}^{+\infty} k \cos(k\eta^z) K_1(k\eta^\rho) \right. \\
 &\quad \left. + \frac{16\pi^2}{3L_z^3} \times \sum_{k=1}^{+\infty} k^2 \cos(k\eta^z) K_0(k\eta^\rho) \right]. \quad (\text{A.115})
 \end{aligned}$$

Group 5 ($s = 5/2$) $|_{\xi=0, k \neq 0}$

$$GR_5(s = 5/2) |_{\xi=0, k \neq 0} = (\vec{\mu}_j^\rho \cdot \vec{\rho}) \mu_i^z \left[-\frac{16\pi^2}{3L_z^3 \rho} \sum_{k=1}^{+\infty} k^2 \sin(k\eta^z) K_1(k\eta^\rho) \right]. \quad (\text{A.116})$$

We can now compute the summation from Equation A.111:

$$\begin{aligned}
 \sum_{i=1}^5 GR_i(s = 5/2) |_{\xi=0, k \neq 0} &= -\frac{8\pi}{3L_z^2} \left[\frac{2(\vec{\mu}_i^\rho \cdot \vec{\rho}_{ij})(\vec{\mu}_j^\rho \cdot \vec{\rho}_{ij})}{\rho_{ij}^3} + \frac{\mu_i^z \mu_j^z}{\rho_{ij}} \right] \\
 &\quad \times \sum_{k=1}^{+\infty} k \cos(k\eta_{ij}^z) K_1(k\eta_{ij}^\rho) \\
 &\quad - \frac{16\pi^2}{3L_z^3} \left[\frac{(\vec{\mu}_i^\rho \cdot \vec{\rho}_{ij}) \mu_j^z + (\vec{\mu}_j^\rho \cdot \vec{\rho}_{ij}) \mu_i^z}{\rho_{ij}} \right] \\
 &\quad \times \sum_{k=1}^{+\infty} k^2 \sin(k\eta_{ij}^z) K_1(k\eta_{ij}^\rho) \\
 &\quad - \frac{16\pi^2}{3L_z^3} \left[\frac{(\vec{\mu}_i^\rho \cdot \vec{\rho}_{ij})(\vec{\mu}_j^\rho \cdot \vec{\rho}_{ij})}{\rho_{ij}^2} - \mu_i^z \mu_j^z \right] \\
 &\quad \times \sum_{k=1}^{+\infty} k^2 \cos(k\eta_{ij}^z) K_0(k\eta_{ij}^\rho). \quad (\text{A.117})
 \end{aligned}$$

Adding up the result from Equation A.110 for $k = 0$ to the result from Equa-

tion A.117 for $k \neq 0$ we obtain:

$$\begin{aligned}
 (\vec{\mu}_i \cdot \nabla_\xi)(\vec{\mu}_j \cdot \nabla_\xi) \Xi_{r_{ij}, \xi}(5/2)|_{\xi=0} &= -\frac{8\pi}{3L_z^2} \left[\frac{2(\vec{\mu}_i^\rho \cdot \vec{\rho}_{ij}) (\vec{\mu}_j^\rho \cdot \vec{\rho}_{ij})}{\rho_{ij}^3} + \frac{\mu_i^z \mu_j^z}{\rho_{ij}} \right] \\
 &\times \sum_{k=1}^{+\infty} k \cos(k\eta_{ij}^z) K_1(k\eta_{ij}^\rho) \\
 &- \frac{16\pi^2}{3L_z^3} \left[\frac{(\vec{\mu}_i^\rho \cdot \vec{\rho}_{ij}) \mu_j^z + (\vec{\mu}_j^\rho \cdot \vec{\rho}_{ij}) \mu_i^z}{\rho_{ij}} \right] \\
 &\times \sum_{k=1}^{+\infty} k^2 \sin(k\eta_{ij}^z) K_1(k\eta_{ij}^\rho) \\
 &- \frac{16\pi^2}{3L_z^3} \left[\frac{(\vec{\mu}_i^\rho \cdot \vec{\rho}_{ij}) (\vec{\mu}_j^\rho \cdot \vec{\rho}_{ij})}{\rho_{ij}^2} - \mu_i^z \mu_j^z \right] \\
 &\times \sum_{k=1}^{+\infty} k^2 \cos(k\eta_{ij}^z) K_0(k\eta_{ij}^\rho) - \frac{2}{3L_z} \\
 &\times \left[\frac{2(\vec{\mu}_i^\rho \cdot \vec{\rho}_{ij}) (\vec{\mu}_j^\rho \cdot \vec{\rho}_{ij})}{\rho_{ij}^4} + \frac{\mu_i^z \mu_j^z}{\rho_{ij}^2} \right]. \quad (\text{A.118})
 \end{aligned}$$

At this point, let us rewrite the expression defining the cross energy:

$$E_{\text{cross}} = \frac{1}{2} \sum_{i=1}^N \sum_{j=1, j \neq i}^N \left[\vec{\mu}_i \vec{\mu}_j \Psi_{r_{ij}}(3/2) + 3(\vec{\mu}_i \cdot \nabla_\xi)(\vec{\mu}_j \cdot \nabla_\xi) \Xi_{r_{ij}, \xi}(5/2)|_{\xi=0} \right]. \quad (\text{A.119})$$

From Equation A.76 we take the term $\vec{\mu}_i \vec{\mu}_j \Psi_{r_{ij}}(3/2)$ and from Equation A.118 we take the term $(\vec{\mu}_i \cdot \nabla_\xi)(\vec{\mu}_j \cdot \nabla_\xi) \Xi_{r_{ij}, \xi}(5/2)|_{\xi=0}$ and multiply it by 3, which leads to

the final form of the cross energy:

$$\begin{aligned}
 E_{\text{cross}} = & \frac{1}{2} \sum_{i=1}^N \sum_{j=1, j \neq i}^N \left\{ -\frac{8\pi}{L_z^2} \left[\frac{2(\vec{\mu}_i^\rho \cdot \vec{\rho}_{ij}) (\vec{\mu}_j^\rho \cdot \vec{\rho}_{ij})}{\rho_{ij}^3} - \frac{(\vec{\mu}_i^\rho \cdot \vec{\mu}_j^\rho)}{\rho_{ij}} \right] \right. \\
 & \times \sum_{k=1}^{+\infty} k \cos(k\eta_{ij}^z) K_1(k\eta_{ij}^\rho) \\
 & - \frac{16\pi^2}{L_z^3} \left[\frac{(\vec{\mu}_i^\rho \cdot \vec{\rho}_{ij}) \mu_j^z + (\vec{\mu}_j^\rho \cdot \vec{\rho}_{ij}) \mu_i^z}{\rho_{ij}} \right] \\
 & \times \sum_{k=1}^{+\infty} k^2 \sin(k\eta_{ij}^z) K_1(k\eta_{ij}^\rho) \\
 & - \frac{16\pi^2}{L_z^3} \left[\frac{(\vec{\mu}_i^\rho \cdot \vec{\rho}_{ij}) (\vec{\mu}_j^\rho \cdot \vec{\rho}_{ij})}{\rho_{ij}^2} - \mu_i^z \mu_j^z \right] \\
 & \times \sum_{k=1}^{+\infty} k^2 \cos(k\eta_{ij}^z) K_0(k\eta_{ij}^\rho) \\
 & \left. - \frac{2}{L_z} \left[\frac{2(\vec{\mu}_i^\rho \cdot \vec{\rho}_{ij}) (\vec{\mu}_j^\rho \cdot \vec{\rho}_{ij})}{\rho_{ij}^4} - \frac{(\vec{\mu}_i^\rho \cdot \vec{\mu}_j^\rho)}{\rho_{ij}^2} \right] \right\}. \quad (\text{A.120})
 \end{aligned}$$

We should note that the expressions for $\Psi_r(s)$, $\Xi_{r,\xi}(s)$ and consequently for E_{cross} are undefined in case $\vec{\rho} = 0$. Hence, the previously written expressions are valid under the condition $\vec{\rho} \neq 0$. For the special case $\vec{\rho} = 0$, i.e., when two dipoles have the same x and y coordinate (the position vector connecting them is parallel to the z axis), the next equation for $\Psi_r(s = 3/2)$ applies [89]:

$$\Psi_r(3/2)|_{\vec{\rho}=0} = -\frac{1}{L_z^3} \left[\Psi'' \left(\frac{|z|}{L_z} \right) + \pi^3 \cos \left(\frac{\pi|z|}{L_z} \right) \sin^{-3} \left(\frac{\pi|z|}{L_z} \right) \right], \quad (\text{A.121})$$

where Ψ'' is the tetra-gamma function [123]. Using Equations A.118 and A.121 we obtain the cross energy in case $\vec{\rho}_{ij} = 0$ as:

$$E_{\text{cross}}|_{\vec{\rho}_{ij}=0} = \frac{1}{2} \sum_{i=1}^N \sum_{j=1, j \neq i}^N \left\{ T_p \left[\Psi'' \left(\frac{|z_{ij}|}{L_z} \right) + \pi^3 \cos \left(\frac{\pi|z_{ij}|}{L_z} \right) \sin^{-3} \left(\frac{\pi|z_{ij}|}{L_z} \right) \right] \right\}, \quad (\text{A.122})$$

where the term T_p is defined as:

$$T_p = -\frac{(\vec{\mu}_i^\rho \cdot \vec{\mu}_j^\rho) - 2\mu_i^z \mu_j^z}{L_z^3}. \quad (\text{A.123})$$

Appendix B Conjugate gradient method

The conjugate gradient (*CG*) method represents a general method for minimizing function $f(\vec{x})$, where f can be any function of argument \vec{x} in N -dimensional space [124]. In our case, we want to minimize the potential energy of atoms in the system, hence $f = V$, where the independent variable \vec{x} are the positions of our atoms $\vec{r}_i, i = 1, \dots, N$. The parameter space over which the minimization is realized is $3N$ -dimensional, since it stands that:

$$\vec{r} = (r_{1x}, r_{1y}, r_{1z}, r_{2x}, r_{2y}, r_{2z}, r_{3x}, r_{3y}, r_{3z}, \dots, r_{Nx}, r_{Ny}, r_{Nz}). \quad (\text{B.1})$$

We can state that we are interested in minimization of the function $V(\vec{r})$. In the *CG* method, the gradient of the function, which is in our case the force, since it stands $\vec{F} = -\nabla V$, is used for finding the minimum of the function. The gradient determines in which direction the function changes the most rapidly. Bearing this in mind, we can come up with a natural, but not very efficient way to minimize the energy, which is to always move in the direction of the negative gradient, since negative gradient means lowering the function value. This method is known as *steepest descent method* and for *MD* systems its algorithm can be defined as [125]:

Step(0): start from the point \vec{r}_0 setting up $j = 0$

Step(1): calculate $V_j(\vec{r}_j)$ and $\vec{F}_j = -\nabla V_j(\vec{r}_j)$

Step(2): if $V_{j-1} - V_j < \epsilon$ (where ϵ is the chosen convergence tolerance, usually at the order of 10^{-6}) then end the algorithm

Step(3): minimize $V(\vec{r}_j + \alpha \vec{F}_j)$ by varying the scalar quantity α

Step(4): update $\vec{r}_{j+1} = \vec{r}_j + \alpha \vec{F}_j; j = j + 1$

Step(5): return to the step (1)

The line minimization in step (3) is a one dimensional operation in which the min-

imum of a function is looked for by moving in a defined direction $\alpha\vec{F}_j$. Let us now explain how does the line minimization work. The line minimization is a straightforward operation which is carried out in two steps [124]:

- (i) confirm that there is a minimum and bracket it
- (ii) search for that minimum with a given accuracy

Step (i) is easy to conduct: starting from a point \vec{r} and known direction \vec{F} , we move forward along some direction $\beta\vec{F}$. If the following conditions are met (for the illustration check Figure B.1):

$$V\left(\vec{r} + \frac{\beta\vec{F}}{2}\right) < V(\vec{r}), V\left(\vec{r} + \frac{\beta\vec{F}}{2}\right) < V\left(\vec{r} + \beta\vec{F}\right), V(\vec{r}) < V\left(\vec{r} + \beta\vec{F}\right) \quad (\text{B.2})$$

then the minimum is bracketed with these three points:

$$\left\{ V(\vec{r}), V\left(\vec{r} + \frac{\beta\vec{F}}{2}\right), V\left(\vec{r} + \beta\vec{F}\right) \right\}. \quad (\text{B.3})$$

In case the above mentioned conditions are not met, we increase β and try again until we meet the conditions.

As the step (i) of bracketing the minimum is completed, we move on to the step (ii) of searching for that minimum within the given accuracy. One way of doing this is applying bisection. However, it turns out that it is better to apply golden section rule, which means that the new guess for the minimum is distant from either ends $\left(\frac{1+\sqrt{5}}{2} - 1\right) \cdot 100\% = 61.803\%$ of the distance between the ends, i.e., points (1) and (2) from Figure B.1 are the ends in the first iteration of the procedure. Later on, the bracketing narrows around the minimum with the goal of converging to it. The golden section rule tells us how should we narrow down the bracketing interval, i.e., the distance between the ends. Besides the line minimization which includes bracketing and golden section rule search for the minimum, there is another method which is called *inverse parabolic interpolation*. The name comes from the fact that a parabola is fitted through the points $\{a, b, c\}$ which correspond to the points (1), (2), (3) from Figure B.1. Our guess for the minimum of the curve we are looking for,

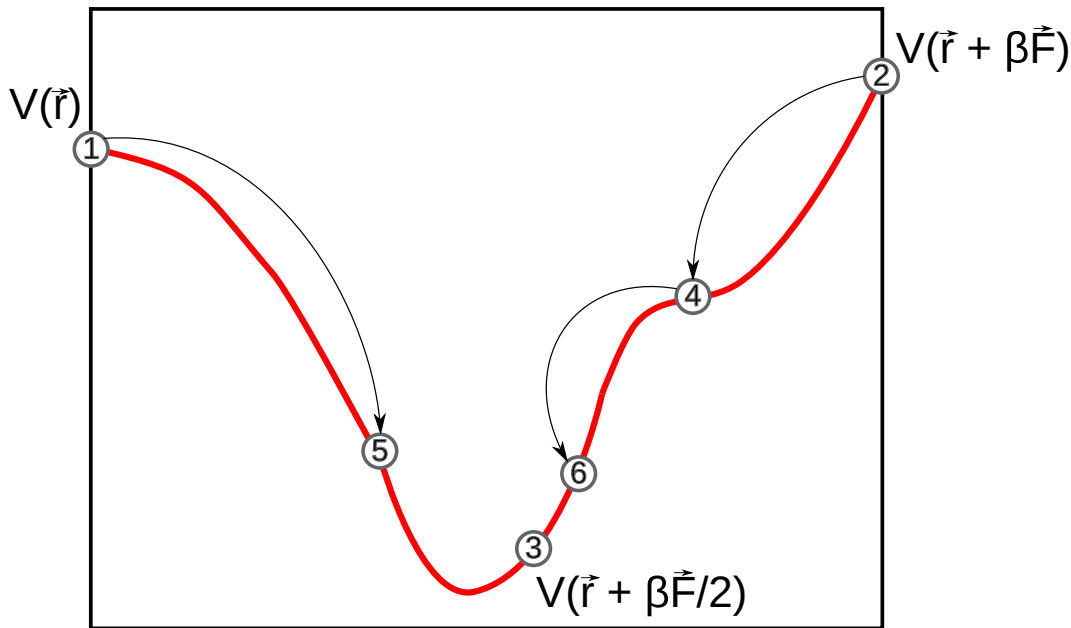


Figure B.1: Bracketing a minimum, points (1), (2) and (3) are the initial bracketing points, jumps to the points (4), (5) and (6), respectively, illustrate the process of line minimization and convergence towards the minimum of the given red curve.

is the minimum of the fitting parabola x , which is computed by the formula [124]:

$$x = b - \frac{1}{2} \frac{(b-a)^2 [V(b) - V(c)] - (b-c)^2 [V(b) - V(a)]}{(b-a)[V(b) - V(c)] - (b-c)[V(b) - V(a)]}. \quad (\text{B.4})$$

After the current parabola is fitted, we replace one of the ending points a or c by point x (this depends on which side of point b is current x) and the inverse parabolic interpolation is repeated. This process of inverse parabolic interpolation continues until the minimum is found with the given accuracy. An advanced method of line minimization built-up upon the previously presented ones is the Brent's method [124]. It employs the inverse parabolic interpolation (IPI) and changes to the golden section in case that there are problems with IPI. We have explained the basis of the steepest descent (SD) approach and the Brent's line minimization. A further step in advancing the minimization algorithms would be their combination. However, such a combined minimization method is not too efficient in many-dimensional parameter spaces because there is a high chance of SD falling into a zig-zag trajectory, which means that the convergence towards the minimum would be very inefficient. A question rises: how can we eliminate this obstacle of the steepest descent method

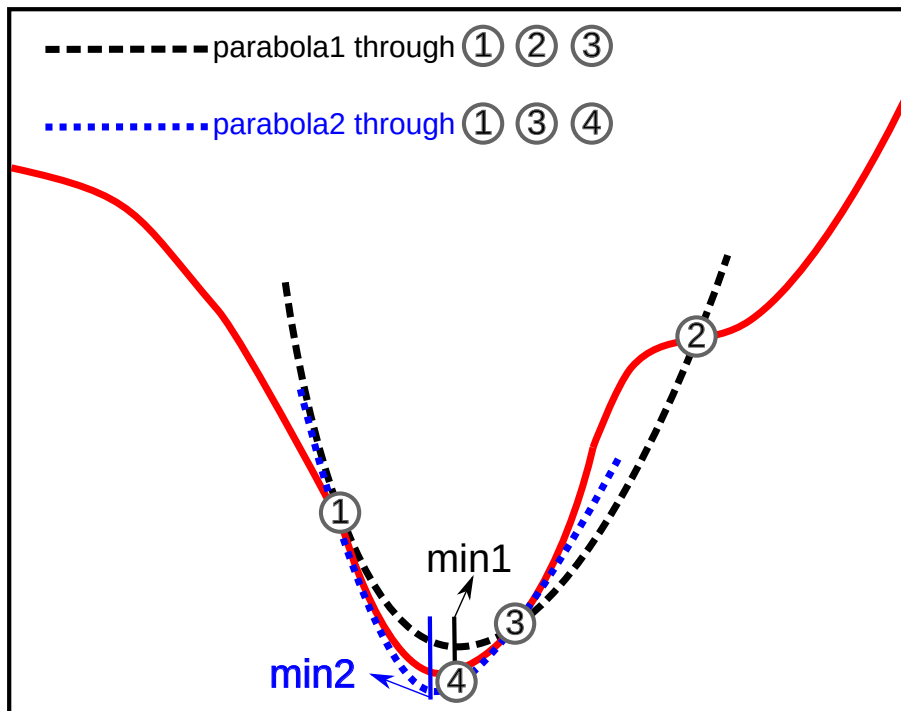


Figure B.2: Inverse parabolic interpolation through the points (1), (2) and (3) via parabola1 leads to the point (4) as that parabola's minimum, noted as *min1*. In the next iteration inverse parabolic interpolation through the points (1), (3) and (4) via parabola2 leads to that parabola's minimum, noted as *min2*, which is closer to the minimum of the red curve which we are looking for. Further inverse parabolic interpolations lead to the convergence towards the minimum of the given red curve.

and achieve efficient convergence? The solution comes with the conjugate gradient (*CG*) method where a new direction, known as *conjugate* direction, is chosen and it depends on the previous direction, hence the zig-zag trajectory can be avoided. Let us explain what does it mean to have two directions that are conjugate. Let us take an arbitrary function $f(\vec{x})$ where the argument \vec{x} is N -dimensional and write down its Taylor series around a certain point \vec{T} [125]:

$$f(\vec{x}) = f(\vec{T}) + \sum_i \frac{\partial f}{\partial x_i} x_i + \frac{1}{2} \sum_{i,j} \frac{\partial^2 f}{\partial x_i \partial x_j} x_i x_j + \dots \approx c - \vec{b} \cdot \vec{x} + \frac{1}{2} \vec{x} \cdot \mathbf{A} \cdot \vec{x}, \quad (\text{B.5})$$

where the scalar c is defined as $c = f(\vec{T})$, the vector \vec{b} is defined as $\vec{b} = -\nabla f|_T$ and the matrix \mathbf{A} is defined as $\mathbf{A} = \frac{\partial^2 f}{\partial x_i \partial x_j}|_T$ and it is known as the *Hessian matrix*. Let us label the previous direction of movement as \vec{u} and the gradient as \vec{g} . We want to

determine the next direction of movement \vec{v} . Bearing in mind that the gradient and the previous direction of movement in a current point are orthogonal, i.e., $\vec{g} \cdot \vec{u} = 0$ and that we want, after the next step, new gradient to be orthogonal to the previous direction of movement, i.e., $\vec{g}^* \cdot \vec{u} = 0$, we come up with the condition:

$$\vec{u} \cdot \delta(\nabla f) = 0 \tag{B.6}$$

which means that the change of the gradient labeled as $\delta(\nabla f)$ should be also perpendicular to the previous direction of movement *vecu*. We start the derivation from the quadratic form of the function f , which is given as: $f(\vec{x}) = c - \vec{b} \cdot \vec{x} + \frac{1}{2} \vec{x} \cdot \mathbf{A} \cdot \vec{x}$. The gradient of the function f derived from its quadratic form is:

$$\nabla f = \mathbf{A} \cdot \vec{x} - \vec{b}. \tag{B.7}$$

Now from the Equation B.7 we calculate the change of the gradient ∇f along a certain distance labeled as $\delta\vec{x}$ is:

$$\delta(\nabla f) = \mathbf{A} \cdot \delta\vec{x} \tag{B.8}$$

and now by setting that $\delta\vec{x}$ corresponds to the new direction of movement \vec{v} , i.e., $\delta\vec{x} = \vec{v}$, we return to Equation B.6:

$$\vec{u} \cdot \delta(\nabla f) = \vec{u} \cdot \mathbf{A} \cdot \vec{v} = 0. \tag{B.9}$$

Summing up the previous discussion, if the relation $\vec{u} \cdot \mathbf{A} \cdot \vec{v} = 0$ holds, we say that the directions \vec{u} and \vec{v} are conjugate. The main task of the *CG* method is the computation of the new direction along which to move, hence the two vectors \vec{g} and \vec{h} are used for the realization of this task. At the start, there are arbitrary initial vectors \vec{g}_0 and $\vec{h}_0 = \vec{g}_0$. The next equations define how are they iterated ($i = 0, 1, 2, 3, \dots$) [124]:

$$\vec{g}_{i+1} = \vec{g}_i - \lambda_i (\mathbf{A} \cdot \vec{h}_i), \vec{h}_{i+1} = \vec{g}_{i+1} + \gamma_i \vec{h}_i. \tag{B.10}$$

In Equation B.10 scalars λ_i and γ_i are figuring, they are defined as [124]:

$$\lambda_i = \frac{\vec{g}_i \cdot \vec{g}_i}{\vec{h}_i \cdot \mathbf{A} \cdot \vec{h}_i} = \frac{\vec{g}_i \cdot \vec{h}_i}{\vec{h}_i \cdot \mathbf{A} \cdot \vec{h}_i} \quad (\text{B.11})$$

and

$$\gamma_i = \frac{\vec{g}_{i+1} \cdot \vec{g}_{i+1}}{\vec{g}_i \cdot \vec{g}_i}. \quad (\text{B.12})$$

Those vectors \vec{g} and \vec{h} fulfill the orthogonality and conjugation conditions [124]:

$$\vec{g}_i \cdot \vec{g}_j = 0, \vec{h}_i \cdot \mathbf{A} \cdot \vec{h}_j = 0, \vec{g}_i \cdot \vec{h}_j = 0 \quad (\text{B.13})$$

From Equations B.10, B.11, B.12 and B.13, by knowing the Hessian matrix \mathbf{A} , we are able to determine successive conjugate directions \vec{h}_i along which the line minimization is conducted. With n such steps, where n is the dimensionality of the problem, we can find the minimum of the quadratic form $f\vec{x}$. However, since the dimensions of the Hessian matrix \mathbf{A} are $3N \times 3N$, the dimensionality of the problem is $n = 3N$ in case of energy minimization of an MD system with N particles. It is highly inefficient to operate with the Hessian matrix in case of MD systems since the number of particles in the system N can be up to 10^6 . Hopefully, there is a theorem which solves the problem by circumventing the usage of the Hessian matrix \mathbf{A} . It claims that if we minimize the function f in the direction \vec{h} to a point \vec{x}_{i+1} , the new gradient can be calculated as [124]:

$$\vec{g}_{i+1} = -\nabla f(\vec{x}_{i+1}) \quad (\text{B.14})$$

In that case, this vector \vec{g}_{i+1} would be the same as if it had been determined via Equation B.10. More details and the proof of this theorem can be found in the chapter 10 "Minimization or maximization of functions" of the book [124]. Based on the previously presented equations we can come up with a sketch of the CG algorithm for the energy minimization of an MD system consisting of N particles [125]:

Step(0): start from the point \vec{r}_0 setting up $j = 0$, $V_0 = V(\vec{r}_0)$, $\vec{q}_0 = -\nabla V(\vec{r}_0)$,
 $\vec{g}_0 = \vec{h}_0 = \vec{q}_0$

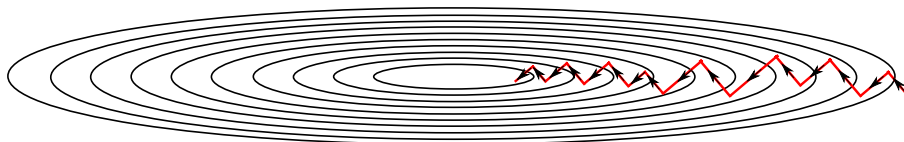


Figure B.3: Steepest descent method can easily fall into a zig-zag trajectory.

Step(1): minimize $V(\vec{r}_j + \alpha \vec{q}_j)$ with respect to the scalar α , after that update $\vec{r}_{j+1} = \vec{r}_j + \alpha \vec{q}_j$ and compute $V(j+1) = V(\vec{r}_{j+1})$

Step(2): if $V_{j+1} - V_j < \epsilon$ (where ϵ is the chosen convergence tolerance, usually at the order of 10^{-6}) then end the algorithm

Step(3): compute $\vec{q}_j = -\nabla V(\vec{r}_{j+1})$ and set $V_j = V(\vec{r}_{j+1})$

Step(4): compute $\gamma = \vec{q}_j \cdot \vec{q}_j / \vec{g}_j \cdot \vec{g}_j$

Step(5): set $\vec{g}_{j+1} = \vec{q}_j$

Step(6): set $\vec{h}_{j+1} = \vec{g}_{j+1} + \gamma \vec{h}_j$ and $\vec{q}_{j+1} = \vec{h}_{j+1}$

Step(7): increase the counter of iterations: $j = j + 1$ and return to the step(1)

The algorithm we have presented is known as *Fletcher-Reeves* algorithm. Sometimes it is more efficient to use its modification, known as *Polak-Ribiere* algorithm. The only difference between the two algorithms is in the step (4) which is in the later case [125]:

Step(4)*: compute $\gamma = (\vec{q}_j + \vec{g}_j) \cdot \vec{q}_j / \vec{g}_j \cdot \vec{g}_j$.

As a concluding remark, *CG* method is efficient in finding a local minimum and it is often the method of choice in *MD* simulations.

Bibliography

- [1] Weijia Wen, Ning Wang, D. W. Zheng, C. Chen, and K. N. Tu, Two- and three-dimensional arrays of magnetic microspheres, *Journal of Materials Research* **14**(4), 1186–1189 (1999). [2](#)
- [2] David J Sellmyer, Applied physics: Strong magnets by self-assembly, *Nature* **420**(6914), 374–375 (2002). [2](#)
- [3] George M. Whitesides and Bartosz Grzybowski, Self-assembly at all scales, *Science* **295**(5564), 2418–2421 (2002). [2](#)
- [4] Ken F Jarrell and Mark J McBride, The surprisingly diverse ways that prokaryotes move, *Nature Reviews Microbiology* **6**(6), 466 (2008). [3](#)
- [5] Iain M Cheeseman and Arshad Desai, Molecular architecture of the kinetochore–microtubule interface, *Nature Reviews Molecular Cell Biology* **9**(1), 33 (2008). [3](#)
- [6] Jonathon Howard and Anthony A Hyman, Growth, fluctuation and switching at microtubule plus ends, *Nature Reviews Molecular Cell Biology* **10**(8), 569–574 (2009). [3](#)
- [7] X. B Zhang, X. F Zhang, D Bernaerts, G. van Tendeloo, S Amelinckx, J. van Landuyt, V Ivanov, J. B Nagy, Ph Lambin, and A. A Lucas, The texture of catalytically grown coil-shaped carbon nanotubules, *Europhysics Letters (EPL)* **27**(2), 141–146 (1994). [3](#)
- [8] Shawn M Douglas, James J Chou, and William M Shih, Dna-nanotube-induced alignment of membrane proteins for nmr structure determination,

-
- Proceedings of the National Academy of Sciences* **104**(16), 6644–6648 (2007). [3](#)
- [9] G Daniel Lilly, Ashish Agarwal, Sudhanshu Srivastava, and Nicholas A Kotov, Helical assemblies of gold nanoparticles, *Small* **7**(14), 2004–2009 (2011). [3](#)
- [10] Toshimi Shimizu, Mitsutoshi Masuda, and Hiroyuki Minamikawa, Supramolecular nanotube architectures based on amphiphilic molecules, *Chemical reviews* **105**(4), 1401–1444 (2005). [3](#)
- [11] Yohei Yamamoto, Takanori Fukushima, Yuki Suna, Noriyuki Ishii, Akinori Saeki, Shu Seki, Seiichi Tagawa, Masateru Taniguchi, Tomoji Kawai, and Takuzo Aida, Photoconductive coaxial nanotubes of molecularly connected electron donor and acceptor layers, *Science* **314**(5806), 1761–1764 (2006). [3](#)
- [12] Wei Zhuang, Edis Kasëmi, Yi Ding, Martin Kröger, A Dieter Schlüter, and Jürgen P Rabe, Self-folding of charged single dendronized polymers, *Advanced Materials* **20**(17), 3204–3210 (2008). [3](#)
- [13] E Alphanbéry, Y Ding, AT Ngo, ZL Wang, LF Wu, and MP Pileni, Assemblies of aligned magnetotactic bacteria and extracted magnetosomes: what is the main factor responsible for the magnetic anisotropy?, *ACS Nano* **3**(6), 1539–1547 (2009). [3](#)
- [14] Peter Atkins and Julio De Paula, *Physical chemistry for the life sciences*, Oxford University Press, USA (2011). [3](#)
- [15] Molly M Bloomfield, Lawrence J Stephens, et al., *Chemistry and the living organism*, J. Wiley (1996). [3](#)
- [16] Hao Zeng, Jing Li, J Ping Liu, Zhong L Wang, and Shouheng Sun, Exchange-coupled nanocomposite magnets by nanoparticle self-assembly, *Nature* **420**(6914), 395 (2002). [3](#)
- [17] Mila Boncheva, Stefan A Andreev, L Mahadevan, Adam Winkleman, David R Reichman, Mara G Prentiss, Sue Whitesides, and George M Whitesides, Mag-

-
- netic self-assembly of three-dimensional surfaces from planar sheets, *Proceedings of the National Academy of Sciences* **102**(11), 3924–3929 (2005). [3](#)
- [18] Taisia A Prokopieva, Victor A Danilov, Sofia S Kantorovich, and Christian Holm, Ground state structures in ferrofluid monolayers, *Phys. Rev. E: Stat. Phys., Plasmas, Fluids, Relat. Interdiscip. Top.* **80**(3), 031404 (2009). [3](#)
- [19] Gurvinder Singh, Henry Chan, Artem Baskin, Elijah Gelman, Nikita Reppin, Petr Král, and Rafal Klajn, Self-assembly of magnetite nanocubes into helical superstructures, *Science* p. 1254132 (2014). [3](#)
- [20] Djamal Zerrouki, Jean Baudry, David Pine, Paul Chaikin, and Jérôme Bibette, Chiral colloidal clusters, *Nature* **455**(7211), 380 (2008). [3](#)
- [21] Galen T Pickett, Mark Gross, and Hiroko Okuyama, Spontaneous chirality in simple systems, *Physical Review Letters* **85**(17), 3652 (2000). [3](#)
- [22] EC Oğuz, R Messina, and H Löwen, Helicity in cylindrically confined yukawa systems, *Europhysics Letters (EPL)* **94**(2), 28005 (2011). [3](#)
- [23] Matthew A Lohr, Ahmed M Alsayed, Bryan G Chen, Zexin Zhang, Randall D Kamien, and Arjun G Yodh, Helical packings and phase transformations of soft spheres in cylinders, *Phys. Rev. E: Stat. Phys., Plasmas, Fluids, Relat. Interdiscip. Top.* **81**(4), 040401 (2010). [3](#)
- [24] Andreas Mershin, Alexandre A Kolomenski, Hans A Schuessler, and Dimitri V Nanopoulos, Tubulin dipole moment, dielectric constant and quantum behavior: computer simulations, experimental results and suggestions, *Biosystems* **77**(1-3), 73–85 (2004). [3](#)
- [25] Erik D Spoerke, George D Bachand, Jun Liu, Darryl Sasaki, and Bruce C Bunker, Directing the polar organization of microtubules, *Langmuir* **24**(14), 7039–7043 (2008). [4](#)
- [26] Michal Cifra, Jirí Pokorný, Daniel Havelka, and O Kučera, Electric field generated by axial longitudinal vibration modes of microtubule, *BioSystems* **100**(2), 122–131 (2010). [4](#)

-
- [27] IS Jacobs and CP Bean, An approach to elongated fine-particle magnets, *Physical Review* **100**(4), 1060 (1955). [4](#)
- [28] P. G. de Gennes and P. A. Pincus, Pair correlations in a ferromagnetic colloid, *Physik der kondensierten Materie* **11**(3), 189–198 (1970). [4](#)
- [29] René Messina, Lara Abou Khalil, and Igor Stanković, Self-assembly of magnetic balls: From chains to tubes, *Phys. Rev. E: Stat. Phys., Plasmas, Fluids, Relat. Interdiscip. Top.* **89**(1), 011202 (2014). [4](#), [34](#), [41](#), [43](#), [46](#), [48](#)
- [30] Dominic Vella, Emmanuel du Pontavice, Cameron L Hall, and Alain Goriely, The magneto-elastica: from self-buckling to self-assembly, In *Proc. R. Soc. London, Ser. A* volume 470 p. 20130609 (2014). [4](#)
- [31] David Tománek, Seong Gon Kim, Philippe Jund, Peter Borrmann, Heinrich Stamerjohanns, and Eberhard R. Hilf, Self-assembly of magnetic nanostructures, *Zeitschrift für Physik D Atoms, Molecules and Clusters* **40**(1), 539–541 (1997). [4](#)
- [32] Gergő Pál, Ferenc Kun, Imre Varga, Dóra Sohler, and Gang Sun, Attraction-driven aggregation of dipolar particles in an external magnetic field, *Phys. Rev. E: Stat. Phys., Plasmas, Fluids, Relat. Interdiscip. Top.* **83**(6), 061504 (2011). [4](#)
- [33] Vikash Malik, Andrei V Petukhov, Le He, Yadong Yin, and Marius Schmidt, Colloidal crystallization and structural changes in suspensions of silica/magnetite core-shell nanoparticles, *Langmuir* **28**(41), 14777–14783 (2012). [4](#)
- [34] Nicolas Vandewalle and Stéphane Dorbolo, Magnetic ghosts and monopoles, *New Journal of Physics* **16**(1), 013050 (2014). [4](#)
- [35] D. A. Wood, C. D. Santangelo, and A. D. Dinsmore, Self-assembly on a cylinder: a model system for understanding the constraint of commensurability, *Soft Matter* **9**, 10016–10024 (2013). [4](#), [21](#)

-
- [36] Bharat Bhushan, Jacob N Israelachvili, and Uzi Landman, Nanotribology: friction, wear and lubrication at the atomic scale, *Nature* **374**(6523), 607 (1995). [7](#), [12](#), [96](#), [102](#)
- [37] Seong-Jun Heo, Susan B Sinnott, Donald W Brenner, and Judith A Harrison, Computational modeling of nanometer-scale tribology, In *Nanotribology and Nanomechanics* pages 623–691. Springer (2005). [7](#)
- [38] Kenneth Holmberg, Peter Andersson, and Ali Erdemir, Global energy consumption due to friction in passenger cars, *Tribology International* **47**, 221–234 (2012). [7](#), [10](#), [11](#)
- [39] Ana C. F. Mendonça, Agílio A. H. Pádua, and Patrice Malfreyt, Nonequilibrium molecular simulations of new ionic lubricants at metallic surfaces: Prediction of the friction, *Journal of Chemical Theory and Computation* **9**(3), 1600–1610 (2013). [7](#), [9](#), [13](#), [65](#), [70](#), [107](#), [108](#), [114](#)
- [40] D. M. Heyes, E. R. Smith, D. Dini, H. A. Spikes, and T. A. Zaki, Pressure dependence of confined liquid behavior subjected to boundary-driven shear, *The Journal of Chemical Physics* **136**(13) (2012). [7](#), [13](#)
- [41] Chiara Gattinoni, David M. Heyes, Christian D. Lorenz, and Daniele Dini, Traction and nonequilibrium phase behavior of confined sheared liquids at high pressure, *Phys. Rev. E: Stat. Phys., Plasmas, Fluids, Relat. Interdiscip. Top.* **88**, 052406 (2013). [7](#), [13](#)
- [42] Laetitia Martinie and Philippe Vergne, Lubrication at extreme conditions: A discussion about the limiting shear stress concept, *Tribology Letters* **63**(2) (2016). [7](#), [13](#), [111](#)
- [43] Nicolas Voeltzel, Andrew Giuliani, Nicolas Fillot, Philippe Vergne, and Laurent Joly, Nanolubrication by ionic liquids: molecular dynamics simulations reveal an anomalous effective rheology, *Physical Chemistry Chemical Physics* **17**, 23226–23235 (2015). [7](#), [9](#), [13](#), [66](#)

-
- [44] Feng Zhou, Yongmin Liang, and Weimin Liu, Ionic liquid lubricants: designed chemistry for engineering applications, *Chemical Society Reviews* **38**(9), 2590–2599 (2009). [8](#), [9](#), [11](#), [12](#)
- [45] K Mistry, M F Fox, and M Priest, Lubrication of an electroplated nickel matrix silicon carbide coated eutectic aluminium—silicon alloy automotive cylinder bore with an ionic liquid as a lubricant additive, *Proceedings of the Institution of Mechanical Engineers, Part J: Journal of Engineering Tribology* **223**(3), 563–569 (2009). [8](#)
- [46] Jun Qu, Dinesh G Bansal, Bo Yu, Jane Y Howe, Huimin Luo, Sheng Dai, Huaqing Li, Peter J Blau, Bruce G Bunting, Gregory Mordukhovich, et al., Antiwear performance and mechanism of an oil-miscible ionic liquid as a lubricant additive, *ACS applied materials & interfaces* **4**(2), 997–1002 (2012). [8](#)
- [47] Jun Qu, Peter J Blau, Sheng Dai, Huimin Luo, and Harry M Meyer, Ionic liquids as novel lubricants and additives for diesel engine applications, *Tribology Letters* **35**(3), 181–189 (2009). [8](#)
- [48] María-Dolores Bermúdez, Ana-Eva Jiménez, José Sanes, and Francisco-José Carrión, Ionic liquids as advanced lubricant fluids, *Molecules* **14**(8), 2888–2908 (2009). [8](#)
- [49] Oscar Yovany Fajardo, Fernando Bresme, Alexei A Kornyshev, and Michael Urbakh, Electrotunable friction with ionic liquid lubricants: how important is the molecular structure of the ions?, *The Journal of Physical Chemistry Letters* **6**(20), 3998–4004 (2015). [8](#), [9](#), [10](#), [65](#), [66](#), [68](#), [71](#), [72](#), [73](#), [74](#), [75](#), [90](#)
- [50] Robert Hayes, Gregory G Warr, and Rob Atkin, At the interface: solvation and designing ionic liquids, *Physical Chemistry Chemical Physics* **12**(8), 1709–1723 (2010). [9](#)
- [51] OY Fajardo, F Bresme, AA Kornyshev, and M Urbakh, Electrotunable lu-

- bricity with ionic liquid nanoscale films, *Scientific Reports* **5** (2015). [9](#), [10](#), [65](#), [66](#), [68](#), [69](#), [72](#), [74](#), [75](#)
- [52] R Capozza, A Vanossi, A Benassi, and E Tosatti, Squeezout phenomena and boundary layer formation of a model ionic liquid under confinement and charging, *The Journal of Chemical Physics* **142**(6), 064707 (2015). [9](#), [10](#), [65](#), [66](#), [68](#), [69](#), [71](#), [73](#), [74](#), [76](#), [77](#)
- [53] Christian Dold, Tobias Amann, and Andreas Kailer, Influence of structural variations on imidazolium-based ionic liquids, *Lubrication Science* **4**(25), 251–268 (2013). [9](#), [12](#), [74](#), [136](#)
- [54] F. Varnik, L. Bocquet, J.-L. Barrat, and L. Berthier, Shear localization in a model glass, *Physical Review Letters* **90**, 095702 (2003). [9](#)
- [55] Anatolii V. Mokshin and Jean-Louis Barrat, Shear-induced crystallization of an amorphous system, *Phys. Rev. E: Stat. Phys., Plasmas, Fluids, Relat. Interdiscip. Top.* **77**, 021505 (2008). [9](#)
- [56] Filippo Federici Canova, Hiroki Matsubara, Masashi Mizukami, Kazue Kurihara, and Alexander L. Shluger, Shear dynamics of nanoconfined ionic liquids, *Physical Chemistry Chemical Physics* **16**, 8247–8256 (2014). [9](#), [13](#), [66](#), [107](#), [108](#), [114](#)
- [57] Jianping Gao, W. D. Luedtke, D. Gourdon, M. Ruths, J. N. Israelachvili, and Uzi Landman, Frictional forces and amontons' law: From the molecular to the macroscopic scale, *The Journal of Physical Chemistry B* **108**(11), 3410–3425 (2004). [10](#), [13](#)
- [58] Mark O Robbins and Martin H Müser, Computer simulations of friction, lubrication, and wear, In Bharat Bhushan, editor, *Modern Tribology Handbook, Two Volume Set Mechanics & Materials Science*. CRC Press (2000). [10](#), [13](#)
- [59] R. E. Rudd and J. Q. Broughton, Coarse-grained molecular dynamics and the atomic limit of finite elements, *Physical Review B* **58**, R5893–R5896 (1998). [10](#), [13](#)

- [60] Y. Wang, W. Jiang, T. Yan, and G. A. Voth, Understanding ionic liquids through atomistic and coarse-grained molecular dynamics simulations, *Accounts of Chemical Research* **40**(11), 1193–1199 (2007). [10](#), [13](#)
- [61] Zhantao Wang and Craig Priest, Impact of nanoscale surface heterogeneity on precursor film growth and macroscopic spreading of [rmim][ntf2] ionic liquids on mica, *Langmuir* **29**(36), 11344–11353 (2013). [10](#), [12](#)
- [62] David A Beattie, Rosa M Espinosa-Marzal, Tracey TM Ho, Mihail N Popescu, John Ralston, Céline JE Richard, Pasindu MF Sellapperumage, and Marta Krasowska, Molecularly-thin precursor films of imidazolium-based ionic liquids on mica, *The Journal of Physical Chemistry C* **117**(45), 23676–23684 (2013). [10](#), [12](#)
- [63] Alexander M Smith, Kevin RJ Lovelock, Nitya Nand Gosvami, Tom Welton, and Susan Perkin, Quantized friction across ionic liquid thin films, *Physical Chemistry Chemical Physics* **15**(37), 15317–15320 (2013). [10](#), [12](#), [93](#)
- [64] Konstantinos Gkagkas, Veerapandian Ponnuchamy, Miljan Dašić, and Igor Stanković, Molecular dynamics investigation of a model ionic liquid lubricant for automotive applications, *Tribology International* **113**, 83–91 (2017). [10](#), [11](#), [68](#), [69](#), [70](#), [71](#), [72](#), [74](#), [92](#), [117](#), [118](#), [136](#)
- [65] W Liu, C Ye, Y Chen, Z Ou, and DC Sun, Tribological behavior of sialon ceramics sliding against steel lubricated by fluorine-containing oils, *Tribology International* **35**(8), 503–509 (2002). [11](#)
- [66] AS Pensado, MJP Comunas, and J Fernández, The pressure–viscosity coefficient of several ionic liquids, *Tribology Letters* **31**(2), 107–118 (2008). [12](#)
- [67] Ichiro Minami, Ionic liquids in tribology, *Molecules* **14**(6), 2286–2305 (2009). [12](#), [74](#)
- [68] Ibrahim Bou-Malham and Lionel Bureau, Nanoconfined ionic liquids: effect of surface charges on flow and molecular layering, *Soft Matter* **6**(17), 4062–4065 (2010). [12](#)

-
- [69] Anthony E. Somers, Patrick C. Howlett, Douglas R. MacFarlane, and Maria Forsyth, A review of ionic liquid lubricants, *Lubricants* **1**(1) (2013). [12](#), [92](#), [93](#), [96](#), [102](#)
- [70] Hideto Kamimura, Takeru Chiba, Tomoo Kubo, Hidetaka Nanao, Ichiro Minami, and Shigeyuki Mori, Relationship between structure and tribological properties of ionic liquids composed of imidazolium cations, *Japanese Journal of Tribology* **51**(6), 675–687 (2006). [12](#)
- [71] Susan Perkin, Lorna Crowhurst, Heiko Niedermeyer, Tom Welton, Alexander M Smith, and Nitya Nand Gosvami, Self-assembly in the electrical double layer of ionic liquids, *Chemical Communications* **47**(23), 6572–6574 (2011). [12](#), [126](#)
- [72] Haizhong Wang, Qiming Lu, Chengfeng Ye, Weimin Liu, and Zhaojie Cui, Friction and wear behaviors of ionic liquid of alkyimidazolium hexafluorophosphates as lubricants for steel/steel contact, *Wear* **256**(1-2), 44–48 (2004). [13](#)
- [73] AE Jiménez, MD Bermudez, P Iglesias, FJ Carrión, and G Martínez-Nicolás, 1-n-alkyl-3-methylimidazolium ionic liquids as neat lubricants and lubricant additives in steel–aluminium contacts, *Wear* **260**(7-8), 766–782 (2006). [13](#)
- [74] Zonggang Mu, Feng Zhou, Shuxiang Zhang, Yongmin Liang, and Weimin Liu, Effect of the functional groups in ionic liquid molecules on the friction and wear behavior of aluminum alloy in lubricated aluminum-on-steel contact, *Tribology International* **38**(8), 725–731 (2005). [13](#)
- [75] Igor Stanković, Miljan Dašić, and René Messina, Structure and cohesive energy of dipolar helices, *Soft Matter* **12**, 3056–3065 (2016). [15](#)
- [76] Wolfram Research, Inc., Mathematica, Version 11.3, Champaign, IL, 2018. [21](#), [147](#), [149](#), [161](#)
- [77] William Thomson Baron Kelvin, *The molecular tactics of a crystal*, Clarendon Press (1894). [22](#)

-
- [78] Simon W de Leeuw, John William Perram, and Edgar Roderick Smith, Simulation of electrostatic systems in periodic boundary conditions. i. lattice sums and dielectric constants, *Proceedings of the Royal Society of London. Series A, Mathematical and Physical Sciences* **373**(1752), 27–56 (1980). [30](#), [31](#)
- [79] DM Heyes, The surface potential of point charge and point dipole lattices, *Surface Science Letters* **110**(2), L619–L624 (1981). [30](#), [31](#)
- [80] David M Heyes, Pressure tensor of partial-charge and point-dipole lattices with bulk and surface geometries, *Physical Review B* **49**(2), 755 (1994). [30](#), [31](#)
- [81] A Grzybowski, E Gwóźdź, and A Bródka, Ewald summation of electrostatic interactions in molecular dynamics of a three-dimensional system with periodicity in two directions, *Physical Review B* **61**(10), 6706 (2000). [30](#), [31](#)
- [82] A Grzybowski and A Bródka, Computationally efficient method for summing interactions of point dipoles in three dimensions with two-dimensional periodicity, *Chemical Physics Letters* **361**(3-4), 329–333 (2002). [30](#), [31](#)
- [83] A Bródka and A Grzybowski, Electrostatic interactions in computer simulations of a three-dimensional system periodic in two directions: Ewald-type summation, *The Journal of Chemical Physics* **117**(18), 8208–8211 (2002). [30](#), [31](#)
- [84] A Bródka, Ewald type summation method for electrostatic interactions in computer simulations of a three-dimensional system periodic in one direction, *Chemical Physics Letters* **363**(5-6), 604–609 (2002). [30](#), [31](#)
- [85] John Lekner, Summation of coulomb fields in computer-simulated disordered systems, *Physica A: Statistical Mechanics and its Applications* **176**(3), 485–498 (1991). [31](#)
- [86] AT Clark, TJ Madden, and PB Warren, Summation of electrostatic interactions in quasi-two-dimensional simulations, *Molecular Physics* **87**(5), 1063–1069 (1996). [31](#)

-
- [87] SY Liem and JH R Clarke, Calculation of coulomb interactions in two-dimensionally periodic systems, *Molecular Physics* **92**(1), 19–25 (1997). [31](#)
- [88] Niels Gronbech-Jensen, Gerhard Hummer, and Keith M Beardmore, Lekner summation of coulomb interactions in partially periodic systems, *Molecular Physics* **92**(5), 941–946 (1997). [31](#)
- [89] A Grzybowski and A Bródka, Electrostatic interactions in molecular dynamics simulation of a three-dimensional system with periodicity in one direction, *Molecular Physics* **100**(5), 635–639 (2002). [31](#), [147](#), [170](#)
- [90] A Grzybowski and A Bródka, Coulomb interactions in a computer simulation of a system periodic in two directions, *Molecular Physics* **100**(7), 1017–1023 (2002). [31](#)
- [91] A Grzybowski and A Bródka, Lekner type method for summing the dipole—dipole interactions in computer simulations of one- and two-dimensionally periodic systems, *Molecular Physics* **101**(8), 1079–1088 (2003). [31](#), [32](#)
- [92] L Assoud and R Messina, Penalty method to predict crystal structures involving hard-core interactions, *Phys. Rev. E: Stat. Phys., Plasmas, Fluids, Relat. Interdiscip. Top.* **83**(3), 036113 (2011). [34](#)
- [93] fmincon description, <https://www.mathworks.com/help/optim/ug/fmincon.html>. [34](#), [35](#), [36](#)
- [94] K De’Bell, AB MacIsaac, IN Booth, and JP Whitehead, Dipolar-induced planar anisotropy in ultrathin magnetic films, *Physical Review B* **55**(22), 15108 (1997). [37](#)
- [95] Sona Prakash and Christopher L Henley, Ordering due to disorder in dipolar magnets on two-dimensional lattices, *Physical Review B* **42**(10), 6574 (1990). [37](#)

-
- [96] Igor Stanković, Miljan Dašić, Jorge A. Otálora, and Carlos García, A platform for nanomagnetism – assembled ferromagnetic and antiferromagnetic dipolar tubes, *Nanoscale* **11**, 2521–2535 (2019). [39](#)
- [97] René Messina and Igor Stanković, Assembly of magnetic spheres in strong homogeneous magnetic field, *Physica A: Statistical Mechanics and its Applications* **466**, 10–20 (2017). [42](#)
- [98] Steve Plimpton, Fast parallel algorithms for short-range molecular dynamics, *Journal of Computational Physics* **117**(1), 1–19 (1995). [51](#), [64](#)
- [99] Michael Rubinstein, Ralph H Colby, et al., *Polymer physics* volume 23, Oxford university press New York (2003). [51](#), [56](#), [59](#), [63](#)
- [100] Ju Li, Basic molecular dynamics, In *Handbook of Materials Modeling* pages 565–588. Springer (2005). [52](#)
- [101] William Humphrey, Andrew Dalke, and Klaus Schulten, VMD – Visual Molecular Dynamics, *Journal of Molecular Graphics* **14**, 33–38 (1996). [64](#), [65](#)
- [102] Jiri Kolafa and John W Perram, Cutoff errors in the ewald summation formulae for point charge systems, *Molecular Simulation* **9**(5), 351–368 (1992). [64](#)
- [103] David S Cerutti, Robert E Duke, Thomas A Darden, and Terry P Lybrand, Staggered mesh ewald: an extension of the smooth particle-mesh ewald method adding great versatility, *Journal of Chemical Theory and Computation* **5**(9), 2322–2338 (2009). [64](#)
- [104] David J Hardy, John E Stone, and Klaus Schulten, Multilevel summation of electrostatic potentials using graphics processing units, *Parallel Computing* **35**(3), 164–177 (2009). [64](#), [69](#)
- [105] Jianping Gao, W. D. Luedtke, and Uzi Landman, Layering transitions and dynamics of confined liquid films, *Physical Review Letters* **79**, 705–708 (1997). [68](#), [92](#), [93](#)

-
- [106] Murray S Daw and Michael I Baskes, Embedded-atom method: Derivation and application to impurities, surfaces, and other defects in metals, *Physical Review B* **29**(12), 6443 (1984). [69](#)
- [107] Igor Stankovic, Siegfried Hess, and Martin Kröger, Structural changes and viscoplastic behavior of a generic embedded-atom model metal in steady shear flow, *Phys. Rev. E: Stat. Phys., Plasmas, Fluids, Relat. Interdiscip. Top.* **69**(2), 021509 (2004). [69](#)
- [108] Astrid Gubbels-Elzas and Barend J Thijsse, Ionic motion during field-assisted oxidation of aluminium studied by molecular dynamics simulations, *Computational Materials Science* **90**, 196–202 (2014). [69](#)
- [109] F. Iori and S. Corni, Including image charge effects in the molecular dynamics simulations of molecules on metal surfaces, *Journal of Computational Chemistry* **29**(10), 1656–1666 (2008). [69](#)
- [110] Miljan Dašić, Igor Stanković, and Konstantinos Gkagkas, Molecular dynamics investigation of the influence of the shape of the cation on the structure and lubrication properties of ionic liquids, *Physical Chemistry Chemical Physics* **21**, 4375–4386 (2019). [71](#)
- [111] Dašić, Miljan, Stanković, Igor, and Gkagkas, Konstantinos, Influence of confinement on flow and lubrication properties of a salt model ionic liquid investigated with molecular dynamics, *The European Physical Journal E* **41**(11), 130 (2018). [71](#)
- [112] Sébastien Viscardy, James Servantie, and Pierre Gaspard, Transport and Helfand moments in the Lennard-Jones fluid. I. Shear viscosity, *The Journal of Chemical Physics* **126**(18), 184512 (2007). [79](#)
- [113] Denis J Evans and GP Morriss, Nonlinear-response theory for steady planar Couette flow, *Physical Review A* **30**(3), 1528 (1984). [79](#)
- [114] Peter J Daivis and BD Todd, A simple, direct derivation and proof of the

- validity of the slod equations of motion for generalized homogeneous flows, *The Journal of Chemical Physics* **124**(19), 194103 (2006). [79](#)
- [115] Robert Hayes, Gregory G Warr, and Rob Atkin, Structure and nanostructure in ionic liquids, *Chemical Reviews* **115**(13), 6357–6426 (2015). [87](#)
- [116] Susan Perkin, Ionic liquids in confined geometries, *Physical Chemistry Chemical Physics* **14**, 5052–5062 (2012). [92](#), [93](#), [117](#)
- [117] Robert Hayes, Natalia Borisenko, Matthew K Tam, Patrick C Howlett, Frank Endres, and Rob Atkin, Double layer structure of ionic liquids at the au (111) electrode interface: an atomic force microscopy investigation, *The Journal of Physical Chemistry C* **115**(14), 6855–6863 (2011). [93](#), [118](#)
- [118] P. D. Kaplan, J. L. Rouke, A. G. Yodh, and D. J. Pine, Entropically driven surface phase separation in binary colloidal mixtures, *Physical Review Letters* **72**(4), 582–585 (1994). [96](#)
- [119] Scott Bair, Laetitia Martinie, and Philippe Vergne, Classical ehl versus quantitative ehl: A perspective part ii—super-arrhenius piezoviscosity, an essential component of elastohydrodynamic friction missing from classical ehl, *Tribology Letters* **63**(3), 37 (2016). [107](#), [136](#)
- [120] Kamil Paduszyn´ski and Urszula Doman´ska, Viscosity of ionic liquids: an extensive database and a new group contribution model based on a feed-forward artificial neural network, *Journal of Chemical Information and Modeling* **54**(5), 1311–1324 (2014). [143](#)
- [121] IS Gradshteyn and IM Ryzhik, *Table of integrals, series and products* (New York: Academic), Elsevier (1980). [147](#)
- [122] Erwin Madelung, *Die mathematischen hilfsmittel des physikers* volume 4, Springer-Verlag (2013). [148](#)
- [123] Milton Abramowitz and Irene A Stegun, *Handbook of mathematical functions: with formulas, graphs, and mathematical tables* volume 55, Courier Corporation (1965). [149](#), [163](#), [167](#), [170](#)

- [124] William H Press, Saul A Teukolsky, William T Vetterling, and Brian P Flannery, *Numerical recipes in C* volume 2, Cambridge university press Cambridge (1982). [171](#), [172](#), [173](#), [175](#), [176](#)
- [125] Introduction to atomistic simulations 2008, http://www.acclab.helsinki.fi/~aakurone/atomistiset/lecturenotes/lecture_all.pdf. [171](#), [174](#), [176](#), [177](#)

Publications list

This doctoral thesis is based on the next published journal papers:

- [1] I. Stanković, **M. Dašić** and R. Messina, Structure and cohesive energy of dipolar helices, *Soft Matter* **12**, 3056 (2016).

- [2] K. Gkagkas, V. Ponnuchamy, **M. Dašić** and I. Stanković, Molecular dynamics investigation of a model ionic liquid lubricant for automotive applications, *Tribology International* **113**, 83 (2017).

- [3] **M. Dašić**, I. Stanković and K. Gkagkas, Influence of confinement on flow and lubrication properties of a salt model ionic liquid investigated with molecular dynamics, *The European Physical Journal E* **41**, 130 (2018).

- [4] I. Stanković, **M. Dašić**, J. A. Otálora and C. García, A platform for nanomagnetism - assembled ferromagnetic and antiferromagnetic dipolar tubes, *Nanoscale* **11**, 2521 (2019).

- [5] **M. Dašić**, I. Stanković and K. Gkagkas, Molecular dynamics investigation of the influence of the shape of the cation on the structure and lubrication properties of ionic liquids, *Physical Chemistry Chemical Physics* **21**, 4375 (2019).

Biography

Miljan Dašić was born on 3.11.1990. in Paraćin, Republic of Serbia. He has finished elementary school "Momčilo Popović-Ozren" and "Gymnasium Paraćin" in Paraćin, both as the best student of generation. He has won numerous prizes at competitions in physics, mathematics, programming and chemistry. He has participated at Petnica Science Center (PSC) physics seminars. Miljan Dašić was a participant of "SciTech 2009", an international scientific summer programme, held at Technion (Israel Institute of Technology), where he worked on an applied mathematics project. The results of that project he presented together with his teammates at a conference held at Technion in August 2009.

Miljan Dašić graduated at the Faculty of Electrical Engineering, University of Belgrade, in July 2013, with a GPA of 9.93/10.00. His undergraduate thesis is based on the research conducted at the Nanophotonic Systems Laboratory of the University of Colorado Boulder (USA) under the mentorship of Prof. Dr. Miloš Popović. During the undergraduate studies he performed several international internships: in 2011 he participated at "UREKA 2011" summer internship at Tyndall National Institute (Cork, Ireland); in 2012 he worked as a research assistant at University of Colorado (Boulder, USA); in 2013 he participated in IAESTE programme at Lappeenranta University of Technology (Lappeenranta, Finland).

Miljan Dašić completed his master studies at the Faculty of Electrical Engineering, University of Belgrade, in July 2014, with a GPA of 10.00. His master thesis was done in the Scientific Computing Laboratory (SCL) of the Institute of Physics Belgrade (IPB) under the mentorship of Dr. Igor Stanković, in the framework of a bilateral Serbian-French project related to the self-assembly of magnetic particles.

In October 2014, Miljan Dašić started his PhD studies at the Faculty of Physics, University of Belgrade, with specialization in condensed matter physics. Since

November 2014, Miljan Dašić has participated in the National Project No. OI171017 "Modeling and Numerical Simulations of Complex Many-Particle Systems" funded by the Ministry of Education, Science and Technological Development of the Republic of Serbia, under the mentorship of Dr. Igor Stanković. He has realized a six-month internship in the Advanced Technology Division of the Technical Centre of Toyota Motor Europe in Zaventem (Belgium). During that internship he worked on the development of molecular dynamics simulations related to the nanoscopic lubrication performance of ionic liquid lubricants.

Miljan Dašić has participated in the PSC physics seminars as a lecturer and mentor on yearly projects. He has also participated in the National Committee for High School Physics Competitions as a Committee member at National-level competitions. Miljan Dašić has worked as a reviewer for international scientific journals "Tribology International" and "Optical and Quantum Electronics".

Miljan Dašić was elected as the member of the "Club Superste" for the year of 2014, in the field of natural sciences, on a competition organized by the ERSTE bank, with the goal of supporting young talents of Serbia. At the international IEEEESTEC conference, held in November 2014 at the Faculty of Electronics (Niš, Serbia), he won the "Best paper award".

During his PhD studies Miljan Dašić published five papers in high quality international scientific journals and participated at several international workshops and conferences.

Прилог 1.

Изјава о ауторству

Име и презиме аутора: **Миљан Дашић**

Број индекса: **8004/2014**

Изјављујем

да је докторска дисертација под насловом

Modeling the behaviour of confined dipolar and ionic systems

(Моделовање понашања просторно ограничених диполних и јонских система)

- резултат сопственог истраживачког рада;
- да дисертација у целини ни у деловима није била предложена за стицање друге дипломе према студијским програмима других високошколских установа;
- да су резултати коректно наведени и
- да нисам кршио ауторска права и користио интелектуалну својину других лица.

Потпис аутора

У Београду, 30.8.2019.



Прилог 2.

**Изјава о истоветности штампане и електронске
верзије докторског рада**

Име и презиме аутора: **Миљан Дашић**

Број индекса: **8004/2014**

Студијски програм: **Физика кондензоване материје и статистичка физика**

Наслов рада: **Modeling the behaviour of confined dipolar and ionic systems
(Моделовање понашања просторно ограничених диполних и јонских
система)**

Ментор: **др Игор Станковић**

Изјављујем да је штампана верзија мог докторског рада истоветна електронској верзији коју сам предао за објављивање на порталу **Дигиталног репозиторијума Универзитета у Београду**.

Дозвољавам да се објаве моји лични подаци везани за добијање академског звања доктора наука, као што су име и презиме, година и место рођења и датум одбране рада.

Ови лични подаци могу се објавити на мрежним страницама дигиталне библиотеке, у електронском каталогу и у публикацијама Универзитета у Београду.

Потпис аутора

У Београду, 30.8.2019.



Прилог 3.

Изјава о коришћењу

Овлашћујем Универзитетску библиотеку „Светозар Марковић“ да у Дигитални репозиторијум Универзитета у Београду унесе моју докторску дисертацију под насловом:

Modeling the behaviour of confined dipolar and ionic systems (Моделовање понашања просторно ограничених диполних и јонских система)

која је моје ауторско дело.

Дисертацију са свим прилозима предао сам у електронском формату погодном за трајно архивирање.

Моју докторску дисертацију похрањену у Дигитални репозиторијум Универзитета у Београду могу да користе сви који поштују одредбе садржане у одабраном типу лиценце Креативне заједнице (Creative Commons) за коју сам се одлучио.

1. Ауторство (CC BY)
2. Ауторство – некомерцијално (CC BY - NC)
3. Ауторство – некомерцијално – без прераде (CC BY-NC-ND)
4. Ауторство – некомерцијално – делити под истим условима (CC BY-NC-SA)
5. Ауторство – без прераде (CC BY-ND)
6. Ауторство – делити под истим условима (CC BY-SA)

(Молимо да заокружите само једну од шест понуђених лиценци. Кратак опис лиценци је саставни део ове изјаве).

У Београду, 30.8.2019.

Потпис аутора



1. **Ауторство.** Дозвољаваате умножавање, дистрибуцију и јавно саопштавање дела, и прераде, ако се наведе име аутора на начин одређен од стране аутора или даваоца лиценце, чак и у комерцијалне сврхе. Ово је најслободнија од свих лиценци.

2. **Ауторство – некомерцијално.** Дозвољаваате умножавање, дистрибуцију и јавно саопштавање дела, и прераде, ако се наведе име аутора на начин одређен од стране аутора или даваоца лиценце. Ова лиценца не дозвољава комерцијалну употребу дела.

3. **Ауторство – некомерцијално – без прераде.** Дозвољаваате умножавање, дистрибуцију и јавно саопштавање дела, без промена, преобликовања или употребе дела у свом делу, ако се наведе име аутора на начин одређен од стране аутора или даваоца лиценце. Ова лиценца не дозвољава комерцијалну употребу дела. У односу на све остале лиценце, овом лиценцом се ограничава највећи обим права коришћења дела.

4. **Ауторство – некомерцијално – делити под истим условима.** Дозвољаваате умножавање, дистрибуцију и јавно саопштавање дела, и прераде, ако се наведе име аутора на начин одређен од стране аутора или даваоца лиценце и ако се прерада дистрибуира под истом или сличном лиценцом. Ова лиценца не дозвољава комерцијалну употребу дела и прерада.

5. **Ауторство – без прераде.** Дозвољаваате умножавање, дистрибуцију и јавно саопштавање дела, без промена, преобликовања или употребе дела у свом делу, ако се наведе име аутора на начин одређен од стране аутора или даваоца лиценце. Ова лиценца дозвољава комерцијалну употребу дела.

6. **Ауторство – делити под истим условима.** Дозвољаваате умножавање, дистрибуцију и јавно саопштавање дела, и прераде, ако се наведе име аутора на начин одређен од стране аутора или даваоца лиценце и ако се прерада дистрибуира под истом или сличном лиценцом. Ова лиценца дозвољава комерцијалну употребу дела и прерада. Слична је софтверским лиценцама, односно лиценцама отвореног кода.